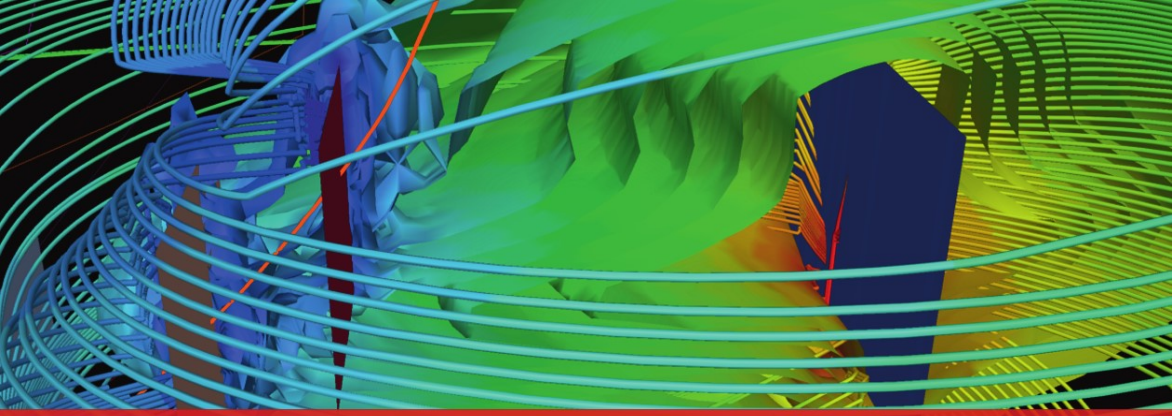

LECTURE NOTES IN COMPUTATIONAL SCIENCE AND ENGINEERING 86

# Olaf Kolditz · Uwe-Jens Görke
# Hua Shao · Wenqing Wang *Editors*

Lecture Notes
in Computational Science
and Engineering

86

Editors:



For further volumes:
http://www.springer.com/series/3527

Olaf Kolditz • Uwe-Jens Görke
Hua Shao • Wenqing Wang
*Editors*

# Thermo-Hydro-Mechanical-Chemical Processes in Fractured Porous Media

## Benchmarks and Examples

Springer

*Editors*
Olaf Kolditz
Uwe-Jens Görke
Wenqing Wang
Helmholtz Centre
for Environmental Research UFZ
Technische Universität Dresden (TUD)
Leipzig
Germany

Hua Shao
Federal Institute
for Geosciences and Natural Resources
Hannover
Germany

ISSN 1439-7358
ISBN 978-3-642-27176-2 e-ISBN 978-3-642-27177-9
DOI 10.1007/978-3-642-27177-9
Springer Heidelberg Dordrecht London New York

Library of Congress Control Number: 2012934370

Mathematics Subject Classification (2010): 35Mxx, 35Qxx, 35G61, 65M60, 68Uxx, 76S05, 76T10, 86-08, 92E20



*Cover illustration*: The cover image represents a snapshot in time during a numerical simulation, illustrating fluid and heat flow pathways in a deep geothermal reservoir exhibiting several large hydraulic fractures.

Printed on acid-free paper

Springer is part of Springer Science+Business Media (www.springer.com)

# Contents

**Book editors:**

Olaf Kolditz, Uwe-Jens Görke, Hua Shao, and Wenqing Wang

**Coordinating Editor:** Alissa Hafele

**Chapter editors:**

1. Hua Shao (Introduction)
2. Olaf Kolditz (Theory)
3. Wenqing Wang, Norihiro Watanabe (Numerical methods)
4. Norbert Böttcher (Heat transport)
5. Feng Sun (Groundwater flow)
6. Thomas Kalbacher (Richards flow)
7. Jens-Olaf Delfs (Overland flow)
8. Ashok Kumar Singh (Gas flow)
9. Uwe-Jens Görke (Deformation processes)
10. Sebastian Bauer (Mass transport)
11. Marc Walther (Density-dependent flow)
12. Chan-Hee Park (Multi-phase flow)
13. Joshua Taron (Consolidation processes)
14. Wenjie Xu (Thermomechanics)
15. Haibing Shao (Reactive Transport)

# Contributors

**Sabine Attinger** Department of Computational Hydrosystems, Helmholtz Centre for Environmental Research (UFZ), Friedrich-Schiller-Universtität Jena, Leipzig, Germany

**Sebastian Bauer** Department of Geohydromodelling, University of Kiel (CAU), Kiel, Germany

**Martin Beinhorn** Center for Applied Geoscience, Universität Tübingen, Tübingen, Germany

**Christof Beyer** Department of Geohydromodelling, University of Kiel (CAU), Kiel, Germany

**Lars Bilke** Department of Environmental Informatics, Helmholtz Centre for Environmental Research (UFZ), Leipzig, Germany

**Guido Blöcher** Department of Chemistry and Material Cycles; Reservoir Technologies, Helmholtz Centre Potsdam (GFZ) German Research Centre for Geosciences, Potsdam, Germany

**Norbert Böttcher** Institute for Groundwater Management, Technische Universität Dresden (TUD), Dresden, Germany

**Mauro Cacace** Department of Chemistry and Material Cycles; Basin Analysis, Helmholtz Centre Potsdam (GFZ) German Research Centre for Geosciences, Potsdam, Germany

**Florian Centler** Department of Environmental Microbiology, Helmholtz Centre for Environmental Research (UFZ), Leipzig, Germany

**Jens-Olaf Delfs** Department of Environmental Informatics, Helmholtz Centre for Environmental Research (UFZ), Leipzig, Germany

**Yanliang Du** IWHR, Beijing, China

**Thomas Fischer** Department of Environmental Informatics, Helmholtz Centre for Environmental Research (UFZ), Leipzig, Germany

**Uwe-Jens Görke** Department of Environmental Informatics, Helmholtz Centre for Environmental Research (UFZ), Leipzig, Germany

**Jürgen Hesser** Underground Space for Storage and Economic Use, Federal Institute for Geosciences and Natural Resources (BGR), Hannover, Germany

**Shuang Jin** Department of Earth Sciences - Geochemistry, Utrecht University (UU), Utrecht, The Netherlands

**Thomas Kalbacher** Department of Environmental Informatics, Helmholtz Centre for Environmental Research (UFZ), Leipzig, Germany

**Olaf Kolditz** Department of Environmental Informatics, Helmholtz Centre for Environmental Research (UFZ), Technische Universität Dresden (TUD), Leipzig, Germany

**Georg Kosakowski** Department of Nuclear Energy and Safety Research, Paul-Scherrer-Institute (PSI), Villigen, Switzerland

**Stefanie Krug** Underground Space for Storage and Economic Use, Federal Institute for Geosciences and Natural Resources (BGR), Hannover, Germany

**Herbert Kunz** Underground Space for Storage and Economic Use, Federal Institute for Geosciences and Natural Resources (BGR), Hannover, Germany

**Rudolf Liedl** Institute for Groundwater Management, Technische Universität Dresden (TUD), Dresden, Germany

**Chris McDermott** School of Geosciences, University of Edinburgh (UE), Edinburgh, UK

**Jude Musuuza** Institute for Earth Sciences: Hydrogeology, Friedrich-Schiller-Universität, Jena, Germany

**Chan-Hee Park** Korea Institute of Geoscience and Mineral Resources (KIGAM), Daejeon, Korea

**Geraldine Pichot** Simulations and Algorithms on Grids for Environment, Inria, Rennes, France

**Florin Adrian Radu** Department of Environmental Informatics, Helmholtz Centre for Environmental Research (UFZ), Leipzig, Germany

**Karsten Rink** Department of Environmental Informatics, Helmholtz Centre for Environmental Research (UFZ), Leipzig, Germany

**Haibing Shao** Department of Environmental Informatics, Helmholtz Centre for Environmental Research (UFZ), Technische Universität Dresden (TUD), Leipzig, Germany

**Hua Shao** Underground Space for Storage and Economic Use, Federal Institute for Geosciences and Natural Resources (BGR), Hannover, Germany

**Ashok Kumar Singh** Department of Environmental Informatics, Helmholtz Centre for Environmental Research (UFZ), Leipzig, Germany

**Feng Sun** Department of Water Monitoring Management, Beijing Hydrological Center, Beijing, China

**Yuanyuan Sun** Department of Environmental Informatics, Helmholtz Centre for Environmental Research (UFZ), Technische Universität Dresden (TUD), Leipzig, Germany

**Joshua Taron** Department of Environmental Informatics, Helmholtz Centre for Environmental Research (UFZ), Leipzig, Germany

**Martin Thullner** Department of Environmental Microbiology, Helmholtz Centre for Environmental Research (UFZ), Leipzig, Germany

**Marc Walther** Institute for Groundwater Management, Technische Universität Dresden (TUD), Dresden, Germany

**Wenqing Wang** Department of Environmental Informatics, Helmholtz Centre for Environmental Research (UFZ), Leipzig, Germany

**Norihiro Watanabe** Department of Environmental Informatics, Helmholtz Centre for Environmental Research (UFZ), Technische Universität Dresden (TUD), Leipzig, Germany

**Yajie Wu** College of Engineering, Ocean University of China, Qingdao, China

**Mingliang Xie** Bereich Endlagersicherheitsforschung Abteilung Prozessanalysen, Gesellschaft für Anlagen- und Reaktorsicherheit (GRS) mbH, Braunschweig, Germany

**Wenjie Xu** Underground Space for Storage and Economic Use, Federal Institute for Geosciences and Natural Resources (BGR), Hannover, Germany

**Björn Zehner** Department of Environmental Informatics, Helmholtz Centre for Environmental Research (UFZ), Leipzig, Germany

# Chapter 1

# Introduction

*by Olaf Kolditz, Uwe-Jens Görke, Hua Shao, and Wenqing Wang*

Coupled process modelling has been considered in the various engineering problems and geo-scientific applications since the computation method was introduced for problems of soil consolidation and dam construction, and oil/gas filed exploration in early 1970. However, substantial progress in experimental and theoretical studies regarding the fully coupled effects of temperature, hydraulics and mechanics, as well as chemistry, in fractured porous media was just made in the last two decades due mainly to demands from the performance and safety assessment of high-level nuclear waste repositories. Numerical methods and computer codes have been developed successfully within the international DECOVALEX project (1992–2011). Meanwhile a wider range of applications associated with THMC coupled problems such as geothermal reservoir engineering, CO2-storage, construction of underground opening etc. can be found in the different international conferences, e.g. GeoProc (www.mech.uwa.edu.au/research/geoproc), ComGeo (www.com-geo.org/).

For a long-term performance and safety assessment of a nuclear waste repository in a deep geological formation, an important issue is to guarantee the isolation of an underground repository. To answer this question, solute transport processes under the coupled conditions involving mechanical stability; thermal loading from the high-level waste, and chemistry in the groundwater should be predicted numerically. Also, for construction planning of such a complex and the implementation of experimental data gained from in situ tests, a multiple process coupled code is required.

Through the rapid development of computer technology, complicated geoscientific and geotechnical problems can be analysed in a coupled manner using

O. Kolditz et al. (eds.), *Thermo-Hydro-Mechanical-Chemical Processes in Fractured Porous Media*, Lecture Notes in Computational Science and Engineering 86,
DOI 10.1007/978-3-642-27177-9_1, © Springer-Verlag Berlin Heidelberg 2012

modern numerical codes. However, the understanding of the complicated coupled processes based on the experimental data available and implementation of the developed algorithm into the numerical codes are major challenge for scientists, which require interdisciplinary cooperation and interactive procedure.

Quality management is nowadays a standard tool for production and development to ensure the high quality of a produced result. A numerical code dealing with the coupled THMC process is a highly complicated software product since the different processes have different characteristic features, e.g. time and spatial scales, nonlinearities, and interaction degree etc. To maintain a high quality of the developed code, benchmark testing is therefore necessary, especially in the case that scientists from different disciplines and organisations are working on the same code. Therefore, code verification and validation of selected test case are documented during the code development, and finally a benchmarking book for the code developer (DBB) is produced and quality ensured.

## 1.1 Scope of This Book

The intention of this book is multifold and can be summarised as the following:

- Outline the theoretical background of THMC processes in porous media for applications in geotechnics and hydrology (Part I),
- Provide collected test cases which can be used for benchmarking the numerical code development for single (Part II) as well as coupled processes (Part III),
- Help to develop and set-up applications (www.opengeosys.net and connected OpenGeoSys development platform available through the internet, see also Appendix for more details)

## 1.2 Application Areas

### 1.2.1 Geotechnics

The coupling phenomena of thermal (T), hydraulic (H), and mechanical (M) processes are important for the analysis of deep geosystems under high temperature, pressure and stress conditions. Application areas of THM coupled models are e.g. geothermal energy utilization, nuclear waste disposal, and carbon dioxide storage in the deep geological formation.

The following slides illustrate that the understanding of THM processes, including chemical reactions (C process) is important to a large variety of geotechnical and geothermal applications. The physical basics are exactly the same for these applications. Different is simply

- the geological environment and different rock types, i.e. crystalline rocks, volcanic rocks, sandstones, clay, bentonite, ...

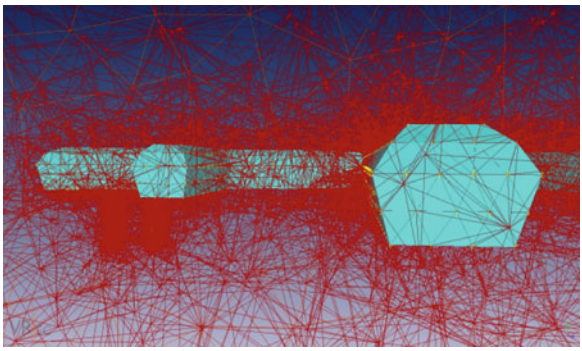

Figure 1.1: Tunnel system (Visualization by B. Zehner)

- the geofluids, i.e. water, brines, vapour, methane, carbon dioxide ...
- the thermodynamic conditions, i.e. temperature, stress, pressure, salinity, ...

There are several concepts concerning host rock for the disposal of hazardous waste in deep geological media, i.e. crystalline, salt, sediment, and volcanic formations. Different concepts use different buffer systems as geotechnical barriers for the waste isolation, i.e. crushed salt, bentonite, and bentonite/sand mixture. THM/C coupled modelling is required for the long-term analysis of possible processes which might result in a release of contaminants from the repository [1]. In that case it is important to know, how long it will take until the contaminants return into the biosphere (Fig. 1.1).

Figure 1.2 illustrates the application area: Carbon Capture Storage (CCS). The idea is to capture the $CO_2$ from the power plants, liquefy it and inject it into the subsurface for long-term storage. Two basic concepts for appropriate geological systems are under proof now: depleted gas reservoirs and deep saline aquifers. After many years of operation many former gas reservoirs are depleted. These reservoirs are in an underpressurized status and can take up large volumes of fluids. Keeping the reservoir underpressurized and the impervious cap rocks are important considerations for storage. THM/C modelling is required in order to calculate the possible fluid storage capacity and to better understand the highly coupled processes in the $CO_2$ injection area as well as their consequences for the storage concept [2].

Figure 1.3 depicts the application area: Geothermal energy, which is one of the alternative future energy resources under consideration. So-called shallow and deep geothermal systems are distinguished. Shallow systems are already commercially used e.g. for heating purposes. Deep geothermal reservoirs can be used for electric power production as high temperatures up to 200 C can be produced. THM/C modeling is required to design these geothermal power plants, e.g. in order to optimize production efficiency and reservoir lifetime. The significant cooling of the reservoir due to fluid reinjection gives rise to

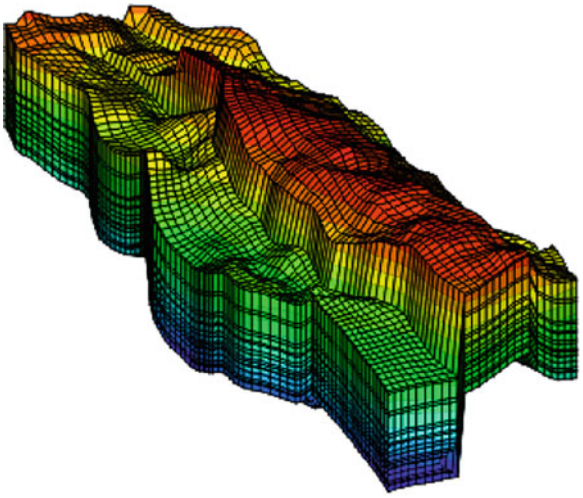

Figure 1.2: Subsurface reservoir for CO2 storage

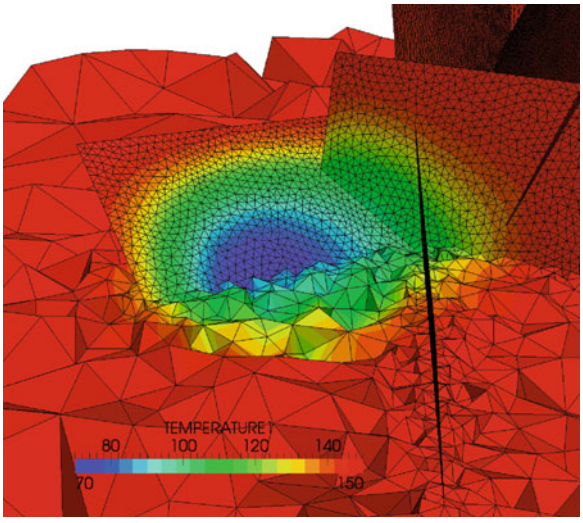


Figure 1.3: Simulated temperature field of water reinjection

thermo-mechanical effects which need to be controlled in order to avoid reservoir damage [3].

The second application area for coupled process simulation is hydrology. River basins or catchments are also subject to THMC coupled processes, but include however a completely different range of thermodynamic conditions than deep geological systems. Hydrological processes are very complex to describe as they vary highly in time and space. The evaluation of groundwater recharge is vital

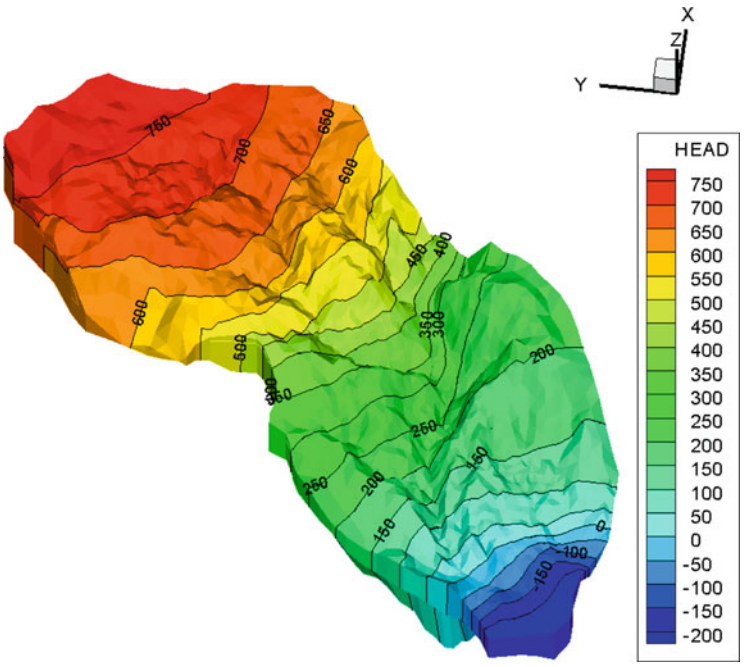


Figure 1.4: Groundwater model for the Wadi Kafrein catchment in Jordan

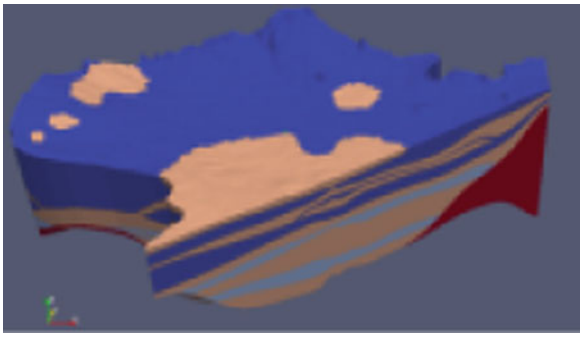

Figure 1.5: Nankou groundwater quality model

to a sustainable water resources management (so called safe yield). To this purpose, i.e. the understanding of small scale phenomena such as root / soil water interaction is of tremendous significance [4]. Typically groundwater models are used for management purposes particularly in semi-arid areas such as the Jordan Valley in the Middle East [5] (Fig. 1.4).

Because water availability is an important issue in semi-arid and arid regions, groundwater quality deterioration is a critical concernin many urban areas of the world. Figure 1.5 shows as an example part of a groundwater quality model

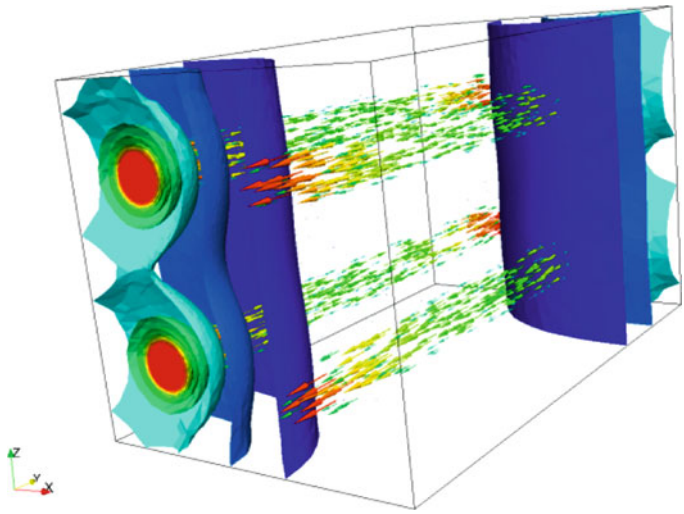

Figure 1.6: Optimizing energy storage concepts by modelling (OGS simulation by Wenqing Wang), [7]

prepared for the Nankou basin in the greater Beijing area. The idea of this modelling project is to identify possible sources of nitrate contamination originating from intense agriculture and fertilizer production [6]. Land use and climate changes will impact the availability and quality of water resources to a large degree in the future. The modelling should help to develop scenarios for improving the groundwater quality in the long term. Areas subject to large groundwater extraction are also subject to severe land subsidence.

A very recent research area for THMC modelling has become energy storage. The economy and feasibility of renewable energy sources will depend a large degree on efficient energy storage systems. Figure 1.6 shows the numerical simulation of flow and heat distribution in a solid thermal energy storage block, which will be used to store solar energy collected during the daytime for use at night (so called solar-thermics). The long term stability and efficiency of those energy storage devices can be optimized using THMC modelling (i.e. solving the inverse geothermal problem). In addition to thermal storage, thermo-chemical concepts are under development, i.e. storing thermal energy by triggering endothermic reactions and gaining thermal energy back on demand with the reverse reaction (exothermic).

# Part I

# Theory and Numerics

# Chapter 2

# Theory

*by Olaf Kolditz, Norbert Böttcher, and Uwe-Jens Görke*

Concerning the theoretical background of flow, transport, deformation, and reaction processes in porous media, there is a considerable amount of monographic literature available [8–15]. The idea of this chapter is to provide a concise, brief-as-possible description (compendium-like) of governing equations for thermo-hydro-mechanical / chemical [THM/C] processes in porous media. We will point to literature references rather than giving detailed derivations of the governing equations. This part is the theoretical basis for all benchmarks and examples found in Part II and III of this book. We will refer to this part in the examples sections where the working equations are briefly repeated.

From the mechanical point of view we consider non-isothermal flow of multiple fluid phases (compressible and incompressible fluids) in a deformable thermo-poro-elastic porous medium based on Biot's consolidation concept. A short introduction to continuum mechanics is given in Sect. 2.1, followed by basic conservations principles (Sect. 2.1.4) as well as an introduction to theory of porous medium (Sect. 2.2). The followings steps are conducted to derive the general field equations:

- Macroscopic balance equations for mass, momentum and energy conservation of porous media (Sect. 2.3),
- Constitutive relationships for non-isothermal multiphase flow and deformation processes in porous media, (Sects. 2.4 and 2.5),

O. Kolditz et al. (eds.), *Thermo-Hydro-Mechanical-Chemical Processes in Fractured Porous Media*, Lecture Notes in Computational Science and Engineering 86,
DOI 10.1007/978-3-642-27177-9_2, © Springer-Verlag Berlin Heidelberg 2012

- Applying the constitutive relationships and introducing physically based simplifications to the balance equations for the derivation of the general field equations. (Parts II and III).

## 2.1 Continuum Mechanics

The basic idea of continuum mechanics is that the evolution of a physical system is completely determined by conservation laws, i.e. basic properties such as mass, momentum, and energy are conserved during the considered process at all times. Any physical system can be completely determined by these conservation properties. In contrast, other quantities such as pressure or entropy do not obey conservation laws. The only additional information concerned are the consistencies of the material (e.g. fluids, solids, porous medium) in the form of constitutive laws.

The concept of conservation means that the variation of a conservation quantity within a given control volume is due to the net effect of internal *sources* and of the amount of the quantity which is crossing the boundary surface of the considered volume—*fluxes*. Sources and fluxes are, in general, dependent on space-time coordinates as well as mechanical and thermodynamic factors. Fluxes result from two contributions: first due to advective transport by fluid motion and second due to diffusion/dispersion processes. Diffusion is always present even when the fluid is at rest. Diffusion is the tendency towards equilibrium or homogeneity of a physical system.

The mechanical description of coupled thermo-hydro-mechanical (THM) processes in porous media is closely associated with the deformation of the solid phase, and the interaction of deformation and flow processes. Each solid material body (including the solid phase of a porous medium) can exhibit different kinds of motion (Sect. 2.1.2):

- rigid body motion (translation or rotation of the body without changing its volume or shape), and
- deformation (local relative change of lengths and/or angles referred to neighboring particles, resulting in variations of the shape and/or volume of the material body under consideration).

Deformation processes of a porous medium interact with hydraulic processes of the coupled physical system particularly in the following ways:

- effects on the stress state within the solid phase due to pore pressure evolution (with possible risk of rock failure), and
- variations of the pore size distribution due to the deformation of the solid skeleton, which affect the hydraulic properties, and thus, have an impact on the flow processes in the porous medium.

The analysis of deformation processes considered as a mechanical response of the material body to the action of applied external forces is one of the objects of mechanics (micromechanics, continuum mechanics). Porous media distinguish themselves by a sophisticated complex microstructure, whose realistic simulation is extremely challenging, and from a practical point of view generally not efficient. Therefore, continuum mechanics (which is based on the assumption that matter is continuously distributed in space) provides the preferred approaches for the mathematical modeling of deformation processes in porous media. Appropriate models are not based on a physical characterization of the real microstructure, but consider their effects on the physical behavior in a phenomenological manner (Sect. 2.2).

General statements of mechanics, which are independent of the specific material under consideration, refer to the kinematics of motion (shortly described in a following section) and the balance relations (Sect. 2.3). By contrast, individual material dependent statements refer to the constitutive relations (Sect. 2.5). Both the balance relations as well as the constitutive relations comprise a mathematically closed system of equations to solve initial-boundary value problems of mechanics.

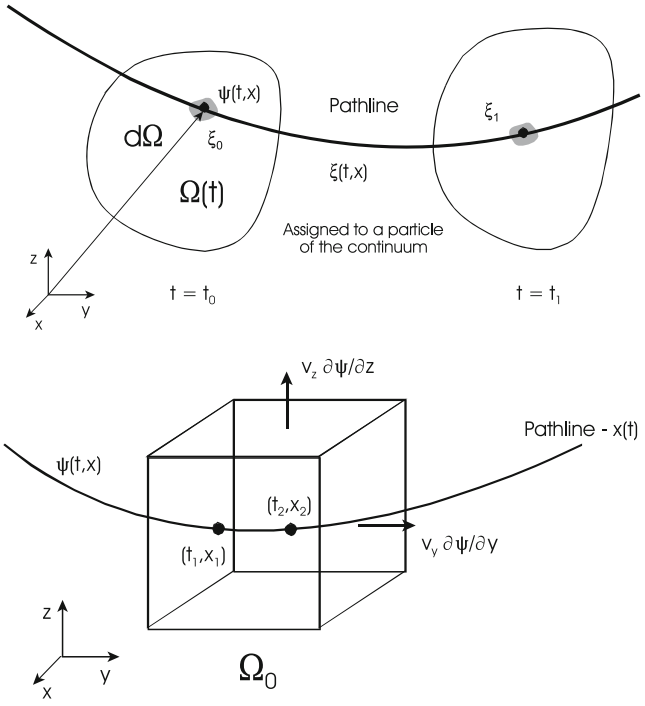


Figure 2.1: Two basic descriptions of motion—Langrangian (*top*) and Eulerian principles (*bottom*), adopted from [16]

### 2.1.1 Lagrangian and Eulerian Principles

In the Lagrangian formulation we follow the quantity along a pathline, i.e. following particles (Fig. 2.1, top). In the Eulerian formulation of motion we consider variations of the quantity with respect to a fixed control volume at fixed places (Fig. 2.1, bottom).

A pathline is a curve along which a fixed particle of a continuum moves during a sequence of time. Pathline is Lagrangian concept of motion. A streamline is a curve along which a sequence of particles moves at a given time. By definition, the tangent to a streamline coincides with the velocity vector at that point. Streamline is Eulerian concept of motion. Note, for unsteady flow the streamline may vary from one instant to the next, whereas for steady flow streamlines remain unchanged with time. For steady motion both pathlines and streamlines coincide. Any particle will remain on a given streamline as time proceeds. Additional terms associated with kinematics of continua are the following (see also Sect. 2.1.2).

### 2.1.2 Kinematics of Continua

Kinematics analyzes the geometry of motion in general and of deformation processes in particular. It is based on the assumption that a material (physical) body $\mathcal{B}$, which represents a set of elements $\mathcal{P}$ called material points (aka: material elements, particles), at each moment of time can be uniquely defined with certain parts (usually different if motion occurs) of space. Assigning the material body specificially to its image in the three-dimensional Euclidean space of physical observations, the location of each material point at each time can be identified with the position vector $\mathbf{x}(t)$ in a physically well-founded manner. Consequently, the position vector can be represented by its Cartesian coordinates $x_1$, $x_2$, $x_3$. In order to characterize the motion of a material body uniquely with respect to a reference state, the domain in space occupied by the material body at an arbitrarily selected time $t_0$ is of emphasized significance. Usually in porous media mechanics, an appropriately chosen initial state of the solid skeleton is chosen as the reference state. The position vectors to define the positions of the material points at $t_0$ are denoted as $\mathbf{X}$.

One of the primary variables within the context of numerical simulation of coupled THM processes is the displacement vector $\mathbf{u}$ of the solid phase. The displacement vector is a commonly used kinematic variable to describe the motion (rigid body motion and/or deformation) of a solid material, and quantifies the change in the position of a given material point (cf. Fig. 2.2).

$$\mathbf{u}(\mathbf{X}, t) = \mathbf{x}(\mathbf{X}, t) - \mathbf{X} \tag{2.1}$$

In other words: the displacement vector connects the current position $\mathbf{x}$ of a material point which under the impact of external forces has been moved, and was located at time $t_0$ at the position $\mathbf{X}$. Because, in general, the displacement

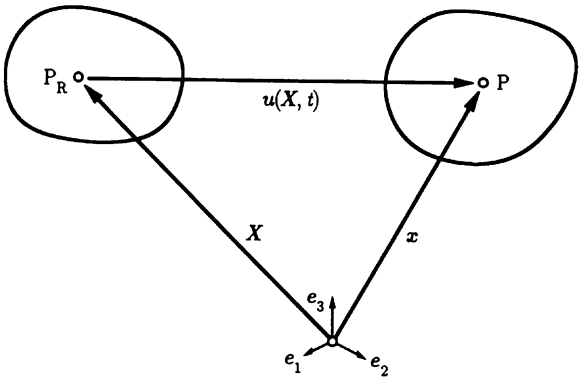


Figure 2.2: Definition of the displacement vector as the difference of the position vectors $\mathbf{x}$ and $\mathbf{X}$ of a material point (particle) of the body under consideration at various time $t$ (current time) and $t_0$ [17]

vector will vary locally and temporally, $\mathbf{u}(\mathbf{X}, t) = \mathbf{u}(\mathbf{X}(\mathbf{x}, t), t) = \bar{\mathbf{u}}(\mathbf{x}, t) \equiv \mathbf{u}$ represents a vector field as function of space and time.

For the possible comparison of the response of material bodies (which are composed of different materials and/or have a different geometry) to the impact of external forces, it is not reasonable to deal with the physically obvious variables displacement and force, but rather to introduce relative physical variables like strain and stress measures. Strain measures represent second-order kinematic tensor variables characterizing the local deformation processes, which deviate from the rigid body motion of a material body.

Based on the definition of the displacement gradient

$$\nabla \bar{\mathbf{u}}(\mathbf{x}, t) = \frac{\partial u_i}{\partial x_j} \boldsymbol{e}_i \otimes \boldsymbol{e}_j \tag{2.2}$$

with the orthonormal system of Cartesian base vectors $\boldsymbol{e}_i$ $(i = 1, 2, 3)$, the strain tensor $\boldsymbol{\varepsilon}(\mathbf{x}, t)$ in the case of small (infinitesimal) deformations is established as the symmetric part of the displacement gradient.

$$\boldsymbol{\varepsilon}(\mathbf{x}, t) = \frac{1}{2} \left( \nabla \bar{\mathbf{u}}(\mathbf{x}, t) + (\nabla \bar{\mathbf{u}}(\mathbf{x}, t))^{\mathrm{T}} \right) \tag{2.3}$$

The matrix of the coefficients of the strain tensor consists of so-called normal components

$$\varepsilon_{ii} = \frac{\partial u_i}{\partial x_i} \tag{2.4}$$

and shear components.

$$\varepsilon_{ij} = \frac{1}{2} \left( \frac{\partial u_i}{\partial x_j} + \frac{\partial u_j}{\partial x_i} \right) \qquad (i \neq j) \tag{2.5}$$

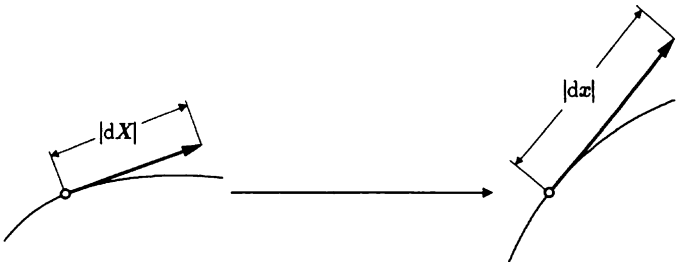


Figure 2.3: Extension (normal strain) of a material line element $d\mathbf{X} = |d\mathbf{X}|\boldsymbol{e}$ [17]

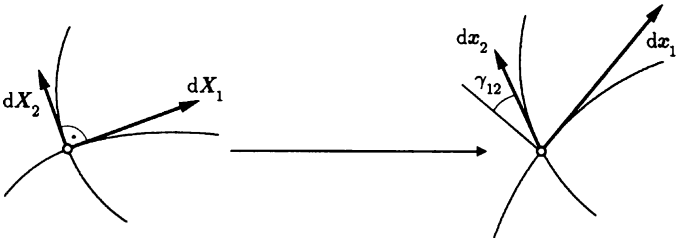


Figure 2.4: Shear (shear strain) of two material line elements $d\mathbf{X}_1 = |d\mathbf{X}_1|\boldsymbol{e}_1$ and $d\mathbf{X}_2 = |d\mathbf{X}_2|\boldsymbol{e}_2$, which are orthogonal in the undeformed state [17]

For special cases it can be easily shown that normal strain is geometrically interpreted as elongation of material line elements (Fig. 2.3), and shear strain represents the change of the angle between two material line elements, which initially were perpendicular to each other (Fig. 2.4).

For the analysis of certain deformation processes it is reasonable to consider local volume changes and shape changes separately. Within this context, the strain tensor can be additively split into two parts: a volumetric $\boldsymbol{\varepsilon}_v$ and a so-called deviatoric (volume-preserving) $\boldsymbol{\varepsilon}_d$ one.

$$\boldsymbol{\varepsilon} = \boldsymbol{\varepsilon}_d + \boldsymbol{\varepsilon}_v \tag{2.6}$$

The individual partial strain tensors are defined as follows:

$$\boldsymbol{\varepsilon}_v = \frac{1}{3}\mathrm{tr}(\boldsymbol{\varepsilon})\,\mathbf{I} = \frac{1}{3}(\varepsilon_{11} + \varepsilon_{22} + \varepsilon_{33})\,\mathbf{I} \tag{2.7}$$

$$\boldsymbol{\varepsilon}_d = \boldsymbol{\varepsilon} - \boldsymbol{\varepsilon}_v \tag{2.8}$$

Based on the definition

$$\mathbf{v}^s(\mathbf{x}, t) = \dot{\mathbf{u}}(\mathbf{x}, t) \tag{2.9}$$

of the velocity of material points of the solid skeleton, the strain rate tensor

$$\dot{\boldsymbol{\varepsilon}}(\mathbf{x},t) \;=\; \mathbf{d}(\mathbf{x},t) \;=\; \frac{1}{2}\left(\nabla\mathbf{v}^s(\mathbf{x},t) \;+\; (\nabla\mathbf{v}^s(\mathbf{x},t))^{\mathrm{T}}\right) \tag{2.10}$$

with its coefficients

$$d_{ij} \;=\; \frac{1}{2}\left(\frac{\partial v_i^s}{\partial x_j} \;+\; \frac{\partial v_j^s}{\partial x_i}\right) \tag{2.11}$$

can be defined, which is necessary for the investigation of deformation processes in the case of rate-dependent material behavior.

In the case of small strains, which was assumed here, the relation between the strain tensor and the displacement vector is a linear one (see (2.3)). Considering large strains, the definition of appropriate strain measures requires more sophisticated reflections about the kinematics of motion. As a result, different strain tensors can be obtained representing non-linear functions of the displacement vector.

### 2.1.3 Stress Tensor

The momentum, as well as the moment of momentum, of a material body are affected by external forces acting on it, which represent the mechanical effect of the surroundings (cf. Fig. 2.5). Summarizing all local forces, the resultant force $\mathcal{F}$ can be defined.

$$\mathcal{F} \;=\; \int_{\partial\mathcal{B}} \mathbf{t}\,da \;+\; \int_{\mathcal{B}} \mathbf{f}\,dm \;=\; \int_{\Gamma} \mathbf{t}(\mathbf{x},t,\mathbf{n})\,d\Gamma \;+\; \int_{\Omega} \mathbf{f}_v(\mathbf{x},t)\,\varrho(\mathbf{x},t)\,d\Omega \tag{2.12}$$

Generally, the material body under consideration bears forces distributed over its surface with the surface force density $\mathbf{t}$ (traction, Cauchy stress vector), and forces distributed over the volume of the material body with the volume force

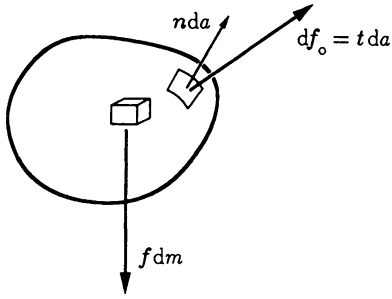


Figure 2.5: External volume and surface forces acting on infinitesimal geometrical elements of a material body [17]

density (mass distributed specific volume force) $\mathbf{f}_v$. As mentioned above, only gravity $\varrho\mathbf{g}$ should be considered as specific volume force.

The traction vector $\mathbf{t}(\mathbf{x}, t, \mathbf{n})$ is considered to be a function of the location of its action on the surface, a function of time and of the normal vector, which characterizes the orientation of the surface element $d\boldsymbol{\Gamma}$. Assuming a linear relation between the traction and the normal vector (Cauchy's theorem), the stress measure $\boldsymbol{\sigma}(\mathbf{x}, t)$ (Cauchy stress tensor) is defined as a link between surface traction and surface orientation.

$$\mathbf{t}(\mathbf{x}, t, \mathbf{n}) = \boldsymbol{\sigma}(\mathbf{x}, t)\,\mathbf{n} \qquad \Rightarrow \qquad \boldsymbol{\sigma} = \sigma_{ij}\,\boldsymbol{e}_i \otimes \boldsymbol{e}_j \tag{2.13}$$

Based on Cauchy's theorem, the differential surface force $d\mathbf{f}_0$ acting on a surface element can be obtained.

$$d\mathbf{f}_0 = \mathbf{t}\,d\Gamma = (\boldsymbol{\sigma}\,\mathbf{n})\,d\Gamma = \boldsymbol{\sigma}\,(\mathbf{n}\,d\Gamma) = \boldsymbol{\sigma}\,d\boldsymbol{\Gamma} \tag{2.14}$$

For certain cases it is reasonable to use the so-called Kirchhoff stress tensor $\boldsymbol{\tau}$, a weighted Cauchy stress measure, instead of the Cauchy stress tensor itself.

$$\boldsymbol{\tau} = \frac{\varrho_0}{\varrho}\,\boldsymbol{\sigma} \tag{2.15}$$

The second-order stress tensor characterizes the local internal load state referring to a material point of the body under consideration. Generally, it can be defined by three stress vectors acting on three faces of an infinitesimal tetrahedron, which are perpendicular to each other when analyzing the equilibrium of forces for this domain. The coefficients of the resulting stress tensor are denoted by two indices—the first indicates the direction of the normal vector of the face under consideration, the second one the direction of the stress coefficient (see Fig. 2.6 for the three-dimensional case).

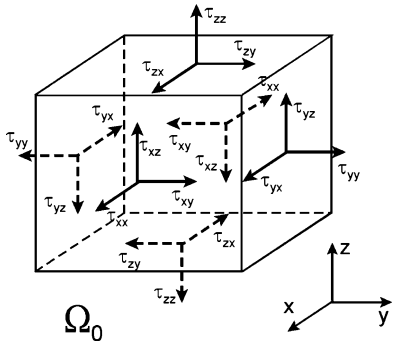


Figure 2.6: Coefficients of the stress tensor acting on a small hexahedral element [16]

The sign convention, usually applied in continuum mechanics, implies positive stress coefficients coinciding with the directions of the axes of coordinates at faces and with normal vectors also coinciding with the directions of the axes of coordinates. Consequently, tensile stress coefficients are positive, compressive stresses negative. Positive stress coefficients on opposite faces are oppositely directed (but of equal absolute value). The matrix of the coefficients of the (Kirchhoff) stress tensor is composed as follows:

$$\tau_{ij} = \begin{pmatrix} \tau_{xx} & \tau_{xy} & \tau_{xz} \\ \tau_{yx} & \tau_{yy} & \tau_{yz} \\ \tau_{zx} & \tau_{zy} & \tau_{zz} \end{pmatrix} \tag{2.16}$$

Analogous to the strain tensor, the coefficients $\tau_{xx}$, $\tau_{yy}$, $\tau_{zz}$ are called normal stresses, the coefficients $\tau_{ij} \quad (i \neq j)$ shear stresses with $\tau_{ij} = \tau_{ji}$ (symmetry of the stress tensor, which results from the balance of moment of momentum).

In the special uniaxial stress case only at one face of a volume element a normal stress occurs, whereas all the other faces are stress-free. Consequently, the stress coefficient is calculated as the force acting on the face under consideration divided by its area.

### 2.1.4 Conservation Principles

Based on the kinematical foundation (Sect. 2.1.2) we formulate the general conservation principle of continuum mechanics for both Eulerian and Lagrangian points of view (Sect. 2.1.1). The amount of a (conservation) quantity in a defined volume $\Omega$ is given by

$$\Psi = \int_{\Omega} \psi d\Omega(t) \tag{2.17}$$

where $\Psi$ is an extensive conservation quantity (i.e. mass, momentum, energy) and $\psi$ is the corresponding intensive conservation quantity such as mass density $\rho$, momentum density $\rho\mathbf{v}$ or energy density $e$ (see Table 2.1).

The balance equations for mass, momentum and energy conservation can be derived based on two fundamental principles, i.e. Eulerian and Lagrangian frameworks (e.g. [16]) Both conservation principles are related by two different forms of derivatives

$$\frac{d\psi}{dt} = \frac{\partial \psi}{\partial t} + \mathbf{v} \cdot \nabla \psi \tag{2.18}$$

Table 2.1: Conservation quantities

| Extensive quantity | Symbol | Intensive quantity | Symbol |
|---|---|---|---|
| Mass | $M$,$M_k$ | Mass density | $\rho$,$\rho_k$ |
| Linear momentum | $\mathbf{m}$ | Linear momentum density | $\rho\mathbf{v}$ |
| Energy | $E$ | Energy density | $e = \rho i + \frac{1}{2}\rho v^2$ |

the total (or material) $d$ and partial derivatives $\partial$, respectively. The general integral balance equation is given by

$$\frac{d}{dt}\int_{\Omega} \psi \, d\Omega = \int_{\Omega} \left( \frac{\partial \psi}{\partial t} + \nabla \cdot \mathbf{\Phi} \right) d\Omega = \int_{\Omega} q^{\psi} d\Omega \tag{2.19}$$

where $\psi$ is a general conservation quantity, $\mathbf{\Phi}$ is the total flux of $\psi$, and $Q$ is a source/sink term for $\psi$. The corresponding extensive and intensive conservation quantities are summarized in Table 2.1.

The total flux $\mathbf{\Phi}^{\psi}$ of a quantity $\psi$ is defined as

$$\mathbf{\Phi}^{\psi} = \mathbf{v}^{E}\psi \tag{2.20}$$

where $\mathbf{v}^{E}$ is a mean particle velocity. Physically $\mathbf{\Phi}^{\psi}$ represents the quantity of $\psi$ passing through a unit area of the continuum, collinear with $\mathbf{v}^{E}$, per unit time with respect to a fixed coordinate system, i.e. Eulerian point of view.

For the case of a multi-component continuum let $\mathbf{v}$ denote the mass-weighted velocity describing a more ordered motion of the particles of a fluid element. The total flux can be written as

$$\mathbf{\Phi}^{\psi} = \mathbf{v}^{E}\psi = \underbrace{\mathbf{v}\psi}_{\mathbf{\Phi}^{\psi}_{A}} + \underbrace{(\mathbf{v}^{E} - \mathbf{v})\psi}_{\mathbf{\Phi}^{\psi}_{D}} \tag{2.21}$$

and, therefore, decomposed into two parts: an advective flux $\mathbf{\Phi}^{\psi}_{A}$ and a diffusive flux $\mathbf{\Phi}^{\psi}_{D}$ relative to the mass-weighted velocity:

- Advective flux of quantity $\psi$

$$\mathbf{\Phi}^{\psi}_{A} = \mathbf{v}\psi \tag{2.22}$$

- Diffusive flux of quantity $\psi$ (Fick's law)

$$\mathbf{\Phi}^{\psi}_{D} = -\alpha \nabla \psi \tag{2.23}$$

where $\alpha$ is a diffusivity coefficient. The negative sign indicates that diffusive flux is positive in the direction of a negative gradient.

If the conservation quantity is a vector (e.g. linear momentum) then the flux becomes a tensor and the source term a vector (e.g. body forces):

- Advective flux of vector quantity $\psi$

$$\mathbf{\Phi}_A^{\psi} = \mathbf{v} : \psi = \begin{bmatrix} v_x & v_y & v_z \end{bmatrix} \begin{bmatrix} \psi_x \\ \psi_y \\ \psi_z \end{bmatrix} = \begin{vmatrix} v_x\psi_x & v_x\psi_y & v_x\psi_z \\ v_y\psi_x & v_y\psi_y & v_y\psi_z \\ v_z\psi_x & v_z\psi_y & v_z\psi_z \end{vmatrix} \tag{2.24}$$

- Diffusive flux of vector quantity $\psi$

$$\mathbf{\Phi}_D^{\psi} = -\rho\nabla : \psi = -\alpha \begin{vmatrix} \frac{\partial\psi_x}{\partial x} & \frac{\partial\psi_y}{\partial y} & \frac{\partial\psi_z}{\partial z} \\ \frac{\partial\psi_x}{\partial x} & \frac{\partial\psi_y}{\partial y} & \frac{\partial\psi_z}{\partial z} \\ \frac{\partial\psi_x}{\partial x} & \frac{\partial\psi_y}{\partial y} & \frac{\partial\psi_z}{\partial z} \end{vmatrix} \tag{2.25}$$

When substituting the flux definition into the general balance equation (2.19), we yield the so-called transport equation

$$\frac{d}{dt}\int_{\Omega} \psi \, d\Omega = \underbrace{\int_{\Omega} \frac{\partial\psi}{\partial t} \, d\Omega}_{1} + \underbrace{\int_{\Omega} \nabla\cdot(\mathbf{v}\psi) \, d\Omega}_{2} - \underbrace{\int_{\Omega} \nabla\cdot(\alpha\nabla\psi) \, d\Omega}_{3} = \underbrace{\int_{\Omega} q^{\psi}}_{4} \tag{2.26}$$

with the following terms:

1. Rate of increase of $\psi$ within a fluid element
2. Net rate of $\psi$ due to flux out of the fluid element
3. Rate of increase / decrease of $\psi$ due to diffusion
4. Rate of increase / decrease of $\psi$ due to sources

## 2.2 Porous Medium

Soil and rock can both be considered a multiphase medium consisting of a solid phase (solid matrix) and of one or more fluid phases (gas and liquids), which occupy the void space (Fig. 2.8). Fluids are immiscible, if a sharp interface is maintained between them. In general, a phase is defined as part of a continuum, which is characterized by distinct material properties and by a well-defined set of thermodynamic state variables. State variables describe the physical

behaviour at all points of the phase. They must vary continuously within the considered phase of a continuum. Phases are separated from each other by surfaces referred to as interphase boundaries. Transport of components may occur within a phase and/or across interphase boundaries. Those interphasic exchange processes between adjacent phases can result from diffusive and/or advective mechanisms.

In fact, it is impossible to describe the complex geometry of the solid matrix and the topology of the void space at the microscopic level, i.e. the topology of the pore space will never be known in detail. As a consequence, boundary conditions for a mathematical model cannot be stated at this scale, since they are not known at the microscopic level. Moreover, it will be extremely difficult to measure values of state variables at each point within a phase in order to observe processes, to calibrate and to verify any model. Finally, the complete formulation and resolution of balance equations at the microscopic level is impossible and may not be reasonable. Therefore, it is necessary to transform the problem from a microscopic scale to a macroscopic level. Starting from the microscopic balance equations for extensive quantities (masses, momentum, energy), this procedure is the subject of the theory of the porous medium [8–15] The entire problem is rewritten in terms of averages of microscopic quantities, which have measurable values. The resulting macroscopic model is referred to as the continuum approach. This conceptual model implies that a real system is replaced by a number of overlapping continua representing the corresponding phases. It is assumed that each phase, occupying a certain part of the porous domain, is regarded as a continuum. These individual phases interact with each other at any place within the entire domain, because they are present at each point within the porous medium, i.e. all phases are completely mixed.

$$\Omega_0 = \sum_\alpha \Omega^\alpha \tag{2.27}$$

In addition to the porous medium approach, there exist different types of structural models for fractured rocks, which characterize the degree of inhomogeneity: the fractured medium and the fractured porous medium. The term fractured medium means that only the fractures are important for the considered process, so blocks surrounded by the fractures may be neglected in the model. The term fractured porous medium means that both the fracture system and the porous matrix are significant for the considered process. The domain of a fractured porous medium consists of two subdomains, representing heterogeneities at different scales, i.e. the diameter of pores in the matrix and the characteristic length of the fractures.

Appropriate averaging rules must be defined in order to realize the above described transformation from a microscopic to a macroscopic level. For this purpose, a well-defined sample size of an averaging volume must be found, which is referred to as the representative elementary volume (abbreviated REV). On the one hand, this averaging unit has to be sufficiently large, so that the influence of microscopic inhomogeneity on the values of averaged (macroscopic)

quantities will vanish, i.e. they become independent of size, shape, and orientation of the REV. On the other hand, the REV must be small enough to reflect the macroscopic heterogeneity. In particular, the REV must be much smaller than the domain of interest, which may vary in size for a flow or a transport problem, respectively. From the mathematical point of view, the macroscopic (averaged) quantities must be continuous and differentiable functions (in space and in time), so that solutions of the governing differential balance equations can be determined. Finally, the continuum approach cannot be employed unless a common range of a REV can be selected for all material properties (e.g. porosity, permeability, dispersivity) as well as for all relevant state variables. This requirement is important with respect to the different conceptual models for fractured rock, which are introduced in the following.

### 2.2.1 Macroscopic Equations

As stated above, it is impossible to describe the complex geometry of the solid matrix and the topology of the void space at the microscopic level, i.e. the topology of the pore space will never be known in detail. Therefore, a statistical approach is used for the derivation of balance equations at a macroscopic level. The physical property of a porous medium is decomposed in phase-related mean values $\overline{\psi^\alpha}$ and local fluctuations $\psi'^\alpha$.

$$\psi^\alpha = \overline{\psi^\alpha} + \psi'^\alpha \tag{2.28}$$

An appropriate averaging volume is called the Representative Elementary Volume (REV) (Fig. 2.7).

Several averaging procedures can be defined [11]. As an example we consider volumetric averaging which is also denoted as the concept of volume fractions. The volumetric averaging operator is given by

$$\overline{\psi^\alpha}^\alpha = \frac{1}{\epsilon^\alpha \Omega_0} \int_{\Omega_0} f^\alpha \psi^\alpha d\Omega \tag{2.29}$$

where $\alpha$ is the phase indicator, $\epsilon^\alpha = \Omega^\alpha / \Omega_0$ is the volumetric fraction of the $\alpha$ phase, $\Omega_0$ is the averaging volume (corresponding to the representative elementary volume), and $f^\alpha = 1/0$ (inside or outside $\alpha$ phase) is the phase distribution function.

Due to the above definition the following averaging rules can be derived.

- Sum

$$\overline{\psi_1^\alpha + \psi_2^\alpha} = \overline{\psi_1^\alpha} + \overline{\psi_2^\alpha} \tag{2.30}$$

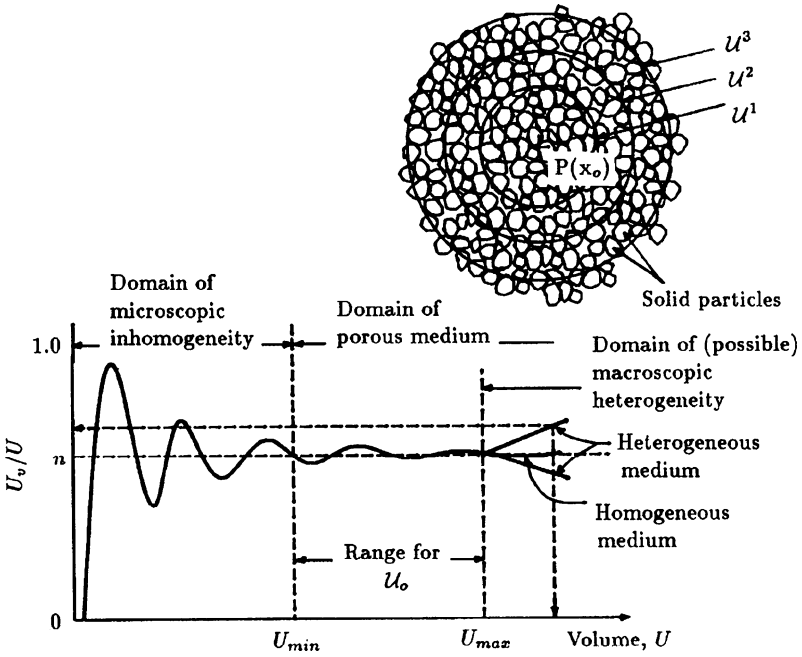


Figure 2.7: Definition of the representative elementary volume (REV) [11]

- Product

$$\overline{\psi_1^\alpha \psi_2^\alpha} = \overline{\psi_1^\alpha}\,\overline{\psi_2^\alpha} + \overline{\psi_1'^\alpha \psi_2'^\alpha} \tag{2.31}$$

- Time derivative

$$\epsilon^\alpha \overline{\frac{\partial \psi^\alpha}{\partial t}} = \frac{\partial \epsilon^\alpha \overline{\psi^\alpha}}{\partial t} - \frac{1}{\Omega_0} \int\limits_{S^{\alpha\beta}} \psi^\alpha \mathbf{w} \cdot d\mathbf{S} \tag{2.32}$$

- Spatial derivative

$$\epsilon^\alpha \overline{\nabla \psi^\alpha} = \nabla(\epsilon^\alpha \overline{\psi^\alpha}) + \frac{1}{\Omega_0} \int\limits_{S^{\alpha\beta}} \psi^\alpha \cdot d\mathbf{S} \tag{2.33}$$

where $\mathbf{w}$ is the velocity of the $\alpha\beta$-phase interface.

To derive a phase related macroscopic balance equation, we have to average the balance equation in differential form for a certain phase (2.19). By use of the above averaging operators and rules the following general macroscopic balance equation can be obtained.

$$\frac{\partial \epsilon^\alpha \overline{\psi^\alpha}}{\partial t} = -\nabla \cdot (\epsilon^\alpha \bar{\psi}^\alpha \overline{\mathbf{v}^\alpha} + \epsilon^\alpha \overline{\psi'^\alpha \mathbf{v}'^\alpha} + \epsilon^\alpha \overline{\mathbf{\Phi}_{\mathrm{Diff}}^{\psi^\alpha}})$$
$$-\frac{1}{\Omega_0} \int_{S^{\alpha\beta}} \mathbf{\Phi}_{\mathrm{Diff}}^{\psi^\alpha} \cdot d\mathbf{S} - \frac{1}{\Omega_0} \int_{S^{\alpha\beta}} \psi^\alpha (\mathbf{v} - \mathbf{w}) \cdot d\mathbf{S} + q^{\psi^\alpha} \tag{2.34}$$

with the dispersive flux

$$\mathbf{\Phi}_{\mathrm{Disp}}^{\psi^\alpha} = \epsilon^\alpha \overline{\psi'^\alpha \mathbf{v}'^\alpha} \tag{2.35}$$

### 2.2.2 Theory of Mixtures

The Theory of Mixtures as one of the basic approaches to model the complex behavior of porous media has been developed over decades (concerning basic assumptions see e.g. [18, 19]). As the Theory of Mixtures does not incorporate any information about the microscopic structure of the material,[1] it has been combined with the Concept of Volume Fractions by e.g. [14, 20–22]. Within the context of this enhanced Theory of Mixtures (also known as Theory of Porous Media), all kinematical and physical quantities can be considered at the macroscale as local statistical averages of their values at the underlying microscale. Concerning a detailed overview of the history of the modeling of the behavior of multiphase multicomponent porous media, the reader is referred to e.g. [15]. Comprehensive studies about the theoretical foundation and numerical algorithms for the simulation of coupled problems of multiphase continua are given in e.g. [14, 15, 23] and the quotations therein.

The individual constituents $\varphi^\alpha$ of a porous material represent the phases of the overall aggregate or components within a phase. Below, $\alpha = s$ marks one immiscible solid phase (no sorption processes are considered), and $\alpha = \gamma$ denotes several immiscible pore fluid phases. A porous medium, however, consists of multiple phases (fluids such as water, air and non-aqueous phase liquids (NAPLs) as well as solids). Moreover, these phases can contain several chemical components which can be dissolved in liquids or adsorbed to the solid phase (Fig. 2.8).

Within the framework of the Concept of Volume Fractions, scalar variables like volume fractions and saturations are defined to describe the microstructure of a porous medium in a macroscopic manner neglecting the real topology and distribution of the pores. These variables serve as measures of local fractions of the individual constituents. The volume fractions $n^\alpha$ represent the ratio of the partial volume $dv^\alpha$ of a given constituent $\varphi^\alpha$ of a multiphase body with respect to the overall volume $dv$ of a representative elementary volume (REV) of the control domain $\Omega$ under consideration. Consequently, based on the definitions

[1] Within the context of the Theory of Mixtures the ideal mixture of all constituents of a multiphase medium is postulated. Consequently, the realistic modeling of the mutual interactions of the constituents is difficult.

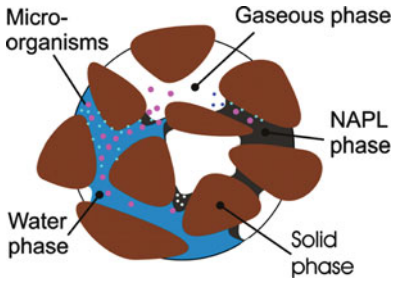


Figure 2.8: Conceptual approach of a porous medium model, adopted from [16]

of the overall volume of the control domain

$$V = \int_{\Omega} dv \tag{2.36}$$

and the corresponding partial volumes of the individual constituents

$$V^{\alpha} = \int_{\Omega} dv^{\alpha} \qquad \text{with} \qquad V = \sum_{\alpha} V^{\alpha} \tag{2.37}$$

the volume fractions

$$n^{\alpha} = \frac{dv^{\alpha}}{dv} \tag{2.38}$$

provide some information about the local volume distribution of the individual constituents.

$$V^{\alpha} = \int_{\Omega} dv^{\alpha} = \int_{\Omega} n^{\alpha}\, dv \tag{2.39}$$

One of the most characteristic media properties of a porous material is the porosity, the local amount of fluid volume fractions.

$$n = \sum_{\gamma} n^{\gamma} = 1 - n^{s} \tag{2.40}$$

Since, in general, the overall medium is completely filled with matter, from (2.37) follows the saturation condition regarding the overall aggregate.

$$\sum_{\alpha} n^{\alpha} = 1 \tag{2.41}$$

If multiphase flow occurs, it is more convenient for various applications to use the (partial) fluid saturations $S^{\gamma}$ instead of the volume fractions. These local functions are given by

$$S^{\gamma} = \frac{dv^{\gamma}}{dv - dv^{s}} = \frac{n^{\gamma}}{n} \tag{2.42}$$

obviously fulfilling the saturation condition regarding the pore content.

$$\sum_{\gamma} S^{\gamma} = 1 \tag{2.43}$$

Usually, constraint conditions addressing real physical effects are formulated to simplify complex mathematical and numerical models. Within the context of porous media, it is reasonable in most applications to assume the (material) incompressibility of constituents as a substantial constraint condition. The issue of (in)compressibility of a material is closely connected to the possible temporal evolution of its mass density.

Within the framework of the Concept of Volume Fractions, two different formulations of mass density related to the constituents of a porous medium are introduced. The so-called material (effective, realistic) density $\rho^{\alpha R}$ is defined as the ratio of the mass fraction $dm^{\alpha}$ of the given individual constituent $\varphi^{\alpha}$ with respect to its partial volume fraction.

$$\rho^{\alpha R} = \frac{dm^{\alpha}}{dv^{\alpha}} \tag{2.44}$$

In contrast, the so-called partial (global, bulk) density is given by the ratio of the mass fraction of the constituent under consideration with respect to the volume fraction of the overall aggregate.

$$\rho^{\alpha} = \frac{dm^{\alpha}}{dv} \tag{2.45}$$

Based on the definition of the volume fractions (2.38), the material and the partial densities are correlated to each other.

$$\rho^{\alpha} = n^{\alpha}\, \rho^{\alpha R} \tag{2.46}$$

If the volume fractions change with time under external loading, from (2.46) follows that for an intrinsically incompressible individual constituent (constant material mass density) compressibility referred to the overall aggregate is observed.

$$\rho^{\alpha R} = \text{const} \quad \Rightarrow \quad \rho^{\alpha} \neq \text{const} \quad \text{as} \quad n^{\alpha} \neq \text{const} \tag{2.47}$$

Obviously, the mass density of the porous medium (homogenized overall aggregate) is defined as the sum of the partial densities of its constituents.

$$\rho = \sum_{\alpha} \rho^{\alpha} \tag{2.48}$$

The conceptual idea behind the formulations and relations presented above consists in the assumption that the mass fractions of all constituents of the multiphase medium are simultaneously present and statistically uniformly distributed over the entire control domain. Within this context, the material body under

consideration is theoretically substituted by an aggregate completely and continuously filled by superimposed (overlapping) homogenized partial continua. In other words, all constituents of a porous medium are characterized as smeared substitute continua with reduced mass densities. Consequently, the motion and physics of the individual constituents, as well as the overall aggregate, can be specified by well-accepted phenomenological methods of continuum mechanics.

When describing the transport and deformation of the constituents of porous media within the framework of continuum mechanics, it is assumed that the geometry of the control domain under consideration is characterized at each time by the solid skeleton, whereas the fluid pore content is able to flow across the boundary of the surface. This assumption serves as the conceptual nucleus for the simulation of complex, coupled physical processes in multiphase porous media, particularly if a deformable solid skeleton is observed. Within this context, it proves to be reasonable not to model the absolute motion state of the pore content, but its motion relative to the motion of the solid phase, considering the porous medium as a local thermodynamic open system with the solid skeleton as volume under observation.

The macroscopic characterization of the physical processes considering the real microstructural situation in a statistically averaged manner is completely adequate for the most hydrological, geotechnological and biomechanical problems under consideration (cf. [24] and others).

## 2.3 Balance Equations

We derive the balance equations for phase and component masses as well as for momentum and energy of a porous medium.

### 2.3.1 Phase Mass Balance

We consider the mass balance of individual phases of a porous medium. Neglecting mass exchange between the phases (no dissolution and sorption processes), the local mass balance for the individual constituent $\varphi^\alpha$ of the porous medium is given by

$$\frac{d_\alpha \rho^\alpha}{dt} + \rho^\alpha \nabla \cdot \boldsymbol{v}^\alpha = \frac{\partial \rho^\alpha}{dt} + \nabla \cdot (\rho^\alpha \boldsymbol{v}^\alpha) = 0 \tag{2.49}$$

with the velocity $\boldsymbol{v}^\alpha$ of the constituent under consideration, and the usual divergence operator $\nabla \cdot ()$. From the velocity-displacement relation for the solid skeleton follows

$$\boldsymbol{v}^s = \dot{\boldsymbol{u}}^s \tag{2.50}$$

with the solid displacement vector $\boldsymbol{u}^s$. The derivative

$$\frac{d_\alpha A}{dt} = \frac{\partial A}{dt} + \boldsymbol{v}^\alpha \cdot \nabla A \tag{2.51}$$

with the usual gradient operator $\nabla()$ denotes the material time derivative of an arbitrary variable $A$ with respect to the motion of a material point of the constituent $\varphi^\alpha$ (cf. (2.18)). It consists of a local (diffusive) part and a convective part associated with the velocity of the constituent.

As mentioned above, the transport processes of the fluid constituents of a porous medium are considered as their relative motion with respect to the motion of the deformable solid skeleton. Consequently, the relations between the material time derivatives (here, of an arbitrary variable $A$) with respect to the solid skeleton, and with respect to the individual fluid constituent $\varphi^\gamma$ is of crucial interest in terms of a unified numerical characterization of the different processes.

$$\frac{d_\gamma A}{dt} = \frac{d_s A}{dt} + \boldsymbol{v}^{\gamma s} \cdot \nabla A \tag{2.52}$$

Here,

$$\boldsymbol{v}^{\gamma s} = \boldsymbol{v}^\gamma - \dot{\boldsymbol{u}}^s \tag{2.53}$$

is the so-called seepage velocity describing the fluid motions with respect to the deforming skeleton material.

According to the generalized formulation (2.49), considering equations (2.40) and (2.46), the local solid phase mass balance is given by

$$\frac{d_s\left[(1-n)\rho^{sR}\right]}{dt} + (1-n)\,\rho^{sR}\,\nabla\cdot\dot{\boldsymbol{u}}^s = 0 \tag{2.54}$$

Assuming material incompressibility of the solid phase, i.e. $d_s\rho^{sR}/dt = 0$ we derive the following expression for porosity changes.

$$\frac{d_s n}{dt} = (1-n)\,\nabla\cdot\dot{\boldsymbol{u}}^s = 0 \tag{2.55}$$

Following the same procedure, additionally considering (2.42) and (2.52), the mass balance relations for the fluid constituents $\varphi^\gamma$ can be defined with respect to the solid phase motion.

$$\frac{d_s\left(nS^\gamma\rho^{\gamma R}\right)}{dt} + \nabla\cdot\left(nS^\gamma\rho^{\gamma R}\boldsymbol{v}^{\gamma s}\right) + nS^\gamma\rho^{\gamma R}\nabla\cdot\dot{\boldsymbol{u}}^s = 0 \tag{2.56}$$

Applying the solid phase mass balance (2.54), (2.56) can be represented in a more detailed description.

$$\begin{aligned} &nS^\gamma\frac{d_s\rho^{\gamma R}}{dt} + n\rho^{\gamma R}\frac{d_s S^\gamma}{dt} \\ &+\nabla\cdot(\rho^\gamma\boldsymbol{w}^{\gamma s}) + S^\gamma\rho^{\gamma R}\nabla\cdot\dot{\boldsymbol{u}}^s = 0 \end{aligned} \tag{2.57}$$

Here

$$\boldsymbol{w}^{\gamma s} = nS^{\gamma}\boldsymbol{v}^{\gamma s} \tag{2.58}$$

is usually denoted as filter velocity of the motion of the pore fluid constituent $\varphi^{\gamma}$. Rewriting (2.57) in terms of partial derivatives we yield

$$\begin{aligned} nS^{\gamma}\frac{\partial \rho^{\gamma R}}{\partial t} + nS^{\gamma}\boldsymbol{v}^{\gamma s}\cdot\nabla\rho^{\gamma R} + n\rho^{\gamma R}\frac{\partial S^{\gamma}}{\partial t} + n\rho^{\gamma R}\boldsymbol{v}^{\gamma s}\cdot\nabla S^{\gamma} \\ +\nabla\cdot(\rho^{\gamma} nS^{\gamma}\boldsymbol{v}^{\gamma s}) + S^{\gamma}\rho^{\gamma R}\nabla\cdot\dot{\boldsymbol{u}}^{s} = 0 \end{aligned} \tag{2.59}$$

**Primary Variables**

The selection of primary variables is important and is ruled by our interest in non-isothermal and non-isobaric processes which promotes the choice of pressure $p$ and temperature $T$ as primary variables. The substitutions of phase density

$$d\rho^{\alpha}(p,T) = \frac{\partial \rho^{\alpha}}{\partial p}dp + \frac{\partial \rho^{\alpha}}{\partial T}dT \tag{2.60}$$

and phase saturation

$$dS^{\alpha}(p,T)\frac{\partial S^{\alpha}}{\partial p}dp + \frac{\partial S^{\alpha}}{\partial T}dT \tag{2.61}$$

will result in formulations of the phase mass balance equations in terms of the selected primary variables.

### 2.3.2 Momentum Balance

When dealing with flow in porous and fractured media we have to consider the mechanics of fluids in tubes and channels. The governing equation for flow of incompressible viscous fluids is the well-known Navier–Stokes equation

$$\underbrace{\frac{\partial \mathbf{v}}{\partial t} + (\mathbf{v}\cdot\nabla)\mathbf{v}}_{\text{inertial terms}} = \mathbf{g} - \frac{1}{\rho}\nabla p + \underbrace{\frac{\mu}{\rho}\nabla^2\mathbf{v}}_{\text{viscous term}} \tag{2.62}$$

The Navier–Stokes equation can be integrated for laminar flow in straight, circular tubes when steady-state boundary conditions are applied. In this case convective acceleration term $(\mathbf{v}\cdot\nabla)\mathbf{v}$ becomes zero. This solution is called the Hagen-Poiseuille equation [25].

$$\Delta p = \frac{8\mu L}{\pi R^4}\,Q \tag{2.63}$$

where $Q$ is the volumetric flow rate, which is velocity multiplied by tube cross-section area, $L$ is tube length and $R$ is tube radius. The linear relationship

between pressure drop and flow rate $Q$ breaks down if convective acceleration and/or transient effects become important. The first case denotes **non-linear laminar flow**, when inertial effects become important, e.g. due to curvature of tubes or channels. The second case is related to **turbulent flow**, when flow pattern become transient due to velocity fluctuations.

Confusion between non-linear laminar flow and 'true' turbulent flow may arise from the fact that—concerning the relationship between pressure drop and the flow rate—inertia effects in laminar flow are expressed in the same fashion as in turbulent flows

$$\Delta p = AQ + BQ^2 \,. \tag{2.64}$$

This means if inertia effects or turbulence effects become significant, the relationship between pressure drop and flow rate (2.63) is no longer linear. Therefore, we have to distinguish between three different flow regimes: linear laminar flow, non-linear laminar flow and 'true' turbulent flow. Equation (2.64) is known as the Forchheimer equation [26].

[27] found that the volume of fluid percolating through a sand column is proportional to the applied pressure difference

$$Q = qA = A\frac{k}{\mu}\frac{\Delta p}{L} \quad \rightarrow \quad \Delta p = \frac{L}{A}\frac{\mu}{k}Q \,. \tag{2.65}$$

Comparing the structure of (2.65) and (2.63), the analogy between porous media flow and tube flow becomes obvious. Both equations are characterized by linear relationships between pressure drop and flow rate.

Darcy's law can be derived from the Navier–Stokes equations. To this purpose a spatial averaging procedure over a representative elementary volume (REV) has to be conducted, where microscopic quantities are transformed into macroscopic ones [9]

$$\langle \psi \rangle = \frac{1}{\mathrm{REV}} \int_{\mathrm{REV}} \psi \, dV \tag{2.66}$$

where $\psi$ is a local, microscopic quantity and $\langle \psi \rangle$ is a spatially averaged macroscopic quantity. [2] For fractures the averaging procedure can be split into two steps

$$\langle \psi \rangle = \frac{1}{2b\,\mathrm{REA}} \int_{-b}^{+b} \int_{\mathrm{REA}} \psi \, dx \, dA \tag{2.67}$$

where $b$ is half fracture aperture and REA is a representative elementary area. In the following we deal with quantities which are averaged over fracture thickness and, therefore, are representative for a certain area of fracture surface.

[2] See also (2.29) for general definition of a mean value for a porous medium. Both notations $\overline{\psi}$ and $\langle \psi \rangle$ are common in literature.

Darcy's law is based essentially on the assumption that fluid motion is inertialess, i.e. inertial terms can be neglected with regard to viscous forces

$$0 = \langle \mathbf{g} \rangle - \frac{1}{\langle \rho \rangle} \nabla \langle p \rangle + \frac{\langle \mu \rangle}{\langle \rho \rangle} \nabla^2 \langle \mathbf{v} \rangle \,. \tag{2.68}$$

Brackets indicate macroscopic quantities. Thus Darcian flow is a special case of creeping flow for which viscous forces prevail over inertial forces. A central topic in porous medium theory is the determination of the viscous drag term. This leads to the concept of permeability for characterization of the hydromechanical properties of porous media [28]. Introducing permeability in the following manner

$$\nabla^2 \langle \mathbf{v} \rangle = -\mathbf{k}^{-1}\, \mathbf{w} \tag{2.69}$$

where $k$ is the permeability of the porous medium and $\mathbf{v}$ is the Darcy or seepage velocity, which are macroscopic quantities by definition. Substituting this expression into (2.68) we obtain

$$0 = \mathbf{g} - \frac{1}{\langle \rho \rangle} \nabla \langle p \rangle - \frac{\langle \mu \rangle}{\langle \rho \rangle} \mathbf{k}^{-1} \mathbf{w} \,. \tag{2.70}$$

Rearranging the terms, we yield the usual form of Darcy's law. We omit the averaging brackets in the following to keep the notation brief.

$$\boldsymbol{w} = -\frac{\mathbf{k}}{\mu} (\nabla p - \rho \mathbf{g}) \,. \tag{2.71}$$

We emphasize that quantities in the above Darcy equation are macroscopic ones related to a certain REV of a porous medium, whereas quantities in the Navier–Stokes equation (2.62) have local meaning.

Darcy's law has been accepted as a fundamental relationship for porous medium hydraulics. However, its validity is restricted to a certain range of geometric and physical conditions. Deviations from linearity between seepage velocity and pressure drop are denoted as non-Darcian flow. Geometric issues are concerned with pore and fracture geometry.

As described above we used the analogy of flow in straight tubes for explanation of hydromechanical processes in porous media. A tube bundles model is one approach to hydromechanics of porous media. However in real geologic materials pores are curved, have varying cross-sections, may be sealed, and suffer from dead-end effects. Rock fractures are characterized by rough surfaces. Physical causes underlying non-linear effects can be high flow rates, molecular effects, ionic effects and non-Newtonian behavior of the fluid itself [29].

### Darcy's Law

For linear momentum conservation in porous media we assume, in general, that inertial forces can be neglected (i.e. $d\mathbf{v}/dt \approx 0$) and body forces are gravity at all. Assuming furthermore that internal fluid friction is small in comparison to friction on the fluid–solid interface and that turbulence effects can be neglected we obtain the Darcy law for each fluid phase $\gamma$ in multiphase flow (cf. (2.58)).

$$\boldsymbol{w}^{\gamma s} = nS^{\gamma}(\boldsymbol{v}^{\gamma} - \boldsymbol{v}^{s}) = -nS^{\gamma}\left(\frac{k_{\mathrm{rel}}^{\gamma}\mathbf{k}}{\mu^{\gamma}}(\nabla p^{\gamma} - \rho^{\gamma}\boldsymbol{g})\right) \tag{2.72}$$

## 2.3.3 Energy Balance

### Heat Transport

The equation of energy conservation is derived from the first law of thermodynamics which states that the variation of the total energy of a system is due to the work of acting forces and heat transmitted to the system.

The total energy per unit mass $e$ specific energy) can be defined as the sum of internal (thermal) energy $i$ and specific kinetic energy $v^2/2$. Internal energy is due to molecular movement. Gravitation is considered as an energy source term, i.e. a body force which does work on the fluid element as it moves through the gravity field. The conservation quantity for energy balance is total energy density

$$\psi^{e} = \rho e = \rho(i + v^2/2) \tag{2.73}$$

Using mass and momentum conservation we can derive the following balance equation for the internal energy

$$\rho\frac{di}{dt} = \rho q^{i} - \nabla\cdot\mathbf{j}_{\mathrm{th}} + \sigma\cdot\nabla\mathbf{v} \tag{2.74}$$

where $q^i$ is the internal energy (heat) source, and $\mathbf{j}_{\mathrm{th}}$ is the diffusive heat flux. Applying the chain rule to the left hand side of the above equation yields

$$\rho\frac{di}{dt} = \rho\frac{dcT}{dt} = \rho c\frac{dT}{dt} + \rho T\frac{dc}{dt} \tag{2.75}$$

and utilizing the definition of the material derivative

$$\frac{dT}{dt} = \frac{\partial T}{\partial t} + \mathbf{v}\cdot\nabla T \tag{2.76}$$

we obtain the heat energy balance equation

$$\rho c\frac{\partial T}{\partial t} + \rho c\mathbf{v}\cdot\nabla T - \nabla\cdot\lambda\nabla T + \rho T\frac{dc}{dt} - \sigma\cdot\nabla\mathbf{v} = \rho q_{\mathrm{th}} \tag{2.77}$$

**Porous Medium**

The heat balance equation for the porous medium consisting of several solid and fluid phases is given by

$$(\sum_{\alpha} \epsilon^{\alpha} c^{\alpha} \rho^{\alpha}) \frac{\partial T}{\partial t} + \nabla \cdot \left( (\sum_{\gamma} n S^{\gamma} \rho^{\gamma} c^{\gamma} \boldsymbol{v}^{\gamma}) T - (\sum_{\alpha} \epsilon^{\alpha} \lambda^{\alpha}) \nabla T \right) = \sum_{\alpha} \epsilon^{\alpha} \rho^{\alpha} q_{\mathrm{th}} + (\sum_{\gamma} n S^{\gamma} \boldsymbol{v}^{\gamma}) \cdot \nabla \sigma \qquad (2.78)$$

where $\alpha$ is all phases and $\gamma$ is fluid phases, respectively.

Most important is the assumption of local thermodynamic equilibrium, meaning that all phase temperatures are equal and, therefore, phase contributions can be superposed. The phase change terms are canceled out with the addition of the individual phases.

## 2.4 Fluid Properties

The above balance equations derived from first principles (Sect. 2.3) are "material-less", i.e. they are valid for any kind of material. Constitutive relationships are necessary to close the balance equations as well as to specify the properties for fluid flow, heat transfer and mechanical stress/deformation of the specific material under consideration. For determination of material properties laboratory tests have to be conducted. A number of material properties cannot be determined directly. This must be done by back analysis using inverse modeling. We organized the description of material properties into two sections: Fluid and mechanical properties (2.5) for THM/C processes in porous media.

As we have to deal with a large variety of geotechnical and hydrological applications (Sect. 1) we allow the most complex case for fluid properties including phase changes. We consider very general equations of state (EOS) such as Redlich-Kwong [30], Peng-Robinson [31] equations as well as the fundamental Helmholtz free energy equation (2.89).

Figure 2.9 shows as an example the phase diagram in case of $CO_2$ as working fluid. If we are interested in different fluids (e.g. $CH_4$, $H_2O$, and $N_2$) Table 2.2 gives an overview of the corresponding fluid property correlations.

### 2.4.1 Density

In subsurface oil and gas reservoirs, properties of gases and liquids strongly depend on environmental pressure and temperature conditions. Equations of state (EOS) may be used to describe the relationship of volume, pressure and

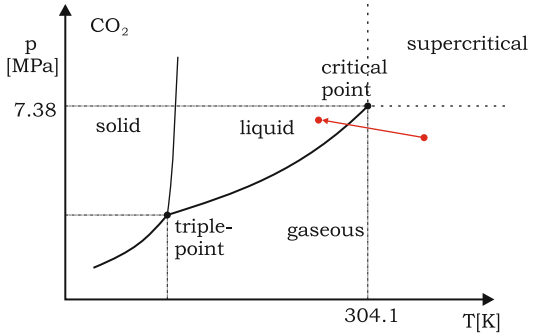


Figure 2.9: Phase diagram of carbon dioxide. The two extreme conditions ( [400] K at [6.5] MPa and [300] K at [7] MPa) are crossing a phase boundary of $CO_2$, so a phase change from hot gas to a liquid state will be forced

Table 2.2: References for fluid properties of $CH_4$, $CO_2$, $H_2O$, and $N_2$

| Fluid | Specifier | Density | Viscosity |
|---|---|---|---|
| Methane $CH_4$ | CH4-RK | [30] | Friend, 1989 [32] |
| | CH4-PR | [31] | |
| | CH4-HE | [33] | |
| Carbon dioxide $CO_2$ | CO2-RK | [30] | Fenghour, 1998 [34] |
| | CO2-PR | [31] | |
| | CO2-HE | [35] | |
| Water $H_2O$ | H2O-RK | [30] | IAPWS, 1998 [36] |
| | H2O-PR | [31] | |
| | H2O-HE | [37] | |
| Nitrogen $N_2$ | N2-RK | [30] | Stephan, 1987 [38] |
| | N2-PR | [31] | |
| | N2-HE | [39] | |

temperature of a real fluid. The knowledge of a fluid's volume or its density is essential to estimate further thermodynamic properties. The first EOS for real gases, which was based on the ideal gas law, was presented by Johannes Diderik van der Waals in 1873 [40]. In 1910 he received the Nobel Prize for the development of the equation

$$p = \frac{RT}{V_m - b} - \frac{a}{V_m^2} \tag{2.79}$$

where $p$ is the pressure, $R$ is the gas constant, $T$ is the temperature, $V_m$ is the molar volume and $a$ and $b$ are correcting parameters.

Table 2.3: Fluid properties used in equations of state, where $\omega$ is the acentric factor, $T_c$ and $p_c$ are temperature and pressure at the critical point and $R$ is the gas constant

| Fluid | $\omega$ [-] | $T_c$ [K] | $p_c$ [MPa] | $R$ [J/kg/K] |
|---|---|---|---|---|
| Carbon dioxide | 0.239 | 304.13 | 7.38 | 188.9 |
| Ethane | 0.099 | 305.32 | 4.87 | 276.5 |
| Methane | 0.011 | 190.56 | 4.60 | 518.3 |
| Water | 0.344 | 647.10 | 22.06 | 461.5 |

**Redlich-Kwong equation of state (RKEOS)** The equation of Redlich and Kwong from 1949 (2.80) represents just a little improvement of the van der Waals equation [30]. It is given as

$$p = \frac{RT}{V_m - b} - \frac{a}{T^{0.5} V_m (V_m + b)}. \tag{2.80}$$

The results are satisfactory only for temperatures above the critical point (see Table 2.3).

Equation (2.80) can be recasted as a cubic equation in terms of volume

$$V_m^3 - \frac{RT}{p} V_m^2 - \left( \frac{RTb}{p} - \frac{a}{T^{0.5} p} + b^2 \right) V_m - \frac{ab}{T^{0.5} p} = 0. \tag{2.81}$$

This equation yields to one or three real roots depending on the number of phases in the system. In the two-phase region, the largest positive root represents the molar volume of the gas phase while the smallest root corresponds to the volume of the liquid phase. The correcting terms $a$ and $b$ are given as

$$a = 0.4275 \frac{R^2 T_c^{2.5}}{p_c} \tag{2.82}$$

and

$$b = 0.0866 \frac{RT_c}{p_c} \tag{2.83}$$

where $T_c$ and $p_c$ are temperature and pressure at the critical point (see Table 2.3). Figures 2.10 and 2.11 show the results of the RKEOS for several substances at four different temperatures in comparison to other equations of state.

**Peng-Robinson equation of state (PREOS)** D. Y. Peng and D. B. Robinson presented an improvement of the RKEOS in 1975 [31]. The proposed equation is also a two-constant van der Waals-Type equation and combines simplicity and accuracy. The PREOS is very simple to solve and gives satisfying

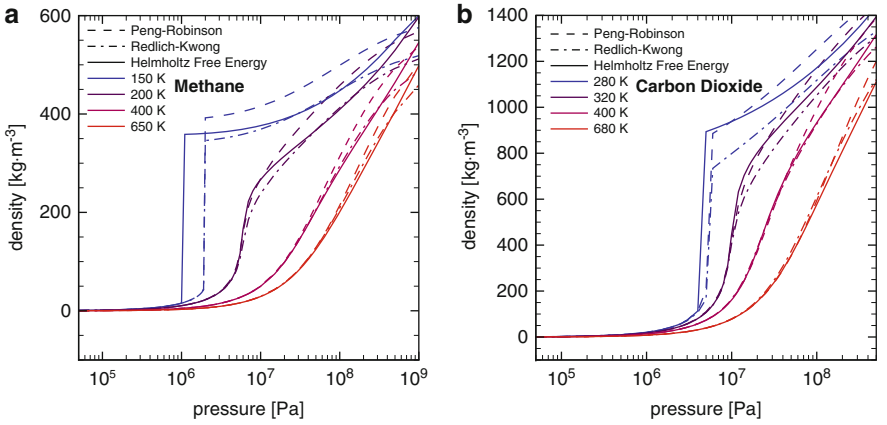


Figure 2.10: Density of $CH_4$ (**a**) and $CO_2$ (**b**) derived by different EOS. Here ——— stands for the HELMHOLTZ Free Energy, – – – for the PREOS and –·–·– for the RKEOS. The colours refer to different temperatures (*blue* - [280] K, *violet* - [320] K, *pink* - [400] K, *red* - [680] K)

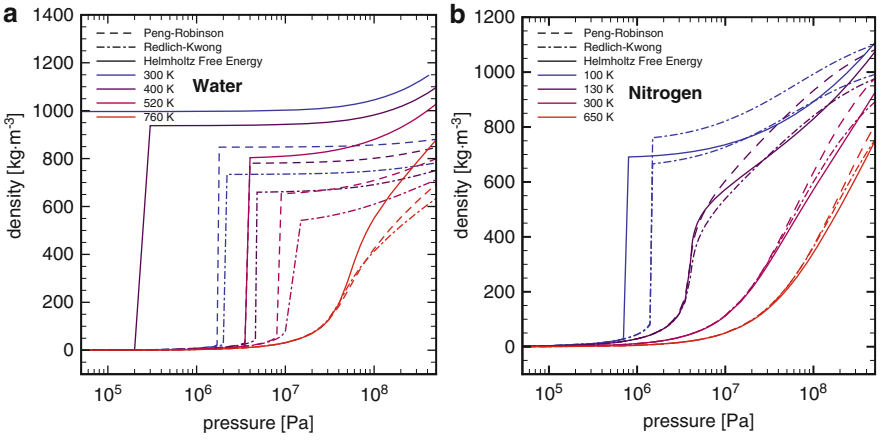


Figure 2.11: Density of $H_2O$ (**a**) and $N_2$ (**b**) derived by different EOS. Here ——— stands for the HELMHOLTZ Free Energy, – – – for the PREOS and –·–·– for the RKEOS. The colours refer to different temperatures (*blue* - [280] K, *violet* - [320] K, *pink* - [400] K, *red* - [680] K)

results within the whole fluid region of a gas. It is given in the form

$$p = \frac{RT}{V_m - b} - \frac{a(T_c) \cdot \alpha(T_r, \omega)}{V_m^2 + 2 \cdot bV_m - b^2} \tag{2.84}$$

where $a$ and $b$ are correcting terms. They can be derived by

$$a(T_c) = 0.45724 \frac{R^2 T_c^2}{p_c} \tag{2.85}$$

and

$$b(T_c) = 0.07780 \frac{RT_c}{p_c} \tag{2.86}$$

for the particular fluids under specification of pressure and temperature at the critical point. Parameter $\alpha(T_r, \omega)$ is a dimensionless function of reduced temperature $T_r$ and acentric factor $\omega$. It is given as

$$\alpha = \left(1 + \left(0.37464 + 1.54226\,\omega - 0.26992\,\omega^2\right)\left(1 - T_r^{0.5}\right)\right)^2 \tag{2.87}$$

for $\omega \leq 0.49$ and

$$\alpha = \left(1 + \left(0.379642 + \left(1.48503 - \left(1.164423 - 1.016666\,\omega\right)\omega\right)\omega\right)\left(1 - T_r^{0.5}\right)\right)^2 \tag{2.88}$$

for $\omega > 0.49$. Table 2.3 shows acentric factors and critical parameters for different real gases. The resulting density distribution of the PREOS is shown in Figs. 2.10 and 2.11 at four different temperatures.

**Fundamental equations** For highly precise results it is necessary to adapt fundamental equations based on the free energy. The HELMHOLTZ free energy is given as

$$\frac{f(\rho, T)}{RT} = \phi(\delta, \tau) = \phi^o(\delta, \tau) + \phi^r(\delta, \tau) \tag{2.89}$$

in dependence from density $\rho$ and temperature $T$ in its dimensionless form. These dimensionless parts are given as the terms $\delta = \rho/\rho_c$ and $\tau = T_c/T$, whereas $\rho_c$ and $T_c$ are density and temperature at the critical point (see Table 2.3). The HELMHOLTZ free energy provides relations between density, temperature and all thermodynamic properties of a fluid, which are expressed in the parameter $\phi^o$ as the ideal gas part and $\phi^r$ as the residual part. For their derivatives in the short forms like $\phi^r_\delta$, $\phi^r_{\delta\delta}$, $\phi^r_\tau$, $\phi^r_{\tau\tau}$, $\phi^r_{\delta\tau}$, $\phi^o_\tau$, $\phi^o_{\tau\tau}$ refer to [35].

Several authors have used the approach of HELMHOLTZ free energy to develop EOS for different substances, e. g.:

- Span & Wagner [35], [41], [39] for carbon dioxide and for nitrogen,
- Pruss & Wagner [42], [37] for water,
- Bücker & Wagner [43] for ethane and
- Setzmann & Wagner [33] for methane.

Table 2.4: Ranges of validity of the free HELMHOLTZ equation (2.89) for several fluids valid from the melting point up to the indicated values

| Fluid | $T$ [K] | $p$ [MPa] | Reference |
|---|---|---|---|
| Carbon dioxide | 216 | 1,100 | [35], [41] |
| Nitrogen | 1,000 | 2,200 | [39] |
| Ethane | 520 | 30 | [43] |
| Methane | 625 | 1,000 | [33] |
| Water | 1,273 | 1,000 | [42], [37] |

The fundamental equation (2.89) according to Wagner et al. ([35],[42],[43], and [33]) is one of the most precise EOS at present. The equation and its derivatives can be used to describe all thermodynamic properties of a pure substance depending on density and temperature. So, it is necessary to solve the relationship between density, pressure and temperature iteratively, as (2.90) shows

$$\frac{p(\delta,\tau)}{\rho RT} = 1 + \delta\frac{\partial\phi^r}{\partial\delta}. \tag{2.90}$$

For water, fluid properties are provided by the IAPWS [3] 1995 steam table equations. To ease computational time, it is also possible to choose an iterative algorithm or to interpolate density values out of a database.

The semi-empirical fundamental equation (2.89) has to be fitted to measurement data by computer algorithms for each substance. Depending on the fluid, there are up to 200 adjusting coefficients to ensure a very accurate fit to the real gas behaviour. For each substance, (2.89) has separate ranges of validity, which are shown in Table 2.4.

### 2.4.2 Enthalpy

The specific enthalpy $h$ is the whole amount of energy of a fluid. It consists of the internal energy and the volume changing work. It can be expressed by deviations of the free HELMHOLTZ energy as

$$\frac{h(\delta,\tau)}{RT} = 1 + \tau\left(\phi^o_\tau + \phi^r_\tau\right) + \delta\phi^r_\delta. \tag{2.91}$$

### 2.4.3 Entropy

The entropy $s$ represents which amount of the energy of a system is potentially available to do work and which amount of it is potentially defined as heat. In

[3] International Association for the Properties of Water and Steam.

classical thermodynamics, the validity for the entropy is the thermodynamical system in equilibrium. The following equation is given for the entropy:

$$\frac{s(\delta,\tau)}{R} = \tau\left(\phi^o_\tau + \phi^r_\tau\right) - \phi^o - \phi^r. \tag{2.92}$$

### 2.4.4 Heat Capacity

The specific heat capacity of a fluid is defined as the amount of heat which is needed to increase the temperature of a fluid of [1] kg by [1] K. In thermodynamics, it is distinguished between a heat capacity at constant pressure, the isobaric heat capacity, and a heat capacity at a constant volume, the isochoric heat capacity. Both can be expressed in terms of free HELMHOLTZ energy, like the following equations show:

isobaric heat capacity

$$\frac{c_p(\delta,\tau)}{R} = -\tau^2\left(\phi^o_{\tau\tau} + \phi^r_{\tau\tau}\right) + \frac{\left(1+\delta\phi^r_\delta - \delta\tau\phi^r_{\delta\tau}\right)^2}{\left(1+2\delta\phi^r_\delta + \delta^2\phi^r_{\delta\delta}\right)} \tag{2.93}$$

isochoric heat capacity

$$\frac{c_v(\delta,\tau)}{R} = -\tau^2\left(\phi^o_{\tau\tau} + \phi^r_{\tau\tau}\right). \tag{2.94}$$

Due to the high number of adjusting coefficients, the properties based on the HELMHOLTZ free energy may be seen as very accurate. On the other hand, the iterative solution of (2.90) requires long computing times, so for long-term simulations or for simulations with a high number of elements, it would be better to use the van der Waals-type equations of Redlich-Kwong or Peng-Robinson. These cubic equations are easy to solve and lead to results very fast. Figures 2.12 and 2.13 illustrate, in which range of temperature and pressure those simple EOS may be used. Here, thermodynamical properties of carbon dioxide based on temperature and density are shown calculated by different EOS. In general, if temperature rises while pressure is declining, the behaviour of a fluid approaches that of the ideal gas and the cubic equations of state give suitable results. For instance, the resulting entropy and enthalpy values of carbon dioxide at low pressures and high temperatures are identical, regardless of the density model they are based on (see Fig. 2.12a and 2.12b). In the liquid and the dense supercritical region, the results based on different EOS diverge increasingly.

In addition, in the vicinity of the saturation curve, the results based on the van der Waals-type EOS may show large variations compared to the fundamental equation based curves (HELMHOLTZ free energy). Particularly, this becomes apparent from Fig. 2.13a and 2.13b, where the heat capacities of $CO_2$ are given. The heat capacities at [400] K and [680] K (in the supercritical region of $CO_2$,

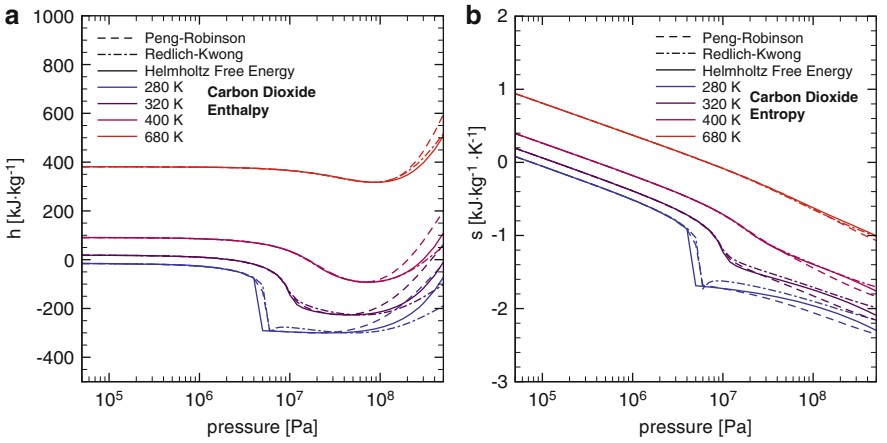


Figure 2.12: Enthalpy (**a**) and entropy (**b**) of $CO_2$ based on different EOS. Here —— stands for the HELMHOLTZ Free Energy, – – – for the PREOS and –·–·– for the RKEOS. The colours refer to different temperatures (*blue* - [280] K, *violet* - [320] K, *pink* - [400] K, *red* - [680] K)

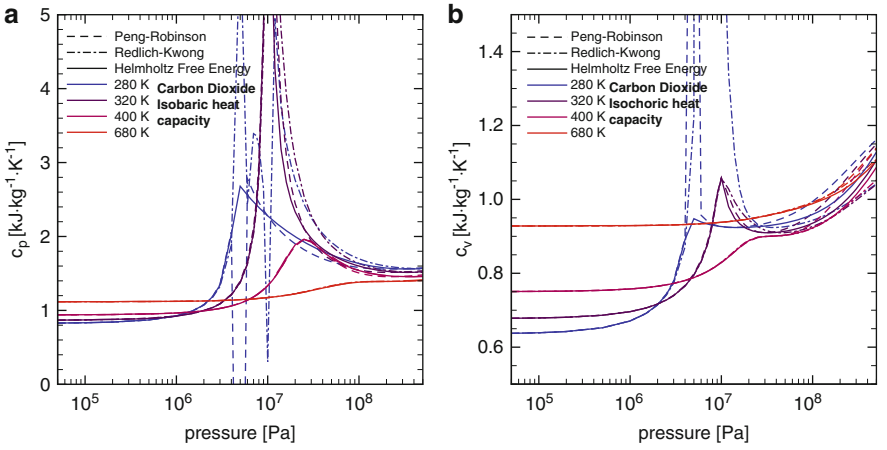


Figure 2.13: Isobaric heat capacity (**a**) and isochoric heat capacity (**b**) of $CO_2$ based on different EOS. Here —— stands for the HELMHOLTZ Free Energy, – – – for the PREOS and –·–·– for the RKEOS. The colours refer to different temperatures (*blue* - [280] K, *violet* - [320] K, *pink* - [400] K, *red* - [680] K)

where no phase boundary exists) are identical, independent from the according density model. Within the two-phase region at [280] K and [320] K, a strong deviation at the phase boundary can be seen.

For water, the cubic EOS are not suitable. Water is a high critical fluid, so its properties are too complex to be described by simple approaches. As we

can see in Fig. 2.11a, the RKEOS, as well as the PREOS equation give viable results only at pressures below [1] MPa and at high temperatures. Therefore it is recommended to use the fundamental equation of the HELMHOLTZ free energy to estimate the density of water.

### 2.4.5 Viscosity

Many authors have developed correlation equations for viscosity $\eta$ of fluids at a density $\rho$ and a temperature $T$. Those correlation equations may be composed of two or three terms, like

$$\eta(\rho, T) = \eta_0(T) + \eta_{ex}(\rho, T) \tag{2.95}$$

or

$$\eta(\rho, T) = \eta_0(T) + \Delta\eta(\rho, T) + \Delta\eta_c(\rho, T). \tag{2.96}$$

In the two-term form, the viscosity correlation consists of a zero-density limit viscosity $\eta_0(T)$ at a temperature $T$, and an excess contribution viscosity $\eta_{ex}(\rho, T)$ at a density $\rho$ and a temperature $T$. This type of correlation function is used (among others) by FRIEND et al. [32] or STEPHAN et al. [38]. The formulation can be enhanced by a term describing the viscosity in the immediate vicinity of the critical point, $\Delta\eta(\rho, T)$ (2.96), as described in FENGHOUR et al. [34] or HUBER et al. [36]. An overview about the used viscosity correlations for several substances is given in Table 2.5. To show an example, Fig. 2.14a portrays the resulting viscosities for carbon dioxide based on densities of different EOS.

### 2.4.6 Thermal Conductivity

Similar to the correlations between viscosity and $T$ and $p$, the thermal conductivity $\lambda$ can be expressed by an equation consisting of the following three parts (see [45]): A conductivity in the limit of zero-density $\lambda^0(0, T)$, where only two-body interaction occurs, a term $\Delta_c\lambda(\rho, T)$ which enhances the property function in the critical region of the fluid, and finally $\Delta\lambda(\rho, T)$ which represents the contribution of all other effects to the thermal conductivity at elevated densities

Table 2.5: Ranges of $T$ and $p$ validity for viscosity correlations for several substances

| Fluid | $T$ [K] | $p$ [MPa] | Reference |
|---|---|---|---|
| Carbon dioxide | 200–1,500 | $\leq 300$ | [34] |
| Nitrogen | 70–1,100 | $\leq 100$ | [38] |
| Ethane | 90–625 | $\leq 30$ | [44] |
| Methane | 91–600 | $\leq 100$ | [32] |
| Water | 273–1,173 | $\leq 100$ | [36] |

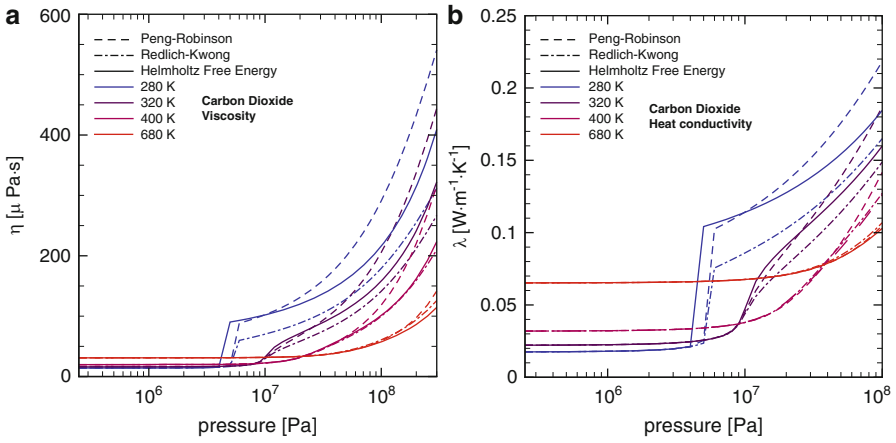


Figure 2.14: Viscosity (**a**) and thermal conductivity (**b**) of $CO_2$ based on different EOS. Here —— stands for the HELMHOLTZ Free Energy, – – – for the PREOS and –·–·– for the RKEOS. The colours refer to different temperatures (*blue* - [280] K, *violet* - [320] K, *pink* - [400] K, *red* - [680] K)

Table 2.6: Ranges of $T$ and $p$ validity for thermal conductivity correlations for several substances

| Fluid | $T$ [K] | $p$ [MPa] | Reference |
|---|---|---|---|
| Carbon dioxide | 200–1,000 | $\leq 100$ | [34] |
| Nitrogen | 70–1,100 | $\leq 100$ | [38] |
| Ethane | $\leq 600$ | $\leq 70$ | [46] |
| Methane | $\leq 200$ | $\leq 600$ | [46] |
| Water | $\leq 800$ | $\leq 100$ | [47] |

including many-body collisions, molecular-velocity correlations and collisional transfer. This equation is

$$\lambda(\rho, T) = \lambda^0(T) + \Delta\lambda(\rho) + \Delta_c\lambda(\rho, T). \tag{2.97}$$

Figure 2.14b shows the thermal conductivity of carbon dioxide at four temperatures based on different EOS. In Table 2.6 the ranges for the validity of $T$ and $p$ concerning thermal conductivity correlations for several substances are shown.

## 2.5 Mechanical Properties

Constitutive equations (i.e. constitutive relations, material laws) are relations between measures of deformation (e.g. strain tensor) and internal force density functions (stress tensor) resulting from the action of external forces. Usually,

they are not laws of nature but represent mathematical models intended to characterize the typical material behavior based on physically reasonable assumptions (particularly consistent with the thermodynamic balance relations) and mathematically correct approaches.

### 2.5.1 Effective Stress Principle

The total Cauchy's stress tensor in porous media is decomposed in partial stresses referring to the participating phases (note the sign convention of positive fluid phase pressure $p^\gamma$, but negative compressive normal stress for the solid phase).

$$\boldsymbol{\sigma} = (1-n)\,\boldsymbol{\sigma}^s - n\left(\sum_\gamma S^\gamma\, p^\gamma\right)\mathbf{I} \tag{2.98}$$

Considering the effective stress principle, relation (2.98) can be modified defining the effective solid stress $\boldsymbol{\sigma}^s_{eff}$ as well as the overall fluid pressure $p^\gamma$

$$\begin{aligned}\boldsymbol{\sigma} &= (1-n)\left[\boldsymbol{\sigma}^s + \left(\sum_\gamma S^\gamma\, p^\gamma\right)\mathbf{I}\right] - \left(\sum_\gamma S^\gamma\, p^\gamma\right)\mathbf{I} \\ &= \boldsymbol{\sigma}_{\text{eff}} - \left(\sum_\gamma S^\gamma\, p^\gamma\right)\mathbf{I}\end{aligned} \tag{2.99}$$

Effective stress is the difference between the total stress and pore fluid pressure. Consequently, its absolute value is lower than the intrinsic stress of the solid skeleton. Constitutive relations for the solid phase of porous media combine the solid skeleton deformation (in terms of the strain tensor) with the effective solid stress. Selected models are presented in the next paragraphs. As they are equally valid for single-phase solid materials as well as for the solid phase of porous media, the special notation of the effective stress tensor will be omitted without loss of generality.

Based on the stress decomposition (2.99), the equilibrium condition for the porous medium becomes

$$\rho\boldsymbol{g} + \nabla\cdot\boldsymbol{\sigma}_{\text{eff}} - \left(\sum_\gamma S^\gamma\, p^\gamma\right)\mathbf{I} = \mathbf{0} \tag{2.100}$$

### 2.5.2 Material Classes

Usually laboratory tests are performed on specimens to investigate the mechanical behavior. Within this context, similar stress-strain curves can be caused by different physical effects, e.g. a nonlinear stress-strain curve does not necessarily suggest inelastic material behavior. For the sake of clarity, it is possible to

introduce a classification of materials based on some essential, distinctly identifiable material phenomena. For instance, comparatively simple experiments can be performed to investigate if the stress-strain curves are rate-dependent, and if hysteresis phenomena occur, indicating dissipative effects.

Based on these assumptions the observable material behavior can be divided into four different basic classes:

- rate-independent without hysteresis,
- rate-independent with hysteresis,
- rate-dependent without hysteresis, and
- rate-dependent with hysteresis.

Figures 2.15 and 2.16 schematically show typical cyclic stress-strain curves for these material classes. The equilibrium curves, presented in Fig. 2.16 can be observed as a result of relaxation experiments.

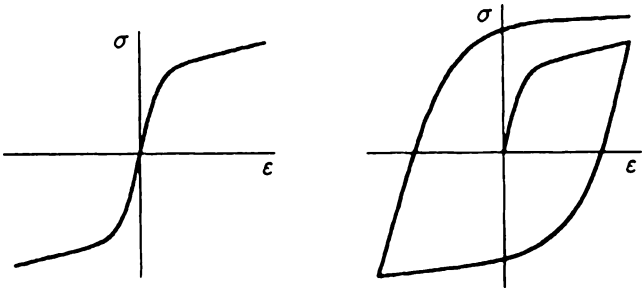


Figure 2.15: Experimentally observed rate-independent solid material behavior. Cyclic uniaxial stress-strain curves [17]: elasticity (*left*) and elastoplasticity (*right*)

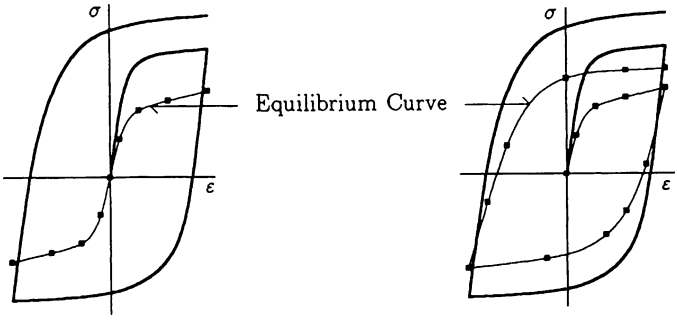


Figure 2.16: Experimentally observed rate-dependent solid material behavior. Cyclic uniaxial stress-strain curves [17]: viscoelasticity (*left*) and viscoplasticity (*right*)

According to the experimental observations, there are four classes of mathematical models matching the material classes defined above:

- the theory of elasticity describes rate-independent material behavior without hysteresis,
- the theory of (elasto)plasticity describes rate-independent material behavior with hysteresis,
- the theory of viscoelasticity describes rate-dependent material behavior without hysteresis, and
- the theory of viscoplasticity describes rate-dependent material behavior with hysteresis.

Physically significant constitutive relations in the uniaxial case can be defined for the four classes of material theories based on so-called rheological models. These complex models consist of a simple networks of individual rheological elements (cf. Fig. 2.17), like

- elastic springs, which correspond to the linear stress-strain relation

$$\sigma = k\,\varepsilon \tag{2.101}$$

  with the spring constant $k$ representing the proportionality factor,

- viscous dashpots, which represent Newtonian viscous substances, and obey a linear relation between stress and strain rate

$$\sigma = \eta\,\dot{\varepsilon} \tag{2.102}$$

  with the proportionality factor $\eta$ characterizing the viscosity, and

- Coulomb friction elements, resisting any motion until a threshold stress $\sigma^\star$ is reached, whereas behind the threshold irreversible deformations occur

$$\varepsilon = \begin{cases} 0, & \text{if} \quad \sigma < \sigma^\star \\ \varepsilon(t), & \text{if} \quad \sigma \geq \sigma^\star \end{cases} \tag{2.103}$$

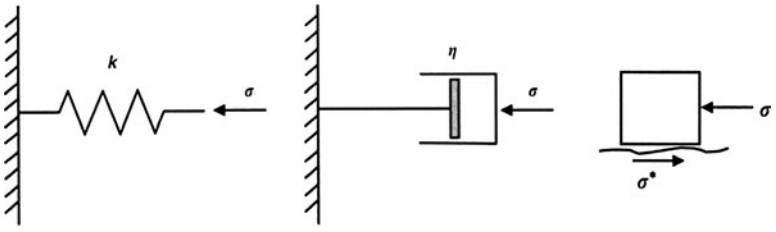


Figure 2.17: Mathematical modeling of solid material behavior. Basic individual elements of rheological models [48]: spring element (*left*), dashpot element (*middle*) and frictional element (*right*)

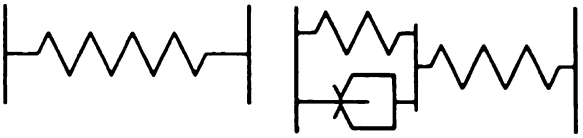

Figure 2.18: Mathematical modeling of rate-independent solid material behavior. Cyclic uniaxial stress-strain curves [17]: elasticity (spring element – *left*) and elastoplasticity (spring and frictional elements – *right*)

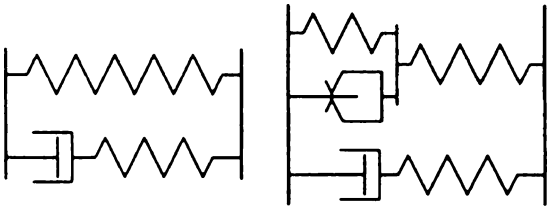

Figure 2.19: Mathematical modeling of rate-dependent solid material behavior. Cyclic uniaxial stress-strain curves [17]: viscoelasticity (spring and dashpot elements – *left*) and viscoplasticity (spring, dashpot, and frictional elements – *right*)

Differential equations, which are defined based on an appropriate composition of rheological models are only in a few special cases suitable to describe material response to external loading observed in reality. They can however serve for marking the physical significance of mathematical models within the context of material theories. In Figs. 2.18 and 2.19 typical rheological models are presented, which characterize the material behavior of the four material classes defined above.

In Table 2.7 some typical technical, as well as natural (including geological), materials are assigned to the generalized material classes considering their material behavior, which can be observed for characteristic application cases. Generally, the classification of the material behavior depends on the real loading regime (e.g. small or large strains), environmental conditions (e.g. temperature), and the time scale of the physical processes under consideration. Changing one or more of these conditions on the same material can demonstrate different mechanical behavior. Basically, no materials are actually purely elastic over a wide range of stresses, temperature, and time. Otherwise, developing and using complex constitutive models, which include all observable phenomena is not advisable for practical reasons. Constitutive relations, rather, should represent idealized and simplified models according to the most dominating conditions appearing in the practical applications under consideration.

Table 2.7: Generalized classes of solid material behavior, and selected, typical representatives

| Material class | Technical/natural material | Geomaterial |
|---|---|---|
| Elasticity | Metals at small strains,<br>ceramics,<br>bone,<br>most other materials at small strains | Igneous rocks<br>(e.g. granite),<br>hard sedimentary rocks<br>(e.g. sandstone) |
| Elastoplasticity | Metals at large strains | Most soils,<br>soft sedimentary rocks (e.g. tuff) |
| Viscoelasticity | Rubber,<br>glass,<br>soft biological tissues | Rock salt (halite) |
| Viscoplasticity | Polymers (plastics),<br>wood,<br>bitumen,<br>metals at high temperature | Clay soils,<br>clay stone |

### 2.5.3 Elasticity

In a micromechanical point of view, elasticity is predominantly caused by the evolution of interatomic forces in response to the impact of external forces. It can be observed for crystalline substances (where the atoms are established in regular structures) as well as for amorphous materials (where the atoms compose irregular structures), and is characterized by reversibility of the deformation processes and the absence of any hysteresis. Furthermore, it is assumed that the current stress state is uniquely defined by the current strain state, and does not depend on the strain history. Consequently, within the context of the constitutive model, the stress tensor is a function of the strain tensor, but it does not depend on the strain rate.

The isothermal isotropic linear elastic material model

$$\boldsymbol{\sigma} = 2\mu\,\boldsymbol{\varepsilon} + \lambda\,\mathrm{tr}(\boldsymbol{\varepsilon})\,\mathbf{I} \tag{2.104}$$

known as generalized Hooke's law is the simplest of all constitutive models for solid material behavior. Instead of the so-called Lamé constants $\mu$ and $\lambda$, Hooke's law is often represented in terms of other material parameters like the Young's modulus (i.e. elastic modulus, coefficient of elasticity, modulus of elasticity et al.) $E$, the Poisson's ratio $\nu$, the shear modulus $G$, and the bulk

modulus $K$. Some useful relations between these parameters are as follows:

$$\begin{aligned} E &= \mu\,\frac{2\mu+3\lambda}{\mu+\lambda}, \qquad \nu = \frac{\lambda}{2(\mu+\lambda)} \\ \mu &= \frac{E}{2(1+\nu)}, \qquad \lambda = \frac{\nu E}{(1+\nu)(1-2\nu)} \\ G &= \frac{E}{2(1+\nu)} = \mu \\ K &= \frac{E}{3(1-2\nu)} = \frac{(\mu+\lambda)(2\mu+3\lambda)}{3} \end{aligned}$$

Thus, the coefficients of the consistent material matrix $d\boldsymbol{\sigma}/d\boldsymbol{\varepsilon}$, which are required for the numerical simulation of mechanical material behavior can be represented clearly in the case of linear elasticity.

$$\underset{\mathbf{4}}{\boldsymbol{C}} \equiv C_{ijkl} = \frac{d\sigma_{ij}}{d\varepsilon_{kl}} = 2\mu\,\delta_{ik}\,\delta_{jl} + \lambda\,\delta_{ij}\,\delta_{kl} \tag{2.105}$$

If a coupling of mechanical and thermal processes occurs (non-isothermal mechanical processes), in addition to the strain caused by the impact of external forces a volumetric thermal strain can be observed, which usually is linearly related to the temperature difference.

$$\boldsymbol{\varepsilon}_{\mathrm{th}} = \alpha_T\,(T - T_0)\,\mathbf{I} \tag{2.106}$$

Here, $\alpha_T$ denotes the linear thermal expansion coefficient, and $T_0$ the initial temperature. In small strain solid mechanics it is common practice to consider additive decompositions of the overall strain tensor into several constitutive parts according to the observed physical phenomena. Considering thermoelastic material behavior, the overall strain tensor consists of an elastic part and a thermal part.

$$\boldsymbol{\varepsilon} = \boldsymbol{\varepsilon}_{\mathrm{el}} + \boldsymbol{\varepsilon}_{\mathrm{th}} \tag{2.107}$$

As Hooke's law (2.104) has to be perceived as a constitutive model, which assigns the local stress state to local elastic strains, a non-isothermal generalization can be defined easily.

$$\boldsymbol{\sigma} = 2\mu\,\boldsymbol{\varepsilon}_{\mathrm{el}} + \lambda\,\mathrm{tr}(\boldsymbol{\varepsilon}_{\mathrm{el}})\,\mathbf{I} = 2\mu\,\boldsymbol{\varepsilon} + \lambda\,\mathrm{tr}(\boldsymbol{\varepsilon})\,\mathbf{I} - (2\mu+3\lambda)\,\boldsymbol{\varepsilon}_{\mathrm{th}} \tag{2.108}$$

A conclusion drawn from Hooke's law of linear elasticity is the specific representation of the equilibrium condition for a thermo-poro-elastic porous medium in the case of small strains.

$$\nabla\cdot\left(\boldsymbol{\sigma}_{\mathrm{eff}}(\boldsymbol{\varepsilon}) - \left(\sum_{\gamma} S^{\gamma}\,p^{\gamma}\right)\mathbf{I} - \frac{2\mu+3\lambda}{3}\,\alpha_T\,(T-T_0)\,\mathbf{I}\right) = \rho\,\boldsymbol{g} \tag{2.109}$$

Table 2.8: Elastic material parameters for selected geomaterials

| Material | Young's modulus [GPa] | Poisson's ratio |
|---|---|---|
| Sand | 0.03...0.6 | 0.10...0.40 |
| Clay | 0.03...0.3 | 0.12...0.40 |
| Clay stone | 3...11 | 0.10...0.27 |
| Salt rock | 12...42 | 0.09...0.49 |
| Sandstone | 4...19 | 0.12...0.20 |
| Granite | 17...56 | 0.11...0.27 |
| Basalt | 31...97 | 0.19...0.30 |
| Limestone | 13...53 | 0.11...0.40 |

Although no materials are actually linearly elastic over a wide range of stresses, elastic constitutive models are often quite useful and accurate in many practical applications, e.g. in rock mechanics. The elastic material parameters given in Table 2.8 for selected soils and rocks show the large variation of material parameters, which is typical for geomaterials.

### 2.5.4 Elastoplasticity

The phenomenon of plastic yielding can be mainly observed in crystalline solid materials. It is associated with the motion of defects (so-called dislocations, discontinuities) of the regular atomic structure during deformation. Elastoplastic material behavior is characterized by elastic material response at the beginning of the deformation process. If a critical stress (the so-called yield stress) is reached, plastic flow occurs, whereas elastic material behavior can be observed again at the beginning of each unloading phase of a cyclic loading process.

In the case of elastic-perfectly plastic material behavior, the stresses remain unchanged during plastic flow keeping the yield stress value. Usually, real materials show elastoplastic material behavior with hardening effects, which are distinguished by an increase of stresses during plastic flow with a much lower slope of the stress-strain curve compared to the elastic phases of the entire deformation process. Elastoplastic material behavior with negligible elastic share is called rigid plasticity (see Fig. 2.20).

During plastic flow a certain fraction of the strain energy is transformed into thermal energy or stored as internal energy due to a remodeling of the microstructure. Therefore, when analyzing cyclic elastoplastic processes rate-independent hystereses can be observed. Additionally, plastic deformation processes prove themselves to be irreversible.

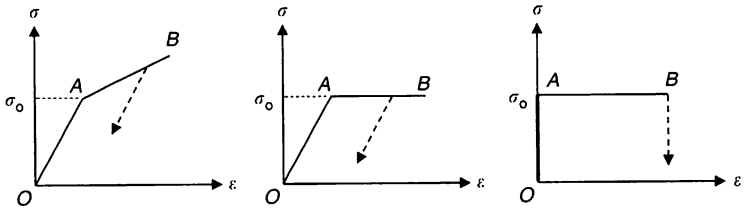


Figure 2.20: Schematic representation of material behavior exhibiting plastic yielding [48]: elastic-plastic with strain hardening (*left*), elastic-perfectly plastic (*middle*), and rigid-perfectly plastic (*right*)

In terms of the mathematical modeling of elastoplasticity, no explicit stress-strain relation can be defined (no biunique relationship between these quantities exists) due to the hysteresis effects. Instead, a mathematically ascertainable functional relation can be created between the stress rate and the elastic strain rate.

$$\dot{\boldsymbol{\sigma}} = \underset{4}{\boldsymbol{C}}\ \dot{\boldsymbol{\varepsilon}}_{\mathrm{el}} \tag{2.110}$$

As shown in the case of thermoelasticity, the overall strain tensor can be additively split into two constitutive parts: an elastic one $\boldsymbol{\varepsilon}_{\mathrm{el}}$ and the partial plastic strain tensor $\boldsymbol{\varepsilon}_{\mathrm{pl}}$.

$$\dot{\boldsymbol{\varepsilon}} = \dot{\boldsymbol{\varepsilon}}_{\mathrm{el}} + \dot{\boldsymbol{\varepsilon}}_{\mathrm{pl}} \tag{2.111}$$

Usually, the plastic yielding is mathematically characterized based on appropriately defined so-called yield conditions $\Phi_{\mathrm{pl}}(\boldsymbol{\sigma})$ (i.e. flow condition, yield criterion). A yield condition is a relationship among the coefficients of the stress tensor separating the elastic domain in the stress space (which represents the area inside the yield condition) from the region of plastic yielding. Within this context, the plastic strain rate tensor is defined as follows:

$$\dot{\boldsymbol{\varepsilon}}_{\mathrm{pl}} = \lambda_{\mathrm{pl}} \frac{\partial \Phi_{\mathrm{pl}}(\boldsymbol{\sigma})}{\partial \boldsymbol{\sigma}} \tag{2.112}$$

with the so-called plastic multiplier $\lambda_{\mathrm{pl}}$. Consequently, the constitutive relation (2.110) can be reformulated.

$$\dot{\boldsymbol{\sigma}} = \underset{4}{\boldsymbol{C}} \left( \dot{\boldsymbol{\varepsilon}} - \lambda_{\mathrm{pl}} \frac{\partial \Phi_{\mathrm{pl}}(\boldsymbol{\sigma})}{\partial \boldsymbol{\sigma}} \right) \tag{2.113}$$

It is generally accepted that plastic yielding is accompanied by incompressible (volume-preserving) deformation processes. Thus, yield conditions are usually defined in terms of the deviatoric stress tensor.

$$\boldsymbol{\sigma}_d = \boldsymbol{\sigma} - \frac{1}{3}\mathrm{tr}(\boldsymbol{\sigma})\,\mathbf{I} \tag{2.114}$$

One of the most widely-used and simplest models is known as von Mises yield condition

$$\Phi_{\mathrm{pl}}(\boldsymbol{\sigma}) = \sqrt{\frac{3}{2}\boldsymbol{\sigma}_d \cdot\cdot \boldsymbol{\sigma}_d} - \sigma_0 = 0 \tag{2.115}$$

with the initial yield stress $\sigma_0$ and the second invariant of the stress deviator.

$$\boldsymbol{\sigma}_d \cdot\cdot \boldsymbol{\sigma}_d = (\sigma_d)_{ij}(\sigma_d)_{ij} = (\sigma)_{ij}(\sigma)_{ij} - \frac{1}{3}(\sigma_{ij}\delta_{ij})^2 \tag{2.116}$$

A generalization of the von Mises yield condition is the Drucker-Prager model with the material parameters $a$ and $b$.

$$\Phi_{\mathrm{pl}}(\boldsymbol{\sigma}) = \sqrt{\frac{2}{3}\boldsymbol{\sigma}_d \cdot\cdot \boldsymbol{\sigma}_d} - b\,\mathrm{tr}(\boldsymbol{\sigma}) - a = 0 \tag{2.117}$$

Within the context of the analysis of geomaterials, elastic-plastic material models play a specific role for soils, whereas their relevance in rock mechanics for subsurface studies is rather minor due to the hardly observable cyclic processes.

### 2.5.5 Viscoelasticity

Viscoelasticity is a typical material property of amorphous substances, particularly polymeric materials. If a wide variety of individual macromolecular chains exhibit elastic material behavior under external loading, networks of macromolecular chains are characterized by internal friction causing rate-dependent effects. Additionally, during mechanical loading, a certain part of strain energy transforms into heat, which is responsible for the existence of hysteresis effects. Relaxation (decrease of stress values at constant strain after instantaneous loading) and retardation (creep—increase of strain values at constant stress after instantaneous loading) are typical mechanical phenomena for viscoelastic materials. Both, relaxation and creep, tend towards asymptotic values, which represent the equilibrium elastic state. In the equilibrium state of viscoelastic materials (at sufficiently small loading rates) no hysteresis occurs. Additionally, no hysteresis is observed at very high loading rates. In this case, the viscoelastic material behavior can be approximated by elastic models using instantaneous parameters.

In contrast to elastoplastic materials, viscoelastic dissipative hysteresis effects are not necessarily accompanied by irreversible deformation processes. A certain heat supply and/or a sufficiently long recovery period can reestablish the shape of a viscoelastic body after mechanical loading.

There exists a wide variety of viscoelastic material models in terms of integral equations or differential relations. A large number of them represent the generalization and modification of uniaxial approaches, which are based on more or less complex rheological models. The simplest viscoelastic rheological models consist of one spring and one dashpot element, respectively (see Fig. 2.21).

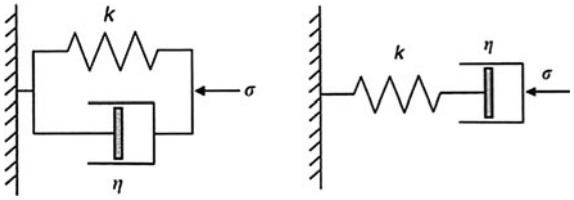


Figure 2.21: Mathematical modeling of reversible rate-dependent solid material behavior. Different combinations of a spring element with a dashpot element [48]: Kelvin-Voigt model (*left*) and Maxwell model (*right*)

The parallel connection of the spring and the dashpot elements is known as Kelvin-Voigt model. It is characterized by equal displacements (and therefore equal strain values) in both of the individual elements, whereas the stress value of the model will be the sum of the stresses in the spring and the dashpot. The constitutive behavior of the Kelvin-Voigt model is described by a differential equation.

$$\sigma = k\,\varepsilon + \eta\,\dot{\varepsilon} \tag{2.118}$$

If a stress $\sigma_0$ is instantaneously applied to a Kelvin-Voigt model, which is held constant thereafter, the solution of the differential equation (2.118) is given as follows:

$$\varepsilon = \frac{\sigma_0}{k}\left[1 - \mathrm{e}^{-kt/\eta}\right] \tag{2.119}$$

which indicates that the strain increases asymptotically to its steady-state (elastic) value $\sigma_0/k$. Thus, the Kelvin-Voigt model represents the typical strain retardation, but neglecting any instantaneous strain.

The series connection of the spring and the dashpot elements is known as the Maxwell model. Within this context, equal stress values occur in both of the individual elements, whereas the total displacement (and therefore the strain) of the model will be the sum of the displacements in the spring and the dashpot. The constitutive behavior of the Maxwell model can again be described by a differential equation.

$$\dot{\varepsilon} = \frac{1}{\eta}\,\sigma + \frac{1}{k}\,\dot{\sigma} \tag{2.120}$$

Applying an instantaneous stress, a Maxwell element exhibits an instantaneous elastic response characterized by the spring constant $k$, and a long-term viscous response specified by the viscosity $\eta$. If the Maxwell substance is subjected to an instantaneous jump in strain with the amplitude $\varepsilon_0$, which is held constant thereafter, the differential equation (2.120) can be solved closely. The solution

$$\sigma = k\,\varepsilon_0\,\mathrm{e}^{-kt/\eta} \tag{2.121}$$

indicates a stress decrease (relaxation) at constant (non-zero) strain, whereas in case of the Maxwell model the stress relaxes to zero, simulating the behavior of a viscoelastic fluid.

### 2.5.6 Viscoplasticity

Viscoplasticity is the most general material class, and the constitutive theories of viscoplasticity must be defined, on principle, to model all macroscopically observable phenomena of material behavior. The viscoplastic material class combines elements of all the other classes presented above. Micromechanical phenomena causing viscoplastic material behavior are exceptionally complex.

Here we will focus on only one typical effect of viscoplastic material behavior particularly relevant for geomaterials—creep processes. Although in both cases characterizing the strain evolution at constant stress, viscoplastic creep differs from the viscoelastic creep (retardation) mentioned above, because no asymptotical strain value will be reached in the viscoplastic case. A typical viscoplastic creep curve is shown in Fig. 2.22.

Generally, for the viscoplastic creep behavior, three typical periods can be observed. Whereas at all creep periods strain increases without reaching any asymptotical value, they differ in the strain rate. The first period, called primary creep, is characterized by a decreasing creep rate (transient creep), while for the second creep period, called secondary creep, a constant strain rate is observed (stationary creep, steady-state creep). The period of more or less constant strain rate is followed by the tertiary creep with an ever-increasing strain rate, eventually causing mechanical failure of the structure under consideration. The total reduction of the applied stresses results in a strain relaxation. Unloading in the primary creep period is characterized by a complete strain relaxation (similar to viscoelatic behavior). However, if stress is removed during the secondary creep period, residual strains remain (effect of plasticity).

Similar to elastoplasticity, a viscoplastic stress-strain constitutive relationship begins with the relationship between stress rate and elastic strain rate given by

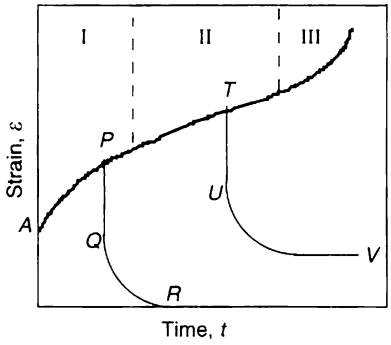


Figure 2.22: Schematical representation of a viscoplastic creep curve showing the three typical periods: primary, secondary, and tertiary creep [48]. The three periods are indicated by the Roman numerals I, II and III, the point $A$ indicates the instantaneous elastic strain

(2.110). The overall strain tensor is additively decomposed into several constitutive parts: apart from the partial elastic and plastic strain tensors a creep strain tensor is introduced $\boldsymbol{\varepsilon}_{\mathrm{c}}$.

$$\dot{\boldsymbol{\varepsilon}} = \dot{\boldsymbol{\varepsilon}}_{\mathrm{el}} + \dot{\boldsymbol{\varepsilon}}_{\mathrm{pl}} + \dot{\boldsymbol{\varepsilon}}_{\mathrm{c}} \tag{2.122}$$

Similar to the plastic potential (yield condition), the creep behavior is mathematically characterized based on appropriately defined creep potentials $\Phi_{\mathrm{c}}(\boldsymbol{\sigma})$ representing, again, relationships among the coefficients of the stress tensor. Consequently, the creep strain rate tensor is defined as follows:

$$\dot{\boldsymbol{\varepsilon}}_{\mathrm{c}} = \lambda_{\mathrm{c}} \frac{\partial \Phi_{\mathrm{c}}(\boldsymbol{\sigma})}{\partial \boldsymbol{\sigma}} \tag{2.123}$$

with the so-called creep multiplier $\lambda_{\mathrm{c}}$. Consequently, the constitutive relation (2.110) can be reformulated.

$$\dot{\boldsymbol{\sigma}} = \underset{\mathbf{4}}{\boldsymbol{C}} \left( \dot{\boldsymbol{\varepsilon}} - \lambda_{\mathrm{pl}} \frac{\partial \Phi_{\mathrm{pl}}(\boldsymbol{\sigma})}{\partial \boldsymbol{\sigma}} - \lambda_{\mathrm{c}} \frac{\partial \Phi_{\mathrm{c}}(\boldsymbol{\sigma})}{\partial \boldsymbol{\sigma}} \right) \tag{2.124}$$

In geomechanics, the long-term rock behavior during the stationary creep period is the main focus of interest. One widely-used creep potential characterizing secondary creep is the so-called Norton's model

$$\Phi_{\mathrm{c}}(\boldsymbol{\sigma}) = \frac{\alpha}{n+1} \left( \sqrt{\frac{3}{2} \boldsymbol{\sigma}_d \cdot\cdot \boldsymbol{\sigma}_d} \right)^{n+1} \tag{2.125}$$

with the material parameters $\alpha$ and $n$.

All of the constitutive models mentioned above are idealized approximations of the actual material behavior. The presented models are relatively simple, and allow a first insight into the material theory of deformable solid substances. Some other aspects, which are relevant for rock mechanical analysis of material behavior, could not be considered here and are subject of further studies, such as:

- Rate-dependent deformation processes in porous media are caused by the pore pressure diffusion through the solid skeleton at a finite rate, and intrinsic viscous properties of the matrix material. A separate experimental observation of these effects is quite challenging with according consequences to the constitutive modeling.
- Certain geomaterials show a layered structure (e.g. shale, sandstone). Consequently, material properties of these substances depend on the direction of the impact of external forces (known as anisotropic material behavior), which has to be considered in constitutive relations.
- The damage and failure of rock plays an important role in real geoprocesses, and require individual consideration.

- The analysis of wave propagation (dynamic phenomena) in geomaterials is relevant for all kinds of seismic activities or seismic analyses.
- The design of appropriate lab tests is essential for the fundamental characterization of material behavior, and the calibration of constitutive models.

## 2.6 Porous Medium Properties

We have considered the properties of fluid (Sect. 2.4) and solid phases (Sect. 2.5), respectively. Many of the properties of a porous medium can be determined based on the assumption of the local thermodynamic equilibrium allowing a superposition of phase related characteristics—except of the hydraulic properties for multiphase flow, which are discussed in more detail in this section. We begin with the different definitions of saturation.

### 2.6.1 Saturation

Saturation of a fluid phase $\gamma$ is defined as the volumetric fraction $\epsilon^\gamma$ related to the sum of all fluid phases volumetric fractions.

$$S^\gamma = \frac{\epsilon^\gamma}{\sum_\gamma \epsilon^\gamma} \tag{2.126}$$

The sum of saturations of all fluid phases must be equal to unity (Sect. 2.2.2). Effective saturation is defined as [49]

$$S^\gamma_{\text{eff}} = \frac{S^\gamma - S^\gamma_r}{1 - S^\gamma_r} \tag{2.127}$$

Moisture content (volumetric water content) is defined as the product of porosity and saturation.

$$\theta^\gamma = nS^\gamma \tag{2.128}$$

Gravimetric water content is defined as

$$\omega^\gamma = nS^\gamma \frac{\rho^s_d}{\rho^\gamma} \tag{2.129}$$

Applying the chain rule, we can express saturation changes in following way.

$$dS^\gamma = \frac{dS^\gamma}{dp^\gamma} dp^\gamma \tag{2.130}$$

The capillary pressure-saturation functions, as well as the relations between relative permeability and saturation, are substantial constitutive equations required for multiphase flow. Within this context, usually algebraic expressions are fit to the corresponding experimentally observed curves. Among the most widely-used of these algebraic expressions are the Brooks-Corey [50] and van

Genuchten [51] relations. If both are realized within the scientific software code developed by the authors, the numerical results presented in this chapter are based on Brooks-Corey's approach.

### 2.6.2 Capillary Pressure and Relative Permeability

As a consequence of interfacial tension, a discontinuity in fluid pressure exists across the interface that separates two immiscible fluids. The partial pressure difference between two phases is denoted as capillary pressure, which is a function of saturation.

$$p_c^{\alpha\beta} = p^\beta - p^\alpha = f(S^\alpha) \tag{2.131}$$

In general, capillary pressure is the difference between partial pressures of non-wetting and wetting phases.

$$p_c = p^{nw} - p^w = f(S^w) \tag{2.132}$$

Capillary pressure is always positive: $p_c > 0, \forall S$. It is often assumed that air is at a constant atmospheric pressure taken as zero $p^g = 0$. This means, the macroscopic pressure of water in the unsaturated zone is always negative due to suction. Capillary pressure must be measured for given soils and pairs of fluids. In general, these experiments are conducted for equilibrium conditions with no fluid in motion. Various authors have proposed analytical functions for capillary pressure—saturation—relationships.

The capillary pressure/saturation relationships differ for drainage and rewetting (imbibition) [52]. This phenomenon is called hysteresis (Fig. 2.23). Reasons for

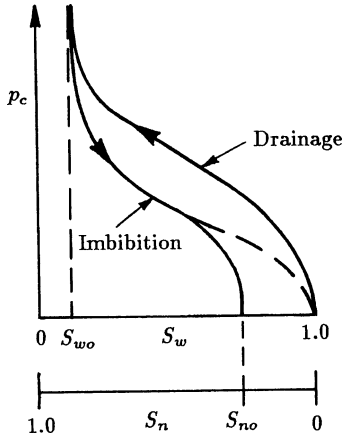


Figure 2.23: Capillary hysteresis [8], with $S_w = S^w$, $S_{w0} = S_r^w$, $S_n = S^{nw}$, $S_{n0} = S_r^{nw}$

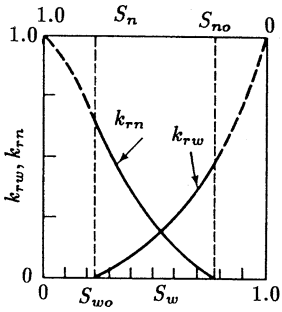


Figure 2.24: Relative permeability functions [8] with $S_w = S^w$, $S_{w0} = S^w_r$, $S_n = S^{nw}$, $S_{n0} = S^{nw}_r$, $k_{rn} = k^{nw}$, $k_{rw} = k^w$

capillary pressure hysteresis are: (i) varying pore shape (ink-bottle effect), (ii) contact angle hysteresis (raindrop effect), (iii) entrapment of non-wetting fluids, (iv) swelling and shrinking of solid grains.

To introduce the concept of relative permeability we recall the Darcy law for flow of multiple fluid phases through porous media, (2.72). Figure 2.24 shows an example of relative permeabilities for both wetting and non-wetting phases.

We consider some of the most used models after van Genuchten, Haverkamp and Brooks–Corey.

**van Genuchten Model [51]**

The definitions of effective saturation, capillary pressure and relative permeability for the van Genuchten model are as follows

$$S_{\text{eff}} = \frac{S^w - S^w_r}{1 - S^w_r} = (1 + (\alpha\, p_c)^n)^m\,, \qquad p_c > 0 \tag{2.133}$$

$$p_c = \begin{cases} 0 & S^w > S^w_{\max} \\ \frac{\rho^w g}{\alpha}(S^{-1/m}_{\text{eff}} - 1)^{1/n} & S^w_r < S^w < S^w_{\max} \\ p_{c\max} & S^w < S^w_r \end{cases} \tag{2.134}$$

with

$$m = 1 - \frac{1}{n} \tag{2.135}$$

$$\mathbf{k}_{\text{rel}}(h) = \frac{1 - (\alpha h)^{n-2}\,[1 + (\alpha h)^n]^{-m}}{[1 + (\alpha h)^n]^{2m}} \tag{2.136}$$

Figures 2.25 and 2.26 show the capillary pressure and relative permeability functions corresponding to the parameters given in Table 2.9, respectively.

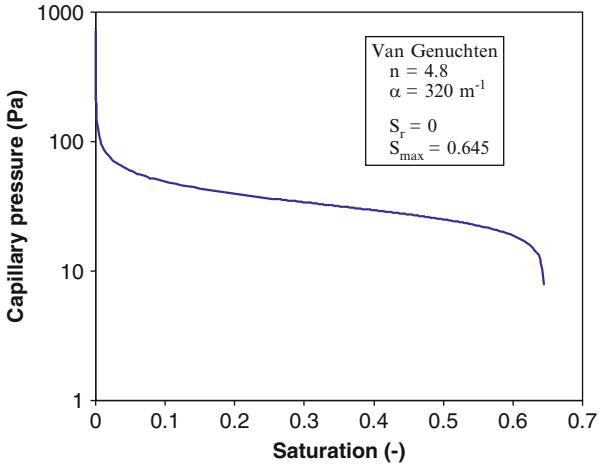


Figure 2.25: Capillary pressure / saturation relationship (Tuebingen experiment 2005)

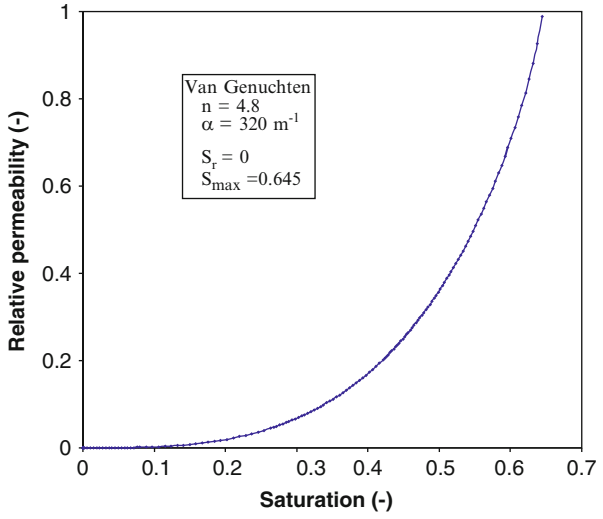


Figure 2.26: Relative permeability / saturation relationship (Tuebingen experiment 2005)

### Haverkamp Model [53]

The formulas for the Haverkamp model are given in terms of pressure head $h = p^w/g\rho^w$ and moisture content $\theta = nS^w$. The definitions of effective saturation, capillary pressure and relative permeability for the Haverkamp model are

Table 2.9: Model parameter

| | | | |
|---|---|---|---|
| $S_r^w$ | Residual water saturation | 0 | |
| $S_{max}^w$ | Maximal water saturation | 0.645 | |
| $n$ | vG parameter | 4.8 | |
| $\alpha$ | vG coefficient | 320 | $[m^{-1}]$ |

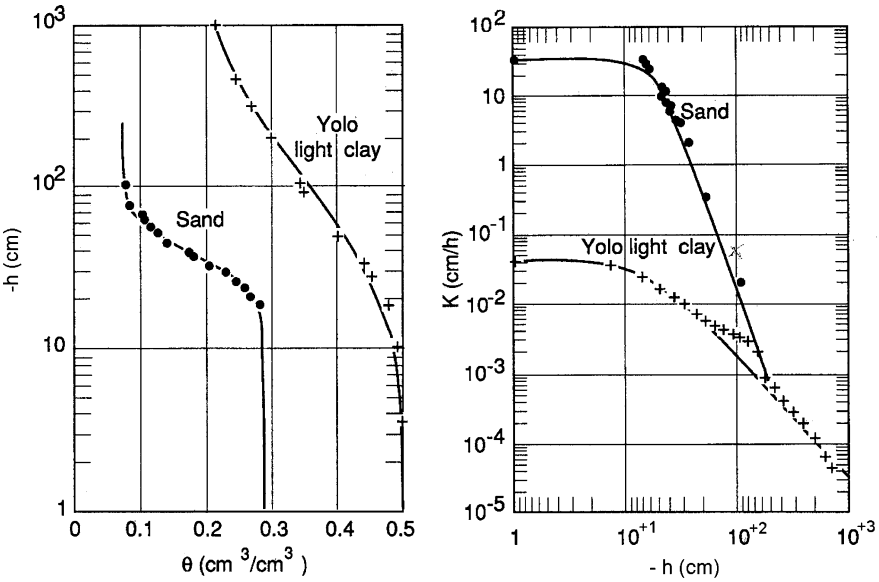


Figure 2.27: Hydraulic properties of unsaturated soil [53]

as follows

$$\theta = \frac{\alpha(\theta_s - \theta_r)}{\alpha + |h|^\beta} + \theta_r \tag{2.137}$$

$$h = \left(-\frac{\alpha}{\theta}(\theta - \theta_s + \theta_r)\right)^{1/\beta} \tag{2.138}$$

$$\mathbf{k}_{\text{rel}}(h) = K_s \frac{A}{A + |h|^\beta} \tag{2.139}$$

Figure 2.27 shows the capillary pressure saturation function corresponding to the parameters given in Table 2.10.

**Brooks & Corey Model [49]**

The Brooks–Corey equations relating the saturation to the capillary pressure are

$$p^c = p^D S_{\text{eff}}^{-(1/\lambda)} \quad \text{for} \quad p^c \geq p^D \tag{2.140}$$

Table 2.10: Model parameter

| | | | |
|---|---|---|---|
| $\theta$ | Volumetric water (moisture) content | | $[cm^3/cm^3]$ |
| $\theta_r$ | Residual volumetric water content | 0.075 | $[cm^3/cm^3]$ |
| $\theta_s$ | Saturated volumetric water content | 0.287 | $[cm^3/cm^3]$ |
| $h(\theta)$ | Soil water pressure head relative to the atmosphere | | [cm] |
| $\alpha$ | | $1.611 \times 10^6$ | $[Pa^{-1}]$ |
| $\beta$ | | 3.96 | |

where $p^D$ is usually known as entry pressure, $\lambda$ is a pore-size distribution index. $S_{\text{eff}}$ is a normalized wetting fluid saturation. For the case of $CO_2$ as wetting fluid into a saline aquifer it is defined as

$$S_{\text{eff}} = \frac{S^l - S^l_{\text{res}}}{1 - S^l_{\text{res}} - S^{CO_2}_{\text{res}}} \tag{2.141}$$

where $S^l_{\text{res}}$ is the wetting phase residual or irreducible saturation, and $S^{CO_2}_{\text{res}}$ is the nonwetting phase residual saturation. The constitutive parameters $p^D$, $\lambda$, $S^l_{\text{res}}$ and $S^{CO_2}_{\text{res}}$ are identified by fitting (2.140) to experimental data. Within this context, the entry pressure is to be understood as the minimum pressure that the nonwetting fluid must have to enter the largest pores. The relations between the relative permeability and the saturation are given by

$$k^l_{\text{rel}} = (S_{\text{eff}})^{(2+3\lambda)/\lambda} \tag{2.142}$$

$$k^{CO_2}_{\text{rel}} = (1 - S_{\text{eff}})^2 \left(1 - (S_{\text{eff}})^{(2+\lambda)/\lambda}\right) \tag{2.143}$$

# Chapter 3

# Numerical Methods

*by Wenqing Wang, Chan-Hee Park, Norihiro Watanabe, and Olaf Kolditz*

The design, implementation and application of the object-oriented programming (OOP) concept in the finite element analysis of multi-field problems is presented in this chapter.

The basic idea of this concept is that the underlying governing equations of porous media mechanics can be classified into different types of partial differential equations (PDEs). In principle, equal types of PDEs for diverse physical problems differ only in material coefficients. Local element matrices and vectors arising fromthe finite element discretization of the PDEs are categorized into several types, regardless of which physical problem they belong to (i.e. fluid flow, mass and heat transport or deformation processes). Element (ELE) objects are introduced to carry out the local assembly of the algebraic equations. The object-orientation includes a strict encapsulation of geometrical (GEO), topological (MSH), process-related (FEM) data and methods of element objects. Geometric entities of an element such as nodes, edges, faces and neighbors are abstracted into corresponding geometric element objects (ELE-GEO). The relationships among these geometric entities form the topology of element meshes (ELE-MSH). Finite element object (ELE-FEM) is presented for the local element calculations, in which each classification type of the matrices and vectors is computed by a unique function. These element functions are able to deal with different element types (lines, triangles, quadrilaterals, tetrahedra, prisms, hexhedra) by automatically choosing the related element interpolation functions. For each process of a multi-field problem, only a single instance of the finite element object is required. The element objects provide a flexible coding environment for multi-field problems with different element types. Here, the

O. Kolditz et al. (eds.), *Thermo-Hydro-Mechanical-Chemical Processes in Fractured Porous Media*, Lecture Notes in Computational Science and Engineering 86,
DOI 10.1007/978-3-642-27177-9_3, © Springer-Verlag Berlin Heidelberg 2012

C++ implementations of the objects are given and described in detail. The efficiency of the new element objects is demonstrated by several test cases dealing with thermo-hydro-mechanical (THM) coupled problems for geotechnical applications.

## 3.1 Introduction

The numerical analysis of complex multi-field problems is an important issue for many engineering problems. A representative example is nuclear waste disposal. Nuclear waste repositories are constructed in deep geologic underground. Normally, the radioactive waste will generate heat for a long period of time with temperatures over 100°C. Possibly, ground water flow may be developed and gas will be produced due to the heating of the ground water. The coupling of thermal and hydraulic processes can cause mechanical damage in the near field of the host rock mass. To assess the safety of the underground repositories, the problem needs to be addressed as a thermo-hydro-mechanical (THM) coupled problem [54–60]. Although some commercial tools are already available, there is a tremendous demand for the development of fully coupled THM codes. Existing concepts couple obtainable codes which are specialized to hydraulic, mechanic or deformation problems. The coupling is then realized by data exchange between these codes. This procedure causes a rigorous restriction of the modeling of coupling phenomena. In this work we present a finite element class which can deal with thermal, hydraulic as well as mechanic problems.

For the programming paradigms, there are two alternatives for finite element code design and development, i.e. procedure-oriented or object-oriented. The former does not encapsulate data and methods manipulating the data together, the latter does encapsulate data and methods and provides regulated communication between data and methods to perform tasks [61, 62]. The object oriented paradigm facilitates the management of abstract data with its capabilities of data encapsulation, polymorphism, and inheritance. Therefore, it provides an easy way to develop and to maintain a code. This is one reason why more and more researchers are shifting from using a procedure oriented to an OOP paradigm in numerical analysis. Other reasons for its popularity include that procedure oriented software of such complexity has to be developed by an ever increasing number of programmer teams. OOP has significant advantages by allowing rapid software development through capsulation, inheritance and polymorphism of data and methods. The advantages of object-oriented programming for the development of engineering software was described in detail by [63].

Although the fundamentals of object-orientated programming (OOP) were established in the 1960s, it remains a very important concept when facing challenges in scientific computation, such as the solution of coupled multi-field problems. One of the first applications of the object-oriented paradigm to finite element analysis was published in 1990 [64], where essential components of finite element methods such as elements, nodes and materials were abstracted

into classes. More efforts have been made by [65–71] in order to demonstrate the advantages of OOP over the procedure oriented programming. Moreover, the applications to many different physical problems have been investigated, such as linear stress analysis [67–69], hypersonic shock waves [72], structural dynamics [73], 2D Mises plasticity [74], linear static problems [75, 76], electro-magnetics [77], solidification process [78], heat transfer as well as topological buildup [79]. A process-oriented approach for the solution of multi-field problems in porous media is presented in [59, 80]. Numerical objects for algebraic calculations in finite element analysis have been developed by [81–83]. In order to provide an automatic coding environment for finite element analysis, a symbolic code development concept is presented for the weak forms arising from the partial differential equations [84–87].

Object design is the fundamental step in object-oriented programming. The utilization of OOP to finite element analysis is mainly focused on three aspects: (1) pre/post processing such as mesh generation and graphical user interface, (2) linear algebra and (3) finite element methods. In all these aspects, the core object is the element object. The design of element objects is associated with other objects corresponding to material properties, numerical methods, local geometry and topology of element etc. Specific material objects are described in most of references cited above.

In this part we present the design, implementation and application of object-orientation in finite element analysis for multi-physics problems. The development of a universal object for local finite element calculation and assembly is capable of coping with different kinds of physical problems (i.e. different types of partial differential equations) and is, in particular, designed for strongly coupled problems. Additionally, object-orientation is used in description of mesh topology for the global assembly of system equations. The description of the programming semantics of these objects is given in C++. All the developments of this work are conducted within the framework of the scientific software project OGS (`http://www.opengeosys.net`). The OO-FEM concept is verified by numerous test cases dealing with thermo-hydro-mechanical (THM) coupled problems in geotechnical as well as hydrological applications (Parts II and III of this book.)

## 3.2 Object-Orientation in Finite Element Analysis

Almost all numerical methods eventually have to deal with the solution of algebraic equation systems. The basic algorithms for the discretization of partial differential equations (PDEs) resulting from the initial-boundary-value-problems (IBVPs) of continuum mechanics can be generalized in principle as follows: time discretization, calculation of problem-specific node (finite difference method: FDM), element (finite element method: FEM), volume (finite volume method:

FVM) contributions, incorporating initial and boundary conditions, assembling and solving the resulting equation system. For non-linear problems, iteration schemes, such as Picard or Newton methods, have to be used.

The general solution algorithm for the finite element method is given in Table 3.1.

The implementation of the general solution algorithm for multi-field IBVPs according to Table 3.1 is illustrated in Fig. 3.1. The time loop represents time discretization. Within the time loop, specified physical processes (e.g. flow, transport, deformation) are solved using the finite element method (left box).

Table 3.1: General solution procedure of the finite element method

1. Domain discretization (i.e. mesh generation): Creation of individual geometric elements (e.g. triangles, tetrahedra) and their topological relationships (mesh topology).
2. Local element assembly: Depending on PDE type (Sect. 3.3) all element matrices and vectors have to be computed. The element integration requires geometric operations such as interpolation with shape functions, calculation of inverse Jacobians and determinants. Additionally material functions have to be computed in Gauss points. Material functions can depend on field variables.
   - Geometric element operations (shape functions, Jacobian),
   - Material parameter calculation at Gauss points,
3. Global assembly of the algebraic equation $\mathbf{Ax} = \mathbf{b}$: The local element entries are assembled into the global system matrix $\mathbf{A}$ and global RHS vector $\mathbf{b}$. The system of equations is established after incorporating boundary conditions and source/sink terms.
   - Assembly of system matrix $\mathbf{A}$ (including incorporation of boundary conditions),
   - Assembly of RHS vector $\mathbf{b}$ (including incorporation of source/sink terms),
4. Solving the system equations,
5. Iterative methods to handle non-linearities,
6. Iterative methods to handle couplings (partitioned and monolithic schemes).

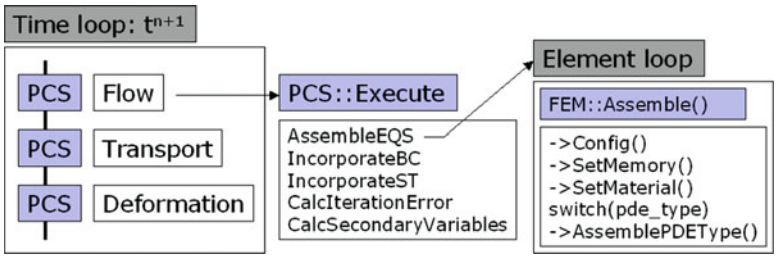


Figure 3.1: Implementation of solution algorithm

The solution procedure of each process is unique (middle box). The basic part is the calculation and assembly of element contribution (right box).

Based on above described general solution algorithm for multi-field IBVPs, the fundamental concept of object-orientation in finite element analysis is the generalization of

- Process (PCS) types (Sect. 3.2.1),
- Equation (PDE) types (Sect. 3.2.2),
- Element (ELE) types (Sect. 3.2.3).

### 3.2.1 Process (PCS) Types

The central idea behind object-orientation of processes is that the basic steps of the solution procedure: calculation of element contributions, assembly of equation system (including treatment of boundary conditions and source terms), solution of the equations system, linearization methods and calculation of secondary variables, are independent of the specific problem (e.g. flow, transport, deformation processes) [80, 88]. The process (PCS) class provides basic methods in order to solve a PDE in a very general way. The central part of the PCS object is the member function `PCS::Execute()` (Fig. 3.1, middle box) conducting these basic steps. Specific properties of the mechanical problem, such as PDE type, primary and secondary variables and material functions, are assigned during process configuration (member function `PCS::Config()`). In order to configure PCS instances we take advantage of polymorphism.

Figure 3.2 illustrates the object-orientation of PCS types for the solution of IBVPs. The PCS object was designed to manage the complete solution algorithm in order to build the global equation system (EQS). In fact, the PCS object 'only' administrates references to geometric (GEO) objects (points, polylines, surfaces, volumes); MSH objects (mesh nodes, elements and mesh topology), node-related data such as initial (IC) and boundary (BC) conditions as well as source terms (ST); material data of porous media (fluid (MFP), solid (MSP), medium (MMP) and chemical (MCP) properties); parameters of the different

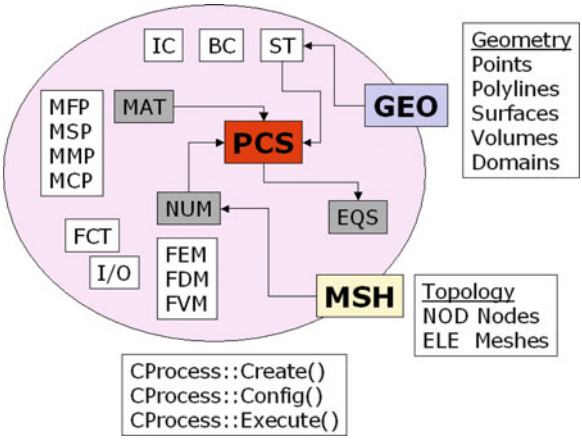


Figure 3.2: Structure of the process (PCS) object

numerical methods (NUM). PCS instances have 'only' pointers to the related objects as members. Objects IC, BC and ST have pointers to object GEO to specify geometrical entities, which are managed by PCS to find element nodes on them. The values in IC and BC and ST are assigned to element nodes found be their GEO members. Object GEO also play a key role in the pre/post-process of the data of the finite element method.

### 3.2.2 PDE Types

When dealing with IBVPs in porous media mechanics, such as fluid flow, mass and heat transport, deformation can be categorized into elliptic, parabolic, hyperbolic or mixed equation types.

As an example to explain the generalization of PDE types, we illustrate the treatment of Laplace terms, which appear in flow, transport as well as deformation processes. In Fig. 3.3 the evaluation of finite element matrices for Laplace terms, i.e. $\mathbb{D}\partial^2/\partial x^2$ is given, where $\mathbb{D}$ is a problem-specific material tensor. The special part of diffusion terms is the calculation of second order space derivatives. The second line of the equation in Fig. 3.3 represents the numerical integration of the matrix being transformaed into reference coordinates. From the view point of object-orientation we are faced with the following operations: tensor coordinate transformation ($\mathbf{T}$), Jacobian ($\mathbf{J}$), integration ($\int$) and computation of material properties ($\mathbb{D}$, e.g. diffusivity, conductivity tensor). The latter is the only problem-specific.

$$\mathbf{K}_e = \int_{\Omega_e} \nabla \boldsymbol{N} \mathbb{D} (\nabla \boldsymbol{N})^{\mathrm{T}} d\Omega \tag{3.1}$$

$$= \sum_{gp=1}^{no\_gp} \int_{\Omega_r} w_{gp} \left[ \nabla \boldsymbol{N} \mathbb{D} (\nabla \boldsymbol{N})^{\mathrm{T}} \det \mathbf{J} \right] |_{gp} d\Omega \tag{3.2}$$

```
void CFiniteElement::CalcLaplace()
{
  // Loop over Gauss points
  for (gp = 0; gp < no_gp; gp++)
  {
     GaussData();                  // Integration points and weights
     Jacobian();                   // det J, J^-1
     GradShapefct();               // ∇N
     LaplaceMATFunction();         // Material parameters, 𝔻
     for (i=0; i<nnodes; i++)      // Loop over element nodes
        for (j = 0; j < nnodes; j++)
         {
            if(j>i) continue;      // Symmetry
            for (k = 0; k < ele_dim; k++)
               for(l=0; l<ele_dim; l++)
                  (*Laplace)(i,j) += fkt * dshapefct[k*nnodes+i]
                                     * mat[ele_dim*k+l]
                                     * dshapefct[l*nnodes+j];
         }
  }
}
```

Figure 3.3: Finite element Laplace matrix and implementation

Figure 3.3 shows the implementation of the Laplace term calculation, in which $\Omega_r$ is the domain by the reference element. The `CalcLaplace()` member function of the finite element class works for different processes with different material functions (Fig. 3.4) and geometric element types. A short description is given in the table below.

| Code | Description |
|---|---|
| `gp` | Gauss integration points |
| `GaussData()` | Calculation of Gauss weights |
| `Jacobian()` | Calculation of Jacobian determinant and inverse |
| `GradShapeFunction()` | Calculation of shape function derivatives |
| `LaplaceMATFunction()` | Calculation of material coefficients |
| `(*Laplace)(i,j)` | Finite element matrix |

### 3.2.3 Element (ELE) Types

The basic concept we apply is that: element data, such as geometrical and topological properties, as well as operations of elements, such as element matrix calculations and treatment of boundary conditions, can be generalized.

```
void CFiniteElementPCS::LaplaceMATFunction()
{
  // Calculate conductivity tensor 𝔻 for Laplacian
   switch(PcsType){
      case L: // Liquid flow
      case U: // Unconfined flow
      case G: // Gas flow
      case T: // Two-phase flow
      case C: // Componental flow
      case H: // Heat transport
      case M: // Mass transport
      case O: // Overland flow
      case R: // Richard flow
   }
}
```

Figure 3.4: Implementation of process dependent material functions

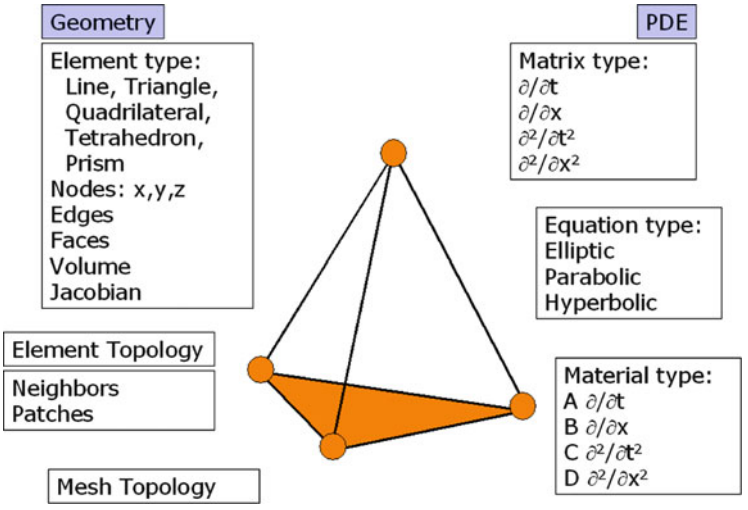


Figure 3.5: Structure of element object

The element object is the fundamental entity in both PDE and element types. In Fig. 3.5 the structure of the element object is illustrated. The element has two kinds of properties, connected geometry and PDE types.

Element geometry includes the geometric type (line, triangle, quad, tetrahedron, prism, hexahedron), node coordinates, edges, faces and volume. Coordinate transformation functionalities are considered as geometric element properties. Element topology is defined by element neighbor relationships. Patch properties are available for finite volume approaches and flux calculations. The elements form the mesh topology. Different geometric element types can be combined

(Fig. 3.5) together to establish a mesh. Additionally, elements can be assigned to different meshes.

Depending on PDE type (elliptic, parabolic, hyperbolic, mixed), different first or second order differential terms have to be evaluated ($\partial/\partial t, \partial/\partial x, \partial^2/\partial t^2$, $\partial^2/\partial x^2$). These differential terms are categorized in corresponding FE matrix types (see Sect. 3.3), mass matrix, Laplacian matrix, tangential matrix and coupling matrices. An obvious advantage of this element concept is that, depending on the geometric element type, interpolations (shape functions) and derivations as well as tensor operations and Gaussian integrations are conducted automatically in a correct way (see Sect. 3.4.2). For material tensor properties in 1D, 2D or 3D ($\mathbf{A}, \mathbf{B}, \mathbf{C}, \mathbf{D}(\mathbf{x})$ in Fig. 3.5), the correct matrix multiplications are conducted automatically. Material functions ($A, B, C, D(u)$ in Fig. 3.5) are evaluated accordingly at corresponding Gaussian points of the selected element.

For the sake of object-orientation for numerical methods a so-called process (PCS) object was designed, implemented ([80], Sect. 3.2.1) and successfully applied to different numerical methods (FEM: [59], FDM: [89], FVM: [90]).

## 3.3 General Finite Element Formulations

The method of weighted residuals is applied to derive the weak formulation of the balance equations given in Sect. 2.3.

Assume $\mathcal{V}^{\mathrm{n}} \subset H^1_{\Gamma}(\Omega)^{\mathrm{n}}$ is the test function space. For all $w \in \mathcal{V}^1$, we have the weak form of the mass balance equation (2.59) as

$$\int_{\Omega} \left( nS^{\gamma} \frac{\partial \rho^{\gamma R}}{\partial t} + nS^{\gamma} \boldsymbol{v}^{\gamma s} \cdot \nabla \rho^{\gamma R} + n\rho^{\gamma R} \frac{\partial S^{\gamma}}{\partial t} + n\rho^{\gamma R} \boldsymbol{v}^{\gamma s} \cdot \nabla S^{\gamma} + \nabla \cdot (\rho^{\gamma} n S^{\gamma} \boldsymbol{v}^{\gamma s}) + S^{\gamma} \rho^{\gamma R} \nabla \cdot \dot{\boldsymbol{u}}^{s} - q^{\gamma} \right) w \, \mathrm{d}\Omega = 0 \tag{3.3}$$

Applying integration by parts, divergence terms can be rewritten as

$$\int_{\Omega} \nabla \cdot \boldsymbol{A} \omega d\Omega = \int_{\Omega} \boldsymbol{A} \cdot \nabla \omega \, \mathrm{d}\Omega + \int_{\Gamma} \boldsymbol{A} \cdot \mathbf{n} \omega \, \mathrm{d}\Gamma \tag{3.4}$$

Under the same assumption, the weak form of heat balance equation (2.78) can be obtained as

$$\int_{\Omega} \sum_{\gamma} (\varepsilon^{\alpha} \rho^{\alpha} c_p^{\alpha}) \frac{\partial T}{\partial t} w \, \mathrm{d}\Omega - \int_{\Omega} \boldsymbol{j}_{\mathrm{th}} \cdot \nabla \omega \, \mathrm{d}\Omega + \int_{\Gamma} \boldsymbol{j}_{\mathrm{th}} \cdot \mathbf{n} \omega \, \mathrm{d}\Gamma - \int_{\Omega} Q_{\mathrm{T}}^{\gamma} w \, \mathrm{d}\Omega = 0 \tag{3.5}$$

Taking into account nonlinearity, the weak form of the momentum balance

equation (2.100) must be fulfilled throughout the load history, i.e.,

$$\int_{\Omega} \frac{1}{2}\left(\boldsymbol{\sigma}_{\text{eff}} - \sum_{\gamma} S^{\gamma} p^{\gamma} \mathbf{I}\right) : \left(\nabla \boldsymbol{w} + (\nabla \boldsymbol{w})^{\mathrm{T}}\right) \, \mathrm{d}\Omega + \int_{\Omega} \boldsymbol{w}^{\mathrm{T}} \cdot \rho \mathbf{g} \, \mathrm{d}\Omega - \int_{\Gamma} \boldsymbol{w}^{\mathrm{T}} \cdot \mathbf{t} \, \mathrm{d}\Gamma = 0 \tag{3.6}$$

for all $\boldsymbol{w} \in \mathcal{V}^{\mathrm{n}}$, $\mathrm{n} = 2, 3$. In principle, the vector form of stress and strain tensor are used to developing the system equation of the discretized weak form of (3.6). Under this form, the constitutive law for the effective stress tensor can be expressed as

$$\boldsymbol{\sigma}_{\text{eff}} = \boldsymbol{C} \, \boldsymbol{\varepsilon}$$

with the corresponding strain-displacement relationship

$$\boldsymbol{\varepsilon} = \mathcal{L} \, \boldsymbol{u}^{s}$$

where $\mathcal{L}$ is an differential operator.

$$\mathcal{L} = \begin{pmatrix} \partial/\partial x & 0 & 0 \\ 0 & \partial/\partial y & 0 \\ 0 & 0 & \partial/\partial z \\ \partial/\partial y & \partial/\partial x & 0 \\ 0 & \partial/\partial z & \partial/\partial y \\ \partial/\partial z & 0 & \partial/\partial x \end{pmatrix} \tag{3.7}$$

We use the Galerkin finite element method to solve the weak forms of balance equations above. All variables are approximated by admissible finite element functions in the Taylor-Hood finite element space, i.e, low order interpolation $\boldsymbol{N}_1 \in \mathbb{R}^{\mathrm{n}}$ for pressure and temperature variables and high order interpolation $\boldsymbol{N}_2 \in \mathbb{R}^{\mathrm{n}}$ for displacement, respectively. As a result of the finite element discretization of the weak forms (3.4), (3.5) and (3.6), we obtain local matrices and vectors for the global system equations [16]. Element matrices and vectors can be classified into following types (Table 3.2)

Table 3.2: Matrix and vector types

| Type | Name | Equations |
|---|---|---|
| $\int_{\Omega} \boldsymbol{N}_1^{\mathrm{T}} \mathcal{M} \boldsymbol{N}_1 \, \mathrm{d}\Omega$ | Mass matrix | (3.4),(3.5) |
| $\int_{\Omega} (\boldsymbol{N}_1)^{\mathrm{T}} \mathcal{M} \nabla \boldsymbol{N}_1 \, \mathrm{d}\Omega$ | Advection matrix | (3.5) |
| $\int_{\Omega} (\nabla \boldsymbol{N}_1)^{\mathrm{T}} \mathcal{M} \nabla \boldsymbol{N}_1 \, \mathrm{d}\Omega$ | Laplace matrix | (3.4),(3.5) |
| $\int_{\Omega} \mathbf{B}^{\mathrm{T}} \mathcal{M} \mathbf{B} \, \mathrm{d}\Omega$ | Tangential matrix | (3.6) |
| $\int_{\Omega} \mathcal{M} \mathbf{B}^{\mathrm{T}} \mathbf{m} \boldsymbol{N}_1 \, \mathrm{d}\Omega$ | Displacement coupling matrix | (3.4) |
| $\int_{\Omega} \mathcal{M} \boldsymbol{N}_1^{\mathrm{T}} \mathbf{m}^{\mathrm{T}} \mathbf{B} \, \mathrm{d}\Omega$ | Pressure coupling matrix | (3.6) |
| $\int_{\Omega} Q \boldsymbol{N}_1 \, \mathrm{d}\Omega \quad , \int_{\Omega} Q \boldsymbol{N}_2 \, \mathrm{d}\Omega$ | Source term vector | (3.4),(3.5),(3.6) |
| $\int_{\Gamma} q \boldsymbol{N}^{\mathrm{r}} \, \mathrm{d}\Gamma$ | Neumann vector | (3.4),(3.5),(3.6) |

where $\mathcal{M}$ are process-specific material functions, $\mathbf{B} = \mathcal{L}\boldsymbol{N}_2$ is so called strain-displacement matrix, $\mathbf{m} = (1, 1, 1, 0, 0, 0)^T$ is mapping vector. Based on this classification of matrix and vector types the finite element object is designed (Sect. 3.4.2).

## 3.4 Element Objects: ELE

In this section, the details of the implementation of the element objects are described. The relationship of element objects is shown in Fig. 3.6. For the simulation of each process in a coupled problem or each single problem, only an instance of mesh object (ELE-MSH) and an instance of finite element object are required. Geometric element object (ELE-GEO) manufactures the foundation of this concept (Sect. 3.4.1). Meshes (ELE-MSH) are formed based from geometric element entities (Sect. 3.4.4). Finite element object (ELE-FEM) basically compute the finite element matrices for different PDE types and geometric element types automatically using the corresponding shape functions (Sect. 3.4.2). ELE-PCS object assembles the equation systems for the problem type, i.e. THM coupled ELE-PCS object problems for porous media (Sect. 3.4.3). To this purpose, objects ELE-PCS and ELE-FEM have a pointer member pointing to each other. When an instance of ELE-PCS object for a process in a coupled problem or a single problem is constructed, an instance of ELE-FEM object is created accordingly. During the construction of the instance of ELE-FEM object, the degree of freedom of the problem is initialize by the type the ELE-PCS instance, i.e. the specific problem. This means only one instance of ELE-PCS and one instance of ELE-FEM have to been created for each process in a coupled problems or for each single problem. Moreover, ELE-FEM has a pointer member pointing to interpolation function. This member is initialized by the messages from the instance of ELE-PCS and each instance of ELE-GEO for each finite element during the local assembly. Such initialization guarantees that interpolation function and its derivatives are set properly for each geometric element for a process or a problem.

For an instance of ELE-FEM object, its pointer type members of the interpolation functions and its derivative functions are initialized by both of the process type and the element geometry type. Moreover, ELE-FEM object has a pointer type member to ELE-GEO object as well. When local assembly comes to an element, or an instance of ELE-GEO, the ELE-FEM instance have the ELE-GEO pointer point to the element and initialized its numerical methods such as

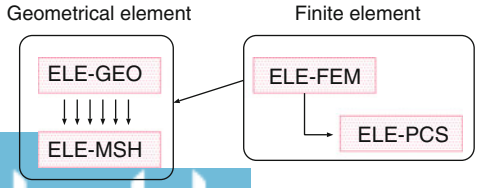


Figure 3.6: Relationship of element objects

interpolation, Guass integration accordingly. This is very helpful for the finite element analysis of consolidation in porous media, in which, the Talyor-Hood finite element spaces, i.e. linear interpolation for flow process and quadratic interpolation for deformation process, is required for stability reason[54]. In default, the order of interpolation of each element is linear and the nodes of an element are its geometrical vertices. If the high order interpolation is required by a process or a problem, additional nodes are created for each instance of ELE-FEM during the construction of the mesh topology. The idea of this concept is, that specific process-related information is introduced as late as possible to keep the software concept as flexible as possible.

### 3.4.1 Geometric Element Object: ELE-GEO

As described in Sect. 3.2, the first step of finite element analysis is the domain discretization. As a result we obtain element meshes. Hereafter, we refer to a mesh element as the geometric element object `ELE-GEO`. The intrinsic properties of a geometric element object are: nodes, edges, faces, volume and neighbors (Fig. 3.7). Neighbor relationships connect geometric element objects within a mesh and, therefore, represent topological properties.

We design the following element property classes to encapsulate all geometric and topological element information.

- `CCore` for `CORE` object,
- `CNode` for `NODE` object,
- `CEdge` for `EDGE` object,
- `CElem` for `ELEM` object.

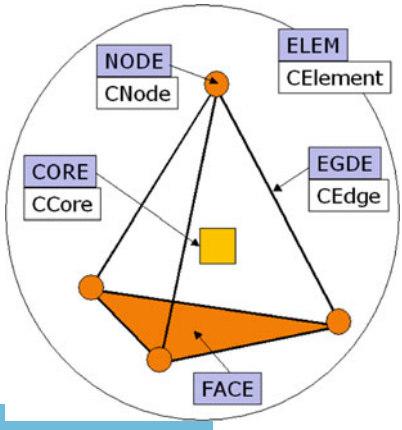


Figure 3.7: Mesh element

```
class CCore
{
   protected:  // Properties
      long index; // global element index
      char position; // position indicator
      bool status; // status in usage
      int order; // order of interpolation
   public:  // Methods
      // Set members
      void SetIndex(const long index) {index = index;}
      void SetPosition(const char BC_type) {boundary = BC_type;}
      void SetStatus(const bool status) {status = status;}
      void SetOrder(const int order) {order = order;}
      // Get members
      long GetIndex() const {return index;}
      char GetPosition() const {return position;}
      bool GetStatus() const {return status;}
      int GetOrder() const {return order;}
      // Construction
      CCore(const int id); // constructor
      virtual  ~CCore(); // destructor
      // Operators
      virtual void operator = (const CCore & g) {}
      virtual bool operator == (const CCore & g) {return false;}
      // Output
      virtual void output(ostream& os=cout) const {};
};
```

Figure 3.8: `CCore` implementation for basic geometric element properties and methods

Faces and neighbors belong to `ELEM` object. Indeed, edges could be also assigned to the `ELEM` object. However, we consider an edge as an individual entity for two reasons. First, some numerical methods, such as mixed finite elements, require edges as a basic geometric property as nodes for the Galerkin FEM. Second, edges are frequently used as basic properties in the automatic mesh generation. As `NODE`, `EDGE` and `ELEM` objects share common data and methods, we abstract these into the `CCore` class as a base class (Fig. 3.8).

### Core Object: `CORE`–Geometric Element Base Class

Common data of a geometric element are: global element index; position indicator within the whole domain, which indicates whether the geometric element is inside the domain or on the domain surface; status flag, which indicates whether this element is marked for some usage. Assign = as well as identity operators == are virtually defined. The C++ implementation of the `CCore` base class is given in Fig. 3.9.

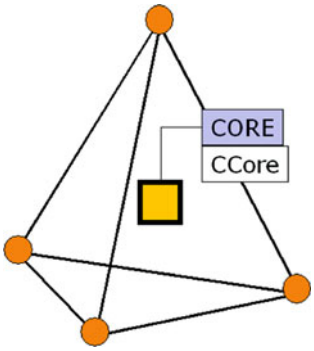


Figure 3.9: Core of mesh element

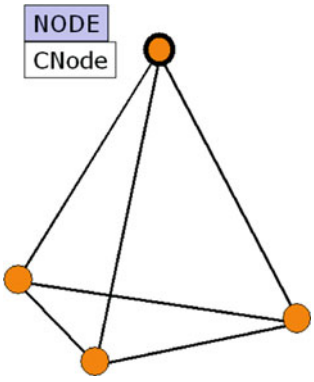


Figure 3.10: Node of element object

Member `char position` is used to determine the location of the geometrical entity within a domain, e.g. it is inside the domain or on the boundary of the domain.

Classes `CNode`, `CEdge` and `CElem` are directly derived from the base class `CCore`. Assign = as well as the identity operator == are overloaded in these objects. With such overloading operators, passing data of an class instance, `A`, to another class instance, `B`, can be simply realized with the instruction `A=B`. Whether two instances are identical can be checked by the instruction `if(A==B)`.

### Node Object: `NODE`

The node object (`NODE`) is derived from the `CCore` class. In addition, the `CNode` class provides the geometrical position of an element in real space, i.e. the coordinates of element nodes (Fig. 3.10).

Mesh elements having this node in common are determined immediately after mesh data is generated. Elements sharing this node are stored in vector `ConnectedElements`. This node-element relationship is very important information of the mesh topology. It is required e.g. for extrapolation of Gauss point values to node values or for projecting element properties to nodes. Using the

ConnectedElements vector, the calculation of mesh topology can be enormously accelerated. For extrapolation of gauss point values to nodes, we only need to know the size of the vector, i.e. how many element connected to the nodes. Since extrapolation takes place element-wise, node values are accumulated from the contribution of its connected elements, we have to average the accumulated node value by dividing it with the number of connected elements after extrapolation is finished. Member vector ConnectedNodes stores indices of all nodes of connected elements and it is used together with the degree of freedom of the process/problem to store indices of all nodes of connected elements and it can be used together with the degree of freedom of the process/problem to create the sparse matrix of the system equations to create the sparse matrix of the system equations. The memory of ConnectedNodes is released as soon as the sparse matrix is created. Classes CEdge and CElem are set as friend classes of CNode so that they can access to CNode private members directly. The C++ implementation of class CNode is given in Fig. 3.11.

```
class CNode:public CCore
{
   private:  // Members
      double coordinate[3];
      Vector<long> ConnectedElements;
      mboxVector<long> ConnectedNodes;
   public:
      // Construction
      Node(const int Index, const double x,
           const double y, const double z=0.0);
      Node() {}
      ~Node() {ConnectedElements.resize(0); ConnectedNodes.resize(0);}
      // Operators
      void operator = (const Node& n);
      bool operator == (const Node & n);
      // Set members
      void SetX(const double argX) { coordinate[0] = argX;}
      void SetY(const double argY) { coordinate[1] = argY;}
      void SetZ(const double argZ) { coordinate[2] = argZ;}
      void SetCoordinates(const double* argCoord);
      // Get members
      double GetX() const {return coordinate[0];}
      double GetY() const {return coordinate[1];}
      double GetZ() const {return coordinate[2];}
      int GetNumberOfConnectedElements() const {return
ConnectedElements.size(); }
      mboxint GetNumberOfConnectedNodes() const {return
ConnectedNodes.size(); }
      // Output
      void Write(ostream& os=cout) const;
   private:  // Class relations
      friend class CEdge;
      friend class CElem;
};
```

Figure 3.11: CNode implementation

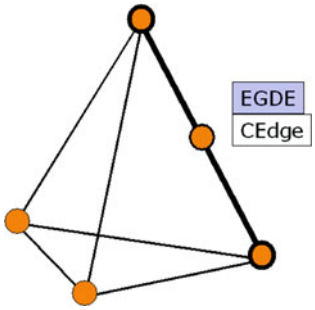


Figure 3.12: Edge of mesh element

```
class CEdge:public CCore
{
   private:  // Members
      vec<CNode* > nodes_of_edges;
   public:  // Member functions
      // Construction
      Edge(const int Index, bool quadr=false);
      ~Edge();
      // Operators
      void operator = (CEdge& edg);
      bool operator == (CEdge& edg);
      // Member access
      void SetNodes( vec<CNode* >& Nodes)
      { for(int i=0; i<(int)Nodes.Size(); i++)  Nodes[i] = nodes_of_edges[i]; }
      void SetNodes( vec<CNode* >& Nodes) const { Nodes = nodes_of_edges;}
      // Output
      void Write(ostream& osm=cout) const;
   private:  // Class relations
      Vector<CNode* >  nodes_of_edges;
      friend class CElem;
};
```

Figure 3.13: `CEdge` implementation

Instances of `NODE` object are stored in a global vector: `vector<CNode*>node_vector`.

### Edge Object: `EDGE`

The edge object (`EDGE`) is derived from the `CCore` class. Edges are used to build up the frame of a geometric element object (Fig. 3.12). It is sufficient to use two nodes to form a geometric edge. However, for higher order finite elements, more points are required along an edge. Therefore, we use a vector of `CNode` pointers as a class member for edge nodes (see Fig. 3.12). In case of quadratic finite elements, the first two nodes are element corner nodes and the last one is the middle point of this edge.

The C++ implementation of the `CEdge` class is given in Fig. 3.13.

`Vector` is a "clone" of the standard C++ vector template, as `template Vector-<class V> class V` with less memory consuming but sufficient and efficient functionality of vector algebraic calculation.

For node based finite elements (i.e. linear interpolation), edges are only used to compute the topological mesh structure and to process Dirichlet boundary conditions and source terms. For instance, if a Dirichlet boundary condition of a PDE is assigned by a polyline, edges of elements on the polyline will be found and the Gauss integration will be performed on these edges to produce node values of nodes of these edges. They are not needed to be stored for the later computations anymore. On the other hand, mixed finite elements or higher order finite elements require edges through all computations. In this case we save all edges of a mesh in a standard C++ vector: `vector<CEdge*>egde_vector`.

**Element Object: `ELEM`**

The element object (`ELEM`) is also derived from the `CCore` class. `ELEM` represents an individual element of a mesh. Node and edge objects are employed to construct the element object. An abstract mesh element object is designed for different geometric element types, i.e. lines, triangles, quadrilaterals, tetrahedra, triangle based prisms, hexahedra (Table 3.3, Fig. 3.15). These geometric element types are defined by an ID, i.e, integer numbers represent element type. The C++ implementation of `class CElem` is given in Fig. 3.14.

Basic members of the element object are identification, geometrical as well as topological properties and mesh relationships. Element ID (index) is inherited from the `CORE` object. Dimension and volume are basic geometric members. Depending on the geometric type of an element (`ele_type`), the following geometrical and topological properties are specified:

Element nodes and edges are kept in the following two member vectors

```
Vector<CNode* > nodes;
```

Table 3.3: Basic topology information of an geometrical element

| Geometric type | `ele_type` | `nnodes` | `nnodesHQ` | `nfaces` | `nedges` |
|---|---|---|---|---|---|
| Line | 1 | 2 | 3 | | |
| Quadrilateral | 2 | 4 | 9 | 4 | 4 |
| Hexehedron | 3 | 8 | 20 | 6 | 12 |
| Triangle | 4 | 3 | 6 | 3 | 3 |
| Tetrahedron | 5 | 4 | 10 | 4 | 6 |
| Prism | 6 | 6 | 15 | 5 | 9 |

```
class CElement:public CCore
{
   private: // Members
      // ID
      CElem* owner;
      int ele_type;  // Element type
      // Geometrical properties
      int dim;       // dimension of element
      double volume; // element volume
      // Topological properties
      int nnodes;    // number of element corner nodes
      int nnodesHQ;  // number of element nodes for quadratic interpolation
      Vector<CNode* >  nodes;
      int nedges;    // number of edges
      Vector<CEdge* >  edges;
      int nfaces;    // number of faces
      // Mesh topology
      int sub_domain;
      Vector<CElem* >  neighbors;
      Vector<CElem* >  sons;
      Vector<long>   nodes_index;
}
```

Figure 3.14: `CElem` implementation

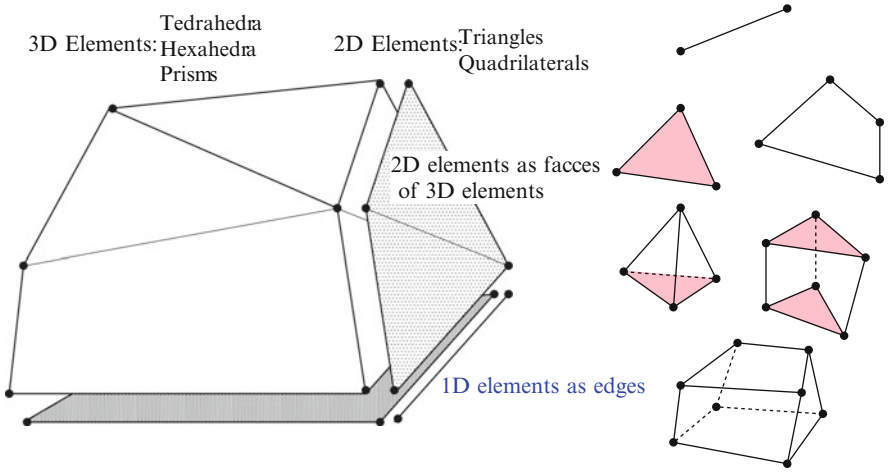


Figure 3.15: Geometric elements types

and

```
Vector<CEdge* > edges;
```

### 3.4.2 Finite Element Object: ELE-FEM

In this section we present the design of the finite element object, i.e. properties and methods, which are required to conduct the finite element analysis. In

particular, we discuss the implementation of steps 2 and 3 described in Table 3.1, i.e., local element assembly and global assembly of the system equation.

According to the principles of object-oriented programming, we encapsulate common data and functionalities of finite elements into a base class. There are two general tasks of the finite element object. First, local finite element calculations and, second, contributions of the element to the global equation system. Afterwards, we derive specific finite element objects for different problem types (i.e. PDE types) in the framework of THM porous media mechanics (see Fig. 3.5).

*Finite element base class:* Local element calculations require the selection of specific interpolation functions as well as their derivatives at integration points corresponding to different element types. Therefore, element interpolation functions are regarded as basic items of the finite element object. These interpolation functions have two arguments: first, values of shape functions or the derivative of shape functions; second, reference points, e.g. Gauss points. Therefore, for each kind of geometric element type, we have four functions associated with element interpolation as

```
void ShapeFunctionXXXX(double*,double*);
void ShapeFunctionHQXXXX(double*,double*);
void GradShapeFunctionXXXX(double*,double*);
void GradShapeFunctionHQXXXX(double*,double*);
```

where `XXXX` is specifying the different geometric element types. `ShapeFunctionXXXX` provides linear interpolation functions $\boldsymbol{N}_1$, whereas `ShapeFunctionHQXXXX` gives quadratic interpolation functions $\boldsymbol{N}_2$, mentioned in Sect. 3.3. `GradShapeFunctionXXXX` and `GradShapeFunctionHQXXXX` offer the derivatives of the corresponding interpolation functions $\boldsymbol{N}_1$ and $\boldsymbol{N}_2$, respectively. Interpolation functions for all kinds of element types are declared as global functions. The function pointer `void (*VoidFuncDXCDX) (double*,double*)` is defined to point to the addresses of the global interpolation functions. The C++ implementation of the finite element base class `CElement` is given in Fig. 3.16.

Member variable, `m_ele_geo`, is a pointer to the corresponding geometric element object `CElem`, which links the finite element object to geometry. When the local assembly takes place for an element, the instance of this element is obtained by finite element object with its member function, `void Config(CElem m_ele_geo)`. With this, the finite element object has all geometrical and topological properties such as geometric type, coordinate nodes and neighbors for local element calculation.

Different weak forms arise from the different governing equations of flow problem, heat transport problem and mechanical problem ((3.4)–(3.6)). This requires different element level computations for the specific problem. Since the root finite element object provides the basic numerical functionality, we can use this object directly for the benefit of the polymorphism mechanism of object oriented programming.

```
class CFiniteElement {
  protected: // Member data
    CElem* m_ele_geo; // Instance of geometric element
    int order; //Order of shape functions
    int n_gauss_points; // Number of Gauss points
    int n_gauss; // Number of sample points for Gauss integration
    mutable double unit[4]; // Local element coordinates
    double* Jacobian; // Jacobian matrix
    double* invJacobian; // Inverse Jacobian matrix
    double* shape_fct; // Linear shape function values at Gauss points
    double* shape_fct_HQ; // Quadratic shape function values at Gauss points
    double* d_shape_fct; // Linear shape function derivative values at Gauss points
    double* d_shape_fct_HQ; // Quadratic shape function derivative values at
                            // Gauss points
  public: // Member functions
    CFiniteElement(const int order=1);
    virtual ~CFiniteElement();
    virtual void Config(CElem* m_ele_geo);
    virtual void ConfigNumerics(const int type);
    double GetGaussData(const int gp,int& gp_r,int& gp_s,int& gp_t)
    virtual void ComputeShapeFct(const int order);
    virtual void ComputeGradShapeFct(const int order);
    virtual double ComputeJacobian(const int order);
    virtual void RealCoordinates(double*xyz);
    virtual void RefCoordinates(double*xyz);
    virtual void LocalAssembly();
    virtual void FaceIntegration();
  protected: // Member functions
    VoidFuncDXCDX ShapeFunction; // Prototype for linear shape functions
    VoidFuncDXCDX ShapeFunctionHQ; // Prototype for quadratic shape functions
    VoidFuncDXCDX GradShapeFunction; // Prototype for linear shape function derivatives
    VoidFuncDXCDX GradShapeFunctionHQ; // Prototype for quadratic shape
                                       // function derivatives
}
```

Figure 3.16: Finite element base class

### 3.4.3 Process Related Finite Element Objects: ELE-PCS

Only at this stage (the last part of the element object concept) do we introduce process-related data. The element object `CFiniteElementPCS` should work for all processes: fluid flow, heat transport, deformation and reaction processes regardless of PDE type and type of unknown field functions (scalar or vector quantities).

The finite element object ELE-PCS has two tasks: First, calculation of element matrices, which are formed by shape functions ($\boldsymbol{N}_1, \nabla \boldsymbol{N}_1$) and process-specific material properties (`MAT` objects) (Step 2 in Table 3.1). Second, to provide local element contributions to the global equation system: $A_{ij} x_i = b_j$, where $i, j$ are global node indices (Step 3 in Table 3.1).

The C++ implementation of the process-related finite element object ELE-PCS is given in Fig. 3.17.

- ELE-FEM relation: Process related instances are derived from the finite element base class `CFiniteElement`. Therefore, they inherit all necessary

```
class CFiniteElementPCS::public CFiniteElement {
  private: // Member data
    // PCS relation
    CProcess* m_pcs;
    // MAT relations
    CFluidProperties* m_mfp;
    CSolidProperties* m_mfp;
    CMediumProperties* m_mmp;
    // Element matrices
    SymMatrix* MassMatrix;
    SymMatrix* LaplaceMatrix;
    SymMatrix* PressureCouplingMatrix;
    Matrix*    AdvectionMatrix;
    Matrix*    StrainMatrix;
    Matrix*    StrainCouplingMatrix;
    ...
    Matrix*    LHSMatrix;
    Vec*       RHSVector;
  public:  // Member functions
    // Construction
    CFiniteElementPCS(CProcess* m_pcs);
    ~CFiniteElementPCS();
    // MAT functions
    void SetMaterial();
    inline void CalcMassMatrixCoefficient();
    inline void CalcAdvectionMatrixCoefficient();
    inline void CalcLaplaceMatrixCoefficient();
    inline void CalcStrainMatrixCoefficient();
    inline void CalcStrainCouplingMatrixCoefficient();
    inline void CalcPressureCouplingMatrixCoefficient();
    // Element matrices
    inline double InterpolateGPValues(double*);
    // Interpolation at Gauss points
    void SetMemory();
    void CalcMassMatrix();
    void CalcLumpedMassMatrix();
    void CalcAdvectionMatrix();
    void CalcLaplaceMatrix();
    void CalcStrainMatrix();
    void CalcStrainCouplingMatrix();
    void CalcPressureCouplingMatrix();
    void CalcGravityVector();
    void LocalAssembly(); // LHS element contribution
    ...
    // Element contribution to global equation system
    void GlobalAssembly(); // LHS matrix contribution
}
```

Figure 3.17: Process related finite element class

geometric and topological data from ELE-GEO, ELE-FEM, and ELE-MSH objects.

- PCS relation: Process related finite element objects need a reference to the related PCS instance, which is conducted by the ELE-PCS class constructor.

- MAT relations: References to all `MAT` objects, i.e. `CFluidProperties* m_mfp`, `CSolidProperties* m_msp` and `CMediumProperties* m_mmp`, are used to get the required material parameters of the specified process (`CProcess* m_pcs`). Member function `SetMaterial()` prepares the references to process-specific material properties to accelerate later computations. This insures that the ELE-FEM object works properly for all THM processes, i.e. fluid flow, heat transport and deformation.

- Local assembly: Element matrices: Based on geometric and finite element base data (ELE-FEM relation) and the references to material data (PCS-MAT relation) the process-specific element matrices can be calculated now (`CalcXXXXMatrix()`). Member functions are used to calculate the material coefficients in the Gauss integration points (`CalcXXXXMatrixCoefficients()`). They are defined as `inline` types to improve the computation efficiency. Local element matrices and vectors are stored in the corresponding symmetric/unsymmetric matrix and vector constructs.

- Global assembly: Equation system: The global assembly is conducted by the `Assemble()` function. It updates the individual element contributions in the equation system, i.e. global left-hand-side (LHS) matrix ($A_{ij}$) and global right-hand-side (RHS) vector ($b_j$). To this purpose the assembly functions needs the relations between local element node and global mesh node numbers, which is provided by the ELE-MSH topology (Sect. 3.4.4). `Assemble()` functions are available for different PDE types. How the `Assemble()` is implemented for a parabolic PDE is shown in Fig. 3.18.

### 3.4.4 Element-Mesh Relations: ELE-MSH

From Fig. 3.6 it can be seen, that element-mesh relations have multiple functions in the element concept, e.g.

```
void CFiniteElementPCS::AssembleParabolicPDEType()
{
  // MAT relations
  SetMaterial();
  // Calculation and assembly of element matrices
  CalcMassMatrix();
  CalcLaplaceMatrix();
  CalcStrainCouplingMatrix();
  // Calculation and assembly of RHS vector
  CalcRHSVector();
}
```

Figure 3.18: Linear element assemble function

- ELE-GEO relation: mesh topology, neighbor relationships of geometric elements, element connectivity, incorporation of boundary conditions,
- ELE-FEM relation: coordinate transformation between local element and global coordinates,
- ELE-PCS relation: local element nodes and node index in the global equation system, material domains.

### ELE-GEO Relation

Apart from the individual/intrinsic element properties, the `ELEM` object contains information about mesh topology, i.e. how this element is emplaced in the element mesh. For instance, the (`sub_domain`) index indicates the part of the domain to which this element belongs. This number is used e.g. to distinguish elements in different areas of the domain with different material properties. Neighbor relationships of geometric elements are important topological properties of an element mesh. Neighbors of an element are all those elements adjacent to the faces of the element. Since the definition of `ELEM` object provides necessary functionality of different geometric element types, we use pointers to `ELEM` object itself to recode neighbors as

```
Vector<CElem* > neighbors;
```

As an example Fig. 3.19 illustrates the arrangement of neighbor relationships in 2D space, in which quadrilateral element A has three neighbor elements adjacent to its faces (i.e. edges in 2D) 1, 2 and 3. Neighbors 1 and 2 are triangle elements, while neighbor 3 is a quadrilateral element. Face 4 is on the domain boundary, which is not shared by any other element. Vector member, `neighbors`, is initialized with size of 4 and assigned during mesh construction. The first three entries are assigned with pointers to neighbors 1, 2 and 3. The

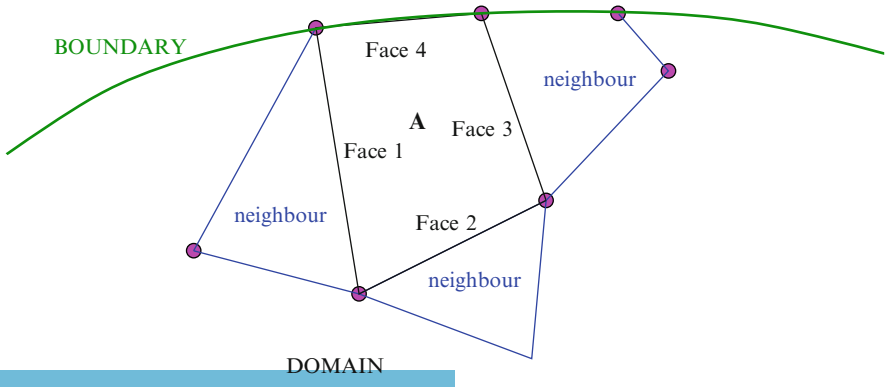


Figure 3.19: Definition of element neighbors

last entry of the vector is filled with a pointer to a surface (Face 4), which is an instance of `ELEM` object configured for a line element. The boundary type `position` of this instance is set as 'B'. The coding of the element neighboring process is given below:

```
neighbors[0] = (CElem*) Neighbour1;
neighbors[1] = (CElem*) Neighbour2;
neighbors[2] = (CElem*) Neighbour3;
neighbors[3] = (CElem*) Face4;
Face4->position = 'B'; // on domain boundary
Face4->owner = this; // this element
```

The above neighbor vector is a member of element, i.e., ELEM, object.

#### ELE-FEM Relation

The ELE-FEM association concerns coordinate transformation between local elements and global coordinates. Depending on the geometric and numerical type of a finite element, related shape functions and their derivatives are available (Sect. 3.4.2). Jacobian calculations are another typical ELE-FEM method.

#### ELE-PCS Relation

Subdomain properties of elements are used to describe heterogeneity, i.e. local variation of material properties for different problems. Element neighbor relationships are essential data for constructing the mesh and determine the propagation orientation of discontinuities in failure analysis (Sect. 9.2.2). Moreover, the proposed element concept allows the assignment of different processes (PCS objects) and meshes (MSH objects).

## 3.5 Parallel Computing and Automatic Control for Time Stepping

The present finite element object and geometric element objects have already been extended to the extended finite method [91]. In addition to the process object, finite element object and geometric element objects, we need to provide more objects to manage the time discretization, assembly and solving of the global system of equations and so on. Since the stiffness matrix of the global system of equations by the finite element method is a sparse matrix, we designed and implemented a sparse object and a linear solver object [92]. The sparse object serves to keep the stiffness matrix and to perform the matrix algebraic calculations for both sequential and parallel computing [93]. The sparse object determines the sparse pattern of the stiffness matrix by the topology of the whole domain mesh for sequential simulations or by the topology of the partitioned

domain meshes for parallel simulations. Consequently, the linear solver object uses the matrix algebraic functions of the sparse object to solve the system of equations. For the temporal discretization, we used the first order difference method and employed an adaptive time stepping method with automatic control [94], moreover all data and functions of which and the coupling of multi-physics processes are encapsulated into a problem oriented object.

# Part II

# Benchmarks for Single Processes

# Chapter 4

# Heat Transport

*by Norbert Böttcher, Guido Blöcher, Mauro Cacace, and Olaf Kolditz*

In the first benchmark chapter we consider heat transport in a porous medium described by the heat balance equation (2.78). With the following assumptions:

- Constant material properties,
- Neglecting viscous dissipation effects,
- Local thermal equillibrium, $c\rho = \sum_\alpha c^\alpha \rho^\alpha$, $\lambda = \sum_\alpha \lambda^\alpha$

we obtain the **linear heat transport** equation

$$c\rho \frac{\partial T}{\partial t} + c\rho \mathbf{v} \cdot \nabla T - \nabla \cdot (\lambda \nabla T) = q_{\mathrm{th}}, \tag{4.1}$$

where $c$ is specific heat capacity, $\rho$ is density, $T$ is temperature, $\mathbf{v}$ is advection velocity and $\lambda$ is thermal conductivity.

Conduction takes place when a temperature gradient in a solid or a stationary fluid medium occurs. It runs into the direction of decreasing temperature. The thermal conductivity is defined in order to quantify the ease with which a particular medium conducts heat. Against it, convection is caused by moving fluids of different temperatures.

The equation for the heat conduction is

$$\frac{\partial T}{\partial t} = \nabla \cdot (\alpha \nabla T), \tag{4.2}$$

where $\alpha = \lambda / c\rho$ is the heat diffusivity constant.

O. Kolditz et al. (eds.), *Thermo-Hydro-Mechanical-Chemical Processes in Fractured Porous Media*, Lecture Notes in Computational Science and Engineering 86,
DOI 10.1007/978-3-642-27177-9_4, © Springer-Verlag Berlin Heidelberg 2012

Temperature changes cause a change of fluid density and viscosity which influences again the behaviour of the fluid while flowing through a porous medium and therefore the velocity of heat transport by groundwater flow. The dependence of density on temperature changes is regarded by using the relation given in (4.3)

$$\rho(T) = \rho_0 \cdot (1 + \beta_T (T - T_0)) . \tag{4.3}$$

Here $\rho_0$ represents the initial density, $T$ the temperature, $T_0$ the initial temperature and $\beta_T$ is the thermal expansion coefficient assumed to be a material constant. A more comprehensive description of thermal material behavior of fluids and solids is given in Sects. 2.4 and 2.5, respectively. Temperature dependent material behavior results in **non-linear heat transport** which is discussed in the coupled processes part of this book.

We consider the following series of benchmarks for heat transport with slightly increasing complexity.

- Linear heat conduction in a semi-infinite domain (4)
- Linear heat conduction in a finite domain (4.1)
- Radial heat conduction in a solid (4.1.3)
- Heat transport in a fracture (4.3)
- Heat transport in a porous medium (4.5)
- Heat transport in a fracture-matrix system (4.6)

## 4.1 Linear Heat Conduction in a Finite Solid

### 4.1.1 Definition

We consider a 1D half-domain which is infinite in one coordinate direction ($z \to \infty$) (Fig. 4.1).

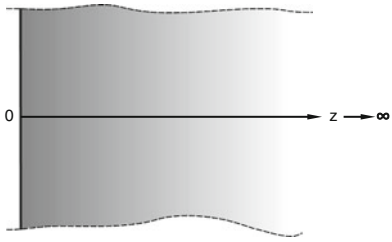


Figure 4.1: Model domain

Table 4.1: Solid phase material properties

| Symbol | Parameter | Value | Unit |
|---|---|---|---|
| $\rho$ | Density | 2,500 | $\mathrm{kg}\cdot\mathrm{m}^{-3}$ |
| $c$ | Heat capacity | 1,000 | $\mathrm{J}\cdot\mathrm{kg}^{-1}\cdot\mathrm{K}^{-1}$ |
| $\lambda$ | Thermal conductivity | 3.2 | $\mathrm{W}\cdot\mathrm{m}^{-1}\cdot\mathrm{K}^{-1}$ |

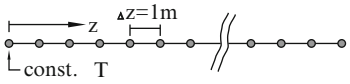


Figure 4.2: Spatial discretisation of the numerical model

### 4.1.2 Solution

#### Analytical Solution

The analytical solution for the 1D linear heat conduction equation (4.2) is

$$T(x,t) = T_0 \operatorname{erfc}\left(\frac{x}{\sqrt{4\alpha t}}\right), \tag{4.4}$$

where $T_0$ is the initial temperature. The boundary conditions are $T(z=0)=1$ and $T(z\to\infty)=0$.

The material properties for this model setup are given in Table 4.1.

Using these values, the heat diffusivity constant is $\alpha = \lambda/c\rho = 1.28\cdot 10^{-6}\,\mathrm{m}^2/\mathrm{s}$.

#### Numerical Solution

The numerical model consists of 60 line elements connected by 61 nodes along the z-axis (Fig. 4.2). The distances of the nodes $\Delta z$ is one meter. At $z = [0]\,\mathrm{m}$ there is a constant temperature boundary condition.

The *Neumann* stability criteria has to be restrained so that the temperature gradient can not be inverted by diffusive fluxes. Using (4.5) the best time step can be estimated by

$$\mathrm{Ne} = \frac{\alpha\Delta t}{(\Delta z)^2} \leq \frac{1}{2}. \tag{4.5}$$

With $\Delta z = [1]\,\mathrm{m}$ and $\alpha = [1.28\cdot 10^{-6}]\,\mathrm{m}^2/\mathrm{s}$ the outcome for the time step is $\Delta t \leq [390625]\,\mathrm{s}$ or 4.5 days, respectively.

### 4.1.3 Results

Figure 4.3 shows the comparison of the solution of (4.4) and the numerical simulation results. The temperature distribution is demonstrated along the model domain after 2 months, 1 year, 2 years and 4 years.

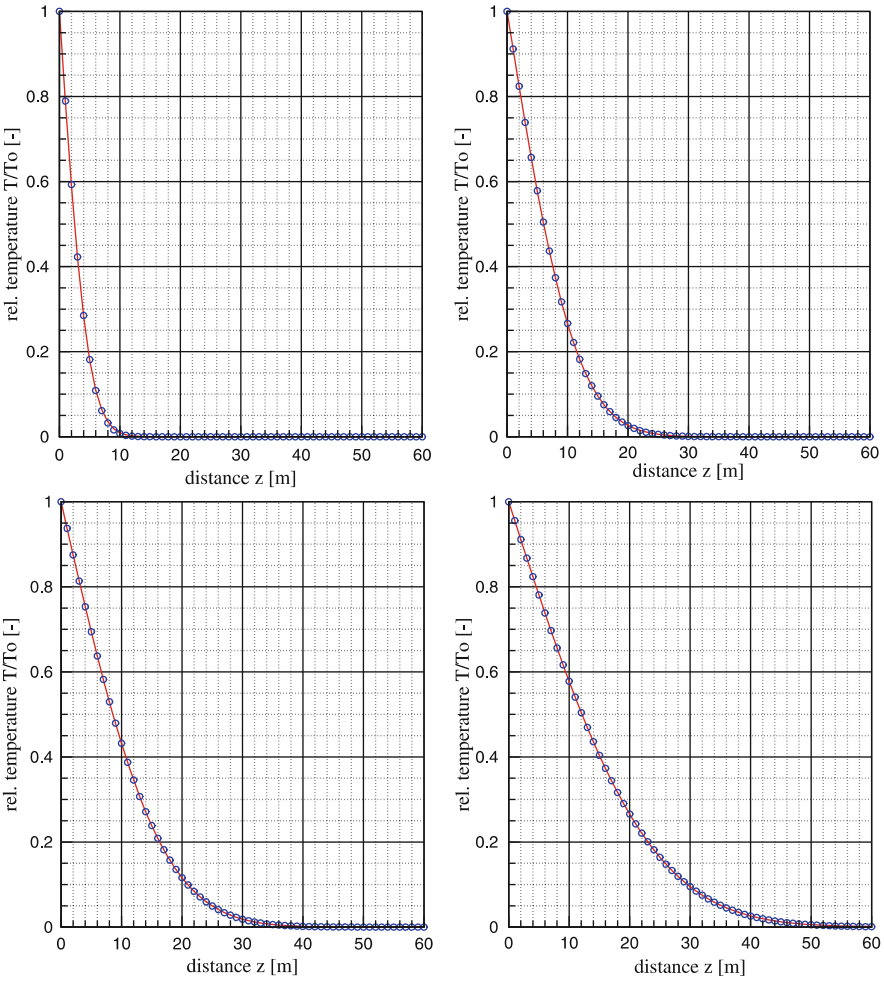


Figure 4.3: Temperature distribution along the z-axis after 2 months, 1 year, 2 years and 4 years (from top left to bottom right)

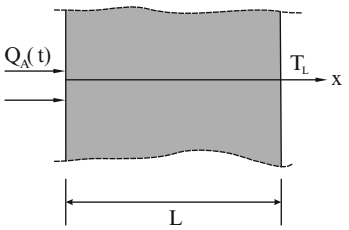


Figure 4.4: Heat conduction through a wall

## 4.2 Radial Heat Conduction in a Solid

### 4.2.1 Definition

In the first example (Sect. 4) there was a domain limited only by one side with a constant temperature at the boundary. The following problem shows the profile of a homogeneous and isotropic wall with a constant heat flow $q_{\text{th}}$ on the left and a constant temperature $T_L$ on the right boundary (Fig. 4.4). We consider diffusive heat transport on a two-side bounded domain.

### 4.2.2 Solution

#### Analytical Solution

A solution for this problem can be found by solving the heat conduction equation (4.2) using *Fourier*'s method (see [95])

$$\begin{aligned} T(x,t) &= T_L + \frac{q_{\text{th}}}{\lambda}(L-x) \\ &+ \sum_{n=1}^{\infty} -\frac{8L}{(2n-1)^2\pi^2}\,\frac{q_{\text{th}}}{\lambda}\cos\frac{(2n-1)\pi x}{2L}\; e^{\left(-\frac{(2n-1)^2\pi^2}{4L^2}\alpha\, t\right)} \end{aligned} \tag{4.6}$$

with $T_L$ is the initial temperature, $Q_A$ is the constant heat source, $\lambda$ is the thermal conductivity and $\alpha$ is the heat diffusivity constant.

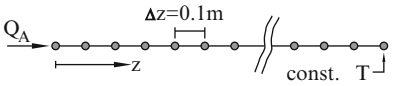


Figure 4.5: Boundary conditions and discretisation for the numerical model

#### Numerical Solution

The numerical model consists of 40 line elements and 41 nodes along the $x$-axis (Fig. 4.5). The step size $\Delta z$ is set to $[0.1]$ m. On the left boundary a constant

Table 4.2: Material properties

| Symbol | Parameter | Value | Unit |
|---|---|---|---|
| $q_{\text{th}}$ | Heat source | [30] | $\text{W}\cdot\text{m}^{-2}$ |
| $T_L$ | Initial temperature | [25] | °C |
| $L$ | Wall thickness | [4] | m |
| $\rho$ | Density of the solid | [2000] | $\text{kg}\cdot\text{m}^{-3}$ |
| $c$ | Heat capacity | [900] | $\text{J}\cdot\text{kg}^{-1}\cdot\text{K}^{-1}$ |
| $\lambda$ | Thermal conductivity | [5.5] | $\text{W}\cdot\text{m}^{-1}\cdot\text{K}^{-1}$ |

source term is set. The right side obtains a constant temperature condition. Table 4.2 shows the values of the used material properties. The heat diffusivity constant is $\alpha = [3.1 \cdot 10^{-6}]\,\text{m}^2/\text{s}$.

### 4.2.3 Results

The comparison of the analytical and numerical solutions is presented in Fig. 4.6. It shows the distribution of the temperature along the profile of the wall. Due to the thickness of the wall, the heat transport takes substantial time, after $5\times10^6$ seconds ($\approx$ 58 days) the temperature distribution becomes a steady-state.

## 4.3 Heat Transport in a Fracture

### 4.3.1 Definition

A slice with a hole in its centre, meaning a 2D annulus, which consists of a solid of a constant temperature, is exposed to a higher temperature at the surface of its hole. The aim of this calculation is to simulate the heat transfer through a homogeneous solid by the use of an axisymmetric model. Figure 4.7 shows a sketch of the calculation area assuming a homogeneous solid, a constant temperature in the whole body at the beginning and a heating of the slice at the inner surface of the hole.

The inner radius $R_1$ of the axisymmetric model is $[1]\,\text{m}$ and the outer radius $R_2$ is $[5]\,\text{m}$. The numerical model consists of 40 elements and 41 nodes. The initial temperature in the whole area is [25]°C. At the right boundary of the numerical model a thermal boundary condition is set with a constant value of [25]°C. At the left boundary a source term for heat flux of $q_{\text{th}} = [30]\text{W/m}^2$ is defined. Thereby the continuous heating of the solid is simulated. The used parameters of the solid are listed in Table 4.3. The simulation of 5,000 time steps with a constant time step length of $[1,000]$s is done.

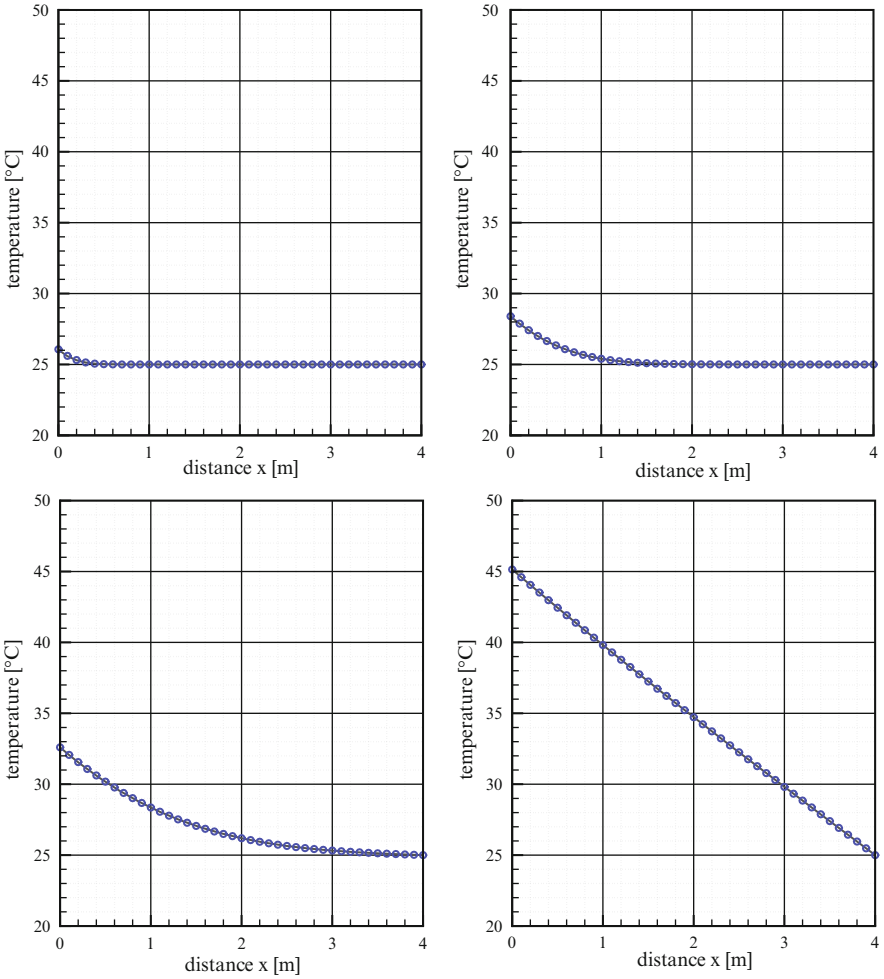


Figure 4.6: Temperature distribution along the wall profile after 10.000, 100.000, 500.000 and 5.000.000 seconds (from top left to bottom right)

### 4.3.2 Solution

For the heating of the annulus with the inner radius $R_1$ and the outer radius $R_2$ the following analytical solution exists for temperature as a function of the radius $r$. The parameters are according to Table 4.3.

$$T(r) = \frac{R_1 q}{\kappa} \ln\left(\frac{R_2}{r}\right) + T_0. \tag{4.7}$$

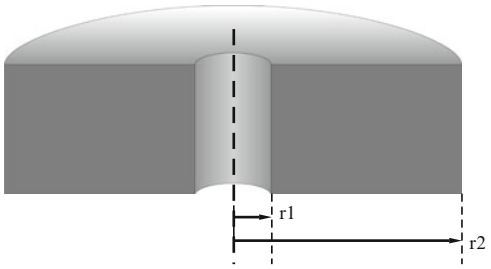


Figure 4.7: Radial heat conduction

Table 4.3: Model parameters

| Symbol | Parameter | Value | Unit |
|---|---|---|---|
| $\rho^s$ | Density of the solid | [2.0] | $\mathrm{t} \cdot \mathrm{m}^{-3}$ |
| $c^s$ | Heat capacity | [900] | $\mathrm{J} \cdot \mathrm{kg}^{-1} \cdot \mathrm{K}^{-1}$ |
| $\lambda^s$ | Thermal conductivity | [5.5] | $\mathrm{W} \cdot \mathrm{m}^{-1} \cdot \mathrm{K}^{-1}$ |
| $q_{\mathrm{th}}$ | Heat flux | 30 | $\mathrm{W/m}^2$ |
| $R_1, R_2$ | Inner and outer radius | 1,5 | m |
| $T_0, T_2$ | Initial and boundary temperatures | 25,25 | K |

### 4.3.3 Results

The results of the analytical equation for the temperature distribution over the model length are compared to those of the numerical simulation. Figure 4.8 shows the temperature distribution over the radius of the annulus. Obviously, with the axisymmetric numerical simulation generates comprehensible results that agree well with the analytical solution.

## 4.4 Heat Transport in a Porous Medium

### 4.4.1 Definition

This problem shows 1D heat transport by advection and diffusion in a $[100]\,\mathrm{m}$ long fracture. The fracture is fully saturated with water, flowing with constant velocity. There is no rock matrix around the fracture considered which could store heat (this will be examined in the next example). Figure 4.9 depicts the model set-up.

The fracture is described as a porous medium with $[100]\%$ porosity, so that no solid material influences the heat transport process. The properties of the fluid are in Table 4.4.

These values cause a diffusivity constant for water of $\alpha = [1.5 \cdot 10^{-7}]\,\mathrm{m}^2/\mathrm{s}$. The groundwater velocity in the fracture is $v = [3.0 \cdot 10^{-7}]\,\mathrm{m/s}$.

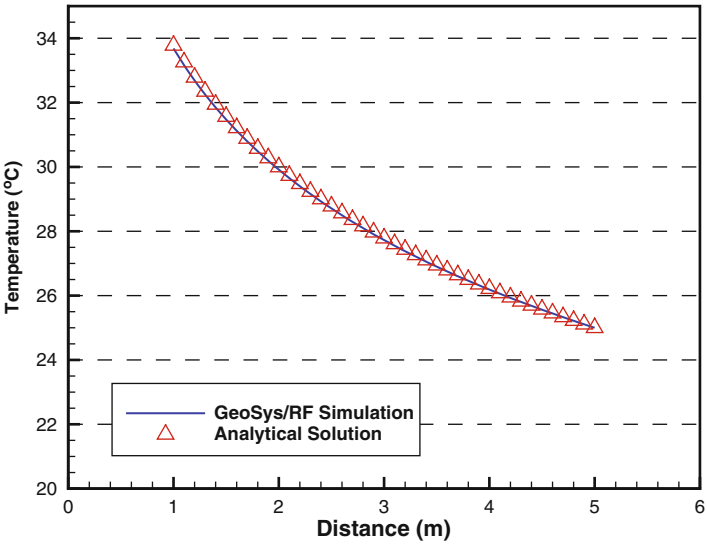


Figure 4.8: Temperature distribution along the radial distance

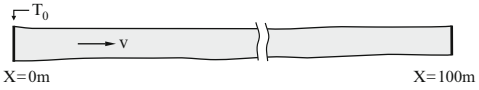


Figure 4.9: A fully saturated fracture with flowing water and a constant temperature at the left border

Table 4.4: Model parameters

| Symbol | Parameter | Value | Unit |
|---|---|---|---|
| $\rho^l$ | Density of water | $[1,000]$ | $\mathrm{kg}\cdot\mathrm{m}^{-3}$ |
| $c^l$ | Heat capacity of water | $[4,000]$ | $\mathrm{J}\cdot\mathrm{kg}^{-1}\cdot\mathrm{K}^{-1}$ |
| $\lambda^l$ | Thermal conductivity of water | $[0.6]$ | $\mathrm{W}\cdot\mathrm{m}^{-1}\cdot\mathrm{K}^{-1}$ |
| $v$ | Water velocity | $3\times10^{-7}$ | m/s |
| $L$ | Fracture length | 100 | m |

### 4.4.2 Solution

For 1D-advective/diffusive transport, an analytical solution is given by Ogata & Banks [96] as

$$T(x,t) = \frac{T_0}{2}\left(\operatorname{erfc}\frac{x - v_x\cdot t}{\sqrt{4\alpha t}} + e^{\frac{v_x\cdot x}{\alpha}}\operatorname{erfc}\frac{x + v_x\cdot t}{\sqrt{4\alpha t}}\right), \tag{4.8}$$

where $T_0$ is the constant temperature at $x = 0$, $v$ is the groundwater velocity and $\alpha$ is the heat diffusivity coefficient of water. More information can be found e.g. in [95, 97].

The mesh for the numerical model consists of 501 nodes combining 500 line elements. The distance between the nodes is $\Delta x = [0.2]\,\mathrm{m}$. The boundary conditions applied are as follows:

- Left border:
  - constant source term (liquid flow) with $Q = [3.0 \cdot 10^{-7}]\,\mathrm{m}^3/\mathrm{s}$
  - constant temperature with $T = [1]°\mathrm{C}$
- Right border:
  - constant pressure with $P = [100]\,\mathrm{kPa}$
- Initial conditions:
  - pressure with $P = [100]\,\mathrm{kPa}$ for whole domain
  - temperature $T = [0]°\mathrm{C}$ for whole domain
- Time step:
  - $\Delta t = [133]\,\mathrm{s}$

With the given parameters, the NEUMANN criteria (4.5) results on Ne = 0.5 which guarantees the numerical stability of the diffusion part of the transport process. The *Courant* criteria, given by

$$C = \frac{v_x \cdot \Delta t}{\Delta x} \leq 1 \tag{4.9}$$

is equal to $C = 0.2$.

### 4.4.3 Results

In Fig. 4.10 a comparison of the analytical and numerical solutions is plotted. The figure shows the temperature breakthrough curve at the end of the fracture at $x = [100]\,\mathrm{m}$. The numerical results show acceptable agreement with the analytical solution. In a further step, the diffusion part of the heat transport process was avoided by minimizing the thermal conductivity of the fluid. Figure 4.11 shows the breakthrough curve for only advective heat transport.

## 4.5 Heat Transport in a Porous Medium

### 4.5.1 Definition

In addition to the previous example (Sect. 4.3) now we consider heat transport in a two-phase homogeneous porous medium consisting of a solid and liquid phase, i.e. a 1D test example for groundwater flow and simultaneous heat transport in

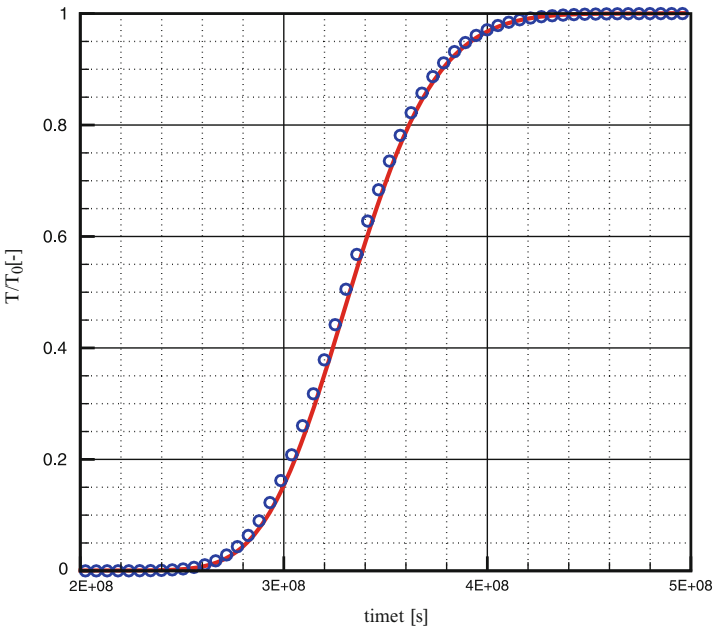


Figure 4.10: Temperature breakthrough curve at the point $x = [100]\,\mathrm{m}$

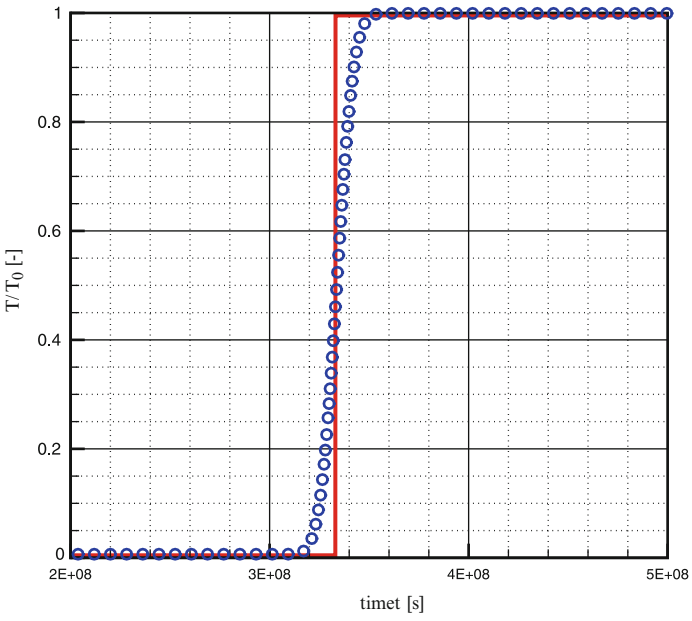


Figure 4.11: Temperature breakthrough curve when diffusion is neglected (shows numerical diffusion)

Table 4.5: Used soil and fluid parameters

| Symbol | Parameter | Value | Unit |
|---|---|---|---|
| | *Soil parameters* | | |
| $\phi$ | Porosity | 0.01 | – |
| $k$ | Permeability | $[1.0 \cdot 10^{-11}]$ | $m^2$ |
| $\rho^s$ | Density | $[2,850]$ | $kg \cdot m^{-3}$ |
| $c^s$ | Heat capacity | $[1,000]$ | $J \cdot kg^{-1} \cdot K^{-1}$ |
| $\lambda^s$ | Heat conductivity | $[3.2]$ | $W \cdot m^{-1} \cdot K^{-1}$ |
| | *Fluid parameters* | | |
| $\rho_0^f$ | Initial density | $[1,000]$ | $kg \cdot m^{-3}$ |
| $\eta$ | Viscosity | $[0.001]$ | $N \cdot s \cdot m^{-2}$ |
| $c^f$ | Heat capacity | $[4,000]$ | $J \cdot kg^{-1} \cdot K^{-1}$ |
| $\lambda^f$ | Heat conductivity | $[0.6]$ | $W \cdot m^{-1} \cdot K^{-1}$ |

an aquifer. The aim of the numerical simulation is also to determine the effect of varying density value with temperature changes.

### 4.5.2 Solution

For the 1-dimensional calculation, the calculation area is simplified as a line with the length of $[5.2]$ m. The calculation model includes 25 elements and 26 nodes. The initial pressure in the whole area is $[100]$ kPa and the initial temperature $[300]$ K. As boundary conditions a constant pressure of $[101]$ kPa is given at the left boundary and of $[100]$ kPa at the right boundary. A constant temperature of $[400]$ K is set at the left boundary. The used soil parameters are listed in Table 4.5. The fluid density is decreasing with increasing temperature. The viscosity, capacity and conductivity of water are set to constant values. The fluid parameters also can be found in Table 4.5.

In order to find out whether the consideration of varying water density with temperature changes is possible, one simulation run is done with a constant density of $[1,000]kg/m^3$, which is the initial water density before heating, and one run with a constant density of $[900]kg/m^3$, the density after the heating process. The temperature results for a heat transport with varying density have to be in between both temperature envelopes.

### 4.5.3 Results

The curve for temperature evolution, which is shown in Fig. 4.12 for the right boundary (node 26), shows the expected characteristics. Therefore it can be stated, that the consideration of temperature dependent fluid density is possible.

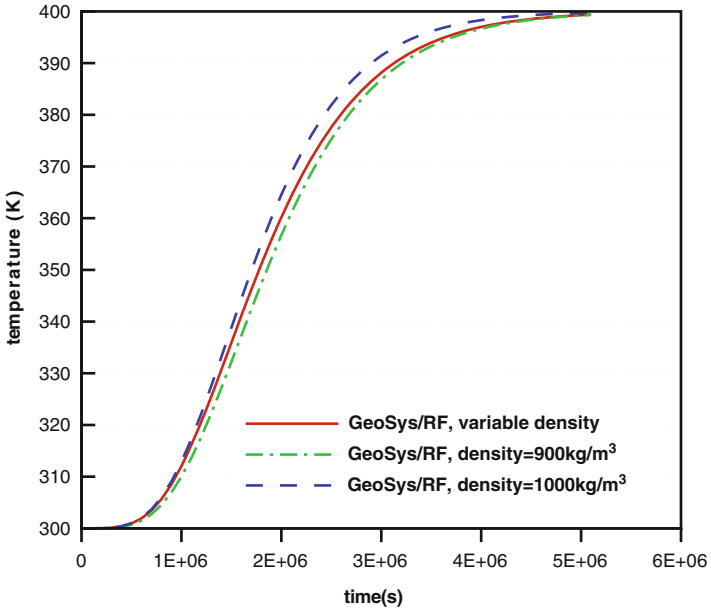


Figure 4.12: Temperature evolution with constant and variable fluid densities

## 4.6 Heat Transport in a Fracture-Matrix System

### 4.6.1 Definition

Based on the example for heat transport in a fluid filled fracture (Sect. 4.3), this problem is extended by heat diffusion through a rock matrix orthogonal to the fracture (Fig. 4.13).

The model and material parameters for the fracture and rock matrix, respectively, are given in Table 4.6.

### 4.6.2 Solution

For this problem an analytical solution was derived by Lauwerier (1955) (see [97]) with following assumptions:

- in the fracture, heat is transported only by advection,
- in the rock matrix, heat transport takes place by diffusion (only along the z-axis).

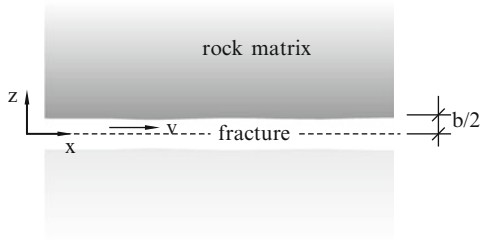


Figure 4.13: Heat transport in a fracture-matrix system

Table 4.6: Model parameters for the LAUWERIER-problem

| Symbol | Parameter | Value | Unit |
|---|---|---|---|
| | *Spatial discretisation* | | |
| $L$ | Fracture length | [50] | m |
| $W$ | Matrix width | [63.25] | m |
| $\Delta x$ | Step size X | [2] | m |
| $\Delta z$ | Step size Z | [0.1265] | m |
| $b/2$ | Half of fracture width | $[1.0 \cdot 10^{-3}]$ | m |
| $v_x$ | Groundwater velocity | $[1.0 \cdot 10^{-4}]$ | m/s |
| | *Temporal discretisation* | | |
| $\Delta t$ | Time step length | $[2.0 \cdot 10^{5}]$ | $s$ |
| | Number of time steps | 2,500 | |
| | Total time | $[5.0 \cdot 10^{8}]$ | $s$ |
| | *Material properties—solid* | | |
| $\lambda$ | Thermal conductivity | [1] | $\mathrm{W} \cdot m^{-1} \cdot \mathrm{K}^{-1}$ |
| $c$ | Heat capacity | [1,000] | $\mathrm{J} \cdot \mathrm{kg}^{-1} \cdot \mathrm{K}^{-1}$ |
| $\rho$ | Density | [2,500] | $\mathrm{kg} \cdot m^{-3}$ |
| | *Material properties—fluid* | | |
| $c$ | Heat capacity | [4,000] | $\mathrm{J} \cdot \mathrm{kg}^{-1} \cdot \mathrm{K}^{-1}$ |
| $\rho$ | Density | [1,000] | $\mathrm{kg} \cdot m^{-3}$ |

The LAUWERIER solution is given by

$$T_D = \begin{cases} 0, & t_D < x_D \\ \operatorname{erfc}\left\{ \frac{\beta}{\sqrt{\alpha(t_D - x_d)}} \left[ x_D + \frac{1}{2\beta}\left(z_D - \frac{1}{2}\right)\right]\right\}, & t_D > x_D \end{cases}, z_D \geq \frac{1}{2} \tag{4.10}$$

with the following dimensionless parameters:

$$t_D = \frac{v_x}{b}t, \quad x_D = \frac{x}{b}, \quad z_D = \frac{z}{b}, \quad \alpha = \frac{\lambda^s}{c^s \rho^s}\frac{1}{bv_x}, \quad \beta = \frac{\lambda^s}{c^l \rho^l}\frac{1}{bv_x} \tag{4.11}$$

where $b$ is the fracture width, $\lambda$ is the thermal conductivity, $c$ is the heat capacity, $\rho$ is the density and the suffixes $s$ and $f$ denote the solid (rock) and liquid (water) phases, respectively.

The numerical LAUWERIER model is formed as a coupling of advective 1D heat transport in x-direction and diffusive 1D heat transport in z-direction. This means, that nodes in the rock matrix are not influenced by their left or right neighbors. The matrix elements are connected to the fracture elements orthogonally. Figure 4.14 shows a schematical description of the model setup. Because of the symmetry, the numerical model calculates just the domain above the x-axis.

Figure 4.15 shows the positions of observation points which were chosen to evaluate the numerical model in comparison with analytical solutions.

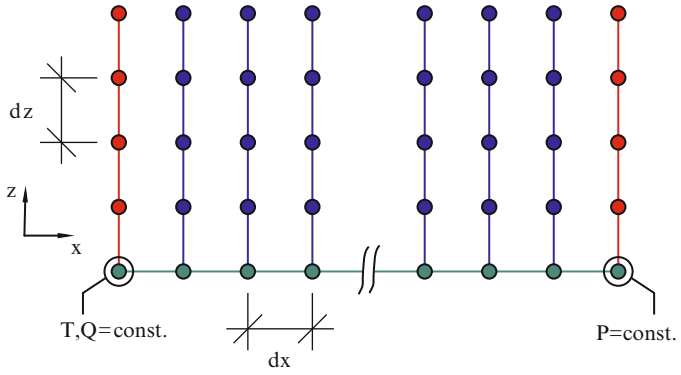


Figure 4.14: Alignment of the grid for the numerical model

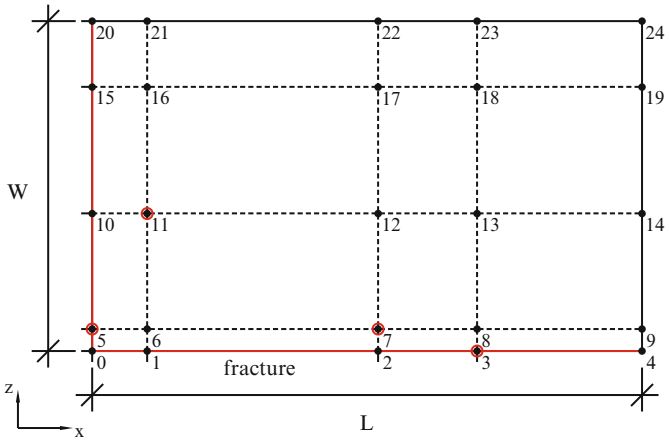


Figure 4.15: Positions of observation points for temperature breakthrough curves

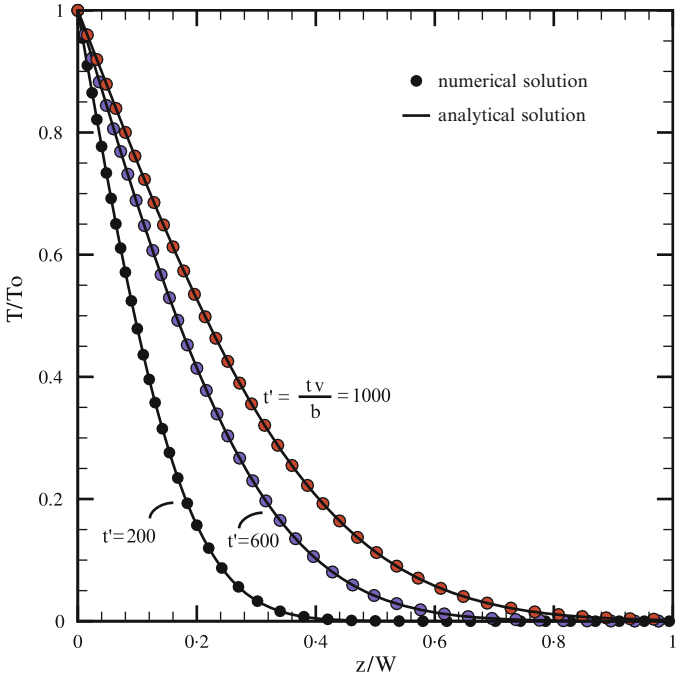


Figure 4.16: Temperature distribution orthogonal to the fracture at $x = 0$ at three different times

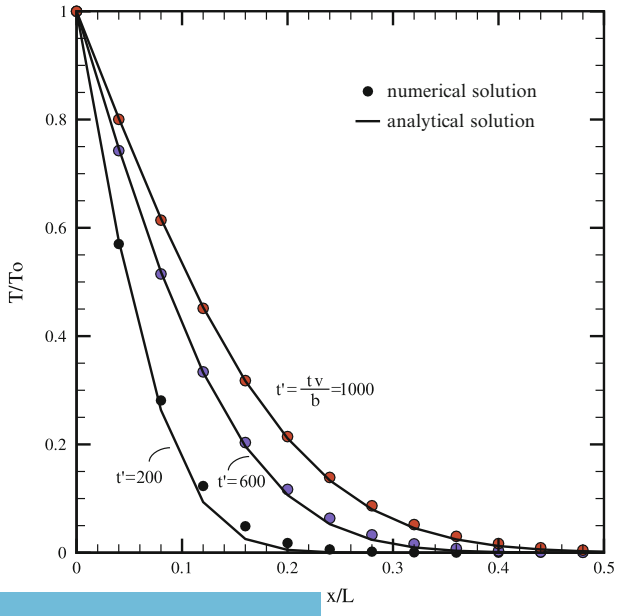


Figure 4.17: Temperature distribution along the fracture at three different times

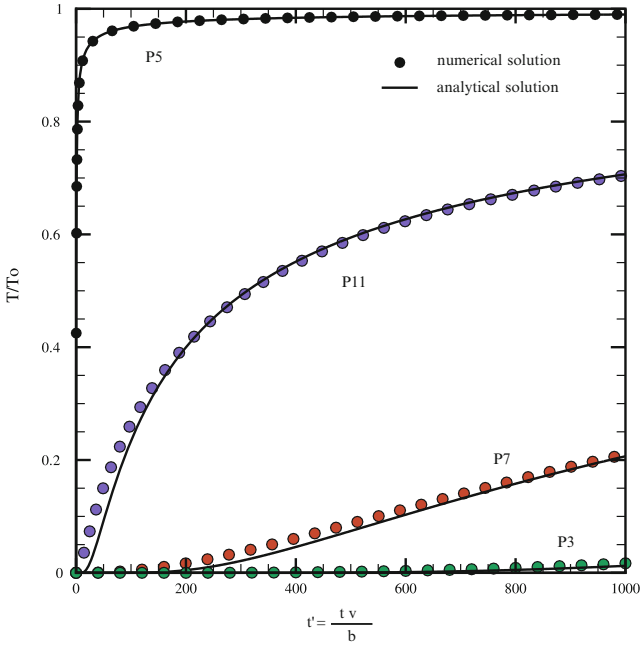


Figure 4.18: Temperature breakthrough curves at certain points in the rock matrix

### 4.6.3 Results

The quality of the numerical results can be shown by temperature distribution curves for several times in the rock matrix. Figure 4.16 shows the temperature profiles for $x = [0]\,\mathrm{m}$ at three moments $t'$. The numerical solution is in very good agreement with the analytical results. Temperature profiles along the fracture at $z = [0]\,\mathrm{m}$ are plotted in Fig. 4.17.

For long simulation times ($t' = 1,000; t' = 600$) both solutions fit very well together. For short simulation times, the numerical solution differs slightly from the analytical results. This discrepancy for short simulation times can be examined in Fig. 4.18, where temperature breakthrough curves for certain points (see Fig. 4.15) are plotted.

# Chapter 5

# Groundwater Flow

*by Feng Sun, Norihiro Watanabe, and Jens-Olaf Delfs*

## 5.1 Groundwater Flow in an Anisotropic Medium

### 5.1.1 Definition

The aim of this example is to simulate the stationary groundwater flow in an anisotropic porous medium. In order to consider the permeability anisotropy, a 2-D numerical model is built which contains a higher permeability in the vertical direction than that in the horizontal direction. The aquifer is assumed saturated and stationary.

For the two-dimensional simulation, the cube consisting of a porous medium is simplified as a square with an area of 1 $m^2$. The calculation model includes 736 triangular elements and 409 nodes. At the lower left corner of the model a constant pressure of 1,000 Pa is specified along two polylines of the length of 0.3 m (Fig. 5.1). At the top and the right borders the pressures are set to 0 in order to create the pressure gradient. As the porous medium is assumed to be anisotropic, which influences the groundwater flow, the values for the permeabilities are equal to $1.0\times10^{-15}$ $m^2$ in x-direction and $1.0\times10^{-14}$ $m^2$ in y-direction. Other properties of the anisotropic media are shown in Table 5.1.

O. Kolditz et al. (eds.), *Thermo-Hydro-Mechanical-Chemical Processes in Fractured Porous Media*, Lecture Notes in Computational Science and Engineering 86,
DOI 10.1007/978-3-642-27177-9_5, 

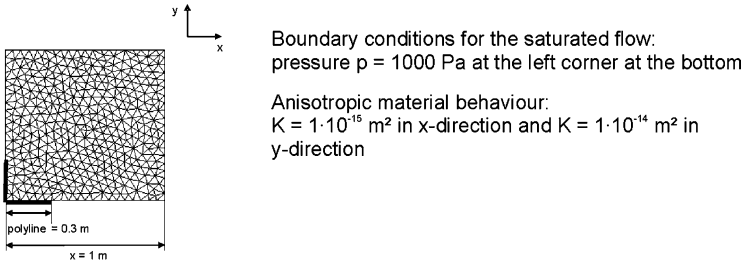


Figure 5.1: Calculation model (2-D) of the anisotropic media

Table 5.1: The parameters defined in the anisotropic media

| Symbol | Parameter | Value | Unit |
|---|---|---|---|
| $n$ | Porosity | 0.2 | – |
| $\kappa_x$ | Permeability | $1.0 \times 10^{-15}$ | $m^2$ |
| $\kappa_y$ | Permeability | $1.0 \times 10^{-14}$ | $m^2$ |

### 5.1.2 Evaluation Method

This test example was not created in order to introduce a new process, however to show the OGS user the possibility of giving a specific permeability for each direction. Therefore, the interpretation of OGS results comprises merely the comparison between pressure distributions due to the anisotropic permeability that were simulated by the use of RockFlow (RF) and OGS. This comparison is possible because both versions were developed separately concerning anisotropy of soils.

### 5.1.3 Results

In Fig. 5.2 the horizontal and vertical pressure distributions of an anisotropic groundwater flow model which was developed using the program code RF are depicted next to those calculated from the above described anisotropic model with OGS. While presuming an anisotropic medium, an inhomogeneous pressure field is developing because the groundwater is not able to spread out uniformly. This can be recognized at the different curve gradients in x- and y-direction. There are slight differences between the curve characteristics of the RF and OGS simulation results. These differences are due to different element types (square in the RF model) and the resulting different x- or y-coordinates. Therefore, the pressure distributions obtained by the simulation with OGS are evaluated to be correct.

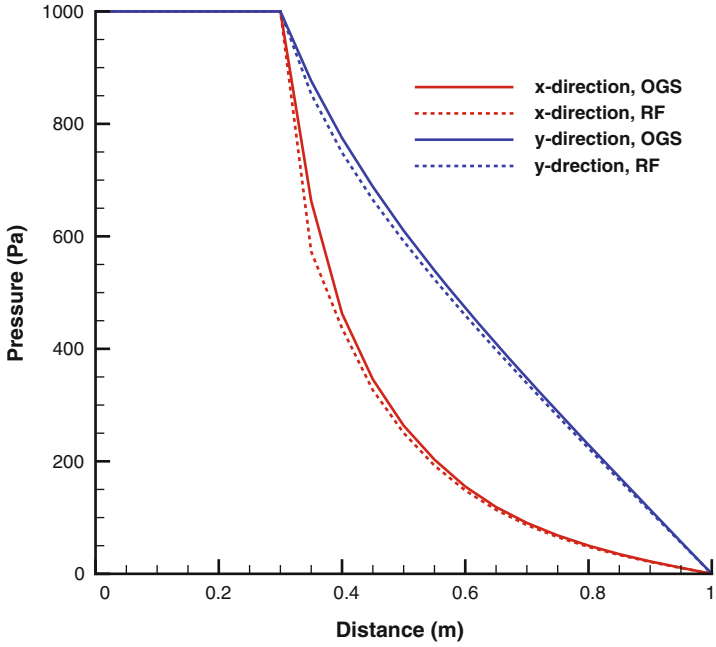


Figure 5.2: Pressure distribution caused by anisotropic saturated flow

## 5.2 Groundwater Flow in a Heterogeneous Medium

### 5.2.1 Definition (2-D)

The aim of this example is to simulate the stationary groundwater flow in an isotropic and heterogeneous porous medium. In order to consider the heterogeneous of hydraulic conductivity, a 2-D numerical model is built. The heterogeneous distribution of hydraulic conductivity is shown in Fig. 5.3. The aquifer is assumed isotropic, heterogeneous, saturated and stationary.

For the two-dimensional simulation, the cube consisting of a porous medium is simplified as a square with an area of 10,000 $m^2$. The calculation model includes 10,000 quad elements and 10,201 nodes. At the left boundary a constant head of 10 m and the right boundary a constant head of 9 m are specified in order to create a pressure gradient.

### 5.2.2 Results (2-D)

As shown in Fig. 5.4, the head distribution of the groundwater flow in a heterogeneous medium is depicted complying with the distribution of the hydraulic conductivity.

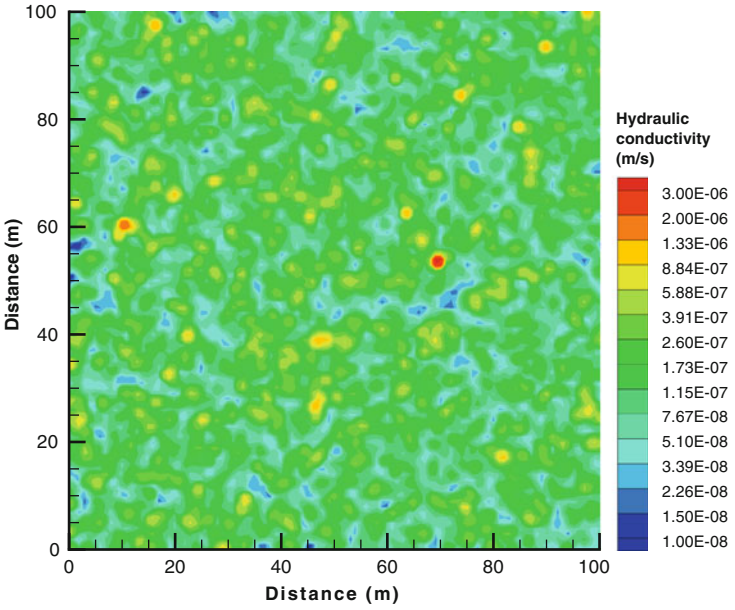


Figure 5.3: Calculation model (2-D): hetergeneous hydraulic conductivity distribution

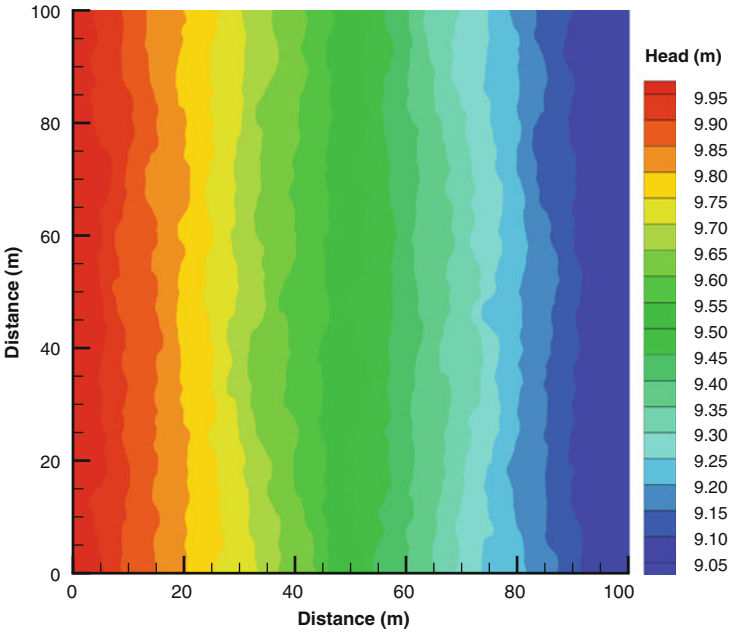


Figure 5.4: Head distribution in response to isotropic and heterogeneous medium

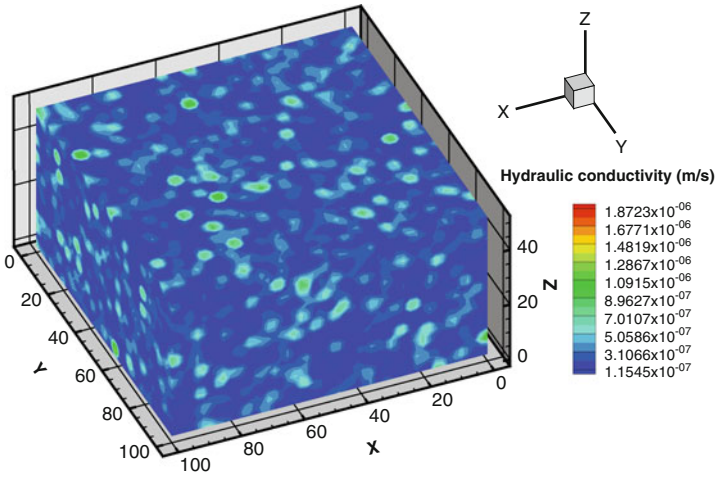


Figure 5.5: Calculation model (3-D): hetergeneous hydraulic conductivity distribution

### 5.2.3 Definition (3-D)

For the three-dimensional simulation, the aquifer is defined as a 100 m× 100 m× 50 m cuboid. The calculation model includes 60,025 hex elements and 65,000 nodes. A constant head of 10 m at the left surface and a constant head of 9 m at the right surface are specified in order to create a pressure gradient. The heterogeneous distribution of hydraulic conductivity is shown in Fig. 5.5.

### 5.2.4 Results (3-D)

As shown in Fig. 5.6, the 3-D head distribution of the groundwater flow in a heterogeneous medium is depicted in response to the distribution of the hydraulic conductivity.

## 5.3 Confined Aquifer with Constant Channel Source Term

### 5.3.1 Definition

This example deals with an aquifer which is subject to a constant recharge line source. The channel is assumed to be independent of the groundwater head and not affected by the water loss or the exchange flux. Therefore, the source term represents a steady and uniform channel located above the aquifer. The cross-section of the channel is rectangular (Fig. 5.7).

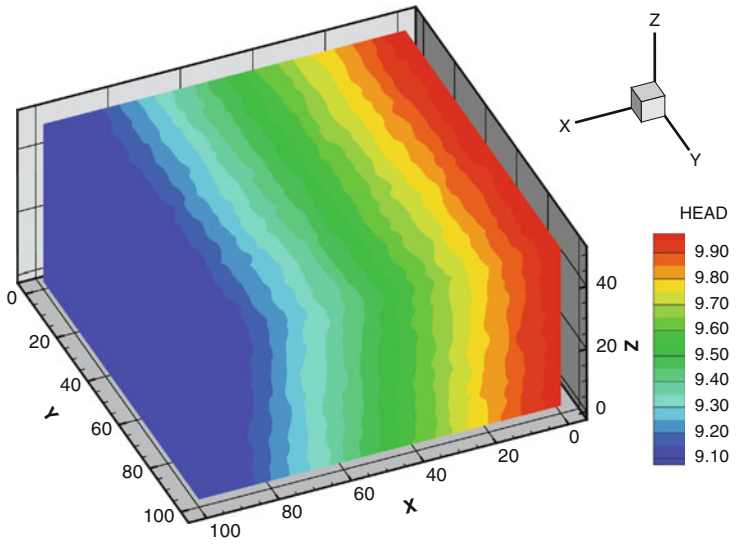


Figure 5.6: Head distribution in response to isotropic and heterogeneous medium (3-D)

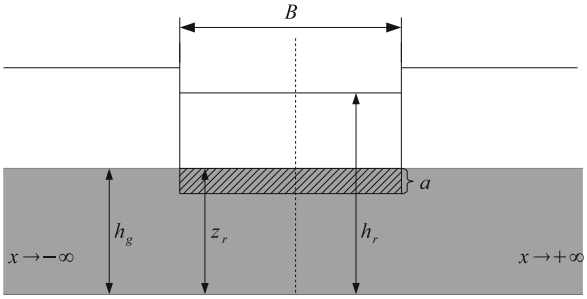


Figure 5.7: The illustration of the cross section of the channel/groundwater

The integrated recharge flow that provides the link between the channel and the groundwater is defined by 5.1 [98].

$$q^{ex} = \begin{cases} -K_\Lambda P \frac{(h_r - h_g)}{a} & h_g > (z_r - a) \\ -K_\Lambda P \frac{(h_r - (z_r - a))}{a} & h_g \leq (z_r - a) \end{cases} \tag{5.1}$$

where $K_\Lambda$ is the channel bed conductivity, $B$ is the channel width, $a$ is the channel bed thickness and $h_r$ is the channel flow head, $h_g$ is the groundwater table. The wetted perimeter $P = 2(h_r - z_r) + B$ for rectangular channel where $z_r$ is the height of the top of the channel bed.

In this benchmark, the aquifer size is 20 m× 10 m with the source term at the left boundary (See Fig. 5.10). The initial groundwater head is 0 m. The channel source term is the boundary condition at one side, at the opposite boundary the head is fixed with 0 m. At the remaining boundaries no-flow is imposed.

For the spatial discretization either 24 × 12 quadrants or hexahedra are used as well as prisms which are generated by cutting the hexahedra into two parts. The hexahedra or prism height is 1 m. The time step is 1 minute. Simulation parameters for the aquifer and the channel source term are given in Table 5.2.

A constant recharge value of $4.0\times10^{-4}\mathrm{m}^2/\mathrm{s}$ is obtained from (5.1) when the properties of the channel are defined as those values in Table 5.2. Because this problem is symmetric for uniform and isotropic conditions in the aquifer,only half of the domain is taken into account. Therefore, the constant Neuman boundary condition is assigned with half of the recharge value ($2.0\times10^{-4}\mathrm{m}^2/\mathrm{s}$).

### 5.3.2 Solution

R. E. Glover [99] presented an analytical solution for a constant line source in an infinite aquifer domain in 1978, which gives the groundwater head at any point of the source line by the following equation,

$$h = q^{ex}\sqrt{\frac{\mu t}{\pi\rho g\kappa L S_y}} \tag{5.2}$$

where $q^{ex}$ is the recharge rate [$\mathrm{L}^2/\mathrm{T}$], $L$ is the saturated thickness of the aquifer [L], $\kappa$ is the permeability of the aquifer [$\mathrm{L}^2/\mathrm{T}$], $S_y$ is the specific yield of the aquifer [-] and $t$ is the time [T].

Table 5.2: Parameters for channel source term examples

| Symbol | Parameter | Value | Unit |
|---|---|---|---|
| | Aquifer | | |
| $S$ | Storage | 0.2 | – |
| $\mu$ | Viscosity | $1.0 \times 10^{-3}$ | Pa· |
| $K$ | Conductivity | $1.0 \times 10^{-3}$ | m/s |
| $L$ | Thickness | 25 | m |
| | Channel source term | | |
| $h_r$ | Channel water surface | 3 | m |
| $z_r$ | Bed top location | 0 | m |
| $a$ | Bottom sediment thickness | 0.3 | m |
| $B$ | Channel width | 34 | m |
| $K_\Lambda$ | Bed conductivity | $1.0 \times 10^{-6}$ | m/s |

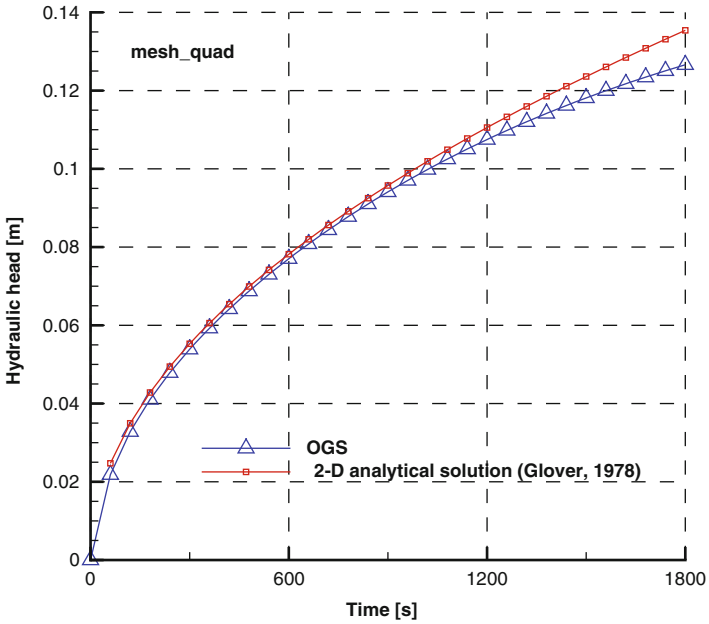


Figure 5.8: Results with quadratic elements and the analytical solution for a confined aquifer below a uniform and steady channel

### 5.3.3 Results

Comparison of simulation results and the analytical solution is given in Fig. 5.8 for quadrants and in Fig. 5.9 for hexahedra.

The small differences between Figs. 5.8 and 5.9 are mainly caused by the channel source term. In the model with hexahedral elements, the channel source term is defined as a line source at the left-top boundary of the domain (Fig. 5.10).

## 5.4 Theis' Problem

### 5.4.1 Definition

Theis' problem examines the transient lowering of the water table induced by a pumping well. Theis' fundamental insight was to recognize that Darcy's law is analogous to the law of heat flow by conduction, i.e., hydraulic pressure being analogous to temperature, pressure-gradient to thermal gradient. The assumptions required by the Theis solution are:

- the aquifer is homogeneous, isotropic, confined, infinite in radial extent,
- the aquifer has uniform thickness, horizontal piezometric surface

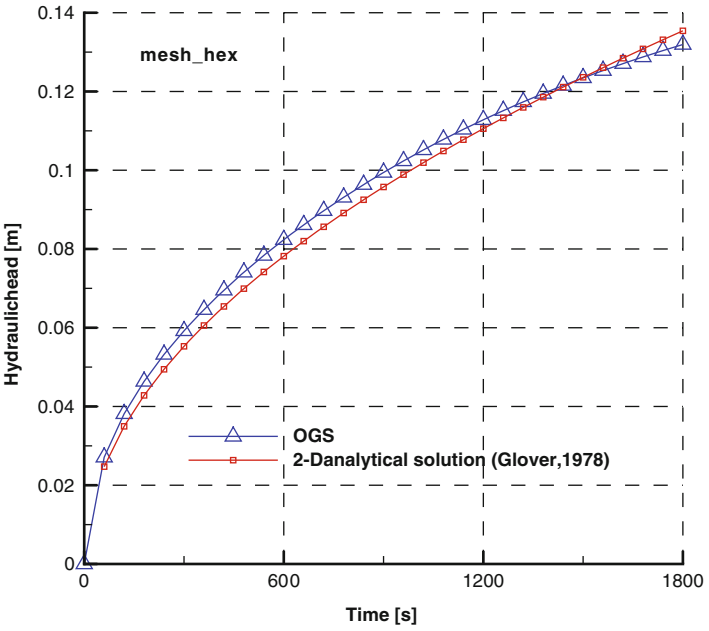


Figure 5.9: Results with hexahedral elements compared with the analytical solution for a confined aquifer below a uniform and steady channel

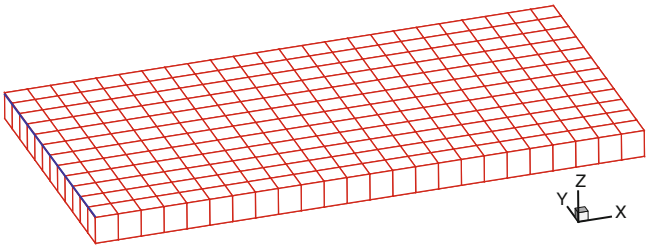


Figure 5.10: Computational domain and source term location

- the well is fully penetrating the entire aquifer thickness,
- the well storage effects can be neglected,
- the well has a constant pumping rate,
- no other wells or long term changes in regional water levels.

### 5.4.2 Solution

The analytical solution of the drawdown as a function of time and distance is expressed by (5.3):

Table 5.3: The parameters defined in 1-D Theis' problem

| Symbol | Parameter | Value | Unit |
|---|---|---|---|
| $h(0,r)$ | Initial conditions | 0 | m |
| $Q$ | Well pumping rate | $1.2233\times10^{3}$ | $m^3/d$ |
| $h(t,304.8)$ | Boundary conditions | 0 | m |
| $K$ | Hydraulic conductivity | $9.2903\times10^{-4}$ | m/s |
| $S$ | Storage coefficient | 0.0010 | – |
| $r$ | 0.3048 | Wellbore radius | m |

$$h_0 - h(t,x,y) = \frac{Q}{4\pi T} W(u) \tag{5.3}$$

$$u = \frac{(x^2+y^2)S}{4Tt} \tag{5.4}$$

where $h_0$ is the constant initial hydraulic head $[L]$, $Q$ is the constant discharge rate $[L^3T^{-1}]$, $T$ is the aquifer transmissivity $[L^2T^{-1}]$, $t$ is time $[T]$, $x, y$ is the coordinate at any point $[L]$ and $S$ is the aquifer storage $[-]$. $W(u)$ is the well function defined by an infinite series for a confined aquifer as

$$W(u) = \int_u^{+\infty} \frac{e^{-u}}{u} du = -\gamma - lnu + \sum_{k=1}^{\infty} \frac{(-1)^{k+1} u^k}{k \cdot k!} \tag{5.5}$$

where $\gamma \approx 0.5772$ is the Euler-Mascheroni constant. For practical purposes, the simplest approximation of $W(u)$ was proposed as $W(u) = -0.5772 - lnu$ for $u < 0.05$. Other more exact approximations of the well function were summarized by R. Srivastava and A. Guzman-Guzman [100].

The parameters and initial & boundary conditions are defined in Table 5.3.

### 5.4.3 Results

Figure 5.11 shows the comparison of analytically and numerically calculated drawdown of hydraulic head versus time at the distance of 9.639 m from the well.

### 5.4.4 2-D Application

The 2-D application is solved in the following situation (Table 5.4).

The aquifer's horizontal domain size is 1,000 m × 750 m with the pumping well at the location coordinate (500, 375). The discretization of space is 10 m × 10 m

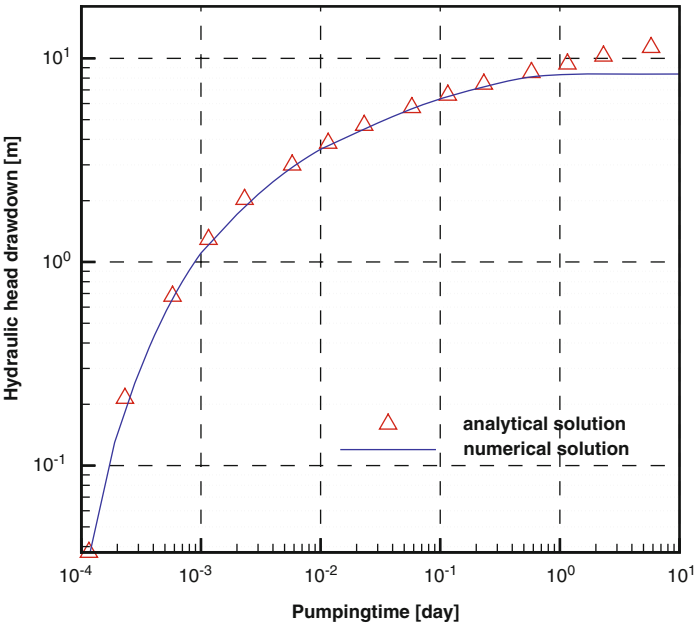


Figure 5.11: Calculated drawdowns at a distance of 9.639 m from the well

Table 5.4: The parameters defined in 2-D Theis' problem

| Symbol | Parameter | Value | Unit |
|---|---|---|---|
| $Q$ | Discharge rate | 1,000 | $m^3/d$ |
| $S$ | Specific storage | $1.0 \times 10^{-5}$ | $1/m$ |
| $T$ | Transmissivity | 1,000 | $m^2/d$ |
| $B$ | Thickness of aquifer | 20 | m |

grid. The simulation time is 151.2 seconds and the time step is 1.036 seconds. The initial head is 20 m in the whole domain and the boundary condition is 0 m drawdown at the left and right boundaries. There is no flux through the top and bottom boundaries. The cone of depression induced by the pumping well at the end of the simulation is plotted in Fig. 5.12.

## 5.5 Unconfined Aquifer

### 5.5.1 Definition

In this example the aquifer consists of a small strip with the size of 100 m × 2 m (see Fig. 5.13). At both ends the head is fixed and constant recharge is imposed on the whole domain which leads to steady state flow. This setting

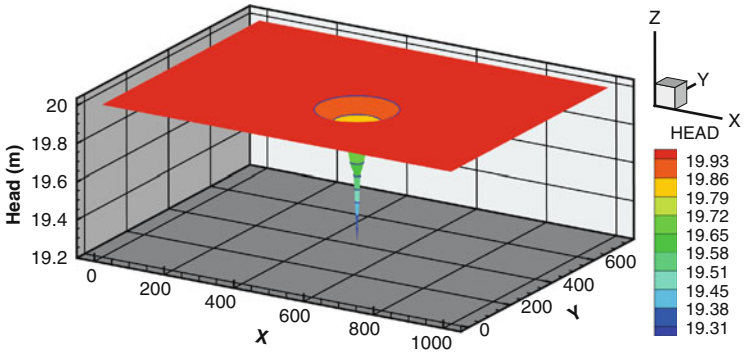


Figure 5.12: Cone of depression at the end of the simulation

allows the comparison with an analytical solution. Initial groundwater head is 0 m. At one end of the strip the head is 1 m at the other 5 m. At the top a source term is $1.0\times10^{-8}$ m/s and at the remaining parts no-flow is imposed. For the spatial discretization 100 equal quadrants and 410 triangles or prisms are used. In the later case, the three-dimensional unconfined groundwater equation is solved with elements adapting to the water height. One time step with the size of 100 s is used. The specific storage $S_s = 0$ m$^{-1}$ or specific yield $S_y = 0$ and a hydraulic conductivity $K$ of $9.9\times10^{-6}$ m/s are used.

### 5.5.2 Analytical Solution

In an unconfined aquifer, the saturated thickness is defined as the vertical distance between the water table surface and the aquifer base. If the aquifer base is at the zero datum, then the unconfined saturated thickness ($b$) is equal to the head ($h$). With the Dupuit assumption (or Dupuit-Forcheimer assumption), where it is assumed that heads do not vary in the vertical direction (i.e., $\frac{\partial h}{\partial z} = 0$), a horizontal water balance is only applied to a long vertical column with area ($\delta x \delta y$) extending from the aquifer base to the unsaturated surface. For this vertical column, applying Darcy's law and a mass balance expression, the groundwater flow equation for an unconfined aquifer can be obtained:

$$S_y \frac{\partial h}{\partial t} = \nabla \cdot (kh\nabla h) + N \tag{5.6}$$

where $N$ [L/T] is the source term representing the addition of water in the vertical direction, $S_y$ [-]is the specific yield of the aquifer and $k$ [L/T] is the hydraulic conductivity.

The unconfined groundwater flow equation is a non-linear partial differential equation, and it may be linearized by expressing the PDE in terms of the squared head for steady-state flow:

$$\nabla \cdot (k \nabla h^2) = -2N \tag{5.7}$$

and for the homogeneous aquifers, (5.7) becomes

$$\nabla^2 \nabla h^2 = -\frac{2N}{k} \tag{5.8}$$

Equation (5.8) can be solved by the standard integration method for linear PDEs. For the definition of the unconfined aquifer above, the analytical solution is expressed by the following equation.

$$h = \sqrt{-0.001x^2 - 0.14x + 25} \tag{5.9}$$

### 5.5.3 Results

Comparison of simulation results with prisms and the analytical solution is shown in Fig. 5.13.

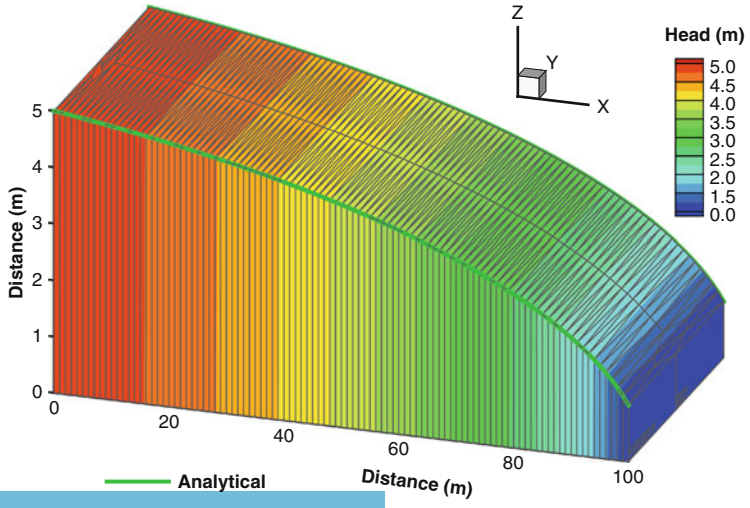


Figure 5.13: Benchmark example results of unconfined aquifer with prisms

## 5.6 2-D Steady State Flow in Porous Media with a Discrete Fracture

### 5.6.1 Definition

This example illustrates the disturbance of the uniform flow in porous media caused by the presence of a fracture. Consider a 2-D infinite horizontal plane of porous media with an embedded fracture. Uniform flow with specific discharge $q_0$ occurs from the left to the right side of the domain. The fracture extends to infinity in the directions normal to the plane. The middle point of the fracture is placed at the center of the plane. The shape of the fracture is shown in Fig. 5.14. The fracture has a length of $L$ and is inclined with angle $\beta$. The fracture aperture $b$ may vary with positions. In this example, it is assumed that the shape corresponds to that obtained from the normal displacements of the sides of a pressurized crack in an elastic medium. This gives

$$b = b_{\max}\sqrt{1 - x'^2} \tag{5.10}$$

where $x'$ is the normalized local coordinate systems. $b_{\max}$ is the aperture at the center $x' = 0$. Assuming the volume of the fracture is sufficiently small as compared to that of porous media, the flow in the porous media can be modeled ignoring the width of the fracture. The flow in the fracture is assumed to be laminar along the fracture surface. Hydraulic conductivity of the fracture is constant and independent of the aperture variation. The pressure variation across the fracture is neglected.

### 5.6.2 Solution

#### Analytical Solution

Strack [101] has derived an exact solution for this problem as the potential flow. The obtained complex potential $\Omega$ is given as

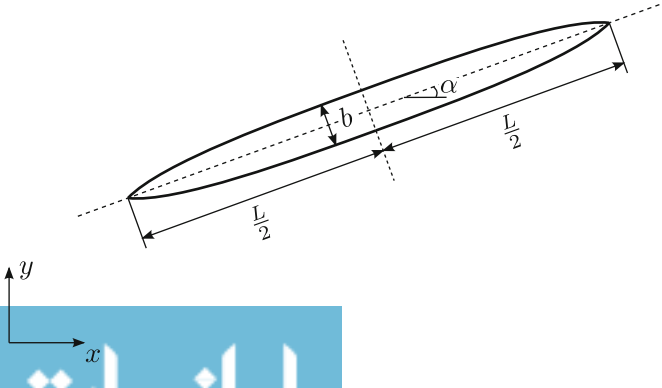


Figure 5.14: Fracture geometry

Table 5.5: Model parameters

| Symbol | Parameter | Value | Unit |
|---|---|---|---|
| $\alpha$ | Fracture angle | 45 | $\circ$ |
| $b_{\mathbf{max}}$ | Maximum fracture aperture | 0.05 | m |
| $L$ | Fracture length | 2.0 | m |
| $K_f$ | Fracture hydraulic conductivity | $1.0 \times 10^{-3}$ | m/s |
| $K_m$ | Porous medium hydraulic conductivity | $1.0 \times 10^{-5}$ | m/s |
| $q_0$ | Specific discharge | $1.0 \times 10^{-4}$ | m/s |

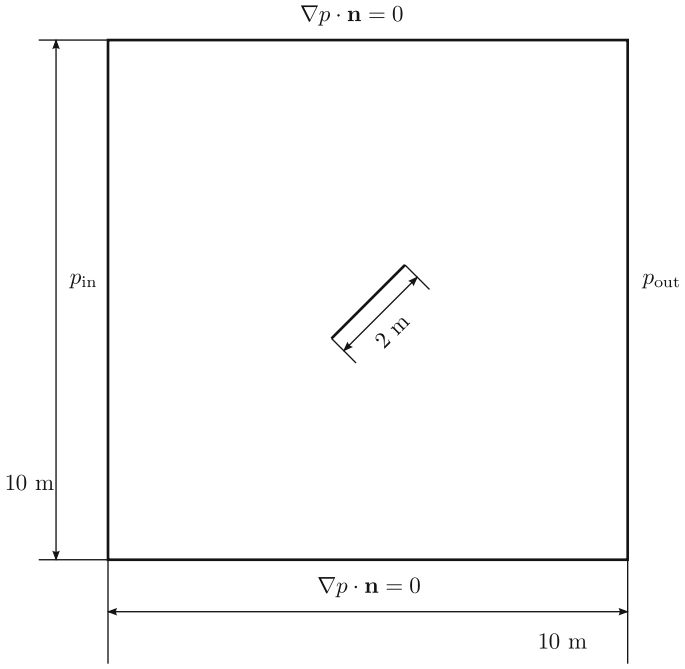


Figure 5.15: Computational area

$$\Omega = -A\sqrt{(Z-1)(Z+1)} + AZ - \frac{1}{2}q_0 L e^{i\alpha} Z + C \tag{5.11}$$

for the dimensionless variable $Z$

$$Z = X + iY = \frac{z - \frac{1}{2}(z_1 + z_2)}{\frac{1}{2}(z_2 - z_1)} \tag{5.12}$$

with the endpoints of the fracture $z_1$ and $z_2$. $A$ is defined as

$$A = \frac{\frac{1}{2}K_f b_{\max}}{K_m L + K_f b_{\max}} q_0 L \cos\alpha \tag{5.13}$$

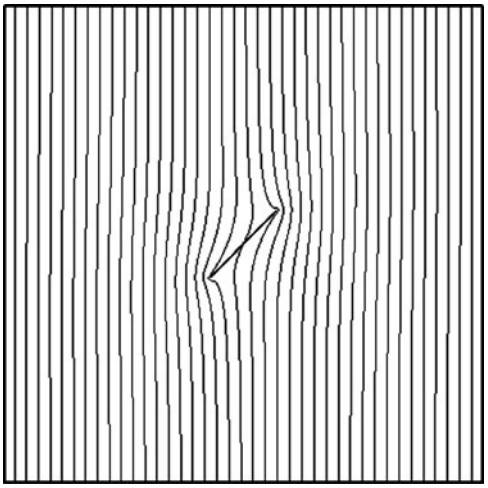

Figure 5.16: Pressure distribution obtained by the analytical solution

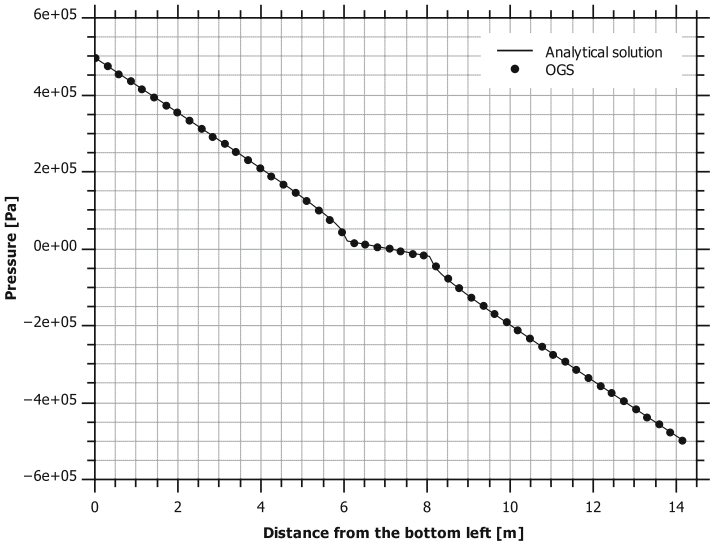


Figure 5.17: Pressure profile along a diagonal line from the bottom-left to the top-right

and $C$ is the integration constant. In this example, the constant is simply considered as zero.

### Numerical Solution

A numerical solution can be obtained by solving the steady state liquid flow problem in a hybrid system of a discrete fracture model and continuum model

(porous media). The fracture is represented as a 1D hydraulic conduit. The domain is set up in a finite space as a square with a length of 10 m as depicted in Fig. 5.15. To compare numerical results with the analytical solution, pressure calculated by the analytical solution is utilized as prescribed pressure at the lateral boundaries, i.e. $p_{\text{in}} = 496465$ Pa and $p_{\text{out}} = -496465$ Pa. It is assumed that the fracture aperture does not vary with positions and has a constant value even at the endpoints, $b = b_{\max}$. Other properties of the numerical model are shown in Table 5.5.

### 5.6.3 Results

Pressure distribution obtained by the analytical solution is shown in Fig. 5.16. Lateral uniform flow is disturbed in the vicinity of the inclined fracture where the flow is faster than in surrounding porous media. Figure 5.17 presents the pressure profile along a diagonal line from the bottom-left to the top-right. Although the numerical solution adopts the idealized fracture geometry, results show good agreement between the numerical and the analytical solution.

# Chapter 6

# Richards Flow

*by Thomas Kalbacher and Yanliang Du*

The upper parts of the ground usually belong to the vadose zone, i.e. the zone between land surface and the top of the upper aquifer. This zone is a transition section between the atmosphere, biosphere, lithosphere and hydrosphere and connects the neighboring compartments via air, water and solids including biomass and organic matter. The vadose zone can be roughly subdivided from top to bottom into a soil water zone, intermediate zone, and the capillary fringe. Only 0.0012% of the global water reservoir or 0.05% of the fresh water budget remains in soil. Compared with groundwater reservoirs, which store over 30% of the global fresh water, the mass fraction of soil water within the hydraulic circle seems to be small, but is actually more dynamic. Water only resides in soil systems a few weeks on average, while groundwater systems can have residence times of several millenniums. Generally, the flow processes in soil take place under unsaturated conditions, i.e. the pore spaces are only partly filled with air and water. Moreover, such unsaturated conditions can occur in any multiphase regime where the water that partly fills the pore system is under suction and the pressure head is negative.

With the single continuum approach, the pore system of each porous media is regarded as the only process environment for flow. Within the pore space, the conductivity for the air flow is much higher than for the water flow. Obviously, a change of the volumetric water content in such regimes causes a change of the air volume. However, if the air phase is considered as continuous and mobile as far as possible, then the air pressure can be assumed as constant and equal to the atmospheric pressure. Since air is much more mobile compared to water, the required driving forces for moving the gas phase in such a system, can be

O. Kolditz et al. (eds.), *Thermo-Hydro-Mechanical-Chemical Processes in Fractured Porous Media*, Lecture Notes in Computational Science and Engineering 86,
DOI 10.1007/978-3-642-27177-9_6, © Springer-Verlag Berlin Heidelberg 2012

neglected. This simplification of a two phase flow system (air and water) is also called the Richards flow regime.

The Richards equation is often used to mathematically describe water movement in the unsaturated zone. It has been introduced by Richards (1931) [102] who suggested that Darcy's law under consideration of the mass conservation principle, is also appropriate for unsaturated flow conditions in porous media. The pressure based formulation of this governing equation (Eq. 6.1), which selects the unknown primary variable as $p$, can be written as:

$$\phi\rho_w \frac{\partial S}{\partial p_c}\frac{\partial p_c}{\partial t} + \bigtriangledown \cdot \left(\rho_w \frac{k_{rel}\mathbf{k}}{\mu_w}(\bigtriangledown p_w - \rho_w \mathbf{g})\right) = Q_w \tag{6.1}$$

where $\phi$ is porosity, $t$ is time, $\rho_w$ is the liquid density, $\mu_w$ is the liquid viscosity, $p_c$ is the capillary pressure with $p_c$ = -$p_w$, $p_w$ is the water pressure, $S$ is the water saturation, $\mathbf{g}$ is gravity acceleration vector, $Q_w$ is the source term, $k_{rel}$ is the relative permeability and $\mathbf{k}$ is the intrinsic permeability which is related to the hydraulic conductivity $\mathbf{K}$ with

$$\mathbf{k} = \frac{\mu_w}{\rho_w \mathrm{g}}\mathbf{K} \tag{6.2}$$

In an unsaturated porous media, the capillary pressure is fundamentally related to the saturation of the gas and liquid phase. If e.g. the water saturation decreases and hence the saturation of air increases, then the water retreats to smaller pores and the capillary pressure increases. The capillary pressure can be seen as a function of the effective saturation $S_{\mathrm{eff}}$. This relationship is primarily determined by the nature of the pore space geometry and interconnectivity and is highly non-linear. Brooks and Corey (1964) [49] and Van Genuchten (1980) [51], among many other scientists, derived functional correlations which contain empiric shape parameters that characterize pore-specific properties. With the Van Genuchten parameterization the capillary pressure can be described as

$$p_c = \frac{\rho_w \mathrm{g}}{\alpha}\left[S_{\mathrm{eff}}^{-1/m} - 1\right]^{1/n} \tag{6.3}$$

where $\alpha$ $[1/m]$ is a conceptualized parameter related to the air entry pressure, $n$ is a dimensionless pore size distribution index and m = 1-$(1/n)$. These parameters are usually used to fit the saturation dependent curves of capillary pressure and hydraulic conductivity to experimental data. The relative permeability can be given as

$$k_{rel} = S_{\mathrm{eff}}^{1/2}\left[1 - (1 - S_{\mathrm{eff}}^{1/m})^m\right]^2 \tag{6.4}$$

The effective saturation is

$$S_{\mathrm{eff}} = \frac{S - S_r}{S_{\max} - S_r} \tag{6.5}$$

with $S_{\max}$ and $S_r$ as the maximum and residual saturation.

With Richards and the single continuum approach, all materials are regarded as continuous porous media, but in porous and fractured media, the fractures and

matrix often exhibit strongly differing hydraulic material properties. The dual permeability method accounts for these differences by assuming two separate but interacting continua that overlap each other in space; one describes flow in the fractures and the other describes flow in the matrix (e.g. Barenblatt et al. 1960 [103], Gerke and van Genuchten 1993 [104] or Vogel et al. 2000 [105]). The dual permeability model, also more generally called the dual porosity model, is composed by coupled Richards equations of the matrix $M$ and fracture $F$ continua, which are combined by additional transfer and specific storage terms.

$$\phi \frac{\partial S^M}{\partial p_c^M} \frac{\partial p_c^M}{\partial t} + \bigtriangledown \cdot \left( \frac{k_{rel} \mathbf{k}^M}{\mu_w} (\bigtriangledown p_w^M - \rho_w \mathbf{g}) \right) = \frac{Q_w^M}{\rho_w} + \frac{\Gamma_w}{w^M} \tag{6.6}$$

$$\phi \frac{\partial S^F}{\partial p_c^F} \frac{\partial p_c^F}{\partial t} + \bigtriangledown \cdot \left( \frac{k_{rel} \mathbf{k}^F}{\mu_w} (\bigtriangledown p_w^F - \rho_w \mathbf{g}) \right) = \frac{Q_w^F}{\rho_w} - \frac{\Gamma_w}{w^F} \tag{6.7}$$

Under quasi-steady exchange conditions, the transfer term $\Gamma_w(t, x)$ is assumed to be proportional to the pressure difference between the pore systems of the matrix and fractures, $p_w^M - p_w^F$. The relationship between the preferential factors $w^M$ and $w^F$ is $w^M + w^F = 1$.

The original definition of the transfer term is adequate for soils, but for fractured porous rock the unsaturated flow in the fractures is more likely to form in channels rather than be uniformly distributed over the entire fracture plane therefore an additional modification is needed as suggested by Birkholzer and Zhang (2006) [106], who introduced an interface reduction factor $R$.

$$\Gamma_w = \alpha^* \frac{k_\alpha}{\mu_w} (p_w^F - p_w^M) R \tag{6.8}$$

$k_\alpha$ is the permeability at the interface between the fracture and matrix continua, but usually defined as the unsaturated permeability $k^M$ of the matrix, since the much smaller hydraulic conductivity of the matrix is the limiting factor for the fracture-matrix flow. The first-order exchange coefficient $\alpha^*$ $[1/m^2]$ is derived from fracture network properties and has to be calibrated using experimental data. The interface reduction factor $R$ is typically equal to the effective fracture liquid saturation.

## 6.1 Single Continuum

All materials used in the benchmarks of the following subsections are regarded as porous media with continuous hydraulic properties. The solution of the single continuum models is based on Eq. (6.1).

### 6.1.1 Infiltration in Homogeneous Soil

#### Definition

This infiltration problem refers to a classical field experiment described by Warrick et al. (1971) [107], who examined simultaneous solute and water

transfer in unsaturated soil within the Panoche clay loam, an alluvial soil of the Central Valley of California. A quadratic 6.10 m plot, which had an average initial saturation of 0.455, was wetted for 2.8 h with 0.076 m of 0.2 N $CaCl_2$, followed by 14.7 h infiltration of 0.229 m solute-free water. The soil-water pressure was monitored by duplicate tensiometer installations at 0.3, 0.6, 0.9, 1.2, 1.5 and 1.8 m below surface.

The numerical infiltration model has been discretized geometrically by a 2.0 m long vertical column with a top surface of 1 $m^2$ (Fig. 6.1). It has been solved by the use of Richards' equation, with a uniform initial condition, fixed boundary condition without source terms, curve descriptions of saturation dependent parameters and homogenous media properties.

Two fixed pressure boundary conditions are used in the flow equation with a uniform initial saturation in the whole domain of 45.5%. At the top, the 2 m high soil column is open to the atmosphere, i.e. the capillary pressure is 0 Pa. The bottom of the column has a capillary pressure of 21,500 Pa (Fig. 6.1). Homogeneous material properties are assumed within the whole domain. The average saturated moisture content, which is equal to the porosity of the soil, is 0.38. The saturated permeability is 9.35e-12 $m^2$. The relative permeability and capillary pressure vs. saturation data are fitted by the soil characteristic functions as shown in Fig. 6.2 respectively and the soil parameters are listed in Table 6.1.

### Results

The simulated and experimental saturation data at various time steps are plotted in Fig. 6.3. The simulated infiltration front (solid line) propagates through the soil column and resembles well the measured saturation results (dashed lines) of Warrick et al. (1971) [107].

To ensure the consistency of different interpolation functions, the soil column has been discretized by one-, two and three-dimensional geometrical models,

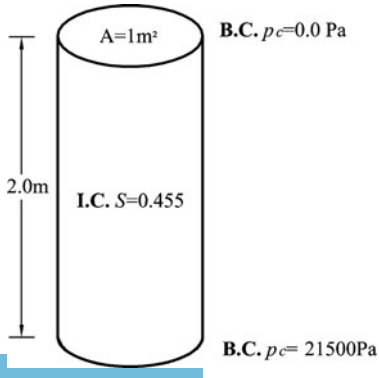


Figure 6.1: Model domain

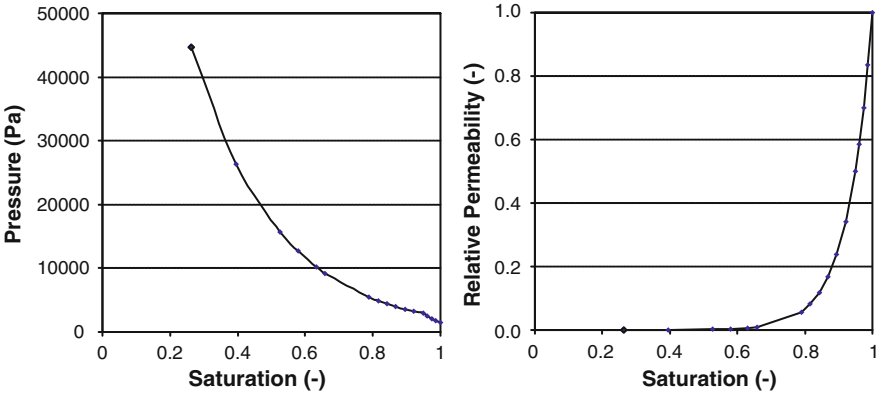


Figure 6.2: Relationship between saturation and capillary pressure as well as between saturation and relative permeability

Table 6.1: Material properties

| Symbol | Parameter | Value | Unit |
|---|---|---|---|
| $p_c$ | Capillary pressure | Curve in Fig. 6.2(l) | Pa |
| $k_{rel}$ | Relative permeability | Curve in Fig. 6.2(r) | – |
| **k** | Intrinsic permeability | 9.35e-12 | $m^2$ |

which contain accordingly consistent finite element types such as lines, triangles, quadrilaterals, tetrahedrons, prisms or hexahedrons. The distinctions of the different discretization cases are presented in Fig. 6.4, which illustrates the temporal evolution of the capillary pressure for the different dimension extensions in the same depth. Figure 6.5 shows the saturation contours after 2, 9 and 17 hours for three different structured and unstructured meshes including elements of lines, triangles or quadrilaterals.

### 6.1.2 Infiltration in Homogeneous Soil (ST/BC)

#### Definition

This example is a one-dimensional infiltration problem which has been used to validate the HYDRUS code [108] as well as the Forsyth model [109], among many others. The experimental study was conducted by Abeele et al. (1981) [110] at Los Alamos National Laboratory and the material properties included in the model are those of the Bandelier Tuff.

Figure 6.6 shows the computational domain of this one-dimensional example, which is a 6m long cylindrical column with a diameter of 3 m. The finite element mesh has a constant mesh density with a node spacing of 3 cm in z direction.

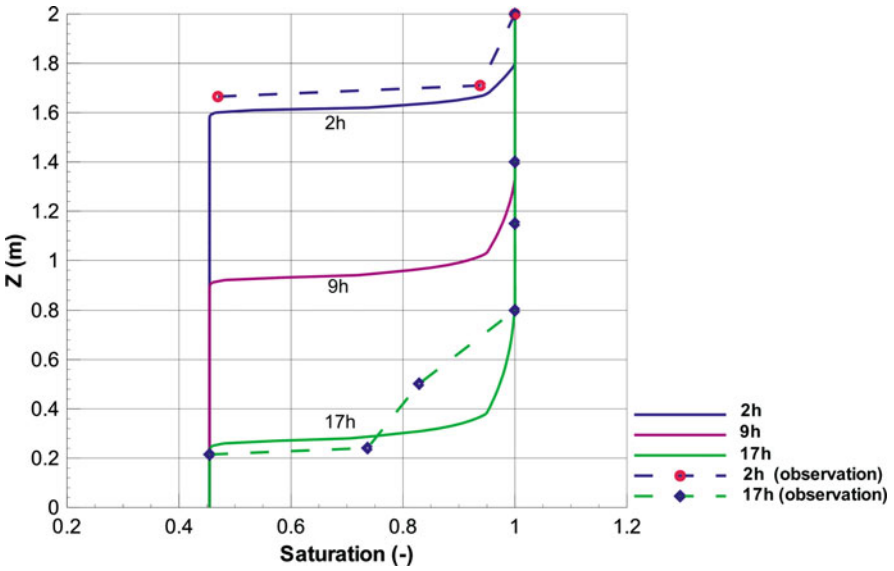


Figure 6.3: Comparison of observed (*symbol and dashed*) and simulated (*solid*) infiltration

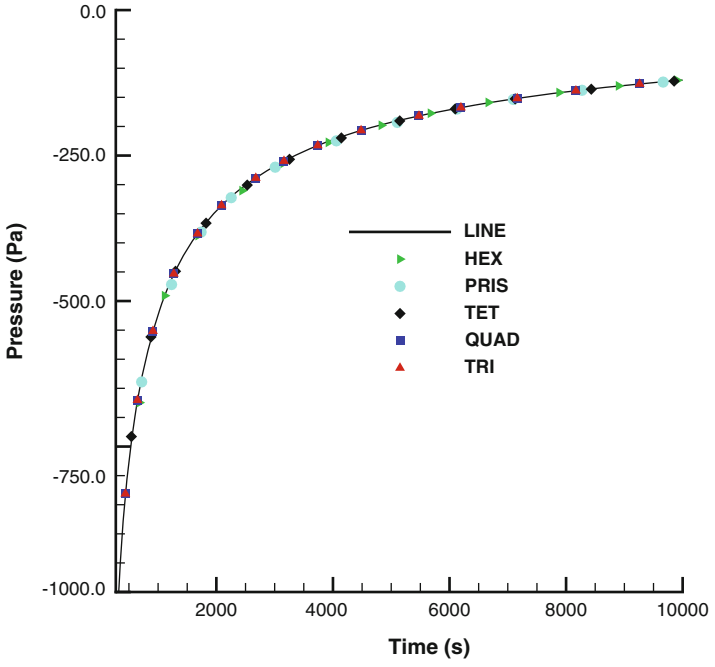


Figure 6.4: Water pressure breakthrough curve. Congruent result for different finite element grids

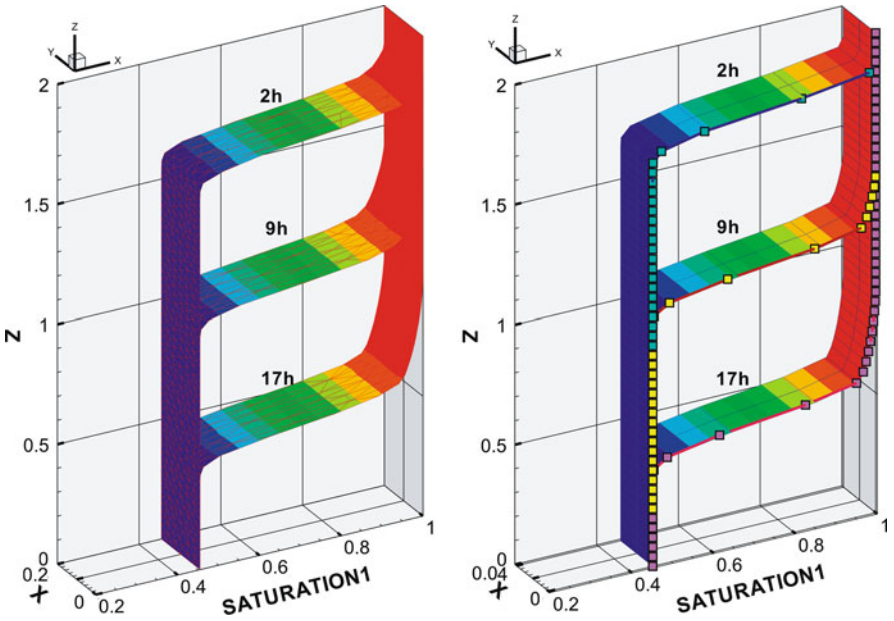


Figure 6.5: Saturation contours and result comparison for different element types. *Left*: unstructured triangular mesh (2D). *Right*: structured quadrilateral mesh (2D) and 1D line mesh (*symbol-solid*)

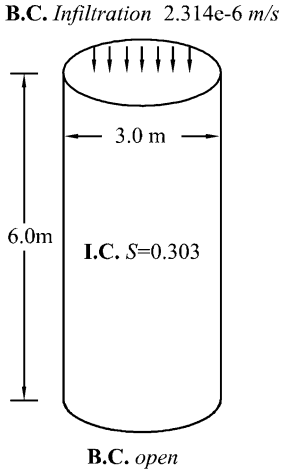


Figure 6.6: Computational domain of the numerical model

Again, the assumption is a homogenous material with unchanging properties within the whole domain. The porosity is 0.33 and the saturated permeability is 2.95e-13 $m^2$. A van Genuchten parameterization is applied for partly saturated conditions. All material specific parameters are listed in Table 6.2.

Table 6.2: Material properties

| Symbol | Parameter | Value | Unit |
|---|---|---|---|
| $\phi$ | Porosity | 0.33 | – |
| $k_s$ | Saturated permeability | 2.95e-13 | $m^2$ |
| $S_r$ | Residual water saturation | 0.0 | – |
| $S_{max}$ | Maximum water saturation | 1.0 | – |
| $\alpha$ | Van Genuchten parameter | 1.43 | 1/m |
| $n$ | Van Genuchten parameter | 1.506 | – |

At the beginning, the material is already relatively wet and does not show super dry conditions. The initial water saturation is S = 0.303 and constant within the whole domain. Therefore the initial condition of pressure is $-71,000$ Pa and constant. The continuous infiltration over 7.16 days at the top of the domain is treated as a source term with 2.314e-6 m/s. Details are illustrated in Fig. 6.6.

**Results**

Figure 6.7 shows the distribution of the water saturation at various times. The left side of Fig. 6.7 is the original result from Forsyth et al. (1995) [109], who compared their code with the HYDRUS simulation. Their problem was solved using both central and upstream weighting and are in close agreement with the HYDRUS results. The OGS simulation results at the right of Fig. 6.7 show similar results as the HYDRUS model, since both are centrally weighted and using a mass conservative formulation.

### 6.1.3 Transient Infiltration in Homogeneous Soil

**Definition**

The following case study was designed by David Kuntz [111] in Tübingen and has been compared with the numerical solutions of Min3P, a multicomponent reactive transport modeling tool for variably saturated porous media (e.g. Mayer et al. 2002 [112]). The model domain depicts a 0.25 m long vertical soil column with a transient water infiltration at the top (Fig. 6.8). Each artificial infiltration event increases drastically, lasts for 24 hours and is repeated weekly, such as for typical surface irrigation scenarios on the lysimeter scale (Fig. 6.9).

The major difference of this test problem, aside from the intermittent infiltration, is that the top fixed boundary condition changes to a source term (flux). The boundary condition at the bottom stays fixed with a pressure of $-31,800$ Pa.

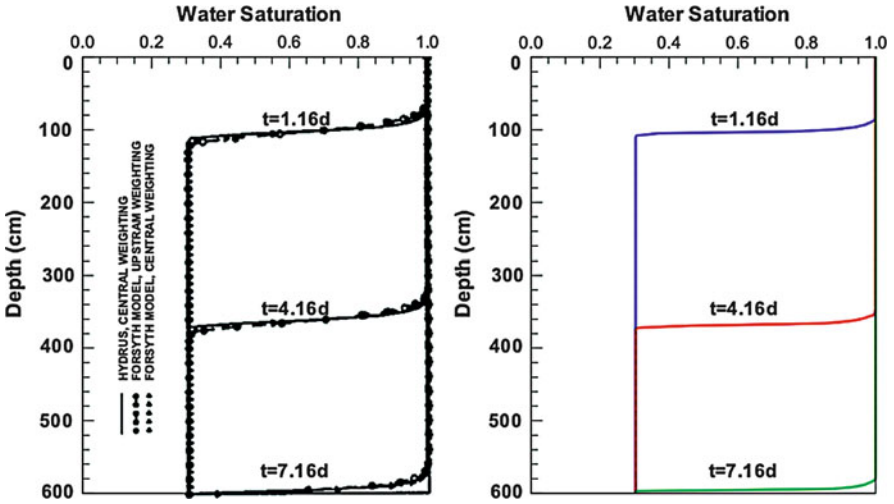


Figure 6.7: Saturation contours and comparison between HYDRUS, Forsyth models (*left*) and OGS (*right*). Source of left diagram: Forsyth et al. (1994) [109]

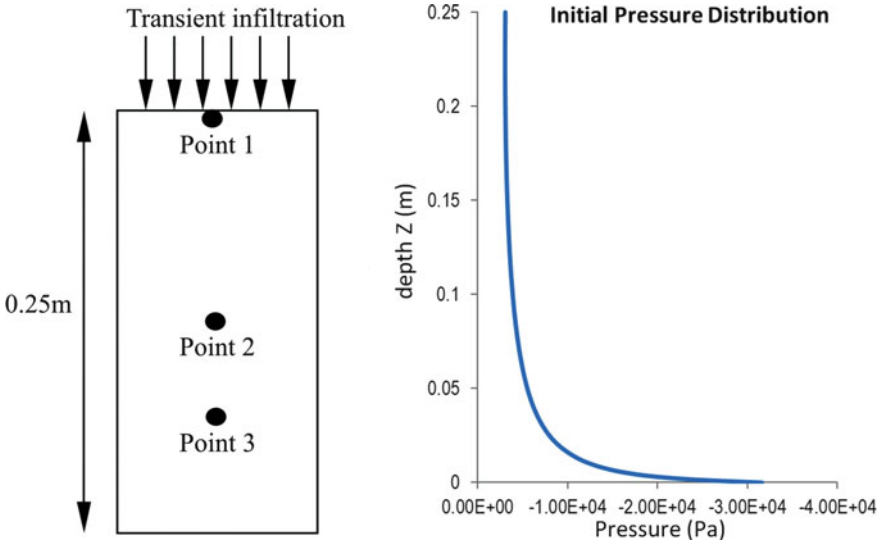


Figure 6.8: Computational domain (*left*) and initial conditions (*right*)

The initial pressure distribution is shown at the right of Fig. 6.8. The homogeneous material properties are given in Table 6.3 and the soil specific parameters are defined by the use of a van Genuchten parameterization.

Table 6.3: Material properties

| Symbol | Parameter | Value | Unit |
|---|---|---|---|
| $\phi$ | Porosity | 0.406 | – |
| $k_s$ | Saturated permeability | 9.35247e-12 | $m^2$ |
| $S_r$ | Residual water saturation | 0.056 | – |
| $S_{max}$ | Maximum water saturation | 1.0 | – |
| $\alpha$ | Van Genuchten parameter | 4.56 | 1/m |
| $n$ | Van Genuchten parameter | 0.254 | – |

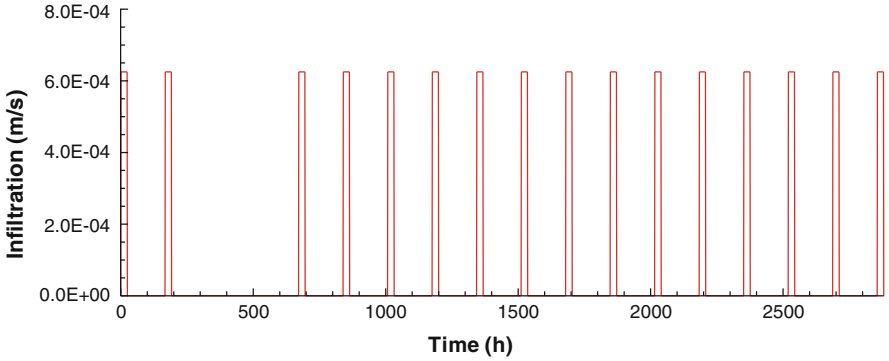


Figure 6.9: Irrigation sequence

**Results**

The numerical model was geometrically discretized in 1D (pseudo 1D in the finite volume model Min3P) with a constant vertical node spacing of 0.00125 m. The contours of Fig. 6.10 display the alternating decrease and increase of the water saturation, modeled with OGS. The results of both software packages were compared at three points in 0.025, 0.15 and 0.2 m depths below the surface. Figure 6.11 shows the comparison of the saturation characteristics over time.

### 6.1.4 Heterogeneous Soil and Non-uniform IC (-/BC)

**Definition**

This problem case was defined within the scope of the DECOVALEX project. The name stands for development of coupled models and their validation against experiments. The general goal of this project is multidisciplinary, interactive and cooperative research on modeling coupled processes in geologic formations, in support of performance assessment for underground storage of radioactive waste.

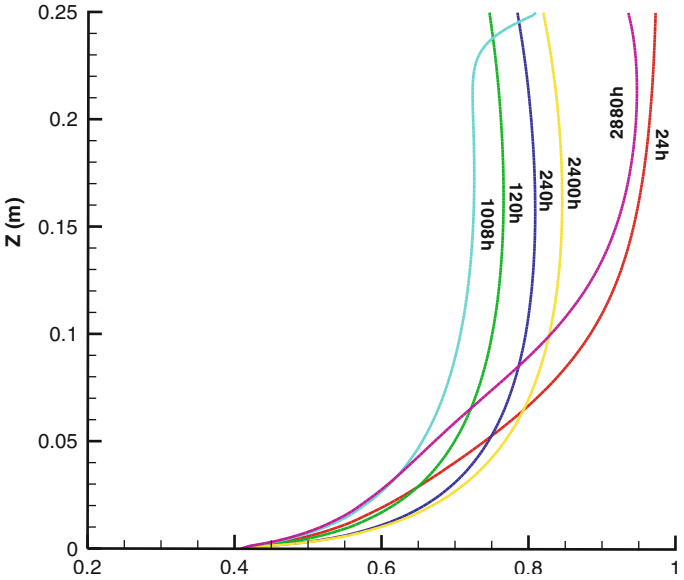


Figure 6.10: Saturation distributions at different times

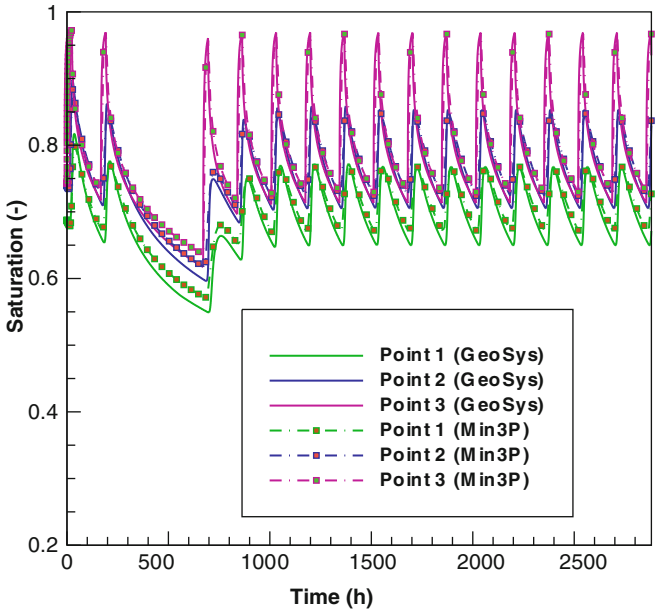


Figure 6.11: Model comparison between OGS (finite element method) and Min3P (finite volume method). Saturation characteristic curves at three different points. Point 1 = 0.025 m , Point 2 = 0.15, and Point 3 = and 0.2 m below top surface

The following test scenario reflects an excavated tunnel in fractured granite, with a waste canister emplaced within a bentonite fill. In this chapter, only liquid flow in bentonite and granite is of interest and both are assumed as porous media. Disregarding the canister, the computational model is a one-dimensional horizontal finite element model with an overall length of 17.05 m, extending from the left end (x=0.45 m) to the right end (x=17.5 m) and discretized into 46 elements (Fig. 6.12). The total simulation time is 20 years. The corresponding material properties are listed in Table 6.4. The relative permeability and suction vs. saturation data are fitted by the characteristic functions which are illustrated in Fig. 6.13. Additionally, the van Genuchten parameters of the rock are given in Table 6.4.

The initial liquid saturation for the bentonite is S = 0.65 and for the rock S=1.0. The only boundary condition is fixed and located in a 16.36 m distance to the bentonite ring, i.e. at the very right side of the model domain, where the rock is assumed to be fully saturated (S = 1.0).


Figure 6.12: Computational domain with IC and BC

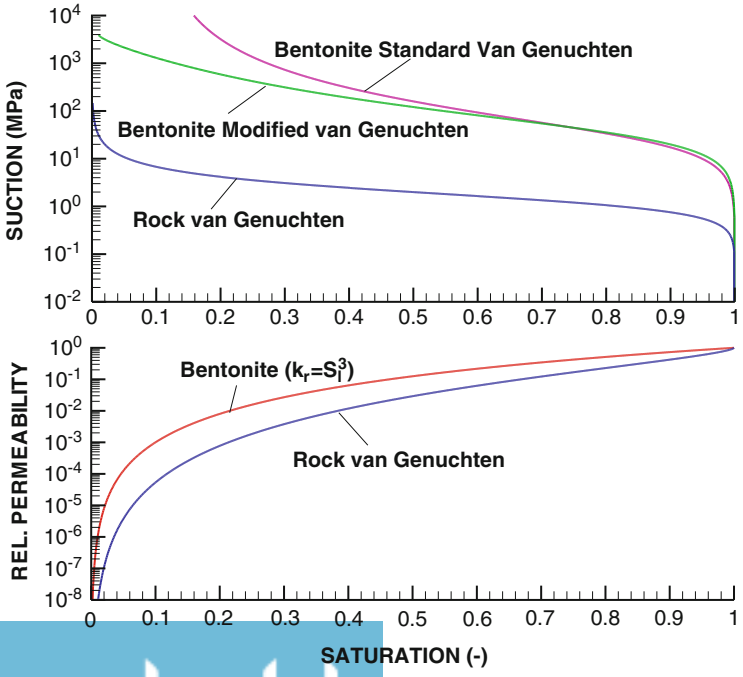


Figure 6.13: Characteristic curves for bentonite and granite rock

### Results

The left diagram of Fig. 6.14 shows the distribution of water saturation along the model domain at different times. The saturation within the bentonite increases continuously with the simulation time. The water flows from right to left, i.e. the water of the rock is draining into the bentonite (Fig. 6.12). Therefore, the water saturation within the granite decreases during the first year, before the boundary condition at the right of the model domain causes an increase of the water content until fully saturated conditions are reached. The diagram on the right of Fig. 6.14 shows the water pressure distribution for different times which generally demonstrates the same behavior as the water saturation; however the pressure within the rock does not change considerably. This is a result of the diverging hydraulic conductivity characteristics of rock and bentonite (Fig. 6.13). Compared to the bentonite, the relative permeability of the granite decreases stronger with reducing water saturation, i.e. the pressure changes stay relatively small.

Table 6.4: Material properties

| Symbol | Parameter | Bentonite | Rock | Unit |
|---|---|---|---|---|
| $\phi$ | Porosity | 0.41 | 0.01 | – |
| $k_s$ | Saturated permeability $k_s$ | 1.03e-17 | 2.0e-21 | $m^2$ |
| $S_r$ | Residual water saturation | 0 | – | – |
| $S_{max}$ | Maximum water saturation | 1.0 | – | – |
| $\alpha$ | Van Genuchten parameter | 6.673 | – | 1/m |
| $n$ | Van Genuchten parameter | 0.6 | – | – |

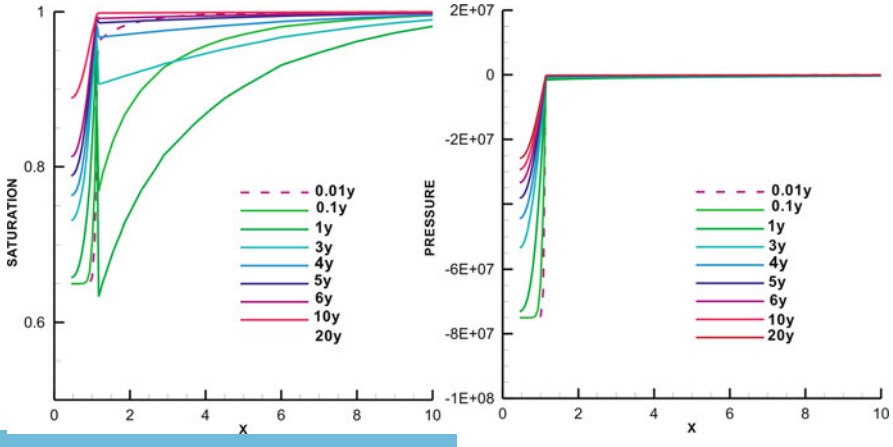


Figure 6.14: Distribution of saturation S [-] (*left*) and water pressure $p$ [Pa](*right*) in bentonite and granite

## 6.2 Dual Continua

The following two dual continua models are based on the assumption that the flow processes in the rock mass are governed by the dual continuum Richards' equations (6.6) and (6.8). The simplified one-dimensional test cases were designed to describe fluid flow in densely fractured rock that could potentially hold a nuclear waste repository and have been applied for code comparison [104, 105].

### Definition

The matrix allocates 95% and the fracture 5% of the overall pore space in both examples (Fig. 6.15). Model A is a 60 cm long vertical column discretized by 60 line elements. Model B has 133 elements and is 40 cm long. Aside from the small finite element sizes (1 cm or 0.3 cm), very small time step sizes (1e-07 - 1e-05 s) are required to ensure an accurate solution.

In model A, the initial conditions of both continua are set as a linear pressure gradient, from $-27,440$ Pa at the top to $-21,560$ Pa at the bottom. The boundary conditions of the fracture and matrix are identical and fixed at the top with 98 Pa but with a free drainage at the bottom (Fig. 6.15). The hydraulic properties of the fracture and matrix pore systems are described by a van Genuchten parameterization and presented in Table 6.5.

Model B is based on the example presented by Gerke and van Genuchten (1993) [104], who assumed a constant infiltration rate of 50 cm/d. The infiltration goes exclusively into the fracture pore area and therefore the matrix continuum

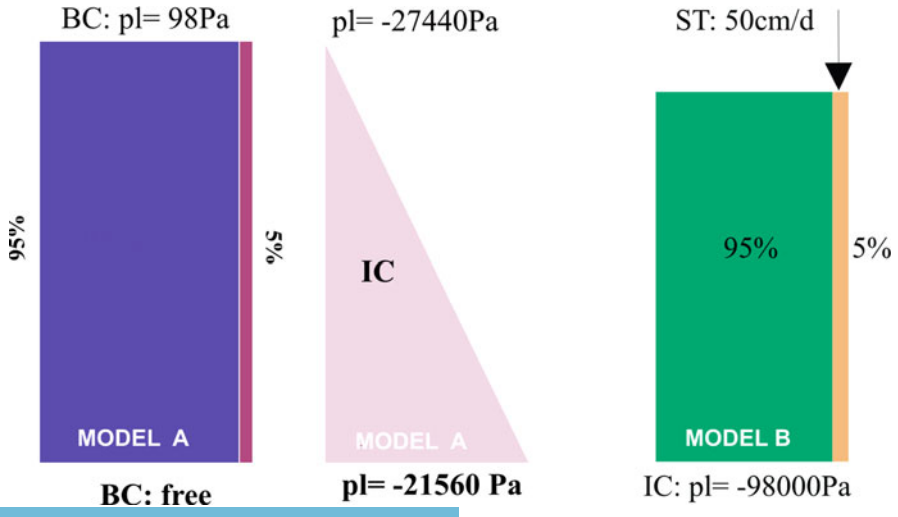


Figure 6.15: Model domain with initial and boundary conditions as well as continuum quantity

Table 6.5: Properties and parameters of model A

| | Symbol | Parameter | Value | Unit |
|---|---|---|---|---|
| | | Preferential factor | 0.95 | – |
| Matrix | $\phi$ | Porosity | 0.498 | – |
| continuum | $S_r$ | Residual water saturation | 0.0 | – |
| | $S_{max}$ | Maximum water saturation | 1.0 | – |
| | $\alpha$ | Van Genuchten parameter | 1.8 | 1/m |
| | $n$ | Van Genuchten parameter | 1.8 | – |
| | $k_s$ | Saturated permeability | 2.32368e-13 | $m^2$ |
| | | Preferential factor | 0.05 | – |
| Fracture | $\phi$ | Porosity | 0.6 | – |
| continuum | $S_r$ | Residual water saturation | 0.0833 | – |
| | $S_{max}$ | Maximum water saturation | 1.0 | – |
| | $\alpha$ | Van Genuchten parameter | 5.6 | 1/m |
| | $n$ | Van Genuchten parameter | 2.68 | – |
| | $k_s$ | Saturated permeability | 1.09000e-11 | $m^2$ |
| Transfer | $\alpha^*$ | Transfer coefficient | 500 | $(1/m^2)$ |

recieves water only from the transfer. The initial conditions for both the matrix and fracture continuum are uniform and identical with $h_w^M = h_w^F = -10$ m or $p_w^M = p_w^F = -98,000$ Pa respectively. The details of model B are illustrated at the right of Fig. 6.15. The apparent permeability of the transfer term is $k_\alpha = 0.01 \times 0.5[k_\alpha(p_w^M) + k_\alpha(p_w^F)]$. All hydraulic parameters for $k_\alpha(p_w)$ are assumed to be identical with those for $k_\alpha^M(p_w^M)$, besides the saturated permeability which is reduced by a factor of 100. The relevant model parameters for the fracture and matrix continuum, as well as the transfer term, are listed in Table 6.6.

### Results

The simulations of model A have been performed first with a single continuum approach to compare the results of OGS and HYDRUS code. Figure 6.16 shows the corresponding water pressure distributions in the column at the time of 20 min and 30 min. The results of HYDRUS are given by symbols. The OGS results are represented by lines, i.e. the pressure fronts in the matrix are illustrated by solid lines and those of the fracture by dashed lines. Second, the dual continua implementation of OGS has been compared with the dual-permeability model S1D_DUAL [105, 113] and is presented in Fig. 6.17. The blue lines are the results without the transfer term, i.e. for the independent single continuum. The red lines (OGS) and symbols (S1D_DUAL) depict the effect of the dual permeability approach. In this model domain, the matrix continuum is the dominant part of

Table 6.6: Properties and parameters of model B

| | Symbol | Parameter | Value | Unit |
|---|---|---|---|---|
| | | Preferential factor | 0.95 | – |
| Matrix | $\phi$ | Porosity | 0.5 | – |
| continuum | $S_r$ | Residual water saturation | 0.21052 | – |
| | $S_{max}$ | Maximum water saturation | 1.0 | – |
| | $\alpha$ | Van Genuchten parameter | 0.05 | 1/m |
| | $n$ | Van Genuchten parameter | 1.5 | – |
| | $k_s$ | Saturated permeability | 1.2419e-14 | $m^2$ |
| | | Preferential factor | 0.05 | – |
| Fracture | $\phi$ | Porosity | 0.5 | – |
| continuum | $S_r$ | Residual water saturation | 0.0 | – |
| | $S_{max}$ | Maximum water saturation | 1.0 | – |
| | $\alpha$ | Van Genuchten parameter | 5.6 | 1/m |
| | $n$ | Van Genuchten parameter | 10 | – |
| | $k_s$ | Saturated permeability | 2.3596e-11 | $m^2$ |
| Transfer | $\alpha^*$ | Transfer coefficient | 120 | $(1/m^2)$ |

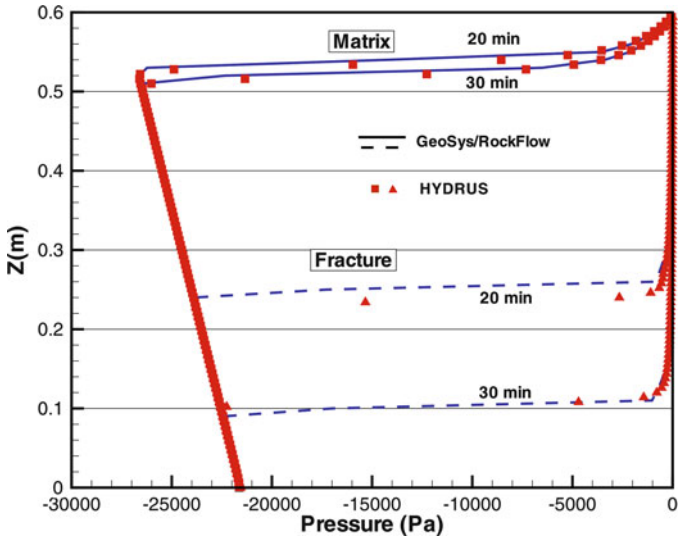


Figure 6.16: Model A with single continuum approach: comparison of the pressure distribution after 20 and 30 min

the whole system and therefore the influence on the water pressure in the matrix is less than in the fracture. The resulting pressure and saturation contours at different times of model B are given in Figs. 6.18 and 6.19.

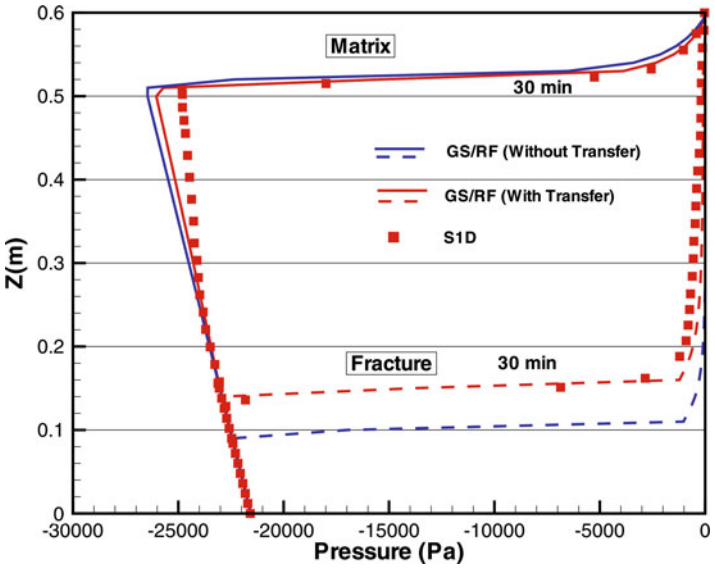


Figure 6.17: Model A with dual permeability approach: comparison of the pressure distribution of two different codes in contrast to the single continuum results

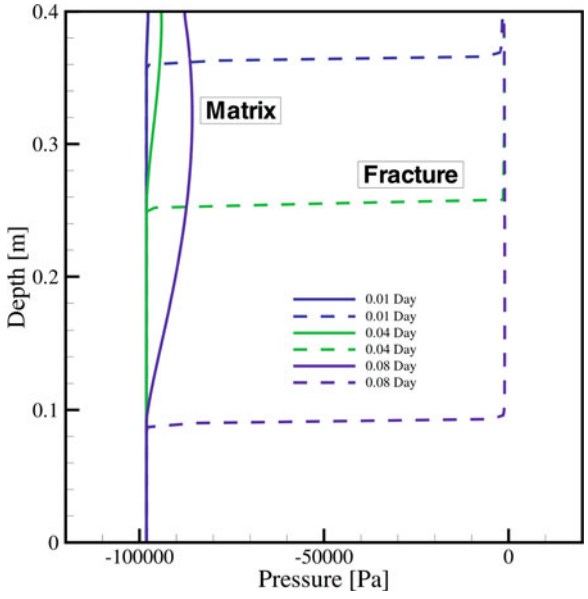


Figure 6.18: Simulated water pressure profiles of model B showing the results in the matrix (*solid lines*) and fracture (*dashed lines*)

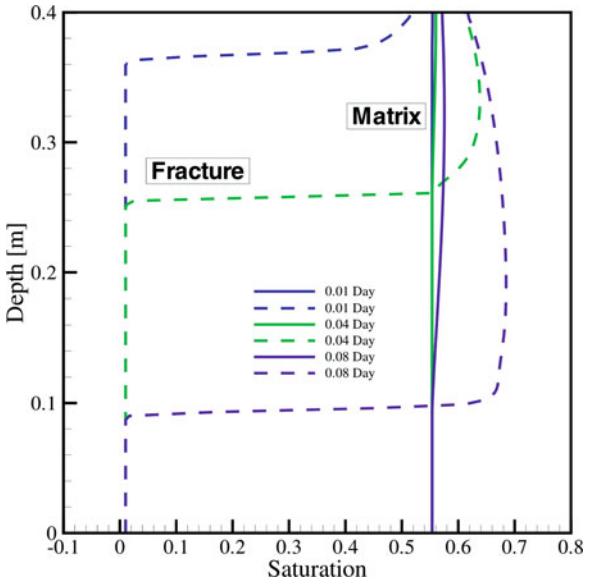


Figure 6.19: Simulated water saturation profiles of model B showing the results in the matrix (*solid lines*) and fracture (*dashed lines*)

# Chapter 7

# Overland Flow

*by Jens-Olaf Delfs, Martin Beinhorn, and Yajie Wu*

This chapter deals with surface runoff which is flow over the land surface generated by precipitation, melting of snow, or other sources. Typically, not all precipitation or snow produces runoff because storage from soil and plant roots can absorb substantial amounts of water. Infiltration excess ([114]) overland flow occurs when precipitation exceeds the rate at which water infiltrates into the soil (Test case Sect. 7.2). Urbanization leads to more pronounced flow maxima during storm events, when impervious surfaces such as pavement force the runoff directly to the stream (Test case Sect. 7.1).

Horizontal flow over a flat or moderately flat surface is described by the Saint-Venant Shallow Water Equations which read

$$\begin{aligned} \phi_o \frac{\partial H}{\partial t} + \nabla H\mathbf{v} &= q \\ \frac{\partial \mathbf{v}}{\partial t} + \mathbf{v}\cdot\nabla\mathbf{v} + g\nabla h &= g(S_0 - S_f) \end{aligned} \tag{7.1}$$

where $H$, surface water depth, and $\mathbf{v}$, flow velocity, are primary variables, $g = 9.81\ \mathrm{m/s^2}$ is the gravitational acceleration, $h = H + b$ the surface water height, $b$ the bottom height, $S_0 = -\nabla b$ the surface slope, $S_f$ the friction slope, $q$ represents external sources / sinks, and $0 \leq \phi_o \leq 1$ is the surface porosity to incorporate depression storage. Equations (7.1) can be derived from the Reynolds averaged Navier Stokes Equations by integrating over water depth $H$ and assuming hydrostatic pressure $p = \rho g(h - z)$, where $\rho$ is the water bulk density (e.g. [115]). The result is a depth-averaged flow field $v(x, y)$,

O. Kolditz et al. (eds.), *Thermo-Hydro-Mechanical-Chemical Processes in Fractured Porous Media*, Lecture Notes in Computational Science and Engineering 86,
DOI 10.1007/978-3-642-27177-9_7, © Springer-Verlag Berlin Heidelberg 2012

where turbulence and surface friction effects are finally incorporated in empiric resistance to flow relationships, i.e. the velocity $v$ is a power function of the water depth $H$. The general form of a resistance to flow relationship for 1D flow in an irregular channel (which involves an additional averaging over the channel breadth) is given by

$$v = CS_f^j R_H^m \tag{7.2}$$

where $j$, m are parameters, $v(l)$ is the flow velocity in the channel course $l$, $R_H(l) = A/P$ the hydraulic radius of the channel, $A(l)$ its cross-section, and $P(l)$ the wetted perimeter. Remark that $R_H = H$ for 2D overland flow, $j = 1/2$, $m = 2/3$ result in the relationship by Manning where $n = 1/C$ is a surface roughness parameter, and $j = 1$, $m = 2$ in the relationship by Darcy-Weisbach for laminar flow. Neglect of the inertial terms simplifies (7.1) to the diffusive wave shallow water equation, which reads

$$\phi_o \frac{\partial H}{\partial t} - \nabla \cdot \frac{CHR_H^m}{|\nabla h|^{1-j}} \nabla h = q \tag{7.3}$$

Further neglect of the hydrostatic pressure term in (7.1) leads to the kinematic wave equation reading

$$\phi_o \frac{\partial H}{\partial t} + C(m+1) R_H^m \nabla H = q \tag{7.4}$$

Equations (7.1)–(7.4) allow to simulate small-amplitude waves (surface runoff, flood waves). The diffusive wave approximation (7.3) can capture backwater phenomena and the Saint-Venant Equations (7.1), further, dam break waves. Conditions for the applicability of the Saint-Venant approximations (kinematic and diffusive wave) are stated for instance in [116], while shallow water equations to reproduce large-amplitude waves (e.g. ocean waves) can be found in [117].

External forcing (precipitation, infiltration, outflow, etc.) can be incorporated in the surface flow Equations (7.1)–(7.4) with source /sink terms $q$. A normal depth $q_{\text{norm}}$ sink term assumes that water flows under uniform (normal) conditions at a downstream boundary while a critical depth $q_{\text{crit}}$ sink term represents free outfall:

$$q_{norm} = -CS_o^j H^m \tag{7.5}$$

$$q_{crit} = -\sqrt{gH^3} \tag{7.6}$$

A [118] term $q_{\text{GA}}$ provides an effective precipitation rate $q_{\text{prec}}^{\text{eff}} = q_{\text{prec}} - q_{\text{GA}}$ for overland flow on an infiltrating surface. Since water infiltrates into dry soil as a sharp wetting front, the Green and Ampt infiltration model assumes that soil saturation above and below the wetting front and the soil-water suction immediately below the wetting front remain constant. The infiltration source term $q_{\text{GA}}(t)$ and the depth of the wetting front $a'(t)$ read

$$q_{\mathrm{GA}} = K' \left( \frac{\Psi_{cd} - H}{a'} \right) \tag{7.7}$$
$$a' = \frac{\int_0^t q_{\mathrm{GA}}(s)\, ds}{\Delta\Theta}.$$

where $\Psi_{\mathrm{cd}}$ the effective capillary drive, $K'$ is related to the saturated soil hydraulic conductivity in Sect. 6, and $\Delta\Theta$ the initial moisture deficit. Interactions between water flowing on the land surface and the underlying soils (Sect. 6) can be addressed with a coupling flux

$$q_{\mathrm{cp}} = -\Lambda \left( H + \frac{p_c}{\rho g} \right) \tag{7.8}$$

where $\Lambda$ is the leakance and $p_c$ the capillary pressure at the surface-soil-interface (6.1).

## 7.1 Surface Flow on a Tilted V-Catchment

### 7.1.1 Definition

In the synthetic test case by [119] precipitation with a rate of $3 \cdot 10^{-6}$ m/s is applied for 90 min on an impervious V-catchment followed by a recession period of an additional 90 min. The V-catchment consists of two sloping planes 800 m wide and 1,000 m long joined by a 20 m wide and 1000 m long channel. At the catchment base (channel region) the surface roughness was reduced (Table 7.1) and the slope set at $S_0 = 0.02$. The hillslopes additionally have a slope of $S_0 = 0.05$ towards the channel. At the channel outlet the water leaves free-falling (critical depth sink term (7.6)) while at the remaining boundaries no-flow is imposed. A structured (rectangular) grid (100 m $\times$ 100m) and a time-step maximum length of 1 min are selected.

### 7.1.2 Solution

Figure 7.1 compares the critical depth outflow of different surface runoff simulators. The simulated hydrographs reach a maximum roughly after 60 min and all water has almost left the catchment after the simulation time of 180 min.

Table 7.1: Material properties

| Symbol | Parameter | Value | Unit |
|---|---|---|---|
| $n$ | Manning friction (Hillslope) | [0.015] | $\mathrm{s/m^{1/3}}$ |
| $n$ | Manning friction (Channel) | [0.15] | $\mathrm{s/m^{1/3}}$ |

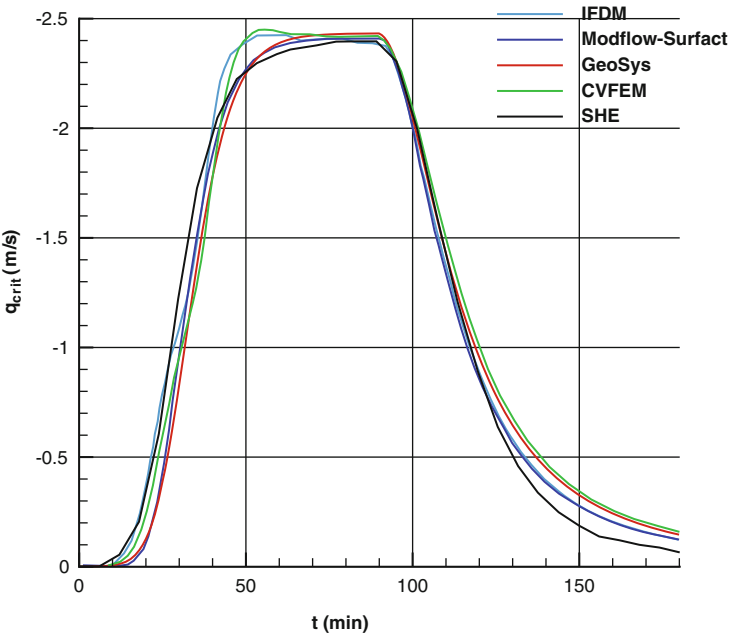


Figure 7.1: Runoff at channel outlet for tilted V-catchment test case.

## 7.2 Infiltration Excess (Horton) Overland Flow

### 7.2.1 Definition

In the classic experiments by [120] a light oil was applied with a constant rate of $q_{\text{prec}} = 6.944 \times 10^{-5}$ m/s for 15 min on an initially drained soil flume with a length of 12.2 m, a width of 0.051 m and a uniform slope of 0.01. Measured outflow at the lower flume end is compared with 1D surface runoff simulations for a grid size of 12.2 cm and a constant time step length of 1 s. Parameters are stated in Table 7.2 for flow resistance (7.2), a Green Ampt source term (7.7), and a Richards model which is coupled via a flux (7.8). A critical depth sink term (7.6) is assigned at the flume outlet.

### 7.2.2 Solution

Figure 7.2 compares measured surface runoff $q_{\text{rf}} = -q_{\text{crit}}/A$, where $A$ is the flume surface area, with model predictions at the flume outlet. First, precipitation completely infiltrates (stage I). After about 7 min surface runoff starts and produces a fast rising hydrograph (stage II). As soon as precipitation from the entire flume surface has reached the outlet, the hydrograph turns flat. The

Table 7.2: Material properties

| Symbol | Parameter | Value | Unit |
|---|---|---|---|
| $n$ | Darcy-Weisbach friction | [1333333] | 1/(ms) |
| $K$ | Conductivity (Green and Ampt model) | $[2.4 \times 10^{-5}]$ | m/s |
| $\Psi_{cd}$ | Effective capillary drive | [0.13] | m |
| $\Delta\Theta$ | Initial moisture deficit | [0.3] | – |
| $K$ | Conductivity (Richards model) | $[2.83 \times 10^{-5}]$ | m/s |
| $\phi$ | Porosity | [0.42] | – |
| $S_r$ | Residual saturation | [0.053] | – |
| $\alpha$ | Van Genuchten parameter | [6] | 1/m |
| $m$ | Van Genuchten parameter | [4] | – |
| $\Lambda$ | Leakance | [0.001] | 1/s |

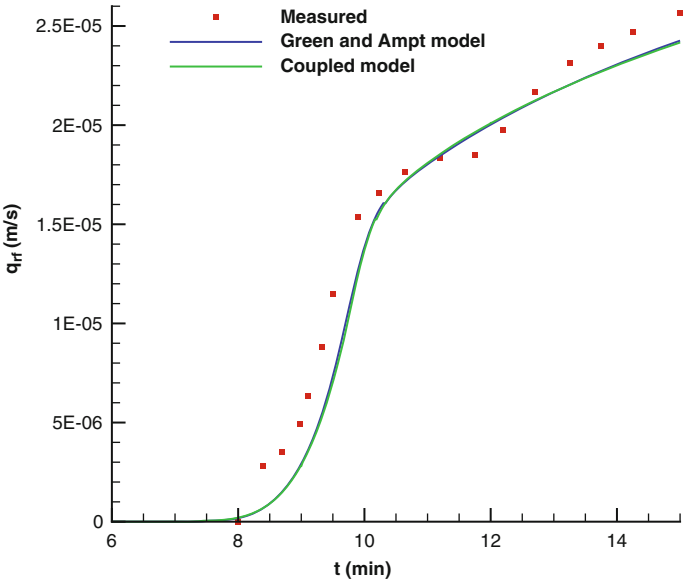


Figure 7.2: Comparison of measured and simulated Horton overland flow

infiltration rate continues to decline as the soil becomes saturated so that surface runoff still increases in the later part of the experiment (stage III). The experimental hydrograph exhibits a considerable dip during stage III which is attributed to gas phase movement ([120]).

# Chapter 8

# Gas Flow

*by Ashok Singh and Olaf Kolditz*

The subject of this chapter is the movement of gases in porous media. In contrast to groundwater hydraulics, gas flow is more complicated because of its compressibility. Significant variations in gas density and viscosity can result also from temperature fluctuations (so-called Klinkenberg effect). According to the kinetic theory of gases, its viscosity should not depend on pressure. This is not necessarily the case for conditions typically existing in natural gas reservoirs [121]. At a fixed temperature, the viscosity of gas can vary by tens of percents as the formation pressure changes by a few Mega Pascale. Another problem concerns the evidence of turbulent flow, which results in additional friction effects. The present study is verified with existing analytical solutions. Simulation of compressible flows in porous media is necessary for different applications such as air movement in soils, gas production or $CO_2$ storage if carbon dioxide is injected in a gaseous state.

The theory of gas seepage was developed first by [122], [123], and [124], who worked out a number of analytical approximations to solve the nonlinear problem. To this end, the following assumption is made

- Gravitational forces are neglected
- No phreatic surfaces are formed
- Idealized material properties

O. Kolditz et al. (eds.), *Thermo-Hydro-Mechanical-Chemical Processes in Fractured Porous Media*, Lecture Notes in Computational Science and Engineering 86,
DOI 10.1007/978-3-642-27177-9_8, © Springer-Verlag Berlin Heidelberg 2012

The state of the compressible fluid within a considered closed system may be isothermal (const. temperature), adiabatic (const. heat content), or polytropic (const. change of heat content).

The equation of gas flow in a porous medium can be derived from the mass balance of gas

$$\frac{\partial(n\rho)}{\partial t} + \nabla \cdot (\rho n \mathbf{v}) = \rho Q_\rho \tag{8.1}$$

where $\rho$ is gas density, $\mathbf{v}$ is velocity vector, $n$ is porosity and $Q_\rho$ is source/sink term.

The equation of state for an ideal gas represents its compressibility as pressure and temperature changes.

$$\rho = \frac{pM}{RT} \tag{8.2}$$

where $p$ is gas pressure, $R$ is the universal gas constant, $M$ is the molecular weight of gas and $T$ is temperature in Kelvin.

Since gas density $\rho$ is dependent on pressure and temperature, for compressible gas flow themass balance equation (8.1) becomes

$$\frac{n}{p}\frac{\partial p}{\partial t} - \frac{n}{T}\frac{\partial T}{\partial t} + \frac{1}{p}\nabla p - \frac{1}{T}\nabla T + \nabla \cdot (n\mathbf{v}) = Q_\rho \tag{8.3}$$

The momentum balance equation can be expressed in the form of an extended Darcy's law for non-linear flow

$$n\mathbf{v} = -\frac{\mathbf{k}}{\mu}\nabla p \tag{8.4}$$

where $\mathbf{k}$ is permeability tensor, $\mu$ is fluid viscosity. The gas mass balance equation reads as

$$\frac{n}{p}\frac{\partial p}{\partial t} - \frac{n}{T}\frac{\partial T}{\partial t} + \frac{1}{p}\nabla p - \frac{1}{T}\nabla T - \nabla \cdot (\frac{\mathbf{k}}{\mu}\nabla p) = Q_\rho \tag{8.5}$$

which is a non-linear equation with respect to gas pressure $p$. For the isothermal case, temperature related term should be neglected and for the nonisothermal case, the temperature value can be obtained from the heat transport equation.

We present the following two benchmarks for verification of the compressible gas flow code. In the first benchmark, density is changing due only to pressure and temperature remaining constant, i.e. isothermal case, whereas in the second benchmark we proved the phenomenon of Joule-Thomson processes during carbon sequestration and enhanced gas recovery.

- Isothermal compressible gas flow (8.4)
- Joule-Thomson cooling processes (8.5)

At the end of the chapter we present an application example dealing with:

- Air flow through porous medium (Sect. 8.6)

## 8.1 Material Functions

For non-isothermal air flow we have to consider the pressure and temperature dependencies of air viscosity $\mu(p,T)$ (Sect. 8.1.1) as well as specific heat capacities $c_p(p,T)$ and heat conductivities $\lambda(p,T)$ (Sect. 8.1.2) ([125]).

### 8.1.1 Air Dynamic Viscosity

The Reichenberg viscosity model ([126]) is used for the non-isothermal flow of air. The pressure and temperature dependencies of air viscosity are shown in Fig. 8.1.

$$\mu(p,T) = \mu_0(T)\left(1 + \frac{Ap_r^{\frac{3}{2}}}{Bp_r + (1 + Cp_r^D)^{-1}}\right) \tag{8.6}$$

with the following parameters:

$$\begin{array}{ll} p_r = \frac{p}{p_{\text{crit}}} & T_r = \frac{T}{T_{\text{crit}}} \\ A = \frac{\alpha_1}{T_r}\exp(\alpha_2 T_r^a) & B = A(\beta_1 T_r - \beta_2) \\ C = \frac{\gamma_1}{T_r}\exp(\gamma_2 T_r^c) & D = \frac{\delta_1}{T_r}\exp(\delta_2 T_r^d) \end{array} \tag{8.7}$$

$$\begin{array}{lll} p_{\text{crit}} = 33.9 \times 10^4 \text{Pa} & T_{\text{crit}} = 126.2\text{K} & \\ \alpha_1 = 1.9824 \times 10^{-3} & \alpha_2 = 5.2683 & a = -0.5767 \\ \beta_1 = 1.6552 & \beta_2 = 1.2760 & \\ \gamma_1 = 0.1319 & \gamma_2 = 3.7035 & c = -79.8678 \\ \delta_1 = 2.9496 & \delta_2 = 2.9190 & d = -16.6169 \end{array}$$

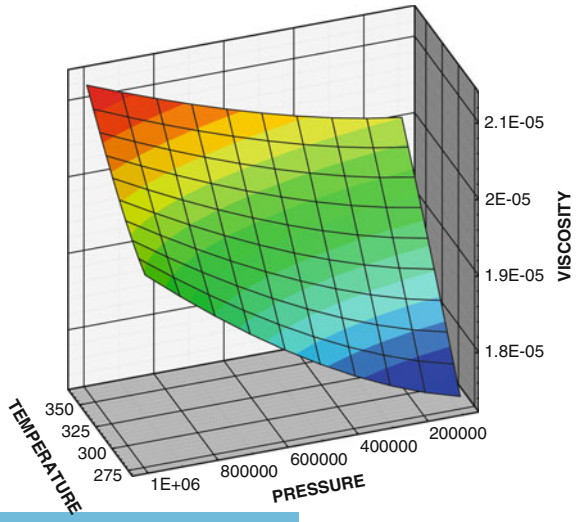


Figure 8.1: Air viscosity as a function of temperature (in Kelvin) and pressure (in Pa)

### 8.1.2 Thermal Properties

Along with the flow characteristics such as air viscosity, the thermal properties, such as heat capacity and thermal conductivity of the gas and solid, are important for heat transport. As an example, Fig. 8.2 depicts the thermal properties of the gas. Figure 8.2 (left) shows the temperature dependence of specific heat capacity of air at atmospheric pressure corresponding to (8.8) from [127] and compared with experimental data by [128]. Figure 8.2 (right) illustrates the temperature dependence of thermal conductivity of air at the atmospheric pressure corresponding to (8.9) from [127] and compared with experimental data by [128]. The pressure dependency of thermal properties can be neglected in the present pressure regimes.

$$c_p = a_0 + a_1 T + a_2 T^2 + a_3 T^3 + a_4 T^4 \tag{8.8}$$

where coefficients $a_0 = 1.0613$; $a_1 = -4.3282 \times 10^{-4}$; $a_2 = 1.0234 \times 10^{-6}$; $a_3 = -6.4747 \times 10^{-10}$; $a_4 = 1.3864 \times 10^{-13}$.

$$\lambda = b_0 + b_1 T + b_2 T^2 + b_3 T^3 + b_4 T^4 + b_5 T^5 \tag{8.9}$$

where coefficients $b_0 = 7.488 \times 10^{-3}$; $b_1 = -1.7082 \times 10^{-4}$; $b_2 = 2.3758 \times 10^{-7}$; $b_3 = -2.2012 \times 10^{-10}$; $b_4 = 9.46 \times 10^{-14}$; $b_5 = -1.579 \times 10^{-17}$.

## 8.2 Element Test

### 8.2.1 Definition

This example is presented for the code verification of different element types, i.e. lines, triangles, quads, tetrahedra, triangle prisms and hexahedra [129]. We

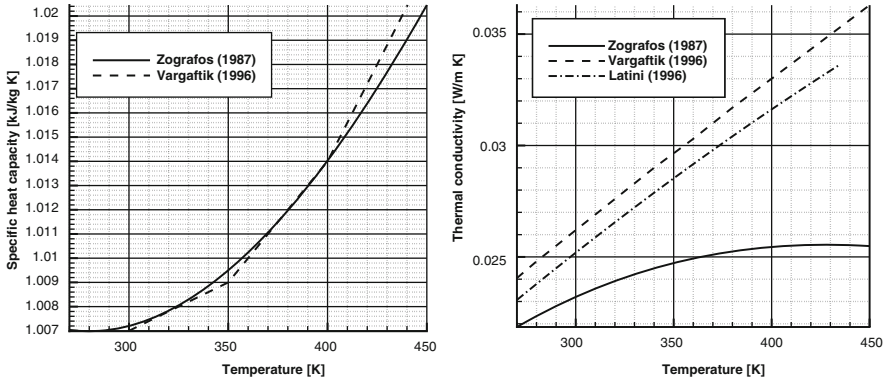


Figure 8.2: Thermal properties of air: specific heat capacity (*left*), thermal conductivity (*right*)

consider flow of a compressible fluid through the porous medium. In this case the hydraulic conductivity is pressure dependent.

The discretization with different element types is shown in Fig. 3.15. The initial gas pressure distribution is equal to $1.01325 \times 10^5$Pa; everywhere in the model domain. There are Dirichlet boundary conditions set at the left end, i.e. $p^g(x = 0\text{m}) = 9.5500 \times 10^4$Pa, and the right end, i.e. $p^g(x = 100\text{m}) = 1.01325 \times 10^5$Pa, in order to extract gas from the domain. The material parameters of the fluid and the porous medium are given in Table 8.1.

### 8.2.2 Results

Figure 8.3 depicts the temporal evolution of gas pressure at the observation point at the outlet. The numerical results of all implemented element types

Table 8.1: Material parameters

| Symbol | Parameter | Value | Unit |
|---|---|---|---|
| $L$ | Model length | 0.05 | m |
| $A$ | Cross section area | 1 | $m^2$ |
| $\mu$ | Dynamic viscosity | $1.78\times10^{-5}$ | Pas |
| $n$ | Porosity | 0.005 | – |
| $\mathbf{k}$ | Permeability | $2.77\times10^{-19}$ | $m^2$ |
| $\Delta t$ | Time step | $3 \times 10^2$ | s |
| $\Delta x$ | Space step | 0.005 | m |

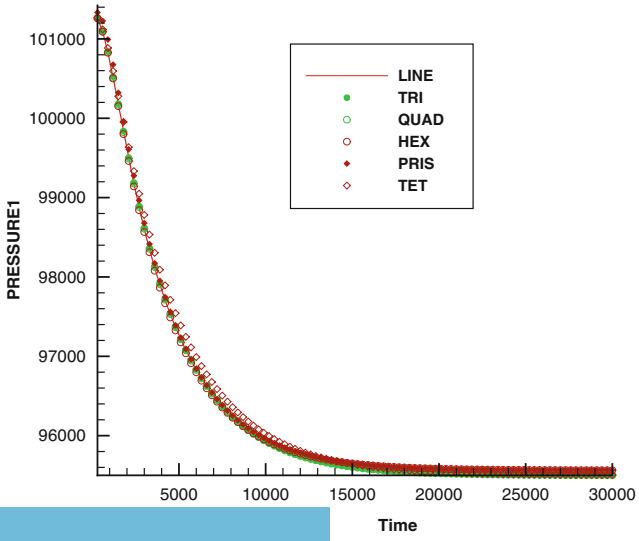


Figure 8.3: Evolution of gas pressure at the outlet observation point

compare very well. Small deviations occur from different numbers of Gauss integration points.

## 8.3 Verifications

Two test examples are presented for 1-D compressible gas flow in a porous media. Analytical solutions exist for both under the steady state condition. The first test case deals with density changing with pressure only, i.e. isothermal case (Sect. 8.4). The second example shows Joule-Thomson processes with heat dissipation during carbon sequestration and enhanced gas recovery.

## 8.4 Isothermal Compressible Gas Flow

### 8.4.1 Definition

We consider a simple 1D test example where gas is injected at a constant pressure into the porous medium. The material parameters are summarized in Table 8.2.

### 8.4.2 Solution

#### Analytical Solution

For isothermal flow with Dirichlet boundary conditions, i.e. $p(x = 0, t) = p_1$ and $p(x = L, t) = p_2$, there exists an analytical solution,

$$p(x) = \sqrt{(p_2^2 - p_1^2)\frac{x}{x_2 - x_1} + p_1^2} \tag{8.10}$$

which is used for verification of the present numerical solution.

According to Darcy's law (8.4) the volumetric gas flux at reference conditions can be approximated as follows

$$Q_0 = A\frac{T_0}{T^* p_0}\frac{\mathbf{k}}{\mu}\frac{(p_2^2 - p_1^2)}{2(x_2 - x_1)} \tag{8.11}$$

#### Numerical Solution

The numerical model consists of 100 line elements connected by 101 nodes along the x-axis. The distances of the nodes $\Delta x$ is one meter. At $x = 0$ m there is a constant pressure boundary value of $3 \times 10^6$ Pa. Whereas at $x = L$ the pressure boundary value is $1.01325 \times 10^5$ Pa.

Table 8.2: Model parameters

| Symbol | Parameter | Value | Unit |
|---|---|---|---|
| $L$ | Model length | 100 | m |
| $A$ | Cross section area | 1 | $m^2$ |
| $n$ | Porosity | 0.35 | – |
| $\mathbf{k}$ | Permeability | $2.7 \times 10^{-11}$ | $m^2$ |
| $\mu$ | Gas dynamic viscosity | $1.76 \times 10^{-5}$ | Pa s |
| $p_0$ | Initial condition | 101325 | Pa |
| $p_1, p_2$ | Boundary conditions | $3 \times 10^6, 1.01325 \times 10^5$ | Pa |
| $\Delta t$ | Time step | $1, 10, 10^2, 10^3, 10^4$ | s |
| $\Delta x$ | Space step | 1 | m |

### 8.4.3 Results

Figure 8.4 shows the comparison of the present numerical solution with the analytical. Steady state is reached after about $1.0 \times 10^4$ s.

## 8.5 Joule-Thomson Cooling Processes

### 8.5.1 Definition

Flow in permeable media is not an isothermal process because there is a temperature change resulting from fluid expansion and viscous dissipation heating. The test benchmark is formulated for the injection of compressed cryogenic $CO_2$ in a one-dimensional horizontal reservoir column. Material parameters are presented in Table 8.3.

### 8.5.2 Solution

#### Analytical Solution

For such a case there exists an analytical solution (Singh et al. [130]) with the boundary value at $x = 0$ is $T_0$ and at $x = L$ is $\nabla T = 0$.

$$T = L_+ \exp(m_+ \, \mathrm{x}) + L_- \exp(m_- \, \mathrm{x}) + \frac{1}{\beta_\mathrm{T}} \tag{8.12}$$

where

$$m_\pm = u_\mathrm{x} \left( \frac{\rho c_p}{\kappa_\mathrm{eff}} \pm \sqrt{\left( \frac{\rho c_p}{\kappa_\mathrm{eff}} \right)^2 + \frac{4\beta_\mathrm{T}\mu}{\mathbf{k}\kappa_\mathrm{eff}}} \right)$$

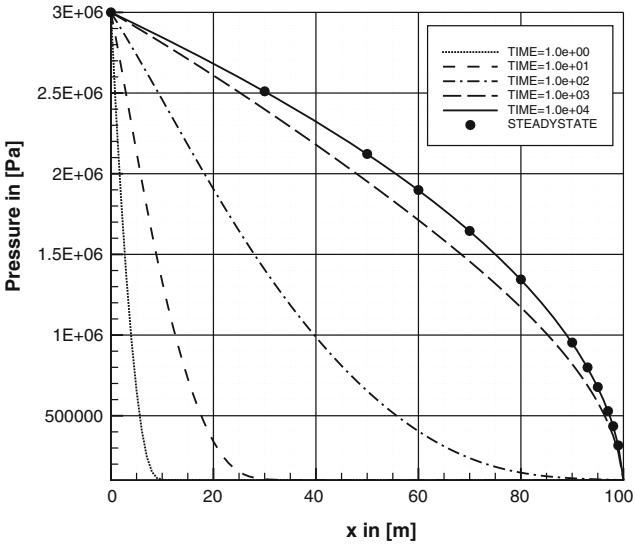


Figure 8.4: Comparison of analytical (•) and numerical solutions

Table 8.3: Model parameters

| Symbol | Parameter | Value | Unit |
|---|---|---|---|
| $L$ | Column radius | 100 | m |
| $n$ | Porosity | 0.35 | – |
| $\rho, \rho^s$ | Densities | $\frac{pM}{z_{\rm sc}RT}, 2460$ | kg m$^{-3}$ |
| $\mathbf{k}$ | Permeability | $2.7 \times 10^{-11}$ | m$^2$ |
| $\mu$ | Dynamic viscosity | $1.9836 \times 10^{-5}$ | Pa s |
| $\kappa, \kappa^s$ | Heat conductivities | $0.02.6374, 2.5$ | W m$^{-1}$K$^{-1}$ |
| $c_p, c_p^s$ | Heat capacities | $1.067 \times 10^3, 1.2 \times 10^3$ | Jkg$^{-1}$K$^{-1}$ |
| $\beta_{\rm T}$ | Thermal expansivity | $-\frac{1}{\rho_0}\frac{\partial \rho}{\partial T}$ | K$^{-1}$ |

and $\rm L_+$ and $\rm L_-$ are integration constants to be determined by boundary conditions.

### Numerical Solution

The finite element solution has been obtained through solving the mass and energy balance equations. Within a time step, the mass balance equation for pressure is solved with temperature changes and in return the energy balance equation is then solved for temperature with obtained fluid velocity. This is the so called staggered approach and is executed until the solution become steady.

The physical domain has been discretized in 100 line elements, in which size varies between $\Delta x = 0.4$ m to $\Delta x = 4.3498$ m. This helps to capture the sharp

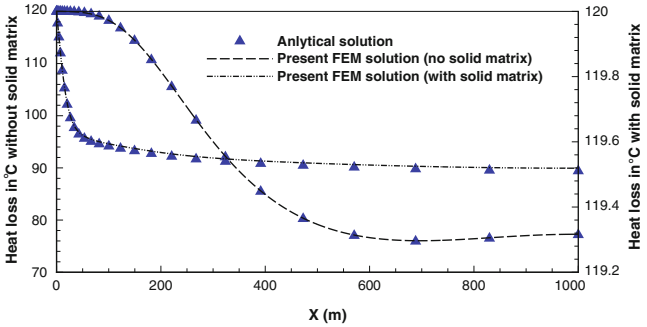


Figure 8.5: Comparison of present solution (FEM) with analytical solution due to (8.12)

gradient of temperature present near the injection point. at the time step size is $\Delta t = 1$ s at the beginning of the simulation, with step by step increases until it reaches $\Delta t = 1.0 \times 10^4$ s.

### 8.5.3 Results

Based on the above findings, OpenGeoSys (OGS) is capable of showing the Joule-Thomson process in carbon sequestration with enhanced gas recovery. In Fig. 8.5 we have presented the comparison of the temperature profile produced from OGS with those of the analytical solution, i.e. (8.12). In the figure, '**without solid matrix**' represents the case in which we do not account for heat provided by the solid matrix by setting $c_p^s = 0, \kappa^s = 0$ whereas '**with solid matrix**' shows the case in which we have accounted for heat provided by the solid matrix.

The figure shows that as we inject $CO_2$ (at temperature 393.15 K which is lower than the inversion temperature $\approx 1,500$ K), its pressure falls with a high gradient. It means as expansion starts, the average distance between molecules grows. Because of intermolecular attractive forces, expansion causes an increase in the potential energy of the gas. As no external work is extracted and the process is adiabatic, the total energy of the gas remains constant due to the conservation of energy. The increase in potential energy thus implies a decrease in kinetic energy and therefore the temperature falls.

## 8.6 Air Flow Example

### 8.6.1 Definition

We consider the same test example definition as for isothermal gas flow in Sect. 8.4. Now we use pressure and temperature dependent material properties described in Sect. 8.1. The model parameters are summarized in Table 8.4.

Table 8.4: Model parameters

| Symbol | Parameter | Value | Unit |
|---|---|---|---|
| $L$ | Model length | 100 | m |
| $n$ | Porosity | 0.35 | – |
| $\rho, \rho^s$ | Densities | (8.2), 2650 | kg m$^{-3}$ |
| $\mathbf{k}$ | Permeability | $2.7 \times 10^{-11}$ | m$^2$ |
| $\mu$ | Dynamic gas viscosity | (8.6) | Pa s |
| $p_0$ | Initial condition | 101325 | Pa |
| $T_0$ | Initial condition | 288 | K |
| $p_2$ | Boundary condition | 101325 | Pa |
| $T_1$ | Boundary condition | 343 | K |
| $Q_\rho$ | Injection rates | $1 - 10$ | kg s$^{-1}$ |
| $\alpha_L, \alpha_T$ | Heat dispersion length | $1, 0.1$ | m |
| $\lambda^g, \lambda^s$ | Heat conductivities | (8.9), 2.5 | W m$^{-1}$K$^{-1}$ |
| $c_p^g, c_p^s$ | Heat capacities | (8.8), 2300 | Jkg$^{-1}$K$^{-1}$ |

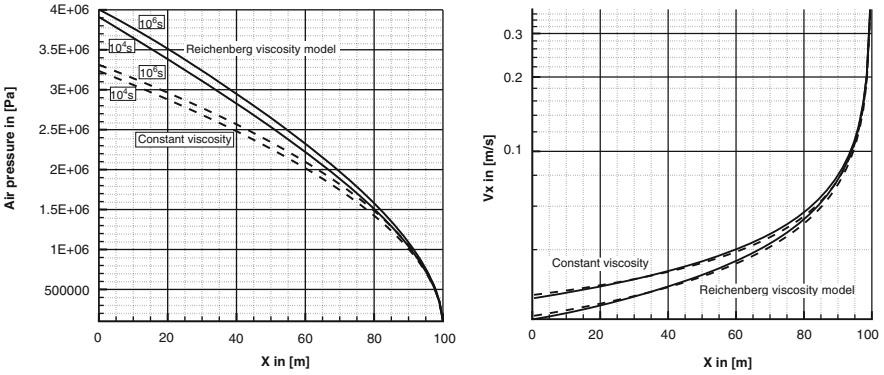


Figure 8.6: Hydraulic profiles evolution: Air pressure (*top*), Air velocity (*bottom*)

### 8.6.2 Solution

The numerical model consists of 100 line elements connected by 101 nodes along the x-axis. The distance of the nodes $\Delta x$ is one meter. At $x = 0$m, we inject air with rates of 1 kg s$^{-1}$ and 10 kg s$^{-1}$, and the temperature is 343 K. At $x = L$ the pressure boundary value is $1.01325 \times 10^5$Pa and $\nabla T = 0$.

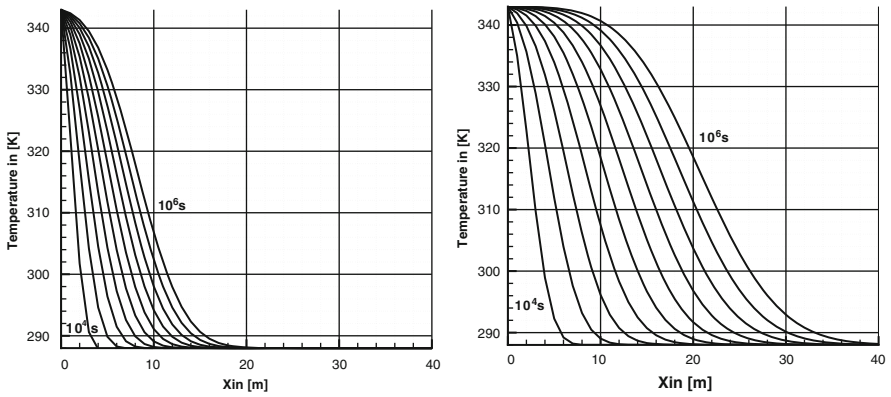


Figure 8.7: Air temperature profiles evolution. 1kg $s^{-1}$ air injection rate (*top*), 10kg $s^{-1}$ air injection rate (*bottom*)

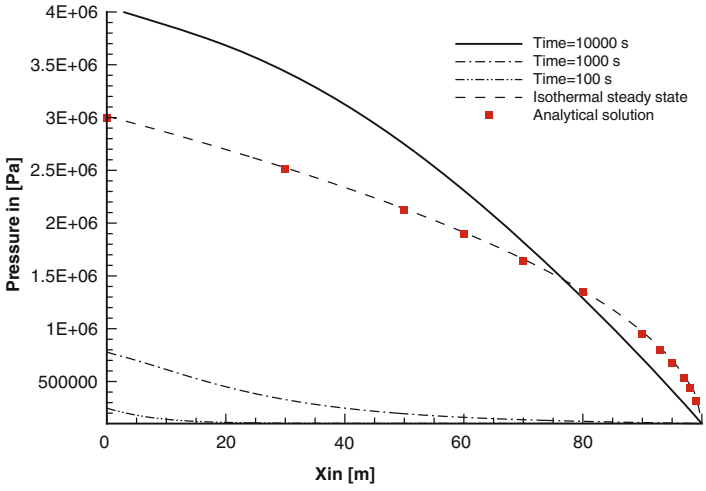


Figure 8.8: Temporal evolution of air pressure profiles for non-isothermal gas flow

### 8.6.3 Results

Figure 8.6 show the air pressure (left) and velocity distributions (right) along the soil column. Simulations were run with constant viscosities and those corresponding to the Reichenberg model (Sect. 8.1.1) which takes pressure and temperature changes into account.

The corresponding temperature profiles for different air injection rates are depicted in Fig. 8.7. The different shapes of the thermal profile curves indicate the transition between diffusion (left) and advection dominated regimes (right).

Figure 8.8 shows the temporal evolution of the air pressure profile for non-isothermal air flow. In order to see the non-isothermal effects we plotted the analytical steady state solution for isothermal flow along with the present numerical solution for non-isothermal flow. As a consequence of the viscosity increase resulting from the Reichenberg model, the steady state pressure is larger for non-isothermal conditions.

# Chapter 9

# Deformation Processes

*by Uwe-Jens Görke, Norihiro Watanabe, Joshua Taron, and Wenqing Wang*

This chapter is dedicated to the analysis of pure deformation processes in solid continua. Within the context of porous media mechanics, the generalized local momentum balance (2.100) discussed in Sect. 2.5.1 serves as the governing equation describing mechanical deformation. In fact, the specific expression of the momentum balance (2.100) defines the equilibrium conditions in porous media here, considering swelling and thermal stresses caused by the coupling of mechanical to other physical and chemical processes. The effective stress principle has been established in order to define the stress state in the solid skeleton of porous media (cf. Sect. 2.5.1). Within this context, $\boldsymbol{\sigma}_{\mathrm{eff}}$ indicates the stress tensor applied to a substitute continuum representing the solid skeleton smeared over the volume of the porous medium under consideration, and being characterized by a reduced partial density compared to the material density of the solid skeleton. Material models, which are well-known from solid mechanics, are transferred directly to the description of the material behavior of the solid skeleton in porous media mechanics.

Assuming small strains, the equilibrium conditions in solid mechanics are defined by the following specific formulation of the balance of linear momentum:

$$\nabla \cdot \boldsymbol{\sigma} + \rho \boldsymbol{g} = 0 \tag{9.1}$$

where $\boldsymbol{\sigma}$ is the Cauchy's stress tensor, $\rho$ is the mass density and $\rho \boldsymbol{g}$ is the volume force with the gravity vector $\boldsymbol{g}$. The coefficients of the displacement vector $\boldsymbol{u}$ are the primary variables, which will become evident introducing an appropriate constitutive relation describing the specific stress-strain behavior of

O. Kolditz et al. (eds.), *Thermo-Hydro-Mechanical-Chemical Processes in Fractured Porous Media*, Lecture Notes in Computational Science and Engineering 86,
DOI 10.1007/978-3-642-27177-9_9, © Springer-Verlag Berlin Heidelberg 2012

the material under consideration into the weak formulation of (9.1). For more details about the systematics of typical material classes see Sect. 2.5.2.

In general, the deformation problem can be considered as an initial-boundary value problem with Neumann type and Dirichlet type boundary conditions, accordingly given by

$$\boldsymbol{\sigma} \cdot\cdot\, \boldsymbol{n} = \boldsymbol{t} \quad \text{or} \quad \boldsymbol{u} = \boldsymbol{u}_\Gamma, \quad \forall\, \boldsymbol{x} \in \partial\Omega \tag{9.2}$$

where $\boldsymbol{n}$ defines the normal vector for the part of the surface with given traction boundary conditions $\boldsymbol{t}$, and $\boldsymbol{u}_\Gamma$ are prescribed boundary displacement values.

Subsequently, the following benchmarks for deformation problems with increasing complexity (e. g., regarding the material behavior) are presented:

*Elasticity:*

- Plane strain confined compression (9.1.1)
- Plane strain confined compression—Excavation in homogeneous media (9.1.2)
- Plane strain confined compression—Excavation in heterogeneous media (9.1.3)
- Strain driven three-dimensional unconfined compression (9.1.4)
- Load driven three-dimensional unconfined compression (9.1.5)
- Nonlinear elastic axisymmetric triaxial compression (9.1.6)
- Transverse isotropic elastic tensile test (9.1.7)

*Elastoplasticity:*

- Compression of a plate with a hole (9.2.1)
- Two-dimensional strain localization problem (9.2.2)
- Cam-Clay plasticity (9.2.3)

*Viscoplastic creep:*

- Creep of a thick-walled cylinder (9.3.1)
- Thermally driven creep in rock salt (9.3.2)
- Stationary creep in rock salt (9.3.3)
- Transient creep in rock salt (9.3.4)

## 9.1 Elasticity

For small strains of solid continua, it is mostly justified to assume isotropic elastic material behavior. Most substantial details of the theory of linear isotropic elasticity, represented by the generalized Hooke's law, are discussed in Sect. 2.5.3. In many technical applications considering small strains, the elastic material parameters are assumed to be constant and the stress-strain curves are nearly linear. However, the typical response of certain geological materials to monotonic

loading (without load reversal) shows a nonlinear stress-strain behavior. Considering only elastic effects during load application, Hooke's law cannot be used to describe the observed material properties. Therefore, so-called pseudo-elastic constitutive models are frequently used for the analysis of nonlinear stress-strain curves, particularly in soil and rock mechanics. In a generalized manner, they are based on the assumption of an explicit stress-strain relation considering a stress- and strain-dependent material matrix:

$$\boldsymbol{\sigma} = \underset{\mathbf{4}}{\boldsymbol{C}}\,(\boldsymbol{\sigma}, \varepsilon) \cdot\cdot\, \boldsymbol{\varepsilon}_{\mathrm{el}}\,. \tag{9.3}$$

Based on the so-called *Lubby1* model (cf. [131]), a nonlinear elastic approach with strain-dependent Young's modulus

$$E(\varepsilon_{\mathrm{v}}) = \frac{E_0}{1 + a\,\varepsilon_{\mathrm{v}}^{n}} \tag{9.4}$$

but constant Poisson's ratio is proposed. Here, $\varepsilon_{\mathrm{v}}$ is the equivalent strain, and $E_0$, $a$, as well as $n$, are material parameters. The equivalent strain is defined by

$$\varepsilon_{\mathrm{v}} = \sqrt{\frac{2}{3}\,\boldsymbol{\varepsilon}_{\mathrm{el}} \cdot\cdot\, \boldsymbol{\varepsilon}_{\mathrm{el}}}\,. \tag{9.5}$$

If the material properties are independent of the orientations and directions of the technical or natural object under consideration, the material behavior is called *isotropic*. Otherwise, the material is known as *anisotropic*. Anisotropy is closely connected with distinguished orientations in the material structure. Among others, fiber-reinforced and layered materials are typical anisotropic materials.

From the point of view of modeling and numerical simulation, special cases of anisotropy such as *orthotropy* are of particular interest. Orthotropic materials are characterized by mutually orthogonal two-fold axes of rotational symmetry. A special class of orthotropic materials represent the so called *transverse isotropic* materials. They are characterized by a plane of isotropy featuring the same material properties independent of the direction of observation within this plane, and different material properties in the direction normal to this plane. Within this context, the normal to the plane of isotropy can be considered as the direction of anisotropy. Most layered materials, biological membranes as well as rocks (e. g. sandstone, shale), can be considered as transverse isotropic ones.

In case of transverse isotropy, the Hooke's law (2.104) has to be modified establishing a unit vector $\boldsymbol{a}$ which defines the direction perpendicular to the plane of isotropy (normal vector, direction of anisotropy—defining, e. g., the direction of a single fiber family of a fiber-reinforced material).

$$\begin{aligned}\sigma_{ij} = {} & \lambda\,\delta_{ij}\,\varepsilon_{kk} \;+\; 2\mu_T\,\varepsilon_{ij} \\ & +\; 2\,(\mu_L - \mu_T)\,(a_i\,\varepsilon_{jl}\,a_l + a_l\,\varepsilon_{li}\,a_j) \\ & +\; \alpha\,(a_i\,a_j\,\varepsilon_{kk} + a_k\,\varepsilon_{kl}\,a_l\,\delta_{ij}) \\ & +\; \beta\,a_k\,\varepsilon_{kl}\,a_l\,a_i\,a_j \end{aligned} \tag{9.6}$$

Linear elastic transverse isotropic material is characterized by five independent material parameters like $\lambda$, $\mu_T$, $\mu_L$, $\alpha$ and $\beta$ given in (9.6). In some cases these parameters are called *invariants* of the transverse isotropic elastic Hooke's law. They can be defined w.l.o.g. by the following (engineering) elastic constants which can be obtained experimentally:

| | | |
|---|---|---|
| $E_i$ | – | Young's modulus within the plane of isotropy, |
| $\nu_i$ | – | Poisson's ratio within the plane of isotropy, |
| $E_a$ | – | Young's modulus w.r.t. the direction of anisotropy, |
| $\nu_{ia}$, $\nu_{ai}$ | – | Poisson's ratio w.r.t. the direction of anisotropy, |
| $G_a$ | – | shear modulus w.r.t. the direction of anisotropy. |

There exist some relations between these parameters.

$$G_i = \frac{E_i}{2(1+\nu_i)} = \mu_i \quad \text{(shear modulus within the plane of isotropy)} \tag{9.7}$$

$$\nu_{ai} = \nu_{ia}\,\frac{E_a}{E_i} \tag{9.8}$$

As mentioned above, the invariants of the transverse isotropic elastic Hooke's law can be expressed by the presented elastic parameters.

$$\begin{aligned}
\lambda &= \frac{E_i(\nu_i + \nu_{ia}\nu_{ai})}{\widetilde{D}} \\
\mu_T &= G_i \\
\mu_L &= G_a \\
\alpha &= \frac{E_i(\nu_{ai}(1+\nu_i-\nu_{ia}) - \nu_i)}{\widetilde{D}} \\
\beta &= \frac{E_a(1-\nu_i^2) - E_i[(\nu_i + \nu_{ia}\nu_{ai}) + 2(\nu_{ai}(1+\nu_i-\nu_{ia}) - \nu_i)]}{\widetilde{D}} \\
&\quad - 4G_a \;+\; 2G_i \\
&\quad \text{with} \quad \widetilde{D} \;=\; 1 \;-\; \nu_i^2 \;-\; 2\,\nu_{ia}\,\nu_{ai} \;-\; 2\,\nu_{ia}\,\nu_i\,\nu_{ai} \\
&\quad\qquad\;\; = (1+\nu_i)(1 \;-\; \nu_i \;-\; 2\,\nu_{ia}\,\nu_{ai})
\end{aligned}$$

The coordinates of the material tensor for a linear elastic transverse isotropic material are defined as follows:

$$\begin{aligned} C_{ijkl} \quad = \quad & \lambda\,\delta_{ij}\,\delta_{kl} \;+\; 2\mu_T\,\delta_{ik}\,\delta_{jl} \\ & +2\,(\mu_L-\mu_T)\,(a_i\,\delta_{jk}\,a_l + a_k\,\delta_{il}\,a_j) \\ & +\alpha\,(a_i\,a_j\,\delta_{kl} + a_k\,a_l\,\delta_{ij}) \\ & +\beta\,a_i\,a_j\,a_k\,a_l \end{aligned} \tag{9.9}$$

### 9.1.1 Plane Strain Confined Compression

#### Definition

This example deals with numerical analyses of a part of the whole rock mass based on special conditions concerning symmetry, structure of the rock mass and material behavior. Imposition of an initial stress state as a function of depth requires the application of a single boundary stress to represent loading from the overburden. In addition to this, the stresses decrease with depth because of the gravity and density of the rock mass (Fig. 9.1).

#### Solution

The calculation area has the size of 50 m × 50 m (length and height), and the problem is simplified under plane strain conditions. The quadrilateral mesh is illustrated in Fig. 9.2(a), which is refined in one corner in order to be used directly to subsequently conduct an elastic excavation simulation.

Regarding boundary conditions, a uniformly distributed pressure of 23.75 MPa is prescribed for the top boundary. Such kinds of boundary conditions are so called tractions in the context of mechanics, and they are treated as Neumann

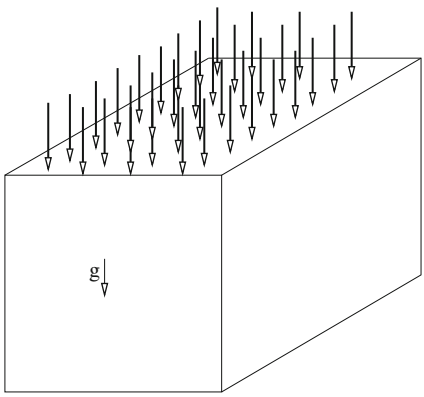


Figure 9.1: Conceptual model of elastic foundation

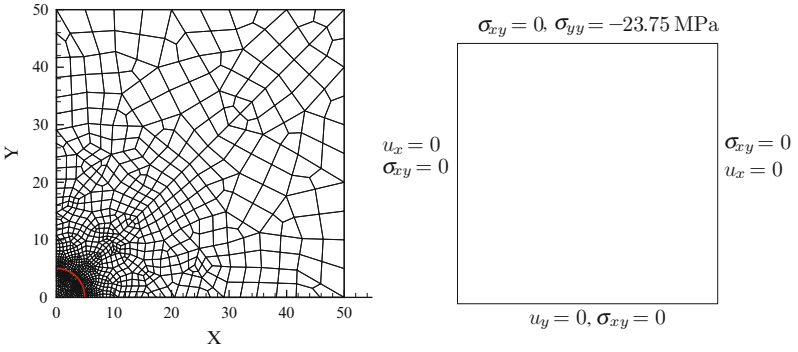


(a) FE mesh (b) Boundary conditions

Figure 9.2: Finite element model. *Left*: Spatial discretization (1,150 quadrilateral elements, 1,101 nodes); *Right*: Boundary conditions

Table 9.1: Material parameters

| Symbol | Parameter | Value | Unit |
|---|---|---|---|
| $E$ | Young's modulus | 25 | GPa |
| $\nu$ | Poisson's ratio | 0.3 | – |
| $\rho$ | Density | 2500 | $\text{kg}\cdot\text{m}^{-3}$ |

type boundary conditions. Boundary conditions are illustrated in more detail in Fig. 9.2(b).

Homogeneous material properties are assumed within the whole domain. Table 9.1 represents the corresponding material parameters.

For this simple elastic problem, the following analytical solution exists:

$$\sigma_{yy} = -23.75 - \rho h \tag{9.10}$$

where $\rho$ is the solid density and $h$ is the height from top to bottom boundary.

**Results**

Figure 9.3 (left) shows the distribution of vertical stress in the domain, which implies that the discretization error is very small. Figure 9.3 (right) shows a linear variation of stress $\sigma_{yy}$ along with height.

The numerical result of $\sigma_{yy}$ at the bottom boundary is $-24.97\,\text{MPa}$, which is very close to the analytic solution, $\sigma_{yy} = -25.0\,\text{MPa}$.

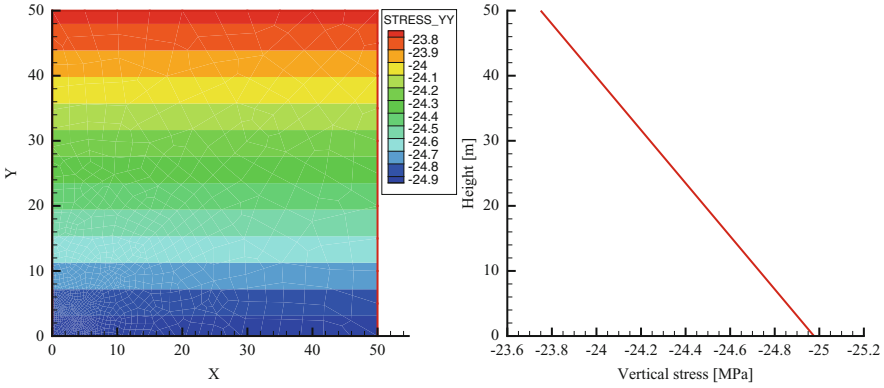


Figure 9.3: Result of vertical stress, $\sigma_{yy}$ (MPa). *Left*: domain distribution. *Right*: Vertical profile

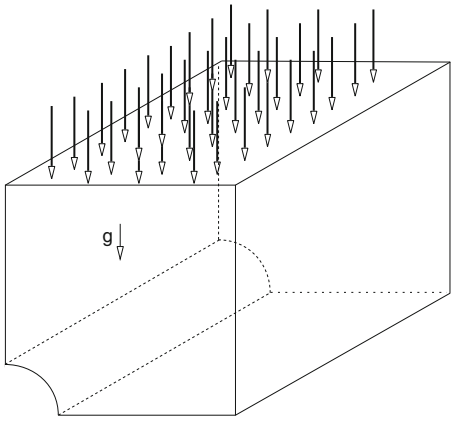


Figure 9.4: Excavation in rock mass

### 9.1.2 Plane Strain Confined Compression: Excavation in Homogeneous Media

#### Definition

This is the second step of the simulation described in the previous section, Sect. 9.1.1. A long cylindrical tunnel is driven in the rock mass, which is schematically shown in Fig. 9.4.

### Solution

The deformation due to the excavation is simulated under the assumption of plane strain. Finite element mesh, initial conditions and material parameters are the same as specified in Sect. 9.1.1. The tunnel has a radius of 5 m. The released loading approach is applied to simulate the excavation.

### Results

Figures 9.5 and 9.6 shows the distribution of vertical displacements and coefficients of the stress tensor in the domain after excavation.

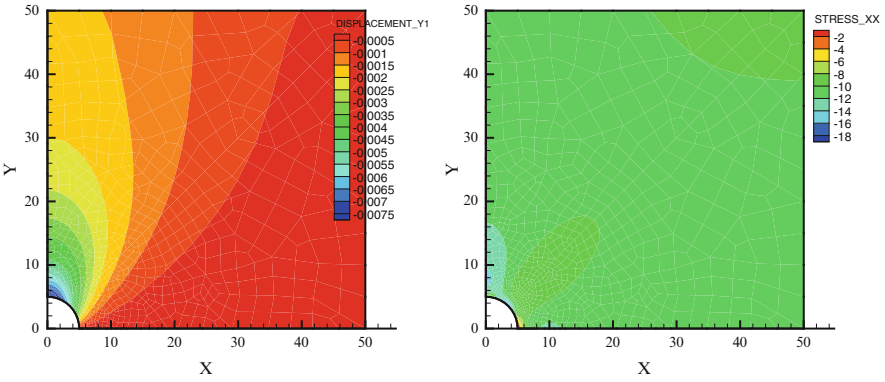


(a) Vertical displacement (m) (b) Horizontal stress (MPa)

Figure 9.5: Vertical displacements and horizontal stress after excavation

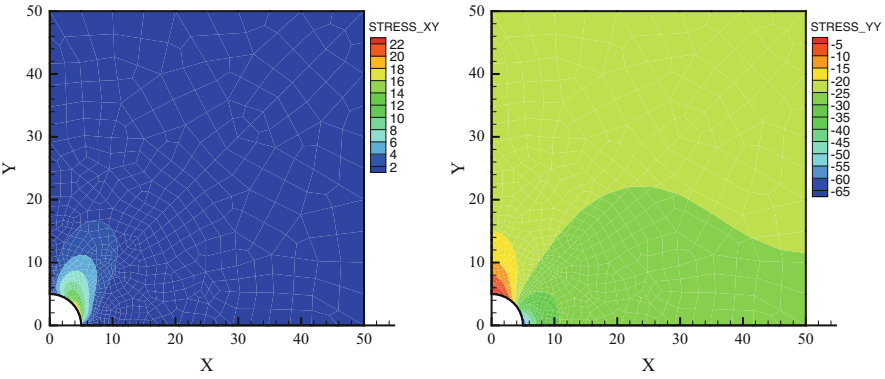


(a) Shear stress (MPa) (b) Vertical stress (MPa)

Figure 9.6: Shear stress and vertical stress after excavation

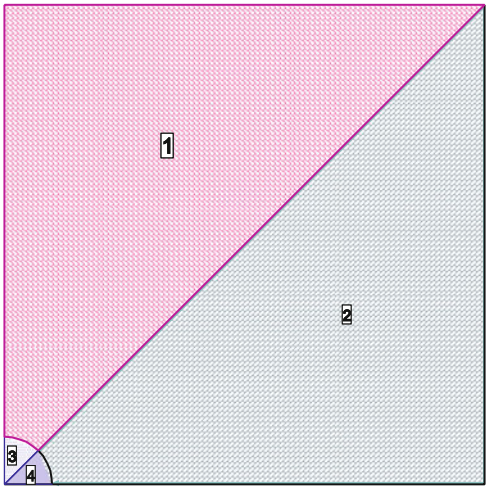


Figure 9.7: Excavation in heterogeneous rock mass

### 9.1.3 Plane Strain Confined Compression: Excavation in Heterogeneous Media

#### Definition

Differing from the homogeneous case, the deformation of the excavation problem defined in Sect. 9.1.2 is analyzed herewith defining the initial conditions as functions of the coordinates, and assuming four different material domains (cf. Fig. 9.7).

#### Solution

The initial stresses are assumed to be linearly distributed within a material domain. The expressions of these distributions are given in Table 9.2.

As depicted in Fig. 9.7, the domain consists of four different materials denoted by 1, 2, 3 and 4. Within this context, only the Young's modulus is assumed to differ for the material domains under consideration (cf. Table 9.3).

#### Results

Figure 9.8 shows the distribution of displacements after excavation, and Fig. 9.9 shows the distribution of different coefficients of the stress tensor after excavation.

Table 9.2: Initial stress distribution as function of coordinates (in kPa; material domains cf. Fig. 9.7)

| Material domain | Functions for stress coefficients $\sigma_{xx}$ | $\sigma_{yy}$ | $\sigma_{zz}$ |
|---|---|---|---|
| 1 | $-23.75 - 0.2y$ | $-23.75 - 0.2y$ | cf. $\sigma_{xx}$ |
| 2 | $-24.75 - 0.5y$ | $-24.75 - 1.3y$ | cf. $\sigma_{xx}$ |
| 3 | $-26.75 - 10.0x - 12.0y$ | $-26.75 - 20.0x - 16.0y$ | cf. $\sigma_{xx}$ |
| 4 | $-27.75 - 10.0x - 14.0y$ | $-27.75 - 20.0x - 18.0y$ | cf. $\sigma_{xx}$ |

Table 9.3: Material parameters (different Young's moduli are given in the order of the material domains)

| Symbol | Parameter | Value | Unit |
|---|---|---|---|
| $E$ | Young's modulus | 25.0; 26.0; 30.0; 28.0 | GPa |
| $\nu$ | Poisson's ratio | 0.3 | – |
| $\rho$ | Density | 2500 | $\mathrm{kg \cdot m^{-3}}$ |

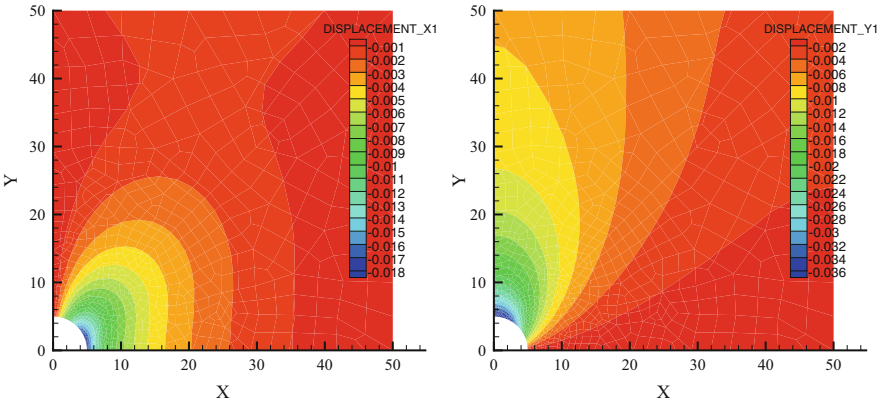


Figure 9.8: Distribution of displacement (m)

### 9.1.4 Strain Driven Three-Dimensional Unconfined Compression

#### Definition

A quarter of an elastic cylinder is compressed at the top, applying prescribed uniform deformations as boundary condition (cf. Fig. 9.10). Assuming homogeneous isotropic linear elastic material behavior and constant loading, the axial

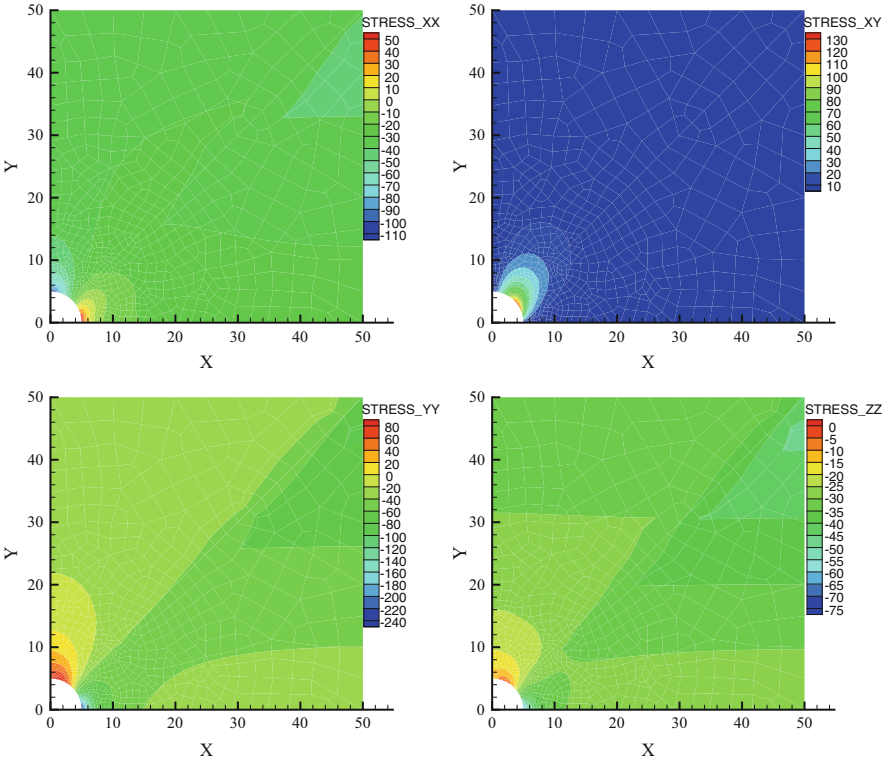


Figure 9.9: Distribution of stresses (kPa)

stress coefficient $\sigma_{zz}$ and the displacement vectors in the nodes of the finite element grid are calculated, which are caused by the given external loading.

**Solution**

The calculation area for the three-dimensional simulation consists of a quarter of the cylinder under consideration (cf. Fig. 9.11). The model includes 4,000 elements and 4,947 nodes. Deformations in the $x$-direction are suppressed in the $y$-$z$-plane and deformations in the $y$-direction are suppressed in the $x$-$z$-plane. Furthermore, axial deformations are suppressed at the bottom of the calculation area. At the top of the model, boundary conditions are prescribed assuming a constant displacement of 0.61 mm causing compression of the cylinder. The used material parameters are shown in Table 9.4.

In order to solve the homogeneous problem analytically, some constraints have to be considered: the stresses in the $x$- and $y$-direction are equal to zero, because

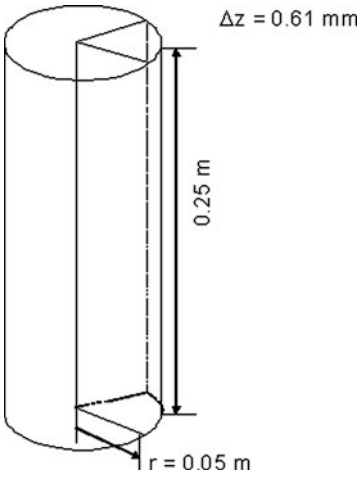


Figure 9.10: Calculation area: a quarter of a cylinder

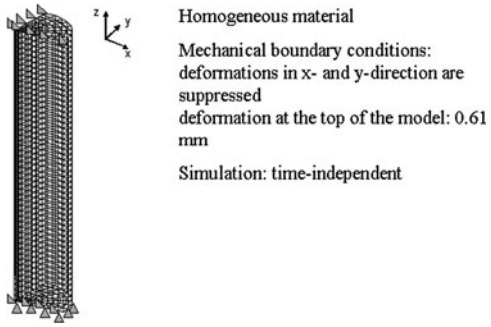


Figure 9.11: Finite element model: spatial discretization and boundary conditions

Table 9.4: Material parameters

| Symbol | Parameter | Value | Unit |
|---|---|---|---|
| $E$ | Young's modulus | 7 | GPa |
| $\nu$ | Poisson's ratio | 0.3 | – |
| $\rho$ | Density | 2,500 | kg·m$^{-3}$ |

the body expands homogeneously in the radial direction. Thus the stress-strain equations defined by Hooke's law (2.104) can be simplified as follows:

$$\varepsilon_{zz} = \frac{\Delta z}{z} = \frac{1}{E} \cdot \sigma_{zz} \tag{9.11}$$

$$\varepsilon_{xx} = \varepsilon_{xx} = \frac{1}{E} \cdot (-\nu \cdot \sigma_{zz}) \tag{9.12}$$

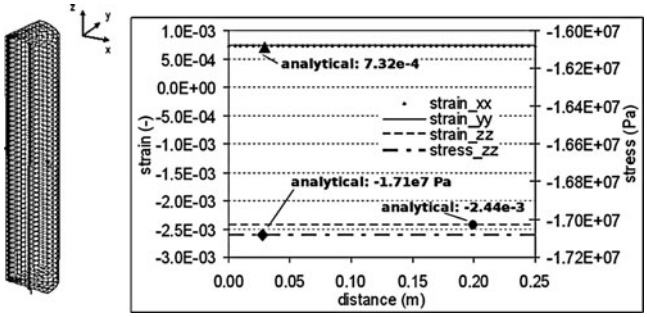


Figure 9.12: Resulting axial strain and axial stress

With the given strain in the $z$-direction, the axial stress $\sigma_{zz}$ is defined using (9.11) as

$$\frac{\Delta z}{z} = -2.44 \times 10^{-3} \quad \text{and} \quad \sigma_{zz} = -1.71 \times 10^{7}\,\text{Pa}$$

In this way, the strains in the $x$- and $y$-direction are known.

$$\varepsilon_{xx} = 7.32 \times 10^{-4}$$

#### Results

As can be seen in Fig. 9.12, the numerical results meet exactly the analytical solutions. In this figure, axial strain and the resulting axial stress are presented along a polyline from the top to bottom of the calculation area.

### 9.1.5 Load Driven Three-Dimensional Unconfined Compression

#### Definition

This example is similar to the previous one, differing in the kind of prescribed external loading: the calculation area undergoes traction boundary conditions (given surface stress) applied to the top of the model, while resulting deformation is unknown. In order to easily investigate whether the simulated results correspond to the analytical solutions, the value of the prescribed axial stress coefficient $\sigma_{zz}$ on the top of the calculation area is chosen to have the same value as the resulting one obtained in the previous example.

#### Solution

The finite element model has the same characteristics as the model in Sect. 9.1.4. At the top of the model a constant compressive surface stress in the axial direction with a value of $1.71 \times 10^7$ Pa is given as the source term. The simulation

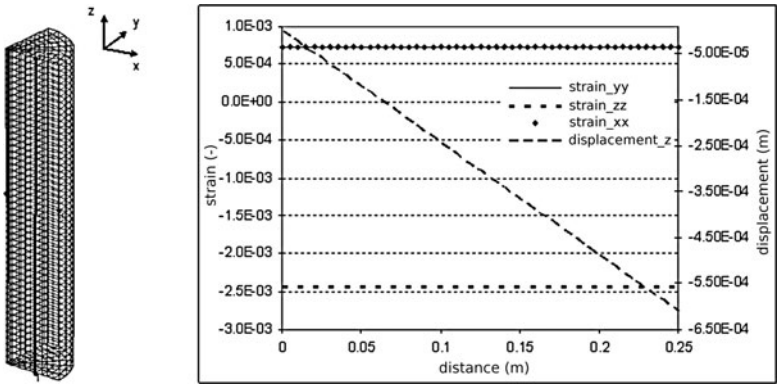


Figure 9.13: Strains and displacement in the $z$-direction

with OpenGeoSys requires the input of the external load in terms of surface tractions as the source term in the $z$-direction at the single nodes of the stressed boundary. The displacement boundary conditions are the same as in the previous example except for the axial displacement on the top of the model. The used material parameters are shown in Table 9.4.

**Results**

The analytical solution and the numerical results are identical to that of the previous example. The calculated axial displacement as a result of the constant load on the top of the model is $6.1\times10^{-4}$ m. The numerical results that are shown in Fig. 9.13 meet the analytical solutions exactly.

### 9.1.6 Nonlinear Elastic Axisymmetric Triaxial Compression

**Definition**

Triaxial short-term compression under axisymmetric conditions is carried out to verify the nonlinear elastic isotropic material model (modified Lubby1 approach). The loading in principal axes includes a radial pressure as well as an axial displacement, and is realized in two steps. It results in a homogeneous stress-strain state.

**Solution**

For the calculation, the cross-section of a cylindrical sample with a radius of 30 mm and a height of 120 mm is studied. Details of the model (geometry, mesh,

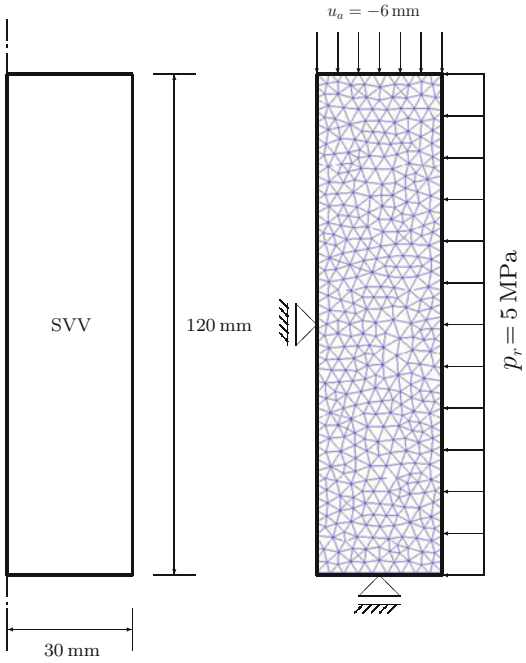


Figure 9.14: Triaxial compression of a cylindrical sample. Axisymmetric model. *Left*: Geometry. *Right*: Finite element grid and boundary conditions

boundary conditions) according to K.-H. Lux and F. Werunsky (unpublished report, 2008) are presented in Fig. 9.14.

Initial conditions do not have to be given for the problem under consideration. As the bottom edge is fixed in the vertical direction, the left-hand edge is fixed in the horizontal direction for symmetry reasons (axis of rotation). On the right-hand edge, initially a radial casing pressure of 5 MPa is applied within 20 seconds with a constant stress rate. While keeping constant this radial pressure, a subsequent stroke-driven axial compressive loading is applied within the following 1,440 seconds with a constant strain rate. The maximum axial displacement is 6 mm which corresponds to a 5% reduction of the sample's height (for the complex loading history cf. Fig. 9.15).

The material parameters referring to the modified Lubby1 relation (9.4) are summarized in Table 9.5. Within this context, the initial Young's modulus and the Poisson's ratio are close to values known for rock salt.

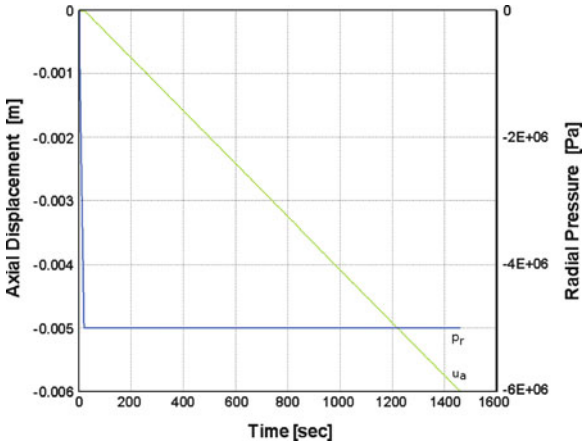


Figure 9.15: Triaxial compression of a cylindrical sample. Loading history for short-term experiments. Radial casing pressure (stress rate $\dot{p}_r = 0.25\,\mathrm{MPa{\cdot}s^{-1}}$) with subsequent axial displacement (strain rate $\dot{\varepsilon}_a = 3.47 \times 10^{-5}\,\mathrm{s^{-1}}$)

Table 9.5: Material parameters

| Symbol | Parameter | Value | Unit |
|---|---|---|---|
| $E_0$ | Initial Young's modulus | 21.4 | GPa |
| $\nu$ | Poisson's ratio | 0.335 | – |
| $a$ | Factor in (9.4) | 2750 | – |
| $n$ | Exponent in (9.4) | 1.0 | – |

**Results**

The representation of the axial stress vs. the axial strain in Fig. 9.16 shows on exemplarily chosen material parameters the noticeable difference between the linear (Hooke's model) and the nonlinear (modified Lubby1 model) elastic models even at small strains. Within the context of the studied case, the stress response will be overestimated by a multiple using the linear Hooke's law.

### 9.1.7 Transverse Isotropic Elastic Tensile Test

**Definition**

Tension of a quadratic plate according to Schröder [132], Kohlmeier [133] and Fiolka [134] is carried out to verify the linear elastic transverse isotropic material model. Within this context, a laminated material structure perpendicular to the

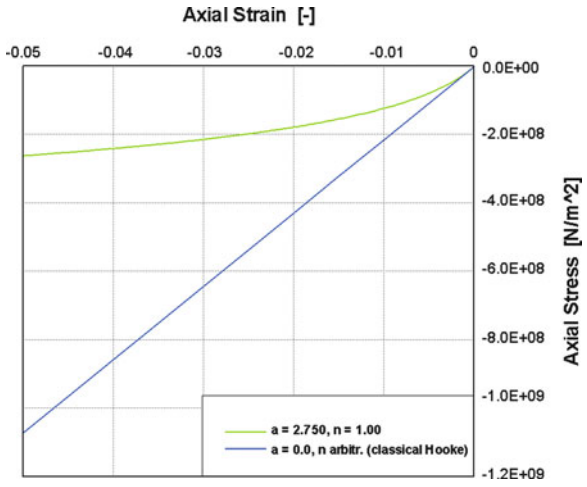


Figure 9.16: Triaxial compression of a cylindrical sample. Stress-strain curves regarding the axial load response. Comparison of linear elastic (Hooke) and nonlinear elastic (modified Lubby1 (9.4)) material models

plane under consideration is assumed. The direction of anisotropy within this plane, which is defined by a vector $\boldsymbol{a}$ is perpendicularly oriented to the material layers.

**Solution**

During simulation, the direction of anisotropy is rotated counterclockwise starting with an angle $\varphi$ of $\varphi = 0°$ and ending with $\varphi = 180°$. Consequently, as in OpenGeoSys, the direction of anisotropy is assumed to be directed parallel to the local $\bar{y}$-axis, and the angle of rotation is defined as the rotation between the global $x$-axis and the local $\bar{x}$-axis, the input angle changes in the range of $\varphi = -90° \ldots 90°$.

Assuming plane strain conditions for the two-dimensional case, the quadratic plate has an edge length of $l = 10\,\text{mm}$, and was analyzed using triangular and rectangular elements respectively. For details of this model (geometry, boundary conditions, material orientation) see Fig. 9.17.

To verify the linear elastic transverse isotropic material model in the three-dimensional case, the tensile test was simulated using a rectangular sample with an edge length $l = 10\,\text{mm}$ and a height $h = 1\,\text{mm}$. According to the two-dimensional case, a vertically arranged laminated material structure is assumed. The direction of anisotropy, which is defined by a vector $\boldsymbol{a}$ is perpendicularly

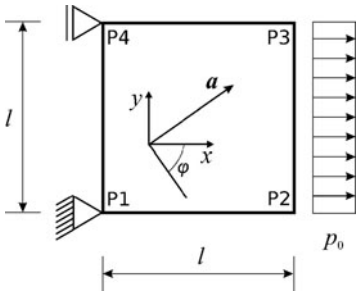


Figure 9.17: Tensile test. Model definition according to Kohlmeier [133]. Vector $\boldsymbol{a}$ defines the direction of anisotropy

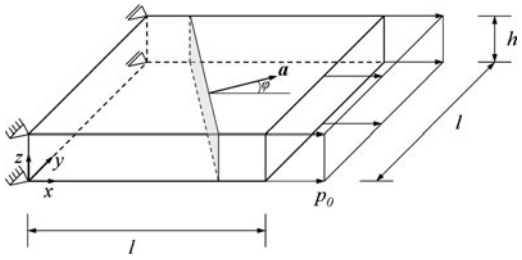


Figure 9.18: Tensile test. Three-dimensional model definition according to Fiolka [134]. Vector $\boldsymbol{a}$ defines the direction of anisotropy

oriented to the material layers. During simulation, the direction of anisotropy is rotated counterclockwise in the $xy$-plane from $\varphi = 0°$ to $\varphi = 180°$.

Within the context of the different opportunities offered by the input structure of OpenGeoSys to define the anisotropy direction, the coefficients of the unit normal vector which is parallel to the direction of anisotropy are given as $n_x = \cos\varphi$, $n_y = \sin\varphi$, and $n_z = 0$. Considering the case that the basis vectors of the local Cartesian coordinate system for transverse isotropic materials are provided by consecutive rotations of the plane of isotropy about the global $y(x_2)$-axis and the $\bar{x}(\bar{x}_1)$-axis of the once rotated system, the angle $\alpha$ has a constant value of 90°, whereas the angle $\beta$ changes from 0° to −180°. Using the angles known from applications in structural geology to generate the constitutive rotation matrices, the dip $\phi$ has the constant value of 90°, and the azimuth varies from 90°...0° (for $0° \leq \varphi \leq 90°$) and 360°...270° (for $90° \leq \varphi \leq 180°$) respectively. For details of the three-dimensional model (geometry, boundary conditions, material orientation) see Fig. 9.18.

Initial conditions do not have to be given for the problem under consideration. The left-hand edge is fixed in the horizontal direction. To avoid rigid body motions, the left lower corner node is fixed in both the vertical and horizontal

directions. A distributed tension load of $p_0 = 0.2\,\text{Mpa}$ is applied at the right-hand edge. In the three-dimensional case, the plane strain condition was realized, preventing any displacement in the $z$-direction on the upper and lower boundary surfaces of the sample.

The material parameters are summarized in Table 9.6.

### Results

The numerical results obtained with OpenGeoSys are compared to values given in [133]. They include displacement coefficients of various corner nodes of the plate depending on the anisotropy direction, and show a good agreement (cf. Fig. 9.19).

Table 9.6: Material parameters

| Symbol | Parameter | Value | Unit |
|---|---|---|---|
| $E_i$ | Young's modulus | 561.12 | MPa |
| $E_a$ | Young's modulus | 1311.83 | MPa |
| $\nu_i$ | Poisson's ratio | 0.6032 | – |
| $\nu_{ia}$ | Poisson's ratio | 0.1838 | – |
| $G_a$ | Shear modulus | 375.00 | MPa |

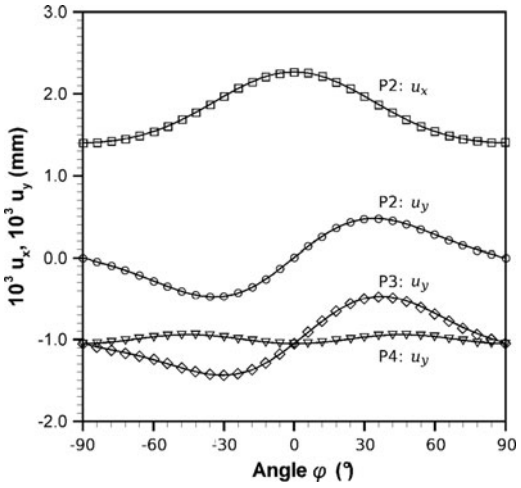


Figure 9.19: Tensile test. OpenGeoSys results (symbols) at length $l = 10\,\text{mm}$ and an edge load of $p_0 = 0.2\,\text{Mpa}$ compared to the reference solution given by Schröder [132] and Kohlmeier [133] (continuous lines)

## 9.2 Elastoplasticity

As discussed in Sect. 2.5.4, plasticity is a property of solid materials, which is characterized by non-reversible deformations and plastic yielding of the material. The last mentioned material property can be mathematically described introducing so-called yield conditions $\Phi_{\mathrm{pl}}(\boldsymbol{\sigma})$. Figure 9.20 illustrates geometrically three typical yield conditions defined in the principal stress space. If the stress path of any material point is located inside one of these surfaces, the point undergoes elastic deformation; if it is located on the boundary of the specific yield surface, plastic yielding is observed. The yield status of a material point is determined checking the Kuhn-Tucker conditions for loading or unloading:

$$\dot{\Phi}_{\mathrm{pl}} \leq 0, \qquad \lambda_{\mathrm{pl}}\, \Phi_{\mathrm{pl}} = 0 \quad \text{or} \quad \lambda_{\mathrm{pl}} \geq 0 \tag{9.13}$$

In metal plasticity, usually so-called associative plasticity models are used, which are characterized by coaxiality of the plastic strain increment and the normal vector established in the current stress point of the yield condition. Usually, the mechanical behavior of geomaterials (in particular soils, and clay-rich materials) is of a more complex nature compared to metals, and depends on porosity, stress state and direction of external loading. Frequently, shear deformation (shear bands) associated with strain localization, dilation and/or a coupling of these properties can be observed. Localization problems are of an unstable nature, i. e., softening may occur at a certain point of loading. As these

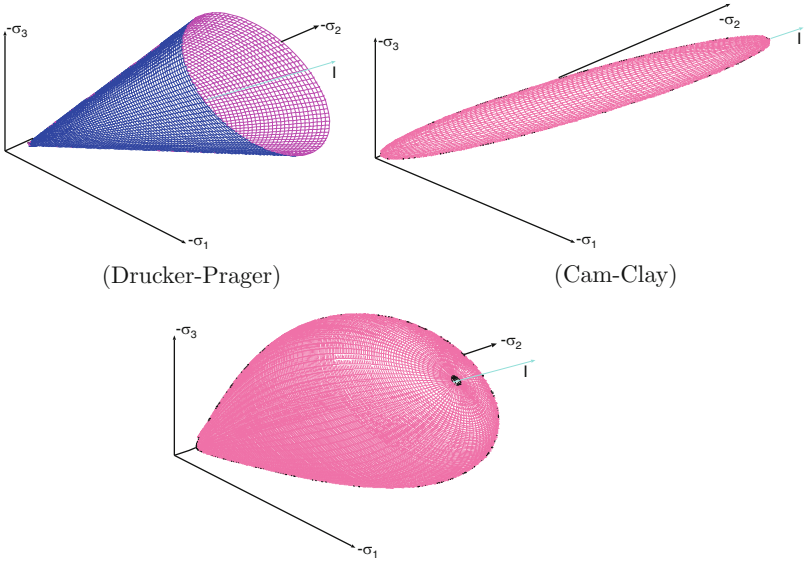


Figure 9.20: Yield surface

phenomena cannot be modeled using classical plasticity approaches, usually so-called non-associated plasticity models are introduced. They are characterized by the definition of a plastic potential $\widehat{\Phi}_{\mathrm{pl}}(\boldsymbol{\sigma})$ instead of the yield condition. Within this context, the increment of the plastic strain tensor will still be defined using (2.112), but substituting the yield condition with the plastic potential. Two typical plastic models suited to address strain localization phenomena are described below.

*Drucker-Prager Model*

This model is a function of two stress invariants and a hardening parameter $\kappa$ with the following yield condition and plastic potential:

$$\Phi_{\mathrm{pl}}(\boldsymbol{\sigma}, \kappa) = \sqrt{\frac{2}{3}\boldsymbol{\sigma}_d \cdot\cdot \boldsymbol{\sigma}_d} + \alpha \,\mathrm{tr}(\boldsymbol{\sigma}) - y(\kappa) = 0 \tag{9.14}$$

$$\widehat{\Phi}_{\mathrm{pl}}(\boldsymbol{\sigma}, \kappa) = \sqrt{\frac{2}{3}\boldsymbol{\sigma}_d \cdot\cdot \boldsymbol{\sigma}_d} + \beta \,\mathrm{tr}(\boldsymbol{\sigma}) - y(\kappa) = 0 \tag{9.15}$$

where $\alpha$ is a coefficient related to the internal frictional angle, $y(\kappa)$ is the yield stress depending on the hardening parameter.

*Cam-Clay model*

Similar to the Drucker-Prager model, the Cam-Clay model is a function of both the first and second stress invariants. The generalized Cam-Clay model is defined as:

$$\Phi_{\mathrm{pl}}(\boldsymbol{\sigma}, \kappa) = \frac{2}{3}\boldsymbol{\sigma}_d \cdot\cdot \boldsymbol{\sigma}_d + M^2 \, p_s \, (p_s - p_{s_{cn}}) = 0 \tag{9.16}$$

with $p_s = \mathrm{tr}(\boldsymbol{\sigma})/3$, where $M$ is the slope of the critical state line and $p_{s_{cn}}$ is the isotropic preconsolidation pressure. The rate of $p_s$ is given by

$$\frac{\mathrm{d}\, p_s}{\mathrm{d}\, \varepsilon^{\mathrm{v}}_{\mathrm{pl}}} = \frac{(1+e)p_s}{\lambda_c - \kappa_c} \tag{9.17}$$

where $e$ is the void ratio, $\varepsilon^{\mathrm{v}}_{\mathrm{pl}}$ defines the volumetric plastic strain, $\lambda_c$ is the virgin compression index and $\kappa_c$ is the swelling/recompression index.

The model also describes the nonlinear elastic behavior of clay-like media before plastic yielding occurs, in which the bulk modulus $K$ is dependent of stress status as

$$K = \frac{1+e}{\kappa_c} p_s = 0 \tag{9.18}$$

### 9.2.1 Compression of a Plate with a Hole

#### Definition

Compression and/or tension of a plate with a hole is a typical plane strain benchmark for the modeling of elastoplastic material behavior, and is defined in [135]. Here, this example is analyzed to compare the behavior of two approaches on pure plastic deformation problems.

#### Solution

In the present simulation, a quarter of the perforated plate is considered because of the symmetry of the problem. The model set-up is shown in Fig. 9.21. The radius of the hole is 10 mm. Two points (point 1 and point 2) are specified to monitor the evolution of variables. Point 1 is located at one third of the distance from point 3 to point 4.

Traction boundary conditions, $p = 100 \cdot \lambda(t)\,\mathrm{MPa}$ are prescribed on the top, where $\lambda(t)$ denotes a time-dependent scaling factor. The particular case of cycling loading is analyzed defining a scaling factor as shown in Fig. 9.22 assuming $\lambda_{\max} = 4.1$.

The finite element grid using triangular elements is shown in Fig. 9.23, and the material parameters obtained from [135] are presented in Table 9.7.

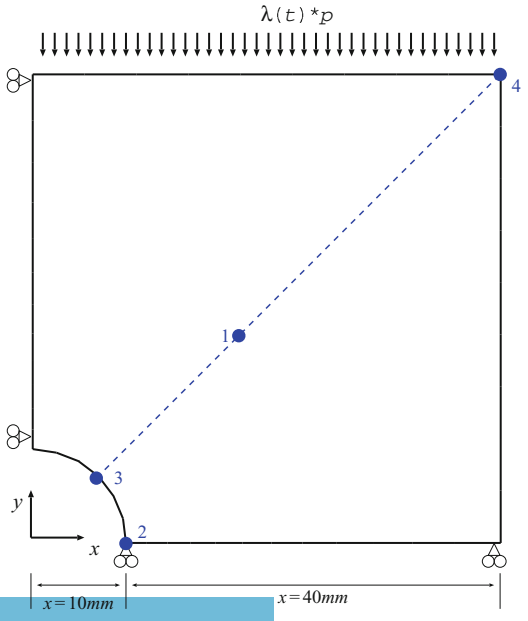


Figure 9.21: One quarter of the compressed steel plate with a hole

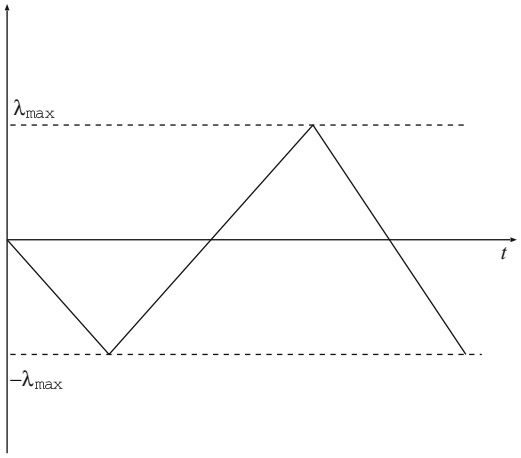


Figure 9.22: Time dependent scaling factor for external loading

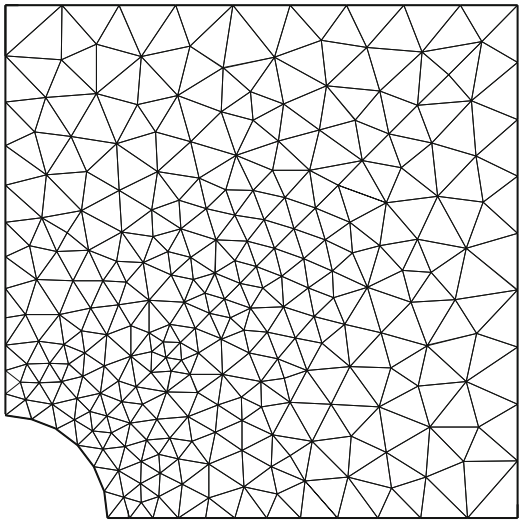

Figure 9.23: Finite element grid: 269 nodes and 484 elements

Table 9.7: Material parameters

| Symbol | Parameter | Value | Unit |
|---|---|---|---|
| $E$ | Young's modulus | 206.9 | GPa |
| $\nu$ | Poisson's ratio | 0.29 | – |
| $\sigma_0$ | Initial yield stress | 0.45 | GPa |

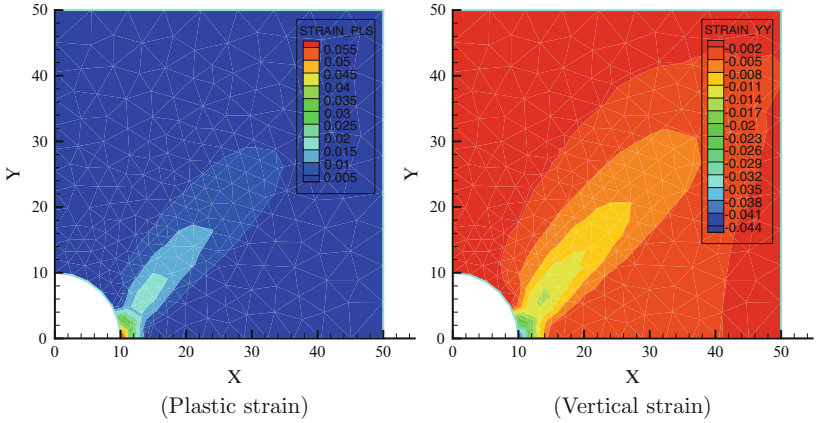


(Plastic strain) (Vertical strain)

Figure 9.24: Distribution of plastic strain and vertical strain at $\lambda_{\max}/10$

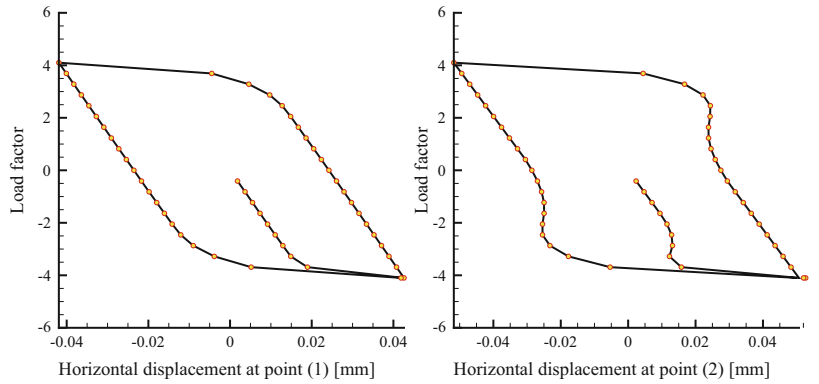


(Point 1) (Point 2)

Figure 9.25: Evolution of horizontal displacement vs. scaling factor

### Results

The load is applied within 60 time steps with a constant increment for the loading factor $\Delta\lambda = \lambda_{\max}/10$. As shown in Fig. 9.24, plastic strain and vertical strain show similar distributions, which are typical for elastoplastic material behavior according to the von Mises model. The evolution of the horizontal displacement at point 1 and at point 2 as functions of the periodic scaling factor $\lambda(t)$ are shown on Fig. 9.25.

### 9.2.2 Two-Dimensional Strain Localization Problem

#### Definition

In this benchmark, a plane strain failure problem is analyzed with triangular and quadrilateral elements, correspondingly. An enhanced strain approximation is used to simulate the displacement discontinuity after failure appears. Neighbor relationships of an element object are essential data for designing the deforming mesh and to determine the evolution of the discontinuity orientation within the context of failure analysis.

From the viewpoint of the bifurcation theory, strain localization is a bifurcation phenomenon, which takes place when the velocity field moves away from the branch of continuous solutions and follows a new path of discontinuous solutions. If standard finite elements are applied to this problem, the mesh has to be refined adaptively near the localization area. Additionally, the system of equations will be an ill-posed one. The strong discontinuity approach with enhanced strain elements avoids an ill-posed system of equations, thus avoiding mesh sensitivity of the analysis [136].

#### Solution

The set-up of the two-dimensional compression problem as proposed by [137] is shown in Fig. 9.26. The geometry of the specimen is simplified as rectangular with the dimensions of 1 m×3 m.

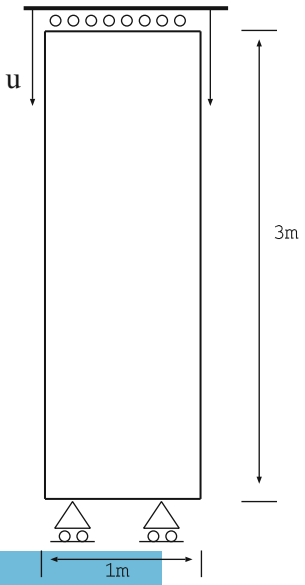


Figure 9.26: Plane strain two-dimensional localization test

Table 9.8: Material parameters

| Symbol | Parameter | Value | Unit |
|---|---|---|---|
| $E$ | Young's modulus | 20.0 | MPa |
| $\nu$ | Poisson's ratio | 0.4 | – |
| $\alpha$ | Factor in (9.15) | 0.233345 | – |
| $\beta$ | Factor in (9.15) | 0.141421 | – |
| $\sigma_0$ | Initial yield stress | 29.69 | kPa |
| $H$ | Hardening modulus | 100 | kPa |
| $H_\delta$ | Localized softening modulus | $-1,000$ | kPa |

The bottom of the specimen is supported by horizontal roles, and its top surface is allowed to move only vertically with the axial displacement $u_z$. Both lateral surfaces are considered to be free of tractions.

The non-associative flow rule is adopted for the Drucker-Prager model with material parameters presented in Table 9.8.

#### Results

Figure 9.27 shows the deformed model exhibiting localization. The stress response at the top surface to the prescribed displacements is discussed in Fig. 9.28. These results agree well with data presented in [137].

### 9.2.3 Cam-Clay Plasticity

#### Definition

This axisymmetric benchmark is usually discussed to verify a critical state plastic mode, e. g., the Cam-Clay model.

#### Solution

For the finite element solution, a quarter of a cylindrical specimen is considered with a diameter of 5 cm and a length of 10 cm. The bottom surface is roller supported, and a vertical (axial) displacement is prescribed at the top surface until the specimen is compressed at 50 % of the initial length. Displacements of the top surface in the radial direction are allowed. The lateral surface of the cylinder is free of tractions. The material parameters are summarized in Table 9.9.

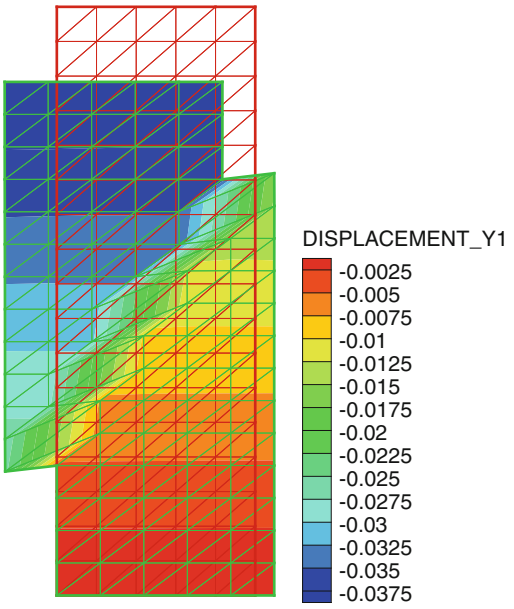


Figure 9.27: Deformed contour with distribution of the axial displacements

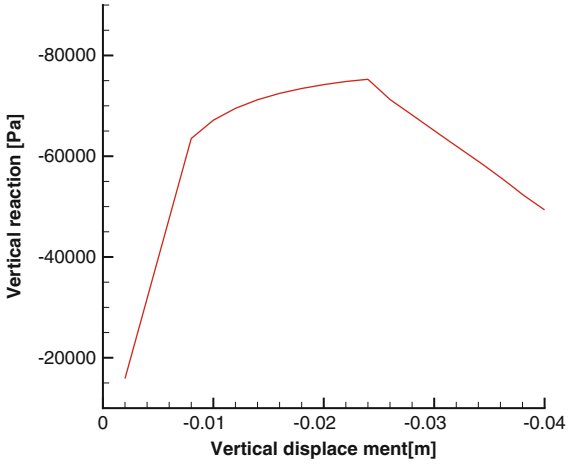


Figure 9.28: Axial stress at the top as a function of the axial displacement

### Results

The relationship between von Mises type stress, the second stress invariant and the axial strain is illustrated in Fig. 9.29. The results agree well with data presented in [138].

Table 9.9: Material parameters

| Symbol | Parameter | Value | Unit |
|---|---|---|---|
| $\nu$ | Poisson's ratio | 0.30 | – |
| $M$ | Slope of critical state line | 1.20 | – |
| $\lambda_c$ | Virgin compression index | 0.20 | – |
| $\kappa_c$ | Swelling / recompression index | 0.02 | – |
| $p_{s_{cn0}}$ | Initial preconsolidation pressure | 60.00 | – |
| $e_0$ | Initial void ratio | 1.50 | – |

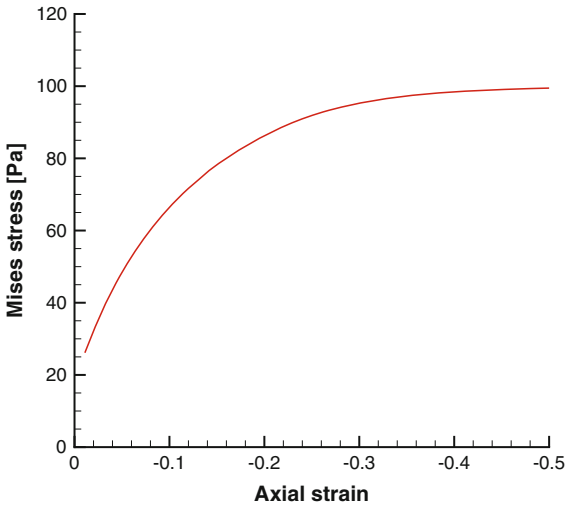


Figure 9.29: Axial strain vs. von Mises type stress

## 9.3 Viscoplastic Creep

Creep is a typical effect of viscoplastic material behavior, and represents a time- and/or temperature-dependent deformation process of solid continua affected by constant load. As discussed in Sect. 2.5.6, similar to plastic potential, a creep potential $\Phi_c$ is introduced in order to describe the creep behavior.

Usually, a stationary creep model is sufficient to describe the creep phenomena in geological media such as soil and rock. The application of Norton's model (2.125) associated with an explicit Euler scheme for time discretization of the differential equation (2.123) results in the following incremental form of the calculation of the creep strain tensor:

$$\Delta\boldsymbol{\varepsilon}_c = \alpha \left(\frac{3}{2}\right)^{\frac{n+1}{2}} \left(\sqrt{\frac{3}{2}\boldsymbol{\sigma}_d \cdot\cdot \boldsymbol{\sigma}_d}\right)^{n-1} \Delta t \ \boldsymbol{\sigma}_d \tag{9.19}$$

with the time step size $\Delta t$.

Viscoplastic creep is mainly caused by diffusion and dislocations at the microscale, and results in hardening as well as recovery aspects. Hou and Lux propose an evolutional equation for the (viscoplastic) creep strain rate considering stationary as well as transient creep, damage impact, hardening and recovery (cf. [139–141]). Neglecting damage effects, this approach is known as Lubby2 model.

$$\dot{\boldsymbol{\varepsilon}}_{\mathrm{c}} = \frac{3}{2}\left[\frac{1}{\eta_k}\left(1 - \frac{\varepsilon_{\mathrm{tr}}}{\max \varepsilon_{\mathrm{tr}}}\right) + \frac{1}{\eta_m}\right]\boldsymbol{\sigma}_d \tag{9.20}$$

Here $\varepsilon^{\mathrm{tr}}$ denotes the equivalent transient creep strain

$$\varepsilon_{\mathrm{tr}} = \sqrt{\frac{2}{3}\boldsymbol{\varepsilon}_{\mathrm{tr}} \cdot\cdot \boldsymbol{\varepsilon}_{\mathrm{tr}}} \tag{9.21}$$

with $\boldsymbol{\varepsilon}_{\mathrm{tr}} = \boldsymbol{\varepsilon}_{\mathrm{c}} - \boldsymbol{\varepsilon}_{\mathrm{st}}$ ($\boldsymbol{\varepsilon}^{\mathrm{st}}$—stationary creep fraction). In addition to the equivalent transient creep strain the generalized representation of the von Mises equivalent deviatoric stress $s_{\mathrm{v}}$ is defined.

$$s_{\mathrm{v}} = \sqrt{\frac{3}{2}\boldsymbol{\sigma}_d \cdot\cdot \boldsymbol{\sigma}_d} \tag{9.22}$$

Furthermore, the following material functions are suggested, considering only hardening, and neglecting recovery effects:

$$\max \varepsilon^{\mathrm{tr}} = \frac{s_{\mathrm{v}}}{G_k} \tag{9.23}$$

$$G_k = \bar{G}_k^* \exp\left(k_1\, s_{\mathrm{v}}\right) \qquad \text{(Kelvin shear modulus)} \tag{9.24}$$

$$\eta_k = \bar{\eta}_k^* \exp\left(k_2\, s_{\mathrm{v}}\right) \qquad \text{(Kelvin viscosity modulus)} \tag{9.25}$$

$$\eta_m = \bar{\eta}_m^* \exp\left(m\, s_{\mathrm{v}}\right) \exp(lT) \qquad \text{(Maxwell viscosity modulus)} \tag{9.26}$$

As $T$ denotes the absolute temperature, the following material parameters are necessary to model various constitutive effects:

- $\bar{G}_k^*$, $k_1$ hardening,
- $\bar{\eta}_k^*$, $k_2$ transient creep, and
- $\bar{\eta}_m^*$, $m$, $l$ stationary creep.

### 9.3.1 Creep of a Thick-Walled Cylinder

#### Definition

In this example, creep behavior of a thick-walled cylinder is discussed, which is subjected to a constant inner normal pressure.

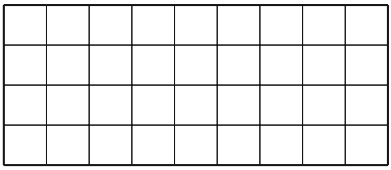

Figure 9.30: Finite element grid of the thick-walled cylinder

Table 9.10: Material parameters of Norton's creep model

| Symbol | Parameter | Value | Unit |
|---|---|---|---|
| $E$ | Young's modulus | 137.8 | GPa |
| $\nu$ | Poisson's ratio | 0.48 | – |
| $\alpha$ | Norton model factor | $6.415 \times 10^{-10}$ | – |
| $n$ | Norton Model exponent | 4 | – |

**Solution**

The inner and the outer radius of the cylinder are 4 mm and 6.4 mm respectively, at a height of 1 mm. Quadrilateral elements are used for the spatial discretization of the axisymmetric finite element model (cf. Fig. 9.30). The boundary conditions are as follows: normal pressure $p = 2.515\,\text{MPa}$ at the inner surface and zero normal stress at the outer surface. Furthermore, displacements in the axial direction are suppressed at the top and bottom surfaces.

A homogeneous initial stress distribution is assumed in the domain, applying the following values for the coefficients of the stress tensor in cylindrical coordinates: $\sigma^0_{rr} = \sigma^0_{\theta\theta} = \sigma^0_{zz} = -50\,\text{Pa}$. The parameters of Norton's creep model are given in Table 9.10.

The numerical results can be compared with Balley's analytical solution for the rate of radial displacements

$$\dot{u}_r = \alpha \frac{3^{\frac{n+1}{2}}}{2n^n} \frac{r_a^2\, r_b^2\, p^n}{(r_b^{2/n} - r_a^{2/n})r}$$

and for the equilibrated state of the first stress invariant

$$\sigma_v = \frac{2\sqrt{3}}{2n} \frac{p\ (r_b/r)^{\frac{2}{n}}}{(r_b/r_a)^{2/n} - 1}$$

**Results**

Figures 9.31 and 9.32 show the distribution of the first stress invariant $\sigma_v$ and of radial displacements along the cross section of the sample wall compared to

the pure elastic solution. This demonstrates that $\sigma_v$ decreases at about 26% at the inner surface of the thick-walled cylinder until the asymptotic creep state is reached. In contrast, the radial displacements increase at about 200%.

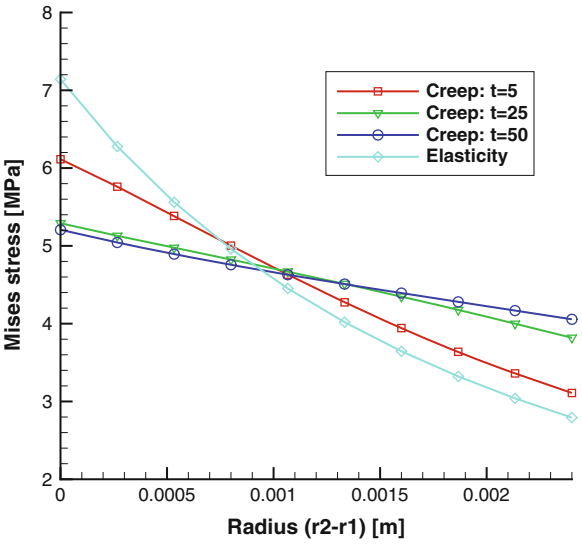


Figure 9.31: Profiles of the first stress invariant during creep at different times, $t = 5,\ 25,\ 50$ sec compared to the elastic solution

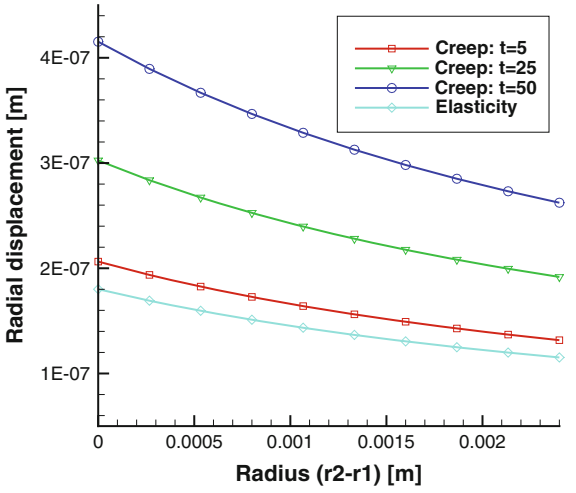


Figure 9.32: Profiles of radial displacements during creep at different times, $t = 5,\ 25,\ 50$ sec compared to the elastic solution

### 9.3.2 Thermally Driven Creep in Rock Salt

#### Definition

Several models exist for the evaluation of the effect of stationary creep in rock salt. One of those models is the so-called BGRa-model (9.27), which is valid for an external load between 5 Mpa and 25 Mpa within a temperature range of 22-200° C ([142]).

$$\dot{\boldsymbol{\varepsilon}}_{\mathrm{c}} = Ae^{-\frac{Q}{RT}} \left(\frac{\sigma}{\sigma^*}\right)^n \tag{9.27}$$

In a cylindrical sample of rock salt, stress relaxation is caused by a temperature decrease of 30 K. The aim of the example is to calculate the resulting strain variation with time within the solid body using the stationary creep model BGRa (9.27). The results of the simulation defining an axisymmetric model are compared to a three-dimensional solution.

#### Solution

For the numerical simulation a cylindrical core sample as shown in Fig. 9.33 is selected.

Figure 9.34 shows the axisymmetric finite element model (mesh, boundary conditions etc.) arranged in the $x$-$z$-plane. The dimensions of this model are: radius ($x$-direction) 0.05 m and height 0.2 m. A relatively coarse mesh consisting of 228 triangular elements and 139 nodes is used.

Vertical deformation at the top and the bottom surfaces are suppressed. The initial temperature in the whole area is 330 K. At the top and bottom of the model, thermal boundary conditions are prescribed defining a temperature of 300 K. Based on these conditions, the stress relaxation during the cooling down is simulated.

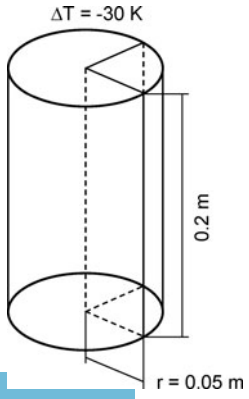


Figure 9.33: Core sample model

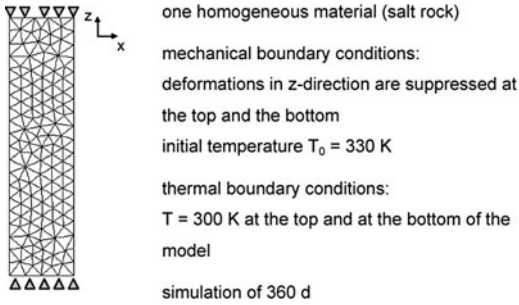


Figure 9.34: Details of the axisymmetric finite element model

Table 9.11: Material parameters of the creep model

| Symbol | Parameter | Value | Unit |
|---|---|---|---|
| $A$ | Factor of the creep model | 0.18 | $\mathrm{d}^{-1}$ |
| $Q$ | Activation energy | 54 | $\mathrm{kJ{\cdot}mol^{-1}}$ |
| $R$ | Gas constant | 8.31447 | $\mathrm{J{\cdot}K^{-1}{\cdot}mol^{-1}}$ |
| $n$ | Material constant | 5 | – |
| $\sigma^*$ | Reference effective stress | 1 | MPa |

Table 9.12: Material parameters and heat process conditions of the thermo-mechanical creep model

| Symbol | Parameter | Value | Unit |
|---|---|---|---|
| $E$ | Young's modulus | 25 | GPa |
| $\nu$ | Poisson's ratio | 0.27 | – |
| $\alpha$ | Thermal expansion coefficient | $4.0 \times 10^{-5}$ | $\mathrm{K^{-1}}$ |
| $c$ | Thermal capacity | 1 | $\mathrm{J{\cdot}kg^{-1}{\cdot}K^{-1}}$ |
| $\lambda$ | Thermal conductivity | 100 | $\mathrm{W{\cdot}m^{-1}{\cdot}K^{-1}}$ |
| $T_0$ | Initial temperature | 330 | K |
| $T$ | Temperature after cooling down | 300 | K |

The material parameters referred to the creep model (9.27) are presented in Table 9.11.

In Table 9.12, material and process parameters of the thermo-elastic part of the constitutive model are given.

The numerical simulation of the stress relaxation process over a time of 360 days is performed within 360 time steps of constant time step length.

In order to evaluate the numerical results of the relaxation problem, the following analytical solution of (9.27) for the problem under consideration has been proposed (Eickemeier 2007, personal communication) in respect of the stress increment for the current time step:

$$\Delta\sigma_{i+1} = \frac{(\dot{\varepsilon}_0^{\mathrm{c}} - A(\sigma/\sigma^*)^n)E_q\Delta t}{1 - E_q/\sigma^* A^* \Delta t\, \xi\, n\, (\sigma/\sigma^*)^{n-1}} \tag{9.28}$$

with

$$A^* = Ae^{-Q/RT} \tag{9.29}$$

Here, the initial creep strain rate $\dot{\varepsilon}_0^{\mathrm{c}}$ is assumed to be zero, $E_q$ is the weighted Young's modulus of the steel plates that are used to apply the external load and support the rock salt sample (in this case, only rock salt is considered), and the paramter $\xi$ is defined as $\xi = 0.5$.

### Results

For the analytical solution of (9.28) the axial stress of the previous time step is used. Time step increment is $\Delta t = 1\,\mathrm{d}$. In the three-dimensional case, the results are shown for node 705, which is located at point ($x$, $y$, $z = 0.05$, 0, 0.12). This node is identical to node 76 of the axisymmetric model (cf. Fig. 9.35).

The comparison of the increment of axial stresses $\Delta\sigma_{i+1}$ analytically obtained using (9.28) shows identical results to the numerical values at node 705 of the three-dimensional model and node 76 of the axisymmetric model. Both stress increments $\Delta\sigma_{i+1}$ obtained by OpenGeoSys and the scientific special purpose finite element code ANSALT (cf. [143]) are equal to $3.05 \times 10^{-3}\,\mathrm{MPa}$. The results of axisymmetric, as well as three-dimensional numerical simulations, are shown in Fig. 9.35 and show an excellent agreement.

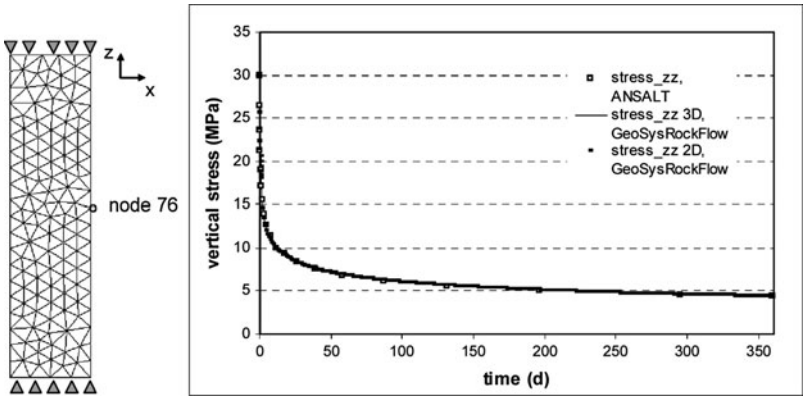


Figure 9.35: Comparison of numerical results (OpenGeoSys vs. ANSALT) for axial stresses

### 9.3.3 Stationary Creep in Rock Salt

#### Definition

With respect to the benchmark discussed in Sect. 9.3.2, the creep process is now assumed to be caused by a constant external load at the bottom of the solid and a constant high temperature at the same time. The aim of this example is to calculate the resulting strain variation with time using the stationary creep model BGRa (9.27).

#### Solution

For the simulation with OpenGeoSys almost the same finite element models (i. e., axisymmetric and three-dimensional case) as for the previous benchmark in Sect. 9.3.2 are selected. The only difference is in the height of the model, which is now 0.25 m. The initial temperature in the whole domain is 373.15 K. A constant load of 5 MPa is applied at the bottom surface of the model. The numerical simulation of the creep process over a time of 100 days is performed within 100 time steps of a constant time step length.

In order to compare numerical solutions with an analytical one, (9.27) is transformed into the following expression:

$$A = \frac{\Delta\varepsilon_{\text{eff}}}{e^{-Q/RT}\sigma_{\text{eff}}} \tag{9.30}$$

with

$$\begin{aligned} \sigma_{\text{eff}} &= \frac{1}{\sqrt{2}}\sqrt{(\sigma_1-\sigma_2)^2+(\sigma_2-\sigma_3)^2+(\sigma_3-\sigma_1)^2} \\ \Delta\varepsilon_{\text{eff}} &= \frac{\varepsilon_{\text{eff}}(t+\Delta t)-\varepsilon_{\text{eff}}(t)}{\Delta t} \\ \varepsilon_{\text{eff}} &= \frac{\sqrt{2}}{3}\sqrt{(\boldsymbol{\varepsilon}_1-\boldsymbol{\varepsilon}_2)^2+(\boldsymbol{\varepsilon}_2-\boldsymbol{\varepsilon}_3)^2+(\boldsymbol{\varepsilon}_3-\boldsymbol{\varepsilon}_1)^2} \end{aligned} \tag{9.31}$$

For the considered calculation steps, the stresses of the corresponding time period are assumed to be constant. Equation (9.30) is solved for node 25 (see Fig. 9.36) of the axisymmetric finite element model.

#### Results

The effective stress value $\sigma_{\text{eff}}$ at node 25 for the given time period is 5.03 MPa, which was calculated using (9.32). The strain at the end of the first time step is $\varepsilon_{\text{eff}}(t_1) = 1.72 \times 10^{-3}$, and at the end of the second time step: $\varepsilon_{\text{eff}}(t_2) = 1.73 \times 10^{-3}$, which again, is calculated using (9.32). Considering (9.30) the analytically obtained value of the parameter $A$ is equal to 0.19, which corresponds

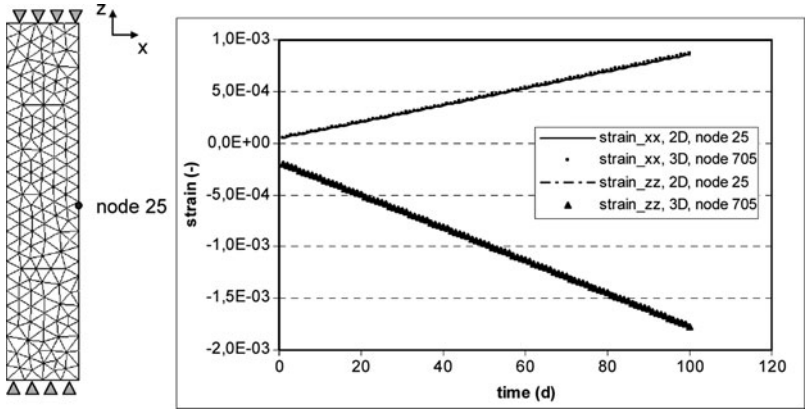


Figure 9.36: Comparison of numerical strain results ($x$- and $z$-directions) for the axisymmetric and the three-dimensional models

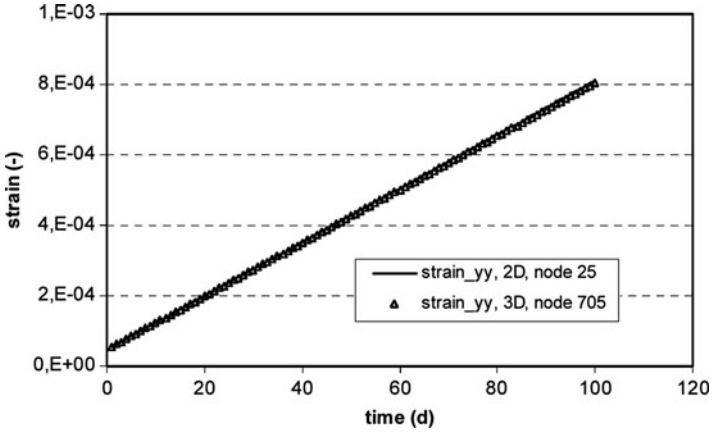


Figure 9.37: Comparison of numerical strain results ($y$-direction) for the axisymmetric and the three-dimensional models

approximately to the input value of $A$ of 0.18 defined in the previous example. The results of the comparison between the axisymmetric model and the three-dimensional model are shown in Figs. 9.36 and 9.37. These results are identical.

### 9.3.4 Transient Creep in Rock Salt

**Definition**

Triaxial long-term compression under axisymmetric conditions is carried out to verify the Lubby2 creep model (9.20) and to study transient as well as

stationary creep behavior, assuming isothermal conditions and neglecting damage processes.

### Solution

As described in Sect. 9.1.6, for the calculation, the cross-section of a cylindrical sample with a radius of 30 mm and a height of 120 mm is studied. The loading in principal axes includes a radial pressure as well as an axial pressure, and is realized in two steps. It is resulting in a homogeneous stress-strain state. Details of the model (geometry, mesh, boundary conditions) according to K.-H. Lux and F. Werunsky (unpublished report, 2008) are presented in Fig. 9.38.

Initial conditions do not have to be given for the problem under consideration. As the bottom edge is fixed in the vertical direction, the left-hand edge is fixed in the horizontal direction for symmetry reasons (axis of rotation). On the right-hand edge, initially a radial casing pressure of 5 MPa is applied within 60 seconds with a constant stress rate. While keeping constant this radial pressure, a subsequent stress-driven axial compressive loading is applied within the

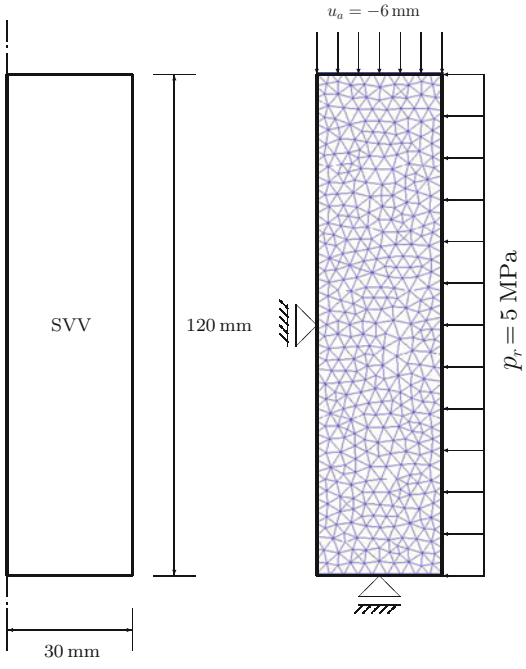


Figure 9.38: Triaxial compression of a cylindrical sample. Axisymmetric model. *Left*: Geometry. *Right*: Finite element grid and boundary conditions

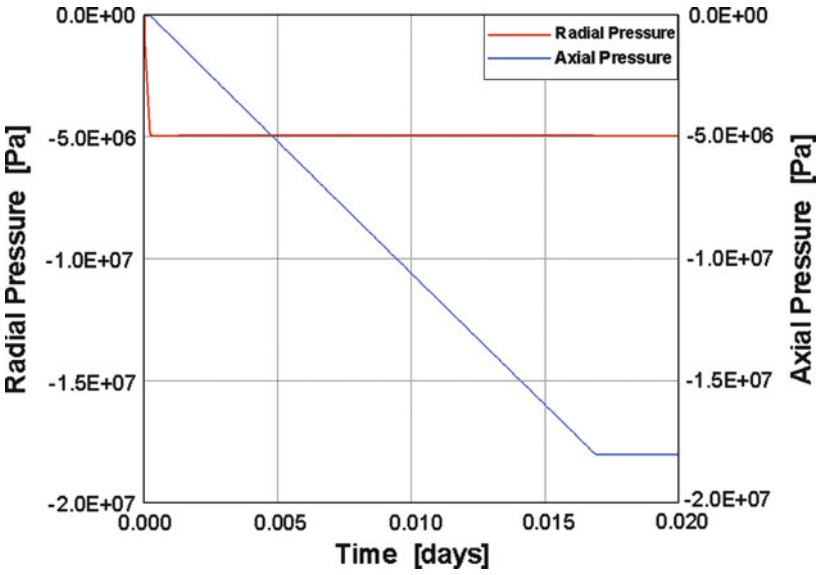


Figure 9.39: Triaxial compression of a cylindrical sample. Loading history for long-term creep experiments. Radial casing pressure (stress rate $\dot{p}_r = 0.083\,\mathrm{MPa{\cdot}s^{-1}}$) with subsequent axial pressure (stress rate $\dot{p}_a = 0.0125\,\mathrm{MPa{\cdot}s^{-1}}$). Each pressure loading with subsequent constant values over 20 days

following 1,440 seconds with a constant stress rate. The maximum axial pressure is 18 MPa. In the following, both the radial and the axial pressures are kept constant for 20 days (for the loading history cf. Fig. 9.39).

The modified Lubby1 model was considered to generate the fourth-order elastic material matrix for the creep model under consideration. Within this context, the material parameters referring to the modified Lubby1 relation (9.4) are given in Table 9.13. The material parameters for the creep fraction (Lubby2 (9.20)) are given in Table 9.14. Within this context, the initial Young's modulus, the Poisson's ratio and all the creep parameters are close to values known for rock salt according to K.-H. Lux, M. Rutenberg and F. Werunsky (unpublished report, 2008).

### Results

The representation of the axial stress vs. the axial strain in Fig. 9.40 shows the complex creep behavior of the sample under consideration.

Table 9.13: Material parameters for the elastic fraction of the material model (cf. Sect. 9.1.6)

| Symbol | Parameter | Value | Unit |
|---|---|---|---|
| $E_0$ | Initial Young's modulus | 21.4 | GPa |
| $\nu$ | Poisson's ratio | 0.335 | – |
| $a$ | Factor in (9.4) | 27500 | – |
| $n$ | Exponent in (9.4) | 1.0 | – |

Table 9.14: Material parameters for the creep fraction of the material model

| Symbol | Parameter | Value | Unit |
|---|---|---|---|
| $\bar{\eta}^*_m$ | Maxwell viscosity in (9.26) | $1.09 \times 10^7$ | MPa·d |
| $m$ | Factor in (9.26) | $-0.219$ | $\text{MPa}^{-1}$ |
| $l$ | Factor in (9.26) | 0.0 | $\text{K}^{-1}$ |
| $\bar{\eta}^*_k$ | Kelvin viscosity in (9.25) | $1.45 \times 10^5$ | MPa·d |
| $k_1$ | Factor in (9.24) | $-0.146$ | $\text{MPa}^{-1}$ |
| $k_2$ | Factor in (9.25) | $-0.121$ | $\text{MPa}^{-1}$ |
| $\bar{G}^*_k$ | Kelvin shear modulus in (9.24) | $7.0 \times 10^4$ | MPa |

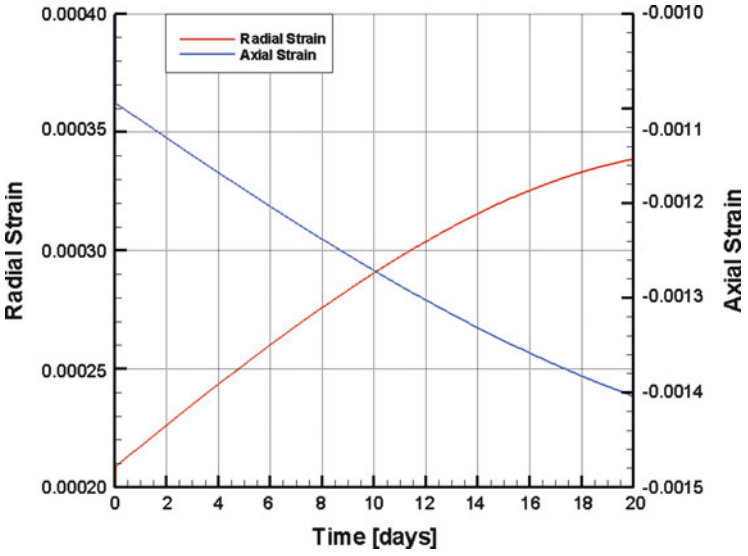


Figure 9.40: Triaxial compression of a cylindrical sample. Numerical simulation of the transient and stationary creep behavior using the Lubby2 model (9.20)

# Chapter 10

# Mass Transport

*by Sebastian Bauer, Christof Beyer, Chris McDermott, Georg Kosakowski, Stefanie Krug, Chan-Hee Park, Geraldine Pichot, Haibing Shao, Yuanyuan Sun, and Joshua Taron*

The mass transport in a homogeneous, saturated aquifer can be influenced by convection, diffusion, decay and biodegradation, sorption and chemical reactions. For a steady state one-dimensional flow through a homogeneous isotropic medium with constant material parameters, the following differential equation (10.1) is applied.

$$\frac{\partial C}{\partial t} + \frac{\rho_b}{R} \cdot \frac{\partial S}{\partial t} + \frac{q}{R} \cdot \frac{\partial C}{\partial x} = D_{xx} \cdot \frac{\partial^2 C}{\partial x^2} - \lambda \cdot C \tag{10.1}$$

with

$C$ – dissolved concentration ($\mathrm{kg \cdot m^{-3}}$),
$S$ – sorbed concentration($\mathrm{kg \cdot kg^{-1}}$),
$t$ – time (s),
$\rho_b$ – bulk density ($\mathrm{kg \cdot m^{-3}}$),
$R$ – retardation factor (-),
$q$ – flow rate ($\mathrm{m \cdot s^{-1}}$),
$x$ – distance (m),
$D_{xx}$ – dispersion coefficient in x-direction ($\mathrm{m^2 \cdot s^{-1}}$),
$\lambda$ – decay rate ($\mathrm{s^{-1}}$).

O. Kolditz et al. (eds.), *Thermo-Hydro-Mechanical-Chemical Processes in Fractured Porous Media*, Lecture Notes in Computational Science and Engineering 86,
DOI 10.1007/978-3-642-27177-9_10, 

This equation is used to calculate the concentration distribution under consideration of decay and sorption with the linear Henry-isotherm. The retardation coefficient $R$ for the Henry isotherm is related to the Henry sorption coefficient $K_D$ in the following way.

$$R = 1 + \frac{\rho_b}{\Phi} K_D = 1 + \frac{1-\Theta}{\Phi} \rho_s K_D \tag{10.2}$$

with

$\Phi$ – porosity (-),
$\rho_s$ – density (kg$\cdot m^{-3}$),

with the initial and boundary conditions

$$C(x, t=0) = C_I \quad \forall x$$

with $C_I$—concentration at time $I$.

$$C(x=0, t) = C_0 \quad \forall t, \qquad \frac{\partial C}{\partial x}(x \to \infty, t) = C_I \quad \forall t > 0$$

with $C_0$—initial concentration.

The following analytical solution is significant:

$$C = C_1 + (C_0 - C_1) \cdot \frac{1}{2} \left[ \exp\left( \frac{v \cdot x(1-\gamma)}{2 \cdot D_{xx}} \right) \cdot \operatorname{erfc}\left( \frac{x - v \cdot \gamma \cdot t/R}{2 \cdot \sqrt{D_{xx} \cdot t/R}} \right) + \exp\left( \frac{v \cdot x(1+\gamma)}{2 \cdot D_{xx}} \right) \cdot \operatorname{erfc}\left( \frac{x + v \cdot \gamma \cdot t/R}{2 \cdot \sqrt{D_{xx} \cdot t/R}} \right) \right] \tag{10.3}$$

with $v$—velocity

$$\gamma = \sqrt{1 + 4 \cdot \lambda \cdot R \cdot D_{xx}/v^2}\,. \tag{10.4}$$

Equation (10.3) is the basis for the verification of the numerical simulation results for the 1-dimensional mass transport. All described equations and all analytical solutions of equation (10.3) are taken from [144].

## 10.1 Diffusion

In both gaseous and aqueous systems, diffusion generates an orderly system; removing gradients of energy or mass concentration. Particles move from higher to lower concentrations via temperature dependent Brownian motion. In an aquifer, diffusive transport appears when convective transport is not particularly relevant (small velocities).

The extent of diffusion is also dependent on the diffusing substance and the medium. In addition, diffusion in soils is influenced by other factors, e.g. tortuosity. The finer a soil, the stronger the interacting forces between the soil matrix and the diffusing molecules. The diffusion coefficient which has to be given in OGS is the so-called apparent diffusion coefficient.

$$D_a = \frac{D_e}{\Phi} \tag{10.5}$$

with $D_e$—effective diffusion coefficient.

### 10.1.1 Axisymmetric Model

#### Definition

This diffusion model is built to reproduce a field study in clay. This in situ test consists of a borehole where a solution is circulated that contains tracer substances such as HTO. These tracers diffuse into the adjacent clay. The aim of the investigation is to simulate the HTO distribution after 300 days, the final test time, and to compare the simulation results of OGS to those that are calculated by HYDRUS 1 D (Simunek et al.) and PHAST (Parkhurst et al.).

To build a proper model of the tracer test, a one-dimensional axisymmetric model with 3.8 cm borehole radius and 21.2 cm horizontal distance in the clay soil is created. As initial conditions a constant pressure of 0 was specified in the whole model and the concentration relation $c/c_0$ of 1 within the distance of the borehole radius and of 0 within the clay domain. The pressure boundary condition corresponds to the initial condition. The calculation model includes 310 elements and 311 nodes. Table 10.1 shows the used parameters for the clay and the apparent diffusion constant $D_a$ of HTO. The calculation is performed for the test duration of 300 days with fitted time step lengths from 0.001 d to 1 d (Bahr, 2007). The porosity in the modelled borehole is assumed to be 1 in order to evoke the simulation of a tracer reservoir that supplies the tracer solution into the clay.

The aim of the presented calculation example is to evaluate the OGS simulation results by comparing them with numerical results of two other simulation programmes. The comparison is made using Hydrus 1 D, which is a one-dimensional

Table 10.1: Model parameters

| Symbol | Parameter | Value | Unit |
|---|---|---|---|
| $\rho$ | Density | 2.5 | $t \cdot m^{-3}$ |
| $\Phi$ | Porosity | 0.15 | – |
| $K$ | Permeability | $1.0{\cdot}10^{-11}$ | $m^2$ |
| $D_a$ | Diffusion coefficient | $3.6{\cdot}10^{-10}$ | $m^2{\cdot}s^{-1}$ |

transport model especially for the solute transport in soils. The second code, PHAST, is linked to the chemical software PHREEQC. The simulation with both programmes was made under consideration of the same boundary conditions and parameters (Bahr, 2007).

### Results

In Fig. 10.1 you can find the concentration distributions over the width of 0.25 m after a simulation time of 300 days, that were calculated by means of OGS, PHAST and Hydrus 1D (Bahr, 2007). The numerical results agree well with each other. Thus, the comparison shows that the diffusion process can be well reproduced by the use of an axisymmetric OGS model.

## 10.1.2 Anisotropy

### Definition

The aim of this example is to simulate the transport of a tracer by molecular diffusion in an anisotropic porous medium. The side length of the square numerical model is 1 m. At the left bottom corner of the model a constant concentration is diffusing into the calculation area. Diffusion is the only process for tracer transport; there are no pressure differences in the whole area. Because of the anisotropy of the soil material the tracer has to diffuse much faster in the x-direction than in the vertical direction. This has to be evaluated by comparing the concentration distributions in both directions.

As initial conditions the pressure and tracer concentrations were set to 0 in the whole area. At the left bottom corner of the model a concentration relation $c/c_0$ of 1 is specified along two polylines 0.3 m in length. The boundary

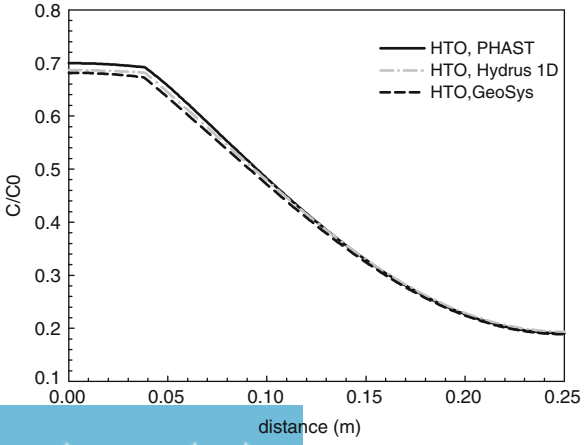


Figure 10.1: Concentration distributions after 300 days

conditions correspond to the initial conditions. The calculation model includes 736 triangular elements and 409 nodes. Table 10.2 shows the parameters used for the simulation. As the porous medium is assumed to be anisotropic, which influences diffusion, the value for tortuosity is set equal to 1 in the x-direction and 0.1 in the y-direction.

The calculation is made for 30 time steps with a length of $1{\cdot}10^7$ seconds. The calculation model is sketched in Fig. 10.2.

As the process of diffusion is dependent on the actual concentration in the porous medium and on the point in time, an analytical solution for the present calculation model is not possible. Therefore, the results of the OGS simulation are evaluated in a solely qualitative way by comparing the concentration distributions in horizontal and vertical directions.

### Results

In Fig. 10.3 you can find the concentration distributions over the model side length of 1 m in the x- and y-directions, respectively, after a simulation time of $1{\cdot}10^8$ seconds. Assuming a small tortuosity of 0.1, the component is not yet

Table 10.2: Model parameters

| Symbol | Parameter | Value | Unit |
|---|---|---|---|
| $\Phi$ | Porosity | 0.4 | – |
| $K$ | Permeability | $1.0{\cdot}10^{-15}$ | $m^2$ |
| $\rho$ | Density water | 1000 | $kg{\cdot}\ m^{-3}$ |
| $\eta$ | Viscosity water | 0.001 | $Pa{\cdot}\ s$ |
| $\alpha_T$ | Dispersion length | 10.0 | m |
| $D_a$ | Diffusion coefficient | $6.0{\cdot}10^{-10}$ | $m^2{\cdot}\ s^{-1}$ |

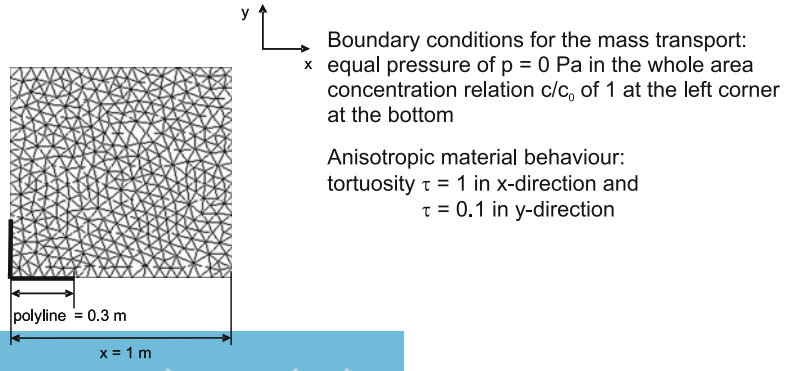


Figure 10.2: Benchmark definition

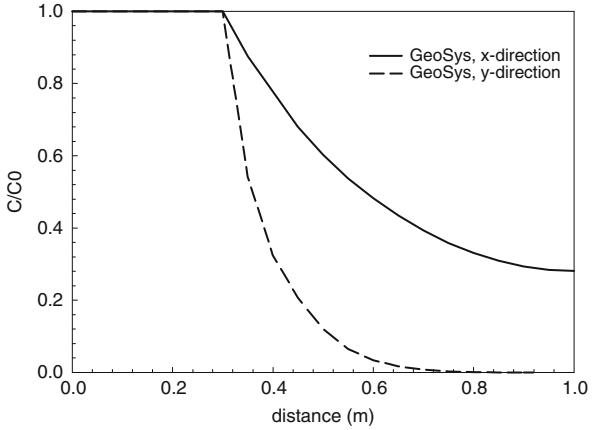


Figure 10.3: Concentration distributions in x- and y-direction

transported over the whole transport length of 1 m in the vertical direction, while in the horizontal direction the concentration relation equals approximately 0.3 at the opposite border of the model. Diffusion velocity depends on tortuosity. For anisotropic materials it can vary in different directions.

## 10.2 Decay

Radioactive decay is the change in the composition of a core by emitting particles and/or electro-magnetic radiation. Different kinds of radioactive decay are i.e. decay as a result of emission of negatrons or positrons and decay under emission of $\gamma$-rays.

$\alpha$-decay $\quad {}^{232}_{90}\mathrm{Th} \rightarrow {}^{228}_{88}\mathrm{Ra} + {}^{4}_{2}\mathrm{He}$

$\beta$-decay $\quad {}^{228}_{88}\mathrm{Ra} \rightarrow {}^{228}_{89}\mathrm{Ac} + {}^{0}_{-1}\mathrm{e}$

$\gamma$-decay $\quad {}^{236}_{92}\mathrm{U}^{\star} \rightarrow {}^{236}_{92}\mathrm{U} + \gamma$

The above given examples show that the radioactive decay is an irreversible process. The following differential equation describes the decay as a first order reaction (without chain development):

$$\frac{\partial C}{\partial t} = -\lambda \cdot C \tag{10.6}$$

with $\lambda$—decay rate ($\mathrm{s}^{-1}$).

The integration of this equation causes an exponential decay term in the following form.

$$C(t) = C_0 \cdot e^{-\lambda \cdot t} \tag{10.7}$$

with $C_0$—initial concentration (kg·m$^{-3}$).

The decay values are commonly expressed as the so-called half life ($t_{1/2}$). This is the point of time when half of the substance is degraded. The relation between the half-life $T$ and the decay rate results from:

$$e^{-\lambda \cdot t} = \frac{1}{2} \Rightarrow \lambda = \frac{\ln(2)}{T} \cong \frac{0.693}{T} \tag{10.8}$$

### 10.2.1 Definition

The aim of this example is to simulate mass transport with the influence of decay, but without any sorption. At the left side of the considered aquifer there is a volume source of 0.1 m$^3$/d, at the right side there is a constant water pressure of 20 kPa. The tracer substance in the source volume is distributed by a stationary flow in the homogeneous aquifer. The mass distribution after 100 days has to be calculated. Figure 10.4 shows a sketch of the calculation area.

The following simplifications are assumed: (1) no sorption, exclusively decay of components (2) homogeneous aquifer, saturated, stationary flow. For the 1-dimensional calculation, the calculation area is simplified as a line with the length of 100 m with 100 elements and 101 nodes. As boundary conditions the relative concentration amounts 1 and the source volume of the fluid phase with 0.1 m$^3$/d is given at the left border of the calculation area and a constant pressure of 20 kPa at the right boundary. The utilized parameters of the soil are listed in Table 10.3. The calculation is divided into 100 time steps with a constant time step length of 1 day. That means, the flow and transport processes in the aquifer within 100 days are simulated.

The concentration distribution at a special point in time and over a given distance is calculated by (10.3). Hereby the retardation coefficient is set equal to 1. The analytical solutions are depicted in Fig. 10.5 as single symbols.

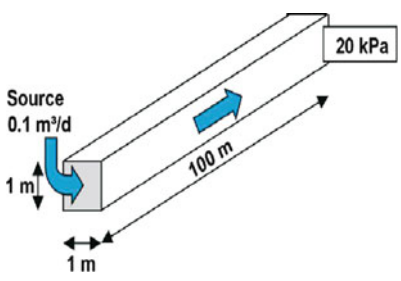


homogeneous aquifer

boundary conditions for the mass transport:
left boundary:
- constant source concentration
  $c/c_0 = 1$
- constant volume source
  $Q = 0.1$ m³/d

right boundary:
- constant pressure p = 20 kPa

simulation of 100 days in 100 timesteps

Figure 10.4: Calculation area: homogeneous aquifer

Table 10.3: Model parameters

| Symbol | Parameter | Value | Unit |
|---|---|---|---|
| $\Phi$ | Porosity | 0.2 | – |
| $K$ | Permeability | $1.0{\cdot}10^{-12}$ | $m^2$ |
| $\rho$ | Density water | 1000 | kg$\cdot$ $m^{-3}$ |
| $\eta$ | Viscosity water | 0.001 | Pa$\cdot$ s |
| $\alpha_L$ | Dispersion length | 5.0 | m |
| $\lambda$ | Decay in solved phase | $2.0{\cdot}10^{-7}$ | $s^{-2}$ |

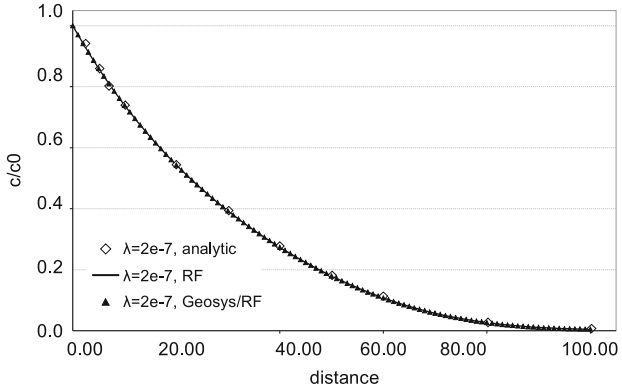


Figure 10.5: Concentration distribution after 100 days (decay)

### 10.2.2 Results

In Fig. 10.5 you can find the concentration distribution over the whole length of the one-dimensional model at the final simulation time of 100 days. It is clear that the numerical results agree well the analytical solutions.

## 10.3 Sorption

Exchange processes, like sorption, between the solid and the liquid phase in the multiphase system of an aquifer can be caused by physical (Van-der-Waals-forces) or chemical bonds. Sorption processes can be reversible (adsorption-desorption) if the chemical environment changes. When transport in a multiphase system is simulated, the mass exchange between the liquid and the solid phase has to be included. The equations that describe the sorption processes are called sorption isotherms. Sorption isotherms describe the relation between the substance that is adsorbed on the solid matrix and the one which is dissolved in the fluid phase. Those equations are only valid under isothermal conditions. The isotherms that

are listed below are based on the assumption that the adsorbed substance and the dissolved one are in a state of equilibrium.

$$\text{Henry}: \qquad S = K_D \cdot C \tag{10.9}$$

$$\text{Freundlich}: \qquad S = K_1 \cdot C^{K_2} \tag{10.10}$$

$$\text{Langmuir}: \qquad S = \frac{K_1 \cdot C}{1 + K_2 \cdot C} \tag{10.11}$$

with

$K_D,\ K_1,\ K_2$ —distribution coefficients,
$S$ —concentration of the adsorbed species (kg· kg$^{-1}$),
$C$ —concentration of the dissolved species (kg· m$^{-3}$).

The distribution coefficients are dependent on the substance and specific soil properties like pH. The linear Henry-isotherm is often used when there are low concentrations of chemical species. Non-linear sorption processes are reproduced by the Freundlich or the Langmuir isotherm. Then the retardation is dependent on the solute concentration. In addition, the use of the Langmuir isotherm assumes a constant amount of sorption space at the solid surface. A maximum concentration for the adsorbed substance on the solid matrix is exclusively considered by the Langmuir isotherm [144]. This maximum concentration $c_{\max}$ is included in the distribution coefficient $K_1$ ($K_1 = c_{\max} \cdot K_2$). The distribution coefficient $K_2$ of the Langmuir isotherm stands for the affinity between solid and sorbed solute. The distribution coefficients do not have comparable values: each sorption isotherm has to be considered separately with its specific constants.

### 10.3.1 Linear Sorption (Henry Isotherm)

The aim of this example is to simulate the solute transport in an aquifer by convection with the influence of retardation as a result of sorption. The solute transport is influenced by linear sorption processes. That means, the Henry-isotherm is relevant to calculate the solute concentration. The calculation area and boundary conditions are the same as described for the precedent example.

The following simplifications are assumed: (1) exclusively linear sorption (Henry isotherm), no decay of components (2) homogeneous aquifer, saturated, stationary flow (Fig. 10.4). The soil parameters are the same as listed in Table 10.3, but decay is not considered during these simulation runs. For the different simulation runs, the Henry-sorption coefficients are varied as listed in Table 10.4 in order to evaluate the influence of sorption on the mass transport. The retardation coefficients $R$ are calculated by solving (10.2).

Table 10.4: Variation of $K_D$-values and retardation coefficients as input variables

| $K_D$ value [$m^3 \cdot kg^{-1}$] | Retardation coefficient [-] |
|---|---|
| 0 | 1 |
| $6.8 \cdot 10^{-6}$ | 1.05 |
| $6.8 \cdot 10^{-5}$ | 1.54 |
| $6.8 \cdot 10^{-4}$ | 6.44 |

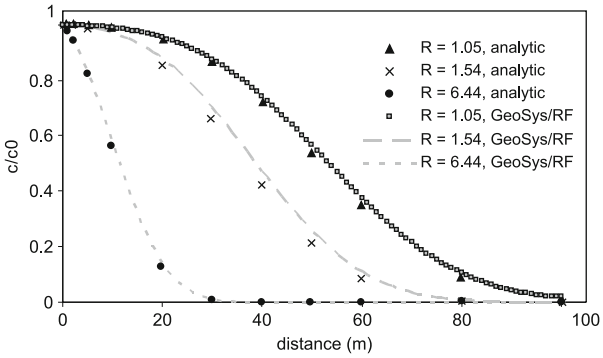


Figure 10.6: Concentration distribution after 100 days (Henry sorption)

**Results**

The concentration distribution at a special point in time and over a given distance is calculated by (10.3). Hereby the decay term $\gamma$ is set equal to 1. The analytical solutions are depicted in Fig. 10.6 as single symbols. In Fig. 10.6 you can find the concentration distribution over the whole length of the one-dimensional model at the final simulation time of 100 days. It is clear that the numerical results agree well the analytical solutions.

### 10.3.2 Non-linear Sorption (Freundlich Isotherm)

**Definition**

The non-linear Freundlich isotherm is often used to describe real sorption processes. Therefore, in this example the transport process, by including the Freundlich isotherm, is calculated in the same way as in the precedent example (same model and boundary conditions). As there exists no opportunity to calculate analytically the solute transport with non-linear sorption, the results of the simulation have to be compared with solutions of the transport equation with linear sorption in order to evaluate the simulation results.

The following simplifications are assumed: (1) non-linear sorption (Freundlich isotherm), no decay of components (2) homogeneous aquifer, saturated, stationary flow (Fig. 10.4).

The soil parameters are the same as listed in Table 10.3 (except decay). For the different simulation runs the Freundlich-sorption coefficients ($K_1$) are varied in the same way as the $K_D$-values that are listed in Table 10.1. The exponent $K_2$ was constant with a value of 1.

The dependence of sorbed molecules on the amount of molecules in dilution is given by equation (10.11). The concentration distribution at a special point in time and over a given distance cannot be calculated analytically by (10.3) when a non-linear sorption process is assumed. A possible way to test the correctness of the simulation results for transport with Freundlich sorption, is to choose values of distribution coefficients that create a concentration distribution which is approximately linear and must therefore be almost equal to the results of transport by use of the Henry isotherm.

### Results

As the values for the Freundlich coefficients were chosen in a way that concentration distribution between sorbed and solute concentrations is almost linear, the results of the simulation runs have to be equal to the results that are obtained by using the linear Henry isotherm. In Fig. 10.7 the concentration distribution of the solute over the model length of 100 m is shown. As the concentrations of the transport simulation by using the Freundlich isotherm match those of the simulation runs with linear sorption, these results for non-linear sorption are reasonable. Additionally, the values for the constant $K_2$ were

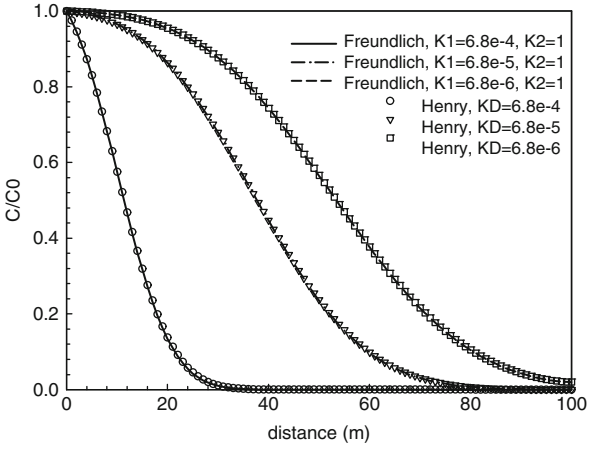


Figure 10.7: Concentration distribution after 100 days (Freundlich compared to Henry sorption)

changed to 0.8 in order to prove a difference between linear and non-linear sorption. The results of the comparison are shown in Fig. 10.8. These numerical results show the effect of the application of a non-linear sorption isotherm: the higher the influence of sorption (large value of sorption coefficient $K_D$ resp. $K_1$) the higher the difference of solute concentration values between non-linear and linear sorption. However, the results for both isotherms were not evaluated quantitatively.

### 10.3.3 Non-linear Sorption (Langmuir Isotherm)

#### Problem Definition

The non-linear Langmuir isotherm is used to describe sorption processes that are restricted by a maximum concentration of sorbed molecules. In this example the transport process, by including the Langmuir isotherm, is calculated in the same way as the precedent examples for mass transport. As there exists no opportunity to calculate analytically the solute transport with non-linear sorption, the results of the simulation have to be compared with solutions of the transport equation with linear sorption in order to evaluate the simulation results.

The following simplifications are assumed: (1) non-linear sorption (Langmuir isotherm), no decay of components (2) homogeneous aquifer, saturated, stationary flow (Fig. 10.4). The soil parameters are the same as listed in Table 10.3 (except decay). In order to create a Langmuir equation which has almost the same linear characteristic as the Henry equation, the Langmuir sorption coefficients, $K_1$, were varied in the same way as the Henry coefficients ($K_D$ values

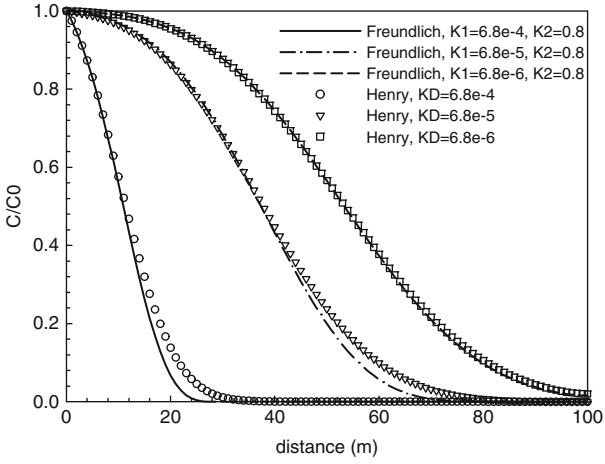


Figure 10.8: Different concentration distributions after 100 days (Freundlich compared to Henry sorption)

in Table 10.4) for the different simulation runs. The $K_2$ coefficients stand for the affinity between solid and sorbed solute. Thus, the $K_2$ value cannot be set equal to 0, because this would cause a transport without any sorption. When $K_2$ equals 1, there is no effect on the binding affinity. Therefore, the coefficient $K_2$ was set constant with a value of 1 in order to approximate the linear characteristic of the Henry equation (10.10).

The dependence of sorbed molecules on the amount of molecules in dilution is given by (10.11). The concentration distribution at a special point in time and over a given distance cannot be calculated analytically by (10.3) when a non-linear sorption process is assumed. Therefore, the simulation results are compared with the results for the mass transport by using the linear Henry isotherm. The non-linear Langmuir isotherm was forced to be almost linear in the way described above. Now the results of the transport, by using the Langmuir isotherm, can be compared with the results that were obtained by the transport simulation with the linear Henry isotherm.

### Results

In Fig. 10.9 the concentration distributions over the whole model length by using the linear Henry isotherm and the non-linear Langmuir isotherm are depicted. Obviously, the results for each specified distribution constant are almost equal. This result is correct, because it was provoked by the choice of the sorption coefficients.

In order to show that the results when using the Langmuir isotherm are actually different to those when using the Henry isotherm, the $K_2$ values were changed

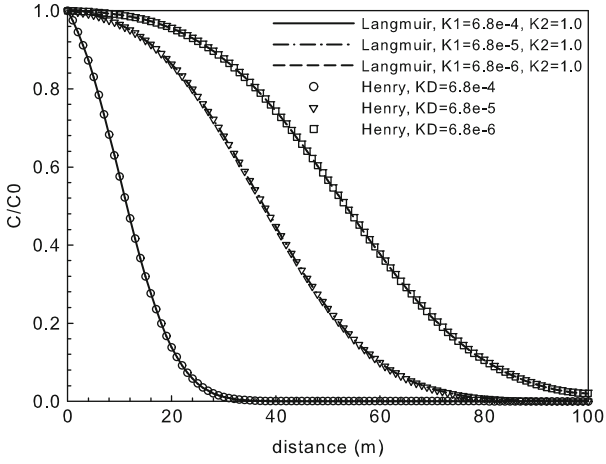


Figure 10.9: Concentration distribution after 100 days (Langmuir compared to Henry sorption)

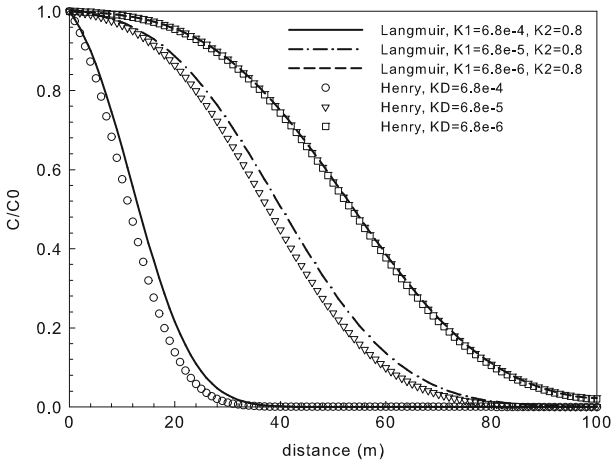


Figure 10.10: Different concentration distributions after 100 days (Langmuir compared to Henry sorption)

to a value of 0.8, so that the Langmuir isotherm received a real non-linear gradient. As the results show (Fig. 10.10), the differences between the concentration distributions are evident.

## 10.4 Sorption and Decay

### 10.4.1 Single Component

#### Definition

The aim of this example is to simulate solute transport in an aquifer by convection with the influence of retardation as a result of sorption. Additionally, the transported mass will be degraded. The calculation area and boundary conditions are the same as described in Sect. 10.2.

The following simplifications are assumed: (1) linear sorption, decay of components (2) homogeneous aquifer, saturated, stationary flow (Fig. 10.4). The soil parameters are the same as listed in Table 10.3. The decay rate $\lambda$ is $2{\cdot}10^{-7}$ $s^{-1}$. For the different simulation runs, the Henry sorption coefficients are varied as listed in Table 10.4, in order to again evaluate the influence of sorption on mass transport. The concentration distribution at a special point in time and over a given distance is calculated by (10.3). The analytical solutions are depicted in Fig. 10.11 as single symbols.

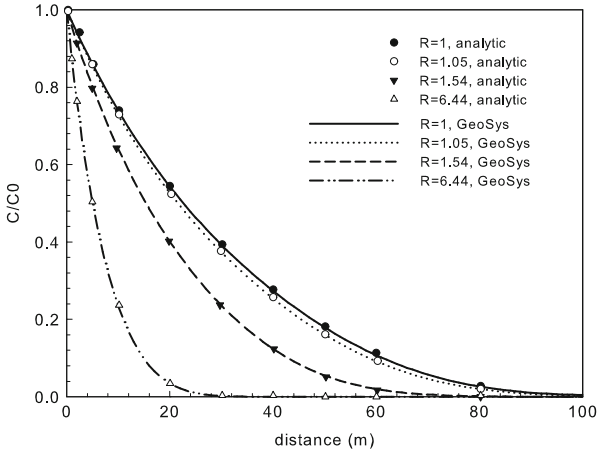


Figure 10.11: Concentration distributions after 100 days (sorption and decay)

**Results**

The influence of radioactive decay on the transport process can be recognized at the typical declining exponential curves in Fig. 10.11. According to the different sorption coefficients, the transport is retarded. Obviously, the numerical results (lines) agree well with the analytical solutions. Therefore, it can be summarized that the transport, under the combined consideration of both decay and sorption, can be reproduced by the OGS simulation.

## 10.4.2 Multi Components

**Definition**

The aim of this example is to simulate the transport of several components with different sorption behaviour and decay. The calculation area and boundary conditions are the same as described for the precedent example. The mass distribution after 100 days has to be calculated.

The following simplifications are assumed (Fig. 10.4):

Component 1: no sorption, no decay
Component 2: decay
Component 3: linear sorption
Component 4: linear sorption, decay
Aquifer: homogeneous, saturated, stationary flow

The soil parameters are the same as listed in Table 10.3. The decay rate $\lambda$ for components 2 and 4 is $2{\cdot}10^{-7}$ $s^{-1}$, the Henry sorption coefficient $K_D$ for

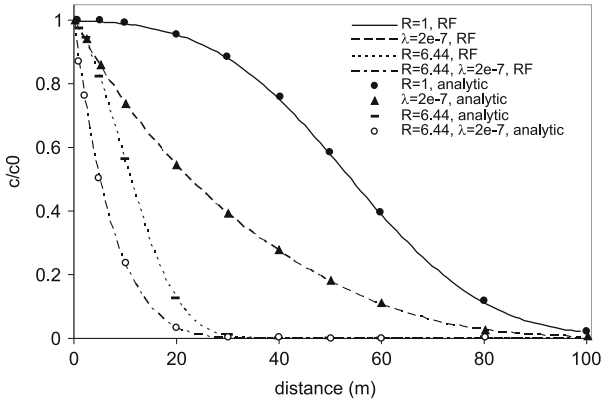


Figure 10.12: Concentration distributions of the four components after 100 days

component 3 is $6.4{\cdot}10^{-4}$ $m^3 \cdot kg^{-1}$ (R = 6.44). The concentration distribution at a special point in time and over a given distance is calculated by equation (2.44). The analytical solutions are depicted in Fig. 10.12 as single symbols.

**Results**

In Fig. 10.12 you can find the concentration distribution of the 4 different components over the whole length of the one-dimensional model at the final simulation time of 100 days. As the comparison of each single component with the analytical results of the "one-component-transport" shows, the numerical results for the multi component transport are reasonable.

## 10.5 Matrix Diffusion

### 10.5.1 Definition

This benchmark is introduced to verify the matrix diffusion function. It simulates advective -dispersive transport of a solute in a one-dimensional fracture with constant aperture, with and without the effect of matrix-diffusion. The geometry and the material parameters are chosen to fit the parameters extracted from experiments conducted during the Colloid Radionuclide Retardation Experiment at Nagra's Grimsel test site [145]. The results from OGS are compared with that from PICNIC, and they fit well.

The geometry and material parameters in PICNIC and OGS are summarized in Table 10.5 and the conceptual model is shown in Fig. 10.13. PICNIC solves the one-dimensional problem, whereas in OGS a two-dimensional discretization was chosen. A rectangular domain of 5.2m × 0.5m was discretized with 1,155

Table 10.5: Geometry and material properties for the simulations

| Symbol | Parameter | Value | Unit |
|---|---|---|---|
| $L$ | Distance between boundary and observation points | 2.5 | m |
| $\alpha_T$ | Transverse dispersion (OGS only) | – | m |
| $\rho$ | Bulk matrix density | $2,670$ | $\mathrm{kg \cdot m^{-3}}$ |
| $2b$ | Fracture aperture | $0.55 \times 10^{-3}$ | m |
| $v$ | Fluid velocity | $7.05 \times 10^{-4}$ | m/s |
| $\alpha_L$ | Longitudinal dispersion (OGS only) | 0.1 | m |
| $Pe$ | Peclet number (PICNIC only) | 25 | – |
| $\varepsilon_p$ | Matrix porosity | 0.3 | – |
| $D_p$ | Diffusion constant in rock matrix | $7.4 \times 10^{-11}$ | $\mathrm{m^2 \cdot s^{-1}}$ |

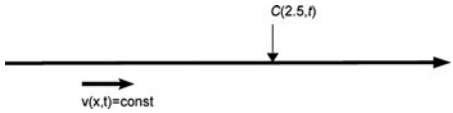


Figure 10.13: Conceptual setup of the 1D problem

nodes and 2,080 triangular elements. One of the shorter domain edges was chosen as an inflow boundary and fluid was injected at the boundary-nodes in such a way that the resulting fluid velocity exactly matches the value from Table 10.5. The concentration is fixed at the inflow boundary. In 2.5m distance the breakthrough curve is recorded. The outflow boundary is assumed to be far away and should not influence the observed breakthrough curve. Picnic V2.2 and OGS (Rev. 1535).

As defining exactly the same transport boundary conditions in OGS and PICNIC is not possible, the following procedure was used to get the inflow boundary condition as similar as possible:

1. The system was calculated for injecting a pulse of solute with a constant flux for a time length of 50s with PICNIC. The concentration vs. time was recorded for the inflow-leg.

2. The concentrations vs. time extracted from PICNIC's inflow-leg was applied (fixed) to the inflow boundary of the OGS system.

These procedures work as long as advective fluxes are much higher than the dispersive-diffusive fluxes over the boundary. The outflow boundary condition is set to infinity, i.e. a semi-infinite problem is calculated. In OGS the domain is set to 5m, double the distance between the inflow boundary and observation

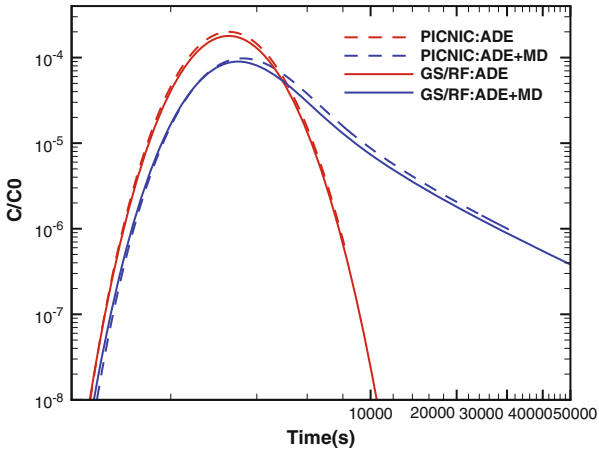


Figure 10.14: Breakthrough of the ADE and the ADE+MD solutions calculated with PICNIC and OGS

point. This prevents the outflow boundary condition from influencing the tracer breakthrough at the observation point.

### 10.5.2 Results

For the investigated two cases, advection and dispersion (ADE) only and ADE plus matrix diffusion(MD), the PICNIC and OGS solutions are, in general, very similar (see Fig. 10.14).

## 10.6 Particle Tracking

The classical advection-dispersion equation of a conservative solute in porous media can be written as [146]

$$\frac{\partial C}{\partial t} = -\nabla \cdot (\boldsymbol{v} C) + \nabla \cdot (\boldsymbol{D} \nabla C) \tag{10.12}$$

where $C$ is the concentration ($\mathrm{kg{\cdot}m^{-3}}$), $\boldsymbol{v}$ is the pore velocity vector ($\mathrm{kg{\cdot}m^{-1}}$) and $\boldsymbol{D}$ is the hydrodynamic dispersion tensor ($\mathrm{m^2{\cdot}s^{-1}}$), t is time ($s$) and $\nabla$is the differential operator.

The random walk particle tracking (RWPT) method is issued from stochastic physics. The stochastic differential equation is [147]

$$\mathbf{x}(t_i) = \mathbf{x}(t_{i-1}) + \mathbf{v}(\mathbf{x}(t_{i-1}))\Delta t + Z\sqrt{2\mathbf{D}(\mathbf{x}(t_{i-1}))\Delta t} \tag{10.13}$$

where $\mathbf{x}$ is the coordinates of the particle location, $\Delta t$ is the time step, and $Z$ is a random number whose mean is zero and variance is unity.

It has been shown that this equation is equivalent to an equation that is slightly different from the advection-dispersion equation (10.12). To be equivalent to equation (10.12), the modified velocity [148] is expressed as

$$\mathbf{v}_i^* = \mathbf{v}_i + \sum_{j=1}^{3} \frac{\partial \mathbf{D}_{ij}}{\partial x_j} \tag{10.14}$$

with dispersion tensor [146]

$$\mathbf{D}_{ij} = \alpha_T |\boldsymbol{v}| \delta_{ij} + (\alpha_L - \alpha_T) \frac{\mathbf{v}_i \mathbf{v}_j}{|\boldsymbol{v}|} + \mathbf{D}_{ii}^d \tag{10.15}$$

where $\delta_{ij}$ is the Kronecker symbol, $\alpha_L$ is the longitudinal dispersion length, $\alpha_T$ is the transverse dispersion length, $D_{ij}^d$ is the tensor of molecular diffusion coefficient and $\mathbf{v}_i$ is the component of the mean pore velocity in the $i$th direction.

The equivalent stochastic differential equation to (10.12) in three-dimensional problems can be written as [149–151]

$$\begin{aligned}
x_{t+\Delta t} &= x_t + \left(\mathbf{v}_x(x_t, y_t, z_t, t) + \tfrac{\partial D_{xx}}{\partial x} + \tfrac{\partial D_{xy}}{\partial y} + \tfrac{\partial D_{xz}}{\partial z}\right)\Delta t \\
&\quad + \sqrt{2D_{xx}\Delta t} Z_1 + \sqrt{2D_{xy}\Delta t} Z_2 + \sqrt{2D_{xz}\Delta t} Z_3 \\
y_{t+\Delta t} &= y_t + \left(\mathbf{v}_y(x_t, y_t, z_t, t) + \tfrac{\partial D_{yx}}{\partial x} + \tfrac{\partial D_{yy}}{\partial y} + \tfrac{\partial D_{yz}}{\partial z}\right)\Delta t \\
&\quad + \sqrt{2D_{yx}\Delta t} Z_1 + \sqrt{2D_{yy}\Delta t} Z_2 + \sqrt{2D_{yz}\Delta t} Z_3 \\
z_{t+\Delta t} &= z_t + \left(\mathbf{v}_z(x_t, y_t, z_t, t) + \tfrac{\partial D_{zx}}{\partial x} + \tfrac{\partial D_{zy}}{\partial y} + \tfrac{\partial D_{zz}}{\partial z}\right)\Delta t \\
&\quad + \sqrt{2D_{zx}\Delta t} Z_1 + \sqrt{2D_{zy}\Delta t} Z_2 + \sqrt{2D_{zz}\Delta t} Z_3
\end{aligned} \tag{10.16}$$

where $Z_i$ is a random number whose mean is zero and variance is unity.

Together with (10.15), the spatial derivatives of the dispersion coefficients can be expressed as a function of the derivatives of velocity. Note that to obtain the derivatives of velocity, velocity has to be continuous mathematically. To this end, we interpolate velocity at any location in an element from the known velocity at the element nodes.

Since the proposed RWPT method makes use of the FEM for velocity estimation, the derivative of velocity within each element is computed as in Fig. 10.15 and written as

$$\begin{aligned}
&\frac{\partial \mathbf{v}_x}{\partial x} = \frac{\mathbf{v}(x_R) - \mathbf{v}(x_L)}{l_x}; \quad \frac{\partial \mathbf{v}_y}{\partial y} = \frac{\mathbf{v}(y_U) - \mathbf{v}(y_D)}{l_y}; \quad \frac{\partial \mathbf{v}_z}{\partial z} = \frac{\mathbf{v}(z_N) - \mathbf{v}(z_S)}{l_z} \\
&\frac{\partial \mathbf{v}_x}{\partial y} = \frac{\partial \mathbf{v}_x}{\partial z} = \frac{\partial \mathbf{v}_y}{\partial z} = \frac{\partial \mathbf{v}_y}{\partial x} = \frac{\partial \mathbf{v}_z}{\partial x} = \frac{\partial \mathbf{v}_z}{\partial y} \simeq 0
\end{aligned} \tag{10.17}$$

where $x_L$ and $x_R$ are intersection points of the element edges with a line parallel to the global $x$ axis at which velocities are $\mathbf{v}(x_L)$ and $\mathbf{v}(x_R)$, $y_D$ and $y_U$ are intersection points of the element edges from down to up with a line parallel to the global $y$ axis at which velocities are $\mathbf{v}(y_D)$ and $\mathbf{v}(y_U)$, $z_S$ and $z_N$ are the

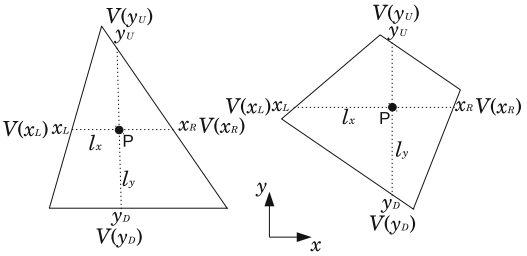


Figure 10.15: Spatial derivatives of velocity for a particle in triangular and quadrilateral elements (V is velocity)

intersection points of the element edges from south to north with a line parallel to the global $z$ axis at which velocities are $\mathbf{v}(z_S)$ and $\mathbf{v}(z_N)$, and $l_x$, $l_y$, and $l_z$ are the length of each intersection line, respectively.

Thus, the derivatives of the dispersion coefficients are as follows [152]

$$
\begin{aligned}
\frac{\partial D_{xx}}{\partial x} &= \mathbf{v}_x \frac{\partial \mathbf{v}_x}{\partial x}\left[\alpha_L\left(\frac{2}{\mathbf{v}} - \frac{\mathbf{v}_x^2}{\mathbf{v}^3}\right) - \alpha_T \frac{\mathbf{v}_y^2+\mathbf{v}_z^2}{\mathbf{v}^3}\right] \\
\frac{\partial D_{xy}}{\partial y} &= (\alpha_L - \alpha_T)\left[\frac{\partial \mathbf{v}_y}{\partial y}\frac{\mathbf{v}_x}{\mathbf{v}} - \frac{\mathbf{v}_x \mathbf{v}_y^2}{\mathbf{v}^3}\frac{\partial \mathbf{v}_y}{\partial y}\right] \\
\frac{\partial D_{xz}}{\partial z} &= (\alpha_L - \alpha_T)\left[\frac{\partial \mathbf{v}_z}{\partial z}\frac{\mathbf{v}_x}{\mathbf{v}} - \frac{\mathbf{v}_x \mathbf{v}_z^2}{\mathbf{v}^3}\frac{\partial \mathbf{v}_z}{\partial z}\right] \\
\frac{\partial D_{yy}}{\partial y} &= \mathbf{v}_y \frac{\partial \mathbf{v}_y}{\partial y}\left[\alpha_L\left(\frac{2}{\mathbf{v}} - \frac{\mathbf{v}_y^2}{\mathbf{v}^3}\right) - \alpha_T \frac{\mathbf{v}_x^2+\mathbf{v}_z^2}{\mathbf{v}^3}\right] \\
\frac{\partial D_{yx}}{\partial x} &= (\alpha_L - \alpha_T)\left[\frac{\partial \mathbf{v}_x}{\partial x}\frac{\mathbf{v}_y}{\mathbf{v}} - \frac{\mathbf{v}_y \mathbf{v}_x^2}{\mathbf{v}^3}\frac{\partial \mathbf{v}_x}{\partial x}\right] \\
\frac{\partial D_{yz}}{\partial z} &= (\alpha_L - \alpha_T)\left[\frac{\partial \mathbf{v}_z}{\partial z}\frac{\mathbf{v}_y}{\mathbf{v}} - \frac{\mathbf{v}_y \mathbf{v}_z^2}{\mathbf{v}^3}\frac{\partial \mathbf{v}_z}{\partial z}\right] \\
\frac{\partial D_{zz}}{\partial z} &= \mathbf{v}_z \frac{\partial \mathbf{v}_z}{\partial z}\left[\alpha_L\left(\frac{2}{\mathbf{v}} - \frac{\mathbf{v}_z^2}{\mathbf{v}^3}\right) - \alpha_T \frac{\mathbf{v}_x^2+\mathbf{v}_y^2}{\mathbf{v}^3}\right] \\
\frac{\partial D_{zx}}{\partial x} &= (\alpha_L - \alpha_T)\left[\frac{\partial \mathbf{v}_x}{\partial x}\frac{\mathbf{v}_z}{\mathbf{v}} - \frac{\mathbf{v}_z \mathbf{v}_x^2}{\mathbf{v}^3}\frac{\partial \mathbf{v}_x}{\partial x}\right] \\
\frac{\partial D_{zy}}{\partial y} &= (\alpha_L - \alpha_T)\left[\frac{\partial \mathbf{v}_y}{\partial y}\frac{\mathbf{v}_z}{\mathbf{v}} - \frac{\mathbf{v}_z \mathbf{v}_y^2}{\mathbf{v}^3}\frac{\partial \mathbf{v}_y}{\partial y}\right]
\end{aligned}
\tag{10.18}
$$

Because velocity is not derivable at the interface of two adjacent elements in a nonuniform flow, computing dispersion coefficient derivatives by using a finite element approach would yield erroneous values [152]. To prevent these errors, a particle is coded to have information of an element index and the velocity estimation is continuous even at the elemental boundaries in this method. Thus, the derivatives of dispersion coefficients will be computed accordingly. This is an improved approach from the work by Hoteit et al. [152].

### 10.6.1 Particle Tracking in Porous Medium: 1D Case Study

#### Definition

A one-dimensional homogenous aquifer is chosen to simulate a soil column experiment conducted by Harter et al. [153]. In the experiment, a constant flow rate was established, 2.5 pore volumes NaCl—tap water solution and 2.5 pore volumes *Cryptosporidium parvum* solution ($1 \times 10^5$ oocysts per mL) were injected respectively, the outflow was continuously collected. Figure 10.16 shows the schematic description of the experiment.

NaCl—tap water solution is used as a tracer, which experiences only advection and dispersion. The *Cryptosporidium parvum* can be classified as a biological colloid. Colloids moving in porous media experience advection, dispersion, sorption-desorption, and filtration.

#### Analytical Solution

For the one-dimensional transport including sorption-desorption and filtration through a homogeneous medium the following differential equation is applied

$$\frac{\partial C}{\partial t} + \frac{\rho_b}{n}\frac{\partial C_S}{\partial t} = v\alpha_L \frac{\partial^2 C}{\partial x^2} - v\left(\frac{\partial C}{\partial x} + \lambda C\right) \tag{10.19}$$

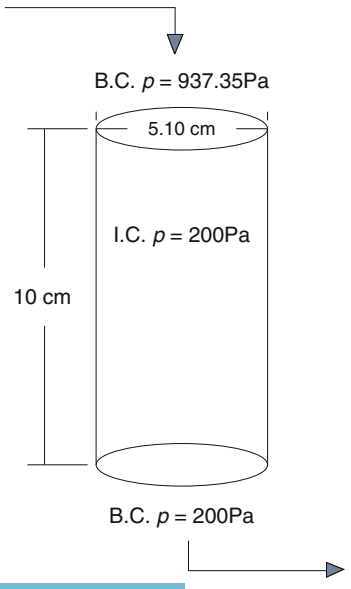


Figure 10.16: Soil column experiment

where $C$ is dissolved concentration ($kg{\cdot}m^{-3}$), $C_S$ is sorbed concentration ($kg{\cdot}kg^{-1}$), $t$ is time (s), $\rho_b$ is bulk density ($kg{\cdot}m^{-3}$), $n$ is porosity (-), $v$ is velocity ($m{\cdot}s^{-1}$), $\alpha_L$ is longitudinal dispertivity (m), $x$ is distance (m) and $\lambda$ is filtration coefficient ($m^{-1}$).

The instantaneous, linear sorption model assumes that

$$C_S = K_d C \tag{10.20}$$

where $K_d$ is the partitioning coefficient ($m^3 \cdot kg^{-1}$). The retardation coefficient $R$ is

$$R = 1 + \frac{\rho_b}{n} K_d \tag{10.21}$$

The dispersion coefficient in the $x$-direction $D_{xx}$ ($m^2 \cdot s^{-1}$) is

$$D_{xx} = v\alpha_L \tag{10.22}$$

The analytical solution for a pulse input (inject time from 0 to $\tau$) is:

$$\begin{aligned} C = \ & \tfrac{1}{2}C_0 \Bigg[ \exp\left(\frac{vx(1-\gamma)}{2D_{xx}}\right) \operatorname{erfc}\left(\frac{x - v\gamma t/R}{2\sqrt{D_{xx}t/R}}\right) \\ & + \exp\left(\frac{vx(1+\gamma)}{2D_{xx}}\right) \operatorname{erfc}\left(\frac{x + v\gamma t/R}{2\sqrt{D_{xx}t/R}}\right) \Bigg] \end{aligned} \tag{10.23}$$

for $t \in (0, \tau)$ ,

$$\begin{aligned} C = \ & \tfrac{1}{2}C_0 \Bigg[ \exp\left(\frac{vx(1-\gamma)}{2D_{xx}}\right) \operatorname{erfc}\left(\frac{x - v\gamma t/R}{2\sqrt{D_{xx}t/R}}\right) \\ & + \exp\left(\frac{vx(1+\gamma)}{2D_{xx}}\right) \operatorname{erfc}\left(\frac{x + v\gamma t/R}{2\sqrt{D_{xx}t/R}}\right) \\ & - \exp\left(\frac{vx(1-\gamma)}{2D_{xx}}\right) \operatorname{erfc}\left(\frac{x - v\gamma (t-\tau)/R}{2\sqrt{D_{xx}(t-\tau)/R}}\right) \\ & - \exp\left(\frac{vx(1+\gamma)}{2D_{xx}}\right) \operatorname{erfc}\left(\frac{x + v\gamma (t-\tau)/R}{2\sqrt{D_{xx}(t-\tau)/R}}\right) \Bigg] \end{aligned} \tag{10.24}$$

for $t \in (\tau, \infty)$ , where

$$\gamma = \sqrt{1 + 4v\lambda R D_{xx}/v^2} \tag{10.25}$$

**Numerical Solution**

The calculation area is simplified to a line with the length of 0.1m. For the numerical model 100 elements and 101 nodes are included. Head gradient is set

by giving two constant pressures at both left and right boundaries to establish a uniform velocity field with the value of 7.1 $\mathrm{md}^{-1}$.

The pore volume ($x$-axis) is calculated by

$$P_V = \frac{vt}{L} \tag{10.26}$$

where $v$ is the seepage velocity, $L$ is the length of the soil column. Considering the Courant number, the time step size is set by assigning $P_V$ to 0.01. In the simulation, 100 particles per time steps are loaded near the left boundary for 250 time steps.

The filtration process is described by using the filtration coefficient. The sorption-desorption process is described by the two-rate model from Johnson et al. [154]. In the two-rate model, desorption is governed by two different rate coefficients

$$N/N_0 = Ae^{-k_1 t} + (1 - A)e^{-k_2 t} \tag{10.27}$$

where $N$ is the number of particles remaining on the medium at time $t$, $N_0$ is the initial number of particles on the medium at the time of initial sorption, $A$ is a weighting factor and $k_1$ and $k_2$ are the fast and slow sorption rate coefficient, respectively. Relevant parameters are listed in Table 10.6.

**Results**

The tracer experiences only advection and dispersion, which means in (10.19), $C_S = 0$, $\lambda = 0$. The results of RWPT simulation for the distribution of concentration over time are compared to those of measured value from the experiment by Harter, the analytical solution and the OGS simulation with the mass transport method. The comparison results are shown in Fig. 10.17.

Table 10.6: Model parameters for the column experiment

| Symbol | Parameter | Value | Unit |
|---|---|---|---|
| $k$ | Permeability | $1.114476^{-11}$ | $\mathrm{m}^2$ |
| $\alpha_L$ | Longitudinal dispersivity | 0.005 | m |
| $n$ | Porosity(tracer) | 0.5 | – |
| $n$ | Porosity(colloid) | 0.42 | – |
| $A$ | Weighting factor | 0.9 | – |
| $k_1$ | Fast sorption rate coefficient | 0.1 | – |
| $k_2$ | Slow sorption rate coefficient | 0.001 | – |
| $\lambda$ | Filtration coefficient | 5.2 | $\mathrm{m}^{-1}$ |

In the colloid transport simulation, the number of particles leaving the right boundary is counted each time step. The number is then converted to concentration in order to obtain the corresponding breakthrough curve over time. The comparison with the measured value from Harter's experiment is shown in Fig. 10.18.

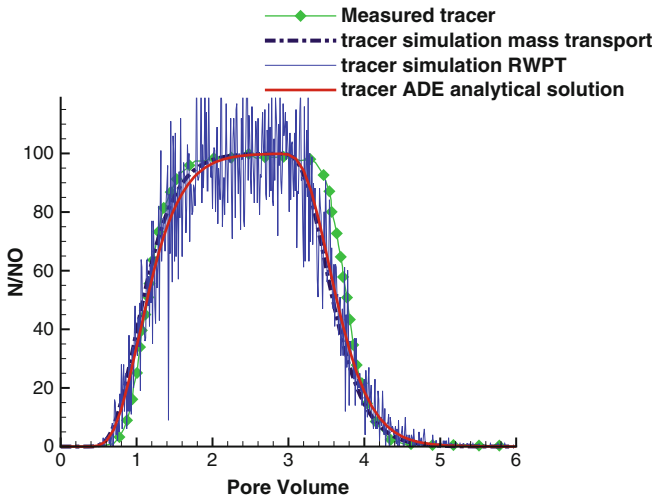


Figure 10.17: Tracer transport with advection and dispertion

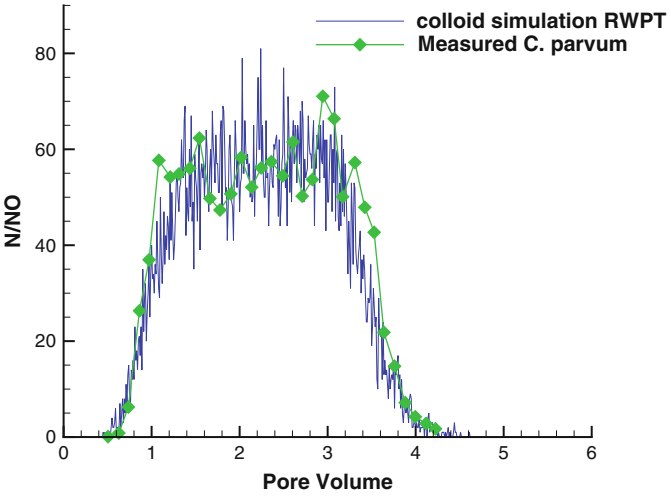


Figure 10.18: Colloid transport with sorption-desorption and decay

### 10.6.2 Particle Tracking in Porous Medium: 2D Case Study

#### Definition

A two-dimensional homogeneous aquifer is chosen to verify advective dispersive transport. The dimension of the model domain is 100 m by 60 m where the uniform velocity field is held constant in the $x$ direction (Fig. 10.19).

#### Analytical Solution

The stated problem can be solved with an analytical solution provided by [96].

$$C(x, y, t) = \frac{C_0 A}{4\pi t \sqrt{D_{xx} + D_{yy}}} \exp\left[-\frac{(x - x_0)^2}{4D_{xx}t} - \frac{(y - y_0)^2}{4D_{yy}t}\right] \tag{10.28}$$

where $C_0$ is the initial concentration.

#### Numerical Solution

The domain is discretized with quadrilateral elements of 0.5 m by 0.5 m. The same grid density is also used for converting particle distributions to element concentrations. The head gradient of one in the $x$ direction is set by assigning two constant boundary conditions along both the left and right sides, thus obtaining the uniform velocity field with the value of 0.5 $\mathrm{md}^{-1}$.

The initial source load is applied to an area with dimensions of 0.1 m by 0.1 m to have an initial concentration of $C_0 = 1\ \mathrm{kg\,m}^{-3}$. The material properties for this model setup are given in Table 10.7.

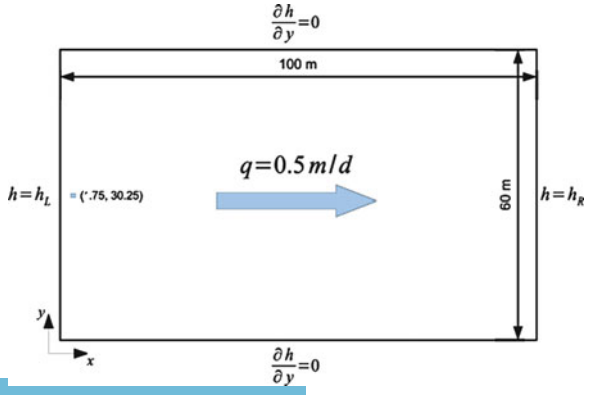


Figure 10.19: Particle tracking in 2D homogeneous aquifer

Table 10.7: Material properties

| Symbol | Parameter | Value | Unit |
|---|---|---|---|
| $k$ | Permeability | $1.114^{-11}$ | $m^2$ |
| $\alpha_L$ | Longitudinal dispersivity | 0.1 | m |
| $\alpha_T$ | Transverse dispersivity | 0.1 | m |

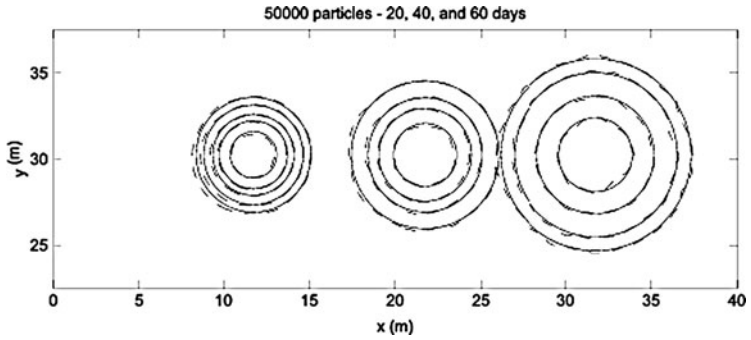


Figure 10.20: Transport results of the RWPT method compared with the analytical solution for 50,000 particles at 20, 40, and 60 days: The solid line is the analytical solution, the dotted line is the RWPT result. Contour lines are shown for $C = 2.6e^{-4}$, $1.6e^{-4}$, $1.0e^{-4}$, and $4e^{-5}$

**Results**

The comparison with the analytical solution is provided in Fig. 10.20. The number of particles used for this simulation is 50,000. This is significantly less than the number of particles reported by [155], who stated that up to 2.5 million particles were necessary to achieve smoothness of the solution due to oscillations around the contours. As the oscillations observed here for the method proposed are smaller than reported by [155], the proposed method allows a dramatic reduction of around two orders of magnitude in the number of particles required for a smooth solution.

In addition, different numbers of particles are used to solve the same problem, producing several different particle clouds as shown in Fig. 10.21.

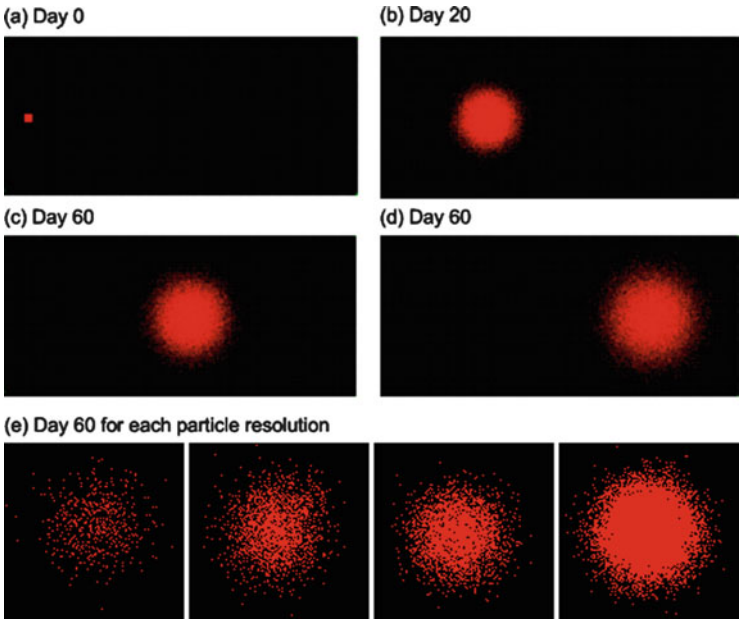


Figure 10.21: (**a**–**d**) Particle clouds of 50,000 particles at 0, 20, 40, and 60 days, (**e**) Particle clouds of 1,000, 5,000, 10,000, and 50,000 particles at 60 days

### 10.6.3 Particle Tracking in Porous Medium: 3D Case Study

#### Definition

A three-dimensional homogeneous cube is chosen to verify advective dispersive transport. The side length of the cube model domain is 100 m. The velocity field is held constant in the diagonal direction from the bottom left to top right (Fig. 10.22).

#### Analytical Solution

The stated problem can be solved with an analytical solution provided by [96].

$$C\left(x,y,z,t\right)=\frac{C_0V}{8\left(\pi t\right)^{3/2}\sqrt{D_{xx}D_{yy}D_{zz}}}\exp\left[-\frac{\left(x-x_0\right)^2}{4D_{xx}t}-\frac{\left(y-y_0\right)^2}{4D_{yy}t}-\frac{\left(z-z_0\right)^2}{4D_{zz}t}\right] \tag{10.29}$$

where $C_0$ is the initial concentration.

### Numerical Solution

The domain is discretized with tetrahedral elements. The same grid density is used for converting particle distributions to element concentrations. The head gradient is set by assigning two constant boundary conditions on the diagonal joint points.

The initial source load is applied to an area close to the bottom left of the domain with an initial concentration of $C_0 = 1\ \mathrm{kg\,m^{-3}}$. The material properties for this model setup are given in Table 10.8.

### Results

The advection-dispersion of the particles pulse across the cube is shown in Fig. 10.23. The number of particles used for this simulation is 500. When particles reached the top right point, the number was counted to generate the breakthrough curves.

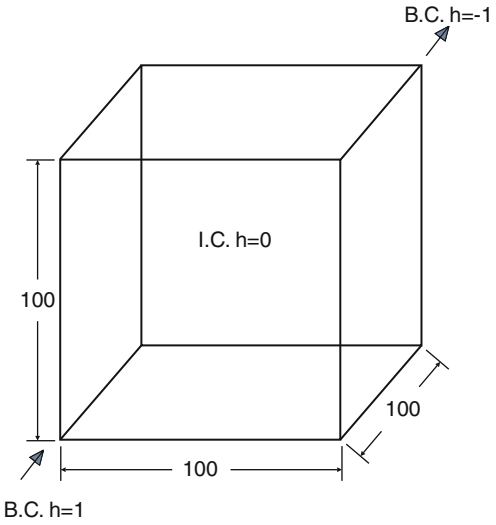


Figure 10.22: Particle tracking in 3D homogeneous aquifer

Table 10.8: Material properties

| Symbol | Parameter | Value | Unit |
|---|---|---|---|
| $k$ | Permeability | $6.0804^{-10}$ | $\mathrm{m^2}$ |
| $\alpha_L$ | Longitudinal dispersivity | 0.005 | m |
| $\alpha_T$ | Transverse dispersivity | 0.005 | m |
| $n$ | Porosity | 0.2 | – |

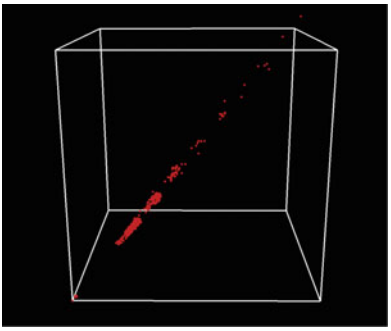

Figure 10.23: Particle clouds in the cube

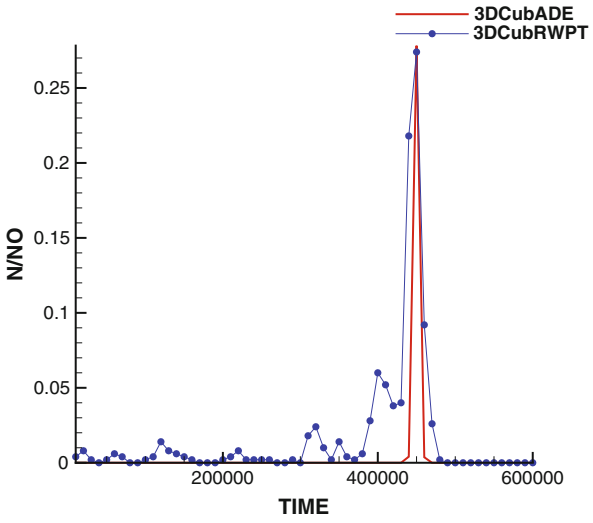


Figure 10.24: Breakthrough curves for particle tracking with advection and dispertion

The result of RWPT simulation for the distribution of concentration over time is compared to the analytical solution. The comparison results are shown in Fig. 10.24.

## 10.7 RWPT in Fractures

Fractures may be defined through direct measurement or geo-statistical reproduction. In the benchmarks of this chapter, both methods will be utilized. Where fractures are directly measured, the methodology utilizes a laser profiler. Profiles (elevation measurements) are taken of each fracture surface and these are manipulated numerically. Point-wise fracture aperture is the difference

between the top and bottom surfaces at corresponding locations. Statistically reproduced fractures reproduce roughness of the aperture (not each surface) in order to achieve a desired mean and standard deviation. The result is used directly as the fracture aperture in numerical simulations.

For a fracture represented by two parallel (planar) plates, permeability is a function of the fracture aperture by the cubic law,

$$k = \frac{b^2}{12} \tag{10.30}$$

For a uniformly fractured rock mass, the cubic law takes form as $b^3/12s$ , where s is fracture spacing.

The aperture, b, however, represents only the mechanical state of the fracture. In reality, observed flow rates are dependent on the hydraulic state of the fracture. In other words, fracture roughness matters. We therefore distinguish two different apertures: the so-called "void" aperture, $b_v$ and the "hydraulic" aperture, $b_h$. The void aperture is the mean geometrically measured distance between the two fracture surfaces, including only those points that are not in contact (as the name implies, including only voids). The hydraulic aperture is a correction from this value ($b_h \leq b_v$), with one possibility known as the geometric correction [156],

$$b_h^3 = \exp\langle \ln(k) \rangle = \exp\left(3 \langle \ln(b_v) \rangle\right) \tag{10.31}$$

where the angled brackets indicate that the mean is taken over the logarithm of the point-wise void aperture. Therefore, as an approximation to reality, the (effective) true permeability of a rough fracture is given by,

$$k = \frac{b_h^2}{12} \tag{10.32}$$

In what follows, we use this permeability to approximate behavior of the fracture and to generate an analytical solution for (qualitative) comparison to simulations within rough fractures, where permeability occurs point-wise (and mechanically) as $k_i = b_i^2/12$ . Therefore, this is an *effective permeability*, and shall be used as an attempt to approximate (or provide reference to) true flow behavior in a rough fracture from a single bulk property.

### 10.7.1 Uncertainty in Flow, Preferential Flow

To examine changes to flow characteristics, we utilize two alternate forms of mass transport: the classical advection-dispersion equation (ADE) and random walk particle tracking (Fig. 10.25). The RWPT simulator within OGS is modified to allow a continuous source of particles (numerically approximate to a Neumann concentration boundary) for comparison with results from ADE simulations. For comparison, dispersion is not allowed within the RWPT simulation: particles are only advected with the flow. Therefore, particles represent

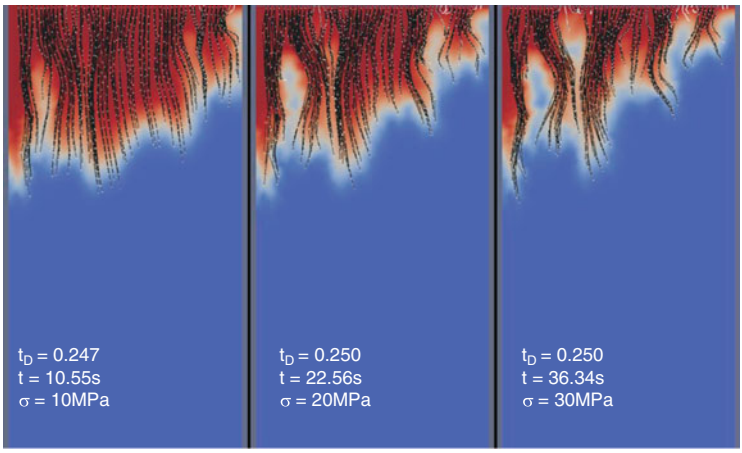


Figure 10.25: RWPT vs. ADE at different stress states. Two separate simulations are conducted and overlay one another. Particle pathlines (*black*) and particles (*white*) are illustrated, and overlay contours (*red* = higher concentration) generated from the ADE simulation

the 50% concentration breakthrough if particles are imagined as concentrations. The plot for each stress state is shown at a different absolute time, but each corresponds to the same dimensionless time, $t_D = v \cdot t/L$, where $t$ is current time and $L$ is total flow length, with $v$ calculated from the mean $b_h$. Therefore, if $b_h$ is a good approximation of behavior, the concentration advance in each plot should be approximately of the same extent. Note that this is true, but also that the increasing tendency for preferential flow with stress lends to increasingly less uniform concentration advance: with increasing stress, a given point in the geometry will record strongly different behavior than its neighbors.

# Part III

# Examples for Coupled Processes

# Chapter 11

# Density Dependent Flow

*by Marc Walther, Jens-Olaf Delfs, Chan-Hee Park, Jude Musuuza, Florin Radu, and Sabine Attinger*

## 11.1 Theory

### 11.1.1 Governing Equations

The governing equations used for variable density flow consist of three fundamental conservation equations: (i) continuity equation of flow, (ii) momentum equation, and (iii) contaminant transport equation. In addition, these three equations are linked to the equations of the bulk fluid density and the hydrodynamic dispersion equations.

#### Equation of the Bulk Fluid Density

The linearized equation of the bulk fluid density under an isothermal state was formulated in terms of hydraulic head as,

$$\rho = \rho_0 \left(1 + \lambda_h \left(h - h_0\right) + \lambda_c C\right) \tag{11.1}$$

where $h$ is the hydraulic head, $\lambda$ is the reference hydraulic head, $\rho$ is the density of fluid, $\rho_0$ is the reference density of the fluid, $\lambda_h$ represents the coefficient of compressibility of the fluid associated with the change of the hydraulic head at constant mass fraction of the solute, $\lambda_C$ is the coefficient of expansivity resulting

O. Kolditz et al. (eds.), *Thermo-Hydro-Mechanical-Chemical Processes in Fractured Porous Media*, Lecture Notes in Computational Science and Engineering 86,
DOI 10.1007/978-3-642-27177-9_11, 

from the change of the mass concentration of the solute at constant hydraulic head and $C$ is the relative concentration.

The relationship between density and concentration can also be approximated using other representations such as an exponential function as given by Kolditz et al. [1998]. The equations describing the relationship between density and other relevant parameters are formulated based on experiments and are approximate relationships.

Another equation for describing the relationship between density and concentration (or mass fraction) is provided by Herbert et al. [1988] and used by Oldenburg and Pruess [1995]. This equation was derived from the assumption that when two liquids are well mixed, the masses or the volumes of respective components are additive. In this study, among these equations which describe the relationship between density and concentration, the linear equation obtained from the experiments is chosen to describe the relation between the bulk fluid density and concentration.

### Continuity Equation of Flow

The macroscopic mass balance equation of the fluid averaged over a representative elementary volume (REV) in a porous medium is

$$\frac{\partial (S\phi\rho)}{\partial t} + \nabla \cdot (\phi\rho\vec{v}) = \rho Q_\rho \tag{11.2}$$

where $S$ is the saturation ratio, $\phi$ is the porosity, $t$ is the time, $\vec{v}$ is the fluid velocity vector and $\rho Q_\rho$ is the source term of the fluid mass in an aquifer. Based on (11.2), the flow equation for a variably saturated porous medium can be written in terms of hydraulic head and mass concentration,

$$\phi\frac{\partial S}{\partial t} + SS_0^h\frac{\partial h}{\partial t} + S\phi\lambda_C\frac{\partial C}{\partial t} + \nabla \cdot \vec{q} + \lambda_c\vec{q} \cdot \nabla C = Q_\rho \tag{11.3}$$

where $S_0^h$ is the specific storativity of a porous medium with respect to hydraulic head change and $\vec{q}$ is the Darcy velocity vector. The head-based flow equation, (11.3), has the advantage over pressure-based flow equations because numerically large static pressures may dominate the dynamic pressure differences that cause motion. The resulting pressure-based numerical scheme may therefore operate at less than optimum numerical efficiency. A more efficient way is to write the flow equation in terms of a quantity that can be directly related to the driving forces. Such a quantity is the equivalent freshwater hydraulic head, defined as $h = \frac{p}{\rho_0 g} + z$ [Frind, 1982].

**Momentum Equation of Flow (the Darcy Equation) and Dispersive Flux**

The momentum balance equation for variable-density fluid flow in a porous medium in terms of hydraulic head can be given as

$$\vec{q} = \phi\vec{v} = -\frac{\hat{k}\rho_0\vec{g}}{\mu}\left(\nabla h + \left(\frac{\rho-\rho_0}{\rho_0}\right)\vec{e}\right) \tag{11.4}$$

where $\hat{k}$ is the tensor of permeability of a porous medium and $\vec{e}$ is the unit vector in the gravitational direction. The dispersion tensor can be written as Bear [1979]

$$\widehat{D} = \gamma D_m\hat{\delta} + \alpha_T\,|v|\,\hat{\delta} + (\alpha_L - \alpha_T)\,\frac{\vec{v}_i\vec{v}_j}{|v|} \tag{11.5}$$

where $\gamma$ is the tortuosity, $D_m$ is the coefficient of molecular diffusion, $\hat{\delta}$ is the Kronecker-delta (unit tensor), $\alpha_T$ is the transverse dispersivity, $v$ is the characteristic value of macroscopic velocity with the subscripts $i$ and $j$ in longitudinal and transversal directions respectively, and $\alpha_L$ is the longitudinal dispersivity.

**Solute Transport Equation**

The solute transport with a source is governed by the following advection-dispersion equation

$$\frac{\partial(\phi C)}{\partial t} + \nabla\cdot(\phi\vec{v}C) - \nabla\cdot\left(\phi\hat{D}\cdot\nabla C\right) = Q_C \tag{11.6}$$

where $Q_C$ is the source term of the solute in terms of mass concentration. Ignoring the expansivity resulting from the change of mass concentration $\lambda_C$, (11.6) can be written as follows

$$\phi\frac{\partial C}{\partial t} + (1-\phi)\,\lambda_h C\frac{\partial h}{\partial t} + \phi\vec{v}\cdot\nabla C - \nabla\cdot\left(\phi\hat{D}\cdot\nabla C\right) + CQ_\rho = Q_C \tag{11.7}$$

Kolditz et al. [1998] defined approximation level of density variations in the mass equations when (11.2) and (11.6) are expanded.

## 11.2 The Elder Problem

### 11.2.1 Definition

The Elder problem is a benchmark to verify density-dependent flow such as free convection, seawater intrusion, and possibly enhanced gas recovery with CO2.

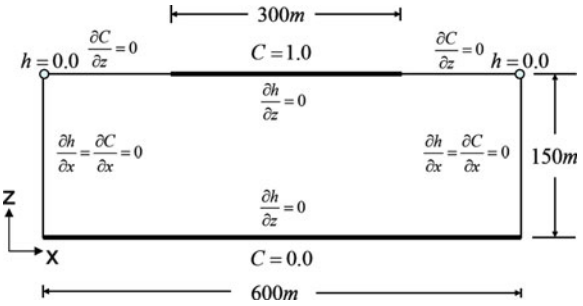


Figure 11.1: Boundary conditions of the Elder problem

Table 11.1: Parameters for the Elder problem

| Symbol | Quantity | Value | Unit |
|---|---|---|---|
| $D_m$ | Molecular diffusion coefficient | 3.565e-6 | $m^2\ s^{-1}$ |
| $k$ | Permeability | 4.845e-13 | $m^2$ |
| $\mu$ | Dynamic viscosity | 10e-6 | $kg\,m^{-1}\ s^{-1}$ |
| $g$ | Gravitational coefficient | 9.81 | $m\,s^{-2}$ |
| $\alpha_L, \alpha_T$ | Longitudinal and transverse dispersivity | 0, 0 | m |
| $\phi$ | porosity | 0.1 | – |
| $\rho_0, \rho_s$ | Density of water and saltwater | (1,1.2)e3 | $kg\,m^{-3}$ |

**Model description.** The Elder Problem is a good example of free convection phenomena, where the fluid flow is driven purely by the density differences of the fluids. Figure 11.1 illustrates the boundary conditions of the Elder problem. Table 11.1 presents the specific parameters for the Elder problem used in this application.

### 11.2.2 Results

The mesh was created with hexahedral elements for further expansion to 3D applications. The grid density level is defined as the $l$th level that consists of $2^{2l+1}$ identical square elements. Based on the definition of the grid density, the number of the hexahedral elements is 8192. The isochlor is defined as a ratio of a density difference to the maximum density difference. Figure 11.2 shows the numerical results obtained from OpenGeoSys as the solution of the Elder problem.

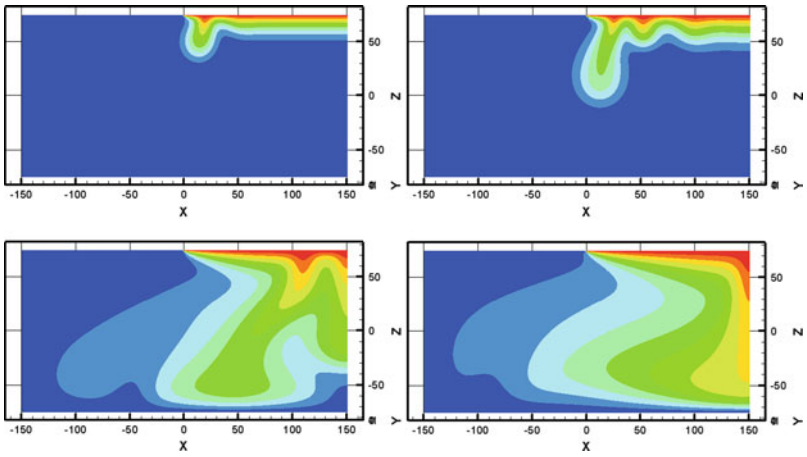


Figure 11.2: Isochlors of the Elder problem for 1, 2, 10, and 20 year at regular grid of level 6

## 11.3 The Goswami Problem

### 11.3.1 Definition

This example shows density dependent groundwater flow under unconfined conditions. The benchmark is based on experimental and modelling data acquired by Goswami et al, 2007 [157], who show a Henry-like (see [158]) saltwater intrusion experiment using a laboratory-scale tank.

Goswami showed three steady-state (SS-1, SS-2, SS-3), differing in the hydraulic gradient, and two transient (TS-1, TS-2) experiments, one advancing front condition (from the final states of experiments SS-1 to SS-2) and one receding front condition (SS-2 to SS-3) experiment, and concurrent simulations with Seawat.

The model set-up will be as close as possible to the one used by Goswami exemplarily showing the simulations of SS-1 and TS-1 with OpenGeoSys.

**Method.** Modifying the Richards-Flow equation [102] with a linear approach as described by Sugio et al, 1987 [159] the hydraulic flow equation is solved for the unconfined flow. Additionally, the Mass_Transport and Richards_Flow processes are coupled via a density correlation as a function of concentration.

**Boundary and Initial Conditions.** Boundary conditions are shown in Fig. 11.3: bottom and top horizontal boundaries are *no-flow*, vertical right and left hand side boundaries are described via linear pressure gradients (including the appropriate densities of fresh water $\rho_f = 1,000\,\mathrm{kg}\cdot\,\mathrm{m}^{-3}$ or salt water

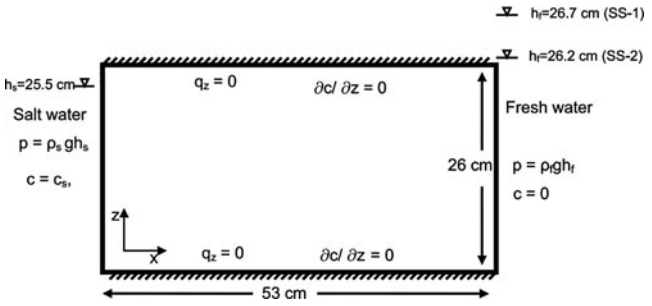


Figure 11.3: Model domain and boundary conditions after GOSWAMI ET AL, 2007 [157]

Table 11.2: Parameters of simulation

| Parameter | Setting |
|---|---|
| Porosity [−] | 0.385 |
| Permeability [m$^2$] | $1.239 \cdot 10^{-9}$ |
| Reduced permeability [m$^2$] | 0.0001 |
| Permeability reduction pressure [Pa] | −100 |

$\rho_s = 1,026\,\mathrm{kg}\cdot\,\mathrm{m}^{-3}$), vertical right and left hand side boundary ISOCHLOR concentrations $C_i$ are fresh water (i.e. $C_i = 0$) and salt water (i.e. $C_i = 1$), respectively.

For the SS-1 simulation, initial conditions are fresh water for the whole domain, i.e. a linear pressure gradient with $p_{(z=0.25\,\mathrm{m})} = 0\mathrm{Pa}$ and $C_i = 0$.

For the TS-1 simulation, initial conditions are the hydraulic and mass transport steady state of SS-1.

**Material properties.** The homogeneous, isotropic domain material equals a medium coarse sand. The corresponding parameters are listed in Table 11.2.

**Model domain, grid discretization.** The dimensions of the laboratory tank were 0.53 x 0.26 x $0.027m^3$; following these measures, a 2D model domain was set up. The grid discretization was uniform with rectangular quad-elements sized $\Delta x = \Delta z = 5 \cdot 10^{-3}m$.

**Time stepping, Dispersivity, Diffusivity.** Time step was chosen to be $\Delta t = 10s$ up to a simulation time of $t_{final} = 4,800\,\mathrm{s} = 80\,\mathrm{min}$ (time until steady state of simulation); to the end of the simulation, time step size was increased up to $\Delta t = 160\,\mathrm{s}$.

Longitudinal dispersivity $\alpha_L$ was determined by GOSWAMI's laboratory experiments to $\alpha_L = 10^{-3}\,\mathrm{m}$, transversal dispersivity $\alpha_T$ was assumed to be $\alpha_T = 0.1 \cdot \alpha_L = 10^{-4}\,\mathrm{m}$.

Diffusion effects were neglected due to the highly advective flow regime.

**Stability** Based on these model configurations, PECLET criterium is met within acceptable ranges with

$$\mathrm{Pe} = \frac{\Delta t \cdot v}{\Delta x} = \frac{10s \cdot 2 \cdot 10^{-4} m s^{-1}}{5 \cdot 10^{-3} m} = 0.4 < 1. \tag{11.8}$$

However, COURANT criterium is exceeded by its reglementations with

$$\mathrm{Co} = \frac{\Delta x}{\alpha} = \frac{5 \cdot 10^{-3} m}{10^{-4} m} = 50 \not< 2, \tag{11.9}$$

which causes some oscillations around the left side ISOCHLOR boundary condition.

### 11.3.2 Results

**Steady State** Figure 11.4 shows the OPENGEOSYS simulation result of the steady-state scenario SS-1 and the typical circulation patterns of a saltwater intrusion, Fig. 11.5 shows the comparison of the experimental measurements with the modeling software outputs of SS-1 for SEAWAT and OPENGEOSYS; the scenario simulations fit very well to the experimental observations. The slight deviations of both simulations may be due to the misfit of the COURANT criterium, to inhomogeneities within the sand material, or to the measurement technique used to obtain the 0.5-ISOCHLOR isolines, which was a simple visual observation of the dyed salt water. GOSWAMI describes it as follows: *"The color variations [...] indicate that the dispersion zone is relatively narrow and is estimated to be about* $1cm$ *wide. Therefore the wedge delineation line [...] (which is assumed to be the 0.5 isochlor) has an error in the range of* $\pm 0.5cm$ *[...]"*. As the dispersion zone was estimated to be about $1cm$ wide, the 0.5-ISOCHLOR isoline (identified as described by Goswami) could very well also be a 0.1 or 0.9-ISOCHLOR isoline.

*Note: Recently, an interesting work was done by this group concerning this issue, i.e. image analysis used for concentration measurements: see [160].*

In addition, Table 11.3 shows an overview of the right boundary's inflow from GOSWAMI's measured experimental data, the SEAWAT results and the equivalent values simulated with OPENGEOSYS. Again, both simulation outputs resemble the measured experimental data within acceptable error limits.

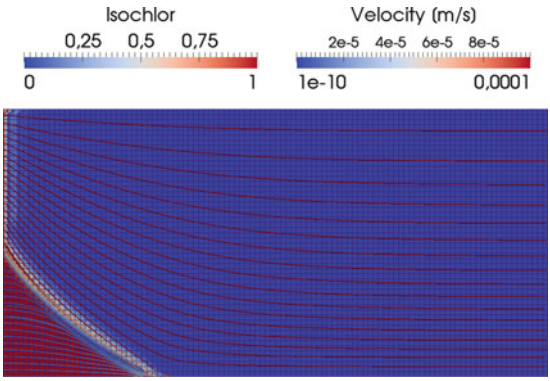


Figure 11.4: ISOCHLOR-concentration, flow field and grid resolution of the OPENGEOSYS steady-state simulation SS-1

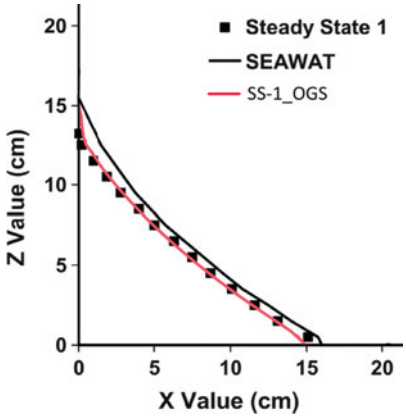


Figure 11.5: Comparison of the 0.5-ISOCHLOR concentration isolines of GOSWAMI's experimental data with his SEAWAT and the OPENGEOSYS steady-state simulation

Table 11.3: Simulation results: right boundary influx [$cm^3 \cdot s^{-1}$]

| Origin of value | SS-1 |
|---|---|
| Experiment | 1.42 |
| SEAWAT | 1.46 |
| OPENGEOSYS | 1.41 |

**Transient State** Figure 11.6 depicts the comparison of the transient simulation of the experiment with both numerical models. While SEAWAT seems to fit the measurements quite well, OPENGEOSYS shows slight differences; both results however, resemble the experimental data in an adequate way.

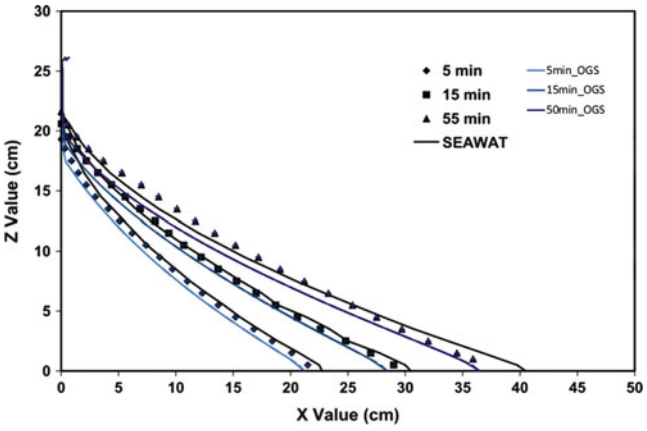


Figure 11.6: Comparison of the 0.5-ISOCHLOR concentration isolines of GOSWAMI's experimental data with his SEAWAT and the OPENGEOSYS transient simulation TS-1

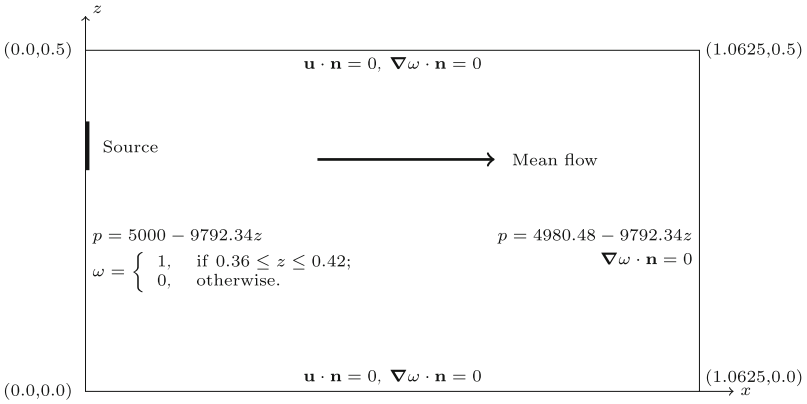


Figure 11.7: Model set-up

## 11.4 The Schincariol Problem

### 11.4.1 Definition

The studies investigated the fingering patterns that result when, for example saline water intrudes into a confined coastal aquifer. The configuration used in [161] was used where a solute was allowed to flow into the study domain shown in Fig. 11.7 with pressure heads maintained over the vertical boundaries to sustain a mean horizontal flow.

Table 11.4: Simulation parameters

| Parameter | Notation | Value | Unit |
|---|---|---|---|
| Porosity | $\phi$ | 0.38 | – |
| Molecular diffusion coefficient of NaCl | $D_m$ | $1.61 \times 10^{-9}$ | $m^2 \cdot s^{-1}$ |
| Longitudinal dispersivity | $\alpha_{\parallel}$ | $1.0 \times 10^{-3}$ | m |
| Transverse dispersivity | $\alpha_{\perp}$ | $2.0 \times 10^{-4}$ | m |
| Mean flow velocity | $v_0$ | $2.75 \times 10^{-6}$ | $m \cdot s^{-1}$ |
| Domain Length in flow direction | $L$ | 1.0625 | m |
| Viscosity of pure water at 20°C | $\mu_0$ | $1.002 \times 10^{-3}$ | Pa· s |
| Maximal viscosity of solution (2,000mg/l NaCl at 20°C) | $\mu_{max}$ | $1.006 \times 10^{-3}$ | Pa·s |
| Density of pure water at 20°C | $\rho_0$ | 998.2 | $kg \cdot m^{-3}$ |
| Maximal density of solution (2,000mg/l NaCl at 20°C) | $\rho_{max}$ | 999.7 | $kg \cdot m^{-3}$ |
| Tortuosity | $\varsigma$ | 0.35 | – |
| Gravity vector | $\mathbf{g}$ | $-9.81$ | $m \cdot s^{-2}$ |
| Mean permeability | $k_0$ | $5.7 \times 10^{-11}$ | $m^2$ |

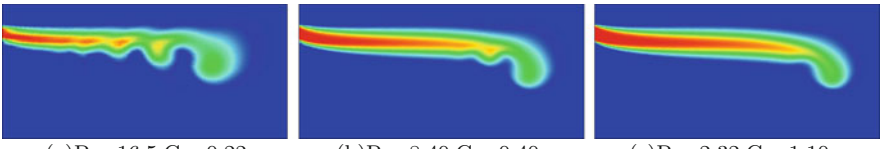

(a)Pe=16.5,Cr=0.22 (b)Pe=8.40,Cr=0.40 (c)Pe=2.32,Cr=1.10

Figure 11.8: A reproduction of Schincariol results with full equations

**Domain setup.** Using the simulation parameters in Table 11.4, the grid and time steps were refined until a solution free of numerical artifacts was obtained.

### 11.4.2 Results

Their results at the approximate Pèclet and Courant numbers were nearly exactly reproduced in [162] as shown in Fig. 11.8. The Pèclet and Courant numbers reported in the figure were obtained with mesh sizes of 0.3 with 4 refinements and a time step of 1 hr; 0.3 with 5 refinements and a time step of 45 min; and 0.2 with 5 refinements and a time step of 57 min. The reproducibility of the results makes the problem defined by [161] a suitable reference from which further investigations can be founded.

Due to the rotation of the velocity field caused by density variations in the boundary layer, some salt accumulates and is trapped in the tip of the of the plume. Therefore, the ever-present lobe at the tip does not count as a finger

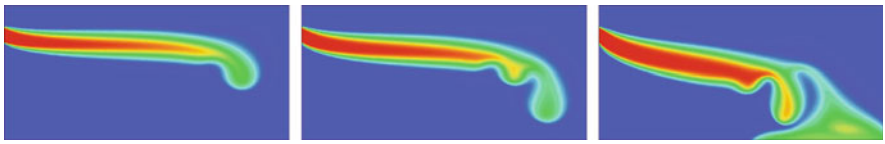

(a) $\rho = 999.7\, kg \cdot m^{-3}$ (b) $\rho = 1000.4\, kg \cdot m^{-3}$ (c) $\rho = 1002.0\, kg \cdot m^{-3}$

Figure 11.9: Fingering patterns at various densities

and Fig. 11.8(c) is considered to be free from instabilities. This numerically stable configuration was further used by [161] to study the effect of periodically varying the width of the inflow region and by [163] to study the effect of medium heterogeneity on fingering patterns. It was also used in [162] to investigate the effects of physical variables like density, viscosity and flow velocity on the evolution of fingers.

Sample results from numerical studies in [162] without the Oberbeck-Boussinesq approximation are shown in Fig. 11.9.

# Chapter 12

# Multiphase Flow Processes

*by Chan-Hee Park, Joshua Taron, Ashok Singh, Wenqing Wang, and Chris McDermott*

In this chapter, we consider two-phase flow processes and examine two alternate combinations of primary variables in the solution of the governing equations: (1) pressure-pressure and (2) pressure-saturation. These combinations are explained in the following sections.

## 12.1 Isothermal Two-Phase Flow

This section ignores temperature effects and the partially saturated sample is treated as an immiscible two-phase system within the voids of the solid skeleton. In the pressure-pressure formulation the primary variables are (1) gas pressure $p^g$ and (2) capillary pressure $p^c$. In the pressure-saturation formulation the primary variables are non-wetting phase saturation $S^{nw}$ and wetting-phase pressure $p^w$. In the benchmarks shown here, both fluids are assumed incompressible.

### 12.1.1 Mass Balance Equation

Consider two-phase flow in porous media, e.g liquid (denoted by $l$) and gas (denoted by $g$). For each phase in two-phase fluid flow, mass conservation is given by the following equation,

$$\frac{\partial}{\partial t}\left(nS^g\rho_k^g + nS^l\rho_k^l\right) + \nabla\cdot\left(\mathbf{J}_k^g + \mathbf{J}_k^l\right) = Q_k, \tag{12.1}$$

O. Kolditz et al. (eds.), *Thermo-Hydro-Mechanical-Chemical Processes in Fractured Porous Media*, Lecture Notes in Computational Science and Engineering 86,
DOI 10.1007/978-3-642-27177-9_12, © Springer-Verlag Berlin Heidelberg 2012

where $S$ is saturation, $\rho$ stands for phase density, $n$ is the porosity, $\mathbf{J}$ is total flux. The subscript $k$ in (12.1) denotes the component, e.g air ($k = a$) or water ($k = w$), within each phase, $\gamma = (g, l)$. For any phase $\gamma = (g, l)$, an advection vector $\mathbf{J}_{A_k^\gamma}$ and a diffusion vector $\mathbf{J}_{D_k^\gamma}$ comprise the total flux, i.e,

$$\mathbf{J}_k^\gamma = \mathbf{J}_{A_k^\gamma} + \mathbf{J}_{D_k^\gamma}. \tag{12.2}$$

According to Darcy's law, the advective part of the total flux may be written as

$$\mathbf{J}_{A_k^\gamma} = -\rho_k^\gamma \frac{\mathbf{k} k_{rel}^\gamma}{\mu^\gamma} \left(\nabla p^\gamma - \rho^\gamma \mathbf{g}\right), \tag{12.3}$$

where $\mathbf{k}$ is the intrinsic permeability, $k_{rel}^\gamma$ is the relative permeability of the phase, and $\mu^\gamma$ is the viscosity.

The diffusive part of the total flux is given by Fick's law

$$\mathbf{J}_{D_k^\gamma} = -nS^\gamma \rho^\gamma \mathbb{D}_k^\gamma \nabla \left(\frac{\rho_k^\gamma}{\rho^\gamma}\right), \tag{12.4}$$

where $\mathbb{D}$ is the diffusion coefficient tensor. Since $\rho^\gamma = \rho_a^\gamma + \rho_w^\gamma$, we have

$$\mathbf{J}_{D_w^\gamma} + \mathbf{J}_{D_a^\gamma} = \mathbf{0} \tag{12.5}$$

under the assumption $\mathbb{D}_a^\gamma = \mathbb{D}_w^\gamma$.

Consider a water-air mixture. We expand the mass balance equation (12.1) with the flux defined in (12.2) based upon the above (12.2)–(12.4). For the water component, the diffusive part of the total flux takes the form

$$\mathbf{J}_{D_w^l} = -nS^l \rho^l \mathbb{D}_w^l \nabla \left(\frac{\rho_w^l}{\rho^l}\right), \quad \mathbf{J}_{D_w^g} = -nS^g \rho^g \mathbb{D}_w^g \nabla \left(\frac{\rho_w^g}{\rho^g}\right). \tag{12.6}$$

Obviously, $\mathbb{D}_w^l = \mathbf{0}$. Therefore, the mass balance equation for water component can be written as follows

$$\begin{aligned} &\frac{\partial}{\partial t}\left(nS^g \rho_w^g + nS^l \rho_w^l\right) - \nabla \cdot \left[\rho_w^l \frac{\mathbf{k} k_{rel}^l}{\mu^l}\left(\nabla p^l - \rho^l \mathbf{g}\right)\right] \\ &-\nabla \cdot \left[\rho_w^g \frac{\mathbf{k} k_{rel}^g}{\mu^g}\left(\nabla p^g - \rho^g \mathbf{g}\right)\right] - \nabla \cdot \left[nS^g \rho^g \mathbb{D}_w^g \nabla \left(\frac{\rho_w^g}{\rho^g}\right)\right] = Q_w. \end{aligned} \tag{12.7}$$

Since the capillary pressure $p^c$ is chosen as one of the two unknowns of (12.1) and $S^g = 1 - S^l$, (12.7) becomes

$$\begin{aligned} &n(\rho_w^l - \rho_w^g)\frac{\partial S^l}{\partial t} + (1 - S^l)n\frac{\partial \rho_w^g}{\partial t} - \nabla \cdot \left[\rho_w^l \frac{\mathbf{k} k_{rel}^l}{\mu^l}\left(\nabla (p^g - p^c) - \rho^l \mathbf{g}\right)\right] \\ &-\nabla \cdot \left[\rho_w^g \frac{\mathbf{k} k_{rel}^g}{\mu^g}\left(\nabla p^g - \rho^g \mathbf{g}\right)\right] - \nabla \cdot \left[nS^g \rho^g \mathbb{D}_w^g \nabla \left(\frac{\rho_w^g}{\rho^g}\right)\right] = Q_w. \end{aligned} \tag{12.8}$$

Similar to the previous procedure, the diffusion part of the total flux of air component can be written as

$$\mathbf{J}_{D_a^l} = -nS^l\rho^l\mathbb{D}_a^l\nabla\left(\frac{\rho_a^l}{\rho^l}\right), \quad \mathbf{J}_{D_a^a} = -nS^g\rho^g\mathbb{D}_a^g\nabla\left(\frac{\rho_a^g}{\rho^g}\right). \tag{12.9}$$

The density shift from air component to liquid $\rho_a^l$ is very small and can be omitted. Therefore, we can assume $\mathbf{J}_{D_a^l} \approx 0$. As a consequence, the mass balance equation for air component is derived:

$$\frac{\partial}{\partial t}\left(nS^g\rho_a^g\right) -$$

$$\nabla\cdot\left[\rho_a^g\frac{\mathbf{k}k_{rel}^g}{\mu^g}\left(\nabla p^g - \rho^g\mathbf{g}\right)\right] - \nabla\cdot\left[nS^g\rho^g\mathbb{D}_a^g\nabla\left(\frac{\rho_a^g}{\rho^g}\right)\right] = Q_a. \tag{12.10}$$

Expanding the temporary derivative term of (12.10) yields

$$-n\rho_a^g\frac{\partial S^l}{\partial t} + (1-S^l)n\frac{\partial\rho_a^g}{\partial t} -$$

$$\nabla\cdot\left[\rho_a^g\frac{\mathbf{k}k_{rel}^g}{\mu^g}\left(\nabla p^g - \rho^g\mathbf{g}\right)\right] - \nabla\cdot\left[nS^g\rho^g\mathbb{D}_a^g\nabla\left(\frac{\rho_a^g}{\rho^g}\right)\right] = Q_a. \tag{12.11}$$

The mass balance equations (12.8) and (12.11) are exactly the same as described in [164].

### 12.1.2 Pressure–Pressure (pp) Scheme

Based on the description of isothermal two-phase flow above, (12.8) and (12.11) can be modified in order to obtain governing equations for isothermal two-phase flow in a porous medium. In this formulation primary variables are gas pressure $p^g$, and capilary pressure $p^c$.

The basic equations of the isothermal two-phase flow system are:

$$n\rho_w\frac{\partial S_w}{\partial p_c}\dot{p}_c + \nabla\cdot\left[\rho_w\frac{\mathbf{k}k_{relw}}{\mu_w}\left(-\nabla p^g + \nabla p^c + \rho_w\mathbf{g}\right)\right] = Q_w \tag{12.12}$$

$$-n\rho^a\frac{\partial S_w}{\partial p_c}\dot{p}_c + n(1-S_w)\left(\frac{\partial\rho_a}{\partial p^g}\dot{p}^g + \frac{\partial\rho_a}{\partial p_c}\dot{p}_c\right) +$$

$$\nabla\cdot\left[\rho_a\frac{\mathbf{k}k_{rela}}{\mu_a}\left(-\nabla p^g + \rho_a\mathbf{g}\right)\right] = Q_a \tag{12.13}$$

### 12.1.3 Pressure-Saturation (pS) Scheme

Based on the description of the isothermal two-phase flow above, (12.8) and (12.11) can be modified in order to obtain governing equations for the isothermal two-phase system. Primary variables of this formulation are wetting phase pressure $p_w$, and non-wetting phase saturation $S_{nw}$. The equations are simply algebraic manipulations of those in the previous section.

### 12.1.4 Liakopoulos Experiment

#### Definition

This benchmark is based on an experiment by Liakopoulus [165] and is proposed by Lewis and Schrefler [14] (pp 167–174). The benchmark is simulated with different element types using the pressure-pressure scheme. The grids used in such simulations are illustrated in Fig. 12.1. Material properties are provided in Table 12.1.

#### Results

The temporal evolution of vertical profiles of primary variables (capillary and gas pressure) are given in Fig. 12.2. Figure 12.3 shows the vertical profiles for

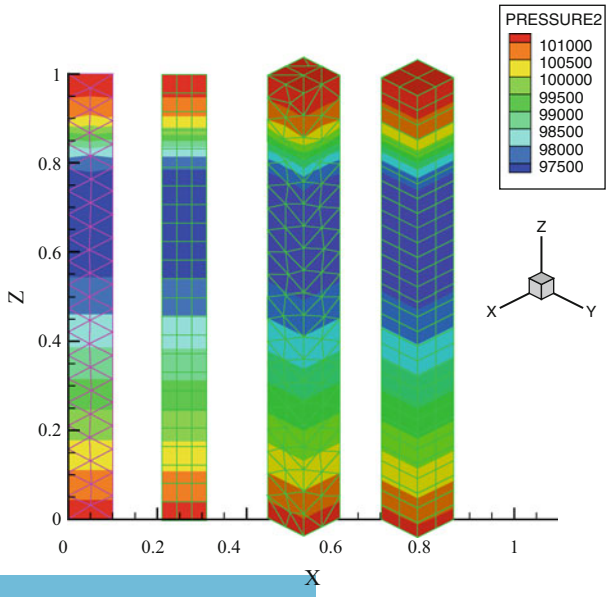


Figure 12.1: Grids with different element types for the Liakopoulos benchmark

Table 12.1: Material parameters for the Liakopoulos problem

| Property | Symbol | Value | Unit |
|---|---|---|---|
| Porosity | $n$ | – | $2.975 \times 10^{-1}$ |
| Permeability | $\kappa$ | $\mathrm{m}^2$ | $4.5000 \times 10^{-13}$ |
| Liquid dynamic viscosity | $\mu_w$ | Pa·s | $1.0000 \times 10^{-3}$ |
| Gas dynamic viscosity | $\mu_a$ | Pa·s | $1.8 \times 10^{-5}$ |
| Liquid density | $\rho_w$ | $\mathrm{kg\,m^{-3}}$ | $1.0000 \times 10^{3}$ |
| Gas density | $\rho_a$ | $\mathrm{kg\,m^{-3}}$ | Ideal Gas Law's |
| Capillary pressure | $p^c$ | Pa | Experimental Curve |
| Relative permeability | $\kappa_{rel\,w}$ | – | Experimenta Curve |
| Relative permeability | $\kappa_{rel\,a}$ | – | Brook–Corey functions |

water saturation as a secondary variable. The results agree well with the findings by Lewis and Schrefler [14].

The results of the element test are depicted in Fig. 12.4 for capillary pressure. A comparison of the results between the two-phase flow model and the Richards model can be found in Chap. 6.

### 12.1.5 Buckley–Leverett Problem

Buckley and Leverett [166] developed a semi-analytical solution for the displacement of two immiscible fluids in porous media. Assuming constant fluid density and porosity, and no source/sink terms, the fluid mass balance equation can be simplified to obtain

$$n\frac{\partial S^\gamma}{\partial t} = -\nabla \cdot \mathbf{q}^\gamma. \tag{12.14}$$

Buckley and Leverett derived the following expression

$$\frac{\partial S^l}{\partial f^l} = \frac{q_{tot}}{n}\frac{\Delta t}{\Delta x} \tag{12.15}$$

with the fractional flow function $f^\gamma = q^\gamma / q_{tot}$

$$f^1 = \left(1 + \frac{\mu_1}{k_1}\frac{k_2}{\mu_2}\right)^{-1} \tag{12.16}$$

where 1 and 2 are the fluid phase numbers. The position of the shock front separating the two fluid phases can be calculated from the following expression

$$\Delta x = -\frac{q_{tot}}{n}\frac{\partial f^l}{\partial S^l}. \tag{12.17}$$

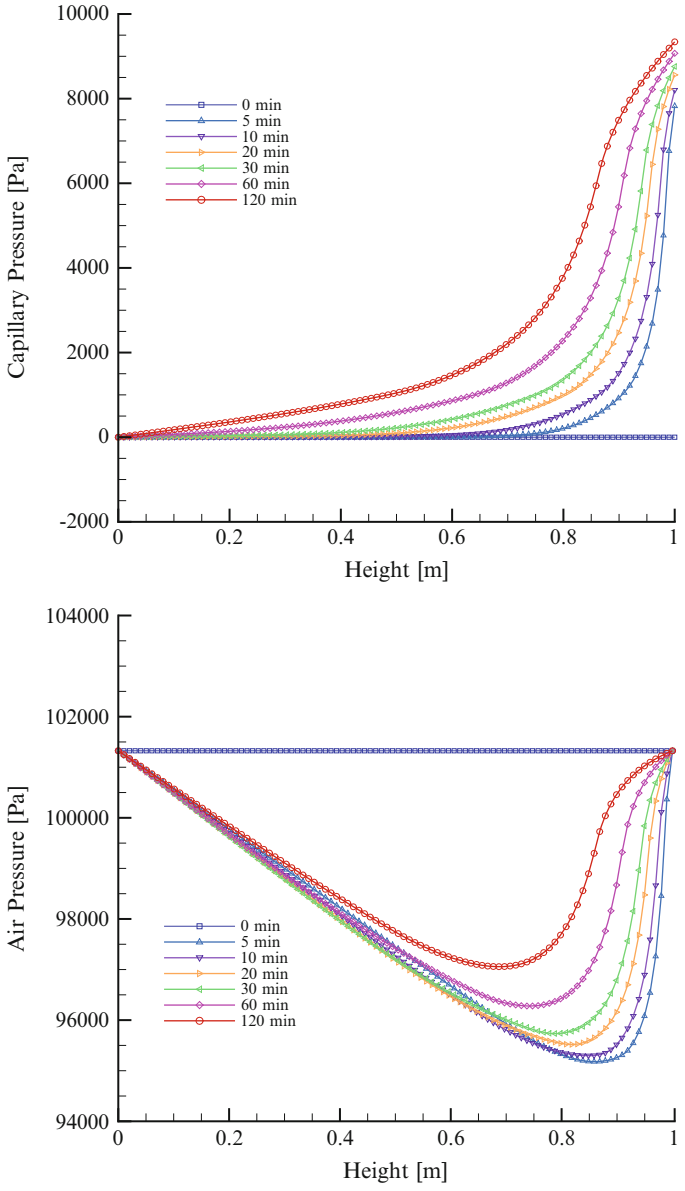


Figure 12.2: Vertical profiles of capillary (*top*) and gas pressures (*bottom*)

Buckley and Leverett suggested that the capillary pressure is a function of the saturation only. Note that the original Buckley–Leverett solution considered phases of water and oil. Moreover, they assumed that the condition that the derivative of capillary pressure with respect to saturation is zero ($dp_{cwo}/dS_{wo} = 0$) is a sufficient rationale to ensure that the spatial gradients of water and oil pressure are equal to one another, as expressed in the following equation,

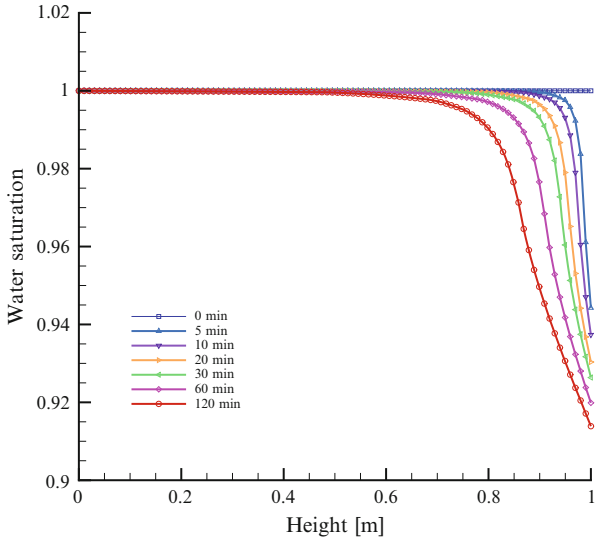


Figure 12.3: Profile of water saturation

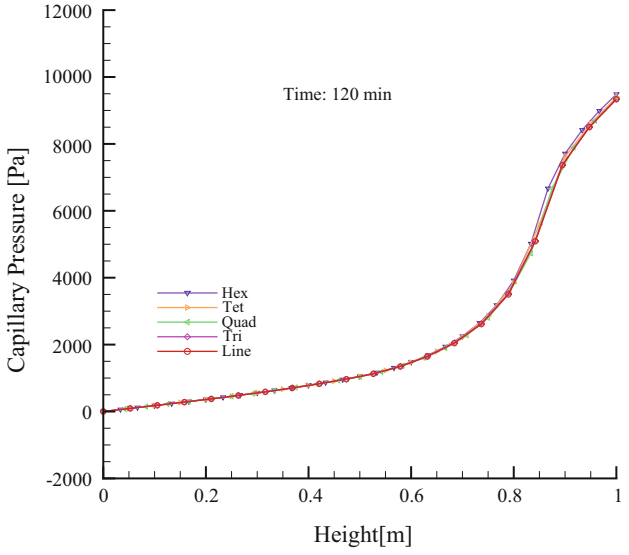


Figure 12.4: Results of element test

$$\frac{\partial p_w}{\partial x} = \frac{\partial p_o}{\partial x} + \frac{\partial p_{cwo}}{\partial x} = \frac{\partial p_o}{\partial x} + \frac{dp_{cwo}}{dS^w}\frac{\partial S^w}{\partial x} = \frac{\partial p_o}{\partial x}. \tag{12.18}$$

**Definition**

The Buckley Leverett problem is frequently used to test numerical models for the functional relation between relative permeability and saturation. In comparison to the analytical solution, the problem is simplified to describe one fluid displacing the other residing fluid in aquifers or reservoirs. In the derivation of the analytical solution, the effect caused by capillary forces between two fluids is not considered.

A non-wetting phase displaces a wetting phase from left to right. The initial total velocity of the two-phase system is 1.0 m/s. The ratio of the dynamic viscosities is one, residual saturations are zero and the Brooks–Corey function ($\lambda = 2$) is used for the relative permeabilities. A space-time discretization of delta x = 0.025 m and delta $t = 0.005$. The total simulation time is 0.4 s.

**Results: pS-Global**

The mass conservation equation is converted to a volumetric one by dividing through by fluid density,

$$n\frac{\partial S_w}{\partial t} - \nabla \cdot \left( \frac{\mathbf{k} k_{rel\,w}}{\mu_w} \left( \nabla p_w - \rho_w \mathbf{g} \right) \right) = q_w \tag{12.19}$$

$$n\frac{\partial S_{nw}}{\partial t} - \nabla \cdot \left( \frac{\mathbf{k} k_{rel\,nw}}{\mu_{nw}} \left( \nabla p_{nw} - \rho_{nw} \mathbf{g} \right) \right) = q_{nw}. \tag{12.20}$$

In the pressure-saturation scheme, OpenGeoSys solves these two equations in a global-implicit scheme or as a total pressure based sequential coupling. As shown in Fig. 12.5, the global-implicit scheme produces more accurate results compared to that obtained by the sequential-coupling scheme. The result has little oscillation and is closer to the analytical solution, particularly in the location of the sharp front of the intruding fluid.

One important note is that the global scheme is sensitive to matrix solvers. The LIS solver (BiCG with Jacobi preconditioned) works well on Windows. However, this iterative solver for this benchmark takes much more time than the PARDISO (a parallel direct solver) that works only on Unix with OpenGeoSys.

**Results: pS-Sequential**

Adding (12.19) and (12.20) and using the relation $S_{nw} + S_w = 1$ and $p^c(S_w) = p_{nw} - p_w$, we get the equation for wetting phase pressure, $p_w$ and non-wetting phase saturation, $S_{nw}$.

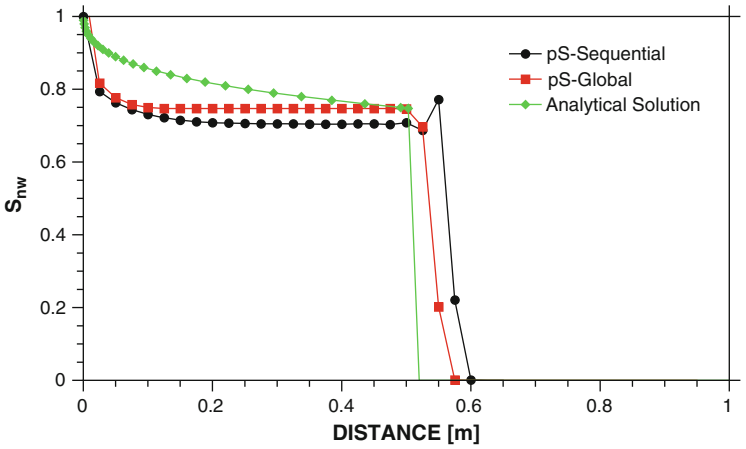


Figure 12.5: Comparison of coupling schemes and analytical solution for the BL problem

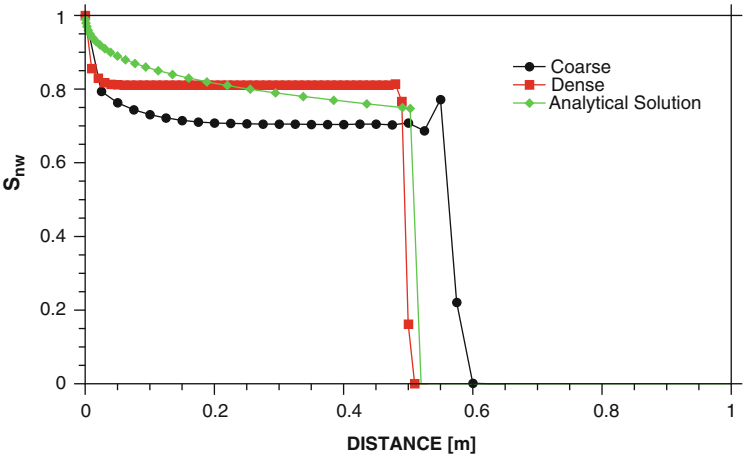


Figure 12.6: Comparison of grid discretizations for the BL problem with sequential coupling

$$-n\frac{\partial S_{nw}}{\partial t} - \nabla \cdot \left( \frac{\mathbf{k} k_{rel\,w}}{\mu_w} \left( \nabla p_w - \rho_w \mathbf{g} \right) \right) = q_w \tag{12.21}$$

$$\nabla \cdot \left( \frac{\mathbf{k} k_{rel\,w}}{\mu_w} \left( \nabla p_w - \rho_w \mathbf{g} \right) \right) + \nabla \cdot \left( \frac{\mathbf{k} k_{rel\,nw}}{\mu_{nw}} \left( \nabla p_w + p_c - \rho_{nw} \mathbf{g} \right) \right) + q_w + q_{nw} = 0 \tag{12.22}$$

In (12.21), non-wetting phase saturation, $S_{nw}$ can be easily solved explicitly with the known pressure obtained from (12.22). The analytical solution for the frontal location of the infiltrating fluid is compared with alternate discretizations in Fig. 12.6. The diffusion term for saturation omitted in the BL equation makes the analytical solution purely advective, with a sharp advancing front. Handling this purely advective transport in numerical models introduces some numerical dispersion, and tighter discretizations will capture the low diffusive front with greater accuracy.

**Results: $CO_2$ Injection**

Based on the Buckley and Leverett solution, we assume saturated $CO_2$ displacing $H_2O$ with constant fluid properties. Figure 12.7 shows the saturation profile, $S_w$, along 1 m column calculated with line element with space-time discretization of $\delta x = 0.025$ m and $\delta t = 0.005$ s. The total simulation time is 0.4 s; using the global implicit pressure-saturation model. Based on linear relation between saturation and relative permeability, the saturation profile, $S_w$ is shown in Fig. 12.8. Material parameters of the problem are provided in Table 12.2.

### 12.1.6 McWhorter Problem

It is assumed that the flow of both wetting and non-wetting phases can be adequately described by Darcy's law if the phases are immiscible and incompressible

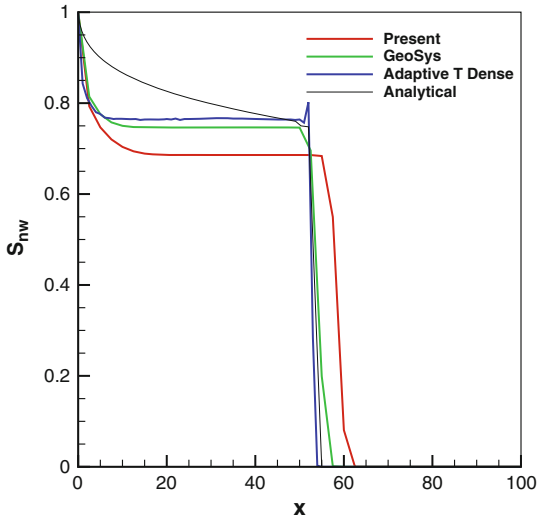


Figure 12.7: Saturation profile obtained with present analysis along with others

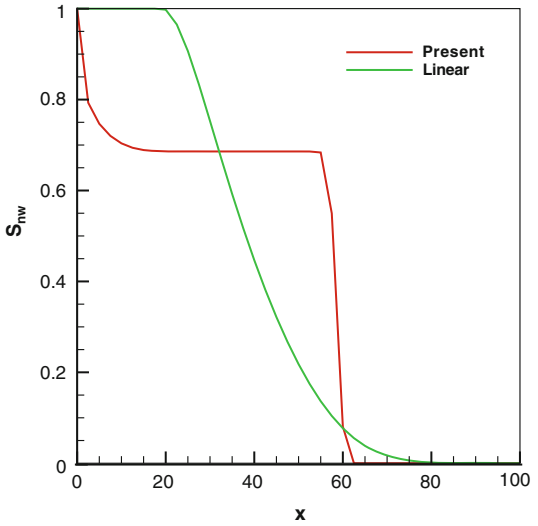


Figure 12.8: Saturation profile obtained with Brooks–Corey relative permeability function and a linear permeability-saturation function

Table 12.2: Material parameters for the BL problem

| Property | Symbol | Value | Unit |
|---|---|---|---|
| Column length | $L$ | m | 1.0 |
| Porosity | $n$ | – | $2.0 \times 10^{-1}$ |
| Permeability | $\kappa$ | $\mathrm{m}^2$ | $1.0 \times 10^{-10}$ |
| Water dynamic viscosity | $\mu_w$ | Pa·s | $1.0 \times 10^{-3}$ |
| Gas dynamic viscosity | $\mu_{nw}$ | Pa·s | $7.0343 \times 10^{-4}$ |
| Water density | $\rho_w$ | $\mathrm{kg\,m}^{-3}$ | $1.0 \times 10^3$ |
| Gas density | $\rho_{nw}$ | $\mathrm{kg\,m}^{-3}$ | $7.73 \times 10^2$ |
| Capillary pressure | $p^c(S)$ | Pa | 0 |
| Relative permeability | $\kappa_{rel}(S)$ | – | Brook–Corey functions |

$$n\frac{\partial S^\gamma}{\partial t} + \nabla \cdot \mathbf{q}^\gamma = 0, \gamma = w, nw \tag{12.23}$$

$$\mathbf{q}^\gamma = -\mathbf{K}\lambda^\gamma \nabla p^\gamma \tag{12.24}$$

where $\lambda_w$ and $\lambda_{nw}$ are mobility of the wetting and non-wetting fluid. Both phase are linked by the state equation $S_w + S_{nw} = 1$ and $p_c = p_g - p_w$. Here total flux, $\mathbf{q}_t = \mathbf{q}_w + \mathbf{q}_{nw}$ and $p_c$ is a function of $S_w$.

A formulation that is often used for two phase flow problems is the so-called fractional flow model. The attractiveness of this formulation is that the model

becomes more accessible to analysis. Subtracting (18.1.24) for both phases we have

$$\mathbf{q}_w = f\mathbf{q}_t - D\frac{\partial S_w}{\partial x} \tag{12.25}$$

where

$$f = \frac{1}{1+\frac{\lambda_{nw}}{\lambda_w}}, \quad D = -\lambda_{nw} f \frac{\partial p_c}{\partial S_w}. \tag{12.26}$$

The first term on the right of (12.25) dictates the rate at which flux is injected on the boundary and the second term represents the additional force due to the gradient of capillary pressure. Inserting (12.25) into (12.28) for the wetting phase and assuming that total flux, $\mathbf{q}_t$ is space invariant

$$\frac{\partial}{\partial x}\left(D\frac{\partial S_w}{\partial x}\right) - \mathbf{q}_t \frac{\partial f}{\partial S_w}\frac{\partial S_w}{\partial x} = n\frac{\partial S_w}{\partial t}. \tag{12.27}$$

In the last benchmark (Buckley and Leveret) it is assumed that the force due to the gradient of capillary pressure is very small relative to total flux, $\mathbf{q}_t$, and hence the second order term is suppressed in the equation.

Including capillarity, model verification can occur against the analytical solution of McWhorter and Sunada ([167]). They developed an exact quasi-analytical solution of (12.27) for unidirectional displacement of a non-wetting phase by a wetting phase using the concept of a fractional flow function.

The fractional flow function is defined as the ratio of wetting phase flux, $\mathbf{q}_w$ to the total flux, $\mathbf{q}_t$. It has been shown that this ratio is function of $S_w$ only, when $\mathbf{q}_t$ is inversely related to the square root of the time.

### Definition

The test benchmark problem for capillary effects is formulated as if the instantaneous displacement occurs in a one-dimensional horizontal reservoir initially occupied by oil (Fig. 12.9). The solution is obtained by solving the governing equations (12.13) with the pressure-pressure scheme described above. Different from the Buckley-Leverett problem, here flow is governed by capillary forces when water saturation at the left end of the horizontal column is kept at one, while the right end is kept at zero flux. Therefore, no source term exists, and flow is by capillary force alone.

### Results

Based on the above discussion, OpenGeoSys produces an agreeable solution. Figure 12.10 shows the water saturation profile, $S_w$ with a fine grid along with 2.6 m long horizontal column for different time steps. Line elements have been

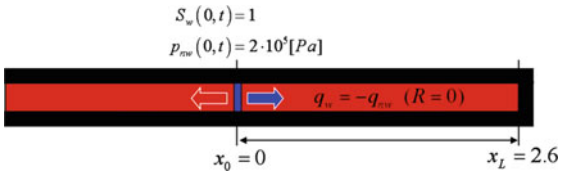


Figure 12.9: Schematic of the benchmark formulated to test McWhorter and Sunada's analytical solution

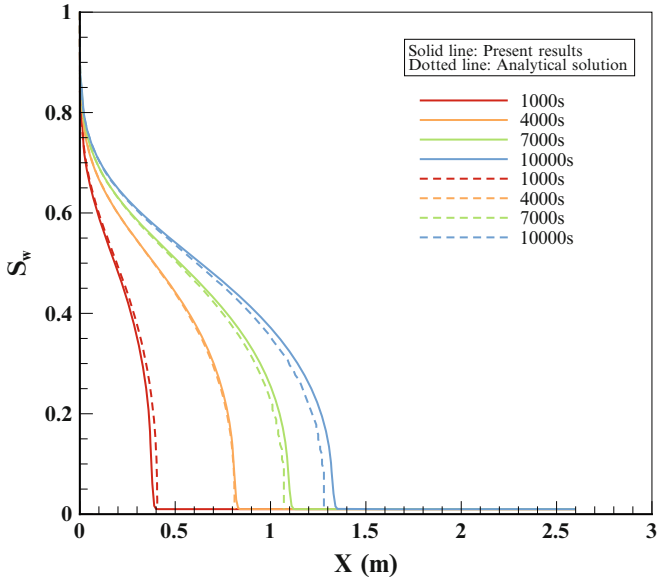


Figure 12.10: Water saturation, $S_w$ profile of the present result along with ananalytical solution based on one by McWhorter

used with the time and space discretization $\delta t = 0.5\,\text{s}$ and $\delta x = 0.05\,\text{m}$ respectively.

Next, we solve exactly the same problem using the total pressure based pressure-saturation model in a sequential iterative coupling scheme. Unlike the pressure-pressure model, one downside for the total-pressure-based saturation model is that it is less accurate for problems dominated by capillarity (see Fig. 12.11). Since the pressure-pressure model directly solves for capillary pressure as a primary variable, the model has an advantage for the capillary related problems. On the other hand, the total-pressure-based saturation model is limited to the problems when $dP_c/dS_w$ is close to zero. The condition for $dP_c/dS_w$ close to zero is caused physically in the case of fractures, shear zones, and transitions between heterogeneities (Table 12.3).

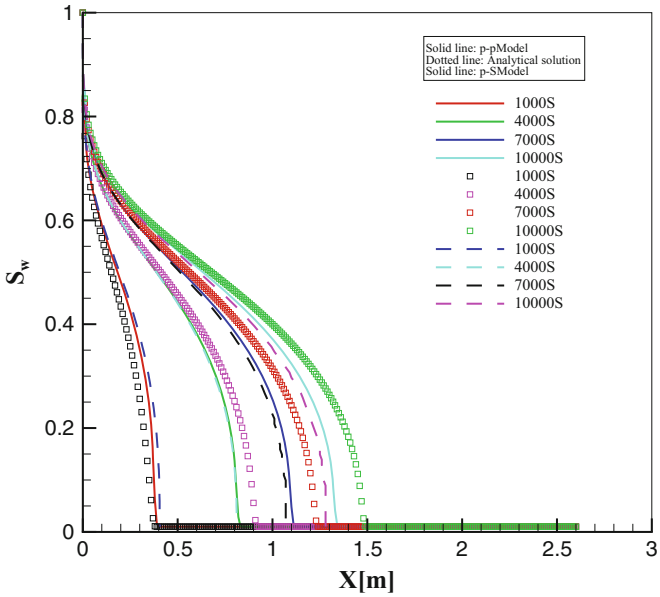


Figure 12.11: Water saturation, $S_w$ profile in sequential iterative coupling scheme

Table 12.3: Material parameters for the McWhorter problem

| Property | Symbol | Value | Unit |
|---|---|---|---|
| Column length | $L$ | $m$ | 2.6 |
| wetting dynamic viscosity | $\mu_w$ | Pa·s | $1.0 \times 10^{-3}$ |
| non-wetting dynamic viscosity | $\mu_{nw}$ | Pa·s | $1.0 \times 10^{-3}$ |
| wetting phase density | $\rho_w$ | $\mathrm{kg\,m^{-3}}$ | $1.0 \times 10^{3}$ |
| Non-wetting phase density | $\rho_{nw}$ | $\mathrm{kg\,m^{-3}}$ | $1.0 \times 10^{3}$ |
| Permeability | $\mathbf{K}$ | $\mathrm{m^2}$ | $1.0 \times 10^{-10}$ |
| Porosity | $n$ | – | $3.0 \times 10^{-1}$ |
| Residual saturation of water | $S_{rw}$ | – | 0 |
| Residual saturation of oil | $S_{nrw}$ | – | 0 |
| Entry pressure | $p_d$ | Pa | $5.0 \times 10^{3}$ |
| Soil distribution index | $\lambda$ | – | 2.0 |
| Capillary pressure | $p^c(S_{eff})$ | Pa | Brooks–Corey model |
| Relative permeability | $\kappa_{rel}(S_{eff})$ | – | Brooks–Corey model |

### 12.1.7 Kueper Problem

Both primary variable schemes are now further tested with a benchmark chosen to examine two-phase flow in heterogeneous media. Kueper and Frind developed a model to simulate their experiment for DNAPL penetration ([168]). The

simultaneous movement of a dense non-wetting phase (DNAPL) through an initially wetting phase (water) saturated heterogeneous porous media may be represented mathematically as a case of two-phase flow. A distinctive feature of the solution is that the primary variables solved for wetting phase pressure and wetting phase saturation, are both existent throughout the solution domain regardless of whether the non-wetting phase is present.

The continuity equation of each phase ($\gamma$) can be defined by

$$\frac{\partial(n\rho^{\gamma}S^{\gamma})}{\partial t} + \nabla \cdot (\rho^{\gamma}\mathbf{q}^{\gamma}) = \mathbf{Q}^{\gamma}, \gamma = w, nw \tag{12.28}$$

where $n$ is porosity, $S^{\gamma}$ is saturation, $\rho^{\gamma}$ is density, $\mathbf{Q}^{\gamma}$ is a source or sink term, and $\mathbf{q}^{\gamma}$ is the Darcy velocity for phase $\gamma$ defined by

$$\mathbf{q}^{\gamma} = -\mathbf{K}\frac{\kappa_r^{\gamma}}{\mu^{\gamma}}(\nabla p^{\gamma} - \rho^{\gamma}\mathbf{g}), \gamma = w, nw \tag{12.29}$$

where $\kappa_r^{\gamma}$ is relative permeability, $\mu^{\gamma}$ is viscosity, $p^{\gamma}$ is pressure for phase $\gamma$, $\mathbf{K}$ is intrinsic permeability tensor and $\mathbf{g}$ is the gravitational vector.

Inherently for saturation, the sum of all saturation in pore space is

$$\sum S^{\gamma} = 1. \tag{12.30}$$

Assuming relative preference (i.e., wettability) of the fluid to media exists and it is not negligible, the capillary pressures relation for a two-phase system is defined over representative elementary volume (REV) by

$$p_c = p_{nw} - p_w \tag{12.31}$$

where $p_c$ is capillary pressure, $p_{nw}$ is pressure for the non-wetting phase fluid and $p_w$ is the wetting phase fluid.

### Definition

A 60 cm × 80 cm × 0.6 cm parallel-plate glass-lined cell was packed with four types of sands and initially fully saturated with water. The configuration of the assembled sand lenses and the two sets of the boundary conditions for the $p_w - S_{nw}$ and $p_c - p_{nw}$ schemes are illustrated in Fig. 12.12. Concerning the constitutive relation between relative permeability and saturation and capillary pressure and saturation, they have used the Brooks–Corey model.

Properties of sands for the Brooks–Corey model are measured experimentally and summarized in the following tables. The numerical solutions obtained from the $p_w - S_{nw}$ scheme and the $p_c - p_{nw}$ scheme for the benchmark of [168] are compared against each other in Fig. 12.13 (Tables 12.4–12.6).

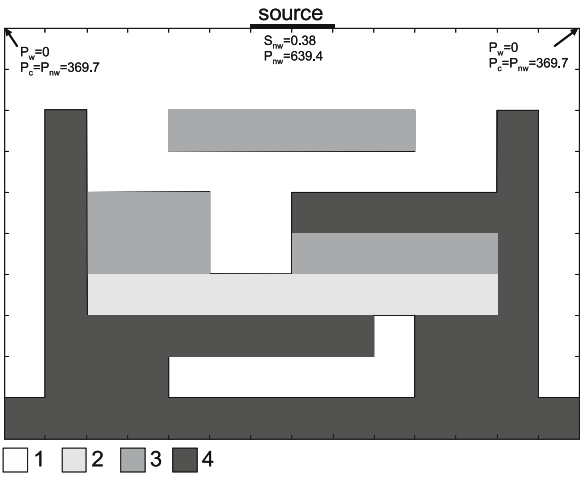


Figure 12.12: Configuration of heterogeneous media in parallel-plate cell

**Results**

Both schemes produce DNAPL plume propagation physically until the plume reaches the less permeable media under the top medium in the model domain. The striking difference occurs at the interface between these two media. While the pwSnw scheme simulates the plume to infiltrate into the less previous medium, the $p_c - p_{nw}$ scheme forces the plume to bypass the less previous medium. A similar experiment and simulation comparison against experimental observation is also conducted by Helmig and Huber [169]. They have reported unphysical fluid behavior captured by the $p_w - S_{nw}$ scheme, a phenomenon that can be avoided with a fully upwind technique ([169]).

## 12.2 Non-isothermal Two-Phase Flow

The multiphase formulation is now extended to examine temperature effects in porous systems.

### 12.2.1 Heat Pipe Problem

When an unsaturated porous medium is subjected to a constant heat flux and the temperature is sufficiently high, water is heated and vaporizes. Vapor flows under its pressure gradient towards the cooler end where it condenses. Vaporization and condensation produce a liquid saturation gradient, creating a capillary pressure gradient inside the porous medium. Condensate flows towards the hot end under the influence of a capillary pressure gradient. This is a heat pipe in an unsaturated porous medium.

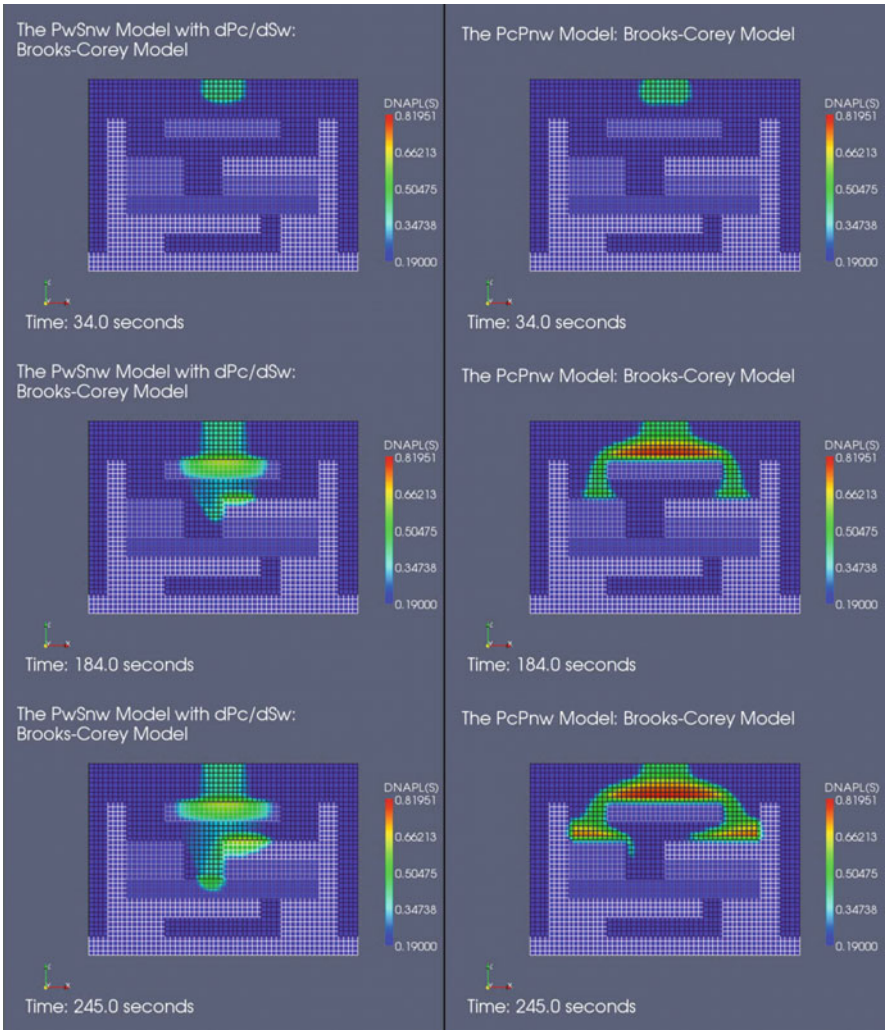


Figure 12.13: Comparison of the results obtained from the $p_w - S_{nw}$ and $p_c - p_{nw}$ schemes. The second column shows good agreement with observed distribution of DNAPL of the experiment [168])

Udell and Fitch derived the pressure gradient of each phase in two-phase flow with heat transfer. The generalized form of the Darcy's law is used to calculate velocity fields

$$\frac{dp^g}{dx} = \frac{\eta q \nu^g}{\mathbf{k} k_{\mathrm{rg}} H_{\mathrm{vap}}} \tag{12.32}$$

$$\frac{dp^l}{dx} = -\frac{\eta q \nu^l}{\mathbf{k} k_{\mathrm{rl}} H_{\mathrm{vap}}} \tag{12.33}$$

Table 12.4: Fluid and medium properties

| Fluid properties | Unit | Wetting fluid | Non-wetting fluid |
|---|---|---|---|
| Density | $\mathrm{kg\,m^{-3}}$ | $1.0 \times 10^3$ | $1.0 \times 10^3$ |
| Viscosity | $Pa \cdots$ | $1.0 \times 10^{-3}$ | $1.0 \times 10^{-3}$ |
| Residual saturation | – | 0.0 | 0.0 |
| Maximum saturation | – | 1.0 | 1.0 |

Table 12.5: Space and time discretization

| Medium properties | Unit | Medium |
|---|---|---|
| $\Delta x$ | m | 0.01 |
| $\Delta t$ | s | 100 |
| Porosity | – | 0.3 |
| Intrinsic permeability | $\mathrm{m^2}$ | $1 \times 10^{-10}$ |
| Brook–Corey's index | – | 2 |
| Entry pressure | Pa | $5 \times 10^3$ |

Table 12.6: Hydraulic properties of sands for the Brooks–Corey model

| Property | $P_d$(Pa) | $\lambda$(-) | $S_{wr}$(-) | k($m^2$) | $n$(-) |
|---|---|---|---|---|---|
| 1 | 369.73 | 3.86 | 0.078 | $5.04 \times 10^{-10}$ | 0.40 |
| 2 | 434.45 | 3.51 | 0.069 | $2.05 \times 10^{-10}$ | 0.39 |
| 3 | 1323.95 | 2.49 | 0.098 | $5.26 \times 10^{-11}$ | 0.39 |
| 4 | 3246.15 | 3.30 | 0.189 | $8.19 \times 10^{-12}$ | 0.41 |

where $\eta$ is the ratio of heat transport caused by convection to the total heat-flux $q$ (see Helming [1997]), $p$ is phase pressure; $\nu^\gamma = \frac{\mu\gamma}{\rho^\gamma}$; $x$ is space coordinate in the x-direction; $\mathbf{k}$ is intrinsic permeability; $k_{r\gamma}$ is relative permeability and $H_{\mathrm{vap}}$ is latent heat of water. $\gamma$ is the phase superscript and $g, l$ stand for gas and liquid phase, respectively. Gas pressure is the sum of two partial pressure, i.e. $p^g = p_a^g + p_w^g$.

The density of the gas phase is the sum of air and vapor density. Air density is according to ideal gas equation,

$$\rho_{\mathrm{ga}} = \frac{M_a p_a}{RT}. \tag{12.34}$$

Energy transport is described by Zhou et al. [1990] as

$$q = -\kappa_{\mathrm{app}} \frac{\partial dT}{dx} + \dot{m}_{\mathrm{vap}} H_{\mathrm{vap}} \tag{12.35}$$

where, $T$ is temperature, $\kappa_{\text{app}}$ is apparent thermal conductivity. Since capillary pressure is the difference of phase pressure, hence from (12.31, 12.32–12.33), the capillary pressure gradient is

$$\frac{dp^c}{dx} = \frac{\eta q}{\mathbf{k} H_{\text{vap}}} \left[ \frac{\nu^g}{k_{\text{rg}}} + \frac{\nu^l}{k_{\text{rl}}} \right]. \tag{12.36}$$

Brooks–Corey presented a water saturation-capillary pressure relation in the following form

$$S = \left( \frac{Pd}{p^c} \right)^{\lambda} \tag{12.37}$$

By comparing this with Leverett's [1941] non-dimensional form we get $Pd = \sigma_0 \left(\frac{n}{\mathbf{k}}\right)^{0.5}$ and $n$ is medium porosity. $\sigma_0$ is interfacial tension at reference temperature $T_0$. Here, $S$ is scaled as following

$$S = \frac{S_{\text{w}} - S_{\text{lr}}}{1 - S_{\text{lr}} - S_{\text{gr}}}. \tag{12.38}$$

The constants $S_{\text{lr}}, S_{\text{gr}}$ are residual saturations. And for interfacial tension we have used the following correlation given by Olivella and Gens [2000]

$$\sigma(T) = 0.3258 C^{1.256} - 0.148 C^{2.256}; \quad T \leq 633.15\text{K}, \tag{12.39}$$

where, $C = 1.0 - \frac{T}{647.3\ K}$. The Brooks–Corey relative permeability relations are

$$\mathbf{k}_{\text{rg}} = (1 - S)^2 \left( 1 - S^{\frac{2+\lambda}{\lambda}} \right); \quad \mathbf{k}_{rl} = S^{\frac{2+3\lambda}{\lambda}}. \tag{12.40}$$

Using (12.36–12.37), we can write the following forms of saturation gradient

$$\frac{dS}{dx} = \frac{S^{1.5}}{P_d} \frac{2\eta q}{\mathbf{k} H_{\text{vap}}} \left[ \frac{\nu^g}{k_{\text{rg}}} + \frac{\nu^l}{k_{\text{rl}}} \right]. \tag{12.41}$$

Now (12.41) is integrated over the two-phase zone. Where the two-phase zone can be defined by imposing the limits of integration (see Udell [1985]): $S = S_0$ at $x = 0$ and $S = S_1$ at $x = L$. The saturation vapor density $\rho_{\text{sat}}$, depends on temperature, and is estimated by following relation

$$\rho_{\text{sat}} = 1.0 \times 10^{-3} \exp\left( a - \frac{b}{T} \right), \tag{12.42}$$

where the constants $a = 19.81$ and $b = 4975.9$. In the porous medium, we must account for a decrease in vapor density due to capillarity. The amount of decrease in vapor density is describe by the Kelvin equation as follows

$$\rho_{\text{gw}} = \rho_{\text{sat}} \exp\left( -\frac{M_{\text{w}} p^c}{\rho^l R T} \right) \tag{12.43}$$

where $M_{\mathrm{w}}$ is water molecular weight; $\rho^l$ is liquid density and $R$ is universal gas constant. From (12.42–12.43), we get temperature as function of vapor density and capillary pressure as

$$T = \frac{A}{B} \tag{12.44}$$

where

$$A = b + \frac{M_{\mathrm{w}} p^c}{\rho^l R}; B = a - 3 - \log\left(\rho_{\mathrm{gw}}\right)$$

$\rho_{\mathrm{gw}}$ is temperature dependent, which introduces difficulty for the temperature calculation. Hence we need to know temperature gradient, which is possible from (12.44) along with the vapor pressure gradient

$$\frac{dp_{\mathrm{gw}}}{dx} = \frac{\eta q \nu_w^g}{\mathbf{k} k_{\mathrm{rg}} H_{\mathrm{vap}}}. \tag{12.45}$$

The form of the temperature gradient is

$$\frac{dT}{dx} = \frac{\frac{BM_{\mathrm{w}}}{\rho^l R}\frac{dp^c}{dx} + \frac{A}{p_{\mathrm{gw}}}\frac{dp_{\mathrm{gw}}}{dx}}{B^2 + \frac{A}{T}}. \tag{12.46}$$

Apparent thermal conductivity can be obtained from heat flux divided by temperature gradient (see Udell [1985]. The coupled differential equations (12.32), (12.36), (12.41) and (12.46 ) are integrated using an Euler method with the following boundary conditions at $x = 0$

$$S = S_0; \quad p^g = p_0^g; \quad p^c = p_0^c; \quad T = T_0. \tag{12.47}$$

Material parameters are presented in Table 12.7.

Table 12.7: Material parameters for the heat pipe problem

| Meaning | Symbol | Value | Unit |
|---|---|---|---|
| Column length | $L$ | m | 2.6 |
| Liquid dynamic viscosity | $\mu^l$ | Pa.s | $1.0 \times 10^{-3}$ |
| Gas dynamic viscosity | $\mu^g$ | Pa.s | $1.0 \times 10^{-5}$ |
| Liquid density | $\rho^l$ | kg.m$^{-3}$ | $1.0 \times 10^3$ |
| Permeability | $\mathbf{k}$ | m$^2$ | $1.0 \times 10^{-13}$ |
| Porosity | $n$ | – | 0.3 |
| Residual saturation of water | $S_{\mathrm{rl}}$ | – | 0.2 |
| Residual saturation of oil | $S_{\mathrm{rg}}$ | – | 0 |
| Soil distribution index | $\lambda$ | – | 2.0 |
| Capillary pressure | $p^c(S)$ | Pa | Brooks–Corey model |
| Relative permeability | $\kappa_{r\gamma}(S)$ | – | Brooks–Corey model |

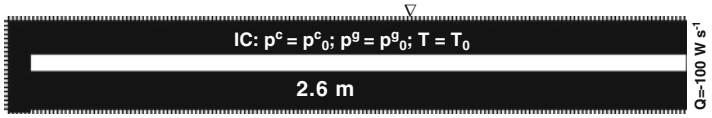


Figure 12.14: Schematic of the benchmark

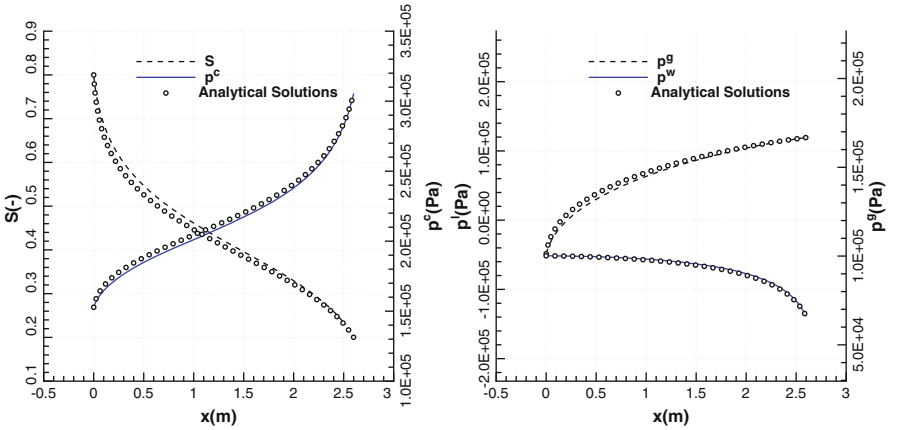


Figure 12.15: Comparison of water saturation and pressure profiles from present solution with an analytical solution

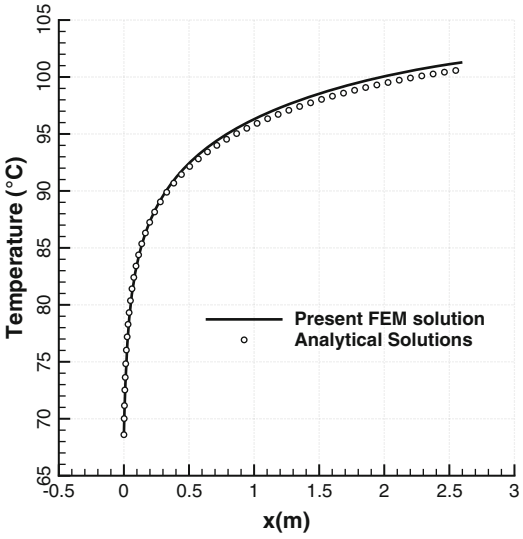


Figure 12.16: Comparison of the temperature profile from present solution with an analytical solution

### Definition

The test benchmark problem for heat pipe effects is formulated in one-dimension. A horizontal column of length 2.6 m is filled with fluid subjected to a constant heat flux at the right end and where the left end temperature is maintained beneath the saturation temperature (Fig. 12.14).

### Results

In order to establish non-isothermal two-phase flow in OpenGeoSys, we have verified numerical solutions with analytical results. Profiles of water saturation $S_{\mathrm{w}}$, gas phase pressure $p^g$, liquid phase pressure $p^l$ and temperature $T$ are presented in Figs. 12.15, and 12.16. Numerical solutions are agreeable. Line elements have been used with variable time steps and a non uniform space discretization. We use a combined monolithic/ staggered coupling scheme i.e. monolithic for the two-phase flow and staggered for the heat transport.

# Chapter 13

# Consolidation ($H^nM$) Processes

*by Joshua Taron, Norihiro Watanabe, and Wenqing Wang*

The purpose of the benchmarks in this chapter is to test the validity of coupled hydro-mechanical (HM) and two-phase hydro-mechanical ($H^2M$) processes. Mechanical compression generates a fluid pressure response, while pressure storage and dissipation modify the mechanical condition via the effective stress. The tests we use are convenient and fundamental validations of the deformation and flow modules, most importantly guaranteeing that the coupling is correct between them.

We examine real systems, where fluids, solids, and solid grains are compressible. In the single phase case, comparisons are made between two finite element coupling schemes: 1) Monolithic: solid and fluid equations solved in a single matrix and 2) Staggered: solid and fluid equations solved iteratively. Two-phase flow consolidation is also examined and then an adapted form of extended finite elements (XFEM) is used to observe the fluid-mechanical interaction in a discrete fracture-matrix system.

## 13.1 Single Phase Consolidation

Let us begin by introducing a few governing equations.

O. Kolditz et al. (eds.), *Thermo-Hydro-Mechanical-Chemical Processes in Fractured Porous Media*, Lecture Notes in Computational Science and Engineering 86,
DOI 10.1007/978-3-642-27177-9_13, © Springer-Verlag Berlin Heidelberg 2012

### 13.1.1 Fluid Mass and Momentum Balance

Linear momentum balance for the fluid follows Darcy:

$$v_{ri} = \phi\left(v_i - v_{si}\right) = -\frac{k_{ij}}{\mu}\left(\frac{\partial p}{\partial x_j} + \rho g_j\right), \tag{13.1}$$

for the intrinsic permeability, $k_{ij}$, dynamic viscosity, $\mu$, and density, $\rho$. The subscript $r$ considers that fluid velocity is relative to motion of the deformable solid ($v_{si}$), so that $v_i$ is absolute fluid velocity, and $v_{ri}$ is relative. Conservation of fluid mass requires,

$$\frac{\partial}{\partial t}\left(\phi\rho\right) + \frac{\partial}{\partial x_i}\left(\phi\rho v_i\right) = 0. \tag{13.2}$$

Fluid properties are functions of temperature and pressure. The fluid density time derivative appearing in the mass balance equation may be expanded to

$$\frac{d\rho}{dt} = \rho\left(\frac{1}{K_f^p}\frac{dp}{dt} - \frac{1}{K_f^T}\frac{dT}{dt}\right), \tag{13.3}$$

with fluid compressibility given by $1/K_f^p = \left(1/\rho\right)\left(\partial\rho/\partial p\right)|_T$ and for the fluid thermal expansion coefficient $1/K_f^T = -\left(1/\rho\right)\left(\partial\rho/\partial T\right)|_p$. In these definitions we utilize moduli ($K$ = inverse compressibility). Also, because thermal effects are not considered in these examples, the temperature dependence may be neglected. Utilizing the Lagrangian total derivative of a component relative to the moving solid, $d_s/dt = \partial/\partial t + v_{si}\partial/\partial x_i$, and a moving fluid, $d_f/dt = \partial/\partial t + v_{fi}\partial/\partial x_i$, substituting for absolute fluid velocity and dividing through by density gives,

$$\phi\left(\frac{1}{K_f^p}\frac{dp}{dt} + \frac{d_s\phi}{dt} + \frac{\partial v_{si}}{\partial x_i}\right) = -\frac{\partial}{\partial x_i}\left(v_{ri}\right). \tag{13.4}$$

To obtain the porosity time derivative, we expand the solid mass balance to obtain

$$\frac{d_s\phi}{dt} = \frac{\left(1-\phi\right)}{\rho_s}\frac{\partial\rho_s}{\partial t} + \left(1-\phi\right)\frac{\partial v_{si}}{\partial x_i}. \tag{13.5}$$

Substituting this gives,

$$\frac{\phi}{K_f^p}\frac{dp}{dt} + \left[\frac{\partial v_{si}}{\partial x_i} + \frac{\left(1-\rho_s\right)}{\rho_s}\frac{\partial\rho_s}{\partial t}\right] = -\frac{\partial}{\partial x_i}\left(v_{ri}\right). \tag{13.6}$$

Utilizing Biot's formulation to represent the solid density time derivative and assuming small strain yields the full fluid mass balance ([170] and [171]),

$$\left( \frac{\phi}{K_f^p} + \overbrace{\frac{(\alpha - \phi)}{K_g}}^{A} \right) \frac{dp}{dt} + \overbrace{\alpha \frac{\partial v_{si}}{\partial x_i}}^{B} = -\frac{\partial}{\partial x_i} \left( v_{ri} \right), \tag{13.7}$$

where $K_g$ is the solid grain bulk modulus, and $\alpha$ is the Biot-Willis coefficient ($\alpha = 1 - K/K_g$ in an ideal, fully interconnected porous media). The bracketed terms $A$ and $B$ represent important couplings from the mechanical system to that of the fluid. All are vital in the HM procedure and without them the equation simplifies to a standard fluid flow equation with fluid compressibility storage in the pressure time derivative.

### 13.1.2 Solid Momentum Balance

We begin with the concept of effective stress,

$$\sigma'_{ij} = \sigma_{ij} + \alpha p \delta_{ij}, \tag{13.8}$$

for the effective stress, $\sigma'$, and the total stress, $\sigma$; negative in compression. Balance of linear momentum is defined by,

$$\frac{\partial \sigma_{ij}}{\partial x_j} + F_i = 0, \tag{13.9}$$

for the body force, $F = \rho_m \mathrm{g}$ and where $\rho_m = \phi \rho_f + (1 - \phi)\rho_s$ is density of the mixture. From the definition of strain, $\varepsilon_{ij} = \left( \partial u_i / \partial x_j + \partial u_j / \partial x_i \right)/2$, and an arbitrary stress-strain relationship of the form $\sigma = \mathbf{D}\varepsilon\left(\mathbf{u}\right)$, we write the displacement formulation of mechanical equilibrium (neglecting thermal effects) for isotropic linear elasticity,

$$\frac{\partial}{\partial x_j} \left[ G \frac{\partial u_i}{\partial x_j} + (\lambda + G) \frac{\partial u_j}{\partial x_i} - \alpha p \delta_{ij} \right] + F_i = 0, \tag{13.10}$$

where $G$ and $\lambda$ are the Lamè constants. Changes to the fluid system are therefore visited in mechanical equilibrium via the effective stress.

### 13.1.3 Numerical Solution Scheme

The numerical solution of (13.7) and (13.10) can be obtained with any convenient method. In these benchmarks, we use a standard Galerkin finite element

spatial discretization with time discretization following a generalized first order finite difference scheme, as implemented in OpenGeoSys. Note that (13.10) is an equilibrium equation, and has no time dependency other than that imposed by coupling terms to fluid behavior. The result is a set of coupled linear equations in pressure, $p$, and solid displacement, $u$. The two equations may be solved sequentially and iteratively, or monolithically as a single system. We present results using both solution schemes in the following benchmarks.

### 13.1.4 Terzaghi Consolidation: Monolithic and Staggered Approaches

In the HM problem, mechanical compression generates a fluid pressure response, while pressure storage and dissipation affect the mechanical condition via the effective stress. Terzaghi has provided the framework to test such a problem. A cartoon of the problem to be examined is shown in Fig. 13.1. This test is a necessary, but not fully sufficient condition for correct implementation of a hydromechanical simulator. It guarantees correct implementation of the coupling relationships between the 1)fluid and 2)mechanical system.

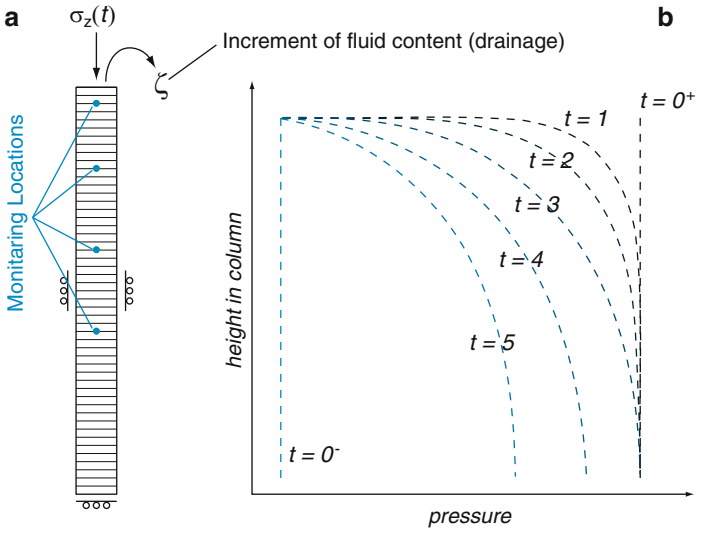


Figure 13.1: Terzaghi problem. (**a**) 2-D column ($p = 0$ initially) stress applied to top of column which is a free draining boundary. Other boundaries are no-flow and roller displacement. Stress may be applied as a single step-load, or as a function of time. Pressure and displacement are monitored in time at specific locations. (**b**) Anticipated (conceptual) pressure profiles within the column with the progression of time for a step-load of applied stress (in full column, not at monitoring locations)

### Definition

For a single fluid phase, the analytical solution for pressure dissipation is available. The analytical solution to this problem has been utilized a number of times for this very purpose. Beginning from the 1-D fluid diffusion equation of hydrogeology (simply a fluid mass balance equation),

$$\frac{\partial p}{\partial t} - c\frac{\partial^2 p}{\partial z^2} = 0, \tag{13.11}$$

where $c$ is 1-D fluid diffusivity. The pore pressure response to a vertical load, $\sigma_z$, applied linearly over time ($\sigma_z^{t=0^-} = 0$) to the top of the column at a rate, $\dot{\sigma}_z = d\sigma_z/dt$, is, ([172], (6.50)),

$$\frac{p\left(z,t\right)}{p_0} = \left\{1 - \left(\frac{L-z}{L}\right)^2 - \frac{32}{\pi^3}\left[\sum_{m=0}^{\infty}\frac{\left(-1\right)^m}{\left(2m+1\right)^3}\exp\left[-\psi^2 ct\right]\cos\left[\psi\left(L-z\right)\right]\right]\right\}, \tag{13.12}$$

where the total pressure generation is

$$p_0 = \frac{L^2}{2c}\left(B_v\dot{\sigma}_z\right), \tag{13.13}$$

for the factor, $\psi = \left(2m+1\right)\pi/\left(2L\right)$, the total column length, $L$, and the location in the column (downward from the applied stress), $z$. The 1-D Skempton coefficient,

$$B_v = -\frac{\delta\bar{p}}{\delta\sigma_{zz}}\bigg|_{\varepsilon_{xx}=\varepsilon_{yy}=\zeta=0} = \frac{\alpha}{K_v S_v}, \tag{13.14}$$

is given purely by micromechanical, poroelastic considerations from the uniaxial drained bulk modulus, $K_v$, and the 1-D specific storage, $S_v$ (Table 13.1). The 1-D diffusivity is also a derivative of the 1-D storage:

$$c = \frac{k}{\mu S_v}, \tag{13.15}$$

and also the permeability, $k$, and viscosity, $\mu$. See Table 13.1, [173], and [172] for additional details regarding poroelastic relationships. If utilizing an applied step load at time $t = 0^+$, we can generate another analytical solution for pressure, and also displacement. For this validation, we utilize only the linear loading rate. Because displacement is the primary variable in our FEM formulation, the displacement must be accurate in order to generate the correct pressure response: we find no need to reproduce the results of a step load analysis here.

We choose a rather long (50 m) column of rock with material properties similar to those of Berea sandstone (Table 13.2). The column is discretized uniformly into 50 FEM grid cells. Geometry is shown in Fig. 13.1, which shows a single column surrounding by displacement roller boundaries allowed to compress from the top where a loading rate, $\dot{\sigma}_z$, is applied at time $t = 0^+$. Fluid pressure is

Table 13.1: Fundamental poroelastic relationships. Many potential combinations are available, these representing only one possibility

| Parameter | Description | Equation |
|---|---|---|
| $B$ | Skempton coefficient | $\alpha/[\alpha - \phi\,(1-\alpha) + \phi K/K_f]$ |
| $K^u$ | Undrained bulk modulus | $K/\,(1-\alpha B)$ |
| $G$ | Shear modulus | $3K\,(1-2\nu)\,/\,(2+2\nu)$ |
| $\nu^u$ | Undrained Poisson's ratio | $(3K^u - 2G)/(6K^u + 2G)$ |
| $B_v$ | Uniaxial Skempton coefficient | $B(1+\nu_u)/(3-3\nu_u)$ |
| $K_v$ | Uniaxial bulk modulus | $3K(1-\nu)/(1+\nu)$ |
| $K_v^u$ | Uniaxial undrained bulk modulus | $3K^u\,(1-\nu^u)/(1+\nu^u)$ |
| $S_v$ | Uniaxial storage | $\alpha/(K_v B_v)$ |

Table 13.2: Solid properties

| Property | Symbol | Unit | Value |
|---|---|---|---|
| *Berea sandstone* | | | |
| Drained bulk modulus | $K$ | GPa | 8.0 |
| Poisson ratio | $\nu$ | – | 0.20 |
| Porosity | $\phi$ | – | 0.19 |
| Permeability | $k$ | m$^2$ | $1.9 \times 10^{-13}$ |
| Biot-Willis coefficient | $\alpha$ | – | 0.8 |
| *Westerly granite* | | | |
| Drained bulk modulus | $K$ | GPa | 25.0 |
| Poisson ratio | $\nu$ | – | 0.25 |
| Porosity | $\phi$ | – | 0.02 |
| Permeability | $k$ | m$^2$ | $5.0 \times 10^{-15}$ |
| Biot-Willis coefficient | $\alpha$ | – | 0.6 |

initially null. Compression of the column leads to a rapid pressure increase and a subsequent drainage of pressure over time from the top of the column. The load is applied quickly enough to allow pressure to build with time. The topmost boundary is free drainage for fluid flow, all others being no-flow (Table 13.3).

**Results**

Simulations are conducted using both a staggered (fluid and solid equations solved iteratively) and monolithic (fluid and solid equations solved in a single matrix) with OpenGeoSys. Results are shown in Fig. 13.2 for two alternate material property scenarios: Berea sandstone and Westerly granite. The solution

Table 13.3: Fluid properties

| Property | Symbol | Unit | Value |
|---|---|---|---|
| Bulk modulus | $K_f$ | GPa | 2.27 |
| Density | $\rho$ | kg/m$^3$ | 997.05 |
| Viscosity | $\mu$ | Pa×s | $8.9008 \times 10^{-4}$ |

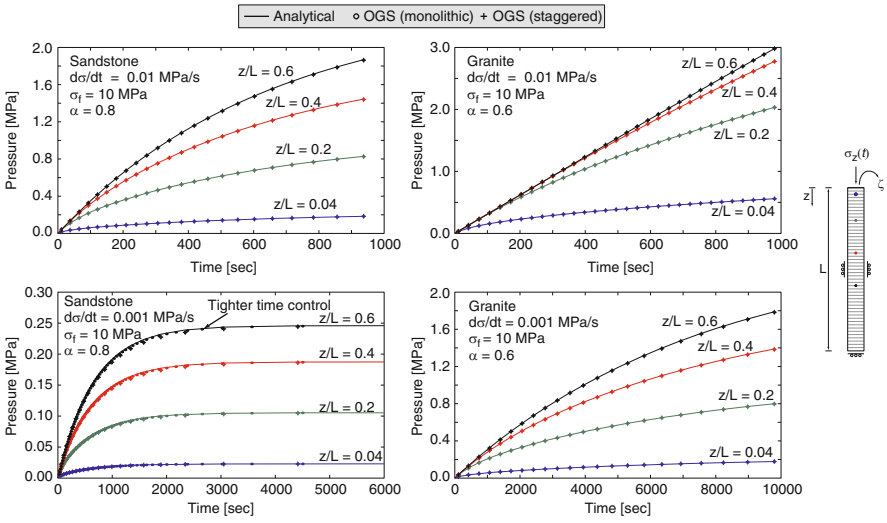


Figure 13.2: Results of HM coupling

is accurate in all cases. We note a small inaccuracy in the slower loading rate for sandstone that illustrates the impact of tolerance in the time step control. Here, we add one extra data set (small dots) with tighter time control, which shows that tighter accuracy can be achieved with this adjustment.

While the monolithic solution is unconditionally stable for an implicit time-stepping scheme, the staggered solution suffers limitations. When the fluid becomes highly incompressible relative to the solid, the solution will diverge. We provide the general criterion that stability is achieved with $B_v < 0.5$. This criterion is generally independent of loading rate. The implications of this are important, such that for Westerly granite if incompressible grains are used the solution is unstable at 25°C for the properties of Table 13.2. Stability can be enforced by increasing the value of porosity that is used, or decreasing $\alpha$, or with any adjustment that brings $B_v$ above 0.5. The staggered solution is stable for all realistic cases (everything compressible) we have tried. For very sharply applied loads such as a step load applied at $t = 0^+$, however, the staggered solution will become unstable even with this criterion. It is important for a

given problem and set of solid/fluid properties to examine stability with the above benchmark before extending to the full system.

Time steps are adaptively controlled with a tolerance based on the rate of pressure change over a time step. Such a scheme is capable of ensuring accuracy in HM or H$^2$M problems. Note the importance of the tolerance in Fig. 13.2.

### 13.1.5 Distributed Footing: Poroelastic Cube (3D)

We consider a vertical cross-section through homogeneous soil. Due to symmetry we can limit the investigation to half of the domain. The model domain is then extending 8 meters in length and 5 meters in height. The problem is solved in 2D and 3D space, respectively.

#### Definition

A strip loading is imposed ($\sigma_{yy} = \sigma_0$ in $x \in [0, 1]$), with zero stresses ($\sigma_{yy} = \sigma_{xy} = 0$ in $x \in (1, 8]$) and zero pressure at the top; no horizontal flux, no horizontal displacements and zero shear stresses at left and right boundaries with no vertical flux and no displacement at the bottom (Fig. 13.3).

#### Results

The 3D geometry expands the 2D domain by extruding the 2D shape by 1m in the off-plane direction (Fig. 13.4). Results at the critical step, i.e., the first step, are shown in Figs. 13.5–13.7. The results produced using the 2D model with triangular elements and the 3D model with tetrahedral elements match each other well, thus providing confidence in higher dimensions.

### 13.1.6 Distributed Footing: Poroelastic Cube (3D) with Dynamic Consolidation

Considering the same problem design as the previous section, the mechanical calculation is now extended to allow for time-dependent deformation. In other words, solid displacements are no longer solved to equilibrium, so that solid velocity may be non-zero following the solution of the mechanical system.

#### Definition

All stresses and pressure are zero at the beginning of deformation. Strip loading ($\sigma_{yy} = \sigma_0$ in $x \in [0, 1]$), zero stresses ($\sigma_{yy} = \sigma_{xy} = 0$ in $x \in (1, 8]$) and zero pressure at the top; no horizontal flux, no horizontal displacements and zero shear stresses at left and right hand sides; no vertical flux and no displacements at bottom (Fig. 13.3).

Material parameters are given in Table 13.4.

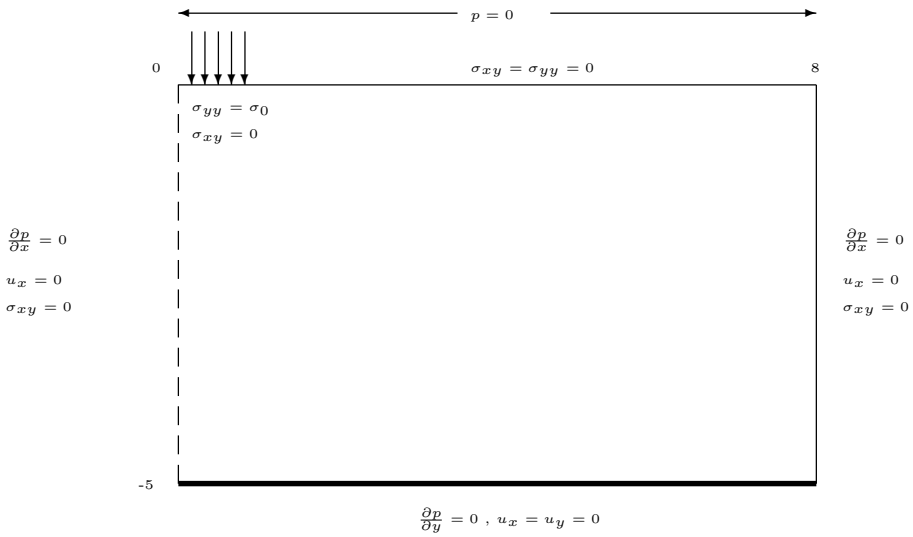


Figure 13.3: Conceptualization of the footing problem. Properties are Young's modulus, $E = 3 \times 10^4$ N/m$^2$, Poisson's ratio, $\nu = 0.2$, permeability, $k = 10^{-10}$ m$^2$, and fluid viscosity, $\mu = 10^{-3}$ Pa s

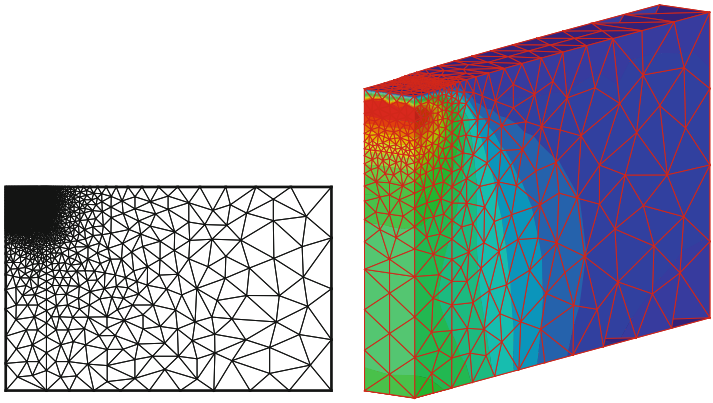

Figure 13.4: Mesh geometry

**Results**

Time duration is ten time steps. The following figures, Figs. 13.8–13.11 show the distribution of state variables within the domain after 10 time steps. Such distribution is similar to the static case illustrated in Fig. 13.6.

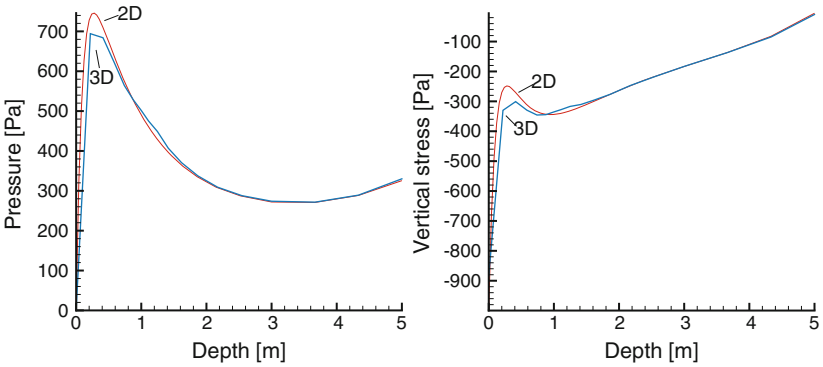


Figure 13.5: Comparison along symmetric axis

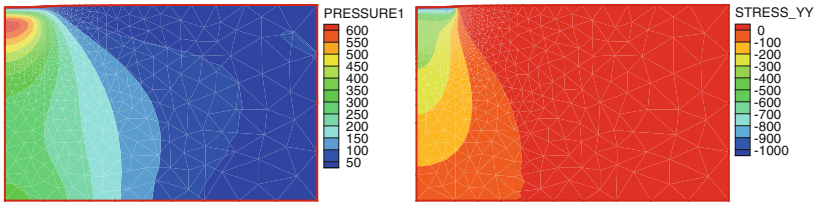


Figure 13.6: 2D contours

Table 13.4: Material properties of dynamic consolidation problem

| Property | Value | Unit |
|---|---|---|
| Young's modulus | $3 \times 10^4$ | $\mathrm{N/m^2}$ |
| Poisson's ratio | $0.2, 0.4$ | – |
| Permeability | $10^{-10}$ | $\mathrm{m^2}$ |
| Fluid viscosity | $10^{-3}$ | Pa s |

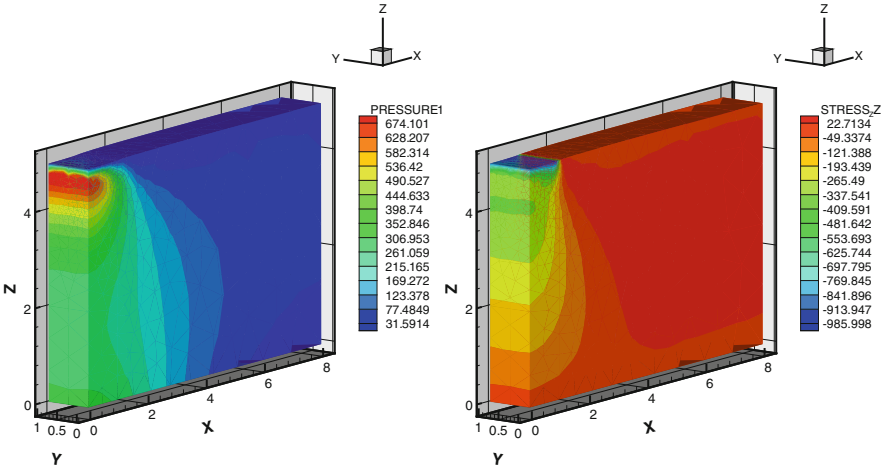


Figure 13.7: 3D contours

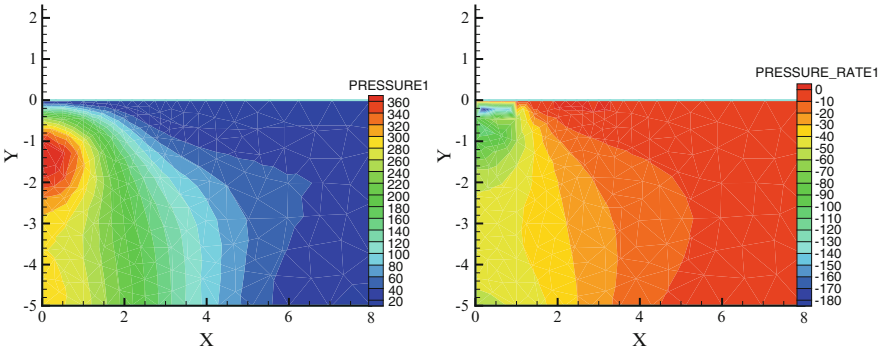


Figure 13.8: Fluid pressures $p$ and rate of fluid pressure $\dot{p}$

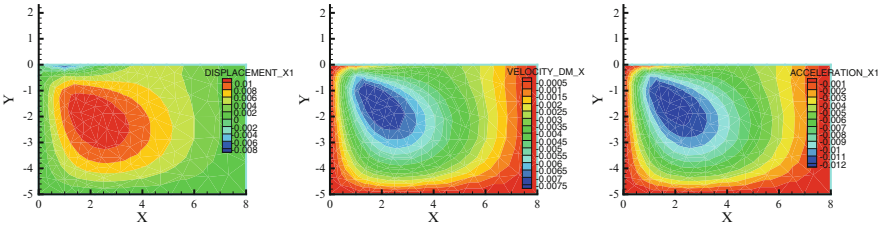


Figure 13.9: Displacement, its rate and acceleration: horizontal component

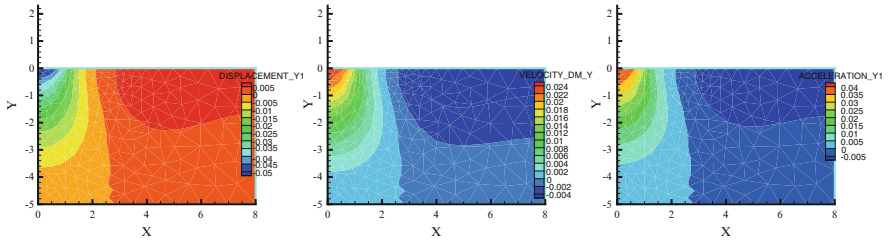


Figure 13.10: Displacement, its rate and acceleration: vertical component

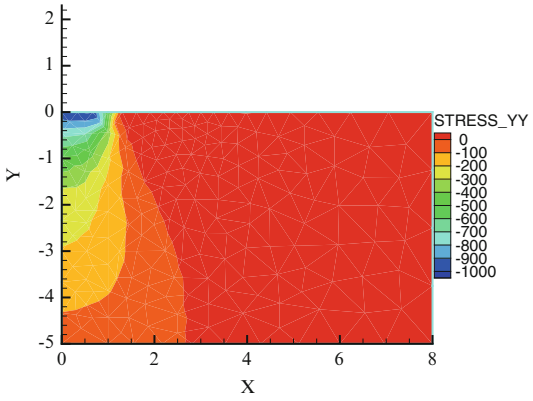


Figure 13.11: Vertical stress

## 13.2 Unsaturated (Richards) Consolidation

### 13.2.1 Fluid Mass and Momentum Balance

The general fluid mass balance equation for a multi-phase fluid system is simply an extension of (13.1),

$$\frac{\partial}{\partial t}\left(\phi S_\alpha \rho\right) + \frac{\partial}{\partial x_i}\left(\phi S_\alpha \rho v_i\right) = Q \tag{13.16}$$

where $S_\alpha$ is saturation of fluid $\alpha$ and $Q$ is the source term. We are interested in a Richards type model for the evolution of fluid pressure under the assumption that the gas phase is immobile, i.e. $v_{gi} = 0$. Assuming incompressible grains, $\alpha = 0$, and expanding terms as in the single phase case, we obtain the following Richards equation for an unsaturated deformable porous medium,

$$\left(S_w \frac{\phi}{K_w}\frac{dp_w}{dt} - \phi\rho_w \frac{dS_{nw}}{dp_c}\right)\frac{dp_w}{dt} + \nabla\cdot\left\{\frac{\mathbf{k}k_w^r}{\mu_w}\left(-\nabla p_w + \rho_w \mathbf{g}\right)\right\} + \mathrm{S}_w\rho_w\nabla\cdot\frac{d\mathbf{u}}{dt} = Q. \tag{13.17}$$

A constitutive equation, the water content function obtained by experiments, characterizes the relationship between $p_c$ and $S_w$, and therefore the derivative $dS_w/dp_c$.

### 13.2.2 Solid Momentum Balance

The deformation process is described in the same manner as for the single phase case, but now fluid pressure acting on the grains is also dependent on the liquid saturation,

$$\nabla \cdot (\sigma - S_w p_w \mathbf{I}) + \rho \mathbf{g} = \mathbf{0} \tag{13.18}$$

### 13.2.3 FEM Solution Scheme

The standard Galerkin finite element approach is applied for the numerical solution of the PDEs (13.17) and (13.18) resulting into the following system of algebraic equations, here solved as a monolithic system,

$$\begin{bmatrix} \mathbf{C}_{pp} & \mathbf{C}_{pu} \\ \mathbf{0} & \mathbf{0} \end{bmatrix} \frac{d}{dt} \begin{Bmatrix} \mathbf{p_w} \\ \mathbf{u} \end{Bmatrix} + \begin{bmatrix} \mathbf{K}_{pp} & \mathbf{0} \\ \mathbf{K}_{up} & \mathbf{K}_{uu} \end{bmatrix} \begin{Bmatrix} \mathbf{p_w} \\ \mathbf{u} \end{Bmatrix} = \begin{Bmatrix} \mathbf{r}_p \\ \mathbf{r}_u \end{Bmatrix} \tag{13.19}$$

### 13.2.4 Terzaghi Consolidation: Unsaturated

#### Definition

This example follows the general form of the Terzaghi consolidation used previously. Boundary conditions and model design follows roughly the experiment of Liakopoulos [165]. The physical experiment of Liakopoulos was conducted in a column packed with so-called Del Monte sand. Moisture content and tension at several points along the column were measured with tensiometers.

In the simulation, the column has a size of 0.1 m × 1 m and is discretized into 20 quadrilateral elements (Fig. 13.12). Initial pressure is zero everywhere in the domain. Boundary conditions for both fluid and displacement fields are depicted in Fig. 13.12. Such initial and boundary conditions imply that the sample in fully saturated at the beginning, the water is allowed to flow out from the bottom boundary.

The capillary pressure, $p_c(S)$, function we use is,

$$p_c = \left( \frac{1 - S}{1.9722} \times 10^{11} \right)^{\frac{1}{2.4279}}, \tag{13.20}$$

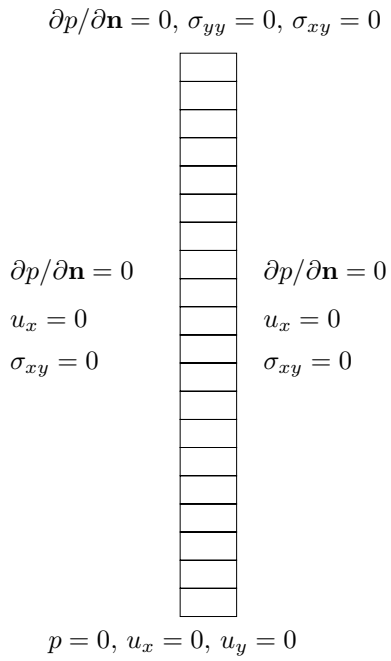


Figure 13.12: Boundary conditions

Table 13.5: Material parameters

| Property | Value | Unit |
|---|---|---|
| Young's modulus, $E$ | MPa | 1.3 |
| Poisson's ratio, $\nu$ | – | 0.4 |
| Solid grain density, $\rho_s$ | $\mathrm{kg\,m^{-3}}$ | 2000 |
| Liquid density, $\rho_w$ | $\mathrm{kg\,m^{-3}}$ | $\mathrm{kg\,m^{-3}}$ |
| Porosity, $\phi$ | – | 0.2975 |
| Permeability, $k$ | $\mathrm{m^2}$ | $4.5 \times 10^{-13}$ |
| Water viscosity, $\mu_w$ | Pa s | $10^{-3}$ |

along with the relative permeability, $k_r(S)$, relationship,

$$k_r = 1 - 2.207(1 - S)^{1.0121} \tag{13.21}$$

fit the measured data for saturations larger than 0.84. The physical parameter are given in Table 13.5.

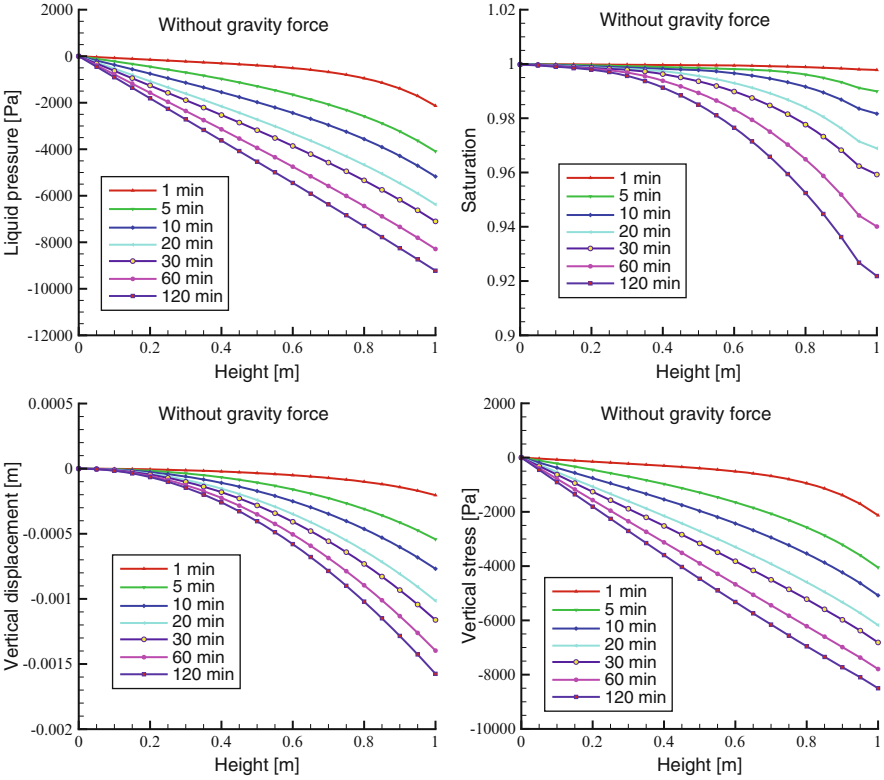


Figure 13.13: Simulated results without gravity force

**Results**

We conduct two kinds of simulations: one including the gravity force as a load for the mechanical displacement field, and the other ignoring gravity. For the case of non-gravity, Fig. 13.13 shows the history profiles of water pressure $p$, water saturation $S$, vertical solid displacement $u_y$ and vertical stress $\sigma_{yy}$.

Vertical profiles of results obtained by taking into account the gravity force are shown in Fig. 13.14. If one compares the saturation result with that obtained by ignoring the gravity force, one can easily see that the desaturation procedure is enhanced by the presence of solid gravity acting on the solid displacement field. This highlights the impact of displacement on water pressure and coupling effects between the two equation systems.

### 13.2.5 DECOVALEX Unsaturated Test Case

DECOVALEX is an international code comparison project for the verification of thermo-hydro-mechanical (THM) and thermo-hydro-chemical (THC) numerical simulators [174].

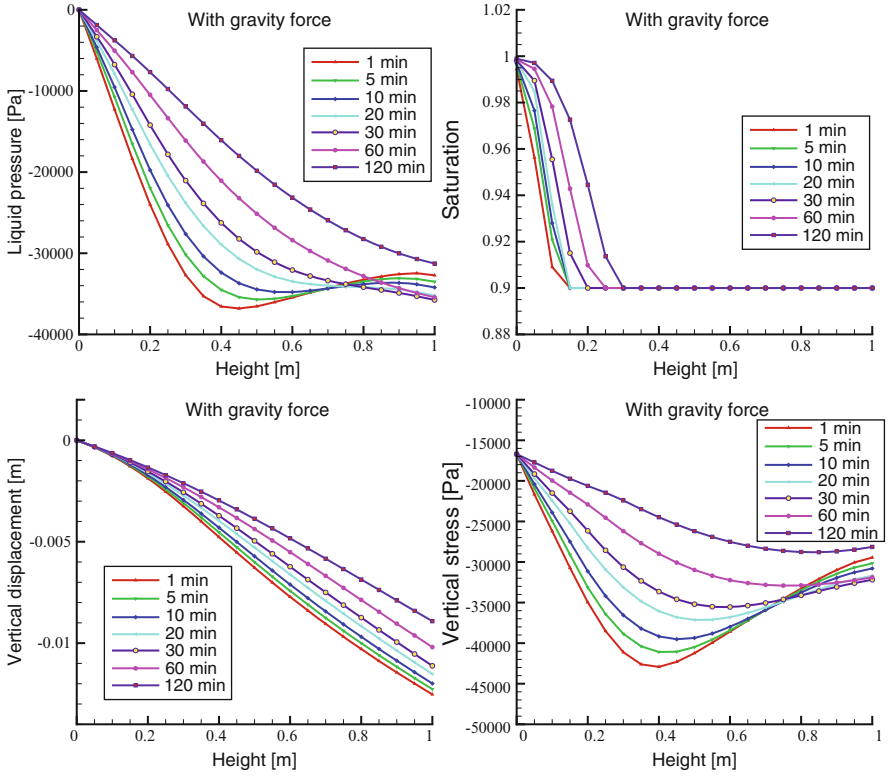


Figure 13.14: Simulated results with gravity force

### Definition

The original DECOVALEX-THM benchmark definition is a 2-D problem [174]. For the comparison of different HM swelling models, we consider a simplified case representing a horizontal cross-section through the 2-D domain. Examined here is the isothermal HM consolidation problem with unsaturated flow (Fig. 13.15).

The simplified model takes a rectangle shape. The mesh of the domain together with material types are shown in Fig. 13.16. Figure 13.17 illustrates the definition of initial and boundary conditions for the horizontal cross-section. Observation points are set at $x = 0.45\,\mathrm{m}$, $x = 1.10\,\mathrm{m}$ to record temporal breakthrough curves. Material parameters for the rock mass and bentonite are given in Table 13.6.

The dependency of capillary pressure and relative permeability on liquid saturation for both rock and bentonite are depicted in Fig. 13.18.

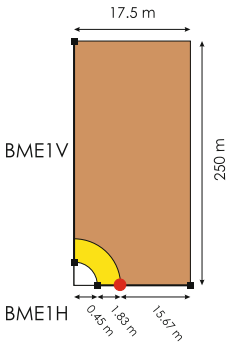


Figure 13.15: 2D DECOVALEX HM definition and simplification for the benchmark exercise BME1H

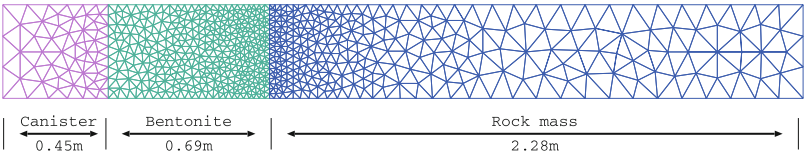


Figure 13.16: Mesh of the simplified BME1H model including canister, bentonite, and rock mass sections

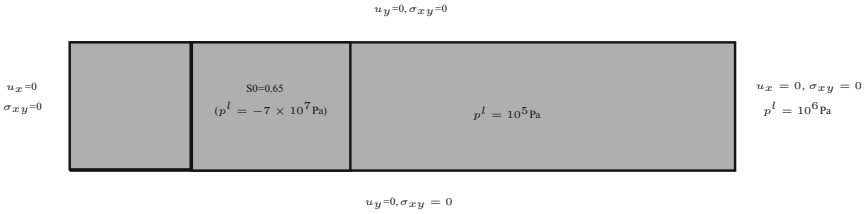


Figure 13.17: Simplified horizontal cross-section model

### Results

Figure 13.19 displays a contour plot of saturation and vertical swelling stress in the domain. Swelling stress in the bentonite is clearly induced by change of water saturation. Figure 13.20 shows the simulated horizontal profiles (top) and temporal evolutions at the observation point (bottom) of water saturation and swelling stress based on the linear swelling model proposed by Rutqvist (2005) [175], which defines the increment of swelling stress to be proportional to liquid saturation increment,

$$\Delta\sigma^{sw} = \beta \Delta S_w, \tag{13.22}$$

Table 13.6: Solid properties of different materials

| Parameter | Unit | Value |
|---|---|---|
| *Rock mass properties* | | |
| Density | kg/m$^3$ | 2,700 |
| Young's modulus | GPa | 35 |
| Poisson ratio | – | 0.3 |
| Porosity | – | 0.01 |
| Saturated permeability | m$^2$ | $1.0 \times 10^{-17}$ |
| | | |
| *Bentonite properties* | | |
| Density | kg/m$^3$ | 1,600 |
| Young's modulus | MPa | 317 |
| Poisson ratio | – | 0.35 |
| Saturated permeability | m$^2$ | $2.0 \times 10^{-21}$ |

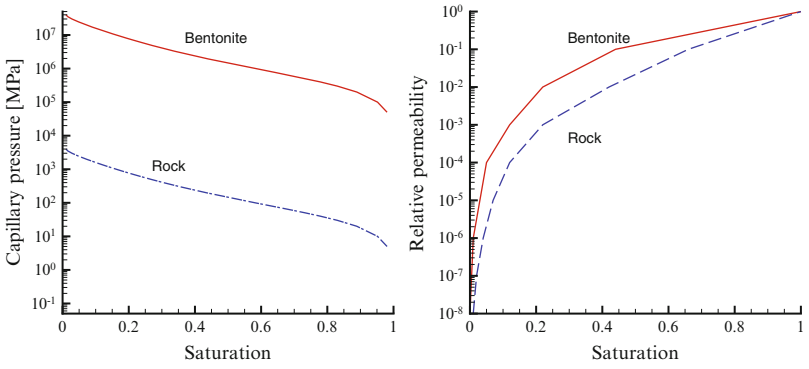


Figure 13.18: Capillary pressure and relative permeability functions

where $\beta$ is a swelling coefficient that could be called the maximum swelling stress. As the saturation change approaches unity, swelling stress approaches $\beta$.

Figure 13.20 shows the simulated horizontal profiles and temporal evolutions at the observation point of water saturation and swelling stress based on the linear swelling model proposed by Rutqvist (2005) [175].

## 13.3 Two-Phase Consolidation

For the two-phase system the governing equations presented in the previous sections must be expanded slightly.

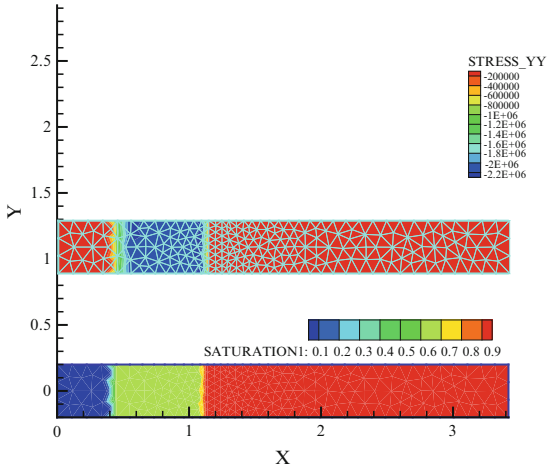


Figure 13.19: Distribution of saturation and vertical swelling stress

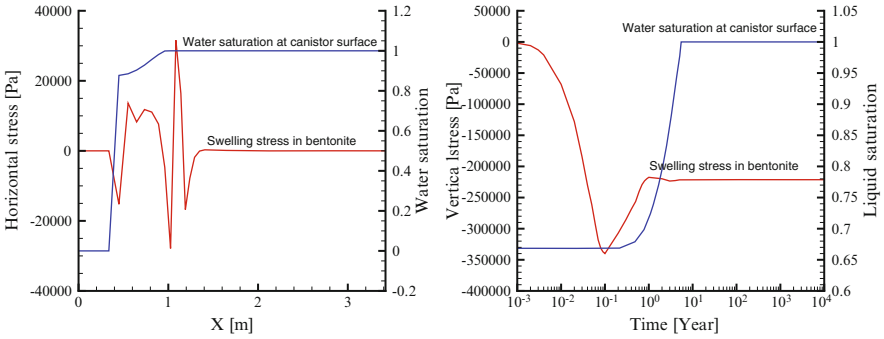


Figure 13.20: Horizontal profile (*top*) and temporal evolution at observation point (*bottom*) of water saturation and swelling stress

### 13.3.1 Fluid Mass and Momentum Balance

Following the same mass balance procedure as for the single phase case, and gathering two mass balance equations, one for a wetting fluid (i.e. liquid) and one for a non-wetting (i.e. gas) fluid, we write,

$$\begin{aligned} S_w \left( \frac{\phi}{K_w} + \frac{\alpha - \phi}{K_s} \right) \frac{dp_w}{dt} - \phi \frac{dS_{nw}}{dt} + \ldots \\ \nabla \cdot \left\{ \frac{\mathbf{k} k_w^r}{\mu_w} \left( -\nabla p_w + \rho_w \mathbf{g} \right) \right\} + \alpha \mathrm{S}_w \nabla \cdot \frac{\partial \mathbf{u}}{\partial t} = 0 \end{aligned} \tag{13.23}$$

for mass balance of the wetting fluid, subscript $w$, and,

$$
\begin{aligned}
&S_{nw}\left(\frac{\phi}{K_{nw}}+\frac{\alpha-\phi}{K_s}\right)\frac{dp_w}{dt}+\phi\left(1-\frac{S_{nw}}{K_{nw}}\frac{\partial p_c}{\partial S_w}\right)\frac{dS_{nw}}{dt}+\ldots\\
&\nabla\cdot\left\{\frac{\mathbf{k}k^r_{nw}}{\mu_{nw}}\left(-\nabla p_w-\frac{\partial p_c}{\partial S_w}\nabla S_{nw}+\rho_{nw}\mathbf{g}\right)\right\}+\alpha S_{nw}\nabla\cdot\frac{\partial\mathbf{u}}{\partial t}=0
\end{aligned}
\tag{13.24}
$$

for mass balance of the non-wetting fluid, subscript $nw$. In these equations, $k^r_\alpha$ is relative permeability of phase $\alpha$, $\rho_\alpha$ is density of phase $\alpha$, and we have chosen wetting pressure, $p_w$, and non-wetting saturation, $S_{nw}$, as primary variables in the solution scheme. Other primary variables, such as capillary pressure, $p_c$, and non-wetting pressure, $p_{nw}$, could also have been chosen with algebraic manipulation, but our benchmark example requires constant, $p_c = 0$, capillary pressure for comparison with an anylitical solution. This is not possible, of course, if $p_c$ is a primary variable. Any viable permeability saturation function may be chosen for the example; we use the Brooks–Corey function.

For the numerical solution, storage due to two different fluids with two different compressibilities and densities is handled implicitly with solution of the above equations. For the analytical solution, we must define an effective compressibility as a function of fluid saturation and properties of each fluid. For immiscible fluids without penetrating bubbles, two compressible materials behave as resistors in series with respect to bulk modulus, thus the effective modulus is

$$
\frac{1}{K_f}=\frac{S_w}{K_w}+\frac{S_{nw}}{K_{nw}}. \tag{13.25}
$$

### 13.3.2 Solid Momentum Balance

As with the single phase case, balance of linear momentum is defined by,

$$
\frac{\partial\sigma_{ij}}{\partial x_j}+F_i=0, \tag{13.26}
$$

but now the body force is a function of two fluids, $F = \rho_m \mathrm{g}$ for the mixture density $\rho_m = \phi(S_w\rho_w + S_{nw}\rho_{nw}) + (1-\phi)\rho_s$, and insertion of the elastic consitutive law yields for solid displacement,

$$
\frac{\partial}{\partial x_j}\left[G\frac{\partial u_i}{\partial x_j}+(\lambda+G)\frac{\partial u_j}{\partial x_i}-\alpha\bar{p}\delta_{ij}\right]+F_i=0, \tag{13.27}
$$

where *mean* fluid pressure is defined as $\bar{p} = S_w p_w + S_{nw} p_{nw}$.

### 13.3.3 FEM Solution Scheme

For the two-phase simulations, the two fluid balance equations are solved in a single global equation, with an iterative coupling to the solid balance equation.

### 13.3.4 Terzaghi Consolidation: Two-Phase

#### Definition

For this comparison, we may utilize the same analytical solution as was done for the single phase case in the previous section, although the solution must represent the mean fluid pressure $\bar{p} = S_w p_w + S_{nw} p_{nw}$, for the final relationship,

$$\frac{\bar{p}\,(z,t)}{\bar{p}_0} = \left\{1.0 - \left(\frac{L-z}{L}\right)^2 - \frac{32}{\pi^3}\left[\sum_{m=0}^{\infty} \frac{(-1)^m}{(2m+1)^3} \exp\left[-\psi^2 ct\right] \cos\left[\psi\,(L-z)\right]\right]\right\}, \tag{13.28}$$

with pressure generation defined in the same manner,

$$\bar{p}_0 = \frac{L^2}{2c}\left(B_v \dot{\sigma}_z\right), \tag{13.29}$$

but where the uniaxial Skempton coefficient, $B_v$, must be defined (see Table 13.1) based upon the effective fluid modulus. Fluid properties are then defined for two separate fluids (Table 13.7)

Table 13.7: Two-phase fluid properties

| Property | Symbol | Unit | Value |
|---|---|---|---|
| *Wetting fluid properties* | | | |
| Bulk modulus | $K_w$ | GPa | 2.933 |
| Density | $\rho_w$ | kg/m$^3$ | 997.05 |
| Viscosity | $\mu_w$ | Pa·s | $8.9008 \times 10^{-4}$ |
| Saturation | $S_w$ | – | 0.8 |
| *Non-wetting fluid properties* | | | |
| Bulk modulus | $K_{nw}$ | GPa | 1.187 |
| Density | $\rho_{nw}$ | kg/m$^3$ | 997.05 |
| Viscosity | $\mu_{nw}$ | Pa·s | $8.9008 \times 10^{-4}$ |
| Saturation | $S_{nw}$ | – | 0.2 |

#### Results

Initially the column is at zero pressure and is saturated uniformly with both fluids ($Sw = 0.8$) and we apply $p_c = 0$ and $k_w^r = k_{nw}^r = 0.5$. Note that we utilize a different compressibility for each fluid in order to exercise both fluid balance equations, with the analytical solution obtained using the *effective* fluid modulus, and with the *effective* modulus having an identical value to the single fluid modulus, 2.27 GPa, used above in the single phase case.

Results are shown in Figs. 13.21 and 13.22 for sandstone and granite (see Table 13.2) for incompressible and compressible grains. With reference to the staggered stability criterion discussed in the HM problem above, because we are examining incompressible grains here the solution becomes unstable for granite. Therefore, an alternate value of porosity (0.06) is utilized (in the granite simulations) to ensure stability, which results in $B_v < 0.5$. Such an adjustment is not required when compressible (real) grains are used, but is utilized none-the-less for comparison with the incompressible grain solution. All results are ideally accurate.

Time steps are adaptively controlled with a tolerance based on the rate of pressure change over a time step. Such a scheme is capable of ensuring accuracy in HM or H2M problems. Note the importance of the tolerance in Fig. 13.2.

### 13.3.5 Invarient Stress: Flow and Storage in a Compressible Medium

It is also possible, and sometimes useful, to test two-phase storage and pressure dissipation in a deformable media at invarient stress. This test guarantees accurate implementation of fluid storage within the mass matrix (time derivative term) of the fluid mass balance PDE.

#### Definition

We utilize the same problem as above, but now no stress is applied and no mechanical equilibrium performed. The analytical solution may be derived from the Carslaw and Jaeger [176] solution for heat dissipation within a solid slab,

$$\bar{p}\,(z,t) = \frac{4p_0}{\pi}\sum_{m=0}^{\infty}\left\{\frac{1}{2m+1}\sin\left[z\left(\frac{(2m+1)\,\pi}{2L}\right)\right]\exp\left[-ct\left(\frac{(2m+1)\,\pi}{2L}\right)^2\right]\right\}, \tag{13.30}$$

where $\bar{p}_0$ is initial mean pressure within the column.

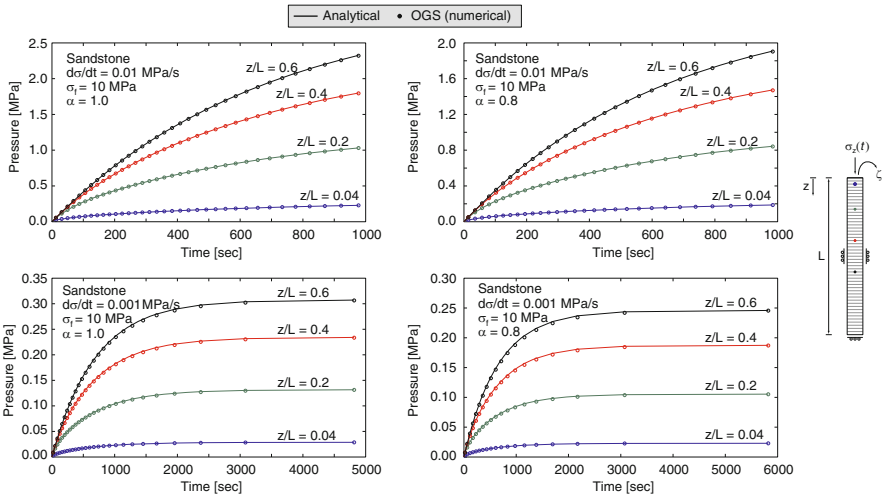


Figure 13.21: Sandstone solutions

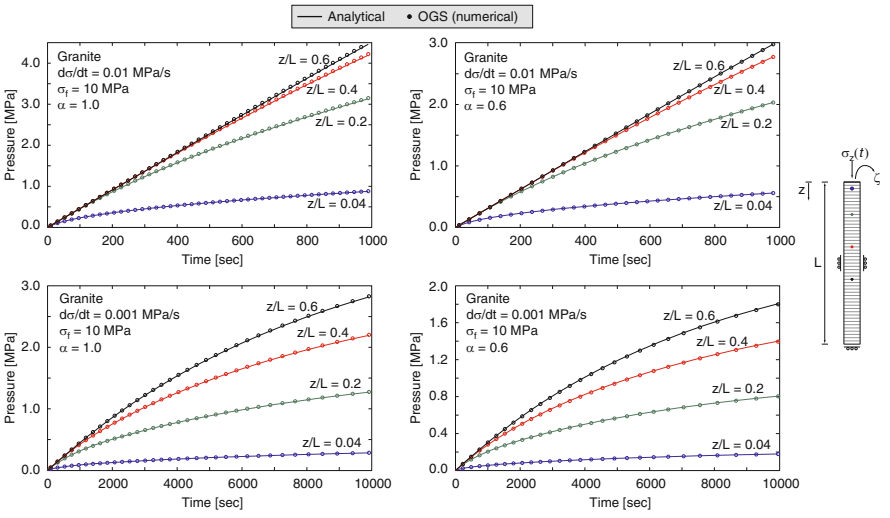


Figure 13.22: Granite solutions. Here, a porosity of 0.06 is used to ensure stability for the incompressible grain simulations (an adjustment that is not needed for compressible grains, but is used there also to maintain consistency)

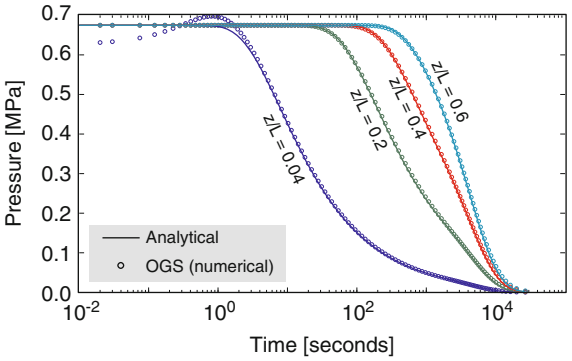


Figure 13.23: Two-phase flow with mechanical storage

**Results**

Results are shown in Fig. 13.23. We note that with an appropriate mixing rule for storage in the two phase formulation, the result is ideal. Very small values of time and $z$ can produce inaccuracies; however, this will always be the case, barring a very small mesh discretization.

### 13.3.6 Cam-Clay Consolidation with Swelling

As before, (13.23) and (13.24) define the fluid system. In this example, however, we choose a numerical solution in OpenGeoSys that accomodates pressure variables in the solution vector. Both equations are therefore algebraically manipulated so that the primary variables to solve for are now the capillary pressure, $p_c$, and the non-wetting pressure, $p_{nw}$,

$$\phi\rho_w \frac{\partial S_w}{\partial p_c}\frac{dp_c}{dt} + \rho_w S_w \nabla\cdot\frac{d\mathbf{u}}{dt} + \nabla\cdot\left[\rho_w \frac{\mathbf{k}k_w^r}{\mu_w}\left(-\nabla p_{nw} + \nabla p_c + \rho_w \mathbf{g}\right)\right] = Q_w \quad (13.31)$$

$$\begin{aligned} &-\phi\rho_{nw}\frac{\partial S_w}{\partial p_c}\frac{dp_c}{dt} + \phi\left(1-S_w\right)\left(\frac{\partial \rho_{nw}}{\partial p_{nw}}\frac{dp_{nw}}{dt} + \frac{\partial \rho_{nw}}{\partial p_c}\frac{dp_c}{dt}\right) + \\ &\left(\rho_w S_w + \rho_{nw}\left(1-S_w\right)\right)\nabla\cdot\frac{d\mathbf{u}}{dt} + \nabla\cdot\left[\rho_{nw}\frac{\mathbf{k}k_{nw}^r}{\mu_{nw}}\left(-\nabla p_{nw} + \rho_{nw}\mathbf{g}\right)\right] = Q_{nw} \end{aligned} \quad (13.32)$$

where in this case we assume that solid grains are incompressible.

As in Sect. 14.2, swelling stress is based on the linear swelling model proposed by Rutqvist (2005) [175], which defines the increment of swelling stress to be proportional to liquid saturation increment,

$$\Delta\sigma^{sw} = \beta\Delta S_w, \quad (13.33)$$

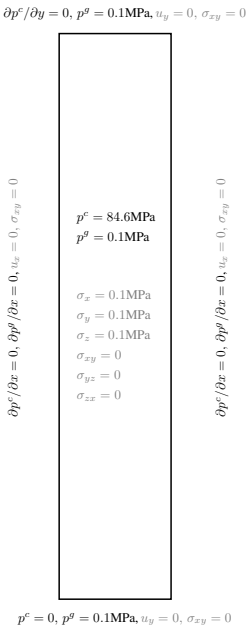


Figure 13.24: Model set-up with initial and boundary conditions

where $\beta$ is a swelling coefficient that could be called the maximum swelling stress. As the saturation change approaches unity, swelling stress approaches $\beta$.

### Definition

Figure 13.24 shows the axi-symmetric model domain for the confined swelling test as well as the initial and boundary conditions for the two-phase flow consolidation problem with hydraulic and fluid properties given in Table 13.8. The parameters of the elasto-plastic swelling model are given in Table 13.9 for Cam-Clay plasticity.

### Results

Figure 13.25 shows the temporal evolution of water saturation on the bottom of the sample between OpenGeoSys and Code-Bright.

Table 13.8: Hydraulic properties

| Meaning | Value | Unit |
|---|---|---|
| Liquid density, $\rho_w$ | $1,000$ | kg/m$^3$ |
| Liquid viscosity, $\mu_w$ | $10^{-3}$ | Pa s |
| Gas density, $\rho_{nw}$ | Clapeyron equation | kg/m$^3$ |
| Gas viscosity, , $\mu_{nw}$ | $1.8 \times 10^{-5}$ | Pa s |
| Intrinsic permeability, $k$ | $0.6 \times 10^{-20}$ | m$^2$ |
| Porosity, $\phi$ | 0.4 | m$^3$/m$^3$ |
| Media properties for liquid: | | |
| *Relative permeability* | Power law $k_w^r = S_e^3$ | |
| Residual saturation | 0 | – |
| Maximum saturation | 1 | – |
| *Water retention* | van Genuchten | |
| Exponential index, m | 0.42 | – |
| Air entry pressure, $p_0$ | 62 | MPa |
| Relative permeability of gas, $k_{nw}^r$ | $5.103 \times 10^{-12} \left[e(1 - S^l)\right]^{4.3}$ | $e$, void ratio |

Table 13.9: Plasticity parameters for the Cam-Clay model

| Parameter | Value | Unit |
|---|---|---|
| Slope of the critical state line, $M$ | 1.5 | – |
| Virgin compression index, $\lambda_p$ | 1.5 | – |
| Swelling/recompression index, $\kappa$ | 0.1 | – |
| Initial preconsolidation pressure, $p_c$ | 8.0 | MPa |
| Initial void ratio, $e$ | 0.7 | – |
| Poisson ratio | 0.4 | – |
| Initial ($s = 0$) elastic slope for $1 + e - p$, $\kappa_{i0}$ | 0.01 | – |
| Initial ($\sigma = 0$) elastic slope for $1 + e - s$, $\kappa_{s0}$ | 0.25 | – |
| Minimum bulk modulus, $K_{min}$ | 10 | MPa |
| First parameter for $\kappa_s$, $\alpha_{ss}$ | $-0.03$ | MPa$^{-1}$ |
| Second parameter for $\kappa_s$, $\alpha_{sp}$ | $-0.1609$ | – |
| Parameter for $\kappa_i$, $\alpha_i$ | $-0.003$ | MPa$^{-1}$ |
| Reference mean stress, $p_{ref}$ | 0.1 | MPa |

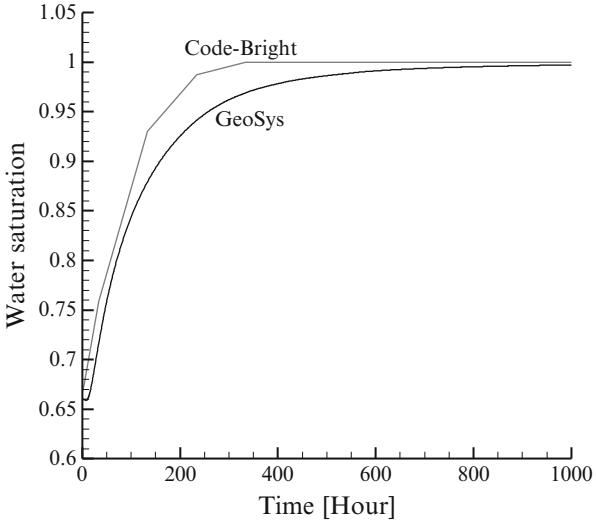


Figure 13.25: Water saturation evolution at the sample bottom

## 13.4 Flow and Mechanics in Discrete Fracture-Matrix Rock Systems

### 13.4.1 Hydro-Mechanical Response of a Single Fracture Within a Rock Matrix (2D)

**Definition**

This example is a fluid injection problem into a single discrete fracture surrounded by an impermeable rock matrix in two-dimensional space and validates the proposed lower-dimensional interface elements with local enrichments for the nonlinear, coupled HM problem. The test case is designed to mimic the semi-analytical similarity solution available in [177], which has been used to verify numerical codes such as ROCMAS II [178], GEOCRACK [179], and FEHM [180]. Test parameters are referred to those of [180]. The solution is available based on the following assumptions:

1. The fluid compressibility is small compared to the compliance of the fracture aperture under normal effective stress. (This is valid for liquid saturated fractures.)

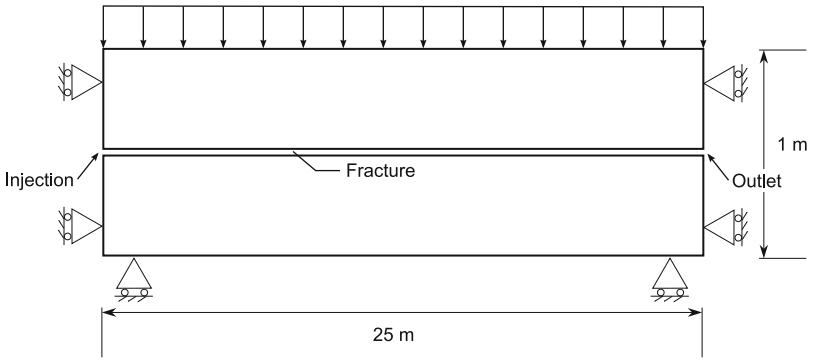


Figure 13.26: Fluid injection into a discrete fracture-rock matrix system

2. Fluid flow in a fracture is laminar flow between parallel surfaces.
3. Fracture deformation is not hysteretic.
4. The gradient in aperture along the fracture is small. There is no shear deformation of the fracture or the fracture does not dilate when sheared.
5. Displacements parallel to the fracture are negligible everywhere within the rock mass.

Figure 13.26 shows a sketch of the calculation model. The major fracture lies horizontally in the middle of an impermeable rock block. The fracture is subjected to a uniform in-situ stress $\sigma_{yy} = 50$ MPa normal to the fracture. Initially, fracture aperture is uniformly $b_0 = 1.0 \cdot 10^{-2}$ mm and fluid pressure is $p_0 = 11.0$ MPa along the fracture. At time $t = 0^+$, fluid is injected at the left-most edge of the fracture (in the form of constant boundary pressure, $p = 11.9$ MPa) and a sudden increase of pressure in the fracture results. The injection pressure induces elastic fracture opening and a subsequent increase of fracture permeability and storage capacity.

### Semi-analytical Solution

Wijesinghe [177] derived the ordinal differential equation with the dimensionless aperture $w$. The semi-analytical solution can be obtained by solving the equation as an initial value problem using the fourth order Runge-Kutta method. For details, please refer to the original work [177] (Table 13.10).

Table 13.10: Model parameters

| Symbol | Parameter | Value | Unit |
|---|---|---|---|
| *Fluid* | | | |
| $\rho^l$ | Density | 1000.0 | $\mathrm{kg} \cdot \mathrm{m}^{-3}$ |
| $\mu$ | Viscosity | 0.001 | Pa·s |
| *Porous medium* | | | |
| $\rho^s$ | Density | 2716.0 | $\mathrm{kg} \cdot \mathrm{m}^{-3}$ |
| $S_s$ | Specific storage | $1.0 \cdot 10^{-10}$ | $\mathrm{Pa}^{-1}$ |
| $k$ | Permeability | $1.0 \cdot 10^{-21}$ | $\mathrm{m}^2 \cdot \mathrm{s}^{-1}$ |
| $\phi$ | Porosity | 0.1 | % |
| $E$ | Young's modulus | 60 | GPa |
| $\nu$ | Poisson ratio | 0.0 | – |
| $\alpha$ | Biot constant | 1.0 | – |
| *Fracture* | | | |
| $b_0$ | Initial aperture | $1.0 \cdot 10^{-5}$ | m |
| $S_s$ | Specific storage | 0.0 | $\mathrm{Pa}^{-1}$ |
| $k_n$ | Joint normal stiffness | 100 | $\mathrm{GPa} \cdot \mathrm{m}^{-1}$ |
| $k_s$ | Joint shear stiffness | 100 | $\mathrm{GPa} \cdot \mathrm{m}^{-1}$ |
| $\alpha$ | Biot constant | 1.0 | – |

### Numerical Solution

Boundary fluid pressure is fixed at $t = 0^+$ to 11.9 MPa at the left and 11 MPa at the right. Line elements with local enrichment were used to represent the discrete fracture and quadrilateral elements for surrounding rock matrix. Very fine vertical discretization is required near the fracture, i.e. $\Delta y$=0.001 m. The time step is selected as 10 s and a Newton–Raphson iteration is utilized to solve the nonlinear equation.

### Results

Simulation results for pressure and fracture aperture are presented in Fig. 13.27 for a lengthwise profile along the fracture. When fluid is injected, the fracture aperture is instantaneously opened to nearly $1.9 \cdot 10^{-2}$ mm at the injection point ($x = 0$ m). With time, this fracture opening behavior gradually propagates

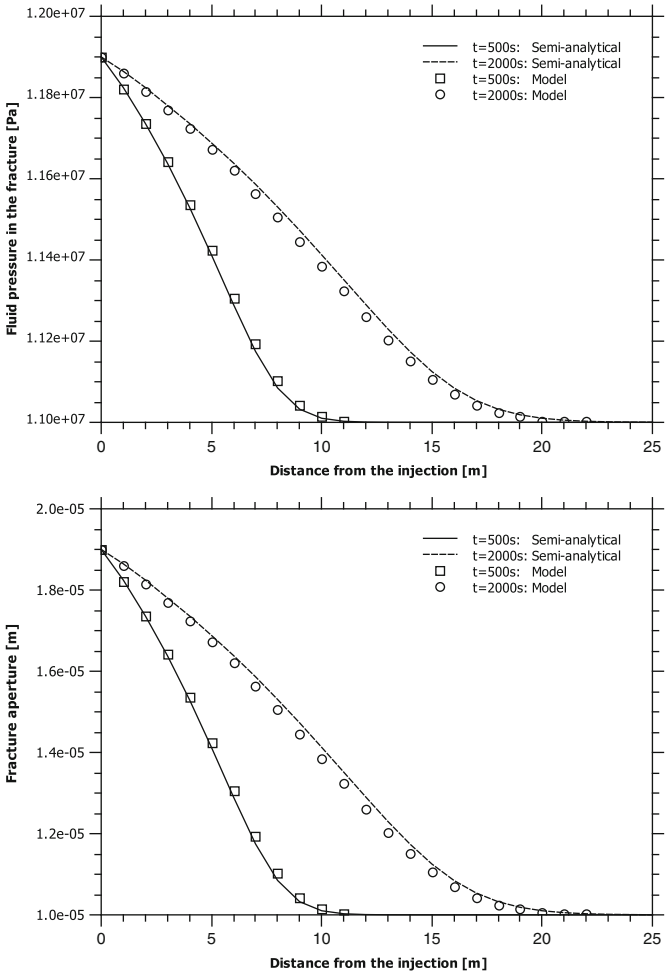


Figure 13.27: Profile along the fracture: pressure (*left*) and aperture (*right*)

toward the right-most, low-pressure edge of the fracture. Linear constitutive laws dictate a linear variation in fracture aperture relative to fluid pressure. Figure 13.27 shows good agreement between the numerical method and the semi-analytical solution.

# Chapter 14

# Thermomechanics

*by Wenjie Xu, Wenqing Wang, Norihiro Watanabe, Jürgen Hesser, and Stephanie Krug*

In this chapter, we consider coupled thermo-mechanical (TM) processes in a porous medium. For a heat transport problem in any medium, the governing equation is given by

$$\rho C_p T' = -\nabla \mathbf{q}_{\mathrm{T}} + Q_{\mathrm{T}}(\boldsymbol{x}, t),\ \boldsymbol{x} \in \mathbb{R}^3 \tag{14.1}$$

where $\rho$ is medium density, $C_p(T)$ is the specific heat capacity, $Q_{\mathrm{T}}$ is the heat source and $\mathbf{q}_{\mathrm{T}}$ is the heat flux, which takes the form

$$\mathbf{q}_{\mathrm{T}} = -K_e \nabla, T \tag{14.2}$$

for solid and

$$\mathbf{q}_{\mathrm{T}} = -K_e \nabla\, T + n \sum_{\gamma}^{phase} (\rho^{\gamma} C_p^{\gamma}) T \mathbf{v},\ \gamma = \text{liquid, gaseous} \tag{14.3}$$

for porous media, considering advective and diffusive fluxes with $K_e$ as the heat conductivity. For porous media, the specific heat capacity consists of portions of solid, liquid and gaseous phases as

$$\rho C_p = \sum_{\gamma}^{phase} (\rho^{\gamma} C_p^{\gamma}) \tag{14.4}$$

O. Kolditz et al. (eds.), *Thermo-Hydro-Mechanical-Chemical Processes in Fractured Porous Media*, Lecture Notes in Computational Science and Engineering 86,
DOI 10.1007/978-3-642-27177-9_14, © Springer-Verlag Berlin Heidelberg 2012

where $\gamma$ specifies a solid, liquid or gaseous phase. The boundary conditions are given by

$$\mathbf{q}_{\mathrm{T}} \cdot \mathbf{n} = q_{\Gamma}^{\mathrm{T}}, \text{ or } \quad T = T_{\Gamma}, \forall \boldsymbol{x} \in \partial\Omega \tag{14.5}$$

and the initial condition reads

$$T(\boldsymbol{x}, t) = T_0(\boldsymbol{x}), \forall \boldsymbol{x} \in \Omega \tag{14.6}$$

with $\mathbf{n}$, the normal direction at $\boldsymbol{x} \in \partial\Omega$

For the mechanical process, the total strain rate $\Delta\boldsymbol{\epsilon}$ can be decomposed into its elastic (reversible) and thermal components,

$$\Delta\boldsymbol{\epsilon} = \mathbb{C}(\Delta\boldsymbol{\epsilon}^e - \alpha\,\mathbf{I}\Delta T) \tag{14.7}$$

where $\mathbb{C}$ is the constitutive tensor, $\alpha$ is the linear thermal expansion coefficient, $\mathbf{I}$ is the identity tensor and $\Delta T$ is temperature change. With the generalized Hook's law, the total stress with the thermal effect can be expressed as

$$\Delta\boldsymbol{\sigma} = \mathbb{C}(\Delta\boldsymbol{\epsilon} - \alpha\,\mathbf{I}\Delta T) \tag{14.8}$$

where $\boldsymbol{\sigma}$ is the stress tensor. The volume of a solid increases or decreases with temperature changes and homogeneous bodies expand evenly in each direction by increasing temperatures. In this case no variation of the stresses occurs. If the deformation of the solid is prevented, the stresses increase or decrease with temperature changes. This phenomenon can be easily calculated by analytical solutions of the Hooke's linear elastic model. The equations of the mechanical behaviour base on the Hooke's law for linear elastic materials are:

$$\varepsilon_x = \frac{1}{E}\left(\sigma_x - \nu\left(\sigma_y + \sigma_z\right)\right) + \alpha\Delta T \tag{14.9}$$

$$\varepsilon_y = \frac{1}{E}\left(\sigma_y - \nu\left(\sigma_x + \sigma_z\right)\right) + \alpha\Delta T \tag{14.10}$$

$$\varepsilon_z = \frac{1}{E}\left(\sigma_z - \nu\left(\sigma_x + \sigma_y\right)\right) + \alpha\Delta T \tag{14.11}$$

where $\varepsilon_{i,\,i=x,y,z}$ are strains, $\sigma_i$ are stresses, $E$ is Young's modulus and $\nu$ is Poisson's ratio.

## 14.1 Thermoelastic Stress Analysis in Homogeneous Material (3 D)

### 14.1.1 Definition

The top and bottom of a solid body that consists of one homogeneous material are heated. The aim of this calculation is to find out the isotropic state of stress

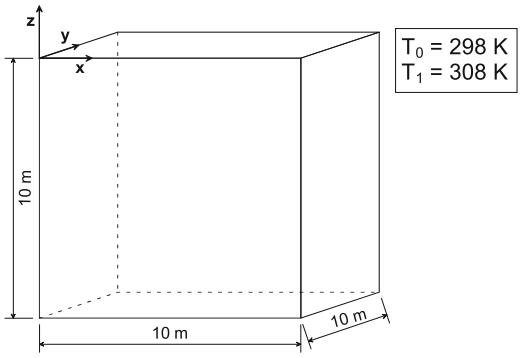


Figure 14.1: Calculation area with one material

Table 14.1: Model parameters

| Symbol | Parameter | Value | Unit |
|---|---|---|---|
| $T_0$ | Initial temperature (before heating) | 298 | K |
| $T_1$ | Temperature after heating | 308 | K |
| $\rho$ | Density of the solid | 2,200 | $\mathrm{kg\,m^{-3}}$ |
| $E$ | Young's modulus of the solid | 25 | GPa |
| $\nu$ | Poisson ratio | 0.27 | – |
| $\alpha$ | Linear thermal expansion | $6.0\times10^{-6}$ | $\mathrm{K^{-1}}$ |
| $c$ | Specific heat capacity | 1.0 | $\mathrm{J\,kg^{-1}\,K^{-1}}$ |
| $\lambda$ | Thermal conductivity | 1.0 | $\mathrm{W\,m^{-1}\,K^{-1}}$ |

that is reached after the whole solid is heated. Figure 14.1 shows a sketch of the calculation area assuming a homogeneous solid, a constant temperature in the whole body at the beginning and a heating of the top and the bottom of the body at about 10 K. Linear elastic material behaviour, isotropic thermal expansion and no gravity effect are assumed. The $xy$-plane is the horizontal plane. The height of the body is in the $z$-direction. The dimensions of this 3 D-model are 10 m in all directions. As deformations in the $x$- and $y$-directions are suppressed, the increasing temperature evokes stresses within the solid. The parameters used for the solid represent the material behaviour of concrete (Table 14.1).

### 14.1.2 Solution

#### Analytical Solution

The analytical solution can be derived from the time independent equation (14.9)–(14.11) with the assumptions of no deformation and an isotropic thermal expansion:

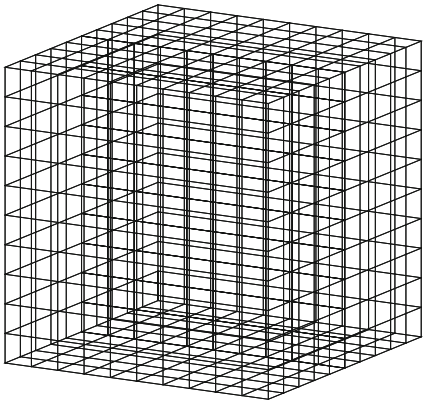

Figure 14.2: Mesh for TM coupling homogeneous material 3D model

$$\begin{aligned} \varepsilon_i &\equiv 0 \\ \sigma_x &= \sigma_y = \sigma_z = -\frac{\alpha \Delta T E}{1-2\nu} \end{aligned} \tag{14.12}$$

Equation (14.12) provides the stresses after heating the solid and shows an isotropic state of stress.

**Numerical Solution**

The dimensions of this 3 D-model are 10 m in all directions. Deformations perpendicular to the outer surfaces are suppressed. The initial temperature in the whole area is 298 K. At the top and at the bottom of the model, the thermal boundary conditions are set with a temperature of 308 K. Thereby the heating of the solid to about 10 K is simulated. A mesh with 1,000 hexahedral elements and 1,331 nodes is used for the simulation. The time duration is divided in 384 time steps with a constant time step size of 900 seconds. This means that heating of the solid within 4 days is simulated. The calculation model is sketched in Fig. 14.2.

### 14.1.3 Results

The calculation of temporal development of the stresses in the centre of the model (at node 665) is presented in Fig. 14.3. The results of the 3 D simulation show an exact agreement with the analytical solutions.

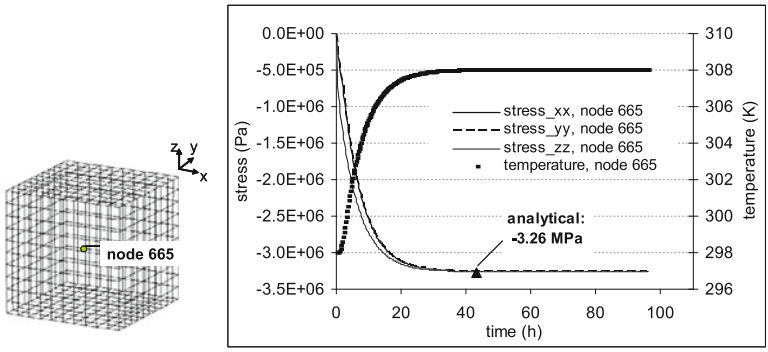


Figure 14.3: Temporal stress development in the centre of the calculation model (node 665)

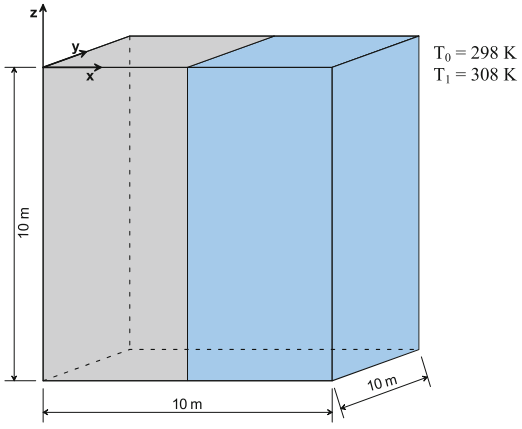


Figure 14.4: Calculation area with two different materials

## 14.2 Thermoelastic Stress Analysis in Composite Materials (3 D)

### 14.2.1 Definition

If there are two materials with different thermal expansions, the volume changes of the materials will be uncommon. The material with the higher thermal expansion expands more than the material with the lower thermal expansion. If deformations at the outer boundaries are prevented, different states of stress will occur in these two materials. But the stresses perpendicular to the parting plane must be equal. The values of the stresses as a result of temperature changes can also easily be calculated by the Hooke's linear elastic model. The aim of this simulation is to specify the stresses at several areas in the solid. Figure 14.4 shows a sketch of the calculation area. The model parameters are given in Table 14.2.

Table 14.2: Model parameters

| Symbol | Parameter | Value | Unit |
|---|---|---|---|
| $T_0$ | Initial temperature (before heating) | 298 | K |
| $T_1$ | Temperature after heating | 308 | K |
| $\rho$ | Density of the solid | 2200 | $\mathrm{kg\,m^{-3}}$ |
| $E$ | Young's modulus of the solid | 25 | GPa |
| $\nu$ | Poisson ratio | 0.27 | – |
| $\alpha_1$ | Linear thermal expansion of material 1 | $6.0\times10^{-6}$ | $\mathrm{K^{-1}}$ |
| $\alpha_2$ | Linear thermal expansion of material 2 | $1.2\times10^{-5}$ | $\mathrm{K^{-1}}$ |
| $c$ | Specific heat capacity | 1.0 | $\mathrm{J\,kg^{-1}K^{-1}}$ |
| $\lambda$ | Thermal conductivity | 1.0 | $\mathrm{W\,m^{-1}\,K^{-1}}$ |

### 14.2.2 Solution

#### Analytical Solution

The equations of the mechanical behaviour are based on the Hooke's law for linear elastic materials (see (14.9)–(14.11)). The analytical solution can be derived from these time independent equations with the assumptions of suppressed deformations in the $y$- and $z$-directions and an isotropic thermal expansion:

$$\varepsilon_x = \varepsilon_z \equiv 0$$

Additionally the stresses in the x-direction (perpendicular to the parting plane between the two materials) must be equal:

$$\sigma_{x1} = \sigma_{x2}$$

where indices denote different materials. Further, the expansion of the one material leads to a compression of the other material with the same value in the x-direction:

$$\varepsilon_{x1} = -\varepsilon_{x2}$$

With these limiting conditions the analytical solutions are:

$$\varepsilon_{x1} = \frac{1}{2}\left(\alpha_1 - \alpha_2\right)\Delta T\left(\frac{1+\nu}{1-\nu}\right) \tag{14.13}$$

$$\varepsilon_{x2} = -\varepsilon_{x1} = -\frac{1}{2}\left(\alpha_1 - \alpha_2\right)\Delta T\left(\frac{1+\nu}{1-\nu}\right) \tag{14.14}$$

$$\sigma_{x1} = \sigma_{x2} = E\frac{\varepsilon_{x2}\left(1-\nu\right) - \alpha_2\Delta T\left(1+\nu\right)}{1-\nu-2\nu^2} \tag{14.15}$$

$$\sigma_{y1} = \sigma_{z1} = \frac{\nu\sigma_{x1} - \alpha_1\Delta T E}{1-\nu} \tag{14.16}$$

$$\sigma_{y2} = \sigma_{z2} = \frac{\nu\sigma_{x2} - \alpha_2\Delta T E}{1-\nu} \tag{14.17}$$

Equations (14.13)–(14.17) provide the strains and stresses after heating the body of two materials. The state of stress is anisotropic.

**Numerical Solution**

The calculation was done with a 3 D model. The $xy$-plane is the horizontal plane. The height of the body is in the $z$-direction. The dimensions of this 3 D model are 10 m in all directions. The model includes 1,000 hexahedral elements and 1331 nodes. Deformations perpendicular to the outer surfaces are suppressed. The initial temperature in the whole area is 298 K. At the top and at the bottom of the model, thermal boundary conditions are set with a temperature of 308 Kthereby the heating of the body to about 10 K is simulated. The parameters used for the solids represent the material behaviour of concrete. The calculation is divided in 1000 time steps with a constant time step length of 0.5 seconds. A sketch of the calculation model is shown in Fig. 14.5.

### 14.2.3 Results

With the analytical solution in (14.13)–(14.17) and the used parameters, the values of the strains in the $x$-direction at the parting plane amount to

$$\varepsilon_{x1} = -5.219178 \times 10^{-5}$$

$$\varepsilon_{x2} = \quad 5.219178 \times 10^{-5}$$

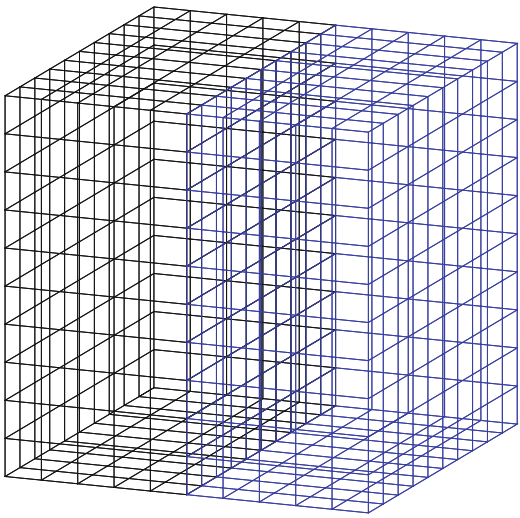

Figure 14.5: Mesh for TM coupling 3D model with 2 materials

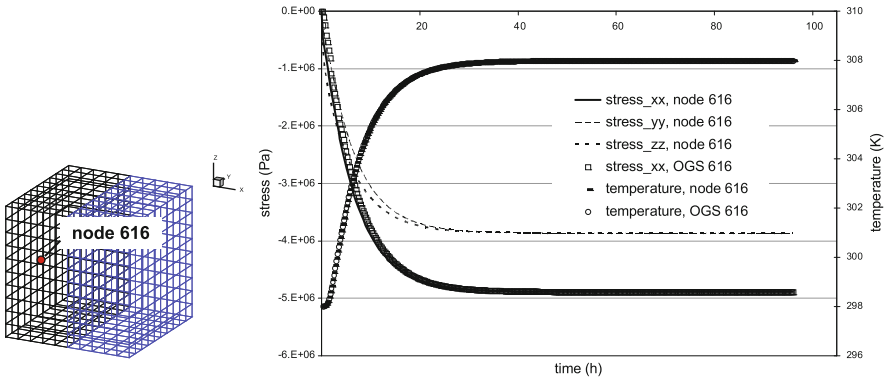


Figure 14.6: Temporal stress development in node 616

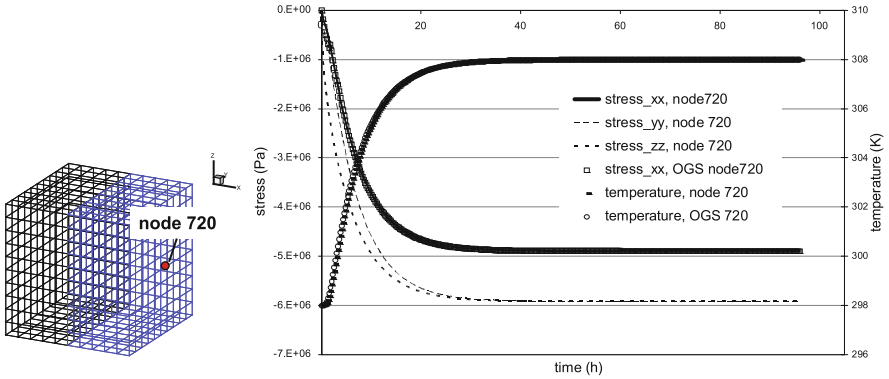


Figure 14.7: Temporal stress development in node 720

The values of the stresses are

$$\sigma_{x1} = \sigma_{x2} = -4891304.34\,\text{Pa} = -4.8913\,\text{MPa}$$

$$\sigma_{y1} = \sigma_{z1} = -3863907.08\,\text{Pa} = -3.8639\,\text{MPa}$$

$$\sigma_{y2} = \sigma_{z2} = -5918701.60\,\text{Pa} = -5.9187\,\text{MPa}$$

This anisotropic state of stress is reached after the whole body is heated. The temporal stress developments in several nodes calculated with both RockFlow and OGS are presented in Figs. 14.6 and 14.7. The results of the 3D simulation show an exact agreement with the analytical solutions.

## 14.3 Thermoelastic Deformation in a Hollow Cylinder

### 14.3.1 Definition

A hollow cylinder which consists of a solid of a constant temperature is exposed to a higher temperature at the surface of its hole. As a result of the increased temperature, the cylinder expands. The aim of this calculation is to get out the radial displacement, as well as the temperature distribution, that is caused by the thermal expansion process, through the use of an axisymmetric model. Figure 14.8 shows a sketch of the calculation area assuming a homogeneous solid, a constant temperature in the whole body at the beginning and a heating of the cylinder at the inner surface. Linear elastic material behaviour and isotropic thermal expansion are assumed. Deformations in the $y$-direction at the bottom and the top and in the $x$-direction at the right border are suppressed. The used parameters of the solid are listed in Table 14.3.

### 14.3.2 Solution

#### Analytical Solution

For the hollow cylinder with the inner radius $R1$ and the outer radius $R2$ the following analytical solution for radial displacement $u_r$, stress $\sigma_r$ and temperature

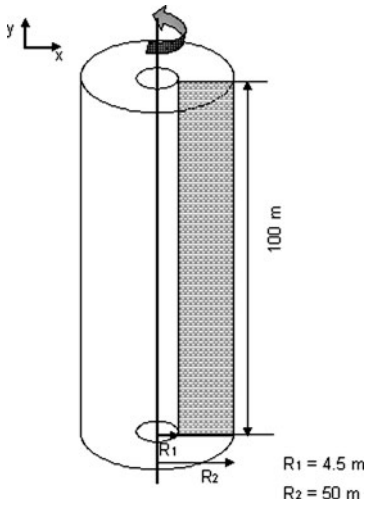


Figure 14.8: Calculation area (*grey area*)

Table 14.3: Model parameters

| Symbol | Parameter | Value | Unit |
|---|---|---|---|
| $T_0$ | Initial temperature (before heating) | 25 | °C |
| $q$ | Heat source | 30 | $\mathrm{W\,m^{-2}}$ |
| $\rho$ | Density of the solid | 2,000 | $\mathrm{kg\,m^{-3}}$ |
| $E$ | Young's modulus of the solid | 2.5 | GPa |
| $\nu$ | Poisson ratio | 0.25 | – |
| $\alpha$ | Thermal expansion | $4.2\times10^{-5}$ | $\mathrm{K^{-1}}$ |
| $\lambda$ | Thermal conductivity | 5.5 | $\mathrm{W\,m^{-1}\,K^{-1}}$ |

in dependency on the radius was used.

$$u_r = \frac{q\,R_1\,\beta}{2\,\psi\,\kappa} r \left(\ln r - \frac{1}{2}\right) + \frac{A_0}{2}\,r + \frac{A_1}{r} \tag{14.18}$$

$$\begin{aligned}\sigma_r = {} & \psi\left[-\frac{q\,R_1\,\beta}{2\,\psi\,\kappa} r \left(\ln r + \frac{1}{2}\right) + \frac{A_0}{2} - \frac{A_1}{r^2}\right] \\ & + \lambda\left[-\frac{q\,R_1\,\beta}{2\,\psi\,\kappa} r \left(\ln r - \frac{1}{2}\right) + \frac{A_0}{2} + \frac{A_1}{r^2}\right] \\ & - \beta\left[\frac{R_1\,q}{\kappa}\,\ln\left(\frac{R_2}{r}\right) + T_0\right]\end{aligned} \tag{14.19}$$

$$T(r) = \frac{R_1\,q}{\kappa}\,\ln\left(\frac{R_2}{r}\right) + T_0 \tag{14.20}$$

where

$$\psi = \lambda + 2\,G \qquad \text{and} \qquad \beta = \alpha\,(3\,\lambda + 2\,G)$$

with

$\lambda$ – Lamé elastic constant
$G$ – shear modulus
$\alpha$ – thermal expansion coefficient
$\kappa$ – thermal conductivity
$A_0$, $A_1$ – integration constants

At the outer surface of the hollow cylinder (where $r = R_2$) there is no deformation, that means the displacement $u_{R2}$ is zero. Therefore (14.18) is set equal to zero for this boundary and adapted to $A_0$.

$$A_0 = -\frac{2\,A_1}{R_2^2} - 2B\left(\ln R_2 - \frac{1}{2}\right) \tag{14.21}$$

where

$$B = \frac{q\, R_1\, \beta}{2\, \psi\, \kappa}$$

At the inner surface of the hollow cylinder (where $r = R_1$) no stress is effected by the expansion because this boundary is phreatic. Therefore (14.19) is set equal to zero and $A_1$ is calculated by using (14.22).

$$A_1 = \frac{\beta\left(\frac{R_1\, q}{\kappa} \ln\left(\frac{R_2}{r}\right) + T_0\right) + \lambda B\left(\ln R_1 - \frac{1}{2}\right) + \psi B\left(\ln R_1 + \frac{1}{2}\right) - \left(\frac{\lambda+\psi}{2}\right) 2B\left(\ln R_2 - \frac{1}{2}\right)}{\frac{\lambda-\psi}{R_1^2} - \frac{\lambda+\psi}{2} \cdot \frac{2}{R_1^2}}. \tag{14.22}$$

After having solved this equation, $A_1$ is used to calculate $A_0$.

### Numerical Solution

The axisymmetric model is in the $xy$-plane. The inner radius $R1$ of the cylindrical model is 4.5 m and the outer radius $R2$ is 50 m. The cylinder is 100 m high. The initial temperature in the whole area is 25°C. As boundary conditions, deformations in the $y$-direction at the bottom and the top are suppressed, as well as deformations in the $x$-direction at the right border. At the right boundary of the model a thermal boundary condition is set with a constant value of 25°C. At the left boundary, a source term for heat flux of $q = 30$ W/m$^2$ is defined and thereby the continuous heating of the solid is simulated. The simulation of only one time step is done. The numerical model consists of 766 triangular elements and 426 nodes as sketched in Fig. 14.9.

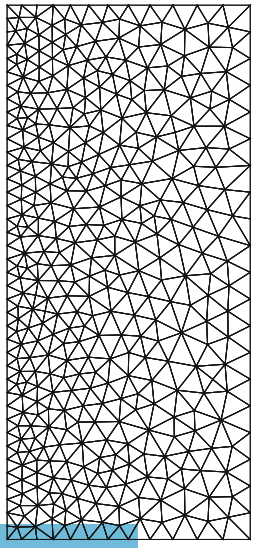

Figure 14.9: Mesh for TM coupling hollow cylinder model (2D axisymmetric)

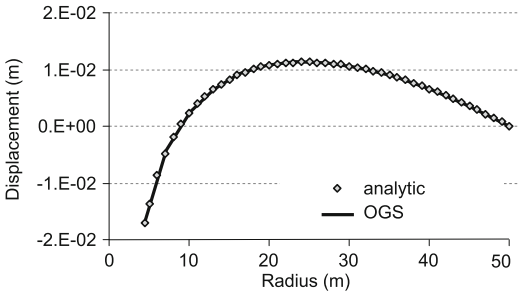


Figure 14.10: Temperature distribution over the radius

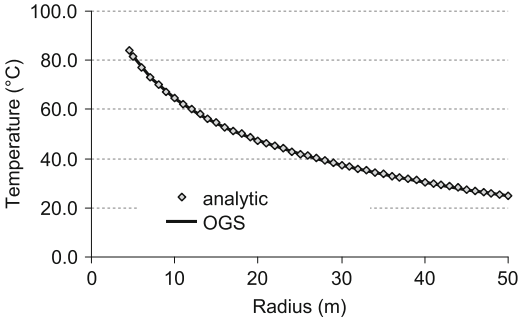


Figure 14.11: Displacements in radial direction

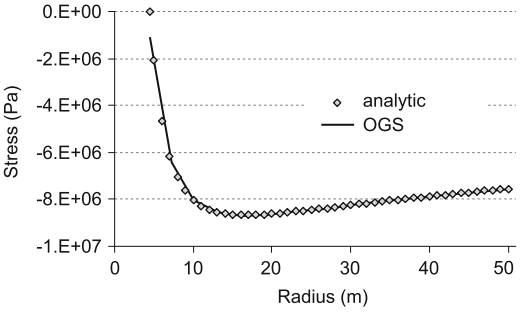


Figure 14.12: Stresses in radial direction

### 14.3.3 Results

The results of the analytical equations for stresses, displacements and temperatures are compared to those of the numerical simulation by OGS. With (14.22) and (14.21) and the used parameters, the integration constants in the analytical solution are obtained as:

$$A_0 = 5.96 \times 10^{-3}$$
$$A_1 = -1.19 \times 10^{-1}$$

Figure 14.10 shows the temperature distribution over the radius of the hollow cylinder. In Fig. 14.11 displacements in radial direction that are caused by the thermal expansion are depicted. In addition you can find the induced stresses in Fig. 14.12. It is clear that with the axisymmetric model, an OGS simulation generates comprehensible results that meet well the analytic solution.

# Chapter 15

# Reactive Transport

*by Haibing Shao, Sebastian Bauer, Florian Centler, Georg Kosakowski, Shuang Jin, and Mingliang Xie*

## 15.1 1D Reactive Transport: Calcite Dissolution and Precipitation

### 15.1.1 Definition

In this example, a one-dimensional column that initially contains calcite mineral is continuously flushed with water that contains magnesium chlorine (Fig. 15.1). With the movement of the water front, calcite starts to dissolve and dolomite is formed temporarily.

#### Media Properties

The media properties of this model are listed in Table 15.1.

For OpenGeoSys-GEMIPM2K calculation, all the possible chemical species need to be explicitly set up for initial and boundary conditions. In this example, all concentration values are given in the unit of mol·kg$^{-1}$ water.

O. Kolditz et al. (eds.), *Thermo-Hydro-Mechanical-Chemical Processes in Fractured Porous Media*, Lecture Notes in Computational Science and Engineering 86,
DOI 10.1007/978-3-642-27177-9_15, 

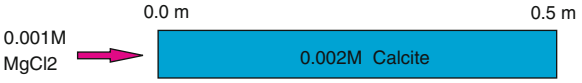


Figure 15.1: Model domain

Table 15.1: Material properties

| Parameter | Value | Unit |
|---|---|---|
| Column length | 0.5 | m |
| Effective porosity | 0.32 | – |
| Bulk density | $1.8 \times 10^3$ | kg $\cdot m^{-3}$ |
| Longitudinal dispersivity | 0.0067 | m |
| Pore velocity | $9.375 \times 10^{-6}$ | m$\cdot$sec$^{-1}$ |
| Flow rate | $3 \times 10^{-6}$ | m$^3\cdot$ sec$^{-1}$ |

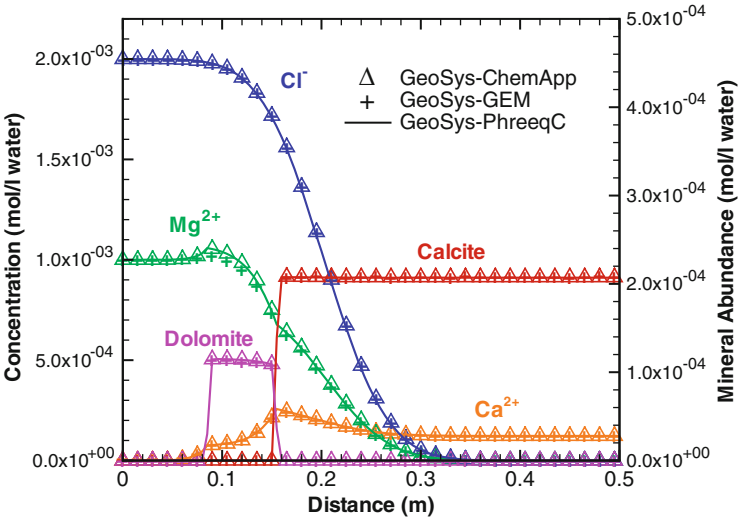


Figure 15.2: Benchmark results from OpenGeoSys-ChemApp, OpenGeoSys-PHREEQC, and OpenGeoSys-GEMIPM2K

### 15.1.2 Solution

This model can be simulated by OpenGeoSys-PHREEQC, OpenGeoSys-ChemApp, and OpenGeoSys-GEMIPM2K. In these benchmarks, we use the Nagra/PSI database [181], which provides same thermodynamic data for all three calculations. Figure 15.2 shows the three simulation results. Solid lines are for OpenGeoSys-PHREEQC, symbols "+" are for OpenGeoSys-GEMIPM2K, and triangles are for OpenGeoSys-ChemApp.

## 15.2 1D Reactive Transport Simulation of Cation Exchange Process

### 15.2.1 Definition

This test example is taken from the PHREEQC User's Guide [182]. The simulation is made in order to reproduce the transport of solutes by saturated flow with the influence of cation exchange. The aim of the example is to check the correctness of the coupling between OpenGeoSys and PHREEQC by comparing the results of the simulations of both programs. With the calculation model, the chemical composition of the effluent, from a column containing a cation exchanger and a sodium-potassium-nitrate-solution, is simulated. This column is flushed with 3 pore volumes of calcium chloride solution. The 8.2 cm long column contains a sodium-potassium-nitrate solution that is in equilibrium with a cation exchanger. For the one-dimensional calculation the calculation area is simplified as a line. The calculation model includes 82 elements and 83 nodes. As an initial condition the water head in the whole domain is assigned to 2 m. The initial state of the solution is given in Table 15.2.

with

pe —redox potential
X —ion exchanger
kgw —kilogram of water.

At the right border of the model the constant head of 2 m is assigned. At the left border a constant flux of $1.388\times10^{-6}$ $m^3 \cdot s^{-1}$ is defined as the source term. The concentration of this infiltrating $CaCl_2$-solution, as well as the pH and pe, are given in Table 15.3.

The soil material is specified by the parameters in Table 15.4. The dispersion of the transported solutes in this soil is set equal to $2 \times 10^{-3}$ m. The calculation

Table 15.2: Used parameters

| Parameter | Value | Unit |
|---|---|---|
| Ca | 0 | mol ·kgw$^{-1}$ |
| Cl | 0 | mol ·kgw$^{-1}$ |
| K | $2.0\times10^{-4}$ | mol ·kgw$^{-1}$ |
| Na | $1.0\times10^{-3}$ | mol ·kgw$^{-1}$ |
| N(5) | $1.2\times10^{-3}$ | mol ·kgw$^{-1}$ |
| pH | 7 | – |
| pe | 12.5 | – |
| Na-X | $5.493\times10^{-4}$ | mol ·kgw$^{-1}$ |
| K-X | $5.507\times10^{-4}$ | mol ·kgw$^{-1}$ |
| Ca-$X_2$ | 0 | mol ·kgw$^{-1}$ |

Table 15.3: State of the infiltration solution

| Parameter | Value | Unit |
|---|---|---|
| Ca | $6.0\times10^{-4}$ | mol $\cdot$kgw$^{-1}$ |
| Cl | $1.2\times10^{-3}$ | mol $\cdot$kgw$^{-1}$ |
| pH | 7 | – |
| pe | 12.5 | – |

Table 15.4: Soil parameters

| Parameter | Value | Unit |
|---|---|---|
| density $\rho$ | 2,000 | kg$\cdot$ m$^{-3}$ |
| porosity $\Phi$ | 0.5 | – |
| permeability $K$ | $1.157\times10^{-5}$ | m$^2$ |

is divided into 480 time steps with a constant time step length of 180 seconds. That meansthe flow and transport processes in the aquifer within 1 day are simulated.

This test example aims to validate the coupling of OpenGeoSys and PHREEQC, merely the comparison between the simulation results of both programs has to be accomplished.

### 15.2.2 Solution

The numerical results are shown in Fig. 15.3. The time-dependent concentrations are the values of the compared OpenGeoSys and PHREEQC models at the end node and end cell, respectively. Within the calculation time of one day the pore volume of the column model is exchanged three times. As chloride is a conservative tracer it arrives already after the exchange of about one pore volume in the effluent. As long as the exchanger contains sodium this component is eluted. Sodium is initially present in the column and exchanges with the incoming calcium. Potassium is released after sodium. When all of the potassium has been released, the concentration of calcium increases to a steady-state value. As depicted in Fig. 15.3, between the OpenGeoSys and the PHREEQC simulation results there are no differences.

## 15.3 1D Reactive Transport: Multispecies Transport with Serial and Parallel Reactions

Reaction networks can be classified as serial and/or parallel reaction networks. In serial reactions, a reactant produces a single product and this product

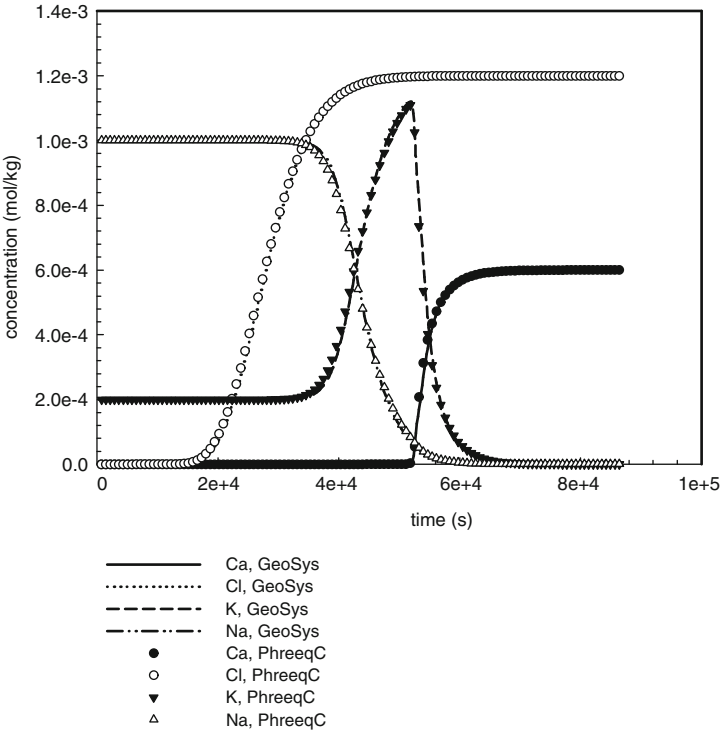


Figure 15.3: Effluent concentrations with time of the OpenGeoSys and PHREEQC simulations

becomes the reactant for the next stage producing reaction. Examples of serial reactions are denitrification, radioactive decay and dechlorination of some chlorinated solvents. In parallel reactions, the parent reactant undergoes two or more independent reactions to produce multiple products. In many biogeochemical systems, the reaction networks are the combination of serial and parallel reactions.

### 15.3.1 Definition

In scenario 1, sequential reductive dechlorination of chlorinated hydrocarbons from trichlorobenzene (TCB) to diclorobenzene (DCB) to monochlorobenzene (MCB) is simulated:

$$TCB \rightarrow DCB \rightarrow MCB \tag{15.1}$$

In scenario 2, a serial-parallel reaction network as shown in Fig. 15.4 is used to perform the verification. It can be decomposed into three serial reactions:

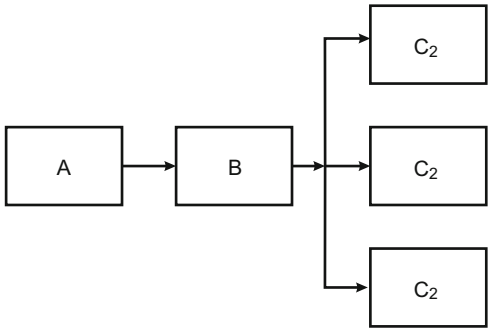


Figure 15.4: An example of serial-parallel reaction network

$A \rightarrow B \rightarrow C_1, A \rightarrow B \rightarrow C_2, A \rightarrow B \rightarrow C_3$. For all the reactions in this scenario, first-order irreversible reactions are assumed.

An analytical solution by [183] has been used to verify the numerical results from OpenGeoSys-BRNS simulation for these two scenarios.

In scenario 1, a sand column of 100 meters in length is flushed constantly with water containing TCB. The microbial groups in the column then start to convert TCB to DCB and further to produce MCB. In the OGS-BRNS model, a line of 100 meters with spatial discretization of 2 meters is defined. Water flows from left to right with a velocity of 20 m/d. The dispersivity is 5 meters. The first order reaction rates of TCB, DCB and MCB are 0.0013, 0.00024 and 0.00019 1/d respectively. The yield factor from TCB to DCB is 0.81 and from DCB to MCB is 0.765. The total simulation time is 1.5 days and temporal discretization of 0.01 day is employed. The initial and boundary conditions are
For $x \geq 0$,

$$C_{TCB}(x,0) = C_{DCB}(x,0) = C_{MCB}(x,0) = 0 \tag{15.2}$$

For $t > 0$,

$$C_{TCB}(0,t) = 10.0 \tag{15.3}$$

$$C_{DCB}(0,t) = C_{MCB}(0,t) = 0 \tag{15.4}$$

$$C_{TCB}(\infty,t) = C_{DCB}(\infty,t) = C_{MCB}(\infty,t) = 0 \tag{15.5}$$

Scenario 2 has similar numerical settings but with different parameter values. The column length is 40 meters with spatial discretization of 1 meter. Water flow velocity is 0.4 m/d. The dispersivity is 10 meters. The total simulation time is 40 days with temporal discretization of 0.04 day. The first order reaction rates and yield factors of the five species are listed in Table 15.5.
For $x \geq 0$,

$$C_A(x,0) = C_B(x,0) = C_{C_1}(x,0) = C_{C_2}(x,0) = C_{C_3}(x,0) \tag{15.6}$$

Table 15.5: Values of first order reaction rates and yield factors for scenario 2

| Parameter | Value | Unit |
|---|---|---|
| Reaction rate of A | 0.2 | $1 \cdot d^{-1}$ |
| Reaction rate of B | 0.1 | $1 \cdot d^{-1}$ |
| Reaction rate of C1 | 0.02 | $1 \cdot d^{-1}$ |
| Reaction rate of C2 | 0.02 | $1 \cdot d^{-1}$ |
| Reaction rate of C3 | 0.02 | $1 \cdot d^{-1}$ |
| Yield factor from A to B | 0.5 | – |
| Yield factor from B to C1 | 0.3 | – |
| Yield factor from B to C2 | 0.2 | – |
| Yield factor from B to C3 | 0.1 | – |

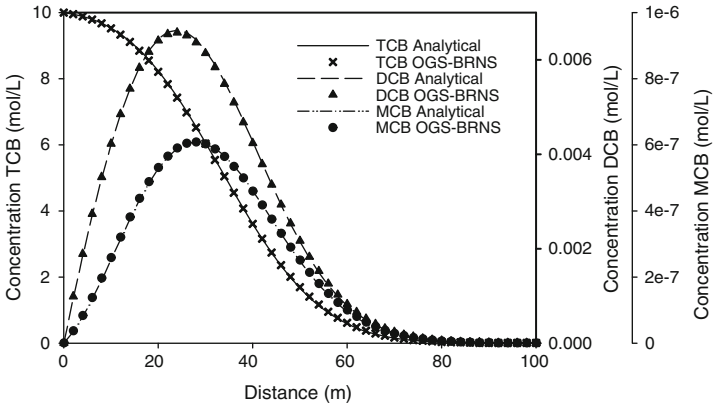


Figure 15.5: Comparison between concentration profiles of TCB, DCB and MCB calculated by analytical solution and OpenGeoSys-BRNS in scenario 1

For $t > 0$,

$$C_A(0,t) = 1.0, \tag{15.7}$$

$$C_B(0,t) = C_{C1}(0,t) = C_{C_2}(0,t) = C_{C_3}(0,t) = 0 \tag{15.8}$$

$$C_A(\infty,t) = C_B(\infty,t) = C_{C_1}(\infty,t) = C_{C_2}(\infty,t) = C_{C_3}(\infty,t) = 0 \tag{15.9}$$

### 15.3.2 Solution

The comparison was conducted for the concentration of all the species for scenario 1 and 2. Figure 15.5 shows a very good agreement between analytical and numerical results for scenario 1. For scenario 2, as we can see from Figs. 15.6 and 15.7, the results obtained from OGS-BRNS also fit well with the analytical solution.

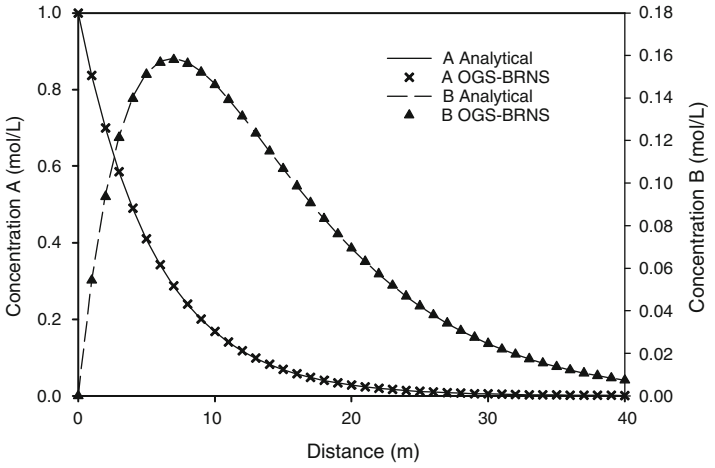


Figure 15.6: Comparison between concentration profiles of species A and B calculated by analytical solution and OpenGeoSys-BRNS in scenario 2

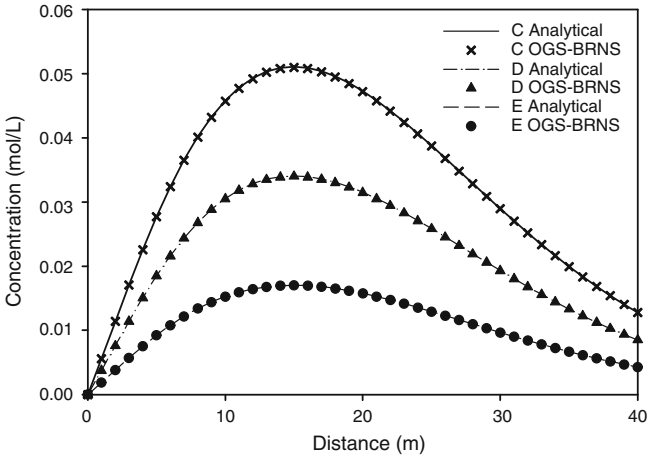


Figure 15.7: Comparison between concentration profiles of species C, D and E calculated by analytical solution and OpenGeoSys-BRNS in scenario 2

## 15.4 1D Reactive Transport: Xylene Degradation with Multiple Monod Kinetics, Exchange Kinetics and Biomass Growth

### 15.4.1 Definition

This benchmark describes the reactive transport of xylene in a homogeneous aquifer. The main purpose is to document the ongoing reactions, which are xylene degradation under aerobic, sulfate reducing and iron reducing conditions, considering growth of the respective biomasses. Also included is the rate limited exchange of iron goethite into bioavailable iron. The aquifer is represented by a one-dimensional model 50 m in length in the x-direction and 1 m in the y-and z directions, respectively. The model is discretized by 100 line elements of a constant 0.5 m length in the x direction. With an isotropic hydraulic conductivity K of $2.13 \times 10^{-3}$ m $\cdot$ $s^{-1}$, a porosity of 0.24 and a hydraulic gradient I of $1.3 \times 10^{-4}$, the steady state transport velocity va is 0.1 m$\cdot$ $d^{-1}$. Longitudinal dispersivity $\alpha_L$ is set to 0.25 m, the diffusion coefficient $D_a$ is set to $1.0 \times 10^{-9}$ $m^2 \cdot s^{-1}$. The physical aquifer parameters are summarized in Table 15.6. The transport simulation is run for a period of 1000 d with a time step length of 5 d.

The model aquifer has a length of 50 m in the x-direction, 1 m in the y-direction and 1 m in the z direction. The whole domain is discretized into 100 line elements with a constant x and y dimension of 1 m. The aquifer is assumed to have a homogeneous and isotropic hydraulic conductivity. Using a gradient of $1.23 \times 10^{-4}$ and a porosity of 0.24 produces a steady state transport velocity of 0.10 m$\cdot d^{-1}$. Xylene degradation is simulated according to the typical redox sequence.

Table 15.6: Parameters used for benchmark HC\1d_xylene_degradation

| Parameter | Value | Unit |
|---|---|---|
| porosity $\Phi = n$ | 0.24 | – |
| matrix volume fraction $VOL_MAT$ | 0.75 | – |
| biomass volume fraction $VOL_BIO$ | 0.01 | – |
| hydraulic conductivity $K$ | $2.13 \times 10^{-3}$ | m$\cdot s^{-1}$ |
| storage coefficient $S$ | 0.0 | $s^{-1}$ |
| solid density $\rho_s$ | 2000 | kg$\cdot m^{-3}$ |
| density of water $\rho_w$ | 1000 | kg$\cdot m^{-3}$ |
| viscosity water $\eta$ | 0.001 | Pa$\cdot$s |
| longitudinal dispersivity $\alpha_l$ | 0.25 | m |
| component diffusion coefficient $D$ | $1.0 \times 10^{-9}$ | $m^2 \cdot$ $s^{-1}$ |

### 15.4.2 Solution

Results of the simulation are shown in Fig. 15.8 for xylene, the electron acceptors oxygen and sulfate, as well as for the biomass of the aerobic microorganisms, the sulfate reducers and the iron reducers simulation time steps of 100 days. For simulation time $t < 500$ d, one can see the advancing xylene front and a reduction of xylene concentrations is only visible for later times, when xylene concentrations reduce to about 90% of the inflow concentration. Also shown is the increasing consumption of oxygen with time accompanied by the growth of the aerobic reducers at the inflow (left) end of the model area. After approximately 800 d, oxygen concentrations in the inflowing groundwater are reduced to almost zero within the first 20 m of the aquifer. Sulfate reducers initially decay from their original amount as growth is inhibited throughout the column by the still high concentrations of oxygen. Once the oxygen is used up, however, sulfate reducers start to grow downstream of the oxygen reducers and sulfate concentrations in the groundwater reduce accordingly. The iron reducers decay from their initial values and start to grow only for late times $t > 80$ d and $x > 30$ m, as xylene degradation from iron reduction is inhibited by both oxygen as well as sulfate, which is still present in concentrations larger than the inhibition concentration for iron reducers. Accordingly, the spatial distribution of bioavailable iron is still almost uniform throughout the aquifer.

## 15.5 1D Reactive Transport: Competition of TCE- and Cis-DCE-Degradation for the Zero Valent Iron Surface

### 15.5.1 Definition

This example simulation demonstrates the use of OpenGeoSys for simulation of multi-species kinetic reactions. The reaction system was set up by D. Schäfer and published in [184]. Further, it was used for model verification of the newly implemented and developed kinetic reaction module in OpenGeoSys. The example considers flow in a one-dimensional column of 1 m in length, resembling the thickness of a reactive iron barrier perpendicular to the flow direction. It involves 19 species and 16 different geochemical reactions, including both first-order degradation reactions of adsorbed substances and kinetic sorption reactions. Competition for the available sorption sites is also considered here.

The model setup consists of a 1D column with saturated ground water flow at a Darcy velocity of $5.0 \times 10^{-4}$ m$\cdot$ d$^{-1}$ from left to right. Geochemical species are added to the inflowing water, and their sorption and degradation behavior is modeled. For a complete description of input parameters see the paper by Schäfer et al. (2003). Every degradation reaction follows a Langmuir-Hinshelwood-Hougen-Watson kinetics with a limited number of sites for the

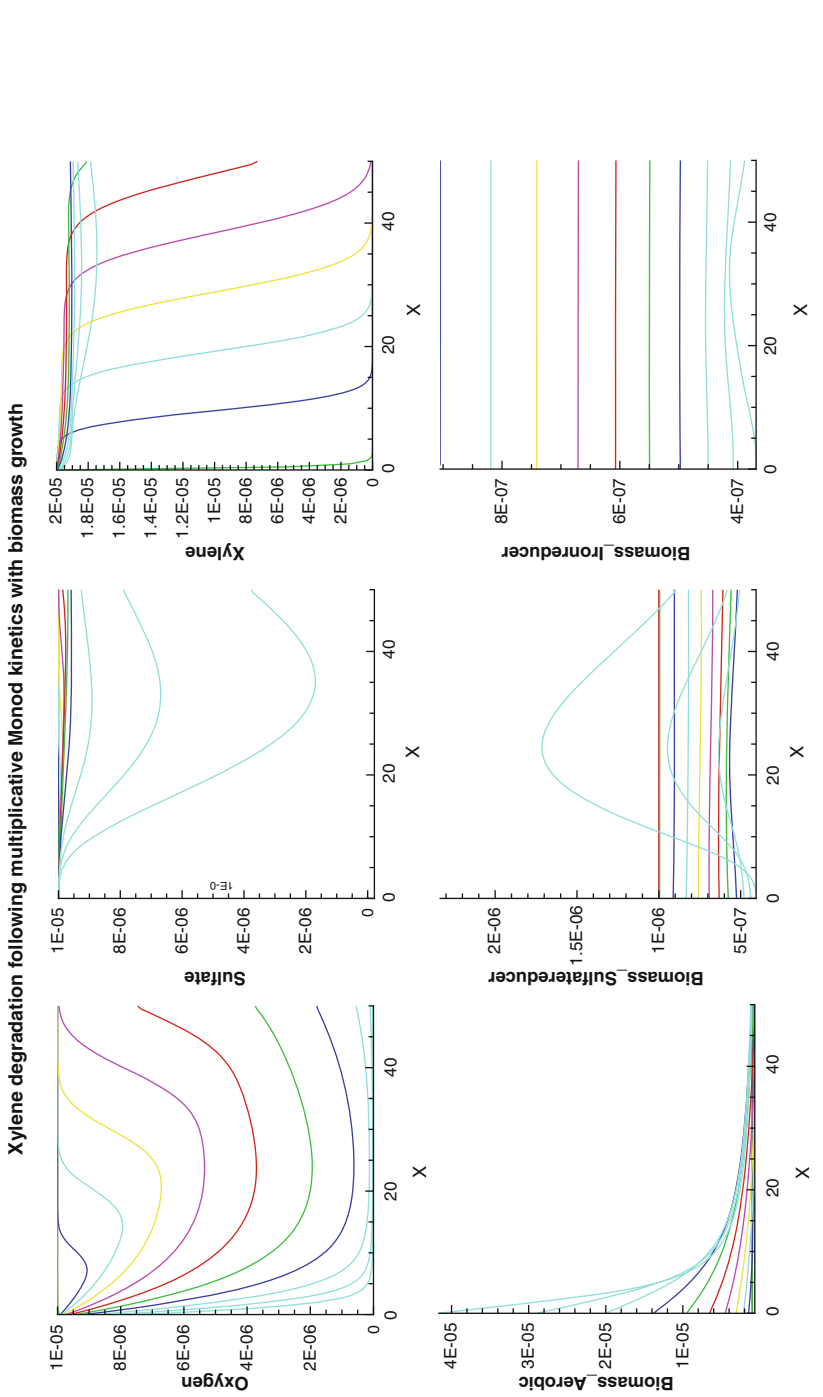


Figure 15.8: Profiles of oxygen, sulfate and xylene (*top row, from left*) and aerobic reducers, sulfate reducers and iron reducers at different times during the 1,000 d simulation period

adsorption and desorption of chlorinated hydrocarbons on the reactive iron surface. Since all the reactive substances involved have to adsorb onto the reactive iron surface in order to be degraded, a competition for the surface sites occurs. This competition has been investigated in column studies and the observed concentration profiles were simulated with the numerical model TBC [184]. Model results are compared with those obtained from an older version of OpenGeoSys, which was compared to the original TBC simulations.

### 15.5.2 Solution

Results of the simulation are shown in Fig. 15.9, where profiles of the dissolved species are depicted. TCE and cis-DCE are added to the inflowing water. They compete for the sorption sites and when sorbed, they degrade according to a first order degradation reaction. The retardation of the reactive species compared to the conservative tracer `mobile` is clearly visible. Also, just downstream of the concentration decrease of TCE or cis-DCE, the degradation products ethane and C4-containing molecules increase. These species are again mobile and are transported with the water, so an instationary behaviour is observed in Fig. 15.9.

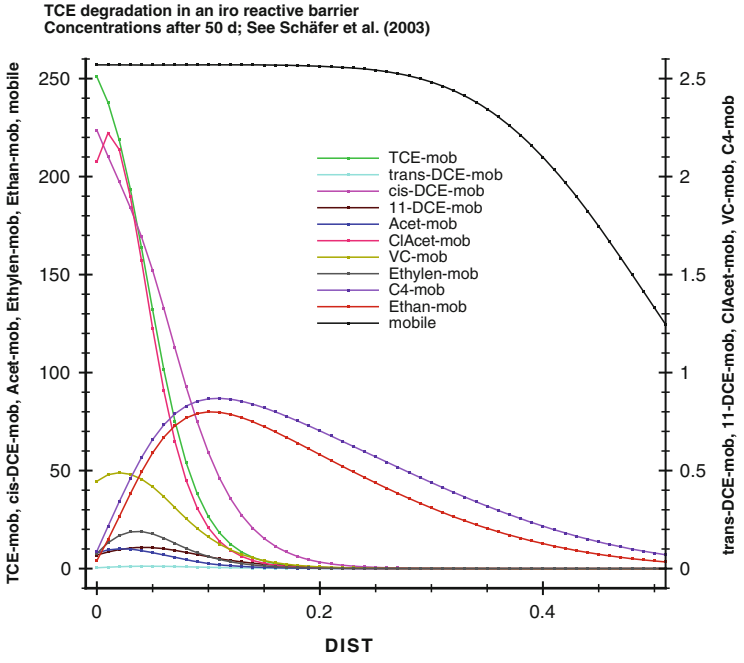


Figure 15.9: Concentration profiles of TCE, trans-DCE, cis-DCE, 1,1-DCE, Acetylene, chloroacetylene, C4, VC, ethene and ethane as well as the conservative tracer mobile after 50 d simulation time

## 15.6 1D Reactive Transport: Sequential CHC Degradation with Isotope Fractionation

### 15.6.1 Reaction Model

When a substrate $C$ is present in the form of light and heavy isotopes $C^l$ and $C^h$, and one of the isotopes is preferentially consumed by a microbial population $X$, a kinetic isotope fractionation effect can be observed, i.e. one of the isotopes will become enriched in the remaining fraction of electron donors relative to its isotope partner. At the same time, the preferentially consumed isotope will become enriched in the reaction product relative to the more recalcitrant isotope. The degree of isotope fractionation can be expressed by means of the fractionation factor $\alpha$ [-], which is a reaction specific constant and relates the isotopic ratio of the degradation reaction's product to the isotope ratio of the substrate. Often, the isotopic enrichment factor $\varepsilon$ [-] is used to quantify the isotope effect of a reaction, which can be related to $\alpha$ for a one step process by

$$\varepsilon = (\alpha - 1) \cdot 1000 \tag{15.10}$$

According to Van Breukelen et al. [185], the degradation rate of the light carbon isotope substrate $d^{12}C_S/dt$ is given by the overall degradation rate $dC_S/dt$ of substrate $C_S$ corrected for the proportion of $^{12}C_S$ to total $C_S$

$$-\frac{d^{12}C_S}{dt} = \frac{d^{12}C_P}{dt} = -\frac{dC_S}{dt}\frac{^{12}C_S}{^{12}C_S + ^{13}C_S} \tag{15.11}$$

The degradation rate of the heavy isotope substrate $d^{13}C_S/dt$ then is given by

$$-\frac{d^{13}C_S}{dt} = \frac{d^{13}C_P}{dt} = -\frac{dC_S}{dt}\frac{^{13}C_S}{^{12}C_S + ^{13}C_S}(\varepsilon \cdot 10^{-3} + 1) \tag{15.12}$$

$dC_S/dt$ can be any rate expression, such as first order, Michaelis-Menten or Monod-kinetics. Based on this concept and using the general formulation of multiple Monod kinetics of first order growth of a microbial species, $X$ from consumption of the light isotope substrate $^{12}C_S$ can be expressed by

$$\left[\frac{\partial X}{\partial t}\right]_{^{12}C_S} = \mu_{max} X \left[\prod_{j=1}^{n_M - 1}\left(\frac{C_j}{K_j^M + C_j}\right)\prod_{j=1}^{n_I}\left(\frac{K_j^I}{K_j^I + C_j}\right)\right]\frac{C_S^{tot}}{C_S^{tot} + K_{C_S}^M}\frac{^{12}C_S}{C_S^{tot}} \tag{15.13}$$

where $C_S^{tot} = ^{12}C_S + ^{13}C_S$ and $\mu_{max}$ [$T^{-1}$] is the maximum growth rate of $X$ with respect to substrate $C$. Growth of $X$ from consumption of the heavy isotope substrate $^{13}C_S$ can be expressed accordingly by

$$\left[\frac{\partial X}{\partial t}\right]_{^{13}C_S} = \mu^*_{max} X \left[\prod_{j=1}^{n_M-1}\left(\frac{C_j}{K_j^M + C_j}\right)\prod_{j=1}^{n_I}\left(\frac{K_j^I}{K_j^I + C_j}\right)\right]\frac{C_S^{tot}}{C_S^{tot} + K_{C_S}^M}\frac{^{13}C_S}{C_S^{tot}} \tag{15.14}$$

where $\mu^*_{max} = \mu_{max}(\varepsilon/1000 - 1)$. The resulting degradation rates of $^{12}C_S$ and $^{13}C_S$ accordingly are given by

$$\frac{\partial\, ^{12}C_S}{\partial t} = -\mu_{max} X \frac{St_{C_S}}{Y_{C_S}}\left[\prod_{j=1}^{n_M-1}\left(\frac{C_j}{K_j^M + C_j}\right)\prod_{j=1}^{n_I}\left(\frac{K_j^I}{K_j^I + C_j}\right)\right]\frac{C_S^{tot}}{C_S^{tot} + K_{C_S}^M}\frac{^{12}C_S}{C_S^{tot}} \tag{15.15}$$

$$\frac{\partial\, ^{13}C_S}{\partial t} = -\mu^*_{max} X \frac{St_{C_S}}{Y_{C_S}}\left[\prod_{j=1}^{n_M-1}\left(\frac{C_j}{K_j^M + C_j}\right)\prod_{j=1}^{n_I}\left(\frac{K_j^I}{K_j^I + C_j}\right)\right]\frac{C_S^{tot}}{C_S^{tot} + K_{C_S}^M}\frac{^{13}C_S}{C_S^{tot}} \tag{15.16}$$

where $St_{C_S}$ [-] and $Y_{C_S}$ [-] are the stoichiometric and yield coefficients for substrate $C_S$. Degradation kinetics for the conceptually more simple Michaelis-Menten, first or zeroth order kinetics may be derived on the basis of (15.13)–(15.16) assuming a constant microorganism mass and choosing appropriate values of $\mu_{max}$, $\mu^*_{max}$, $K^M_{C_S}$, $St_{C_S}$ and $Y_{C_S}$.

For the simulation of biodegradation with isotope fractionation of a substrate species $C_S$ by multiplicative Monod (or one of the more simplified) kinetics, heavy and light isotopes of the fractionating substrate, e.g. $^{12}C_S$ and $^{13}C_S$, must be defined as two individual species with corresponding transport processes. Also, two individual degradation reactions must be defined, requiring identical parameter values for $\mu_{max}$ , $Y_{C_S}$, and all $K_i^M$, $K_i^I$, and $St_i$. The isotopic enrichment factor $\varepsilon$ then is used to calculate the modified maximum growth rate $\mu^*_{max}$ for the more recalcitrant isotope.

### 15.6.2 Definition

In this benchmark, which is based on a model of [185], sequential degradation of chlorinated hydrocarbons (CHC) from PCE to the end product ethylene (Eth), which will not further degrade, is simulated:

$$PCE \rightarrow TCE \rightarrow DCE \rightarrow VC \rightarrow Eth \tag{15.17}$$

A contaminant source located at the upstream model boundary emits a constant concentration of PCE. All degradation reactions follow simple first order

Table 15.7: Parameters used for benchmark

| Parameter | Value | Unit |
|---|---|---|
| porosity $\Phi = n$ | 0.25 | – |
| matrix volume fraction $VOL\_MAT$ | 0.74 | – |
| biomass volume fraction $VOL\_BIO$ | 0.01 | – |
| hydraulic conductivity $K$ | $1.1574\times10^{-4}$ | m $\cdot$s$^{-1}$ |
| flow velocity $q$ | $1.1574\times10^{-6}$ | m$\cdot$s$^{-1}$ |
| longitudinal dispersivity $\alpha_l$ | 1.0 | m |
| component diffusion coefficient $D$ | $3.0\times10^{-9}$ | m$\cdot$s$^{-1}$ |

Table 15.8: Reaction parameters used for benchmark HC\1d_isofrac

| CHC species | enrichment factor $\varepsilon$ [-] | first order rate constant $\lambda$ [$s^{-1}$] |
|---|---|---|
| PCE | $-5.2$ | $6.366\times10^{-8}$ |
| TCE | $-8.5$ | $3.125\times10^{-8}$ |
| DCE | $-17.8$ | $2.199\times10^{-8}$ |
| VC | $-23.2$ | $1.273\times10^{-8}$ |
| Eth | 0.0 | – |

kinetics and involve an isotope fractionation effect. The one-dimensional transport model has a length of 876 m and is discretized by 120 finite line elements of 7.3 m length, respectively. Basic flow and transport model parameters are summarized in Table 15.7, reaction parameters for the individual species in Table 15.8.

Each of the mobile hydrocarbon species is defined twice, once for the light isotopologue and once for the respective heavy isotopologue. Also, an immobile microorganism species $X$ is defined, which has an initial unit concentration of 1.0 throughout the model domain. The microorganisms degrade each of the chlorinated species (i.e. PCE, TCE, DCE and VC). Thus, a total of eight monod-type growth reactions for $X$, one for each isotopologue species, must be defined. Growth of $X$, however, is inhibited by setting the growth parameter in the *.krc file to zero in each of the reactions and microorganism decay is not included in the simulation, i.e. $X$ is constant in time and space. Each reaction contains only a single Monod term for the respective isotopologue species. To achieve degradation kinetics of first order in each case, the half saturation concentrations $K_i^M >> C_i$ and are hence set to a value of $1.0\times10^{10}$. As the effective first order rate constant is given by $\lambda_i = \mu_{max_i}/K_i^M$, parameters $\mu_{max_i}$ are set to proportionally high values in the *.krc file, i.e. ten orders of magnitude larger than indicated in Table 15.8. Also, the yield coefficients $Y_i$ for the individual reactions must be set to 1.0.

Initial concentrations of all species except the microorganisms are 0.0 mol L$^{-1}$ throughout the model domain. For $^{12}$PCE and $^{13}$PCE the upgradient boundary

conditions are constant concentrations of $9.892 \times 10^{-4}$ and $1.078 \times 10^{-4}$ mol $L^{-1}$, respectively. The hydraulic gradient of 0.01 is induced by fixed head boundary conditions of 10.0 and 9.781 m at the up- and downgradient model boundaries. The reactive transport simulation is run for a period of 20 years with 200 time steps of 3153600 s, respectively, and using an explicit-implicit time stepping scheme ($\theta = 0.5$).

Model results are compared against the one-dimensional Domenico analytical solution including first order degradation kinetics as well as by comparison of an equivalent one-dimensional simulation with PHREEQC, which was presented by Van Breukelen et al. [185].

### 15.6.3 Solution

Results at the end of the simulation are presented in Figs. 15.10 and 15.11. In Fig. 15.10, numerical simulation results for the PCE isotopologues in the form of normalized concentrations $C/C_0$ are compared against results of the one-dimensional Domenico analytical solution including first order degradation, in which the first order degradation rate for the heavy PCE isotopologue $\lambda_{^{13}PCE} = \lambda_{^{12}PCE}(\varepsilon/1000 - 1)$. Note that for the comparison with the analytical solution, kinetic reactions are suppressed on the first node of the FE

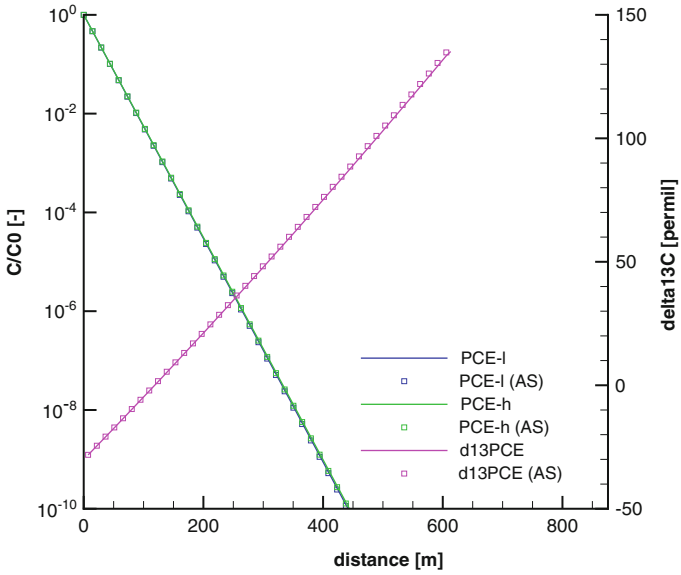


Figure 15.10: PCE isotopologue concentration profiles (left axis) and $\delta^{13}C$ isotope signature (right axis) versus transport distance along the 1D model. Lines represent GeoSys simulation results, symbols represent analytical solution results

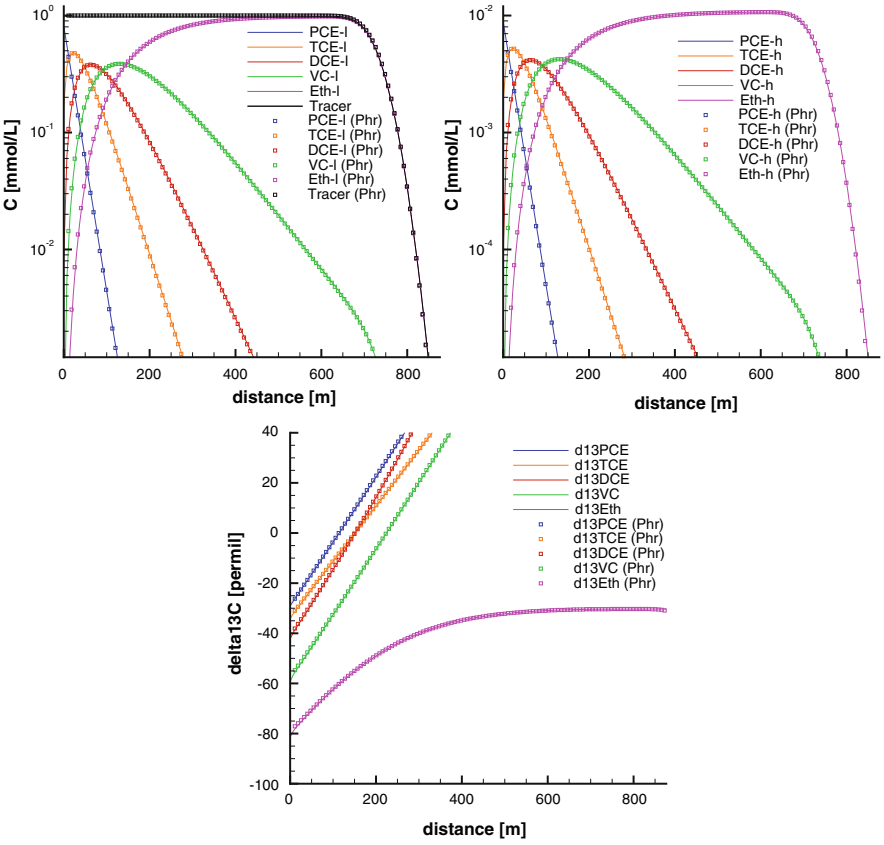


Figure 15.11: Light (upper left diagram), heavy (*upper right diagram*) isotopologue chlorinated hydrocarbon species profiles and $\delta^{13}C$ isotope signatures (*lower diagram*) versus transport distance along the 1D model. *Full lines* represent OpenGeoSys simulation results, symbols represent PHREEQC simulation results

mesh (i.e. on the upstream model boundary) in order to correctly represent the concentration boundary condition of the analytical solution. Concentrations of the PCE isotopologues match the analytical solution over a concentration range of more than 10 orders of magnitude. Also the resulting $\delta^{13}C$ [permil] isotope signatures, which were computed by

$$\delta^{13}C = \left( \frac{R_{C_i}}{R_{Ref}} - 1 \right) 1000 \tag{15.18}$$

where $R_{C_i}$ [-] is the isotope ratio ${}^{13}C_i/{}^{12}C_i$ of species $C_i$ in the simulation, while $R_{Ref}$ [-] is the isotope ratio of the international standard, i.e. in this case

the Vienna Pee Dee Belemnite (V-PDB; $R_{Ref} = 0.011237$), match results of the analytical solution precisely, verifying the correctness of the implementation.

In Fig. 15.11 the upper left and right diagrams show simulated concentration profiles of the individual CHC species versus results obtained by PHREEQC. Note that for the comparison with the PHREEQC simulation, kinetic reactions are not suppressed on the upstream model boundary. The lower diagram shows $\delta^{13}C$ isotope signatures. While concentrations of $^{12}$PCE and $^{13}$PCE decrease exponentially with distance from the source. At the left hand side model boundary, isotopologues of TCE, DCE and VC show concentration peaks in different distances from the source. Eth isotopologues finally accumulate as the end products of the degradation chain and reach the source concentrations of $^{12}$PCE and $^{13}$PCE, respectively. Also, while TCE, DCE and VC isotope signatures increase almost linearly with travel distance demonstrating the increasing enrichment of the heavy isotopologues, the Eth signature approaches the $\delta^{13}C$ of the source, i.e. PCE. For all isotopologue species, concentration profiles and isotope signatures show an excellent agreement with the PHREEQC simulation, verifying the numerical implementation also for sequential degradation reactions.

## 15.7 1D Reactive Transport: Degradation of Organic Contaminants in a Sand Column Experiment by Five Bacterial Groups Forming a Degradation Network

The Biogeochemical Reaction Network Simulator (BRNS, [186, 187]) is coupled to OpenGeoSys following a sequential non-iterative operator splitting scheme yielding the reactive transport model OpenGeoSys-BRNS. The technical coupling is sketched in Fig. 15.12.

### 15.7.1 Definition

An experimental study by von Gunten and Zobrist [188] has been used to validate the reactive transport models TBC [189] and the stand-alone 1D version of BRNS [190]. Both models could reproduce the experimental data set. Here, we use the same simulation scenario to validate GeoSysBRNS and compare simulation results to BRNS results.

In the example referred to as “Scenario 1” in [190], a sand column of 29 centimeters in length is constantly flushed with water containing lactate as an electron donor, and oxygen, nitrate, and sulfate as terminal electron acceptors (TEAs). Manganese and iron oxyhydroxides are bound to the sand matrix in solid phases and act as two additional TEAs. Five distinct microbial

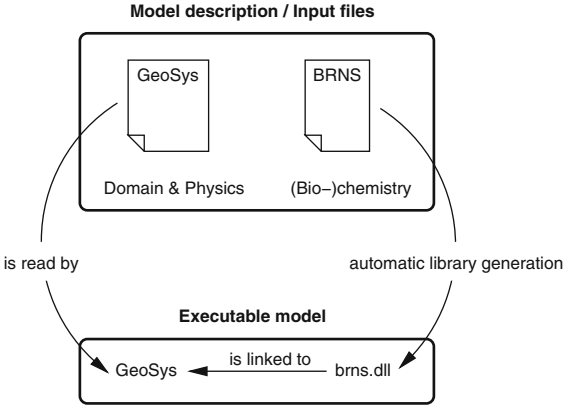


Figure 15.12: The setup of OpenGeoSys-BRNS. The model description is divided into two parts: the model domain definition, physical parameters, hydrogeological flow, and discretization parameters in OpenGeoSys format, and the description of the coupled (bio-)chemical reaction processes in BRNS format. The latter is compiled into a problem specific library that is accessed by OpenGeoSys at runtime

- phase exchange (matrix, biophase, pore water)
- oxidation of sulfide by Fe(III)
- precipitation and dissolution of calcite and Fe(II) minerals
- acid-base reactions for carbonates, sulfides, lactate, propionate, acetate

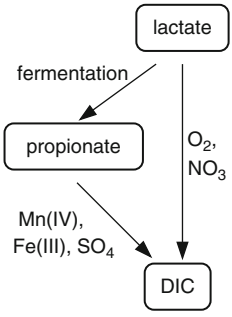


Figure 15.13: Modeling organic carbon degradation in a sand column experiment. Coupled abiotic processes considered in the model (*left*), and microbial degradation pathways with corresponding TAEs (*right*)

groups, which catalyze the reduction of each TEA to sustain their growth, are considered in the model. The experimental results suggest that lactate is concomitantly mineralized into dissolved inorganic carbon (DIC) and fermented to acetate and proprionate, with the latter being further oxidized into DIC. In addition to these microbial degradation pathways, reactive species concentrations are influenced by a set of abiotic reactions (Fig. 15.13). The complete reaction network of the model consists of 21 mobile and 18 immobile

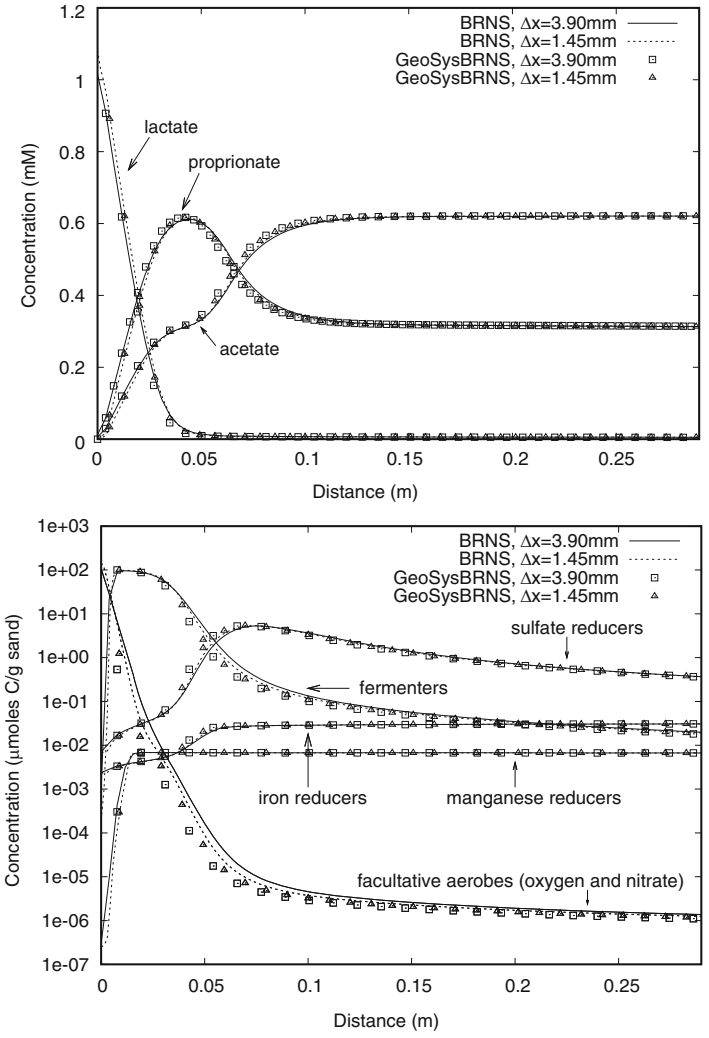


Figure 15.14: Comparison of simulation results obtained with BRNS (*lines*) and OpenGeoSys-BRNS (*symbols*): organic species (*top*) and all five bacterial groups (*bottom*) at day 48 using the highest temporal resolution ($\Delta$t=4 s) and two spatial resolutions

reactive species. The dynamics of the system is determined by 24 kinetically controlled chemical reactions and nine equilibrium reactions describing acid base dissociations.

The coupling of the BRNS to OpenGeoSys is shown to be correct by comparing simulation results of OpenGeoSys-BRNS to BRNS results [191].

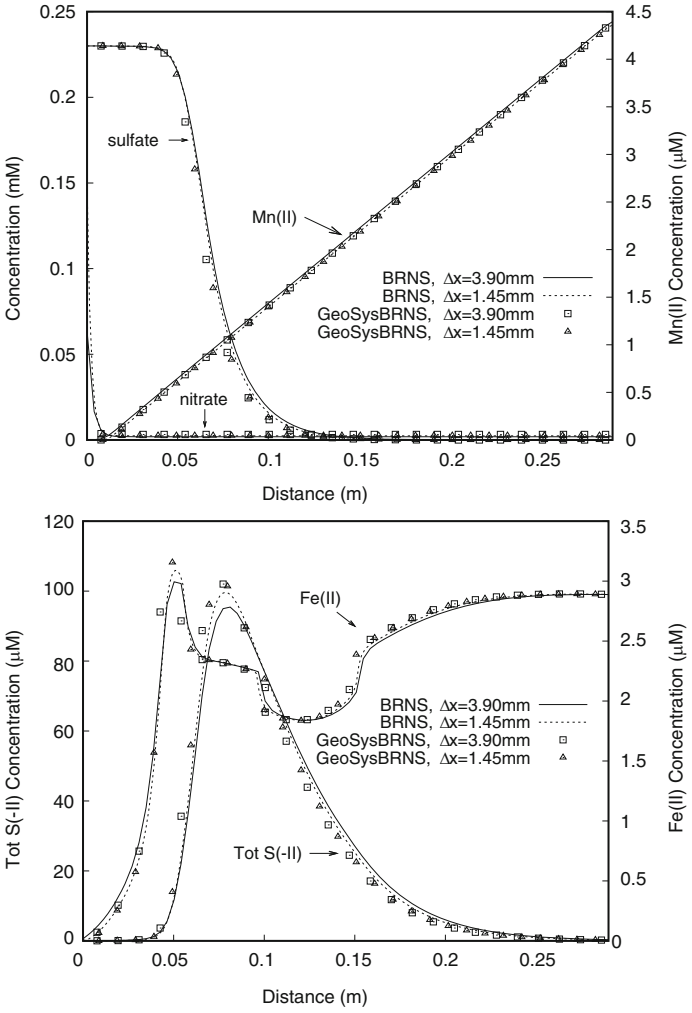


Figure 15.15: Comparison of simulation results obtained with BRNS (*lines*) and OpenGeoSys-BRNS (*symbols*): inorganic species at day 48 using the highest temporal resolution ($\Delta$t=4 s) and two spatial resolutions

### 15.7.2 Solution

We simulate the experiment with OpenGeoSys-BRNS using two spatial resolutions and three different temporal resolutions per spatial setting, ensuring Courant numbers smaller than 1.0 in all cases. As in previous studies [189, 190], we choose 48 days as the target time for comparing the results of the coupled model to those obtained with the BRNS model using the same set of

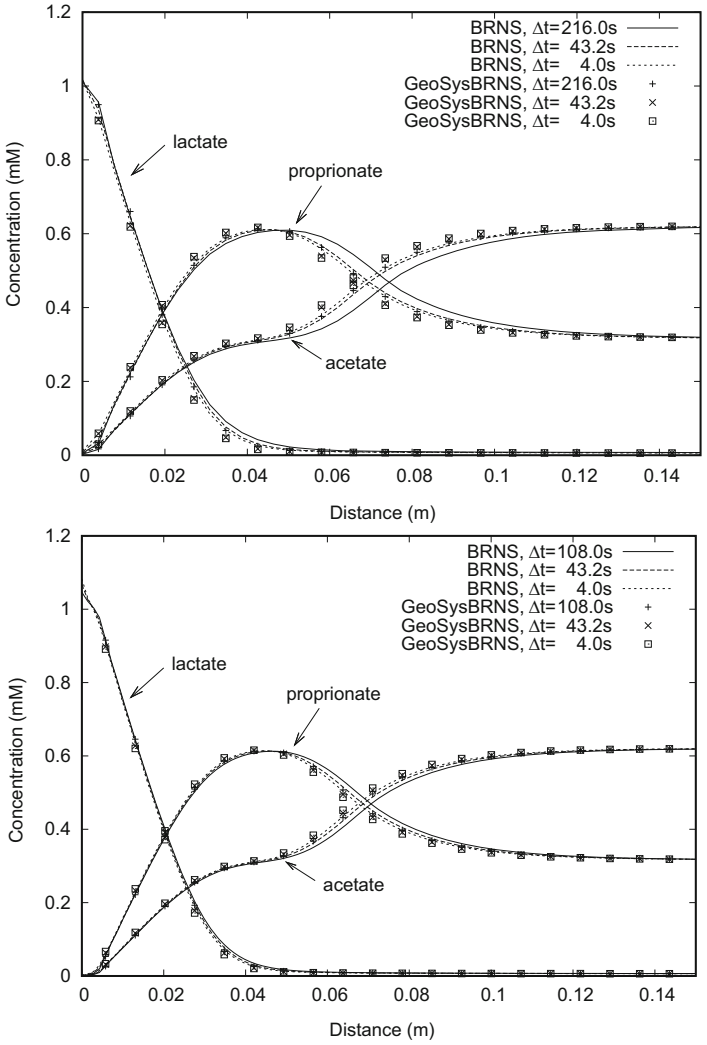


Figure 15.16: Comparison of simulation results obtained with BRNS (*lines*) and OpenGeoSys-BRNS (*symbols*) at day 48 using two spatial resolutions (*top*: Δx=3.9mm, *bottom*: Δx=1.45mm) and different time step sizes for lactate, proprionate, and acetate

spatio-temporal resolution settings. At this target time, the system is still in the transient state.

The simulation results of OpenGeoSys-BRNS and BRNS agree very well for all 39 reactive species at the highest spatial and temporal resolution (see selected species in Figs. 15.14, 15.15). Decreasing the spatial resolution leads to slightly different results, with the coupled model generally staying closer to the high resolution results than the stand-alone version of BRNS (Figs. 15.14, 15.15).

When the time step size is increased, the numerical results of both models diverge from the high resolution results (Fig. 15.16). While increasing the time step from 4 s to 43.2 s does not lead to significant changes for both models and both spatial resolutions, a noticeable deviation is observed when the time step size is increased further to 108 s for the high, and to 216 s for the low spatial resolution. For these larger time step sizes, the results of OpenGeoSys-BRNS are again generally closer to the high resolution results than the BRNS solutions. The observed differences can be attributed to the different numerical schemes used by BRNS (finite differences) and OpenGeoSys-BRNS (finite elements). Further details of the OpenGeoSys-BRNS and its performance can be found in [191].

## 15.8 1D Reactive Transport: Mixing Controlled Biodegradation (2D)

### 15.8.1 Definition

For contaminated groundwater, the natural remediation process is usually limited by the availability of substrates acting as a carbon source for soil bacteria and the availability of electron acceptors. The transport of these chemical compounds is controlled by the dispersion length of the flow system. Recently, Cirpka and Valocchi [192] presented an analytical solution (revised in [193]; see also [194]) for the steady state of a two-dimensional scenario dominated by transversal mixing. This example serves as a first multidimensional benchmark to validate OpenGeoSys-BRNS. [192] and [193] provide analytical solutions for double-monod kinetics with first-order biomass decay. OpenGeoSys-BRNS is also compared to the KinReact module of OpenGeoSys(OpenGeoSys-KRC), which is able to solve the same problem.

In this scenario, bacterial growth is modeled using double-monod terms for the substrates. Biomass decays with a constant decay rate $d$. The overall dynamics is described by four differential equations, with the dynamics of species A, B, and C directly linked to the biomass growth $r$ via yield factor $Y$:

$$\frac{\partial C_{bio}}{\partial t} = \underbrace{\frac{C_A}{K_A + C_A} \cdot \frac{C_B}{K_B + C_B} \cdot \mu_{max} \cdot C_{bio}}_{r} - d \cdot C_{bio} \tag{15.19}$$

$$\frac{\partial C_A}{\partial t} = -\frac{1}{Y} \cdot r \tag{15.20}$$

$$\frac{\partial C_B}{\partial t} = -\frac{1}{Y} \cdot r \tag{15.21}$$

$$\frac{\partial C_C}{\partial t} = +\frac{1}{Y} \cdot r. \tag{15.22}$$

The chemical parameters and their values are listed in Table 15.9.

Table 15.9: Reaction parameters and values

| Symbol | Parameter | Value | Unit |
|---|---|---|---|
| $K_A$ | Monod constant substrate A | $8.33 \times 10^{-5}$ | mol·L$^{-1}$ |
| $K_B$ | Monod constant substrate B | $3.13 \times 10^{-5}$ | mol·L$^{-1}$ |
| $\mu_{max}$ | Maximum growth rate | 1.0 | d$^{-1}$ |
| $d$ | Biomass death rate | 0.1 | d$^{-1}$ |
| $Y$ | Yield coefficient | 1.0 | g·mol$^{-1}$ |

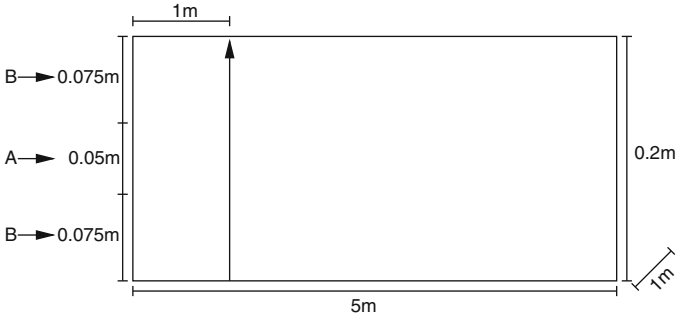


Figure 15.17: The simulation domain. Simulation results are compared using concentration profiles along a transect at a distance of one meter from the inflow boundary, indicated by the arrow

Using OpenGeoSys-BRNS, here we simulate the case as a transient state groundwater flow process coupled with biodegradation. The numerical solutions are compared to the analytical steady state solutions and against the OpenGeoSys-KRC simulation.

The model domain is 5 meters long and 20 cm wide (see Fig. 15.17). Groundwater flows from left to right. Transport velocity is 1 m/d. The transport parameters are listed in Table 15.10. Two substrates are continuously emitted at the left inflow boundary throughout the simulation period. Substrate A is centrally injected over a width of 5 cm with a concentration of $3.3 \times 10^{-4}$ mol/l, while substrate B is emitted at the remaining part of the boundary with a concentration of $2.5 \times 10^{-4}$ mol/l. Initially, the concentration in the whole simulation domain is zero for substrate A, $2.5 \times 10^{-4}$ mol/l for substrate B and $1.0 \times 10^{-6}$ g/l for biomass. Biomass is considered to be immobile.

In the presence of both species A and B, with A representing a generic organic contaminant acting as a carbon source and B representing a generic electron acceptor, the biomass grows, and a waste product C is formed.

For the numerical simulation, a grid spacing of 2.5 cm in flow and 0.4 cm transversal to the flow direction is used. Temporal discretization of 2 min is

Table 15.10: Transport parameters and values

| Parameter | | Value | Unit |
|---|---|---|---|
| $v_a$ | Transport velocity | 1.0 | $\mathrm{m{\cdot}d^{-1}}$ |
| $D_t$ | Transversal dispersion coefficient | 2.5 | $\mathrm{cm^2 \cdot d^{-1}}$ |
| $D_l$ | Longitudinal dispersion coefficient | 0.0[a] | $\mathrm{cm^2 \cdot d^{-1}}$ |

[a]As a zero value cannot be used in the numerical simulation, the value $2.5 \times 10^2 \mathrm{cm^2/d}$ was used instead. When the numerical simulation reaches steady state, this difference can be neglected

employed. The OpenGeoSys-KRC simulation additionally verifies the functionality of three routines, which were implemented to enhance computational efficiency of the numerical simulation:

- The steady state flow field is computed only once (i.e. for the first time step) during the simulation. For later time steps, the velocities calculated for the first time step are reused for all transport processes. This modus is invoked by the flow process keyword

```
$TIM_TYPE
 STEADY.
```

- Mass matrices for all transported (i.e. mobile) species are computed only once (i.e. for the first time step), stored and reused for later time steps. This modus is invoked by mass transport process keyword

```
$MEMORY_TYPE
 1
```

- Source terms are defined as volumetric fluxes $[\mathrm{m^3 \cdot s^{-1}}]$. The flux defined for a polyline is evenly distributed to all nodes of that polyline. This modus is invoked for a source term by the keyword

```
$DIS_TYPE
 CONSTANT_GEO  2.31481E-06
```

  where the number represents the volumetric flux assigned to a polyline.

In the OpenGeoSys-KRC simulation, the downgradient model boundary consists of two polylines with lengths of 0.15 and 0.05 m, respectively. In order to achieve a transport velocity (setting porosity $n = 0.5$) of 1 $\mathrm{m{\cdot}d^{-1}}$ (or $1.15741 \times 10^{-6}$ $\mathrm{m{\cdot}s^{-1}}$) with a given total model cross section of 0.2 $\mathrm{m^2}$ (i.e. assuming a unit width of the model), the volumetric fluxes assigned to the polylines are $-8.75130 \times 10^{-7}$ and $-2.822945 \times 10^{-7}$ $[\mathrm{m^3 \cdot s^{-1}}]$, respectively.

### 15.8.2 Solution

The concentrations of the conservative tracer (i.e. the mixing ratio $X$) fit well with the analytical solution, indicating that the flow field and conservative transport is properly simulated by both models. All of the three routines tested work correctly in the OpenGeoSys-KRC simulation, which allows a reduction of computation time by approximately 50% for this test example. Also, both numerical simulations yield the same results for the reactive species. However, some small discrepancies are found between the numerical and the analytical solutions for the components A, B, C, and (most obvious) for the biomass concentration (see Fig. 15.18). This is mainly due to the problem of exactly defining the transitions between boundary conditions of components A and B on the inflow boundary of the model: polylines defining inflow concentrations of A and B may not share nodes and hence the boundary condition polylines are separated by a distance of one element width (i.e. 0.005 m) which has to be overcome by transverse dispersion before A nd B may react with each other, while in the analytical solution A and B are in direct contact right at the model boundary. This problem and hence differences between numerical and analytical solutions, may be reduced by a local mesh refinement at the left hand side model boundary.

## 15.9 2D Reactive Transport Simulation of COMEDY Clogging Experiment

Clogging is a widely occurring phenomenon in porous media. The change of pore space structure normally leads to different behaviors of hydraulics. In such systems, flow and transport of solutes are strongly coupled with chemical reactions, imposing challenges to numerical simulations. The COMEDY experimental setup [195] was a 2D reactive transport scenario which involves clogging and perforation of an interface. Numerical models such as CRUNCH and HYTECH have been applied to simulate it. In this section, simulation results from OpenGeoSys-GEM are compared against those from other codes.

### 15.9.1 Definition

Figure 15.19 shows the geometry of the model domain. It is a chamber containing 3 regions. Two of them (Q1 and Q3) are made of chemically inert quartz and the central region (Q2) contains the reactant mineral portlandite. Oxalate ions were injected as a constant flux through Inlet 2, and sodium chloride solutions were introduced through Inlet 1 (Table 15.12). In Q2, the chemical reaction between the inlet solution and portlandite leads to the precipitation of calcium oxalate, as in the following.

$$C_2O_4^{2-} + Ca(OH)_2 + H_2O \Rightarrow CaC_2O_4 \cdot H2O + 2OH^- \tag{15.23}$$

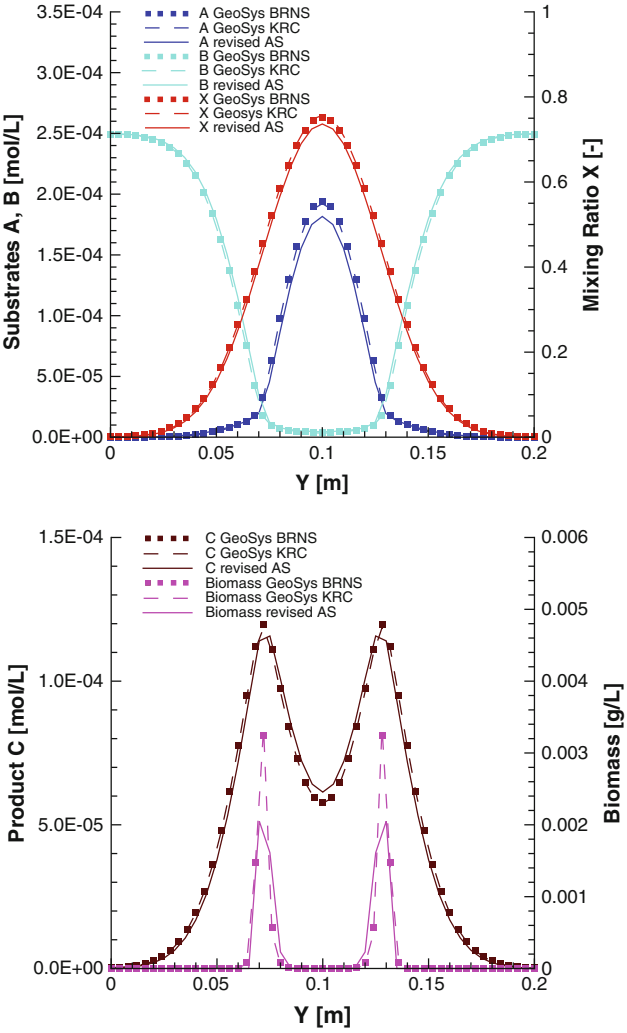


Figure 15.18: Simulation results for the transversal mixing model, using the kinetic approach and the finest temporal and spatial resolution. Analytical solution as solid lines, result of the numerical simulations with OpenGeoSys-BRNS as symbols and of OpenGeoSys-KRC as dashed lines

The initial and boundary chemical was set up using the GEMS-PSI software package. It implements a Gibbs energy minimization algorithm in thermodynamic modeling of equilibrium in heterogeneous aquatic chemical systems. The oxalate ion was introduced as an independent component in the thermodynamic database. The reaction (15.23) was also introduced with equivalent logK values as in [195]. The detailed chemical setup for the different regions are given in

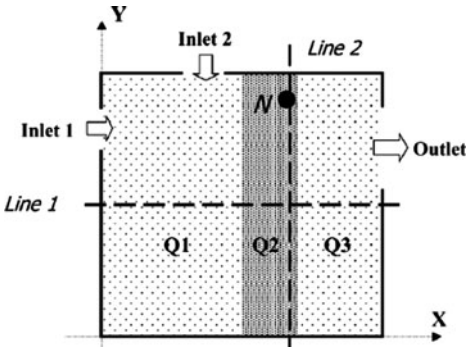


Figure 15.19: 2D model domain for the COMEDY experiment according to [195]. The setup is a square (14 cm of edge size). Lines labeled Line 1 (y = 7.0 cm) and Line 2 (x = 9.5 cm) (respectively node N (x = 9.5 cm; y = 10.8 cm)) are test lines/node on which specific profiles will be compared

Table 15.11: Equilibrium amount of independent components and phases for boundary and initial conditions

| | Component | Q1(=Q3) | Q2 | I1 | I2 |
|---|---|---|---|---|---|
| Amount of chemical species in aqueous phase (mol) | C | 1.00e-5 | 5.50e-8 | 6.20e-8 | 5.51e-8 |
| | Ca | 1.00e-5 | 3.32 | 4.70e-8 | 3.00e-8 |
| | Cl | 1.20e-5 | 1.71e-12 | 0.02 | 4.25e-5 |
| | H | 33.2 | 27.7 | 33.2 | 33.3 |
| | Na | 1.71e-10 | 1.35e-3 | 0.02 | 0.8 |
| | O | 78.3 | 78.9 | 78.3 | 78.4 |
| | Oxa | 2.00e-8 | 1.00e-8 | 2.00e-8 | 0.40 |
| | Si | 30.9 | 30.9 | 30.9 | 30.9 |
| | Zz | 0 | 0 | 0 | 0 |
| Amount of solid phases (mol) | Graphite | 3.50e-8 | 3.50e-8 | 3.50e-8 | 3.50e-8 |
| | Aragonite | 1.00e-8 | 1.00e-8 | 1.70e-8 | 1.00e-8 |
| | Calcite | 1.00e-5 | 1.00e-8 | 1.00e-8 | 1.00e-8 |
| | Portlandite | 0 | 3.33 | 0 | 0 |
| | Calcium Oxalate | 1.00e-8 | 1.00e-8 | 1.00e-8 | 1.00e-8 |
| | Quartz | 30.87 | 30.87 | 30.87 | 30.87 |
| | Amorph Silica | 0 | 0 | 0 | 0 |
| Equilibrium state | pH | 7 | 12.5 | 7 | 7 |
| | Liquid volume (L) | 0.3 | 0.19 | 0.3 | 0.3 |
| | Total volume (L) | 1 | 1 | 1 | 1 |

Table 15.12: Model Setup for the inlets

| Velocity (m/s) | Inlet 1 | Inlet 2 |
|---|---|---|
| x | 5.7143e-10 | 0 |
| y | 0 | 11.429e-10 |

Table 15.13: Hydraulic parameters of the model domain

| Parameters | Q1 | Q2 | Q3 |
|---|---|---|---|
| Hydraulic conductivity ($m^2/s$) | 1.00e-5 | 1.64e-6 | 1.00e-5 |
| Dispersivity (m) | 2.00e-2 | 2.00e-2 | 2.00e-2 |
| Diffusion coefficient ($m^2/s$) | 3.33e-9 | 3.33e-9 | 3.33e-9 |
| Tortuosity | 1.0 | 1.58 | 1.0 |

Table 15.11. At some points, the system is in an undefined redox state. To avoid this, a small amount of dissolved $O_2$ was introduced in the initial bulk composition to keep the system in oxic condition. The value of porosity is obtained using the ratio $V_{Initial}/V_{Total}$.

The chamber is discretized with a finite element mesh of quadrilateral elements of 3.3 mm size. The domain contains 1,849 nodes and 1,764 elements. A variable time step scheme is used to calculate the maximal time step size, which influences the accuracy of simulation results. The pressure at the outlet is set to 1 bar.

The tortuosity is set different for the Q2 region to mimic the initial effective diffusion coefficient, which is the same ($1 \times 10^{-9}$) for the 3 regions in [195] (Table 15.13). In this study diffusion and dispersion are assumed isotropic and $D^*$ reduces to a scalar form, $D* = \alpha \| \overrightarrow{U} \| + D$ where $D$ is the effective diffusion coefficient. It is assumed that all solutes have the same value. $\alpha$ (m) is the dispersivity of the porous medium and $\overrightarrow{U}$ is the Darcy velocity vector. In this benchmark, advection and diffusion govern the transport process. The Archie's diffusion law $D_e = n^m \cdot D_p$ is applied in this model. The dissolution/precipitation reaction rate $r_s$ (mol/s) is defined according to the following formula,

$$r_s = -A_s k_{rate}[1 - (Q_s/K)] \tag{15.24}$$

where $k_{rate}$ is the dissolution and precipitation rate constant (mol $\cdot m^2 \cdot s^{-1}$). $Q_s$ is the ion activity product. $K$ is the equilibrium constant and $A_s$ is the specific surface area ($m^2 \cdot mol^{-1}$). The values used here are $A_{bulk} = 1,000\ m^2_{solid}/m^3_{porousmedium}$, $log_{10}K_{Portlandite} = -5$ and $log_{10}K_{CaOxa} = -5$.

### 15.9.2 Solution

For the flow part, (Fig. 15.20) shows the Darcy velocities on Line 1, compared against the results given by HYTEC. The results obtained with OpenGeosys are in good accordance quantitatively and qualitatively.

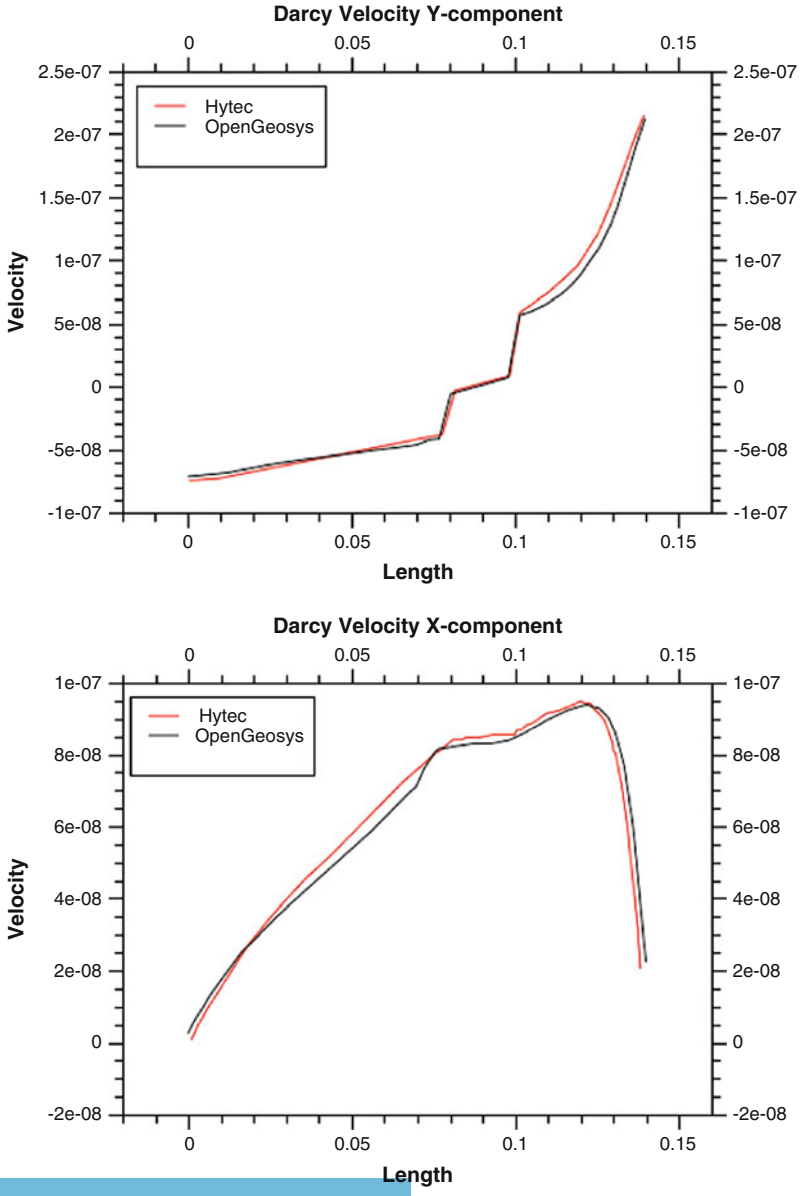


Figure 15.20: Darcy velocity profile on line 1 (x=70 cm)

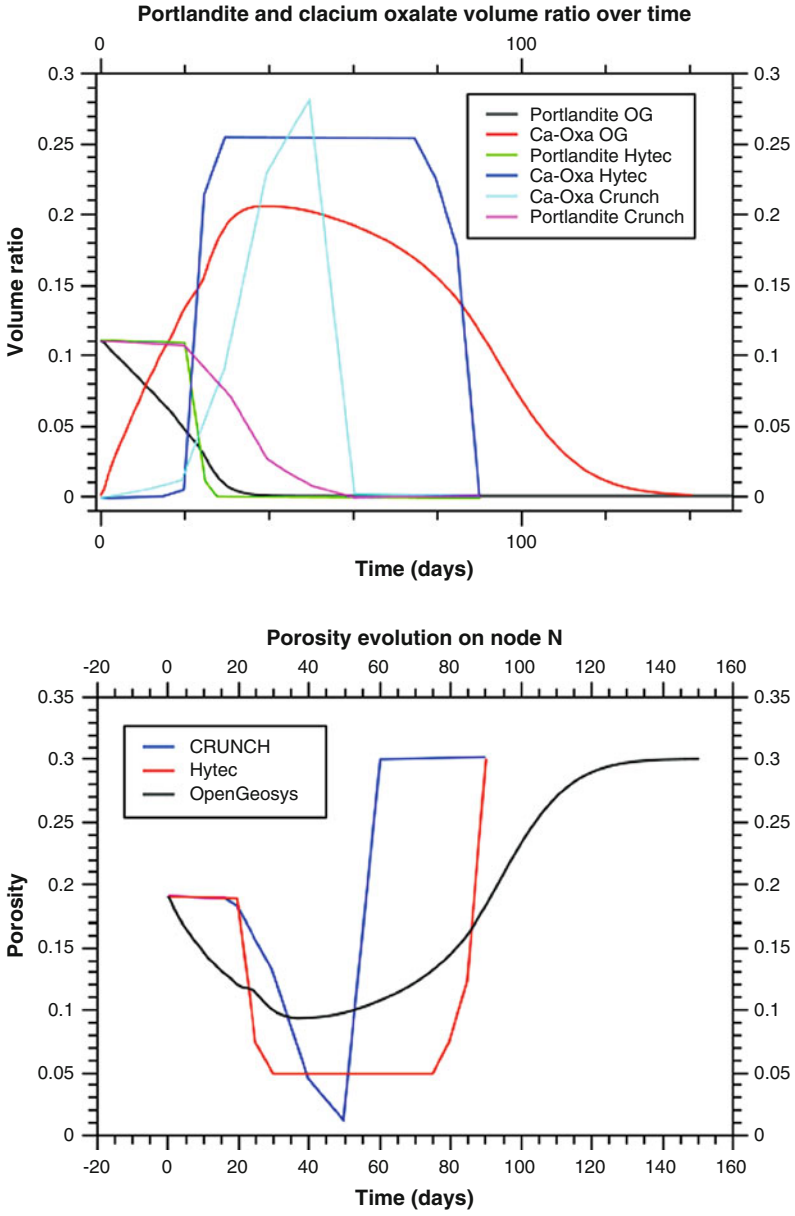


Figure 15.21: Solids volume ratio and porosity evolution on node N (x=0.096m; y=0.11m)

For the clogging process, porosity evolution profile (Fig. 15.21) calculated by OpenGeoSys-GEM is compared against those from HYTEC and CRUNCH [195]. Qualitatively the results are in good accordance. Portlandite dissolves

and calcium oxalate precipitates. After the calcium oxalate volume fraction reaches a maximum it dissolves. The porosity follows the opposite evolution of mineral volume fraction due to the decrease of 33mL per mol of reacted portlandite. When calcium oxalate starts to dissolve, the porosity increases until it reaches the maximal value of 0.3, due to an inert quartz background in Q2.

Quantitatively, the results are different in several aspects. One of them is the evolution of porosity with time. With OpenGeosys, the portlandite dissolves much faster. It took 20 days in OGS, whereas in CRUNCH and HYTEC the complete dissolution happens after 60 and 27 days respectively. The calcium oxalate is completely dissolved after 156 days in the OGS result, and took 60 and 90 days for CRUNCH and HYTEC. The porosity follows the same evolution in time. The dissolution time of calcium oxalate can be slightly reduced by increasing its precipitation/dissolution rate. Another difference is that with HYTEC and CRUNCH, portlandite volume ratios remain approximately constant for the 20 days before dissolving. This difference can be explained by the fact that water in Q1 and Q3 is not in equilibrium with portlandite. When it diffuses into Q2, it starts to dissolve portlandite before oxalate ions reach the node N. Also noticed is, the height of the maximum of calcium oxalate (20% vol. for Opengeosys, 28.1% vol. for CRUNCH, and 25.5% vol. for Hytec) makes the obstacle created with the OpenGeosys simulation more permeable. An increase in the height of the maximum is observed when the precipitation/dissolution rate of calcium oxalate is increased.

# Appendix A

# Software Engineering

*by Lars Bilke*

The OpenGeoSys software development community is distributed all over the world and people with different backgrounds are contributing code to a complex software system. The following points have to be addressed for successful software development:

- Platform independent code
- A single build system
- A version control system
- A collaborative project web site
- Continuous builds and testing
- Providing binaries and documentation for end users

OpenGeoSys should run on a PC as well as on a computing cluster regardless of the operating system. Therefore the code should not include any platform specific feature or library. Instead open source and platform independent libraries like Qt[1] for the graphical user interface or VTK[2] for visualization algorithms are used so that developers can simply use the platform or tools they want.

Despite the use of platform independent code and libraries, in the end there must be platform specific build settings or project files for integrated development environments like Visual Studio or Eclipse. These are generated by the CMake[3] build system which is configured using platform independent configuration files.

[1] Qt: `http://qt.nokia.com/products/`
[2] The Visualization Toolkit: `http://www.vtk.org`
[3] CMake: `http://www.cmake.org`

O. Kolditz et al. (eds.), *Thermo-Hydro-Mechanical-Chemical Processes in Fractured Porous Media*, Lecture Notes in Computational Science and Engineering 86,
DOI 10.1007/978-3-642-27177-9, © Springer-Verlag Berlin Heidelberg 2012

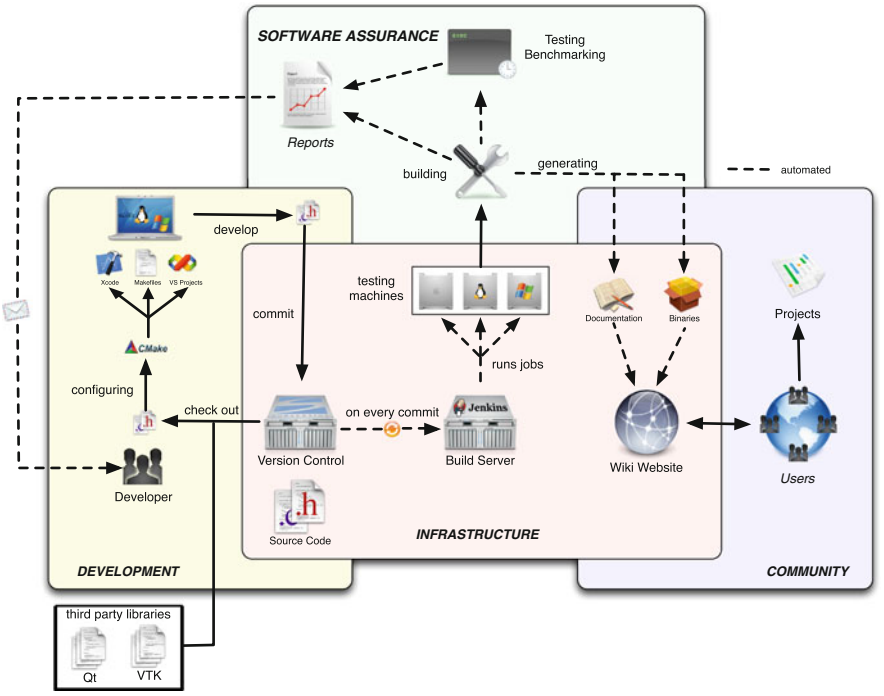


Figure A.1: Overview of the OpenGeoSys software engineering workflow

Also, CMake enables so-called *out of source builds* which means that all the generated files are separated from the source code. This makes it easier to manage the source code in a version control system.

A source code management and version control system is a definite requirement for distributed software development. For this purpose Subversion[4] is used, which enables developers to work on separate versions (*branches*) of the software and to merge those versions at some point to the official one.

The version control system is integrated into an information and collaboration website based on a wiki[5] system. The wiki is used for collecting information such as tutorials, application examples and case studies. Discussions take place in the OpenGeoSys mailing list.[6]

To improve code stability and to verify code correctness a continuous build and testing system, based on the Jenkins Continuous Integration Server,[7] has been established. This server is connected to the version control system and does the following on every code change:

[4]Subversion: `http://subversion.tigris.org/`
[5]TracWiki: `http://trac.edgewall.org/wiki/TracWiki`
[6]OGS-Mailinglist: `http://groups.google.com/group/ogs6`
[7]Jenkins: `http://jenkins-ci.org/`

- Compiles (*builds*) the code on every supported platform (Linux, Windows, MacOS)
- Runs a comprehensive test suite of over 120 benchmarks
- Verifies the test results
- Runs software development related metrics on the code (like compiler warnings, code complexity, static analysis tools)
- Generates source code documentation
- Provides binaries for end users
- Informs developers on errors

These points enhance the software development process considerably. Firstly, t platform independence is maintained. Additionally, errors in the source code, and at which time they were introduced, can be tracked down easily. Lastly, developers gain access to code analysis tools and up-to-date source code documentation without the need to install it on their own machines.

Figure A.1 shows an overview of the software engineering workflow and concludes this section.

# Appendix B

# Data Processing

*by Karsten Rink and Thomas Fischer*

OpenGeoSys is a program for the simulation of (coupled) thermal, hydrological, mechanical and chemical processes that contains a large amount of FEM-related functionality and numerical solvers. It is, however, a command line tool and therefore not intuitive for first time users. Also, it is difficult to get a feeling for the data that is utilized by the program and simulation results cannot be directly verified without the help of other tools.

To address these issues, the OpenGeoSys Data Explorer has been developed as a graphical user interface (GUI) for OpenGeoSys (see Fig. B.1). This allows for a 3D visualization of input and output data of process simulations and will thus convey a better understanding of the data as well as the simulations. As with the simulation software itself, the Data Explorer is platform independent due to the use of the open source application framework Qt and is tested under Windows- and Linux-based operating systems as well as MacOS. It employs the same basic data structures as the command line tool and thus complements OpenGeoSys by giving users a way to visually assess their data sets.

An interactive 3D view (see Fig. B.2) often enhances the understanding of data and makes it easier to discuss certain aspects or problems with other scientists. In addition to handling the native OpenGeoSys file formats, the Data Explorer also provides a large number of interfaces for the import of files created by established geoscientific software products such as the geographic information system ArcGIS, the groundwater modeling software GMS and, to a certain degree, software used in the mining or petroleum industry such as Petrel or Gocad. Non-spatial information, such as time series data or borehole stratigraphies, can

O. Kolditz et al. (eds.), *Thermo-Hydro-Mechanical-Chemical Processes in Fractured Porous Media*, Lecture Notes in Computational Science and Engineering 86,
DOI 10.1007/978-3-642-27177-9, © Springer-Verlag Berlin Heidelberg 2012

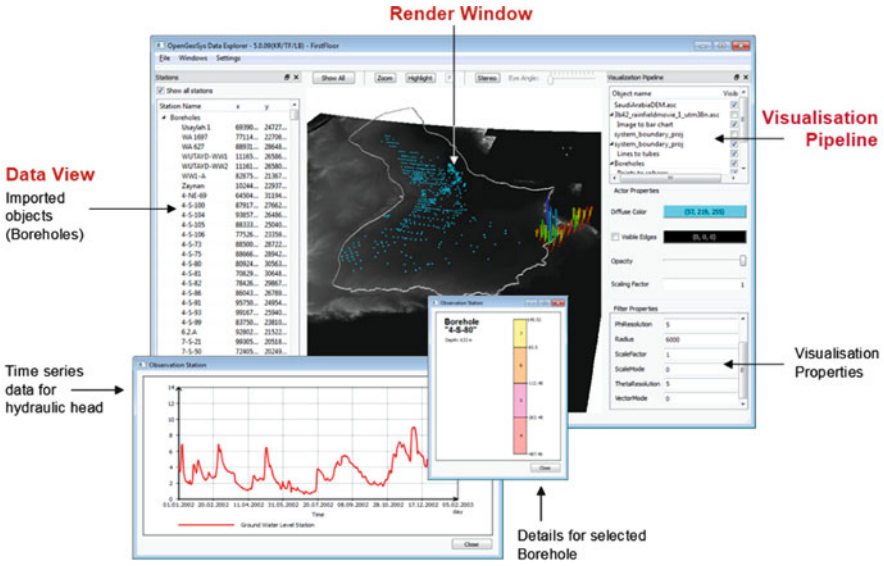


Figure B.1: The graphical user interface of the OpenGeoSys Data Explorer

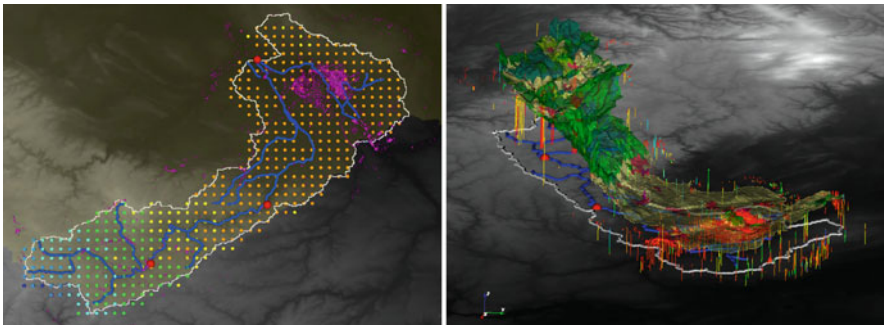

(a) 2D view (b) 3D view

Figure B.2: Example for visualization of multiple data sets. Figure B.2(a) depicts geometrical information such as the boundary of the model region (*white*), the river network (*blue*), gauging stations (*red*) and boreholes (*pink*) in addition to a discrete precipitation map where the *blue dots* mark high precipitation and the *red/orange dots* low precipitation. Figure B.2(b) shows the same scene in 3D (although without the precipitation). Boreholes can now be seen as 3D structures. A semi-transparent surface mesh overlaid with land use classes as been added to the scene

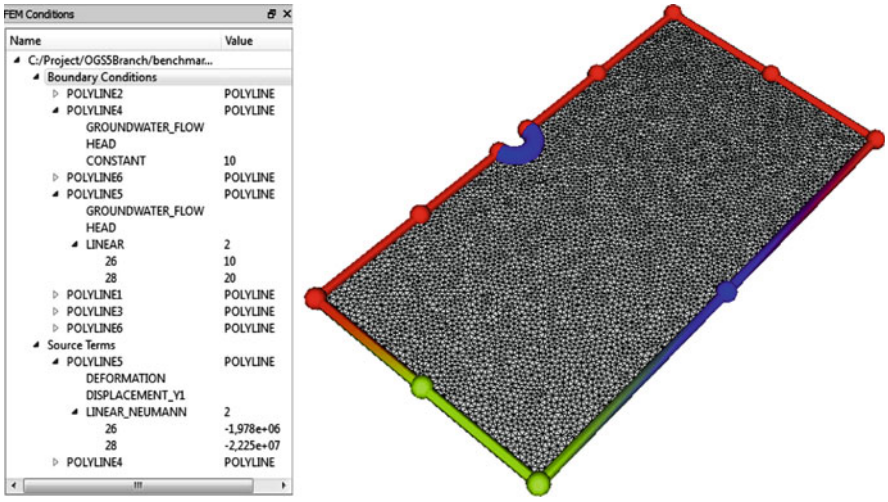


(a) Information (b) 3D visualization

Figure B.3: Example for visualization of FEM related data. Depicted are a number of boundary conditions for a FEM Mesh along with detailed information about their properties

be viewed in separate 2D windows. Furthermore, it is possible to import image data in popular formats such as JPEG or PNG. In addition to all these geoscientific input data formats, it is also possible to visualize FEM-related information like boundary conditions (see Fig. B.3) and 3D object structures in the widespread VTK format. In particular, this format is used to store the time invariant results of process simulations calculated using OpenGeoSys .

The Data Explorer supports users when preparing simulations by allowing them to see how various data sets complement or interact with each other. When heterogeneous data sets from different sources are integrated into a model, it is not uncommon that inconsistencies between those data sets exist. Typical examples in the scope of hydrological data include the course of rivers not quite matching the underlying terrain model, subsurface layers penetrating each other or boreholes not starting at ground level but instead above or below the surface. The reasons for such inconsistencies are manifold and can be attributed to different data acquisition methods (such as remote sensing data scanned from orbit via satellites, borehole logs created manually using core samples, etc.), data conversion problems or human error. However, if models for the simulation of processes such as groundwater recharge are based on faulty or conflicting information they might produce erroneous or deceptive results. An interactive 3D view allows the user to assess the quality of the data and detect inconsistencies, artifacts or missing information.

A number of visualization options are available in the GUI to support users in this assessment process by allowing the adjustment of a number of visualization

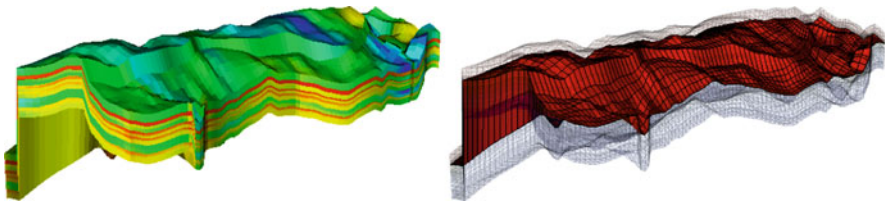

(a) All elements (b) Zero volume elements

Figure B.4: Visualization of mesh element quality. *Blue* signifies good quality; *red* elements might cause problems during simulation. Figure B.4(b) depicts a layer containing zero volume elements blended into the transparent mesh

parameters for each data set. Examples include

- Super elevation of objects
- Adjusting transparency, such that objects occupying the same space can be evaluated
- Application of user defined color tables (e.g. for borehole information)
- Selection of specific materials or stratigraphic layers (e.g. a specific set of lines or a certain subsurface layer) while blanking out the rest of the data set.
- Enlargement of selected features for better visibility

In addition, users can see the underlying data of visualized objects (such as point coordinates, mesh element information, etc.) in a separate menu and can even process geometric data to a certain degree (connecting polylines, triangulation of surfaces, etc.). Furthermore, it is possible to generate parameterized FEM meshes based on existing geometric data with a desired element density and optional mesh refinement towards selected features. For existing meshes it is possible to check the quality of all mesh elements with respect to certain well-establish criteria such as the ratio of the longest to shortest element edge, equi-angle skewness or global element area/volume and then analyze the results of such an analysis directly in the 3D view (see Fig. B.4).

For more information on the topic of evaluation of 3D data sets the interested reader is referred to [196]. A comprehensive specification of the functionality of the OpenGeoSys Data Explorer can be found in the *OpenGeoSys Data Explorer User Manual* [197].

# Appendix C

# GINA_OGS

*by Herbert Kunz*

During the development of the numerical code OpenGeoSys, a program GINA as a pre- and post-processing tool, was developed by the German Federal Institute for Geosciences and Natural Resources (BGR). As an OpenGeoSys user, the development of GINA has continuously matched the requests of applicants. In the field of deep geological disposal of radioactive waste, coupled THMC process modelling is vital for planning and evaluation of experiments in the underground laboratory, for process understanding, and for long-term safety assessment with the complicated geological and geotechnical geometry (Fig. C.1). With the help of GINA, time-consuming handling of pre- and post-processing for a FE-simulation is easy.

The main features of this interactive graphical user interface tool GINA are:

## Pre-processing

- Geometrical data for FE meshing The geometrical objects (points, polylines, surfaces and volumes) can be defined using coordinates input and/or with a mouse, which are the basic objects in the code OpenGeoSys for mesh generating, definition of initial and boundary conditions, and results viewing
- Preparing of finite element parameters Necessary parameters and conditions (initial conditions, boundary conditions, and material properties) can be interactively defined using keyboard and mouse input

O. Kolditz et al. (eds.), *Thermo-Hydro-Mechanical-Chemical Processes in Fractured Porous Media*, Lecture Notes in Computational Science and Engineering 86,
DOI 10.1007/978-3-642-27177-9, © Springer-Verlag Berlin Heidelberg 2012

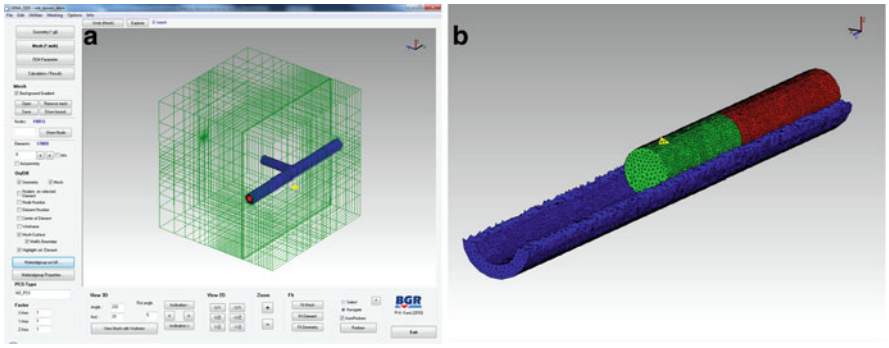


Figure C.1: GINA functions and generated mesh of a rock-EDZ-tunnel system

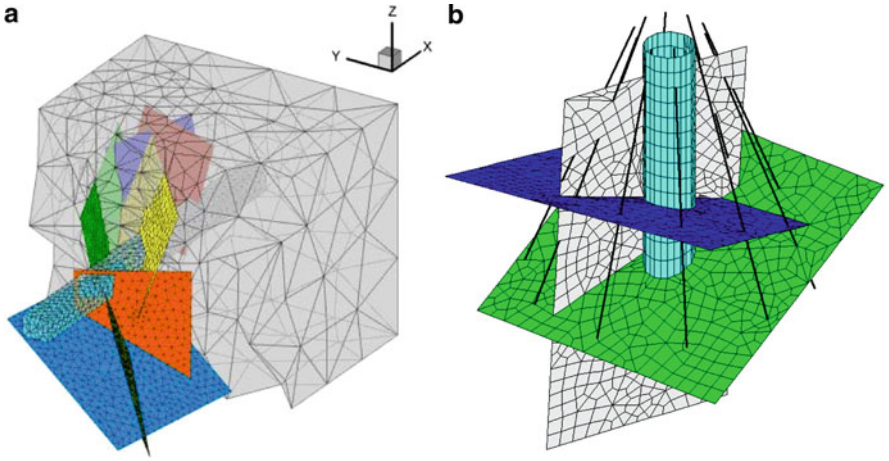


Figure C.2: Finite element mesh for a coupled fracture network and rock mass model (**a**) and fracture-borehole system (**b**)

## Mesh Generation

A mesh generator for structured meshes in 2D (quad) and 3D (prism and hexahedral) elements is implemented in GINA. A special feature for the generation of finite element mesh for a fracture network with surrounding rock mass was developed in the course of the BGR investigation program for fracture flow at Grimsel Test Site (Switzerland) (Fig. C.2).

For the unstructured meshes in 2D and 3D, an interface to the open source software, e.g. GMSH (www.geuz.org/gmsh) for unstructured triangle and quad-elements and TetGen (`http://tetgen.berlios.de`) for tetrahedral elements, is implemented in GINA. With the help of the interface, a high quality mesh of 2D and 3D complex structures can be generated using GMSH and Tetgen based on the geometrical objects in the code OpenGeoSys.

## Post-processing

Using the post-processing functions, simulation results from the OpenGeoSys can be visualized and evaluated during model calculation in the following cases:

- Contour, colour, and isoline plots in the 2D domain
- X/Y—diagram versus time or along a polyline
- Convert to mechanical principle stress from stress field and viewing in vector form

## Data Interface

To interact with other programs GINA has the following import and export formats:

- Import File Formats: GMSH, TetGen, Tecplot, DXF, ASCII.
- Export File Formats: GMSH, TetGen, JPG, VRML, Excel

## Contact Information

For more information, please contact: herbert.kunz@bgr.de

# Appendix D

# Geometric Modelling, Gridding and Visualization

*by Björn Zehner*

Geometric modelling and 3D visualization are two aspects that are important for scientific simulation. The first one is a preprocessing step in which a 3D description of the input model is set up which is later needed for generating the 3D grid on which the simulation is run and for setting the different parameters on the grid's cells and the initial and boundary conditions. The latter one is needed because the output of the simulation is usually a vast amount of numbers. Visualization (and Virtual Reality) deals with the question of how to represent these numbers in an intuitive and comprehensible way. Examples of this are the visualization of tensor fields from geomechanics [198] or of scalar fields with uncertainty [199].

Figure D.1 shows the overall processing workflow, from data interpretation via modelling and simulation, to visualization as it is used in the geoscience domain. As a first step, a 3D model describing the subsurface is constructed from the field data provided. While this 3D model construction can be done using CAD software for geotechnical and engineering applications, more complicated and irregular geological structures require specialized software. One program commonly used for this task by many universities, state agencies and oil companies is GOCAD[1] from Paradigm Ltd, while another example is Petrel[2] from Schlumberger. The next necessary step is the generation of 3D simulation grids from

[1] GOCAD: `http://www.pdgm.com`
[2] Petrel: `http://www.slb.com`

O. Kolditz et al. (eds.), *Thermo-Hydro-Mechanical-Chemical Processes in Fractured Porous Media*, Lecture Notes in Computational Science and Engineering 86,
DOI 10.1007/978-3-642-27177-9, © Springer-Verlag Berlin Heidelberg 2012

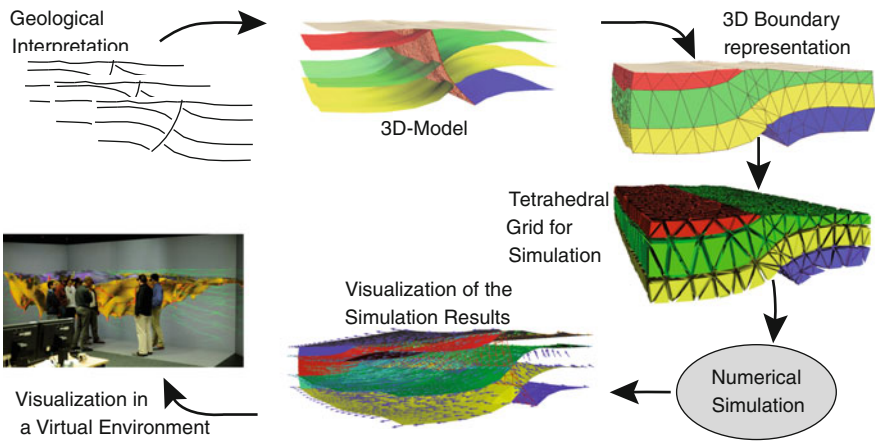


Figure D.1: Processing workflow from geological interpretation and geometrical modelling via simulation to visualization

geometrical models. For the purpose of reservoir simulation, hexahedral grids and finite difference simulation techniques are more common, and the construction of such grids works well in most modelling packages. However, to represent complicated 3D geological structures, such as fault systems, unstructured grids that use tetrahedra are more suitable. In order to generate these grids, the modelling software has to be used to construct a boundary representation of the 3D model from which the simulation grid can be generated using e.g. TetGen[3] (a software that is open source for research purposes). TetGen also recognizes if the volume is partitioned into subspaces and assigns corresponding identifiers to the generated tetrahedra. Furthermore, the geometries from the 3D Model can be used to set the initial and boundary conditions, for example a predefined flow on all vertices along a line.

After running the simulation, the results need to be visualized. A very comprehensive C++ library that provides most of the standard algorithms for visualizing scientific data is the Visualization Toolkit (VTK)[4] [200]. VTK is pipeline-oriented and provides different filters that each take an input data set, do some processing (such as isosurface extraction) and forward the result to the next filter or an object that visualizes it. In this way, complicated pipelines can be constructed in order to assess the data. VTK also defines its own file formats and the finite element software OpenGeoSys (OGS) can output simulation results directly in this format. The VTK library can be used to implement a full visualization application. This has been done, for example, with the OGS Data Explorer (see chapter on data processing). Additionally, the open source software Paraview[5] is based on VTK and makes most of the filters available within a graphical user interface.

[3]TetGen: `http://tetgen.berlios.de/`
[4]VTK: `http://www.vtk.org`
[5]Paraview: `http://www.paraview.org`

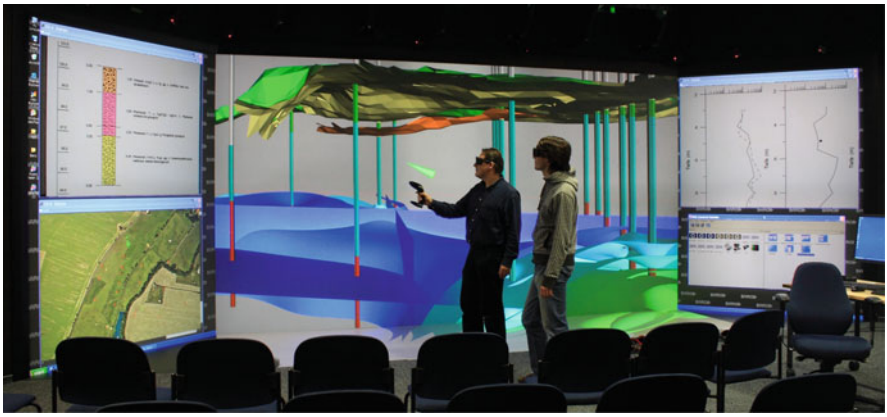

Figure D.2: Combined 2D and 3D visualization in the UFZ's visualization center as suggested in [201]. The rear screen and the floor are used to show the 3D model using head-tracked stereoscopic visualization. On the side screens additional information is shown, such as the stratigraphic profile of a borehole, graphs or a map on which the position of the user is indicated and the direction in which he or she is looking. 2D- and 3D-Views are coupled

If synoptic views are created that visualize simulation results together with the geometrical model and other data on which this model is based, the display quickly becomes cluttered and difficult for viewers to grasp spatial interrelationships of the data. Further, simulation results are often discussed in small groups or presented to stakeholders who are not familiar with the interpretation of the visualization shown to them and for this reason have problems understanding it. Stereoscopic visualization on high resolution display walls can help to overcome these problems as they provide a real 3D impression that is easier for viewers to understand and is capable of showing much more detail. However, these display walls are often more complicated to use as they involve several projectors run by a computer cluster and thus require specialized software. The display at the UFZ-Helmholtz Centre for Environmental Research,[6] for example, uses 13 SXGA+ projectors in a theater-like configuration with a large rear screen, two side screens and a projection on the floor. It can be used either as an immersive VR display or as a display where the rear screen and the floor are used in VR mode, while the side screens show additional 2D information, such as maps, in order to help the users orient themselves within large-scale regional models or borehole data and logs (see Fig. D.2). A full description of the system, its design concept and its use as a visual information system can be found in [201].

To run these types of systems, the open-source scenegraph OpenSG[7] [202] is attractive because it supports the distribution of the scenegraph. A visualization

[6]Homepage of UFZ's Visualization Center:`http://www.ufz.de/index.php?en=14171`
[7]OpenSG: `http://www.opensg.org/`

application runs on the master computer, assembles the scene and reacts to the user input. The scenegraph itself and the changes made to it are continuously distributed to the remote computers on which OpenGL is used in order to render the scene. The scenegraph is relatively well documented and comes with examples that show various features, for example how to run a display wall with a computer cluster. The UFZ uses a commercial application, VRED from PI-VR GmbH[8] that is based on OpenSG, to run its visualization center. We have extended VRED using OpenSG and Nokia's Qt Toolkit for the graphical user interface. We also have extended VTK with a vtkOpenSGActor class so that content that has been created using a VTK pipeline can be easily converted on the fly into OpenSG format. In this way we have integrated some standard features, such as isosurface extraction from scalar fields or glyph rendering and streamline computation for vector fields, into VRED.

As we have seen, the complete workflow and data processing involves several software packages and libraries, each specialized for a certain step of the workflow. For this reason, the data have to be converted between these different formats and the information distributed across several files that must be viewed with various software packages. We have experimented with using GOCAD as a tool for geometric modelling, data exchange with our project partners and model maintenance. GOCAD provides import and export functionality to different data formats, such as ArcGIS Shape files, and it can be extended using C++ and a plugin mechanism, so that we can add our own algorithms, exporters and importers. In contrast to the often applied way of writing data converters that read data in GOCAD ASCII format and output the desired file type, our chosen way of extending GOCAD has the advantage of allowing us to make use of the topological information that GOCAD keeps track of internally but does not write to the files. Further, we have access to the data that describe the appearance of the different objects in GOCAD (e.g. line width or colour of a surface), so that we can very easily create the same visualization using other formats. In order to provide an easier and more rapid data exchange we have added some modelling functionality and the necessary interfaces between GOCAD and Gmsh, TetGen, VTK, OpenSG and our finite element simulation software OpenGeoSys. In this way we support the processing of the data as is described in Fig. D.3.

In order to generate the simulation grids, GOCAD provides algorithms that generate a structured (hexahedral) grid which can be fitted to the geology that delineates the actual reservoir. However, as mentioned earlier, with regard to complicated reservoirs a (tetrahedral) mesh would be preferable. For many geometrical models, one critical step is conversion from the surface- or boundary-based 3D model to the 3D grid, because this step requires the surface model to

[8] VRED: www.pi-vr.de

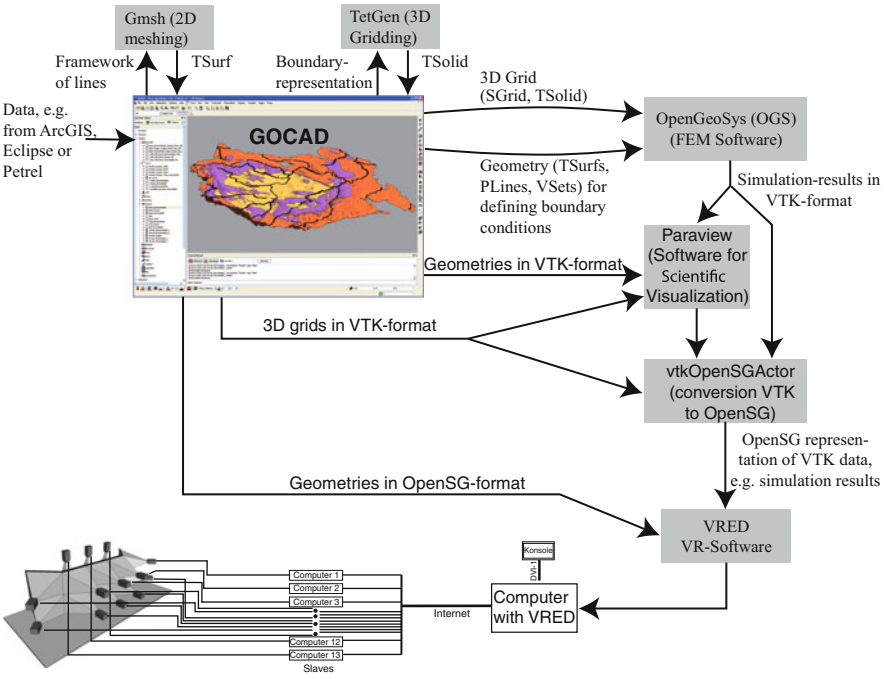


Figure D.3: Processing pipeline for the data from geometrical modelling through simulation to visualization

fulfill different constraints. In order to generate tetrahedral grids, the quality of the triangular meshes must be higher than is normally required for illustration, communication and discussion purposes. The mesh should consist of triangles with not too large an aspect ratio (the longest side length divided by the shortest side length). The lines where one surface intersects another one or is connected to it, for example at the contact of a stratigraphic layer and a fault, are also critical. As is shown in Fig. D.4, it is essential that both surfaces share the same vertices and segments. Additionally, the whole model should be represented by a boundary representation that has no holes and divides the space into volumes fully enclosed by surfaces.

There are several ways of generating or remeshing a model such that it can be used as a boundary representation model. We have extended GOCAD in order to use two different methods, which is described in more detail in [203, 204]. One is more targeted at constructing complicated fault zones and requires a lot of individual work. The other is more suitable for the construction of large-scale regional models. Both of them make use of constrained delaunay triangulation by using the open source software Gmsh.[9]

[9] Gmsh: http://www.geuz.org/gmsh/

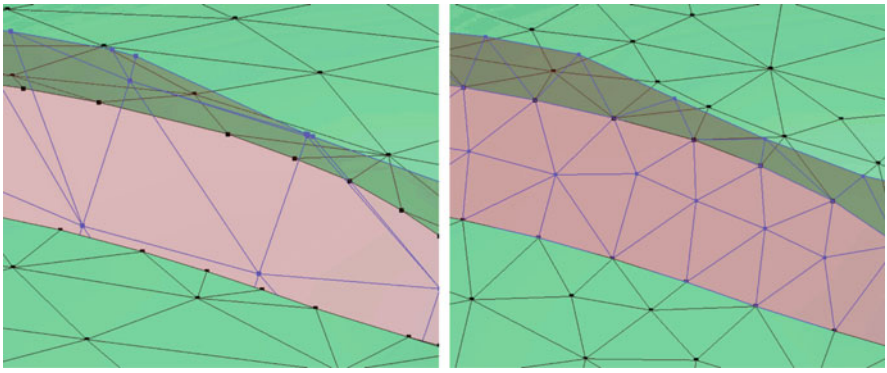

Figure D.4: The same part of a model of two surfaces (*green*) connected to a fault (*reddish*) shown twice. On the left side the three meshes do not share the segments and points where they are in contact. Further, some of the *triangles* have a very poor aspect ratio. Before a tetrahedralization of this model would be possible it would have to be remeshed, so that it looks like the image on the right side

In order to generate a complicated fault zone, the contact lines of the different horizons on the fault need to be constructed. This can be done by extracting the contact lines from the existing model, using standard GOCAD commands, or by constructing them from scratch from a series of geological cross sections. If the points on these lines are very irregularly spaced they should be resampled, using for example, cubic spline interpolation. If the contact lines cross, the intersection must be calculated and a point inserted on both lines at this position. Further, the outline of the fault must be constructed. The fault is now represented by a framework of lines (segments) that must be part of the fault's triangulation. To facilitate further processing, the best-fitting plane is calculated for the framework and the points are projected onto this plane. The framework is then exported to the software Gmsh and Gmsh's constrained Delaunay algorithm is used to create a triangulation that contains all the points and segments of the framework. Subsequently this triangulation is loaded into GOCAD, the points that were part of the initial framework are transformed back to their original location and set as control nodes (which means that they are not allowed to move any more), and the mesh is smoothed using GOCAD's standard interpolation algorithm (DSI).

The method used to construct a boundary representation for a large-scale regional model is shown in Fig. D.5 for a small part of the Thuringian basin in Germany. As a first step, Gmsh is used to generate a triangulation of the whole region that accepts the different outlines of the stratigraphic units and other features, such as well locations and rivers, as constraints (a). This triangulation is then later used in GOCAD as a template for generation of the different horizons. The triangles of the template that are outside the outline of a horizon

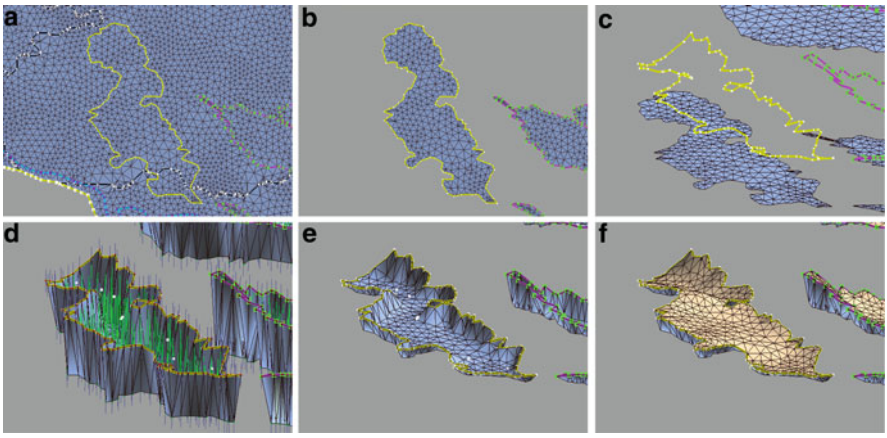


Figure D.5: Construction of a boundary representation for large scale regional models. See text for explanations

are deleted (b). The vertices on the border of the triangulation are then moved onto the line that represents the outline of the horizon on the terrain. Additionally, they are set as control nodes so that they do not move any more during subsequent operations. For the other points, different constraints are set, such as control points against which the surface should converge (step c-d). Using GOCAD's iterative standard interpolation algorithm (DSI) a smooth surface is generated (e). Applying the same sequence of operations for the top of the stratigraphic unit generates a cover as a top that fits exactly over the first horizon, so that we get a closed volume (f).

A model that has been meshed or remeshed using the aforementioned methods has a boundary representation that can easily be gridded using open source gridding software such as TetGen in order to generate a tetrahedral grid. We have extended GOCAD by adding an exporter for TetGen input files and an importer for TetGen output files. The output of TetGen is read into GOCAD as a TSolid where the different subvolumes are represented as different parts. Another implemented exporter for GOCAD allows us to then write this grid directly in the format of our finite element simulation software OpenGeoSys. Further, geometries such as lines, points and surfaces can be exported from GOCAD in an XML format that is used by OpenGeoSys to define geometries that are used for setting boundary and initial conditions. In this way GOCAD can be used as a kind of preprocessor for OpenGeoSys.

The extensions to GOCAD described above have been tested and used within several projects at the UFZ. As part of the INFLUINS project, which deals with fluid flow in sedimentary basins, we have constructed a model of the Thuringian basin that has been partitioned into the stratigraphic units Bunter, Muschelkalk and Keuper. The corresponding simulation grid consisted of more than 600,000 tetrahedra and has been exported to OpenGeoSys to perform ground-

water simulation. Moreover, we have used the exporters to VTK and OpenSG for subsequent visualization of the model in our visualization center. Within the CO2MAN project we have used GOCAD to exchange data and the simulation grid with our project partners and to construct the necessary geometries for setting the boundary conditions.

# Appendix E

# Heat Transport in a Real Fracture-Matrix System

*by Guido Blöcher and Mauro Cacace*

As a last example for linear heat transport we introduce an applied case study for a 3D fracture-matrix system.

## Geology

The following problem deals with simulating fluid flow and heat transport in a three-dimensional heterogeneous faulted geological system.

The model volume consists of two sub-horizontal geological layers, including two dipping faults (Fig. E.1). The horizontal north-south and east-west extensions are 200 m, resulting in a horizontal model area of 40,000 $m^2$. The two geological layers are vertically bordered by three curved surfaces. The elevation of the top, middle and bottom surface is $55 \pm 5$ m, $0 \pm 7$ m and $-45 \pm 5$ m, respectively. Therefore, an average thickness of 55 m for layer 1 and 45 m for layer 2 is established (Table E.1).

Both faults penetrate the two geological layers. Fault 1 has a length of 233 m and is striking North-East, with dip coordinates of 316.7°; 80.6°. Fault 2 has a length of 184 m and is oriented perpendicular to fault 1, having dip coordinates of 225°; 63.2° (Table E.1).

O. Kolditz et al. (eds.), *Thermo-Hydro-Mechanical-Chemical Processes in Fractured Porous Media*, Lecture Notes in Computational Science and Engineering 86,
DOI 10.1007/978-3-642-27177-9, © Springer-Verlag Berlin Heidelberg 2012

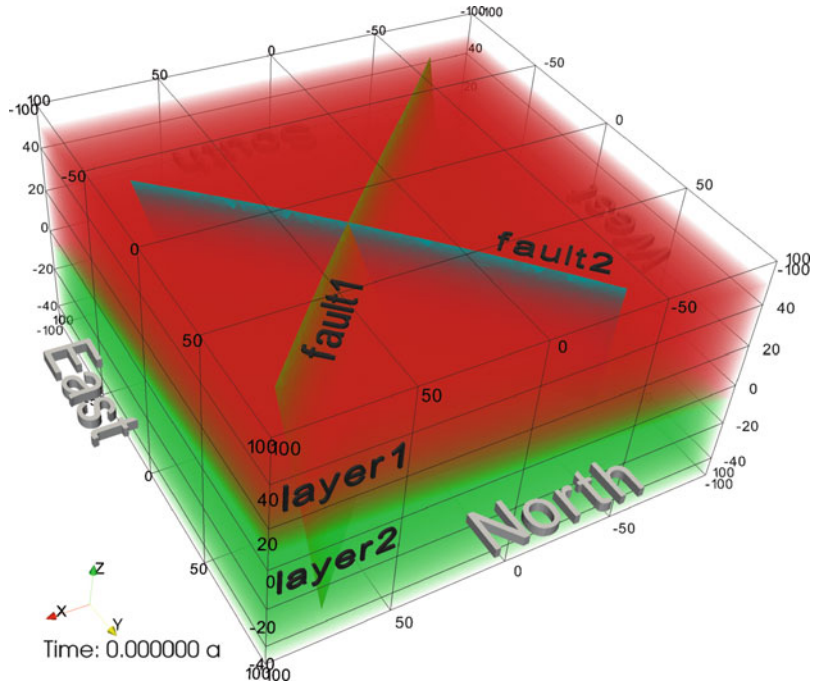


Figure E.1: Sample model consisting of two geological layers cut by a system of two crossing faults

Table E.1: Geometrical attributes of the geological layers and faults

| Property | Unit | Layer 1 | Layer 2 |
|---|---|---|---|
| Average thickness $t$ | (m) | 55 | 45 |
| | | Fault 1 | Fault 2 |
| Dip direction | (°) | 316.7 | 225 |
| Dip | (°) | 80.6 | 63.2 |
| Length $l$ | (m) | 233.5 | 183.8 |

## Initial and Boundary Conditions

During the simulation, a general flow field from South to North is generated. Dirichlet (or first-type) boundary conditions for pressure are set along the southern and northern boundaries (Fig. E.2). According to the definition of hydrostatic pressure, the pressure at the southern border is constant at $p(x, y = -100\,\text{m}, z) = \rho g z + 1.75 \times 10^6$ Pa and at the northern border at $p(x, y = 100\,\text{m}, z) = \rho g z + 1.25 \times 10^6$ Pa (Fig. E.2), where $\rho$ [1,000 kg/m$^3$], g [9.81 m/s$^2$] and z denotes the fluid density, gravitational acceleration and height of liquid column, respectively. An average hydraulic gradient $\nabla h = 5 \times 10^5$ Pa/200 m=0.25 from

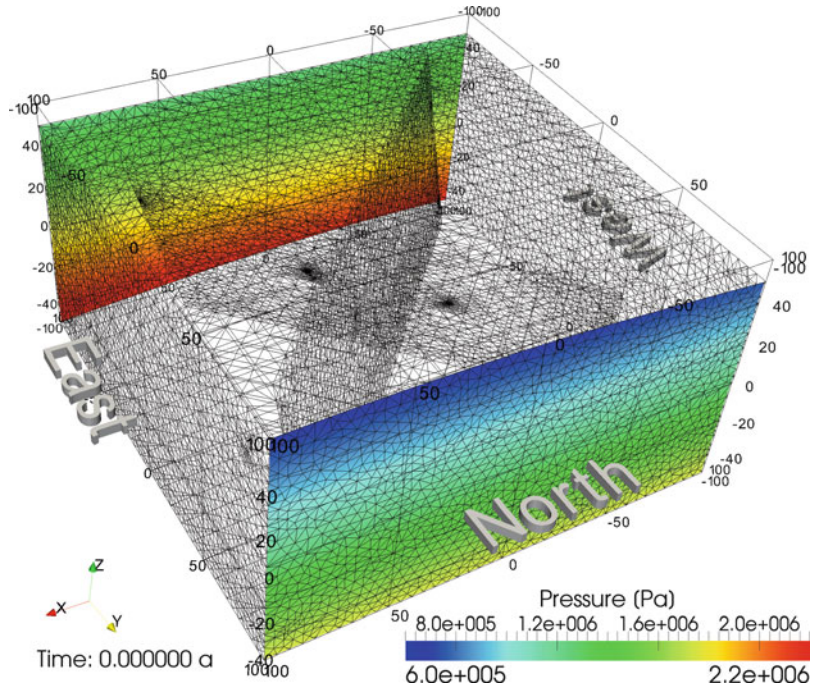


Figure E.2: Pressure boundary condition of the sample model

the South to the North is provided. For the remaining domain, a pressure value of $1.75 \times 10^6$ Pa is initialized.

To generate an inflow of hot and cold water from the southern border, Dirichlet boundary conditions for temperature are applied too (Fig. E.3). Along the southern border, temperature increases from 40°C to 80°C, in going from West to East, resulting in a temperature profile of $T(x, y = -100\,\text{m}, z)$= 0.2°C/m∗x+60°C (Fig. E.3). For the remaining domain, the initial temperature is set to 60°C.

## Parameters

Table E.2 shows the hydraulic properties of the two geological layers.

To assure a variation of the hydraulic properties, the upper geological layer was modeled twice as conductive as the lower layer. The permeability $k$ of layer 1 is set to $2 \times 10^{-14}$ m$^2$ and the porosity $\phi$ to 0.15. For layer 2 the permeability k is set to $10^{-14}$ m$^2$ and the porosity $\phi$ to 0.08. The storage of both layers is derived from the bulk compressibility $\beta$ (1/Pa) of the rock and the embedded fluid. Assuming fissured rocks, the storage is set to $7 \times 10^{-10}$ 1/Pa.

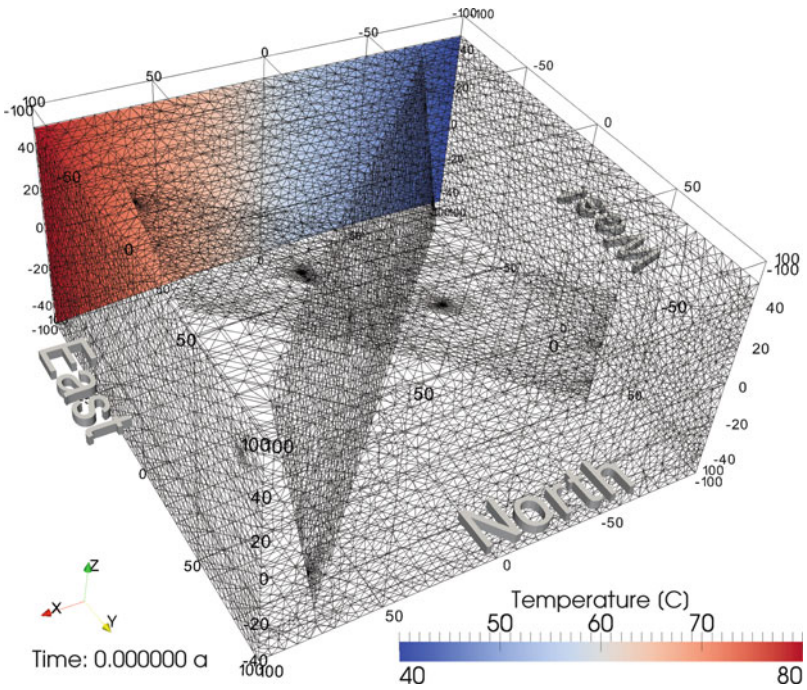


Figure E.3: Temperature boundary conditions of the sample model

Table E.2: Porous medium properties of geological layers

| Property | Unit | Layer 1 | Layer 2 |
|---|---|---|---|
| Porosity $\phi$ | $(-)$ | 0.15 | 0.08 |
| Storage $\beta$ | (1/Pa) | $7 \times 10^{-10}$ | $7 \times 10^{-10}$ |
| Permeability $k$ | $(m^2)$ | $2 \times 10^{-14}$ | $10^{-14}$ |

Table E.3: Medium properties of faults

| Property | Unit | Fault 1 | Fault 2 |
|---|---|---|---|
| Aperture $a$ | (m) | 0.05 | 0.05 |
| Porosity $\phi$ | $(-)$ | 1 | 1 |
| Storage $\beta$ | (1/Pa) | $4.6 \times 10^{-10}$ | $4.6 \times 10^{-10}$ |
| Permeability $k$ | $(m^2)$ | $10^{-8}$ | $5 \times 10^{-9}$ |

In Table E.3 the relevant parameters for the system of the two faults are listed.

The permeability of fault 1 is set to $10^{-8}$ m and that of fault 2 to $5 \times 10^{-9}$ $m^2$. The fault transmissivity is defined as the product of the fault permeability $k$ and aperture $a$. To ensure a high contrast between fault transmissivity and

matrix conductivity, the aperture of both faults is set to 0.05 m. To provide free fluid flow in the faults, a porosity value of 1.0 is chosen. The storage in the faults is due to the fluid compressibility only and $\beta = 4.6 \times 10^{-10}$ 1/Pa is assigned.

The simulation time is set to 145 years in order to observe the major changes characterizing the temperature field.

## Results

After approximately one month, a steady state for the pressure and velocity field is achieved (Fig. E.4).

Due to the fact that the implemented faults do not cut the southern and northern borders of the model, matrix flow is predominant in these areas. Accordingly, the highest pressure gradients are observed at the northern and southern borders of the model (Fig. E.4a). In proximity to the cutting faults, the isobars (surfaces of constant pressure) are sub-horizontal due to high flow rates within the faults. Maximum Darcy velocities of $v = \times 10^{-4}$ m/s can be observed inside the faults (Fig. E.4b). Despite low pressure gradients, high flow rates occur in the fault planes. High values of fluid velocity are the result of the relative high transmissivity of the faults with respect to the surrounding domain.

Figure E.4b shows the stationary flow field. As described above, highest flow velocities can be observed in the fault planes. The applied pressure boundary conditions force a regional flow field from South to North. The average velocity at the southern and northern regions is $10^{-7}$ m/s, with maximum inflow to the faults from the South. In the rest of the domain, outflow from the faults into the rock matrix is pronounced. In the central part of the model, faults act as the predominant flow paths. In contrast, low velocities (less than $10^{-8}$ m/s) characterize the eastern and western boundaries. An additional important fact is that at the southern edge of fault 1 and fault 2, backward flow from the North to the South occurs. Pressure equalisation within the faults results in higher matrix pressure at this area. This causes drainage of the rock matrix by the fault system.

Figure E.5a–d shows the 45°C, 55°C, 65°C and 75°C contours at four different time stages.

Before stationary field conditions for pressure and velocity are reached, conductive heat transfer does not affect the initial temperature field significantly (Fig. E.5a). After achieving the stationary pressure and velocity field, convective heat transfer (advection plus diffusion) becomes predominant. The cold water front ($T = 55$°C) enters fault 1 after approximately 4 months (Fig. E.5b). Due to the geometry of fault 1 with respect to the southern boundary of the domain, cold water enters fault 1 in the upper part. After 35 years, (Fig. E.5c) cold water from fault 1 and hot water from fault 2 are mixed at the fault intersection. The

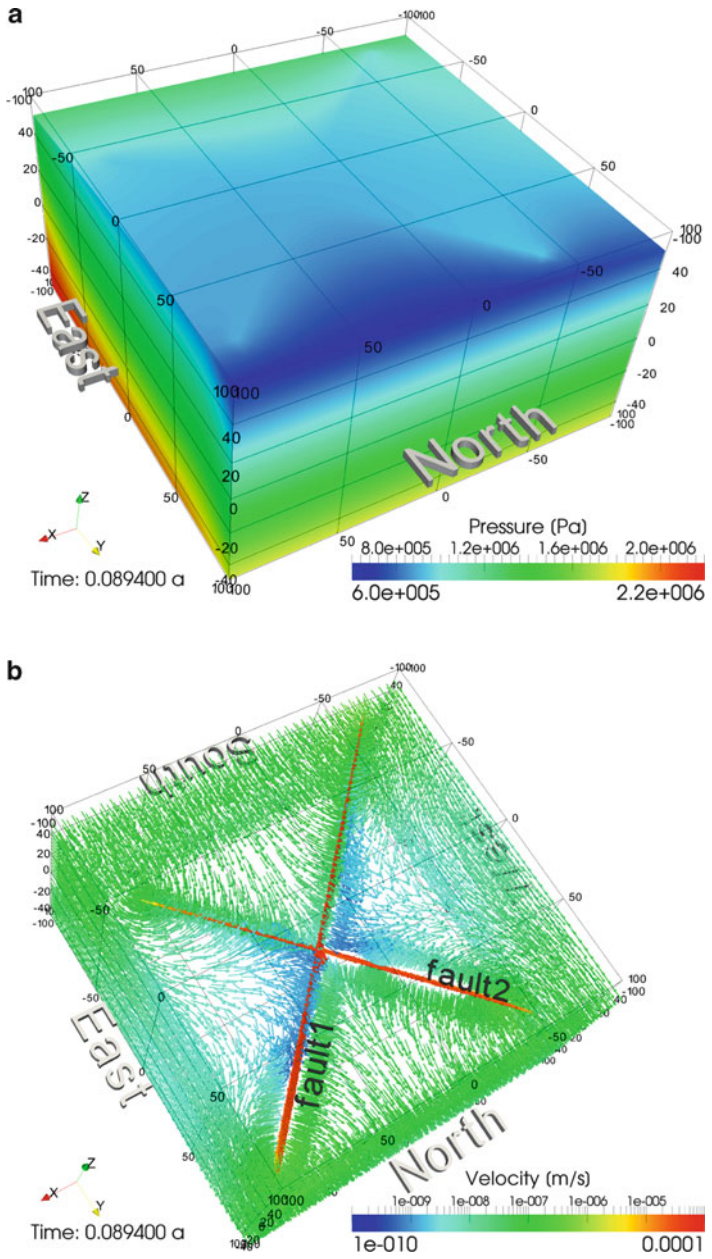


Figure E.4: Simulated steady pressure (**a**) and velocity field (**b**) achieved after approximately 1 month

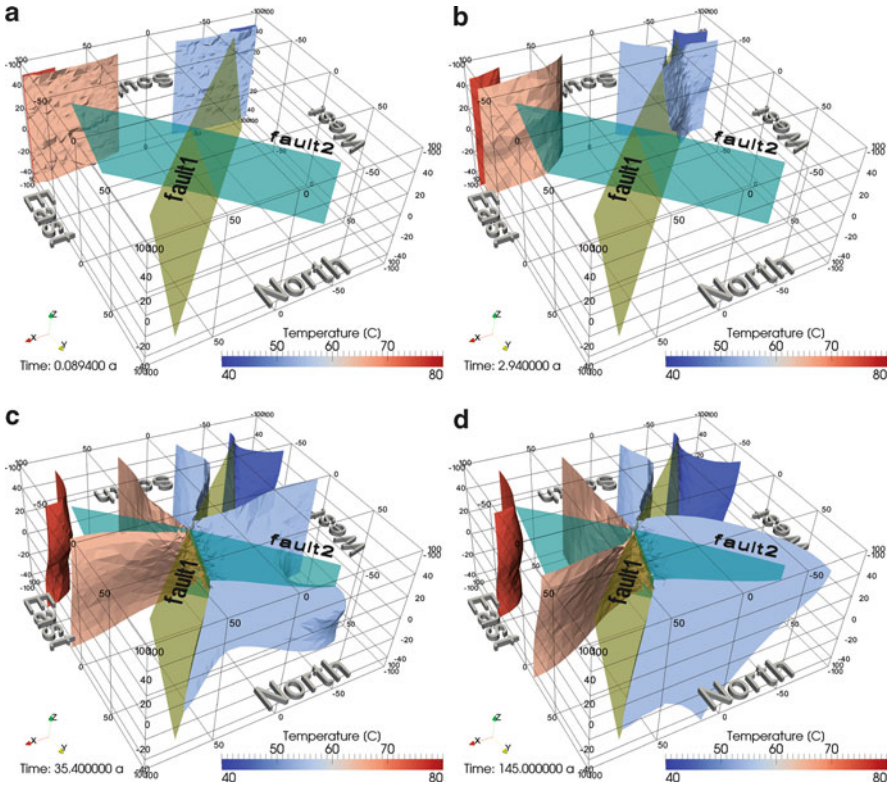


Figure E.5: Temperature contour plots (45°C, 55°C, 65°C and 75°C isosurfaces) at four different time stages

final temperature field (Fig. E.5d) shows an average temperature of $T = 55°C$ in the northern part which is less than the mean initial temperature of 60°C. The depression from the mean value occurs because fault 1 is more conductive than fault 2, which drives higher amounts of cold water into the system.

For a detailed observation of the pressure, velocity and temperature evolution inside the two faults, three observation points were set (Fig. E.6a).

After starting the simulation the pressure increases at all observation points (Fig. E.6b). As shown for observation point 3 (Fig. E.6c), the initial magnitude of the velocity is due to vertical flow only. The observed downward flow is forced by the initial pressure conditions in combination with the chosen pressure boundary. Therefore, an initial increase of fluid pressure is observed. After 1 month, a stationary pressure and velocity field is reached, as indicated by the horizontal lines in Fig. E.6b, c.

The vertical component of velocity decreases over time from $3 \times 10^{-2}$ m/s to $10^{-8}$ m/s, and the horizontal flow from South to North with velocities between $10^{-5}$ m/s and $10^{-4}$ m/s becomes dominant. The cold water reaches the fault

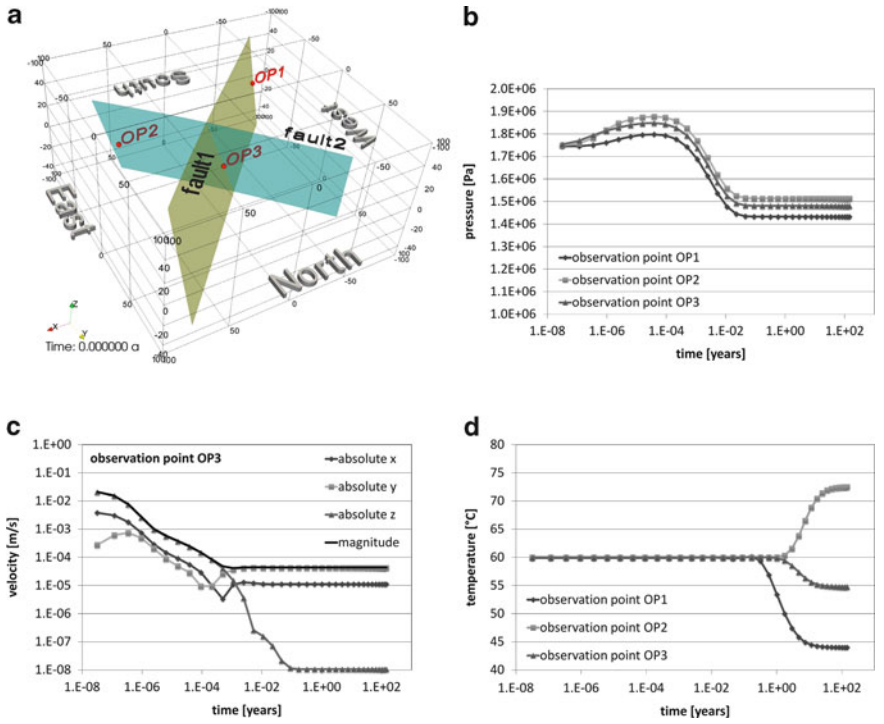


Figure E.6: Location of three observation points within the fault faces (**a**); Simulated pressure (**b**) and temperature (**d**) values at these observation points and simulated velocity components (**c**) at observation point 3

system at the edge of fault 1 (Fig. E.6d) after approximately 4 months. After an additional 17 months, cooling at observation point 3 begins. At the same time, hot water reaches fault 2 first. Due to the lower transmissivity of fault 2, the hot water reaches the intersection point after 10 years, and cooling at observation point 3 stops. Higher amounts of cold water enter the fault intersection (observation point 3) from the more conductive fault 1, causing temperature to decrease to 55°C. This corroborates the observation of the temperature field for the total domain.

In a second run, the same problem described above has been numerically solved using the Flux Corrected Transport (FCT). Figure E.7 illustrates the differences regarding numerical oscillations in solving for the transport field with (dashed lines) and without (solid lines) FCT method. Figure E.7a, b show the calculated temperature profiles along the general flow field for two different stages in the simulation. As shown in Fig. E.7a, the FCT method seems to reduce the amplitudes of numerical oscillations by a maximum factor of three at the beginning of the simulation.

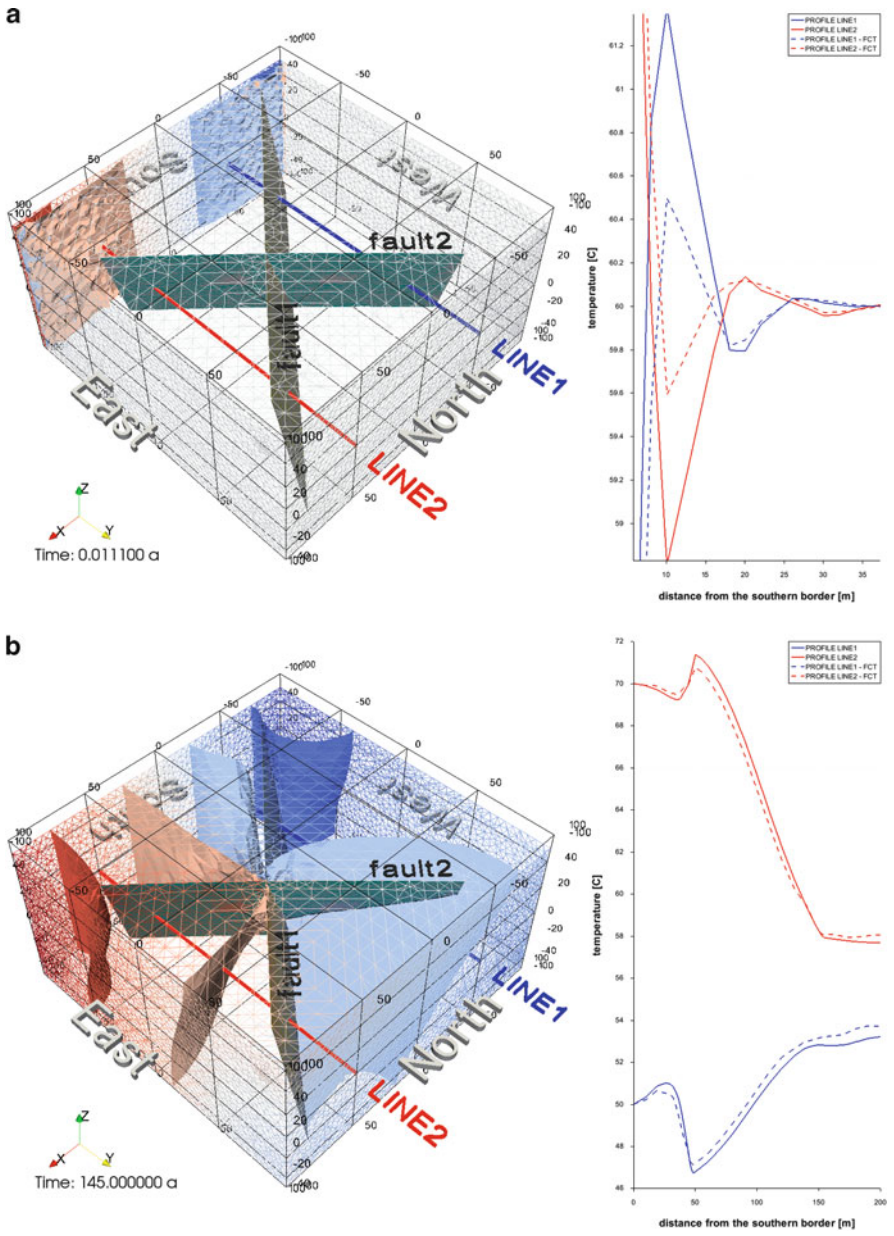


Figure E.7: Simulated temperature along two lines at the beginning (**a**) and at the final simulation time (**b**) with and without flux corrected transport FCT

# Bibliography


[1] Nowak T, Kunz H, Dixon D, Wang W, Göerke U-J, and Kolditz O. Coupled 3-d thermo-hydro-mechanical analysis of geotechnical in situ tests. *Int. J. Numer. Anal. Meth. Geomech*, 48(1):1–15, 2011.

[2] Görke U-J, Park C-H, Wang W, Singh AK, and Kolditz O. Numerical simulation of multiphase hydromechanical processes induced by $co_2$ injection into deep saline aquifers. *Oil and Gas Science and Technology – Rev. IFP Energies nouvelles*, 66(1):3446–118, 2011.

[3] Watanabe N, McDermott C anf Wang W, Taniguchi T, and Kolditz O. Uncertainty analysis of thermo-hydro-mechanical processes in heterogeneous porous media. *Computational Mechanics*, 45(4):263–280, 2010.

[4] T. Kalbacher, C. Schneider, W. Wang, A. Hildebrandt, S. Attinger, and O. Kolditz. Parallelized modelling of soil-coupled 3d water uptake of multiple root systems with automatic adaptive time step control. *Vadoze Zone Journal*, pages 1–11, 2010.

[5] Wu Y, Toll M, Wang W, Sauter M, and Kolditz O. Development of a high-precision groundwater model with scarce data: The wadi kafrein area. *Environ Earth Sci*, 2011.

[6] F. Sun, H. Shao, T. Kalbacher, W. Wang, Z. Yang, Z. Huang, T. Jiang, and O. Kolditz. Change of subsurface flow regime in the nankou area, beijing. *Environmental Earth Sciences*, pages 1–11, 2010.

[7] Umbach E (ed). *Energie Forschung Zukunft*. Helmholtz Gemeinschaft Deutscher Forschungszentren, 2010.

[8] Jacob Bear. *Dynamics of Fluids in Porous Media*. Elsevier, New York, 1972.



O. Kolditz et al. (eds.), *Thermo-Hydro-Mechanical-Chemical Processes in Fractured Porous Media*, Lecture Notes in Computational Science and Engineering 86,
DOI 10.1007/978-3-642-27177-9, © Springer-Verlag Berlin Heidelberg 2012

[9] H.-J. G. Diersch. *Modellierung und numerische Simulation geohydrodynamischer Transportprozesse*. Habilitationsschrift, Akademie der Wissenschaften der DDR, Berlin, 1985.

[10] W. Ehlers. Poröse Medien - ein kontinuumsmechanisches Modell auf der Basis der Mischungstheorie. Forschungsberichte aus dem Fachbereich Bauwesen, Uni Essen, 1989.

[11] J. Bear and Y. Bachmat. *Introduction to modeling of transport phenomena in porous media*. Kluwer Academic Publishers, Dordrecht, 1990.

[12] W. Kinzelbach. *Numerische Methoden zur Modellierung des Transports von Schadstoffen im Grundwasser*. R. Oldenburg Verlag, 1992.

[13] Rainer Helmig. *Multiphase Flow and Transport Processes in the Subsurface*. Springer, Berlin, 1997.

[14] R. W. Lewis and B. A. Schrefler. *The finite element method in the static and dynamic deformation and consolidation of porous media*. Wiley, 1998.

[15] Reint de Boer. *Theory of Porous Media*. Springer, Berlin, 2000.

[16] O. Kolditz. *Computational methods in environmental fluid mechanics*. Graduate Text Book, Springer Science Publisher, Berlin, 2002.

[17] P. Haupt. *Continuum mechanics and theory of materials*. Springer, 2002.

[18] Bowen R.M. *Theory of mixture*, volume III of *Continuum Physics*. Academic Press, New York, 1976. Eringen, A.C. (Ed.).

[19] Truesdell C. and Toupin R.A. *The classical field theories*, volume III/1 of *Handbuch der Physik*. Springer, Berlin, 1960. Flügge, S. (Ed.).

[20] Bowen R.M. Incompressible porous media models by use of the theory of mixtures. *Int. J. Eng. Sci.*, 18:1129–1148, 1980.

[21] de Boer R. and Ehlers W. On the problem of fluid- and gas-filled elastoplastic solids. *Int. J. Sol. Struct.*, 22:1231–1242, 1986.

[22] Prevost P. Mechanics of continuous porous media. *Int. J. Eng. Sci*, 18:787–800, 1980.

[23] Ehlers W. and Bluhm J. *Porous media: Theory, experiments and numerical applications*. Springer, Berlin, 2002.

[24] Görke U.-J., Wimmer M.A., Alini M., Schneider E., and Günther H. Multiscale finite element modeling in tissue engineering of articular cartilage. *Eur. Cells Mater.*, 12(1):19, 2006.

[25] H. Lamb. *Hydrodynamics*. Cambridge University Press, 1932.

[26] P. Forchheimer. *Hydraulik*. Teubner, Berlin, 1914.

[27] H. Darcy. *Les Fontaines Publiques de la Ville de Dijon*. Dalmont, Paris, 1856.

[28] A.E. Scheidegger. *The physics of flow through porous media*. University of Toronto Press, 3rd edition, 1974.

[29] F.A. Dullien. *Porous media: fluid tramsport and pore structure*. Academic Press, 1979.

[30] Otto Redlich and J. N. S. Kwong. On the Thermodynamics of Solutions. v. An Equation of State. Fugacities of Gaseous Solutions. *Chemical Reviews*, 44:233–244, 1949.

[31] D.Y. Peng and D.B. Robinson. A new two-constant equation of state. *Ind. Eng. Chem. Fundam.*, 15:59–64, 1974.

[32] D. G. Friend, J. F. Ely, and H. H. Ingham. Thermophysical properties of methane. *Journal of Physical and Chemical Reference Data*, 18(2), 1989.

[33] Ulrich Setzmann and Wolfgang Wagner. A new equation of state and tables of thermodynamic properties for methane covering the range from the melting line to 625 K at pressures up to 1000 MPa. *J. Phys. Chem. Ref. Data*, 20:1061–1155, 1991.

[34] A. Fenghour, W.A. Wakeham, and V. Vesovic. The Viscosity of Carbon Dioxide. *Journal of Physical and Chemical Reference Data*, 27:31–44, 1998.

[35] R. Span and W. Wagner. A new Equation of State for Carbon Dioxide Covering the Fluid Region from the Triple-Point Temperature to 1100 K at Pressures up to 800 MPa. *Journal of Physical and Chemical Reference Data*, 25(6):1509–1596, 1996.

[36] International Association for the Properties of Water and Steam. *Release on the IAPWS Formulation 2008 for the Viscosity of Ordinary Water Substance*, 2008.

[37] W. Wagner and A. Pruss. The IAPWS formulation 1995 for the thermodynamic properties of ordinary water substance for general and scientific use. *Journal of Physical and Chemical Reference Data*, 31(2), 2002.

[38] K. Stephan, R. Krauss, and A. Laesecke. Viscosity and thermal conductivity of nitrogen for a wide range of fluid states. *Journal of Physical and Chemical Reference Data*, 16(4), 1987.

[39] R. Span, E.W. Lemmon, R.T. Jacobsen, W. Wagner, and A.Yokozeki. A Reference Equation of State for the Thermodynamic Properties of Nitrogen for Temperatures from 63.151 to 1000K and Pressures to 2200MPa. *J. Phys. Chem. Ref. Data*, 29:1361–1431, 2000.

[40] Johannes Diderik van der Waals. *Over de Continuiteit van den gas- en vloeistoftoestand*. Sijthoff, Leiden, 1873.

[41] Roland Span. *Eine neue Fundamentalgleichung für das fluide Zustandsgebiet von Kohlendioxid bei Temperaturen bis zu 1100 K und Drücken bis zu 800 MPa*. VDI Verlag, Düsseldorf, 1993.

[42] Andreas Pruß and Wolfgang Wagner. *Eine neue Fundamentalgleichung für das fluide Zustandsgebiet von Wasser für Temperaturen von der Schmelzlinie bis zu 1273 K bei Drücken bis zu 1000 MPa*. VDI Verlag, Düsseldorf, 1995.

[43] D. Bücker and W. Wagner. A reference equation of state for the thermodynamic properties of ethane for temperatures from the melting line to 675 K and pressures up to 900 MPa. *J. Phys. Chem. Ref. Data*, 35:205–266, 2006.

[44] D. G. Friend, H. Ingham, and J. F. Ely. Thermophysical properties of ethane. *Journal of Physical and Chemical Reference Data*, 20(2), 1991.

[45] V. Vesovic and W.A. Wakeham. The transport properties of carbon dioxide. *Journal of Physical and Chemical Reference Data*, 19(3):763–807, 1990.

[46] B. A. Younglove and J. F. Ely. Thermophysical properties of fluids. ii. methane, ethane, propane, isobutane, and normal butane. *Journal of Physical and Chemical Reference Data*, 16(4), 1987.

[47] International Association for the Properties of Water and Steam. *Revised Release on the IAPWS Formulation 1985 for the Thermal Conductivity of Ordinary Water Substance*, 2008.

[48] Jaeger J.C., Cook N.G.W, and Zimmermann R.W. *Fundamentals of rock mechanics*. Blackwell Publishing, 4 edition, 2007.

[49] R. N. Brooks and A. T. Corey. Properties of porous media affecting fluid flow. *J. Irrig. Drain. Div. ASCE*, 92:61–68, 1964.

[50] RH and Corey AT. Hydraulic properties of porous media. Technical report, Colorado State University, Fort Collins, 1964. Hydrology Paper No. 3.

[51] M. T. Van Genuchten. A closed-form equation for predicting the hydraulic conductivity of unsaturated soils. *Soil Sci. Soc. Am. J.*, 44:892–898, 1980.

[52] Yechezkel Mualem. A new model for predicting the hydraulic conductivity of unsaturated porous media. *Water Resources Research*, 12:513–522, 1976.

[53] R. Haverkamp, M. Vauclin, J. Touma, P. J. Wierenga, and G. Vachaud. A comparison of numerical simulation models for one-dimensional infiltration. *J. Soil Science Society of America*, 41:284–294, 1977.

[54] R. W. Lewis and B. A. Schrefler. *The Finite Element Method in the Static and Dynamic Deformation and Consolidation of Porous Media (Second Edition)*. Wiley, 1998.

[55] R. de Boer. *Theory of Porous Media: Highlights in Historical Development and Current State*. Springer-Verlag, Heidelberg, 2002.

[56] R. de Boer. *Trends in Continuum Mechanics of Porous Media: Theory and Applications of Transport in Porous Media*. Springer-Verlag, Heidelberg, 2005.

[57] *Proceedings of the GeoProc International Conference on Coupled T-H-M-C Process in Geo-Systems*, The Royal Institute of Technology, Stockholm, Sweden, 2003.

[58] W. Ehlers and J. Bluhm. *Porous Media: Theory, Experiments and Numerical Applications*. Springer-Verlag, 2002.

[59] O. Kolditz, W. Wang, J. de Jonge, M. Xie, and S. Bauer. A process-oriented approach to compute thm problems in porous media - part 1: Theoretical and informatics background. In T. Schanz, editor, *Unsaturated Soils: Numerical and Theoretical Approaches*, pages 53–66. Springer, 2004.

[60] O. Kolditz and J. De Jonge. Non-isothermal two-phase flow in low-permeable porous media. *Computational Mechanics*, 33(5):345–364, 2004.

[61] B. Stroustrup. *The C++ Programming Language (Third Edition)*. Addison-Wesley, 2000.

[62] T. Budd. *An Introduction to Object-Oriented Programming*. Addison Wesley, Third edition, 2001.

[63] G. L. Fenvesm. Object-oriented programming for engineering software development. *Engineering With Computers*, 6(Winter):1–15, 1990.

[64] B. Forde, R. O. Foschi, and S. F. Stiemer. Object-oriented finite element analysis. *Computers & Structures*, 34(3):355–374, 1990.

[65] J. Filho and P. Devloo. Object-oriented programming in scientific computations: The beginning of a new era. *Engineering Computations*, 8:81–87, 1991.

[66] R. I. Mackie. Object-oriented programming of the finite element method. *International Journal for Numerical and Analytical Methods in Geomechanics*, 35(2):425–436, 1992.

[67] T. Zimmermann, Y. Duboispelerin, and P. Bomme. Object-oriented finite element programming: I: governing principles. *Computer Methods in Applied Mechanics and Engineering*, 98(2):291–303, 1992.

[68] Y. Duboispelerin, T. Zimmermann, and P. Bomme. Object-oriented finite element in programming: II: a prototype program in smalltalk. *Computer Methods in Applied Mechanics and Engineering*, 98(3):361–397, 1992.

[69] Y. Duboispelerin and T. Zimmermann. Object-oriented finite element in programming: II: an efficient implementation in c++. *Computer Methods in Applied Mechanics and Engineering*, 108(1-2):165–183, 1993.

[70] R. M. V. Pidaparti and A. V. Hudli. Dynamic analysis of structures using object-oriented techniques. *Computers & Structures*, 49(1):149–156, 1993.

[71] B. Raphael and C. S. Krishnamoorthy. Automating finite element development using object-oriented techniques. *Engineering Computations*, 10:267–278, 1993.

[72] K. G. Budge and J. S. Peery. RHALE – A MMALE shock physics code written in c++. *International Journal of Impact Engineering*, 14:107–120, 1993.

[73] A. V. Pidaparti, R. V. M.and Hudli. Dynamic analysis of structures using object-oriented techniques. *Computers & Structures*, 49(1):149–156, 1993.

[74] P. Mentrey and T. Zimmermann. Object-oriented non-linear finite element analysis: application to j2 plasticity. *Computers & Structures*, 49(5):767–773, 1993.

[75] G. Yu and H. Adeli. An integrated computing environment for solution of complex engineering problems using the object-oriented programming paradigm and a blackboard architecture. *Journal Of Structural Engineering–ASCE*, 119(9):2763–281, 1993.

[76] H. Adeli and G. Yu. An integrated computing environment for solution of complex engineering problems using the object-oriented programming paradigm and a blackboard architecture. *Computers & Structures*, 54(2):255–265, 1995.

[77] E. J. Silva, P. Mesquita, R. R. Saldanha, and P. F. M. Palmeira. An object-oriented finite element program for electromagnetic field computation. *IEEE transactions on magnetics*, 30:3618–3621, 1994.

[78] R. Sampath and N. Zabaras. An object oriented implementation of a front tracking finite element method for directional solidification process. *International Journal for Numerical Methods in Engineering*, 44:1227–1265, 1999.

[79] C. Rihaczek and B. Kroplin. Object-oriented design of finite element software for transient, non-linear coupling problems. In ASCE, editor, *Second Congress on Computing in Civil Engineering*, 1994.

[80] O. Kolditz and S. Bauer. A process-orientated approach to compute multi-field problems in porous media. *Int. Journal of Hydroinformatics*, 6:225–244, 2004.

[81] S. P. Scholz. Elements of an object-oriented fem++ program in c++. *Computers & Structures*, 43(3):517–529, 1992.

[82] G. W. Zeglinski, R. P. S. Han, and P. Aitchison. Object-oriented matrix classes for use in a finite element code using c++. *International Journal for Numerical and Analytical Methods in Geomechanics*, 37(22):3921–3937, 1994.

[83] J. Lu, D. W. White, W. F. Chen, and H. E. Dunsmore. A matrix class library in c++ for structural engineering. *Computers & Structures*, 55(1):95–111, 1995.

[84] Th Zimmermann and D Eyheramendy. Object-oriented finite elements: I. principles of symbolic derivation and automatic programming. *Computer Methods in Applied Mechanics and Engineering*, 132(3–4):259–276, 1996.

[85] D Eyheramendy and Th Zimmermann. Object-oriented finite elements ii. a symbolic environment for automatic programming. *Computer Methods in Applied Mechanics and Engineering*, 132(3–4):277–304, 1996.

[86] D Eyheramendy and Th Zimmermann. Object-oriented finite elements iii. theory and application of automatic programming. *Computer Methods in Applied Mechanics and Engineering*, 154(1–2):41–68, 1998.

[87] D Eyheramendy and Th Zimmermann. Object-oriented finite elements. iv. symbolic derivations and automatic programming of nonlinear formulations. *Computer Methods in Applied Mechanics and Engineering*, 190(22–23):2729–2751, 2001.

[88] O. Kolditz, M. Beinhorn, M. Xie, T. Kalbacher, S. Bauer, W. Wang, C. McDermott, C. Chen, C. Beyer, J. Gronewold, D. Kemmler, R. Walsh, C.H. Park, and Y. Du. GeoSys Rockflow, Open Source Software Design. Technical Report, GeoSys–Preprint [2004-25] http://www.uni-tuebingen.de/zag/geohydrology. Technical report, Center for Applied Geosciences, University of Tuebingen, 2004.

[89] O. Kolditz, M. Beinhorn, and R. Liedl. An object-oriented groundwater/river model. *IAHS Publ.*, 297:531–539, 2005.

[90] M. Beinhorn. *Contributions to computational hydrology: Non-linear flow processes in subsurface and surface hydrosystems*. PhD thesis, GeoHydrology and HydroInformatics, Center for Applied Geosciences, Tuebingen University, 2005.

[91] N. Watanabe, W. Wang, J Taron, U. J. Görke, and O. Kolditz. Lower-dimensional interface elements with local enrichment: Application to coupled hydro-mechanical problems in discretely fractured porous media. *International Journal for Numerical Methods in Engineering*, DOI: 10.1002/nme.3353.

[92] W. Wang and O. Kolditz. Sparse matrix and solver objects for parallel finite element simulation of multi-field problems. *Lecture Notes in Computer Science (including subseries Lecture Notes in Artificial Intelligence and Lecture Notes in Bioinformatics)*, 5938 LNCS:418–425, 2010.

[93] W. Wang, G. Kosakowski, and O. Kolditz. A parallel finite element scheme for thermo-hydro-mechanical (thm) coupled problems in porous media. *Computers & Geosciences*, 35(8):1631–1641, 2009.

[94] W. Wang, T. Schnicke, and O. Kolditz. Parallel finite element method and time stepping control for non-isothermal poro-elastic problems. *CMC–Computers Materials & Continua*, 21(3):217–235, 2011.

[95] Frieder Häfner, Dietrich Sames, and Hans-Dieter Voigt. *Wärme- und Stofftransport: Mathematische Methoden*. Springer, Berlin, 1992.

[96] A. Ogata and R. B. Banks. A solution of the differential equation of longitudinal dispersion in porous media. Technical report, U.S. Geological Survey, Washington, D.C., 1961.

[97] O. Kolditz. *Strömung, Stoff- und Wärmetransport im Kluftgestein*. Borntraeger-Verlag, Berlin-Stuttgart, 1997.

[98] O. Gunduz and M. M. Aral. River networks and groundwater flow: a simultaneous solution of a coupled system. *Journal of Hydrology*, 301(1-4):216 – 234, 2005.

[99] R. E. Glover. *Transient Ground Water Hydraulics*. Water Resources Publications, 1978.

[100] Rajesh Srivastava and Amado Guzman-Guzman. Practical approximations of the well function. *Ground Water*, 36(5):844–848, 1998.

[101] O.D.L. Strack. Assessment of effectiveness of geologic isolation systems. analytic modeling of flow in a permeable fissured medium. Technical report, Pacific Northwest Lab., Richland, WA., 1982.

[102] L. A. Richards. Capillary conduction of liquids through porous mediums. *Physics A-J Gen. Appl. Phys.*, 1(1):318–333, 1931.

[103] P. Yu G. Barenblatt, I. Zheltov and I.N. Kochina. Basic concepts in the theory of seepage of homogeneous fluids in fissurized rocks. *J. Applied Mathematics and Mechanics (PMM)*, 24(5):1286–1303, 1960.

[104] H.H. Gerke and M.T. van Genuchten. A dual-porosity model for simulating the preferential movement of water and solutes in structured porous media. *Water Resources Research*, 29(2):305–320, 1993.

[105] R. Zhang T.Vogel, H.H. Gerke and M.T. van Genuchten. Modeling flow and transport in a two-dimensional dual-permeability system with spatially variable hydraulic properties. *J. Hydrol.*, 238:78–89, 2000.

[106] J. Birkholzer and Y. Zhang. The impact of fracture-matrix interaction on thermalhydrological conditions in heated fractured rock. *Vadose Zone Journal*, 5:657–672, 2006.

[107] D.R. Nielsen A. Warrick, J.W. Biggar. Simultaneous solute and water transfer for an unsaturated soil. *Water Resources Research*, 7(5):1216–1225, 1971.

[108] J. Kool and M. van Genuchten. Hydrus. a one dimensional variably saturated flow and transport model, including hysteresis and root water uptake version 3.3. *US Salinity Laboratory Technical Report, US Department of Agriculture, Riverside, CA, USA*, 1991.

[109] P. A. Forsyth, Y. S. Wu, and K. Pruess. Robust numerical methods for saturated-unsaturated flow with dry initial conditions in heterogeneous media. *Advances in Water Resource*, 18:25–38, 1995.

[110] M.L. Wheeler W.V. Abeele and B.W. Burton. Geohydrology of bandelier tuff. *Los Alamos National Laboratory report, LA-8962-MS*, 1981.

[111] P. Grathwohl D. Kuntz. Comparison of steady-state and transient flow conditions on reactive transport of contaminants in the vadose soil zone. *Journal of Hydrology*, 369:233–255, 2009.

[112] E.O. Frind K.U. Mayer and D.W. Blowes. Multicomponent reactive transport modeling in variably saturated porous media using a generalized formulation for kinetically controlled reactions. *Water Resources Research*, 38:1174, 2002.

[113] T. Vogel C. Ray and J. Dusek. Modeling depth-variant and domain-specific sorption and biodegradation in dual-permeability media. *Journal of Contaminant Hydrology*, 70, 2004.

[114] R E Horton. An approach toward physical interpretation of infiltration capacity. *Soil Science Society of America*, 5:399–417, 1940.

[115] S Ferrari and F Saleri. A new two-dimensional shallow water model including pressure effects and slow varying bottom topography. *Math. Modell. Numer. Anal.*, 38(2):211–234, 2004.

[116] R S Govindaraju, S E Jones, and M L Kavvas. On the diffusion wave model for overland flow 1. Solution for steep slopes. *Water Resour. Res.*, 24(5):734–744, 1998.

[117] E Miglio. *Mathematical and Numerical Modeling for Environmental Applications*. PhD thesis, Modeling and Scientific Computation Laboratory, Polytecnic University of Milan, 2000.

[118] W H Green and G A Ampt. Studies on soil physics: 1. Flow of air and water through soils. *J. Agric. Sci.*, 4:1–24, 1911.

[119] P Di Giammarco, P E Todini, and P Lamberti. A conservative finite elements approach to overland flow: The control volume finite element formulation. *Journal of Hydrology*, 175:267–291, 1996.

[120] R E Smith and D A Woolhiser. Overland flow on an infiltrating surface. *Water Resources Research*, 7(4):899–913, 1971.

[121] H D Voigt and M Lauterbach. Druckaufbaumessungen an Gas-Sonden. Technical report, Zentrales Geologisches Institut, Berlin, 1985. Haefner et al. Geohydrodynamische Erkundung von Erdoel-, Ergas- und Grundwasserlagerstaetten.

[122] M Muskat. *The flow of homogenous fluids through porous media*. J.W. Edwards Inc., Ann Arbor, Michigan, 1nd edition, 1937.

[123] I.S. Leibenzon. *The flow of natural fluids in porous media (in Russian)*. Gostekizdat, 1947.

[124] V.I. Aravin and S. N. Numerov. *Theory of fluid flow in undeformable porous media*. Israel Program for Scientific Translations, 1965.

[125] C I McDermott, A L Randriamanjatosoa, H Tenzer, and O Kolditz. Simulation of heat extraction from crystalline rocks: The influence of coupled processes on differential reservoir cooling. *Geothermics*, 35(3):321–344, 2006.

[126] R C Reid, J M Prausnitz, and B E Poling. *The properties of liquids and gases*. McGraw-Hill, 1988.

[127] A I Zografos, W A Martin, and J E Sunderland. Equations of properties as a function of temperature for seven fluids. *Computer Methods in Applied Mechanics and Engineering*, 61:177–187, 1987.

[128] N B Vargaftik, J K Vinogradov, and V S Jargin. *Handbook of physical properties of liquids and gases: Pures substances and mixtures*. Begell House, Redding, 1996.

[129] W. Wang and O. Kolditz. Object-oriented finite element analysis of thermo-hydro-mechanical (thm) problems in porous media. *Int. J. Numerical Methods in Engineering*, 69(1):162–201, 2007.

[130] Singh AK, Göerke U-J and Kolditz O. Numerical simulation of non-isothermal compositional gas flow: Application to carbon dioxide injection into gas reservoirs. *Energy*, 36(5):3446 –3458, 2011.

[131] K.-H. Lux. *Gebirgsmechanischer Entwurf und Felderfahrungen im Salzkavernenbau: Ein Beitrag zur Entwicklung von Prognosemodellen für den Hohlraumbau im duktilen Salzgebirge*. Ferdinand Enke Verlag, Stuttgart, 1984.

[132] J. Schröder. Theoretische und algorithmische Konzepte zur phänomenologischen Beschreibung anisotropen Materialverhaltens. Dissertation, Universität Hannover, 1996.

[133] M. Kohlmeier. Coupling of thermal, hydraulic and mechanical processes for geotechnical simulations of partially saturated porous media. Dissertation, Universität Hannover, 2006.

[134] M. Fiolka. Theorie und Numerik volumetrischer Schalenelemente zur Delaminationsanalyse von Faserverbundlaminaten. Dissertation, Berichte des Instituts für Mechanik 2008/2, 2008.

[135] E. Ramm, E. Rank, R. Rannacher, K. Schweizerhol, E. Stein, W. Wendland, G. Wittum, P. Wriggers, and W. Wunderlich. *Error-controlled Adaptive Finite Elements in Solid Mechanics*. Wiley, England, 2003.

[136] I.S. Sandler and J.P. Wright. Strain softening. In S. Nemat, R. Asaro, and G. Hegemier, editors, *Theoretical foundations for Large Scale Computations of Nonlinear Behavior*, pages 285–315. Matinus Nijhiff, Netherlands, 1984.

[137] R. I. Borja. A finite element model for strain localization analysis of strongly discontinuous fields based on standard Galerkin approximation. *Computer Methods in Applied Mechanics and Engineering*, 190:1529–1549, 2000.

[138] D. Sheng, S. W. Sloan, and H. S. Yu. Aspects of finite element implementation of critical state models. *Computational Mechanis*, 26:185–196, 2000.

[139] Z. Hou. Untersuchungen zum Nachweis der Standsicherheit für Untertagedeponien im Salzgebirge. Dissertation, Technische Universität Clausthal, 1997.

[140] Z. Hou. Geomechanische Planungskonzepte für untertägige Tragwerke mit besonderer Berücksichtigung von Gefügeschädigung, Verheilung und hydromechanischer Kopplung. Habilitation, Technische Universität Clausthal, 2002.

[141] Z. Hou and K.-H. Lux. Ein neues Stoffmodell für duktile Salzgesteine mit Einbeziehung von Gefügeschädigung und tertiärem Kriechen auf der Grundlage der Continuum-Damage-Mechanik. *Geotechnik*, 21(3):259–263, 1998.

[142] U. Hunsche and O. Schulze. Das kriechverhalten von steinsalz. *Kali und Steinsalz*, 11:238–255, 1994.

[143] U. Gabbert, A. Honecker, H. Köppe, and H. Nipp. Numerical analysis of large geomechanical systems in civil engineering by the dynamic relaxation technique. In P.J. Pahl and H. Werner, editors, *Computing in Civil and Building Engineering*, pages 1275–1281. A.A. Balkema Publishers, Rotterdam, 1995.

[144] A. Habbar. Direkte und inverse Modellierung reaktiver Transportprozesse in klüftig-porösen medien. Dissertation, Bericht Nr. 65, Institut für Strömungsmechanik und Elektronisches Rechnen im Bauwesen, 2001.

[145] G. Kosakowski and P. Smith. Modelling the transport of solutes ans colloids in the grimsel migration shear zone. Technical Report 05-03, Paul Scherrer Institut, Villigen, Switzerland, 2005.

[146] J. Bear. *Hydraulics of groundwater*. McGraw-Hill, New York, 1979.

[147] K. Ito. On stochastical differential equations. *American Mathematical Society*, 4:289–302, 1951.

[148] W. Kinzelbach. *Groundwater Modelling*. Elsevier, Amsterdam, 1986.

[149] A F B Tompson and L W Gelhar. Numerical simulation of solute transport in three-dimensional randomly heterogeneous porous media. *Water Resources Research*, 26(10):2451–2562, 1990.

[150] E. M. LaBolle, G. E. Fogg, and A. F. B. Tompson. Random-walk simulation of transport in heterogeneous porous media: Local mass-conservation problem and implementation methods. *Water Resources Research*, 32(3):583–593, 1996.

[151] W. Kinzelbach. The random-walk method in pollutant transport simulation. *NATO ASI Ser*, Ser.(C224):227–246, 1988.

[152] H. Hoteit, R. Mose, A. Younes, F. Lehmann, and Ph. Ackerer. Three-dimensional modeling of mass transfer in porous media using the mixed hybrid finite elements and the random-walk methods. *Mathe. Geology*, 34(4):435–456, 2002.

[153] T. Harter and S. Wagner. Colloid transport and filtration of *Cryptosporidium parvum* in sandy soils and aquifer sediments. *Environ. Sci. Technol.*, 34:62–70, 2000.

[154] W. P. Johnson, K. A. Blue, and B. E. Logan. Modeling bacterial detachment during transport through porous media as a residence-time-dependent process. *Water Resour. Res.*, 31:2649–2658, 1995.

[155] A E Hassan and M M Mohamed. On using particle tracking methods to simulate transport in single-continuum and dual continua porous media. *Journal of Hydrology*, 275(3-4):242–260, 2003.

[156] A.R. Piggott and D. Elsworth. Laboratory assessment of the equivalent apertures of a rock fracture. *Geophysical Research Letters*, 20(13):1387–1390, 1993.

[157] R. R. Goswami and T. P. Clement. Laboratory-scale investigation of saltwater intrusion dynamics. *Water Resour. Res.*, 43, 2007.

[158] H. R. Henry. *Salt intrusion into coastal aquifers*. PhD thesis, Columbia University, New York, USA, 1960.

[159] S. Sugio and C. S. Desai. Residual flow procedure for sea water intrusion in unconfined aquifers. *Int J Num Meth Engng*, 24(8):1439–1450, 1987.

[160] R. R. Goswami, B. Ambale, and T. P. Clement. Estimating errors in concentration measurements obtained from image analysis. *Vadose Zone Journal*, 8(1):108–118, 2009.

[161] R. A. Schincariol, F. W. Schwartz, and C. A. Mendoza. On the generation of instabilities in variable density flow. *Water Resources Research*, 30(4):913–927, 1994.

[162] Jude L. Musuuza, Sabine Attinger, and Florin A. Radu. An extended stability criterion for density-driven flows in homogeneous porous media. *Advances in Water Resources*, 32:796–808, 2009. doi:10.1016/j.advwatres.2009.01.012.

[163] R. A. Schincariol, F. W. Schwartz, and C. A. Mendoza. Instabilities in variable density flows: Stability and sensitivity analyses for homogeneous and heterogeneous media. *Water Resources Research*, 33(1):31–41, 1997.

[164] L. Sanavia, F. Pesavento, and B. A. Schrefler. Finite element analysis of non-isothermal multiphase geomaterials with application to strain localization simulation. *Trans. Amer. Math. Soc.*, 37(4):331–348, 2006.

[165] A. Liakopoulos. Retention and distribution of moisture in soils after infiltration has ceased. *Bull. Intern. Assoc. Scientific Hydrology*, 10:58–69, 1965.

[166] S. E. Buckley and M. C. Leverett. Mechanism of fluid displacements in sands. *Transactions American Institute of Mining and Metallurgical Engineers (TAIME)*, 146:107–116, 1941.

[167] D.B. McWhorter and D.K. Sunada. Exact integral solutions for two-phase flow. *Water Resources Research*, 26(3):399–413, 1990.

[168] B.H. Kueper and E.O. Frind. Two-phase flow in heterogeneous porous media: 1. model development. *Water Resources Research*, 27(6):1049–1057, 1991.

[169] Rainer Helmig and Ralf Huber. Comparison of Galerkin-type discretization techniques for two-phase flow in heterogeneous porous media. *Adv. Water Res.*, 21:697–711, 1998.

[170] N. Khalili and P. S. Selvadurai. A fully coupled constitutive model for thermo-hydro-mechanical analysis in elastic media with double porosity. *Geophysical Research Letters*, 30(24):5, 2003.

[171] J. Rutqvist, L. Börgesson, M. Chijimatsu, A. Kobayashi, L. Jing, T. S. Nguyen, J. Noorishad, and C.-F. Tsang. Thermohydromechanics of partially saturated geologic media: governing equations and formulation of four finite element models. *International Journal of Rock Mechanics & Mining Sciences*, 38:105–127, 2001.

[172] H. F. Wang. *Theory of Linear Poroelasticity*. Princeton University Press, Princeton, 2000.

[173] E. Detournay and H.-D. Cheng. Fundamentals of poroelasticity. In J. A. Hudson, editor, *Comprehensive rock engineering*, pages 113–171. Pergamon, New York, 1993.

[174] J. Birkholzer, J. Rutqvist, E. Sonnenthal, and D. Barr. Decovalex-thmc project, task d: Long-term permeability/porosity changes in the edz and near field due to thm and thc processes in volcanic and crystalline-bentonite systems. Technical Report 2008:45, SKI, Stockholm, 2008.

[175] J. Rutqvist. Coupling thermal-hydrological-mechanical analysis within the framework of (decovalex-thmc), task d_thm, step 1: Model inception. Technical report, Earth Sciences Division, Lawrence Berkeley National Laboratory, USA, 2005.

[176] H. S. Carslaw and J. C. Jaeger. *Conduction of heat in solids*. Oxford University Press, Oxford, 2nd edition, 1959.

[177] A. M. Wijesinghe. An exact similarity solution for coupled deformation and fluid flow in discrete fractures. Technical Report UCID–20675, Lawrence Livermore National Laboratory, Livermore, CA, February 1986.

[178] J. Noorishad, C.F. Tsang, and P.A. Witherspoon. Theoretical and field studies of coupled hydromechanical behaviour of fractured rocks–1. development and verification of a numerical simulator. *International Journal of Rock Mechanics and Mining Sciences & Geomechanics Abstracts*, 29(4):401–409, July 1992.

[179] D. Swenson, R. DuTeau, and T. Sprecker. Modeling flow in a jointed geothermal reservoir. In *World Geothermal Congress 1995, Florence, Italy*, 1995.

[180] K.M. Bower and G. Zyvoloski. A numerical model for thermo-hydro-mechanical coupling in fractured rock. *International Journal of Rock Mechanics and Mining Sciences*, 34(8):1201–1211, 1997.

[181] W. Hummel, U. Berner, E. Curti, F.J. Pearson, and T. Troenen. *The Nagra/PSI Chemical Thermodynamic Data Base 01/01*. Universal Publishers, 2002.

[182] D.L. Parkhurst and C. A. J. Appelo. User's guide to phreeqc (version 2) - a computer program for speciation, batch-reaction, one-dimensional transport, and inverse geochemical calculations, 1999.

[183] T. P. Clement Sun Y., J. N. Petersen and R. S. Skeen. Development of analytical solutions for multispecies transport with serial and parallel reactions. *Water Resources Research*, 35(1):185–190, 1999.

[184] Ralf Köber Dirk Schäfer and Andreas Dahmke. Competing tce- and cis-dce-degradation kinetics by zero-valent iron - experimental results and numerical simulation. *Journal of Contaminant Hydrology*, 65:183–202, 2003.

[185] B.V. Van Breukelen, D. Hunkeler, and F. Volkering. Quantification of sequential chlorinated ethene degradation by use of a reactive transport model incorporating isotope fractionation. *Environ. Sci. Technol.*, 39(11):4189–4197, 2005.

[186] D.R. Aguilera, P. Jourabchi, C. Spiteri, and P. Regnier. A knowledge-based reactive transport approach for the simulation of biogeochemical dynamics in earth systems. *Geochemistry, Geophysics, Geosystems*, 6:Q07012, 2005.

[187] P. Regnier, J.P. O'Kane, C.I. Steefel, and J.P. Vanderborght. Modeling complex multi-component reactive-transport systems: towards a simulation environment based on the concept of a knowledge base. *Applied Mathematical Modelling*, 26:913–927, 2002.

[188] Urs von Gunten and Jürg Zobrist. Biogeochemical changes in groundwater-infiltration systems: Column studies. *Geochimica et Cosmochimica Acta*, 57:3895–3906, 1993.

[189] Dirk Schäfer, Wolfgang Schäfer, and Wolfgang Kinzelbach. Simulation of reactive processes related to biodegradation in aquifers. 2. model application to a column study on organic carbon degradation. *Journal of Contaminant Hydrology*, 31:187–209, 1998.

[190] Martin Thullner, Philippe Van Cappellen, and Pierre Regnier. Modeling the impact of microbial activity on redox dynamics in porous media. *Geochimica et Cosmochimica Acta*, 69(21):5005–5019, 2005.

[191] Florian Centler, Haibing Shao, Cecilia de Bias, Chan-Hee Park, Pierre Regnier, Olaf Kolditz, and Martin Thullner. Geosysbrns - a flexible multidimensional reactive transport model for simulating biogeochemical subsurface processes. *submitted to Computers & Geosciences*, 00:0000, 2009.

[192] Olaf A. Cirpka and Albert J. Valocchi. Two-dimensional concentration distribution for mixing-controlled bioreactive transport in steady state. *Adv Water Resour*, 30:1668–1679, 2007.

[193] Olaf A. Cirpka and Albert J. Valocchi. Reply to comments on two-dimensional concentration distribution for mixing-controlled bioreactive transport in steady state by h. shao et al. *Adv Water Resour*, 32:298–301, 2009.

[194] Haibing Shao, Florian Centler, Cecilia de Bias, Martin Thullner, and Olaf Kolditz. Comments on "two-dimensional concentration distribution for mixing-controlled bioreactive transport in steady state" by o. a. cirpka and a. j. valocchi. *Adv Water Resour*, 32:293–297, 2009.

[195] B Cochepin, L Trotignon, O Bildstein, Carl I Steefel, V Lagneau, and J Vanderlee. Approaches to modelling coupled flow and reaction in a 2d cementation experiment. *Advances in Water Resources*, 31(12):1540–1551, 2008.

[196] Karsten Rink, Thomas Fischer, and Olaf Kolditz. Data Visualisation and Validation for Hydrolocical Models. In *Proc of Int Conf on Computer Graphics, Visualization, Computer Vision and Image Processing (CGVCVIP)*, pages 169–176.

[197] Karsten Rink. The OpenGeoSys Data Explorer Manual. Technical report, Department of Environmental Informatics, Helmholtz Centre for Environmental Research - UFZ, Leipzig, Germany, 2011.

[198] B. Zehner. Interactive exploration of tensor fields in geosciences using volume rendering. *Computers & Geosciences*, 32:73–84, 2006.

[199] B. Zehner, N. Watanabe, and O. Kolditz. Visualization of gridded scalar data with uncertainty in geosciences. *Computers & Geosciences*, 36:1268–1275, 2010.

[200] W. Schroeder, K. Martin, and B. Lorensen. *The Visualization Toolkit, An Object-Oriented Approach to 3D Graphics*. Prentice-Hall Inc., 1996.

[201] B. Zehner. Mixing Virtual Reality and 2D Visualization - Using Virtual Environments as Visual 3D Information Systems for Discussion of Data from Geo- and Environmental Sciences. In *Proceedings of the*

*International Conference on Computer Graphics Theory and Applications (GRAPP2010)*, pages 364–369, 2010. Available from: http://www.ufz.de/index.php?en=19329.

[202] D. Reiners, G. Voss, and J. Behr. Opensg: Basic concepts. In *OpenSG Symposium 2002*, 2002.

[203] B. Zehner. Constructing Models for Finite Element Simulation Using Gocad. In *Proceedings of the 31st Gocad Meeting, June 2011, Nancy*, 2011. CD-ROM.

[204] B. Zehner. Constructing Geometric Models of the Subsurface for Finite Element Simulation. In *Proceedings of the Annual Conference of the International Association for Mathematical Geosciences (IAMG2011), Salzburg, Austria, 5th to 9th September 2011*, 2011. Published on the web, www.iamg2011.at.